

Delving into Group 16 – Increasing the Accessibility and Understanding the  
Optoelectronic Properties of Tellurophenes

By

Christina A. Braun

A thesis submitted in partial fulfillment of the requirements for the degree of  
Doctor of Philosophy

Department of Chemistry

University of Alberta

© Christina A. Braun, 2020

## Abstract

This Thesis describes the investigation of 5-membered heterocycles that contain the heavy atom tellurium (Te), termed tellurophenes, as light emitting materials or the active (light absorbing) component in organic photovoltaics. A particular focus was placed on developing new routes to synthesize tellurophenes as well as studying their room-temperature phosphorescence (RTP).

To begin, the emission of borylated tellurophenes was explored by revisiting the emission of a previously reported bis(pinacolatoboryl)tellurophene. This work concluded that the boron centres in this borylated tellurophene are largely involved in the photophysical process of RTP and found that the Lewis acidity of the boron centres could be used to tune the emission *via* coordination chemistry.

Next, a new tellurophene precursor featuring di(isopropoxy)boryl  $-B(O^iPr)_2$  groups was developed. This  $-B(O^iPr)_2$  substituted tellurophene precursor underwent exchange reactions with alcohols and amines, including catechol, 4-*tert*-butylcatechol, and 1,8-diaminonaphthalene, to replace the  $O^iPr$  groups on the boron centres with either oxygen- or nitrogen-based chelates. This method was used to synthesize three new borylated tellurophenes, which were all emissive when cooled to 77 K. Furthermore, the  $-B(O^iPr)_2$  substituted tellurophene precursor could be reacted with  $MesMgBr$  ( $Mes = 2,4,6-Me_3C_6H_2$ ) to displace one  $O^iPr$  group on each boron centre, yielding a new tellurophene (**Mes(<sup>i</sup>PrO)B-Te-6-B(O<sup>i</sup>Pr)Mes**) that exhibited bright yellow RTP in the solid state.

In addition to their emissive properties, borylated tellurophenes are also desirable precursors for Suzuki-Miyaura cross-coupling, leading to the formation of  $\pi$ -conjugated materials. However, tellurophenes often undergo facile protodeboronation under the basic conditions of these reactions, greatly reducing product yields. Therefore, the conditions for this reaction were optimized for tellurophenes, and the Suzuki-Miyaura cross-coupling of borylated tellurophenes with arylhalides under mild conditions with high isolated yields was reported. This synthetic route was then used to synthesize several 2,5-bis(aryl)tellurophenes, many of which exhibit RTP when incorporated into a rigid poly(methylmethacrylate) (PMMA) matrix.

Finally, a new class of  $\pi$ -extended tellurophenes featuring a fused benzobithiophene core, termed tellura(benzo)bithiophenes (**Te-bbts**), were developed. One such **Te-bbt** with cumenyl (4-isopropylphenyl) side groups exhibited orange coloured phosphorescence in a rigid PMMA environment with an emission maximum ( $\lambda_{em}$ ) centred at 680 nm. A dibrominated **Te-bbt** monomer was also synthesized and later polymerized to give a novel Te-containing homopolymer with a broad absorption profile that extends beyond 600 nm. The results described in this Thesis demonstrate that tellurophenes are an attractive class of heterocycle with many useful properties, making them worthwhile targets for future research explorations.

## Preface

Portions of the work discussed in this Thesis were completed in collaboration with other researchers within the Rivard group, with others in the Department of Chemistry, as well as with researchers outside of the University of Alberta.

All X-ray crystallographic studies described in this Thesis were performed by Dr. R. McDonald, Dr. M. J. Ferguson, or Dr. Y. Zhou, including the mounting of crystals, operation of the diffractometer, data collection, structure refinement, and the preparation of crystallographic data tables. Elemental analyses were performed at the Analytical Instrument Laboratory at the Department of Chemistry, University of Alberta. Mass spectrometric analyses were performed at the Mass Spectrometry Laboratory at the Department of Chemistry, University of Alberta.

The computational studies in this Thesis were made possible by the facilities of the Shared Hierarchical Academic Computing Network (SHARCNET: [www.sharcnet.ca](http://www.sharcnet.ca)), WestGrid ([www.westgrid.ca](http://www.westgrid.ca)), and Compute/Calcul Canada ([www.computecanada.ca](http://www.computecanada.ca)). The work in this Thesis was supported by the Natural Sciences and Engineering Research Council of Canada, the Canada Foundation for Innovation, Alberta Innovates, and the Faculty of Science at the University of Alberta.

In Chapter 2, computations were performed by Inara de Aguiar, Gabriel L. C. de Souza (Universidade Federal de Mato Grosso, Brazil) and Prof. A. Brown (University of Alberta). Photoluminescence measurements (including lifetime and quantum yield) were performed by Prof. G. He (Xi'an Jiaotong University) and his student Y. Qi under the support of the Natural Science Foundation of China. The

attempted synthesis of zirconacycles from the boryl-capped diynes **1**, **2**, and **3** were conducted by W. Torres Delgado (a previous Ph.D. student in the Rivard group) and D. Zomerman (a previous undergraduate student in the Rivard group).

In Chapters 3–5, photoluminescence measurements (including lifetime and quantum yields) were performed in the Analytical Laboratory at the University of Alberta, under the training and guidance of W. Moffat and J. Jones. Computational studies were performed with the help of valuable insight and troubleshooting from Dr. E. Hupf (University of Alberta/ Universität Bremen), who is sincerely thanked for his input.

In Chapters 3 and 4, N. Martinek (a previous undergraduate student in the Rivard group) is gratefully acknowledged for her synthetic assistance.

In Chapter 4, Avik Bhattacharjee (Portland State University) assisted with the synthesis and computational studies regarding the pyridyl and methylpyridinium compounds, **pyr-Te-6-pyr** and **[Mepyr-Te-6-pyrMe][I]<sub>2</sub>**.

In Chapter 5, Dr. M. P. Boone (a postdoctoral fellow in the Rivard group) is sincerely thanked for his preliminary work on the project, including his input regarding the project goal and the synthetic route to access the tellura(benzo)bithiophenes. TGA measurements were conducted by W. Moffat and J. Jones in the Analytical Laboratory at the University of Alberta.

According to the policy within our research group, each chapter of this Thesis is essentially self-contained, and prepared in the form of a paper that is intended for

publication in peer-reviewed journals. A portion of this Thesis has been published previously elsewhere, and these publications are listed below.

Chapter 2: C. A. Braun, D. Zommerman, I. de Aguiar, Y. Qi, W. Torres Delgado, M. J. Ferguson, R. McDonald, G. L. C. de Souza, G. He, A. Brown and E. Rivard, *Faraday Discuss.*, **2017**, *196*, 255–268.

Chapter 3: C. A. Braun, N. Martinek, Y. Zhou, M. J. Ferguson and E. Rivard, *Dalton Trans.*, **2019**, *48*, 10210–10219.

In addition to the work described in this Thesis, contributions were also made to the following papers, published in peer-reviewed journals:

W. Torres Delgado, C. A. Braun, M. P. Boone, O. Shynkaruk, Y. Qi, R. McDonald, M. J. Ferguson, P. Data, S. K. C. Almeida, I. de Aguiar, G. L. C. de Souza, A. Brown, G. He and E. Rivard, *ACS Appl. Mater. Interfaces*, **2018**, *10*, 12124–12134.

K. Takahashi, S. Shimo, E. Hupf, J. Ochiai, C. A. Braun, W. Torres Delgado, L. Xu, G. He, E. Rivard and N. Iwasawa, *Chem. Eur. J.*, **2019**, *25*, 8479–8483.

*The only true wisdom is in knowing you know nothing – Socrates*

*Even a blind squirrel finds an acorn sometimes – Susan Mallery*

## Acknowledgements

First and foremost, I would like to thank my family. My mother Anna, and my father Dave, have never stopped believing in me for a moment and their unconditional support means the world to me. I would also like to thank my sister Linda for being my best friend and making me the proudest aunt to the most wonderful nephews, Gavin and Caleb. Lastly, I would like to thank my brother Jamie. I love you all so very much!

I owe a tremendous thank you to my boyfriend Alvaro Omaña. I can't imagine finishing this degree without your support and encouragement. Thank you for being my rock, making me feel loved, and trying your best to make my life less stressful. Also, thank you for the supply of **B-Te-6-B** that you gave me many years ago!

To my supervisor, Dr. Eric Rivard, thank you for the guidance you've given me throughout my PhD. Thank you for everything you have done for me, especially for the time you've spent elevating my work to a level that I am very proud of. I would also like to thank my supervisory committee members, Dr. Arthur Mar and Dr. Juli Gibbs, for their support and valuable input regarding my projects. Finally, thank you to the rest of my Ph.D. examining committee, Dr. Mariusz Klobukowski and Dr. Derek Gates, as well as the non-examining chair, Dr. Joe Takats.

To all of the Rivard Group members (both past and present), thank you for being my second family. I owe a special shout out to several previous Rivardians: Dr. Melanie Lui, Dr. Anindya Swarnakar, Dr. Alyona Shynkaruk, Dr. Emanuel Hupf, and Dr. Sarah Parke. To all of you, your continued friendship and support even after you left Edmonton is very valuable to me; thank you for being such a positive presence in my



life. To all of the current Rivardians: Bruno Luppi (my older brother/bestie), Ian Watson (the Bungler), Jocelyn Sinclair (Lab Mom), Alvaro Omaña, Sam Baird (Lab Daddy), Brandon Frenette (Rando without BN), and William Medroa (Billiam) thank you for being the most amazing coworkers. It has been such a pleasure working with all of you! I would also like to acknowledge the wonderful undergraduates who have graced the Rivard group with their presence, especially Linkun Miao, Gunwant Matharu, and Nicole Martinek!

I feel privileged to have worked in a department with so many kind and incredibly helpful people. Thank you to all of the technical and support staff in the Department of Chemistry, especially: Dr. Mike Ferguson, Wayne Mofatt, Jennifer Jones, Mark Miskolzie, the machine shop guys (especially Dirk), Dr. Randy Whittal, Jing Zheng, Ryan Lewis, and Jason Dibbs.

I am also very grateful for the many friends I have made here at the University of Alberta including (but not limited to): Dr. Patrick (Party Pat) Moon, Hansol Park, Aaron Kirkey, Jasper Woodard, Ellen Buckie, Jasmine Bhangu, Alyssa Fu, and Max Sirtl. Whether we grabbed drinks or I convinced you to play sports with me, your friendship means a lot to me! I'd also like to thank the people with whom I played drop-in volleyball with on Sunday nights (especially the group of Persian students who were so welcoming and fun to play with)!

Finally, I would like to acknowledge NSERC, Alberta Innovates, and the Department of Chemistry at the University of Alberta for their financial support.

# Table of Contents

|   |           |
|---|-----------|
| <b>Chapter 1 – Introduction</b>   | <b>1</b>  |
| 1.1 Potential Advantages of Incorporating Heavy Main Group Atoms into $\pi$ -Conjugated Systems   | 1         |
| 1.1.1 Unlocking phosphorescence within heavy atom-containing heterocycles                         | 2         |
| 1.1.2 Using triplet excitons to increase the efficiencies of organic photovoltaics                | 9         |
| 1.1.3 Heavy element-containing heterocycles for organic field effect transistors                  | 14        |
| 1.2 Tellurophenes   | 16        |
| 1.2.1 Reactivity of tellurophenes: highlighting the differences from thiophenes and selenophenes  | 17        |
| 1.2.2 Synthesis of tellurophenes  | 23        |
| 1.2.3 Synthesis of $\pi$ -extended tellurophenes  | 28        |
| 1.2.4 Coaxing room temperature phosphorescence from tellurophenes                                 | 30        |
| 1.2.5 Tellurophene-based organic photovoltaics  | 34        |
| 1.2.6 OFETs devices with tellurophenes  | 45        |
| 1.2.7 Future Outlook  | 47        |
| 1.3 References  | 49        |
| <b>Chapter 2 – Probing the Nature of Peripheral Boryl Groups within Luminescent Tellurophenes</b> | <b>60</b> |

|   |           |
|---|-----------|
| 2.1 Introduction  | 60        |
| 2.2 Results and Discussion  | 63        |
| 2.2.1 Attempted synthesis of new luminescent tellurophenes  | 63        |
| 2.2.2 Synthesis of <b>B-Te-6-B</b> adducts  | 66        |
| 2.2.3 Structural characterization of <b>B-Te-6-B</b> adducts  | 68        |
| 2.2.4 Photoluminescence of <b>ImMe<sub>2</sub><sup>i</sup>Pr<sub>2</sub>•B-Te-6-B</b>   | 71        |
| 2.2.5 Computational study on <b>B-Te-6-B</b>  | 72        |
| 2.2.6 TD-DFT study of the <b>B-Te-6-B</b> adducts   | 79        |
| 2.3 Conclusions   | 82        |
| 2.4 Experimental  | 82        |
| 2.4.1 General considerations  | 82        |
| 2.4.2 Synthetic procedures  | 83        |
| 2.4.3 X-ray crystallography   | 86        |
| 2.5 References and Notes  | 88        |
| <br>  |           |
| <b>Chapter 3 – Using Boryl-Substitution and Improved Suzuki-Miyaura Cross-Coupling to Access New Phosphorescent Tellurophenes</b> | <b>93</b> |
| 3.1 Introduction  | 93        |
| 3.2 Results and Discussion  | 95        |
| 3.2.1 Condensation reactions of <b>(<sup>i</sup>PrO)<sub>2</sub>B-Te-6-B(O<sup>i</sup>Pr)<sub>2</sub></b>                         | 95        |
| 3.2.2 Structural characterization of borylated tellurophenes  | 100       |
| 3.2.3 Photoluminescence characterization of borylated tellurophenes   | 103       |

|  |            |
|--|------------|
| 3.2.4 Computational studies  | 109        |
| 3.2.5 Suzuki-Miyaura cross-coupling involving borylated tellurophenes  | 112        |
| 3.3 Conclusions  | 116        |
| 3.4 Experimental   | 117        |
| 3.4.1 General procedures   | 117        |
| 3.4.2 Synthetic procedures   | 118        |
| 3.4.3 Photoluminescence measurements   | 125        |
| 3.4.4 X-ray crystallography  | 127        |
| 3.4.5 Selected NMR spectra   | 129        |
| 3.4.6 Computational methodology  | 139        |
| 3.5 References   | 141        |
| <b>Chapter 4 – New Tellurophenes Derived from the Suzuki-Miyaura Cross-Coupling of a Bis(boryl)tellurophene</b>                  | <b>149</b> |
| 4.1 Introduction   | 149        |
| 4.2 Results and Discussion   | 153        |
| 4.2.1 Synthesis of 2,5-bis(aryl)tellurophenes  | 153        |
| 4.2.2 Solid state structures of the 2,5-bis(aryl)tellurophenes derived from the Suzuki-Miyaura cross-coupling protocol           | 156        |
| 4.2.3 Optical absorption properties of the 2,5-bis(aryl)tellurophenes  | 163        |
| 4.2.4 Photoluminescence of <b>Mes<sub>2</sub>B(C<sub>6</sub>H<sub>4</sub>)-Te-6-(C<sub>6</sub>H<sub>4</sub>)BMes<sub>2</sub></b> | 165        |
| 4.2.5 Photoluminescence of <b>O<sub>2</sub>N(C<sub>6</sub>H<sub>4</sub>)-Te-6-(C<sub>6</sub>H<sub>4</sub>)NO<sub>2</sub></b>     | 170        |

|   |            |
|---|------------|
| 4.2.6 Photoluminescence of <b>pyr-Te-6-pyr</b>  | 173        |
| 4.2.7 Photoluminescence of <b>Mes-Te-6-Mes</b>  | 176        |
| 4.2.8 Photoluminescence of <b>[Mepyr-Te-6-pyrMe][I]<sub>2</sub></b>                                 | 180        |
| 4.2.9 Photoluminescence of <b>dpe-Te-6-dpe</b>  | 182        |
| 4.2.10 Comparing the HOMO/LUMO levels of 2,5-bis(aryl)tellurophenes                                 | 186        |
| 4.3 Conclusion  | 187        |
| 4.4 Experimental  | 188        |
| 4.4.1 General procedures  | 188        |
| 4.4.2 Synthetic procedures  | 190        |
| 4.4.3 X-ray crystallography   | 195        |
| 4.4.4 Photoluminescence data  | 198        |
| 4.4.5 Computational methodology   | 199        |
| 4.5 References  | 200        |
| <b>Chapter 5 – Tellura(benzo)bithiophene: A New Class of <math>\pi</math>-Extended Tellurophene</b> | <b>207</b> |
| 5.1 Introduction  | 207        |
| 5.2 Results and Discussion  | 213        |
| 5.2.1 Synthesis of tellura(benzo)bithiophenes   | 213        |
| 5.2.2 Optical absorption properties of <b>Te-bbt-cumenyl</b>  | 215        |
| 5.2.3 Investigating the oxidative decomposition of <b>Te-bbt-cumenyl</b>                            | 217        |
| 5.2.4 Synthesis of <b>Te-bbt-cumenyl</b> derivatives  | 222        |

|   |            |
|---|------------|
| 5.2.5 Solid state structures of the tellura(benzo)bithiophenes  | 225        |
| 5.2.6 Attempted intramolecular annulation of <b>Te-bbt-cumenyl</b>  | 230        |
| 5.2.7 A computational study on <b>Te-bbt(Me<sub>2</sub>)-cumenyl</b> and its annulated derivative <b>Te-bbt(Me<sub>2</sub>)-f-cumenyl</b> | 235        |
| 5.2.8 Polymerization of <b>Te-bbt(Br<sub>2</sub>)-cumenyl</b>   | 236        |
| 5.2.9 Photoluminescence studies of <b>Te-bbt-cumenyl</b>  | 241        |
| 5.3 Conclusion  | 248        |
| 5.4 Experimental  | 248        |
| 5.4.1 General procedures  | 248        |
| 5.4.2 Synthetic procedures  | 250        |
| 5.4.3 GPC results   | 260        |
| 5.4.4 Photoluminescent lifetimes  | 260        |
| 5.4.5 X-ray crystallography   | 260        |
| 5.4.6 Computational methodology   | 263        |
| 5.5 References  | 264        |
| <b>Chapter 6 –Summary and Future Directions</b>   | <b>271</b> |
| 6.1 Tuning the Emission and Enhancing the Quantum Yield of Phosphorescence from Borylated Tellurophenes                                   | 271        |
| 6.2 Optimizing OPV Devices with Tellurophenes   | 276        |
| 6.3 Future Outlook  | 280        |

|                              |            |
|------------------------------|------------|
| 6.4 References               | 281        |
| <b>Complete Bibliography</b> | <b>283</b> |

## List of Figures

- Figure 1.1** – A simplified Jablonski diagram showing some possible photophysical processes that can occur after the absorption of a photon by a molecule. .... 4
- Figure 1.2** – Heterofluorenes featuring Group 13 elements and their corresponding emission measured in frozen 2-MeTHF. .... 9
- Figure 1.3** – Simplified representations of: a) the architecture of a bulk heterojunction OPV device, and b) the energy level diagram of an OPV device showing exciton (electron/hole pair) dissociation. .... 11
- Figure 1.4** – A depiction of the  $V_{OC}$  as it relates to the HOMO and LUMO levels of the donor and acceptor materials in an OPV device. .... 12
- Figure 1.5** – The donor polymer shown in a) was used to study the influence of the Group 14 element (E) in the dithienyl/heterole subunit on overall OPV device performance, which is summarized in b). .... 14
- Figure 1.6** – Configuration of a bottom-gate, top-contact organic field effect transistor. .... 15
- Figure 1.7** – The structures of chalcogenophenes (**8–10**) with the carbon atoms of the chalcogenophene ring labelled on the left most structure. .... 16
- Figure 1.8** – Photoluminescence data including quantum yield of fluorescence ( $\Phi_F$ ), quantum yield of phosphorescence ( $\Phi_P$ ), and the quantum yield of triplet formation ( $\Phi_T$ ) for benzo- and dibenzochalcogenophenes measured at 77 K in EtOH. .... 32



|  |    |
|--|----|
| <b>Figure 1.9</b> – Selected phosphorescent tellurophenes developed by Rivard and coworkers. ....  | 33 |
| <b>Figure 1.10</b> – Dibenzotellurophenes <b>75–77</b> synthesized by Xu and coworkers exhibiting RTP. ....  | 34 |
| <b>Figure 1.11</b> – Poly(3-alkylchalcogenophene)s incorporated into OPV devices by Seferos and coworkers. ....  | 37 |
| <b>Figure 1.12</b> – Chalcogenophene-containing small molecules studied as donor materials in OPVs. ....   | 38 |
| <b>Figure 1.13</b> – The donor and acceptor polymers used in the all-polymer OPVs studied by Huang and coworkers. ....   | 42 |
| <b>Figure 1.14</b> – Small molecule acceptors <b>99–101</b> containing a tellurophene fused to PDI developed by Huang and coworkers, as well as the donor polymer used to construct OPV devices. ....  | 43 |
| <b>Figure 1.15</b> – Chalcogenophene-containing molecules and polymers that have been incorporated into OFET devices. ....   | 46 |
| <b>Figure 2.1</b> – The structure of the BPin-flanked tellurophene, <b>B-Te-6-B</b> . ....   | 61 |
| <b>Figure 2.2</b> – Selected tellurophenes reported by the Rivard group and their observed photoluminescence under irradiation with a hand-held UV-lamp. ....  | 62 |
| <b>Figure 2.3</b> – Molecular structure of <b>2</b> . ....   | 65 |
| <b>Figure 2.4</b> – Computed vertical excitation energies (in eV) to singlet ( $S_n$ ) and triplet ( $T_n$ ) states from the ground state ( $S_0$ ) at the TD B3LYP/jun-cc-pVTZ-(PP) level of theory in the gas-phase for <b>B-Te-6-B</b> at the B3LYP/cc- |    |

|  |     |
|--|-----|
| pVDZ $S_0$ equilibrium geometry. Also plotted are the HOMO and LUMO<br>for <b>B-Te-6-B</b> . .....   | 67  |
| <b>Figure 2.5</b> – Molecular structure of <b>ImMe<sup>i</sup>Pr<sub>2</sub>•B-Te-6-B•ImMe<sup>i</sup>Pr<sub>2</sub></b> . .....   | 70  |
| <b>Figure 2.6</b> – Molecular structure of <b>ImMe<sup>i</sup>Pr<sub>2</sub>•B-Te-6-B</b> . .....  | 70  |
| <b>Figure 2.7</b> – Excitation and emission spectra for a film of <b>ImMe<sup>i</sup>Pr<sub>2</sub>•B-Te-6-B</b> drop-<br>cast from THF under N <sub>2</sub> . .....   | 72  |
| <b>Figure 2.8</b> – HOMO and LUMO of <b>ImMe<sup>i</sup>Pr<sub>2</sub>•B-Te-6-B</b> for the $S_0$ state at the<br>(B3LYP/cc-pVDZ-(PP)) $S_1$ equilibrium geometry as determined at the<br>B3LYP/ccpVDZ-(PP) level of theory in the gas-phase. ....   | 81  |
| <b>Figure 2.9</b> – HOMO and LUMO of <b>ImMe<sup>i</sup>Pr<sub>2</sub>•B-Te-6-B</b> for the $S_0$ state at the<br>(B3LYP/cc-pVDZ-(PP)) $T_1$ equilibrium geometry as determined at the<br>B3LYP/ccpVDZ-(PP) level of theory in the gas-phase. ....   | 81  |
| <b>Figure 3.1</b> – Tellurophenes developed for photovoltaic and phosphorescence-based<br>applications. ....   | 95  |
| <b>Figure 3.2</b> – Molecular structure of <b>catB-Te-6-Bcat</b> . .....   | 101 |
| <b>Figure 3.3</b> – Molecular structure of <b><sup>t</sup>BucatB-Te-6-Bcat<sup>t</sup>Bu</b> . .....   | 102 |
| <b>Figure 3.4</b> – Molecular structure of <b>danB-Te-6-Bdan</b> . .....   | 102 |
| <b>Figure 3.5</b> – Molecular structure of <b>Mes(<sup>i</sup>PrO)B-Te-6-B(O<sup>i</sup>Pr)Mes</b> . .....   | 103 |
| <b>Figure 3.6</b> – UV-vis absorption spectra recorded for $3 \times 10^{-5}$ M THF solutions. ...   | 104 |
| <b>Figure 3.7</b> – <i>Top</i> : Solutions of a) <b>catB-Te-6-Bcat</b> , b) <b><sup>t</sup>BucatB-Te-6-B<sup>t</sup>Bucat</b> , c) <b>danB-<br/>    Te-6-Bdan</b> and d) <b>Mes(<sup>i</sup>PrO)B-Te-6-B(O<sup>i</sup>Pr)Mes</b> in 2-<br>methyltetrahydrofuran (0.01–0.02 M) at room temperature. <i>Bottom</i> : |     |

Frozen solutions of e) **catB-Te-6-Bcat**, f) **<sup>t</sup>BucatB-Te-6-B<sup>t</sup>Bucat**, g) **danB-Te-6-Bdan** and h) **Mes(<sup>i</sup>PrO)B-Te-6-B(O<sup>i</sup>Pr)Mes** in 2-methyltetrahydrofuran cooled in N<sub>2</sub> (l) and irradiated with a hand-held UV lamp. .... 105

**Figure 3.8** – *Top*: Solid samples of a) **catB-Te-6-Bcat**, b) **<sup>t</sup>BucatB-Te-6-B<sup>t</sup>Bucat**, c) **danB-Te-6-Bdan** and d) **Mes(<sup>i</sup>PrO)B-Te-6-B(O<sup>i</sup>Pr)Mes** at room temperature. *Bottom*: Solid samples of e) **catB-Te-6-Bcat**, f) **<sup>t</sup>BucatB-Te-6-B<sup>t</sup>Bucat**, g) **danB-Te-6-Bdan** and h) **Mes(<sup>i</sup>PrO)B-Te-6-B(O<sup>i</sup>Pr)Mes** cooled in N<sub>2</sub> (l) and irradiated with a hand-held UV lamp. .... 106

**Figure 3.9** – Solid state excitation and emission spectra of an amorphous sample of **<sup>t</sup>BucatB-Te-6-B<sup>t</sup>Bucat**. .... 107

**Figure 3.10** – *Left*: Solid state excitation and emission spectra of an amorphous sample of **Mes(<sup>i</sup>PrO)B-Te-6-B(O<sup>i</sup>Pr)Mes**. *Right*: Image of the solid sample of **Mes(<sup>i</sup>PrO)B-Te-6-B(O<sup>i</sup>Pr)Mes** irradiated with a hand-held UV lamp. .... 107

**Figure 3.11** – The experimental and calculated UV-vis absorption spectra of **Mes(<sup>i</sup>PrO)B-Te-6-B(O<sup>i</sup>Pr)Mes** at the B3LYP/cc-pVDZ(-PP) level of theory. Black bars are shown for the two electronic transitions with the highest oscillator strengths. .... 110

**Figure 3.12** – TD-DFT [B3LYP/cc-pVDZ(-PP)] computed main transitions for **Mes(<sup>i</sup>PrO)B-Te-6-B(O<sup>i</sup>Pr)Mes** including excitation wavelengths and

|                    |  |     |
|--------------------|--|-----|
|                    | oscillator strengths ( <i>f</i> ) for the most intense transitions ( $S_0 \rightarrow S_1$ : black;<br>$S_0 \rightarrow S_4$ : red) along with the associated molecular orbitals. ....   | 111 |
| <b>Figure 3.13</b> | – <i>Left</i> : Singlet and triplet states of <b>Mes(<sup>i</sup>PrO)B-Te-6-B(O<sup>i</sup>Pr)Mes</b><br>calculated at the B3LYP/cc-pVDZ(-PP) level of theory; <i>Right</i> : A close-<br>up of the $S_2$ - $S_4$ and $T_5$ - $T_7$ states. ....   | 111 |
| <b>Figure 3.14</b> | – $^1\text{H}$ NMR spectra ( $\text{CDCl}_3$ ) of the attempted Suzuki-Miyaura cross<br>coupling reactions between borylated tellurophenes and 2 equivalents of<br>2-bromothiophene. a) coupling with <b>B-Te-6-B</b> (16 hrs), b) coupling with<br><b>catB-Te-6-Bcat</b> (40 hrs), c) coupling with <b><sup>t</sup>BucatB-Te-6-B<sup>t</sup>Bucat</b> (40<br>hrs), d) <b>danB-Te-6-Bdan</b> (16 hrs). ....  | 115 |
| <b>Figure 3.15</b> | – $^{13}\text{C}\{^1\text{H}\}$ NMR spectra ( $\text{CDCl}_3$ ) of attempted Suzuki-Miyaura cross<br>coupling reactions between borylated tellurophenes and 2-<br>bromothiophene to produce <b>thienyl-Te-6-thienyl (T-Te-6-T)</b> . a)<br>coupling with <b>B-Te-6-B</b> (16 hrs), b) coupling with <b>catB-Te-6-Bcat</b> (40<br>hrs), c) coupling with <b><sup>t</sup>BucatB-Te-6-B<sup>t</sup>Bucat</b> (40 hrs), d) <b>danB-Te-6-<br/>Bdan</b> (16 hrs). .... | 116 |
| <b>Figure 3.16</b> | – $^1\text{H}$ NMR spectrum of $(^i\text{PrO})_2\text{BC}\equiv\text{C}(\text{CH}_2)_4\text{C}\equiv\text{CB}(\text{O}^i\text{Pr})_2$ in $\text{C}_6\text{D}_6$ . ....   | 129 |
| <b>Figure 3.17</b> | – $^{13}\text{C}\{^1\text{H}\}$ NMR spectrum of $(^i\text{PrO})_2\text{BC}\equiv\text{C}(\text{CH}_2)_4\text{C}\equiv\text{CB}(\text{O}^i\text{Pr})_2$ in $\text{C}_6\text{D}_6$ .<br>.....  | 130 |
| <b>Figure 3.18</b> | – $^{11}\text{B}\{^1\text{H}\}$ NMR spectrum of $(^i\text{PrO})_2\text{BC}\equiv\text{C}(\text{CH}_2)_4\text{C}\equiv\text{CB}(\text{O}^i\text{Pr})_2$ in $\text{C}_6\text{D}_6$ .<br>.....  | 130 |
| <b>Figure 3.19</b> | – $^1\text{H}$ NMR spectrum of $(^i\text{PrO})_2\text{B-Te-6-B}(\text{O}^i\text{Pr})_2$ in $\text{C}_6\text{D}_6$ . ....   | 131 |

|  |     |
|--|-----|
| <b>Figure 3.20</b> – $^{13}\text{C}\{^1\text{H}\}$ NMR spectrum of $(^i\text{PrO})_2\text{B-Te-6-B(O}^i\text{Pr)}_2$ in $\text{C}_6\text{D}_6$ . .....   | 131 |
| <b>Figure 3.21</b> – $^{11}\text{B}\{^1\text{H}\}$ NMR spectrum of $(^i\text{PrO})_2\text{B-Te-6-B(O}^i\text{Pr)}_2$ in $\text{C}_6\text{D}_6$ . .....   | 132 |
| <b>Figure 3.22</b> – $^1\text{H}$ NMR spectrum of <b>catB-Te-6-Bcat</b> in $\text{C}_6\text{D}_6$ . .....  | 132 |
| <b>Figure 3.23</b> – $^{13}\text{C}\{^1\text{H}\}$ NMR spectrum of <b>catB-Te-6-Bcat</b> in $\text{C}_6\text{D}_6$ . .....   | 133 |
| <b>Figure 3.24</b> – $^{11}\text{B}\{^1\text{H}\}$ NMR spectrum of <b>catB-Te-6-Bcat</b> in $\text{C}_6\text{D}_6$ . .....   | 133 |
| <b>Figure 3.25</b> – $^1\text{H}$ NMR spectrum of $^t\text{BucatB-Te-6-B}^t\text{Bucat}$ in $\text{C}_6\text{D}_6$ . .....   | 134 |
| <b>Figure 3.26</b> – $^{13}\text{C}\{^1\text{H}\}$ NMR spectrum of $^t\text{BucatB-Te-6-B}^t\text{Bucat}$ in $\text{C}_6\text{D}_6$ . .....  | 134 |
| <b>Figure 3.27</b> – $^{11}\text{B}\{^1\text{H}\}$ NMR spectrum of $^t\text{BucatB-Te-6-B}^t\text{Bucat}$ in $\text{C}_6\text{D}_6$ . .....  | 135 |
| <b>Figure 3.28</b> – $^1\text{H}$ NMR spectrum of <b>danB-Te-6-Bdan</b> in $\text{C}_6\text{D}_6$ . .....  | 135 |
| <b>Figure 3.29</b> – $^{13}\text{C}\{^1\text{H}\}$ NMR spectrum of <b>danB-Te-6-Bdan</b> in $\text{C}_6\text{D}_6$ . .....   | 136 |
| <b>Figure 3.30</b> – $^{11}\text{B}\{^1\text{H}\}$ NMR spectrum of <b>danB-Te-6-Bdan</b> in $\text{C}_6\text{D}_6$ . .....   | 136 |
| <b>Figure 3.31</b> – $^1\text{H}$ NMR spectrum of <b>Mes(<math>^i\text{PrO}</math>)B-Te-6-B(<math>\text{O}^i\text{Pr}</math>)Mes</b> in $\text{C}_6\text{D}_6$ . .....   | 137 |
| <b>Figure 3.32</b> – $^{13}\text{C}\{^1\text{H}\}$ NMR spectrum of <b>Mes(<math>^i\text{PrO}</math>)B-Te-6-B(<math>\text{O}^i\text{Pr}</math>)Mes</b> in $\text{C}_6\text{D}_6$ .<br>.....   | 137 |
| <b>Figure 3.33</b> – $^{11}\text{B}\{^1\text{H}\}$ NMR spectrum of <b>Mes(<math>^i\text{PrO}</math>)B-Te-6-B(<math>\text{O}^i\text{Pr}</math>)Mes</b> in $\text{C}_6\text{D}_6$ .<br>.....   | 138 |
| <b>Figure 3.34</b> – $^1\text{H}$ NMR spectrum of <b>thienyl-Te-6-thienyl (T-Te-6-T)</b> in $\text{CDCl}_3$<br>produced <i>via</i> the Suzuki-Miyaura cross coupling of <b>B-Te-6-B</b> and 2<br>equivalents of 2-bromothiophene. .... | 138 |
| <b>Figure 4.1</b> – Viologen and examples of extended viologens featuring Group 16<br>heteroles as the aromatic spacer. ....   | 151 |
| <b>Figure 4.2</b> – Chalcogen-bridged viologens developed by He and coworkers. ....  | 152 |

|   |     |
|---|-----|
| <b>Figure 4.3</b> – “Push-pull” tellurophene <b>8</b> with carbon angles used to calculate the torsion angles of interest shown with spheres. ....  | 157 |
| <b>Figure 4.4</b> – Molecular structure of <b>Mes-Te-6-Mes</b> . ....   | 158 |
| <b>Figure 4.5</b> – Molecular structure of <b>O<sub>2</sub>N(C<sub>6</sub>H<sub>4</sub>)-Te-6-(C<sub>6</sub>H<sub>4</sub>)NO<sub>2</sub></b> . ....   | 159 |
| <b>Figure 4.6</b> – Molecular structure of <b>pyr-Te-6-pyr</b> . ....   | 160 |
| <b>Figure 4.7</b> – Molecular structure of <b>[Mepyr-Te-6-pyrMe][I]<sub>2</sub></b> . ....  | 161 |
| <b>Figure 4.8</b> – a) The structure of dibenzotellurophene diiodide <b>9</b> , and b) intramolecular Te···I interactions which drive the solid state packing of <b>9</b> . ....  | 161 |
| <b>Figure 4.9</b> – a) Gas-phase geometry optimizations at the B3LYP/cc-pVDZ(-PP) level of theory for <b>[Mepyr-Te-6-pyrMe]<sup>2+</sup></b> and <b>[Mepyr-Te-pyrMe]<sup>2+</sup></b> showing the difference in energy between structures that are optimized with frozen torsion angles (restricted optimization) and the energy of their respective optimized structures performed with no geometric restrictions (unrestricted optimization); b) structures of <b>[Mepyr-Te-6-pyrMe]<sup>2+</sup></b> and <b>[Mepyr-Te-pyrMe]<sup>2+</sup></b> with the torsion angle of interest shown in grey. .... | 163 |
| <b>Figure 4.10</b> –Experimental UV-vis spectra and computed UV-vis spectra for the 2,5-bis(aryl)tellurophenes discussed in this Chapter at the B3LYP/cc-pVDZ(-PP) level of theory in the gas-phase. ....   | 165 |
| <b>Figure 4.11</b> – a) Excitation and emission spectra of <b>Mes<sub>2</sub>B(C<sub>6</sub>H<sub>4</sub>)-Te-6-(C<sub>6</sub>H<sub>4</sub>)BMes<sub>2</sub></b> ; b) images of films containing 100 % PMMA and 1 wt% of <b>Mes<sub>2</sub>B(C<sub>6</sub>H<sub>4</sub>)-Te-6-(C<sub>6</sub>H<sub>4</sub>)BMes<sub>2</sub></b> in PMMA; c) images of films  |     |

|                    |  |     |
|--------------------|--|-----|
|                    | containing 100 % PMMA and 1 wt% of <b>Mes<sub>2</sub>B(C<sub>6</sub>H<sub>4</sub>)-Te-6-(C<sub>6</sub>H<sub>4</sub>)BMes<sub>2</sub></b> in PMMA irradiated with a hand-held UV lamp. ....   | 166 |
| <b>Figure 4.12</b> | – TD-DFT [B3LYP/cc-pVDZ(-PP)] computed transitions ( $S_0 \rightarrow S_1$ : black, $S_0 \rightarrow S_2$ : blue) for <b>Mes<sub>2</sub>B(C<sub>6</sub>H<sub>4</sub>)-Te-6-(C<sub>6</sub>H<sub>4</sub>)BMes<sub>2</sub></b> in the gas-phase including the excitation wavelength, oscillator strength ( $f$ ), and the associated molecular orbitals. ....   | 168 |
| <b>Figure 4.13</b> | – a) Excitation and emission spectra of <b>O<sub>2</sub>N(C<sub>6</sub>H<sub>4</sub>)-Te-6-(C<sub>6</sub>H<sub>4</sub>)NO<sub>2</sub></b> ; b) images of films containing 100 % PMMA and 1 wt% of <b>O<sub>2</sub>N(C<sub>6</sub>H<sub>4</sub>)-Te-6-(C<sub>6</sub>H<sub>4</sub>)NO<sub>2</sub></b> in PMMA; c) images of films containing 100 % PMMA and 1 wt% of <b>O<sub>2</sub>N(C<sub>6</sub>H<sub>4</sub>)-Te-6-(C<sub>6</sub>H<sub>4</sub>)NO<sub>2</sub></b> in PMMA irradiated with a hand-held UV lamp. .... | 171 |
| <b>Figure 4.14</b> | – The structure asymmetric tellurophenes <b>10</b> and <b>11</b> featuring a <i>p</i> -nitrophenyl group. ....   | 171 |
| <b>Figure 4.15</b> | – TD-DFT [B3LYP/cc-pVDZ(-PP)] computed transitions ( $S_0 \rightarrow S_1$ : black, $S_0 \rightarrow S_2$ : blue) for <b>O<sub>2</sub>N(C<sub>6</sub>H<sub>4</sub>)-Te-6-(C<sub>6</sub>H<sub>4</sub>)NO<sub>2</sub></b> in the gas-phase including the excitation wavelength, oscillator strength ( $f$ ), and the associated molecular orbitals. ....   | 172 |
| <b>Figure 4.16</b> | – a) Excitation and emission spectra of <b>pyr-Te-6-pyr</b> ; b) images of films containing 100 % PMMA and 1 wt% of <b>pyr-Te-6-pyr</b> in PMMA; c) images of films containing 100 % PMMA and 1 wt% of <b>pyr-Te-6-pyr</b> in PMMA irradiated with a hand-held UV lamp. ....   | 174 |

- Figure 4.17** – TD-DFT [B3LYP/cc-pVDZ(-PP)] computed main transitions for **pyr-Te-6-pyr** in the gas-phase including the excitation wavelengths and oscillator strengths ( $f$ ) for the most intense transitions ( $S_0 \rightarrow S_3$ : red;  $S_0 \rightarrow S_4$ : black) along with the associated molecular orbitals. .... 175
- Figure 4.18** – Excitation spectra and emission spectra for a film containing 1 wt% of **Mes-Te-6-Mes** in PMMA shown as a solid lines and a film of pure PMMA shown as dash-dot lines. .... 177
- Figure 4.19** – TD-DFT [B3LYP/cc-pVDZ(-PP)] computed main transitions for **Mes-Te-6-Mes** in the gas-phase including the excitation wavelengths and oscillator strengths ( $f$ ) for the most intense transitions ( $S_0 \rightarrow S_3$ : red;  $S_0 \rightarrow S_8$ : black;  $S_0 \rightarrow S_9$ : blue) along with the associated molecular orbitals. .... 178
- Figure 4.20** – TD-DFT [B3LYP/cc-pVDZ(-PP)] computed main transitions for **[Mepyr-Te-6-pyrMe][I]<sub>2</sub>** in the gas-phase including the excitation wavelengths and oscillator strengths ( $f$ ) for the most intense transitions ( $S_0 \rightarrow S_3$ : red;  $S_0 \rightarrow S_4$ : black) along with the associated molecular orbitals. .... 181
- Figure 4.21** – TD-DFT [B3LYP/cc-pVDZ(-PP)] computed transitions ( $S_0 \rightarrow S_1$ : red;  $S_0 \rightarrow S_5$ : black) for **dpe-Te-6-dpe** in the gas-phase including the excitation wavelengths, oscillator strengths ( $f$ ), and the associated molecular orbitals. .... 184



|   |     |
|---|-----|
| <b>Figure 4.22</b> – Computed HOMO and LUMO energy levels for the optimized ground state of <b>Mes-Te-6-Mes</b> , <b>Mes<sub>2</sub>B(C<sub>6</sub>H<sub>4</sub>)-Te-6-(C<sub>6</sub>H<sub>4</sub>)BMes<sub>2</sub></b> , <b>dpe-Te-6-dpe</b> , <b>O<sub>2</sub>N(C<sub>6</sub>H<sub>4</sub>)-Te-6-(C<sub>6</sub>H<sub>4</sub>)NO<sub>2</sub></b> , <b>pyr-Te-6-pyr</b> , and <b>[Mepyr-Te-6-pyrMe]<sup>2+</sup></b> in the gas-phase using B3LYP/cc-pVDZ(-PP)..... | 187 |
| <b>Figure 5.1</b> – Known tellurophene-containing homopolymers. ....  | 209 |
| <b>Figure 5.2</b> – Examples of tellurophenes incorporated into $\pi$ -extended molecules. ..   | 210 |
| <b>Figure 5.3</b> – The seven possible isomers of benzotrithiophene ( <b>BTT</b> ).....   | 211 |
| <b>Figure 5.4</b> – Phospho(benzo)bithiophene isomers and their fluorescent properties. ....  | 212 |
| <b>Figure 5.5</b> – The $\pi$ -extended tellura(benzo)bithiophenes mentioned in this Chapter. ....  | 213 |
| <b>Figure 5.6</b> – Experimental UV-vis spectrum of <b>Te-bbt-cumenyl</b> in THF (concentration = $2.99 \times 10^{-5}$ M) and computed UV-vis spectrum shown in grey along with oscillator strengths for the main predicted transitions (computed at the B3LYP/cc-pVDZ(-PP) level of theory). ....   | 216 |
| <b>Figure 5.7</b> – TD-DFT [B3LYP/cc-pVDZ(-PP)] computed main transitions for <b>Te-bbt-cumenyl</b> , including excitation wavelengths and oscillator strengths ( $f$ ) for the most intense transitions (S <sub>0</sub> -S <sub>1</sub> : red; S <sub>0</sub> -S <sub>2</sub> : black; S <sub>0</sub> -S <sub>3</sub> : blue) along with the associated molecular orbitals. ....   | 216 |
| <b>Figure 5.8</b> – TGA plot of <b>Te-bbt-cumenyl</b> measured under air at 10 °C/minute. The horizontal dashed line indicates the point at which 5 % mass loss occurs. ....  | 218 |

|  |     |
|--|-----|
| <b>Figure 5.9</b> – UV-vis absorbance spectra recorded after irradiating a solution of <b>Te-bbt-cumenyl</b> in THF with 355 nm (75 W) for 20 minute time intervals. Initial concentration of <b>Te-bbt-cumenyl</b> was $6.00 \times 10^{-5}$ M. ....                          | 218 |
| <b>Figure 5.10</b> – The structure of <b>Te-bbt-cumenyl</b> as well as the potential oxidation products: <b>TeO-bbt-cumenyl</b> , <b>TeO<sub>2</sub>-bbt-cumenyl</b> , and the corresponding ene-dione. ....   | 220 |
| <b>Figure 5.11</b> – LUMO and HOMO of <b>Te-bbt-cumenyl</b> , <b>TeO-bbt-cumenyl</b> , and <b>TeO<sub>2</sub>-bbt-cumenyl</b> at the S <sub>0</sub> state equilibrium geometry as determined at the B3LYP/cc-pVDZ(-PP) level of theory in the gas-phase. ....                  | 221 |
| <b>Figure 5.12</b> – Calculated UV-vis spectra of <b>Te-bbt-cumenyl</b> , <b>TeO-bbt-cumenyl</b> , <b>TeO<sub>2</sub>-bbt-cumenyl</b> , and the ene-dione determined at the B3LYP/cc-pVDZ(-PP) level of theory using a THF polarizable continuum model (PCM). ....             | 222 |
| <b>Figure 5.13</b> – Structurally characterized [ <i>c</i> ]-hetero(benzo)-[ <i>b,b</i> ]-bithiophenes in the literature and <b>Te-bbt-cumenyl</b> . ....  | 225 |
| <b>Figure 5.14</b> – Molecular structure of <b>Te-bbt-SiMe<sub>3</sub></b> . ....  | 227 |
| <b>Figure 5.15</b> – Molecular structure of <b>Te-bbt-(C<sub>6</sub>H<sub>4</sub>)OCH<sub>3</sub></b> . ....   | 228 |
| <b>Figure 5.16</b> – Molecular structure of <b>Te-bbt-cumenyl</b> . ....   | 229 |
| <b>Figure 5.17</b> – Molecular structure of <b>Te-bbt(Br<sub>2</sub>)-cumenyl</b> . ....   | 230 |
| <b>Figure 5.18</b> – Stacked <sup>1</sup> H NMR spectra (recorded in CDCl <sub>3</sub> ) of a) a close-up of the aryl region, b) <b>Te-bbt(Me<sub>2</sub>)-cumenyl</b> , and c) reaction of <b>Te-bbt(Me<sub>2</sub>)-cumenyl</b> with <i>p</i> -chloranil after work-up. .... | 234 |

|   |     |
|---|-----|
| <b>Figure 5.19</b> – Stacked $^{13}\text{C}\{^1\text{H}\}$ NMR spectra (in $\text{CDCl}_3$ ) of a) <b>Te-bbt(Me<sub>2</sub>)-cumenyl</b> ,<br>and b) the result of combining <b>Te-bbt(Me<sub>2</sub>)-cumenyl</b> with <i>p</i> -chloranil.<br>.....   | 234 |
| <b>Figure 5.20</b> – The HOMO and LUMO along with their corresponding energies, of <b>Te-bbt(Me<sub>2</sub>)-cumenyl</b> and <b>Te-bbt(Me<sub>2</sub>)-f-cumenyl</b> computed at the B3LYP/cc-pVDZ(-PP) level of theory. ....   | 236 |
| <b>Figure 5.21</b> – A sample of <b>poly(Te-bbt-cumenyl)</b> as synthesized and after sitting in a lit room for 2 days under ambient conditions. ....   | 238 |
| <b>Figure 5.22</b> – $^1\text{H}$ NMR spectra recorded in $\text{CDCl}_3$ of <b>Te-bbt(Br<sub>2</sub>)-cumenyl</b> and <b>poly(Te-bbt-cumenyl)</b> . ....   | 238 |
| <b>Figure 5.23</b> – $^1\text{H}$ NMR spectra of a sample of polymer in $\text{CDCl}_3$ stored under $\text{N}_2$ ( <i>top</i> ) and then exposed to air for 3 days ( <i>bottom</i> ) close-up of aryl, $^i\text{Pr}(\text{CH})$ and $^i\text{Pr}(\text{CH}_3)$ regions. ....   | 239 |
| <b>Figure 5.24</b> – UV-vis spectra of <b>poly(Te-bbt-cumenyl)</b> , <b>Te-bbt-cumenyl</b> , and <b>Te-bbt(Br<sub>2</sub>)-cumenyl</b> in THF. ....   | 241 |
| <b>Figure 5.25</b> – a) Excitation and emission spectra of <b>Te-bbt-cumenyl</b> in a PMMA matrix collected in air; b) images of films containing 100 % PMMA and 1 wt% of <b>Te-bbt-cumenyl</b> in PMMA under ambient conditions; c) images of films containing 100 % PMMA and 1 wt% of <b>Te-bbt-cumenyl</b> in PMMA irradiated with a hand-held UV lamp. .... | 242 |

|  |     |
|--|-----|
| <b>Figure 5.26</b> – <i>Left</i> : Singlet and triplet states of <b>Te-bbt-cumenyl</b> calculated at the B3LYP/cc-pVDZ(-PP) level of theory; <i>Right</i> : A close-up of the S <sub>1</sub> –S <sub>7</sub> and T <sub>2</sub> –T <sub>10</sub> states. ....  | 244 |
| <b>Figure 5.27</b> – TD-DFT [B3LYP/cc-pVDZ(-PP)] computed main transitions for <b>Te-bbt(Me<sub>2</sub>)-f-cumenyl</b> including excitation wavelengths and oscillator strengths ( <i>f</i> ) for the most intense transitions (S <sub>0</sub> →S <sub>1</sub> : red; S <sub>0</sub> →S <sub>5</sub> : black) along with the associated molecular orbitals. .... | 246 |
| <b>Figure 6.1</b> – The highest reported quantum yield of phosphorescence from a tellurophene. ....  | 272 |
| <b>Figure 6.2</b> – Bis(boryl)tellurophenes discussed in this Thesis. ....   | 273 |
| <b>Figure 6.3</b> – Examples of non-fullerene acceptors for OPVs. ....   | 280 |

## List of Schemes

|   |    |
|---|----|
| <b>Scheme 1.1</b> – The reactivity of tellurophenes towards Br <sub>2</sub> . .....   | 20 |
| <b>Scheme 1.2</b> – a) The oxidation of diaryltellurides (R <sub>2</sub> Te) in the presence of O <sub>2</sub> and a photosensitizer (Rose Bengal); b) the self-sensitized oxidation of a diaminotelluroxanthylum dye <b>17a</b> to produce the fluorescent telluroxide <b>17b</b> ; c) the self-sensitized oxidation of 2,5-diphenyltellurophene <b>18</b> to produce the ene-dione <b>19</b> and TeO <sub>2</sub> . ..... | 21 |
| <b>Scheme 1.3</b> – Te/Li exchange reactions involving tellurophenes. ....  | 23 |
| <b>Scheme 1.4</b> – Early reports of the synthesis of tellurophenes. ....   | 25 |
| <b>Scheme 1.5</b> – Synthesis of a tellurium <i>via</i> a rhodacycle intermediate. ....   | 26 |
| <b>Scheme 1.6</b> – Synthesis of a tellurophene <i>via</i> a zirconacycle intermediate. ....  | 26 |
| <b>Scheme 1.7</b> – The synthesis of 2,5-diaryltellurophenes <i>via</i> hydrazones. ....  | 27 |
| <b>Scheme 1.8</b> – Synthesis of push-pull tellurophenes <i>via</i> an aryl-exchange followed by an intramolecular cyclization of ditellurides. ....  | 27 |
| <b>Scheme 1.9</b> – Synthesis of 3-aryltellurophenes as described by Han and coworkers. ....  | 28 |
| <b>Scheme 1.10</b> – Synthesis of benzotellurophenes ( <b>39a–e</b> ) <i>via</i> a lithiated aryl intermediate, as developed by Sashida and coworkers. ....   | 28 |
| <b>Scheme 1.11</b> – Synthesis of benzotellurophenes ( <b>40–42</b> ) as well as tellurophenes fused with larger heteroacenes ( <i>e.g.</i> , pyrene), as developed by Rivard and coworkers. ....   | 29 |
| <b>Scheme 1.12</b> – The synthesis of $\pi$ -extended tellurophenes <i>via</i> arylzinc precursors as reported by Yoshikai and coworkers. ....  | 30 |

|  |    |
|--|----|
| <b>Scheme 1.13</b> – The synthesis of $\pi$ -extended tellurophenes <b>47</b> and <b>48</b> <i>via</i> diaryliodonium salts as reported by Xu and coworkers. ....  | 30 |
| <b>Scheme 1.14</b> – Electropolymerization of tellurophene-capped monomers <b>49</b> and <b>51</b> to form polytellurophenes <b>50</b> and <b>52</b> , respectively, as described by Data and coworkers. ....            | 31 |
| <b>Scheme 1.15</b> – Synthesis of a phosphorescent platinum-acetylide tellurophene copolymer. ....   | 34 |
| <b>Scheme 1.16</b> – The first reported synthesis of poly(3-alkyltellurophene)s by Seferos and coworkers. ....   | 36 |
| <b>Scheme 1.17</b> – The synthesis of chalcogenophene-containing polymers <b>88</b> and <b>89</b> studied as donor materials in OPVs. ....   | 39 |
| <b>Scheme 1.18</b> – Chalcogenophene-containing polymers <b>90–92</b> developed as donor materials for OPVs. ....  | 40 |
| <b>Scheme 1.19</b> – Chalcogenophene-containing polymers developed as donor materials for OPVs. ....   | 41 |
| <b>Scheme 2.1</b> – Attempted cyclization of borylated diynes with zirconocene reagents.   | 65 |
| <b>Scheme 2.2</b> – Synthesis of mono- and bis-(NHC) adducts of <b>B-Te-6-B</b> . ....   | 68 |
| <b>Scheme 3.1</b> – Synthesis of the di(isopropoxy)borylated tellurophene precursor ( <b><sup>i</sup>PrO</b> ) <sub>2</sub> <b>B-Te-6-B(O<sup>i</sup>Pr)</b> <sub>2</sub> . ....   | 96 |
| <b>Scheme 3.2</b> – Boryl exchange protocol used to access new borylated tellurophenes <i>via</i> the common building block ( <b><sup>i</sup>PrO</b> ) <sub>2</sub> <b>B-Te-6-B(O<sup>i</sup>Pr)</b> <sub>2</sub> . .... | 97 |

|  |     |
|--|-----|
| <b>Scheme 3.3</b> – Attempted reactions between ( <i>i</i> PrO) <sub>2</sub> <b>B-Te-6-B</b> (O <i>i</i> Pr) <sub>2</sub> and 2,6-di- <i>tert</i> -butyl-4-methylphenol, <i>N,N'</i> -dimesityl-1,2-phenylenediamine, or <i>N,N'</i> -dixylyl-1,2-phenylenediamine. .... | 99  |
| <b>Scheme 3.4</b> – Reactions between ( <i>i</i> PrO) <sub>2</sub> <b>B-Te-6-B</b> (O <i>i</i> Pr) <sub>2</sub> and various Brønsted acidic polyols that produce <b>H-Te-6-H</b> as the only tellurium containing product. ....  | 99  |
| <b>Scheme 3.5</b> – Improved Suzuki-Miyaura cross-coupling of <b>B-Te-6-B</b> with 2-bromothiophene to yield <b>thienyl-Te-6-thienyl</b> . ....  | 113 |
| <b>Scheme 4.1</b> – Suzuki-Miyaura cross-coupling of <b>B-Te-6-B</b> with 2-bromothiophene to yield <b>thienyl-Te-6-thienyl</b> . ....   | 150 |
| <b>Scheme 4.2</b> – Synthesis of 2,5-bis(aryl)tellurophenes derived from the Suzuki-Miyaura cross-coupling of <b>B-Te-6-B</b> with arylhalides. ....   | 155 |
| <b>Scheme 4.3</b> – Synthesis of [Mepyr-Te-6-pyrMe][I] <sub>2</sub> . ....   | 156 |
| <b>Scheme 5.1</b> – The synthesis of unsymmetrical benzotrithalcofenophenes <i>via</i> Pd-catalyzed intramolecular dehydrogenative arylation. ....   | 212 |
| <b>Scheme 5.2</b> – Synthetic procedure for 3,3'-bis(trimethylsilylethynyl)-2,2'-bithiophene. ....   | 214 |
| <b>Scheme 5.3</b> – Synthesis of diynes <b>BT1</b> and <b>BT2</b> , <b>Te-bbt-SiMe<sub>3</sub></b> , <b>Te-bbt-(C<sub>6</sub>H<sub>4</sub>)OCH<sub>3</sub></b> , and <b>Te-bbt-cumenyl</b> . ....  | 215 |
| <b>Scheme 5.4</b> – The partial iodination of <b>Te-bbt-cumenyl</b> and the resulting mixture of di-iodinated, mono-iodinated, and unreacted <b>Te-bbt-cumenyl</b> . ....  | 223 |

|  |     |
|--|-----|
| <b>Scheme 5.5</b> – Lithiation of <b>Te-bbt-cumenyl</b> followed by reaction with an electrophile to synthesize: <b>Te-bbt(D<sub>2</sub>)-cumenyl</b> (X = D), <b>Te-bbt(Me<sub>2</sub>)-cumenyl</b> (X = Me), and <b>Te-bbt(Br<sub>2</sub>)-cumenyl</b> (X = Br). ..... | 224 |
| <b>Scheme 5.6</b> – a) Itami’s procedure for annulating thiophene rings with aryl rings around a sumanene core; b) attempting to apply Itami’s protocol to <b>Te-bbt(Me<sub>2</sub>)-cumenyl</b> . .....   | 231 |
| <b>Scheme 5.7</b> – a) Huang’s procedure for annulating a tellurophene ring with adjoining PDI units; b) application of Huang’s protocol to <b>Te-bbt(Me<sub>2</sub>)-cumenyl</b> . ...  | 233 |
| <b>Scheme 5.8</b> – Polymerization of <b>Te-bbt(Br<sub>2</sub>)-cumenyl</b> under KCTP conditions....  | 238 |
| <b>Scheme 6.1</b> – Coordination of an NHC to the boron centres in <b>2</b> to form <b>2•NHC</b> and <b>2•(NHC)<sub>2</sub></b> . .....  | 272 |
| <b>Scheme 6.2</b> – The proposed coordination of aryl salts to <b>4</b> in order to tune the emission wavelength and enhance RTP. ....   | 273 |
| <b>Scheme 6.3</b> – a) Borafluorenes with pendant amines, and b) the proposed use of tellurophenes featuring boryl groups with pendant amines to increase atmospheric stability of the tellurophene and potentially turn the emission “on” and “off”. .....              | 274 |
| <b>Scheme 6.4</b> – The polymerization of <b>11</b> to form polymer <b>12</b> <i>via</i> KCTP. ....  | 277 |
| <b>Scheme 6.5</b> – a) The proposed synthesis, and b) the polymerization, of a <b>Te-bbt</b> monomer with solubilizing alkyl groups <b>13</b> in the hope obtaining higher molecular weights for polymer <b>14</b> <i>via</i> KCTP. ....                                 | 278 |



## List of Tables

|  |    |
|--|----|
| <b>Table 1.1</b> – Properties of sulfur, selenium and tellurium. ....  | 17 |
| <b>Table 1.2</b> – OPV device parameters using poly(3-alkylchalcogenophene)s and PC <sub>71</sub> BM as the active layer components. ....  | 37 |
| <b>Table 1.3</b> – OPV device parameters using active layers comprised of PC <sub>61</sub> BM as the acceptor and small molecules chalcogenophenes <b>85–87</b> as the donor. ....   | 38 |
| <b>Table 1.4</b> – OPV device parameters comparing <b>88</b> to its previously reported thiophene analogue <b>89</b> . ....  | 39 |
| <b>Table 1.5</b> – OPV device parameters using active layers comprised of PC <sub>61</sub> BM as the acceptor and polymers <b>90–92</b> as the donor. ....   | 40 |
| <b>Table 1.6</b> – OPV device parameters using active layers comprised of PC <sub>71</sub> BM as the acceptor and polymers <b>93–95</b> as the donor. ....   | 41 |
| <b>Table 1.7</b> – Summary of OPV device performance parameters using the donor polymer PTB7-Ph and Te-containing acceptor polymers <b>96–98</b> . ....  | 42 |
| <b>Table 1.8</b> – Summary of OPV device performance parameters using the donor polymer PBDB-T and Te-containing acceptors <b>99–101</b> . ....  | 43 |
| <b>Table 1.9</b> – Charge carrier mobilities (cm <sup>2</sup> V <sup>-1</sup> s <sup>-1</sup> ) and on/off ratios of bottom-gate, top-contact OFET devices incorporating chalcogenophene-containing molecules and polymers listed in chronological order. .... | 47 |
| <b>Table 2.1</b> - The excitation energies (in eV) of the three lowest-lying singlet and triplet states for <b>B-Te-6-B</b> with different basis sets <sup>a</sup> at the TD-B3LYP level of  |    |

|  |    |
|--|----|
| theory at the gas-phase $S_0$ geometry (as determined at the B3LYP/cc-pVDZ-(PP) level of theory). .....  | 74 |
| <b>Table 2.2</b> – The excitation energies (in eV) of the three lowest-lying singlet and triplet states for <b>B-Te-6-B</b> at the TD-B3LYP, TD-CAM-B3LYP, and TD-M06-2X levels of theory with the cc-pVDZ-(PP) basis set at the gas-phase $S_0$ geometry (as determined at the B3LYP/ccpVDZ-(PP) level of theory). .                            | 75 |
| <b>Table 2.3</b> – The excitation energies (in eV) of the three lowest-lying singlet and triplet states for <b>B-Te-6-B</b> at the TD-B3LYP/cc-pVDZ-(PP) level of theory for different solvents (THF and H <sub>2</sub> O treated with IEF-PCM) at the gas-phase $S_0$ geometry (as determined at the B3LYP/cc-pVDZ-(PP) level of theory). ..... | 76 |
| <b>Table 2.4</b> – The excitation energies (in eV) using various levels of theory for <b>B-Te-6-B</b> at the optimized $T_1$ geometry. ....  | 77 |
| <b>Table 2.5</b> – The excitation energies (in eV) at the TD-B3LYP/TZVP/ZORA of theory for <b>B-Te-6-B</b> at the specified geometries. ....   | 78 |
| <b>Table 2.6</b> – The excitation energies (in eV) to the lowest-energy “singlet” state (at the $S_1$ geometry) and “triplet” states (at the $T_1$ geometry) at the TD-B3LYP/TZVP/ZORA [+ spin-orbit coupling] level of theory for <b>B-Te-6-B</b> . ....  | 79 |
| <b>Table 2.7</b> – The excitation energies (in eV) at the TD-B3LYP level of theory with the ccpVDZ-(PP) and cc-pVTZ-(PP) basis sets for <b>ImMe<sub>2</sub><sup>i</sup>Pr<sub>2</sub>•B-Te-6-B</b> at the specified geometries. ....   | 80 |

|   |     |
|---|-----|
| <b>Table 2.8</b> – The excitation energies (in eV) at the TD-B3LYP level of theory with the ccpVDZ(-PP) and cc-pVTZ(-PP) basis sets for <b>ImMe<sub>2</sub><sup>i</sup>Pr<sub>2</sub>•B-Te-6-B</b> at the specified geometries. ....            | 80  |
| <b>Table 2.9</b> – Crystallographic data for compounds <b>2</b> , <b>ImMe<sub>2</sub><sup>i</sup>Pr<sub>2</sub>•B-Te-6-B•ImMe<sub>2</sub><sup>i</sup>Pr<sub>2</sub></b> , and <b>ImMe<sub>2</sub><sup>i</sup>Pr<sub>2</sub>•B-Te-6-B</b> . .... | 87  |
| <b>Table 3.1</b> – The photoluminescence decay of <b>Mes(<sup>i</sup>PrO)B-Te-6-B(O<sup>i</sup>Pr)Mes</b> powder, fit with a biexponential and the resulting fitting parameters. ....   | 126 |
| <b>Table 3.2</b> – The photoluminescence decay of <b><sup>t</sup>BucatB-Te-6-B<sup>t</sup>Bucat</b> powder, fit with a biexponential and the resulting fitting parameters. ....   | 126 |
| <b>Table 3.3</b> – Crystallographic data for the tellurophenes derived from <b>(<sup>i</sup>PrO)<sub>2</sub>B-Te-6-B(O<sup>i</sup>Pr)<sub>2</sub></b> . ....  | 128 |
| <b>Table 3.4</b> – TD-DFT calculated excited states of <b>Mes(<sup>i</sup>PrO)B-Te-6-B(O<sup>i</sup>Pr)Mes</b> at the B3LYP-ccpVDZ(-PP) level of theory. ....   | 140 |
| <b>Table 4.1</b> – TD-DFT calculated excited states of <b>Mes<sub>2</sub>B(C<sub>6</sub>H<sub>4</sub>)-Te-6-(C<sub>6</sub>H<sub>4</sub>)BMes<sub>2</sub></b> at the B3LYP-cc-pVDZ(-PP) level of theory. ....                                    | 169 |
| <b>Table 4.2</b> – TD-DFT calculated excited states of <b>O<sub>2</sub>N(C<sub>6</sub>H<sub>4</sub>)-Te-6-(C<sub>6</sub>H<sub>4</sub>)NO<sub>2</sub></b> at the B3LYP-ccpVDZ(-PP) level of theory. ....   | 173 |
| <b>Table 4.3</b> – TD-DFT calculated excited states of <b>pyr-Te-6-pyr</b> at the B3LYP-ccpVDZ(-PP) level of theory. ....   | 176 |
| <b>Table 4.4</b> – TD-DFT calculated excited states of <b>Mes-Te-6-Mes</b> at the B3LYP-cc-pVDZ(-PP) level of theory. ....  | 179 |

|   |     |
|---|-----|
| <b>Table 4.5</b> – TD-DFT calculated excited states of <b>[Mepyr-Te-6-pyrMe]<sup>2+</sup></b> at the B3LYP-ccpVDZ(-PP) level of theory. ....  | 182 |
| <b>Table 4.6</b> – TD-DFT calculated excited states of <b>dpe-Te-6-dpe</b> at the B3LYP-ccpVDZ(-PP) level of theory. ....   | 185 |
| <b>Table 4.7</b> – Crystallographic data for the tellurophenes discussed in Chapter 4. ....   | 197 |
| <b>Table 4.8</b> – The photoluminescence decay of a PMMA film containing 1 wt% of <b>Mes<sub>2</sub>B(C<sub>6</sub>H<sub>4</sub>)-Te-6-(C<sub>6</sub>H<sub>4</sub>)BMes<sub>2</sub></b> , fit with a biexponential and the resulting fitting parameters. .... | 198 |
| <b>Table 4.9</b> – The photoluminescence decay of a PMMA film containing 1 wt% of <b>O<sub>2</sub>N(C<sub>6</sub>H<sub>4</sub>)-Te-6-(C<sub>6</sub>H<sub>4</sub>)NO<sub>2</sub></b> , fit with a biexponential and the resulting fitting parameters. ....     | 198 |
| <b>Table 4.10</b> – The photoluminescence decay of a PMMA film containing 1 wt% of <b>pyr-Te-6-pyr</b> , fit with a biexponential and the resulting fitting parameters. ....  | 199 |
| <b>Table 5.1</b> – TD-DFT calculated excited states of <b>Te-bbt-cumenyl</b> at the B3LYP-ccpVDZ(-PP) level of theory. ....   | 244 |
| <b>Table 5.2</b> – TD-DFT calculated excited states of <b>Te-bbt(Me<sub>2</sub>)-f-cumenyl</b> at the B3LYP-ccpVDZ(-PP) level of theory. ....   | 247 |
| <b>Table 5.3</b> – Initial GPC results for partially oxidized <b>poly(Te-bbt-cumenyl)</b> in THF. ....  | 260 |
| <b>Table 5.4</b> – The photoluminescence decay of a PMMA film containing 1 wt% of <b>Te-bbt-cumenyl</b> and the resulting fitting parameters. ....  | 260 |
| <b>Table 5.5</b> – Crystallographic data for the <b>Te-bbts</b> discussed in this Chapter. ....   | 262 |

## List of Symbols, Nomenclature, and Abbreviations

|             |   |
|-------------|---|
| $\{^nX\}$   | Decoupled to $^nX$ nucleus                  |
| $^1O_2$     | Singlet oxygen                              |
| $^3O_2$     | Triplet oxygen                              |
| 2-MeTHF     | 2-Methyltetrahydrofuran                     |
| Å           | Ångström                                    |
| Ac          | Acyl group ( $-C(O)R$ )                     |
| ACQ         | Aggregation-caused quenching                |
| AIE         | Aggregation-induced emission                |
| Ar          | Aryl group                                  |
| atm         | Atmospheric (unit of pressure)              |
| BHJ         | Bulk heterojunction                         |
| BHT         | Butylated hydroxytoluene                    |
| bipy        | 2,2'-bipyridine                             |
| Bn          | Benzyl group ( $CH_2C_6H_5$ )               |
| BPIn        | Pinacolboronate                             |
| br          | Broad                                       |
| Bu          | Butyl group ( $C_4H_9$ )                    |
| cat         | Catechol (1,2-dihydroxybenzene)             |
| $C_6D_6$    | Benzene- $d_6$                              |
| $CDCl_3$    | Chloroform-d                                |
| $^{\circ}C$ | Degrees Celsius                             |
| <i>ca.</i>  | Circa; approximately                        |
| $cm^{-1}$   | Wavenumbers                                 |
| Cp          | Cyclopentadienyl ligand ( $\eta^5-C_5H_5$ ) |
| CV          | Cyclic voltammetry                          |

|                  |   |
|------------------|---|
| d                | Doublet   |
| D                | Diffusion coefficient   |
| dan              | 1,2-diaminonaphthyl group   |
| dba              | Dibenzylideneacetone  |
| $\bar{D}$        | Dispersity ( $M_w/M_n$ )  |
| dd               | Doublet of doublets   |
| DEPTQ            | Distortionless enhancement by polarization transfer including quaternary nuclei |
| DF               | Delayed fluorescence  |
| DFT              | Density Functional Theory   |
| Dipp             | 2,6-( <sup>i</sup> Pr) <sub>2</sub> C <sub>6</sub> H <sub>3</sub>               |
| DMAc             | Dimethylacetamide   |
| DMAP             | Dimethylaminopyridine   |
| DMF              | <i>N,N'</i> -Dimethylformamide  |
| dpe              | diphenylethene  |
| dppe             | bis(diphenylphosphino)ethane  |
| dppp             | bis(diphenylphosphino)propane   |
| DMSO             | Dimethylsulfoxide   |
| dt               | Doublet of triplets   |
| E                | Variable main group element   |
| E <sub>0-0</sub> | Zero-point corrected adiabatic energy   |
| ECP              | Effective core potential  |
| EI               | Electron ionization   |
| eq               | Molar equivalents   |
| Em               | Emission  |
| Et               | Ethyl (C <sub>2</sub> H <sub>5</sub> )  |
| eV               | Electron volt   |

|  |  |
|--|--|
| Ex   | Excitation   |
| $f$  | Oscillator strength  |
| Fl   | fluorenyl  |
| g  | Gram   |
| GPC  | Gel permeation chromatography                                  |
| HOMO   | Highest occupied molecular orbital                             |
| HRMS   | High resolution mass spectrometry                              |
| Hz   | Hertz  |
| IC   | Internal conversion  |
| IEF-PCM  | Integral equation formalism polarizable continuum model        |
| ImMe <sub>2</sub> <sup>i</sup> Pr <sub>2</sub> | (MeCN <sup>i</sup> Pr) <sub>2</sub> C:                         |
| <sup>i</sup> Pr                                | <i>iso</i> -propyl (Me <sub>2</sub> CH)                        |
| IPrCH <sub>2</sub>                             | HCNDipp) <sub>2</sub> CCH <sub>2</sub>                         |
| IR   | Infrared   |
| ISC  | Intersystem crossing   |
| $J$  | NMR coupling constant  |
| $J_{sc}$                                       | Short-circuit current density                                  |
| K  | Kelvin   |
| KCTP   | Kumada Catalyst-Transfer Polycondensation                      |
| kDa  | Kilodaltons (1,000 g/mol)                                      |
| $L_D$  | Diffusion limit  |
| LUMO   | Lowest Unoccupied Molecular Orbital                            |
| MAD  | Mean average difference  |
| MALDI  | Matrix Assisted Laser Desorption/Ionization                    |
| Me   | Methyl (CH <sub>3</sub> )                                      |
| MeCN   | Acetonitrile   |
| Mes  | Mesityl (2,4,6-Me <sub>3</sub> C <sub>6</sub> H <sub>2</sub> ) |

|                 |  |
|-----------------|--|
| mg              | Milligram  |
| MHz             | Megahertz  |
| mL              | Milliliter                                       |
| mmol            | Millimole  |
| <i>o</i> -tolyl | <i>ortho</i> -MeC <sub>6</sub> H <sub>4</sub>    |
| μ               | Charge carrier mobility                          |
| μ <sub>h</sub>  | Hole mobility                                    |
| <i>m</i> -CPBA  | <i>meta</i> -chloroperoxybenzoic acid            |
| mol%            | Mole percent                                     |
| M <sub>n</sub>  | Number average molecular weight                  |
| M <sub>w</sub>  | Weight average molecular weight                  |
| MO              | Molecular orbital                                |
| mol             | Mole   |
| Mp              | Melting point                                    |
| <sup>n</sup> Bu | <i>n</i> -butyl (C <sub>4</sub> H <sub>9</sub> ) |
| n               | Principle quantum number                         |
| NDI             | naphthalene diimide                              |
| NHC             | <i>N</i> -Heterocyclic carbene                   |
| NHO             | <i>N</i> -Heterocyclic olefin                    |
| NIR             | Near-Infrared Radiation                          |
| NIS             | <i>N</i> -iodosuccinimide                        |
| nm              | Nanometers                                       |
| NMR             | Nuclear Magnetic Resonance                       |
| ns              | Nanoseconds                                      |
| LED             | Light-emitting diode                             |
| OFET            | Organic field effect transistor                  |
| E <sub>g</sub>  | Optical bandgap                                  |



|                    |   |
|--------------------|---|
| OLED               | Organic light-emitting diode                            |
| ORTEP              | Oak Ridge thermal ellipsoid plot                        |
| OPV                | Organic photovoltaic                                    |
| P3HT               | Poly(3-hexylthiophene)                                  |
| PCBM               | [6,6]-phenyl-C <sub>61</sub> -butyric acid methyl ester |
| PCE                | Power conversion efficiency                             |
| PDI                | Perylene diimide  |
| Ph                 | Phenyl (C <sub>6</sub> H <sub>5</sub> )                 |
| PL                 | Photoluminescence                                       |
| PMMA               | Poly(methylmethacrylate)                                |
| ppm                | Parts per million                                       |
| PivOH              | Pivalic acid  |
| pyr                | Pyridine  |
| pyrMe              | Methylpyridinium  |
| R                  | Variable functional group                               |
| rt                 | Room temperature  |
| k                  | Rate constant   |
| RI                 | Refractive index  |
| RTP                | Room temperature phosphorescence                        |
| s                  | Singlet   |
| S <sub>n</sub>     | nth singlet state                                       |
| SOC                | Spin-orbit coupling                                     |
| ζ                  | Spin-orbit coupling constant                            |
| t                  | Triplet   |
| TADF               | Thermally activated delayed fluorescence                |
| <sup>t</sup> Bu    | <i>tert</i> -butyl                                      |
| <sup>t</sup> Bucat | <i>tert</i> -butylcatechol                              |

|                 |   |
|-----------------|---|
| TBAF            | Tetrabutylammonium fluoride                           |
| TD-DFT          | Time dependent-density functional theory              |
| Te-bbt          | Tellura(benzo)bithiophene                             |
| Tf              | Triflate  |
| TGA             | Thermogravimetric analysis                            |
| THF             | Tetrahydrofuran                                       |
| TMEDA           | Tetramethylethylenediamine                            |
| $T_n$           | nth triplet state                                     |
| TPA             | Triphenylamine  |
| Trip            | 2,4,6-triisopropylphenyl                              |
| UFF             | Universal force field                                 |
| UV              | Ultraviolet   |
| UV-vis          | Ultraviolet/visible spectroscopy                      |
| $V_{OC}$        | Open-circuit voltage                                  |
| wt%             | Percent by weight                                     |
| XPhos           | 2-Dicyclohexylphosphino-2',4',6'-triisopropylbiphenyl |
| XRD             | X-ray diffraction                                     |
| Z               | Atomic number   |
| ZORA            | Zeroth order regular approximation                    |
| $\delta$        | Partial charge or chemical shift in ppm               |
| $\Delta E_{ST}$ | Singlet and triplet energy gap                        |
| $\eta$          | Eta (the number of coordinated atoms within a ligand) |
| $\epsilon$      | Epsilon (molar absorptivity)                          |
| $\tau$          | Lifetime  |
| $\tau_F$        | Fluorescence lifetime                                 |
| $\tau_P$        | Phosphorescence lifetime                              |
| $\mu$           | Charge carrier mobility                               |

|                 |                                  |
|-----------------|----------------------------------|
| $\mu_h$         | Hole mobility                    |
| $\mu_s$         | Microseconds                     |
| $\mu$ -wave     | Microwave radiation              |
| $\Phi$          | Quantum yield                    |
| $\Phi_F$        | Quantum yield of fluorescence    |
| $\Phi_P$        | Quantum yield of phosphorescence |
| $\lambda$       | Wavelength                       |
| $\lambda_{ex}$  | Excitation wavelength            |
| $\lambda_{em}$  | Emission wavelength              |
| $\lambda_{max}$ | Wavelength of maximum absorbance |

## Chapter 1 – Introduction

### 1.1 Potential Advantages of Incorporating Heavy Main Group Atoms into $\pi$ -Conjugated Systems

Within the last century, synthetic polymers have entered virtually all aspects of our lives, changing the world and the way that we live in a dramatic fashion. The study of polymers was initially spurred by war-time need, but from here they rapidly grew to include a diverse range of applications, from single-use packaging to drug delivery. More recently, organic  $\pi$ -conjugated polymers are being developed as non-toxic, lightweight, solution processible and possibly flexible, organic electronics.<sup>1,2</sup> However, the study of polymers bearing  $\pi$ -conjugated groups has historically focused on carbon-based materials, leaving the potential of heavy atom-containing materials yet to be explored. One important exception is the inclusion of sulfur-containing thiophenes, which have become widely explored building blocks in the field of organic semiconductors.<sup>3,4</sup> The study of semiconducting polymers incorporating other heavier main group elements (E) remains limited, largely due to synthetic challenges associated with the larger size and lower electronegativity of heavier atoms, leading to weaker orbital overlap and increased polarity within C-E bonds.<sup>5</sup> However, the incorporation of heavy atoms into  $\pi$ -conjugated systems is expected to result in lower optical bandgaps and higher charge carrier mobilities, giving rise to useful semiconductor properties.<sup>6</sup> A lot of progress has been made in the last 20 years to overcome some of the synthetic challenges associated with incorporating heavy main group elements into

$\pi$ -conjugated materials, in order to realize some of their benefits in the context of organic photovoltaics (OPVs), organic light-emitting diodes (OLEDs) and organic field effect transistors (OFETs).

In this Thesis, I will be describing my efforts to synthesize and study the optoelectronic properties of five-membered heterocycles featuring the heavy main-group atom tellurium. In particular, new synthetic routes to access a variety of tellurophenes with previously unexplored side groups were developed. In many cases, the resulting tellurophenes exhibited long-lived luminescence (phosphorescence) in the solid state. In each case, computational and solid state analysis were used to examine the underlying factors behind unlocking phosphorescence from tellurophenes.

### **1.1.1 Unlocking phosphorescence within heavy atom-containing heterocycles**

The importance of electronic displays has resulted in tremendous advancements in the field of light-emitting devices. However, due to the increasing popularity of these devices, alongside growing environmental concern, there is pressure on researchers to develop cheaper and more efficient light-emitting materials. In this regard, organic light-emitting diodes (OLEDs) remains a very active area of exploration.

Fundamentally, light emission from a molecule results when an excited state (created *via* absorption of a photon or an electrochemically injected electron/hole) decays radiatively. After light absorption, many photophysical processes are potentially available for an excited state, as illustrated in the simplified Jablonski diagram shown in Figure 1.1, leading to non-radiative processes that compete with light emission

(luminescence).<sup>7</sup> For example, when a molecule absorbs light, an electron is promoted from the ground state ( $S_0$ ) to an excited singlet state ( $S_n$ ,  $n \geq 1$ ) in a virtually instantaneous process with an extremely high rate constant ( $k > 10^{15} \text{ s}^{-1}$ ). Next, the excited state will undergo non-radiative decay *via* vibrational relaxation to the lowest excited state ( $S_1$ ). The non-radiative decay of any spin-allowed transition (associated with no change in spin multiplicity) is known as internal conversion (IC). Therefore, vibrational relaxation of an excited state is a form of IC, and it is usually associated with an extremely high rate constant, especially when the energy difference between the states involved in the transition are very small (as per the Energy Gap Law). As a result, vibrational relaxation to the lowest excited state ( $S_1$ ) almost always dominates all other processes and therefore emission is typically only possible from the lowest excited state, this is known as Kasha's rule. If emission happens from an excited singlet state (*e.g.*,  $S_1$ ) then it is termed fluorescence; if emission occurs from an excited triplet state (*e.g.*,  $T_1$ ) then the emission is referred to as phosphorescence. Alternatively, the lowest excited state can also decay non-radiatively, through molecular motion or by transferring the energy of the excited state to another species (*i.e.*, to a quencher molecule). Luminescence and non-radiative decay are often in competition with one another and strategies, such as building structurally rigid molecules, are often employed to suppress non-radiative decay and to enhance emission.<sup>8</sup>

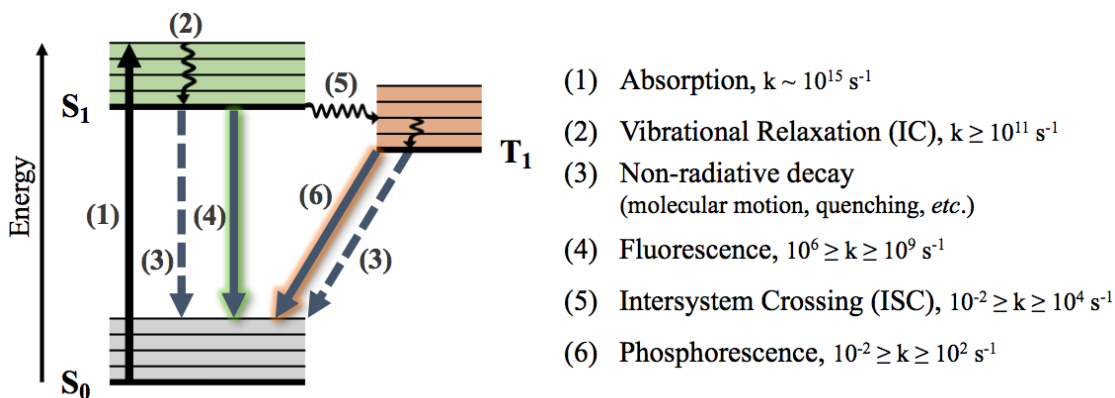


**Figure 1.1** – A simplified Jablonski diagram showing some possible photophysical processes that can occur after the absorption of a photon by a molecule.

In some cases, a change in spin multiplicity in the excited state becomes more favourable, allowing access to excited triplet states ( $T_n, n \geq 1$ ) from singlet excited states ( $S_n, n \geq 1$ ); recall that singlet excited states are initially generated upon the absorption of light. This process is known as intersystem crossing (ISC) and is much slower than internal conversion (IC). As before, vibrational relaxation to the lowest excited state ( $T_1$ ) takes place. Finally, non-radiative decay (*e.g.*, expending energy through molecular motion or transferring energy to a quencher) and radiative decay from  $T_1$  (phosphorescence) are possible routes back to the ground state. Equations 1 and 2 are two expressions for the efficiency of phosphorescence from an excited state, known as quantum yield ( $\Phi$ ). In Equation 1, the quantum yield for phosphorescence  $\Phi_{\text{phos}}$  is expressed in terms of the rate constant ( $k_{\text{phos}}$ ) and lifetime ( $\tau_{\text{phos}}$ ) associated with emission from the  $T_1$  excited state. In Equation 2,  $\Phi_{\text{phos}}$  is expressed as the rate constant for phosphorescence divided by the sum of all the rate constants ( $k$ ) associated with the decay of the excited state, including phosphorescence ( $k_{\text{phos}}$ ), fluorescence ( $k_{\text{fl}}$ ), and all

possible methods of non-radiative decay including internal conversion ( $k_{IC}$ ) and intersystem crossing ( $k_{ISC}$ ).

$$\Phi_{phos} = k_{phos} \times \tau_{phos} \quad (1)$$

$$\Phi_{phos} = \frac{k_{phos}}{\sum k} \quad (2)$$

The radiative decay of organic compounds is typically dominated by emission from singlet excited states because ISC to triplet states is very unfavourable; in fact, converting a singlet excited state to a triplet excited state is referred to as a spin-forbidden process. Due to the forbidden nature of ISC in most organic compounds, emission usually occurs in the form of fluorescence with lifetimes on the order of  $10^{-9}$  s. However, if the rate of ISC can be enhanced, then radiative decay of triplet excited states to give phosphorescence with much longer lifetimes ( $> 10^{-6}$  s) becomes possible. The longer lifetimes associated with phosphorescence are desirable for afterglow applications in persistent luminescence (emergency lighting, traffic signs, anti-counterfeit detection, etc.)<sup>9</sup> as well as for time-gated bioimaging.<sup>10</sup> Furthermore, spin statistics predict that 75 % of all electrically generated excitons (in an OLED) will be of a triplet state, with only 25 % of excited states generated as singlet states. As a consequence, if a system is unable to undergo ISC from singlet to triplet states and/or cannot emit from triplet states, then the theoretical maximum electroluminescent efficiency will be only 25 %.<sup>11</sup> However, phosphorescent materials can undergo ISC and emit light from triplet excited states and therefore have a theoretical maximum electroluminescent efficiency of 100 %.<sup>11</sup> Of note, if a molecule contains triplet and



singlet excited states with very small energy differences, then reverse intersystem crossing can take place to harvest triplet excitons and allow fluorescence to occur with a theoretical maximum efficiency of 100 % (known as thermally activated delayed fluorescence).<sup>12,13</sup>

The most popular method of increasing the rate of ISC to achieve phosphorescence is *via* the heavy atom effect. The incorporation of heavy atoms into a molecule considerably increases the spin-orbit coupling constant ( $\zeta$ ) as shown in Equation 3 ( $n$  = principle quantum number of orbital involved,  $Z$  = atomic number).<sup>14</sup> Spin-orbit coupling facilitates ISC by leading to more effective mixing of singlet and triplet excited states. Therefore, by enhancing spin-orbit coupling, the spin-forbidden nature of ISC (leading to a change in spin multiplicity) becomes relaxed. Thus, heavy atoms enhance the rate of ISC between singlet and triplet excited states and allow for phosphorescence to be a competitive photophysical process.<sup>7,14,15</sup> In the search to find suitable phosphorescent materials to advance light-emitting technologies, research has mainly focused on expensive transition metal complexes based on Ir and Pt centres. A key advance in this area would be the design of phosphors based on less expensive main group elements.

$$\zeta = \frac{0.450 Z^{2.33}}{n^3} \quad (3)$$

Another possible fate of an excited state that has not yet been discussed is quenching, the transfer of the energy of an excited state to another species, preventing

luminescence from occurring. There are two common methods of energy transfer between two species: 1) direct orbital interaction (Dexter), and 2) a through-space coupling of dipoles (Förster). Although quenching is possible from both singlet and triplet excited states, the longer lifetimes of triplet excited states make them especially susceptible to energy transfer quenching pathways.

A common challenge to achieving efficient phosphors is triplet-triplet annihilation, which results when two triplet excited states interact to form a singlet excited state and a ground state. Of note, this process can lead to fluorescence if the singlet excited state that is generated can emit light (known as triplet-triplet annihilation upconversion).<sup>16</sup> Triplet-triplet annihilation can occur between two excited states of the same species (self-quenching) or *via* the interaction of two triplet states from two different species. For example, most phosphors are very sensitive to quenching with molecular O<sub>2</sub>, which exists in its triplet state (<sup>3</sup>O<sub>2</sub>). The quenching pathway results in the production of extremely reactive singlet oxygen (<sup>1</sup>O<sub>2</sub>), with the phosphor returning to the ground state without emitting light.<sup>17</sup> In order to prevent self-quenching and minimize O<sub>2</sub> quenching (which is limited by diffusion), emitters are usually incorporated into a host matrix. Not only does this increase the complexity of OLEDs, but it also introduces a new route for non-radiative decay *via* energy transfer to the host material. Therefore, the design of solid state emitters that are not prone to self-quenching is particularly desirable in the field of OLEDs.<sup>18</sup>

Although close packing of molecules often leads to self-quenching (aggregation-caused quenching, ACQ), in some cases it can actually enhance emission

(aggregation-induced emission, AIE) due to the presence of a rigid environment that suppresses non-radiative decay. Furthermore, dense packing in the solid state can also limit the diffusion of oxygen. As such, designing molecules that emit *via* AIE represents a promising method for achieving higher performance solid state emitters.

The use of heavy main group elements to achieve phosphorescence has been demonstrated for Group 13 heteroles by Chujo and coworkers. These authors studied the emission (both fluorescence and phosphorescence) from heterofluorenes containing Group 13 elements.<sup>19</sup> At room temperature, phosphorescence was only observed from heterofluorenes featuring the heavier atoms Ga and In (compounds **3** and **4**, Figure 1.2), while no phosphorescence was observed from the B and Al analogues **1** and **2** (Figure 1.2). At 77 K, phosphorescence was detected from all four heterofluorenes due to a decrease in molecular motion in the frozen 2-methyltetrahydrofuran (2-MeTHF) matrix, however a clear trend of increasing contribution from triplet excited states to the overall emission was observed from the heterofluorenes containing heavier elements (Figure 1.2). This study suggests that heavy main group elements can unlock room temperature phosphorescence. Of note, phosphors containing other heavy p-block elements, such as Bi,<sup>20-22</sup> and Te, are also known. Phosphorescent molecules incorporating tellurium (Te) will be described later in this Chapter.

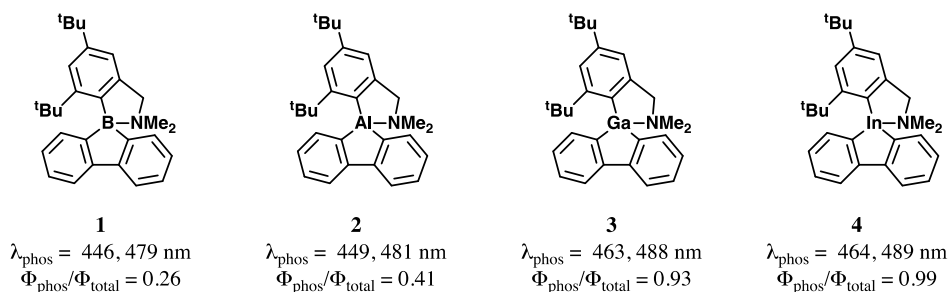


**Figure 1.2** – Heterofluorenes featuring Group 13 elements and their corresponding emission measured in frozen 2-MeTHF (concentration =  $1.0 \times 10^{-4}$  M) under argon at 77 K ( $\Phi_{\text{total}} = \Phi_{\text{phos}} + \Phi_{\text{f}}$ ).<sup>19</sup>

### 1.1.2 Using triplet excitons to increase the efficiencies of organic photovoltaics

Organic photovoltaics (OPVs) are an attractive solution to the world's growing energy demand, providing a potentially inexpensive and flexible alternative to conventional Si-based solar cells.<sup>23</sup> The active layer in an OPV device has two major components: 1) a donor material that absorbs light and generates an exciton (electron-hole pair), and 2) an acceptor material that is able to overcome the binding energy of the exciton and extract the electron. Most OPV studies are focused on thiophene-based polymers as the donor, however these materials typically only generate singlet excitons with diffusion lengths of 3 to 7 nm depending on the degree of crystallinity.<sup>24</sup> As a result, the architecture for most OPV devices relies on an intimate mixing of the donor and acceptor materials on the nanoscale, known as a bulk heterojunction (BHJ), in order for charge separation to be competitive with energy loss through recombination (Figure 1.3). However, the efficiency of a BHJ OPV device is very susceptible to the donor-acceptor blend morphology and any change in morphology that occurs over time. In

this regard, the longer lifetime of triplet excitons have the potential to increase the efficiency of OPV devices in two ways: 1) triplet excitons are able to diffuse over much longer distances ( $> 1 \mu\text{m}$ ) than singlet excitons, increasing the chance of harnessing the energy of the exciton, and 2) obviating the need for intimate mixing of the donor and acceptor layers in a BHJ and moving toward a simplified layered heterojunction device structure. Equation 4 illustrates the direct relationship between exciton diffusion length ( $L_D$ ) and the lifetime of the exciton ( $\tau$ ) ( $Z$  = the number of dimensions considered,  $D$  = the diffusion coefficient).

$$L_D = \sqrt{2ZD\tau} \quad (4)$$

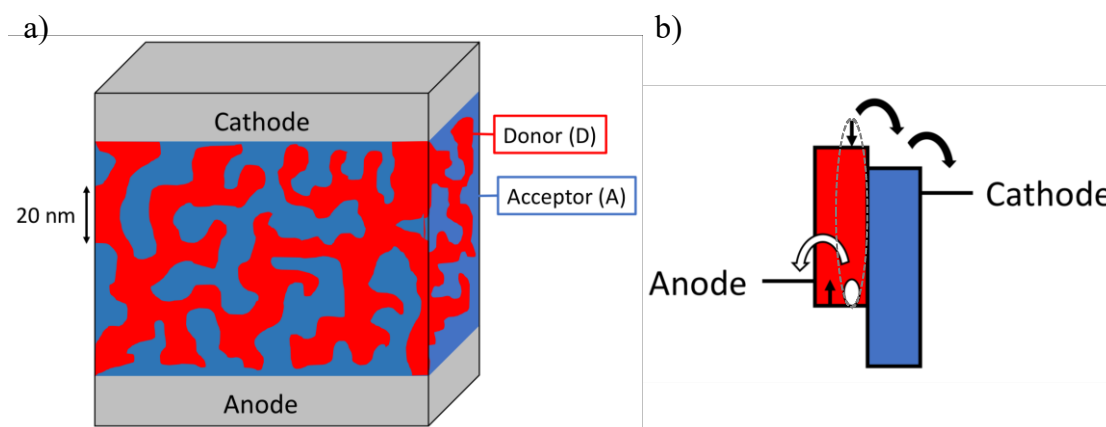


**Figure 1.3** – Simplified representations of: a) the architecture of a bulk heterojunction OPV device, and b) the energy level diagram of an OPV device showing exciton (electron/hole pair) dissociation; red = donor, blue = acceptor.

The efficiency of an OPV device is most often described as the ratio of the maximum power ( $P_{\max}$ ) generated by the device relative to the input power ( $P_{\text{input}}$ ). This is known as the power conversion efficiency (PCE) and is calculated using the experimentally measured short-circuit current density ( $J_{\text{sc}}$ ), open-circuit voltage ( $V_{\text{oc}}$ ), and fill factor (FF) under standard solar irradiation using AM 1.5G 100  $\text{mW}/\text{cm}^2$  (models sunlight travelling through global air mass at mid-latitudes) according to Equation 5. The introduction of a heavy atom is expected to decrease  $V_{\text{oc}}$  due to the smaller optical bandgap of heavy atom-containing compounds, since  $V_{\text{oc}}$  depends on the difference between the LUMO of the donor and the HOMO of the acceptor (Figure 1.4). However, a reduction of the optical bandgap also increases light absorption at longer wavelengths such that more of the sun's energy can be harnessed, generating more excitons.<sup>25</sup> The generation of more excitons from incident solar radiation and the generation of triplet excitons, which can travel over longer distances, are both

anticipated consequences of incorporating heavy atoms into OPVs. Furthermore, both are expected to increase the overall PCE by increasing  $J_{SC}$ .

$$\text{PCE} = \frac{P_{\max}}{P_{\text{input}}} = \frac{J_{SC} \times V_{OC} \times FF}{P_{\text{input}}} \quad (5)$$

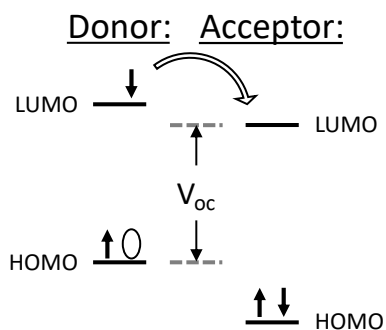


**Figure 1.4** – A depiction of the  $V_{OC}$  as it relates to the HOMO and LUMO levels of the donor and acceptor materials in an OPV device.

Despite these advantages, there are few reports that experimentally investigate the use of triplet excitons in OPV devices, and most focus on palladium and iridium complexes. In one early study, neat PtOEP (PtOEP = 2,3,7,8,12,13,17,18-octaethyl-21*H*,23*H*-porphineplatinum(II)) was used as the donor material in a layered (stacked) heterojunction photovoltaic device with  $C_{60}$  as the acceptor to achieve a PCE of 2.1%.<sup>26</sup> The efficiency of heterojunction devices with different layer thicknesses of PtOEP were studied, and the layer thickness that produced the best PCE was used to estimate an exciton diffusion length ( $L_D$ ) of 30 nm. This diffusion length is much longer than donor materials that produce singlet excitons, like poly(3-hexylthiophene) (P3HT), which typically have  $L_D$  of 3–7 nm.<sup>24</sup> The authors suggest that further improvements to device

efficiency can be achieved if both the charge carrier mobility and lifetime of the triplet exciton are increased in order to achieve even longer diffusion lengths.

Transition metal complexes have also been used as dopants to dramatically increase the short-circuit current density ( $J_{SC}$ ) *via* their ability to form triplet excitons. In one example, an OPV device containing P3HT and PCBM ([6,6]-phenyl-C<sub>61</sub>-butyric acid methyl ester) as the active layer components was doped with Ir(ppy)<sub>3</sub> (fac-tris(2-phenylpyridine) iridium(III)).<sup>27</sup> The authors found that the ideal doping level of Ir(ppy)<sub>3</sub> was 5 wt% leading to a  $J_{SC}$  value over three times greater than the original value for the undoped system. However, at dopant levels above 5 wt% the aggregation of PCBM occurred, resulting in poor device efficiencies since the retention of an ideal phase morphology is necessary for charge extraction. It should be noted that phase aggregation of PCBM is a common challenge and that the field of OPVs has moved beyond PCBM acceptors and towards  $\pi$ -extended molecular species.<sup>28-30</sup> Nevertheless, this early study incorporating transition metal complexes as dopants in OPVs demonstrate that triplet excitons can increase  $J_{SC}$ , but also highlights that many other factors (such as active layer morphology) contribute to the overall efficiency of OPV devices.

Although less studied, the incorporation of heavy main group atoms into OPV devices is becoming more common. The systematic effect of the presence of a heavy Group 14 element in a donor polymer was investigated by Reynolds and coworkers (Figure 1.5).<sup>31</sup> In order to probe the effect of changing a single atom (from C to Ge) the authors used the same synthetic method and work-up for each polymer in order to



achieve similar number average molecular weights and dispersities ( $M_n = 20.8\text{--}26.4$  kDa,  $D = 1.4\text{--}1.7$ ). As shown in Figure 1.5b, the polymer featuring the heaviest atom (Ge) exhibited the highest  $J_{SC}$  value and the best overall PCE, demonstrating that in addition to transition metals, heavy main group elements can also increase PCEs by enhancing  $J_{SC}$  values.

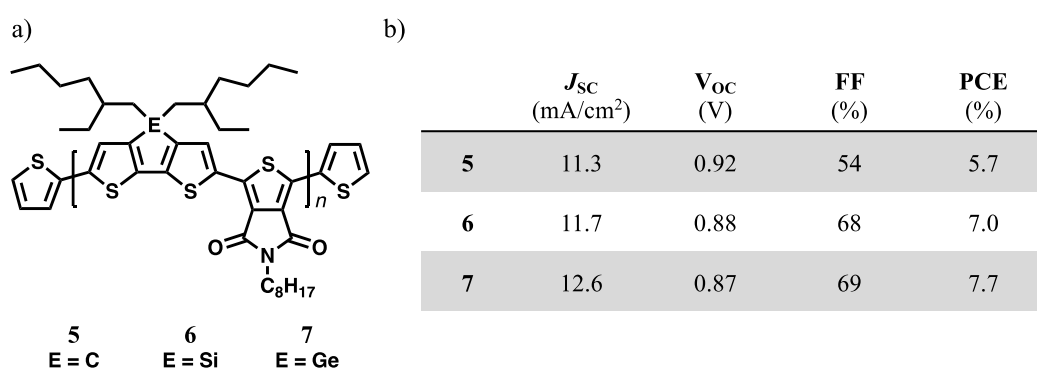


**Figure 1.5** – The donor polymer shown in a) was used to study the influence of the Group 14 element (E) in the dithienyl/heterole subunit on overall OPV device performance, which is summarized in b).

### 1.1.3 Heavy element-containing heterocycles for organic field effect transistors

Although not directly studied in this Thesis, organic field effect transistors (OFETs) are another crucial member of the organic electronic family, comprising the basic building block for flexible, lightweight, solution-processable circuitry. The basic structure of an OFET device is illustrated in Figure 1.6 (bottom-gate, top-contact configuration) featuring an organic semiconductor that allows current to flow from the source to the drain in the presence of an electric field (*i.e.*, when voltage is applied to

the gate). OFETs represent a very active field of study and the development of organic semiconductors for OFETs with charge carrier mobilities ( $\mu$ ) that rival that of polycrystalline Si ( $\mu > 10 \text{ cm}^2 \text{ V}^{-1} \text{ s}^{-1}$ ) has recently been achieved.<sup>2,32</sup> Organic materials are typically p-type semiconductors, and therefore hole mobilities ( $\mu_h$ ) are usually the most relevant parameters discussed in OFETs. However, current challenges that exist in this field include achieving isotropic mobility within the bulk semiconductor, developing inexpensive and efficient synthetic methods, and lastly, developing materials with long-term thermal stability.

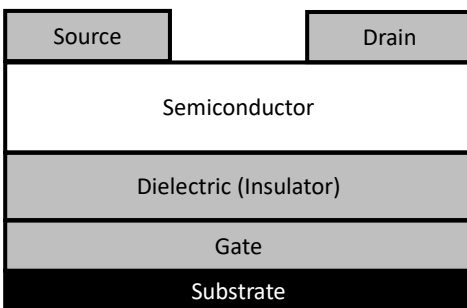


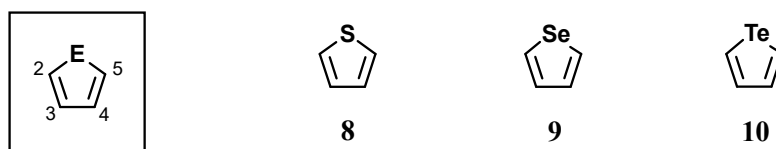
**Figure 1.6** – Configuration of a bottom-gate, top-contact organic field effect transistor.

Ideally, organic semiconductors for OFETs should exhibit intermolecular interactions such that interchain charge transport is possible (*i.e.* charge transport is not limited to one direction such as along a polymer backbone). Thus far, the study of OFETs has been largely focused on planar carbon and/or thiophene-based  $\pi$ -conjugated materials that form  $\pi$ -stacking interactions in the solid state.<sup>2,32</sup> However, the larger size and greater polarizability of heavy atoms make them intrinsically prone to forming stronger element-element interactions. Therefore, the incorporation of heavy atoms

could lead to further enhancement of the charge carrier mobility through increased intermolecular interactions. A discussion on the substitution of heavier group 16 elements on OFET performance is described in section 1.2.6.

## 1.2 Tellurophenes

As discussed previously, there is growing interest in the incorporation of heavy main group elements into optoelectronic devices. Tellurophene (**10**) is the heaviest known Group 16 heterole and is a “big brother” to the ubiquitous thiophene (**8**) moiety in organic electronics (Figure 1.7). In fact, several research groups have recently reviewed the synthesis and use of tellurophenes to access unique semiconductor properties that are not accessible with related S/Se systems.<sup>33-38</sup> This section focuses on the progress and challenges associated with the synthesis of tellurophenes, as well as their application in OLEDs, OPVs, and OFETs.



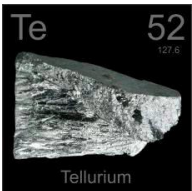


**Figure 1.7** – The structures of chalcogenophenes (**8–10**) with the carbon atoms of the chalcogenophene ring labelled on the left most structure.

### 1.2.1 Reactivity of tellurophenes: highlighting the differences from thiophenes and selenophenes

In contrast to selenium, whose chemistry is often similar to and can be inferred from that of sulfur, the reactivity of tellurium-containing compounds can be substantially different.<sup>39</sup> This is often attributed to significant differences in the atomic radius and electronegativity of the tellurium atom. As shown in Table 1.1, selenium has a larger atomic radius but a similar electronegativity when compared to sulfur, whereas tellurium is much different from sulfur in both aspects. Two important consequences of the larger size and lower electronegativity of tellurium are enhanced polarizability and a greater tendency to form Te...Te interactions.

**Table 1.1** – Properties of sulfur, selenium and tellurium.

|  | Sulfur   | Selenium  | Tellurium   |
|--|--|---|---|
| Images <sup>40</sup>   |  |  |  |
| van der Waals Atomic Radius (Å) <sup>41</sup>                  | 1.80   | 1.90  | 2.06  |
| Pauling Electronegativity <sup>42</sup>                        | 2.58   | 2.55  | 2.10  |
| Ionization Energy (eV) <sup>42</sup>                           | 10.3600  | 9.7524  | 9.0096  |
| Polarizability (Å <sup>3</sup> ) <sup>42</sup>                 | 2.87   | 3.89  | 5.5   |
| E–C bond strengths (kJ/mol) <sup>43</sup>                      | 272  | 234   | 200   |
| Spin-orbit coupling constant (cm <sup>-1</sup> ) <sup>14</sup> | 288  | 1670  | 4480  |

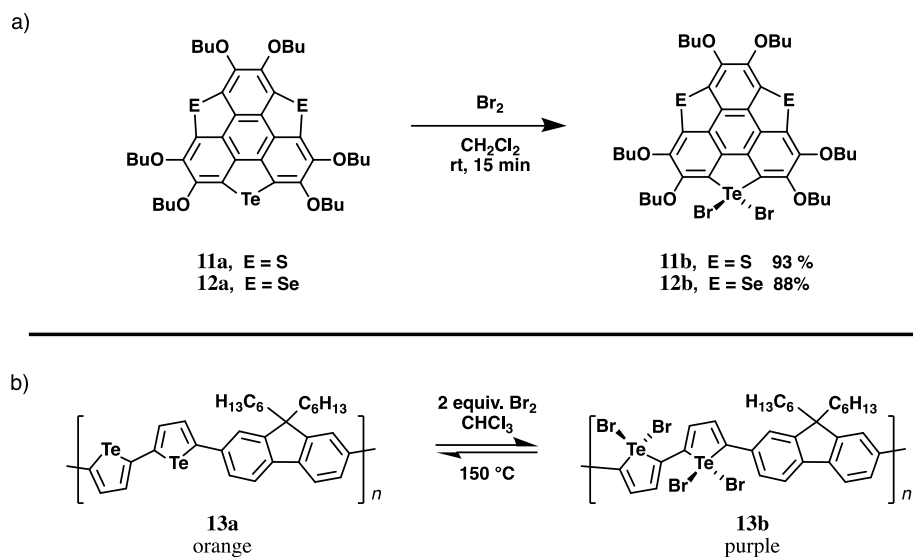
In terms of bonding interactions, the larger, more diffuse orbitals of tellurophene generally result in the formation of weaker bonds with most lighter elements. Table 1.1 illustrates the lowering of the E–C (E = S, Se, Te) bond strength as the Group 16 element becomes heavier. The decreased electronegativity of Te also has implications in the Te–C bond polarities, which invert from  $E^{\delta-}-C^{\delta+}$  for E = S, Se to  $Te^{\delta+}-C^{\delta-}$ .

Although sulfur, selenium, and tellurium are all known to access oxidation states from –2 to +6, the stability of the higher oxidation states increases as the Group 16 element gets heavier.<sup>39</sup> For example, whereas  $SCl_4$  is not thermally stable,  $SeCl_4$  and  $TeCl_4$  are stable isolable solids. However, the higher susceptibility of tellurophenes towards oxidation can be problematic when a compound with a lower oxidation state at Te is targeted.

The differences between sulfur and tellurium result in some interesting implications within a series of five-membered Group 16 heteroles, termed chalcogenophenes (Figure 1.7). First, the optical bandgap of the parent chalcogenophene decreases substantially from 1.9 eV for thiophene (**8**) to 1.44 eV for tellurophene (**10**).<sup>44</sup> Second, although tellurophenes are considered to be aromatic, they have a lower degree of aromaticity than thiophenes/selenophenes (as determined by the relative rates of electrophilic substitution).<sup>45</sup> For example, the early observation that 2,3,4,5-tetraphenyltellurophene ( $TeC_4Ph_4$ ) does not behave like a diyne when subjected to a Diels-Alder reaction with maleic anhydride, but instead remains inert similar to other tetraphenylchalcogenophenes ( $SC_4Ph_4$ ,  $SeC_4Ph_4$ ), offered an early suggestion that tellurophenes have an aromaticity similar to thiophenes and selenophenes.<sup>46</sup>

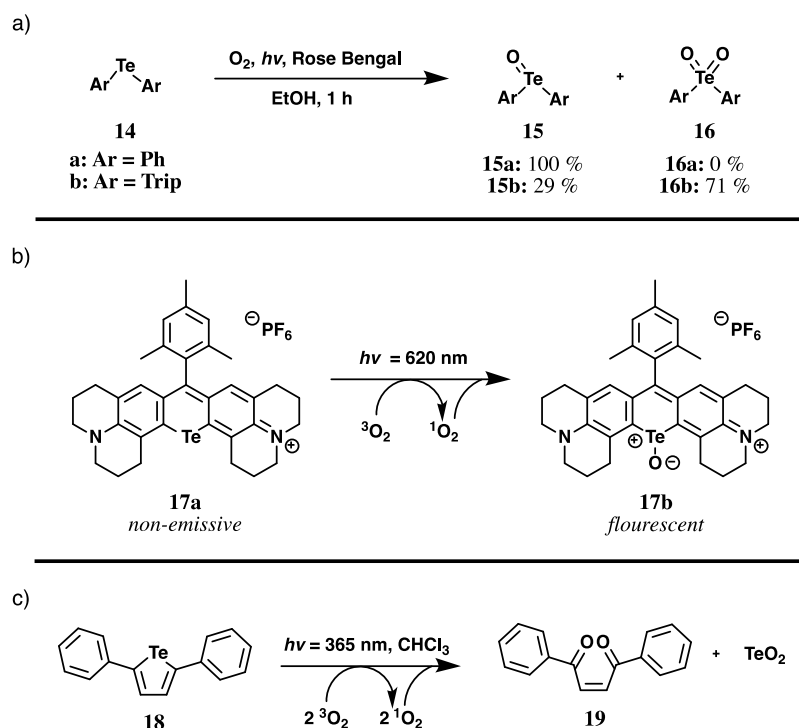
Fringuelli and coworkers were amongst the first researchers to study the reactivity of tellurophenes in detail.<sup>45,47</sup> These authors demonstrated that tellurophenes undergo typical heteroaromatic behaviour such as electrophilic substitution favouring the 2,5-positions of the heterocycle (see Figure 1.7 for the numbering scheme). However, these authors also observed a difference in reactivity between tellurophenes and selenophenes/thiophenes. For example, many reactions that are used to functionalize thiophene and selenophene rings, such as standard conditions for nitration (nitric acid/acetic acid), do not lead to the desired products when applied to tellurophenes (although the authors did not give further details).

Several groups have found that facile oxidation of the Te centre in tellurophenes occurs in the presence of many different halogenating agents ( $\text{Br}_2$ ,  $\text{PhICl}_2$ ,  $\text{ICl}$ ).<sup>48-58</sup> Whereas thiophene can be selectively brominated in the 2,5-positions using  $\text{Br}_2$ , the reaction of  $\text{Br}_2$  with tellurophenes results in the oxidation of the Te centre. The differing reactivity of Te towards  $\text{Br}_2$  relative to S or Se, is also demonstrated in trichalcogenophenesumanenes, which feature a tellurophene ring as well as either two thiophene rings (**11**) or two selenophene rings (**12**); in both **11** and **12**, controlling the stoichiometry of  $\text{Br}_2$  allows for the exclusive bromination at the Te centre in high yields (Scheme 1.1a).<sup>58</sup> Furthermore, the oxidative addition of bromine to tellurophene-containing polymer **13a** yields the Te(IV) polymer **13b**, and is accompanied by a colour change from orange to purple; the elimination of  $\text{Br}_2$  to reform **13a** occurs upon heating to 150 °C (Scheme 1.1b).<sup>48</sup> Other studies have shown that  $\text{Br}_2$  addition to the Te centre in a tellurophene can be reversed upon irradiation with UV or visible light.<sup>50,52,54,56</sup>



**Scheme 1.1** – The reactivity of tellurophenes towards Br<sub>2</sub>.

Tellurophenes are also generally much more reactive towards oxygen than their lighter chalcogen atom counterparts. This is demonstrated by the reaction of Ph<sub>2</sub>Te (**14a**) with O<sub>2</sub> in the presence of a triplet sensitizer (Rose Bengal) to quantitatively form the telluroxide Ph<sub>2</sub>TeO (**15a**). In contrast, both Ph<sub>2</sub>S and Ph<sub>2</sub>Se are inert toward oxygen under these same conditions (Scheme 1.2a).<sup>59</sup> When bulky Trip groups are bound to Te (Trip = 2,4,6-triisopropylphenyl) and the oxidation reaction is conducted in an aprotic solvent, either in dilute solutions or at low temperatures, both the telluroxide (Trip<sub>2</sub>Te(O), **15b**) and the tellurone (Trip<sub>2</sub>Te(O)<sub>2</sub>, **16b**) are formed (Scheme 1.2a).<sup>60</sup> Detty and coworkers also studied the oxidation of diaryltellurides and concluded that electron-withdrawing or electron-donating substituents on the aryl group had little impact on the ability of a diaryltelluride to react with O<sub>2</sub>, possibly due to the poor overlap between the Te-based orbitals and the proximal π-system.<sup>61</sup>



**Scheme 1.2** – a) The oxidation of diaryltellurides ( $\text{R}_2\text{Te}$ ) in the presence of  $\text{O}_2$  and a photosensitizer (Rose Bengal); b) the self-sensitized oxidation of a diaminotelluroxanthylum dye **17a** to produce the fluorescent telluroxide **17b**; c) the self-sensitized oxidation of 2,5-diphenyltellurophene **18** to produce the ene-dione **19** and  $\text{TeO}_2$ .

Unlike diaryltellurides, which require a photosensitizer to produce  $^1\text{O}_2$ , when tellurium is incorporated directly into a heterocyclic  $\pi$ -system, such as in the 6-membered tellurapyrylium compound **17a** (Scheme 1.2b) or 5-membered tellurophenes such as **18** (Scheme 1.2c), the direct reaction with  $\text{O}_2$  becomes possible under UV-light irradiation, obviating the need for a photosensitizer. Utilizing this reactivity, Nagano and coworkers as well as Detty and coworkers have studied the use of tellurapyrylium dyes, such as **17a**, as potential photosensitizers to produce and then react with  $^1\text{O}_2$  to

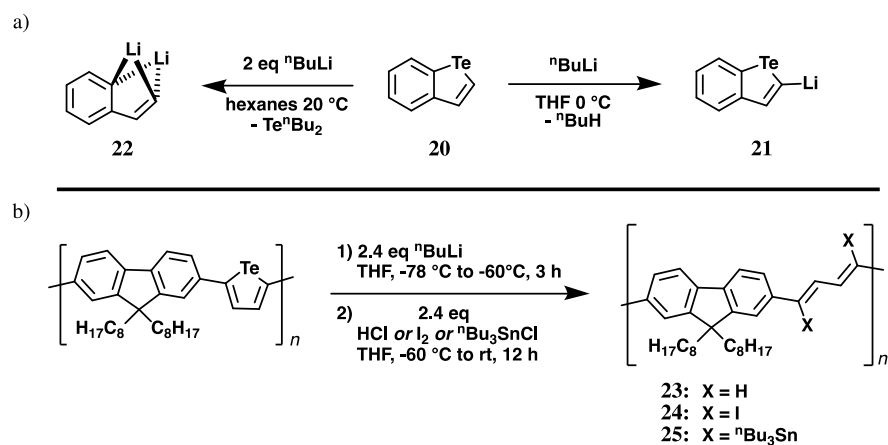


form fluorescent telluroxide compounds (**17b**) for the imaging of live cells (Scheme 1.2b).<sup>62-66</sup> Similarly, Huang and coworkers have demonstrated the use of nanoparticles capped with tellurophene-based semiconducting polymers which form reactive oxygen species (such as cytotoxic  $^1\text{O}_2$ ) for cancer theranostic applications.<sup>67</sup>

In 2010, Seferos and coworkers reported the photochemical decomposition of 2,5-diphenyltellurophene (**18**) leading to the extrusion of  $\text{TeO}_2$  in the presence of oxygen.<sup>68</sup> Contrary to Ando's observation with  $\text{Ph}_2\text{Te}$ , where oxidation occurred exclusively at the Te centre (**14a/b** in Scheme 1.2a), the oxidation of 2,5-diphenyltellurophene occurs to produce the ene-dione **19** with loss of tellurium in the form of  $\text{TeO}_2$  (Scheme 1.2). Interestingly, the chemical oxidation of 2,5-diphenyltellurophene with *m*-CPBA (*meta*-chloroperoxybenzoic acid) also produces  $\text{TeO}_2$  and the ene-dione (**19**), however an intermediate consistent with a telluroxide ( $\text{TeO}$ ) was detected by the emergence of a red-shifted UV-vis absorbance peak, as well as *via*  $^1\text{H}/^{125}\text{Te}$  NMR spectroscopy.

Another important difference in reactivity between tellurophenes and thiophenes is the ability of the former to undergo a Te/Li exchange, as first observed by Winter and coworkers.<sup>69</sup> While the 2,5-positions of thiophenes can be readily lithiated with  $^n\text{BuLi}$ , leaving the S atom intact, Te/Li exchange occurs readily under the right conditions. Maercker and coworkers established that the treatment of benzotellurophene **20** with  $^n\text{BuLi}$  in THF gave the lithiated product **21** in high yield, whereas treatment of **20** with  $^n\text{BuLi}$  in hexanes results in Te/Li exchange to produce the pyrophoric dilithio compound **22** (Scheme 1.3a).<sup>70</sup> This Te/Li exchange reaction was

recently used by Tomita and coworkers to synthesize a variety of element-containing polymers by first lithiating a tellurophene-containing polymer in THF with  $n\text{BuLi}$  and then adding the appropriate electrophile to synthesize polymers **23–25** (Scheme 1.3b).<sup>71</sup>

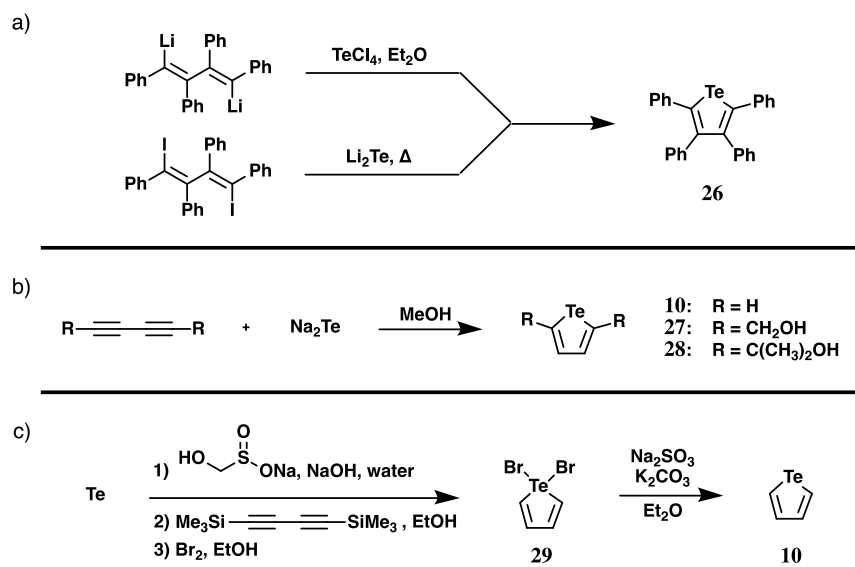


**Scheme 1.3** – Te/Li exchange reactions involving tellurophenes.

### 1.2.2 Synthesis of tellurophenes

The first tellurophene reported in the literature was 2,3,4,5-tetraphenyltellurophene (**26**, Scheme 1.4a).<sup>46</sup> In this early report by Braye and coworkers (1961), two related routes for the synthesis of **26** were reported: 1) reaction of  $\text{TeCl}_4$  with 1,4-dilithio-1,2,3,4-tetraphenylbutadiene, and 2) reaction of  $\text{Li}_2\text{Te}$  with 1,4-diiodo-1,2,3,4-tetraphenylbutadiene (Scheme 1.4a). The first known synthesis of the parent tellurophene (**10**), as well as water-soluble tellurophenes featuring alcohol side groups (**27** and **28**, Scheme 1.4b) were reported by Mack in 1966 *via* the reaction of the requisite diacetylene with sodium telluride ( $\text{Na}_2\text{Te}$ ).<sup>72</sup> The lack of synthetic details and the irreproducible high yield reported by Mack led many others to report

modifications to this procedure. Of note, Fringuelli highlighted the many challenges associated with Mack's initial synthetic route to the parent tellurophene (**10**) including the highly reactive nature of the reaction mixture towards air and moisture, the facile oxidation/polymerization that can occur with butadiyne, and sensitivity of the product yield toward the source of Te (amorphous *vs* crystalline).<sup>47</sup> Barton and Roth set out to circumvent the use of the extremely reactive reagent butadiyne by reacting Na<sub>2</sub>Te with 1,3-bis(trimethylsilyl)-1,3-butadiyne instead, affording the parent tellurophene due to *in situ* cleavage of the C–Si bonds with the basic reaction conditions involved (*i.e.*, Na<sub>2</sub>Te in methanol).<sup>73</sup> Praefcke and coworkers further simplified the procedure by reporting the successful reaction between bis(trimethylsilyl)-1,3-butadiyne and Na<sub>2</sub>Te, with the Na<sub>2</sub>Te generated *in situ* from tellurium and sodium formaldehydesulfoxylate (Scheme 1.4c). These authors also added Br<sub>2</sub> to the reaction mixture, enabling them to isolate the non-volatile brominated tellurophene **29**, which was converted into the parent tellurophene (**10**) upon reaction with sodium sulphite and potassium carbonate with an improved overall yield of up to 59 % (Scheme 1.4c).<sup>74</sup>

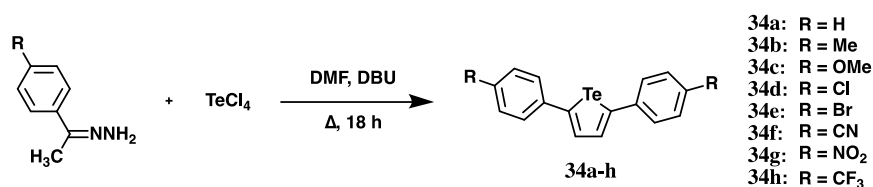


**Scheme 1.4** – Early reports of the synthesis of tellurophenes.

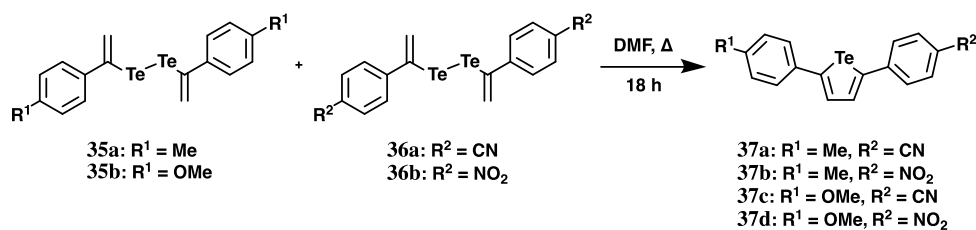
Due to the complicated nature and low yields generally associated with synthesizing tellurophenes from  $\text{Na}_2\text{Te}$  and butadiynes, there was considerable interest in finding an alternative synthetic route. One possibility is to insert a Te atom into a pre-existing heterocycle *via* transmetallation. In 1975, Müller and coworkers were the first to do this by preparing tellurophenes *via* transmetallation from a rhodium-containing heterocycle (**30**); this methodology allowed for the synthesis of more complex tellurophenes, including those with ketonic groups (**31**, Scheme 1.5).<sup>75,76</sup> In 1988 Fagan and Nugent demonstrated that readily accessible zirconacycles could serve as extremely efficient precursors to main group heterocycles,<sup>77</sup> and this methodology was later expanded to include the substitution of the  $\text{Cp}_2\text{Zr}$  group for almost any main group element ( $\text{Cp} = \eta^5\text{-C}_5\text{H}_5$ ).<sup>78</sup> In 2013, Rivard and coworkers were the first to apply Fagan and Nugent's transmetallation of zirconacycles as a route to form tellurophenes, regenerating the zirconocene source  $\text{Cp}_2\text{ZrCl}_2$  in the process, such that it can be recycled



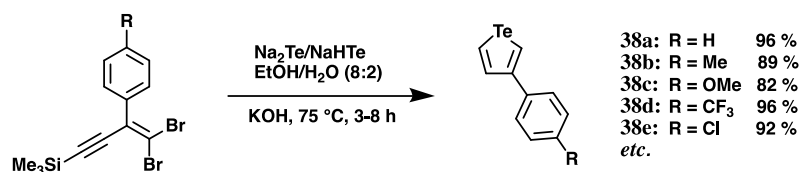
featuring both electron-deficient and electron-rich aryl substituents in order to achieve a “push-pull” system.<sup>81</sup> This was accomplished through arylvinyl exchange between two different starting ditellurides in refluxing DMF, followed by intramolecular cyclization of the vinyl groups to yield an unsymmetric tellurophene (Scheme 1.8). In another recent example, the direct synthesis of 3-substituted tellurophenes (**38a–e**) was accomplished in high yields by Han and coworkers through a multi-step cascade reaction between 1,1-dibromo-1-en-3-yne and telluride salts (Scheme 1.9).<sup>82</sup>



**Scheme 1.7** – The synthesis of 2,5-diaryltellurophenes *via* hydrazones; DBU = 1,8-diazabicyclo[5.4.0]undec-7-ene.<sup>80</sup>



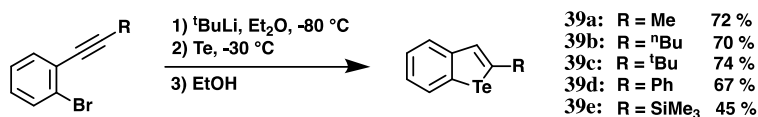
**Scheme 1.8** – Synthesis of push-pull tellurophenes *via* an aryl-exchange followed by an intramolecular cyclization of ditellurides.<sup>81</sup>



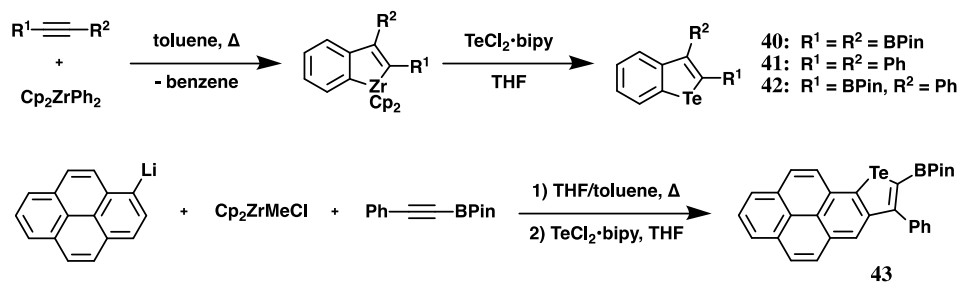
**Scheme 1.9** – Synthesis of 3-aryltellurophenes as described by Han and coworkers.<sup>82</sup>

### 1.2.3 Synthesis of $\pi$ -extended tellurophenes

Tellurium-lithium exchange has long-since been a popular method to synthesize benzotellurophenes.<sup>83-88</sup> Sahshida and coworkers used this reaction to develop a versatile three-step, one-pot procedure for the high-yielding synthesis of benzotellurophenes from *o*-bromoethynylbenzene derivatives, which are readily accessible from the Pd-catalyzed reaction of *o*-bromoiodobenzene with 1-substituted alkynes (Scheme 1.10).<sup>89</sup> Rivard and coworkers also developed a synthesis of benzotellurophenes by heating Cp<sub>2</sub>ZrPh<sub>2</sub> in the presence of an alkyne to form a benzozirconacycle, which can yield the benzotellurophene upon transmetalation with TeCl<sub>2</sub>•bipy (bipy = 2,2'-bipyridine, Scheme 1.11).<sup>90</sup> In 2019, Rivard and coworkers expanded this methodology to allow for the synthesis of tellurophenes with multiple-fused acene rings, including the pyrene analogue **43** shown in Scheme 1.11.<sup>91</sup>



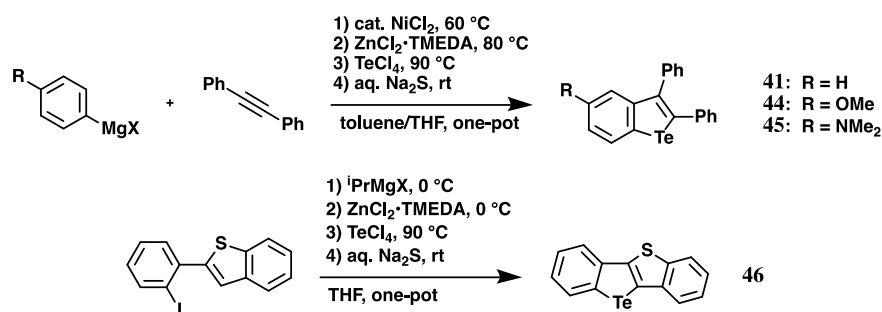
**Scheme 1.10** – Synthesis of benzotellurophenes (**39a–e**) *via* a lithiated aryl intermediate, as developed by Sashida and coworkers.<sup>89</sup>



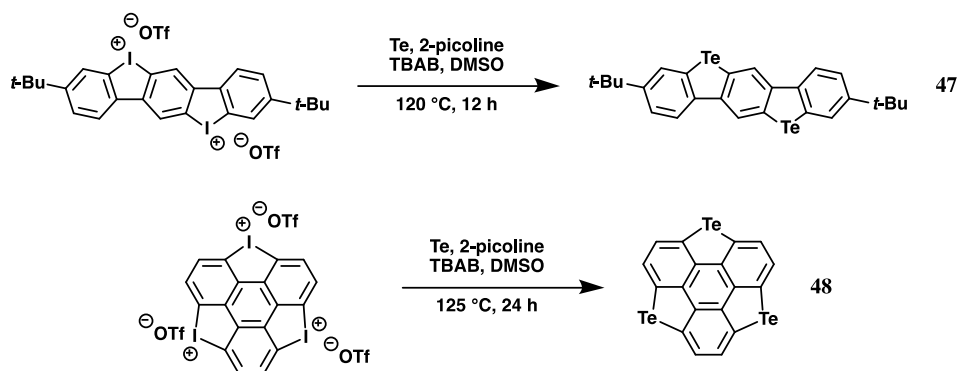
**Scheme 1.11** – Synthesis of benzotellurophenes (**40–42**) as well as tellurophenes fused with larger heteroacenes (*e.g.*, pyrene), as developed by Rivard and coworkers; bipy = 2,2'-bipyridine.<sup>90,91</sup>

Recently, Yoshikai and coworkers successfully achieved the electrophilic telluration of  $C(sp^2)$ -Zn bonds (generated *in situ* from aryl Grignard reagents), which subsequently undergo a transmetalation reaction with  $TeCl_4$ . The resulting aryltelluride participates in an intramolecular cyclization *via* activation of a neighbouring  $C(sp^2)$ -H bond in the presence of  $Na_2S$  to afford Te heterocycles (Scheme 1.12).<sup>92</sup> This method was used to synthesize a library of Te-bridged aromatic systems, including the Te-bridged molecule **46** shown in Scheme 1.12. Furthermore, diaryliodonium salts have been shown to be valuable precursors to tellurium-containing heterocycles including the ladder-type compound **47** as well as the tellurasumanene **48** (Scheme 1.13).<sup>93</sup>





**Scheme 1.12** – The synthesis of  $\pi$ -extended tellurophenes *via* arylzinc precursors as reported by Yoshikai and coworkers; TMEDA =  $N,N,N',N'$ -tetramethylethylenediamine.<sup>92</sup>



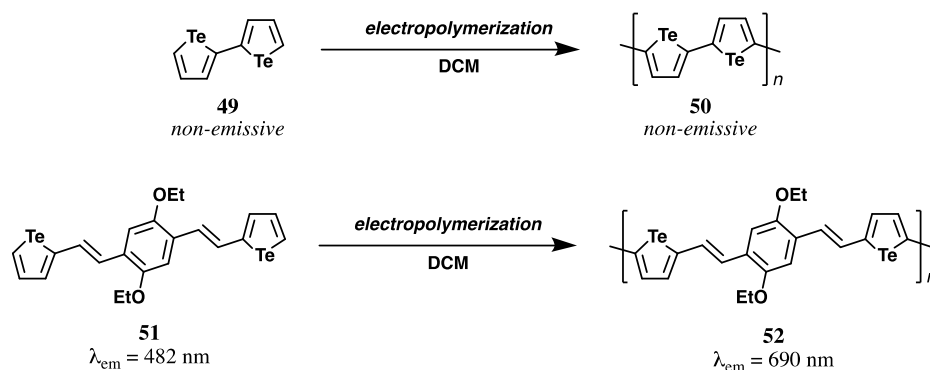
**Scheme 1.13** – The synthesis of  $\pi$ -extended tellurophenes **47** and **48** *via* diaryliodonium salts as reported by Xu and coworkers; TBAB =  $[\text{N}(\text{nBu})_4][\text{Br}]$ .<sup>93</sup>

### 1.2.4 Coaxing room temperature phosphorescence from tellurophenes

Due to the heavy nature of the Te atom, many tellurium-containing compounds are known to exhibit weaker fluorescence behaviour than their lighter congeners, at the expense of either emission or non-radiative decay from triplet excited states (accessed *via* intersystem crossing).<sup>94-96</sup> Nevertheless, many examples of fluorescent compounds with a Te atom incorporated into  $\pi$ -systems exist in the literature.<sup>62,66,96-99</sup> One notable

family of fluorescent Te-containing compounds are oxidized tellurapyrylium dyes based on a rhodamine scaffold, such as compound **17b** mentioned earlier in this Chapter (Scheme 1.2).<sup>62-66</sup>

In regard to the five-membered tellurophenes, push-pull type 2,5-diaryltellurophenes (**37a–d**, Scheme 1.8) exhibit weak fluorescence ( $\Phi_F \leq 2.3\%$ ).<sup>81</sup> Furthermore, Data and coworkers showed that, while 2,2'-bitellurophene (**49**) and its corresponding polymer (**50**) are non-emissive, both **51** and **52** are luminescent with emission maxima at 482 and 690 nm respectively (Scheme 1.14).<sup>97</sup>



**Scheme 1.14** – Electropolymerization of tellurophene-capped monomers **49** and **51** to form polytellurophenes **50** and **52**, respectively, as described by Data and coworkers.<sup>97</sup>

The earliest reported investigation of phosphorescence from tellurophenes was in 1989, when light emission from benzo- and dibenzochalcogenophenes was detected in frozen EtOH at 77 K.<sup>100</sup> As shown in Figure 1.8, the quantum yield of fluorescence ( $\Phi_F$ ) decreases and the quantum yield of triplet formation ( $\Phi_T$ ) increases for the

heterocycles bearing heavier Group 16 elements, giving rise to the first report of tellurophenes (**56** and **60**, Figure 1.8) exhibiting phosphorescence.

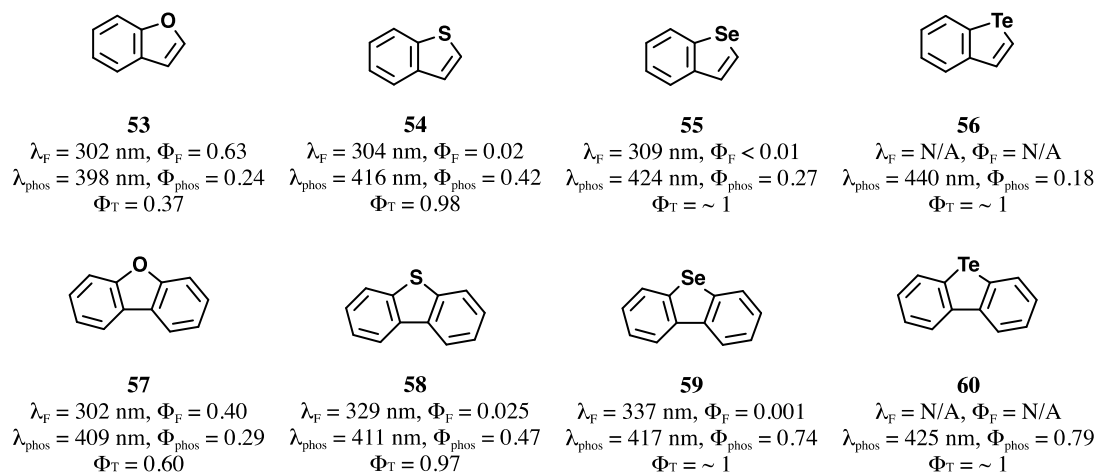


**Figure 1.8** – Photoluminescence data including quantum yield of fluorescence ( $\Phi_F$ ), quantum yield of phosphorescence ( $\Phi_P$ ), and the quantum yield of triplet formation ( $\Phi_T$ ) for benzo- and dibenzochalcogenophenes measured at 77 K in EtOH.<sup>100</sup>

In 2014, Rivard and coworkers reported the first examples of room temperature phosphorescence (RTP) from tellurophenes in the solid state (**33**, **61–64**, Figure 1.9).<sup>51</sup> Shortly thereafter, the library of phosphorescent tellurophenes was expanded to include benzotellurophenes (**40–42**, **67**, **71**, **72**, **74**) and 2,5-diaryltellurophenes (**66–70**), enabling the modulation of emission from green to orange (Figure 1.9).<sup>55,90,91,101</sup> Xu and coworkers also synthesized three dibenzotellurophenes (**75–77**) that exhibit RTP in the solid state (Figure 1.10) as well as other derivatives that were emissive at 77 K.<sup>93</sup> Seferos and coworkers reported the first example of phosphorescence from a Te-

containing polymer (**78**) with an emission maxima ( $\lambda_{em}$ ) of 671 nm in a deaerated chloroform solution (Scheme 1.15).<sup>96</sup>

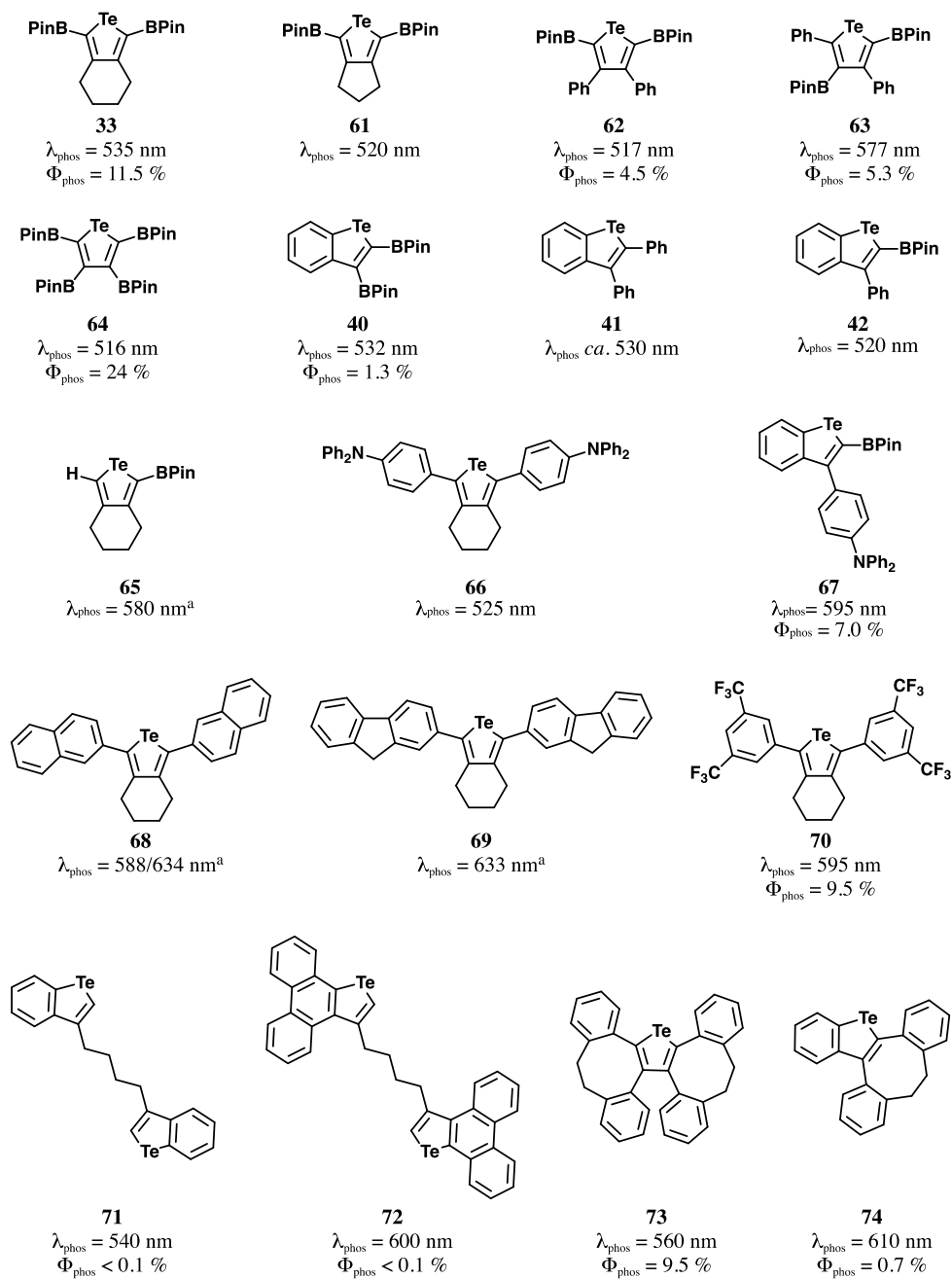


**Figure 1.9** – Selected phosphorescent tellurophenes developed by Rivard and coworkers (<sup>a</sup>luminescence was only observed at 77 K).<sup>51,55,90,91,101</sup>

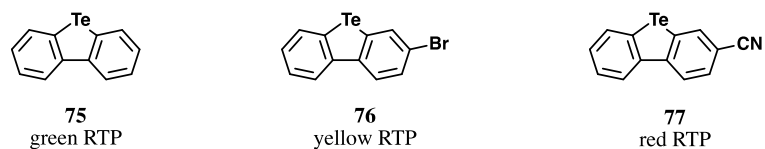
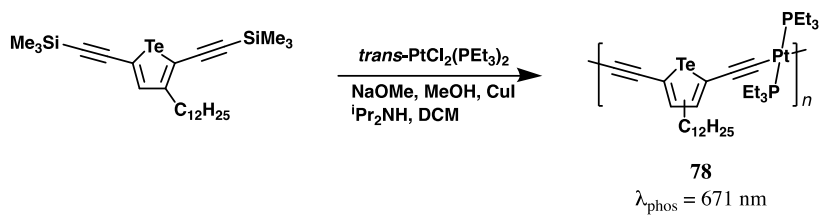


**Figure 1.10** – Dibenzotellurophenes **75–77** synthesized by Xu and coworkers exhibiting RTP.<sup>93</sup>



**Scheme 1.15** – Synthesis of a phosphorescent platinum-acetylide tellurophene copolymer.<sup>96</sup>

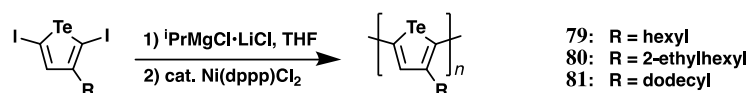
### 1.2.5 Tellurophene-based organic photovoltaics

An active field of study for tellurophenes is their use in enhancing OPV performance. Until recently, the most studied OPV devices were based on poly(3-hexylthiophene) (P3HT) and [6,6]-phenyl- $\text{C}_{61}$ -butyric acid methyl ester (PCBM) as donor and acceptor materials, respectively. This donor-acceptor combination quickly became a benchmarking system in OPV research. The success of P3HT can be attributed to its ability to be synthesized reproducibly in high molecular weights with low dispersities ( $D$ ) and excellent regioregularity. However to date, solar cells based on P3HT/PCBM have never achieved a PCE > 5 % and thus further improvements in optical absorption and hole mobility are necessary to advance the use of chalcogenophene polymers in this field.<sup>102</sup> In particular, lowering the optical bandgap in order to improve the absorption of incident solar irradiation has been actively

explored.<sup>25</sup> Two main strategies have been identified to lower the optical bandgap of polychalcogenophenes, including: 1) the synthesis of materials with alternating electron-donor and electron-acceptor moieties along the polymer backbone, and 2) substitution of S for a heavier element such as Se or Te. Both approaches are designed to raise the HOMO and lower the LUMO, thereby decreasing the optical bandgap and allowing for the absorption of lower energy sunlight. While a lot of research has focused on the donor-acceptor approach and has allowed for devices with PCEs as high as 16.5 %, <sup>103</sup> much less attention has been paid to heavy atom substitution.

The first poly(3-alkyltellurophene)s (**79–81**, analogous to the ubiquitous poly(3-hexylthiophene)) were synthesized by Seferos and coworkers using both electropolymerization and Kumada Catalyst-Transfer Polycondensation (KCTP) to give polymers with modest number average molecular weights ( $M_n$ ) of 5.4–11.3 kDa (Scheme 1.16).<sup>44</sup> These tellurium-containing polymers exhibited the expected red-shift in optical absorbance, giving rise to an optical bandgap of 1.44 eV for poly(3-hexyltellurophene) (**79**), which is substantially smaller than that of P3HT (2.0 eV).<sup>104</sup> The low solubility of **79** prevented the determination of its regioregularity, but the more soluble polymer **81** with dodecyl side groups was obtained with a high degree of regioregularity (93 %), as determined by <sup>1</sup>H NMR spectroscopy. The significantly lower  $\Phi_F$  for the selenophene and tellurophene analogues of P3HT (0.0042 and 0.00014, respectively) in comparison to P3HT itself ( $\Phi_F = 0.30$ ), lends indirect support for the formation of triplet excitons upon irradiating the Se- and Te-containing polymers.<sup>105</sup>

Seferos and coworkers also studied the effect of temperature and solubility on the controlled polymerization of 3-alkyltellurophenes *via* KCTP (Scheme 1.16).<sup>106</sup> Although higher temperatures can be used sometimes to improve solubility and allow for longer polymer chain lengths, it can also increase the favourability of catalyst dissociation, leading to early chain termination. The authors also determined that the inclusion of longer alkyl side chains led to higher  $M_n$  values, and that alkyl side chains with branching sites in close proximity to the tellurophene ring (*e.g.*, 2-ethylhexyl in **80**) were detrimental to the kinetics of polymerization.



**Scheme 1.16** – The first reported synthesis of poly(3-alkyltellurophene)s by Seferos and coworkers; dppp = bis(diphenylphosphino)propane.<sup>44</sup>

Soon after, Kang and coworkers independently synthesized poly(3-dodecyltellurophene) (**81**) *via* Suzuki-Miyaura polycondensation, with a regioregularity of 87%.<sup>107</sup> These authors were the first to report the incorporation of a polytellurophene into an OPV device. Unfortunately, the resulting **81**/PC<sub>71</sub>BM donor/acceptor active layer gave a maximum PCE of only 1.1%. Seferos and coworkers also incorporated their polytellurophenes into OPV devices. In order to make direct comparisons between poly(3-alkyltellurophene)s and the lighter poly(3-alkylselenophene)s and poly(3-alkylthiophene)s, a series of polymers with similar molecular weights, dispersities, and regioregularities were synthesized using 3,7-dimethyloctyl as the side chain (**82–84**,

Figure 1.11).<sup>108</sup> However, of the resulting OPV devices constructed using PC<sub>71</sub>BM as the acceptor, the polytellurophene **84** exhibited both the lowest  $V_{oc}$  and the lowest  $J_{sc}$ , giving rise to the worst PCE of the poly(3-alkylchalcogenophene) series (Table 1.2). The same trend was observed for both a BHJ as well as a planar heterojunction device architecture.

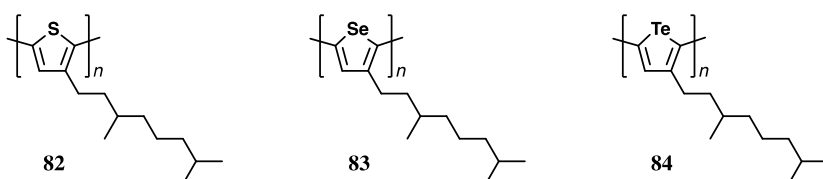


**Figure 1.11** – Poly(3-alkylchalcogenophene)s incorporated into OPV devices by Seferos and coworkers.<sup>108</sup>

**Table 1.2** – OPV device parameters using poly(3-alkylchalcogenophene)s and PC<sub>71</sub>BM as the active layer components;  $M_n$  values given in units of kDa.<sup>108</sup>

| Donor     | $M_n$ (kDa) | $E_g$ (eV) | structure | $V_{oc}$ (V) | $J_{sc}$ (mA cm <sup>-2</sup> ) | PCE (%) |
|-----------|-------------|------------|-----------|--------------|---------------------------------|---------|
| <b>82</b> | 41.0 (1.2)  | 1.91       | BHJ       | 0.67         | 4.11                            | 1.18    |
|           |             |            | planar    | 0.63         | 2.21                            | 0.64    |
| <b>83</b> | 39.0 (1.2)  | 1.65       | BHJ       | 0.67         | 4.74                            | 1.65    |
|           |             |            | planar    | 0.55         | 1.96                            | 0.52    |
| <b>84</b> | 36.6 (1.2)  | 1.45       | BHJ       | 0.59         | 3.69                            | 1.02    |
|           |             |            | planar    | 0.43         | 1.23                            | 0.25    |

Other groups have explored the effect of substituting heavier Group 16 elements within the donor polymer of an OPV device. Grubbs and coworkers synthesized the tellurophene-containing molecules (**85–87**) and polymer (**88**) via ipso-arylation



coupling, both of which were studied as donor components in the active layer of an OPV device (Scheme 1.17).<sup>109,110</sup> Devices containing small molecules featuring different chalcogens (**85–87**, Figure 1.12) and PC<sub>71</sub>BM all behaved similarly, although tellurophene **87** resulted in the lowest PCE (Table 1.3). The Te-containing polymer **88** was also synthesized and compared to the previously reported thiophene analogue **89**.<sup>111</sup> Encouragingly, **88** did show an enhancement in the photoresponse at longer wavelengths than **89**, however this only resulted in a slight increase in  $J_{sc}$  and a similar PCE to that of **89** (Table 1.4). However, care should be taken when making direct comparisons between **88** and **89** because they were synthesized from different methods, leading to polymers with significantly different  $M_n$  values; moreover the devices were built using different electron- and hole-transporting layers (Scheme 1.17, Table 1.4).

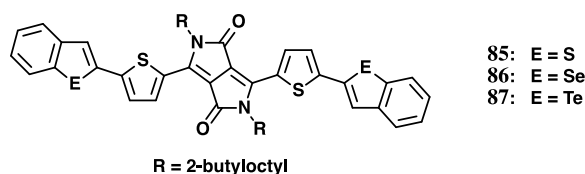
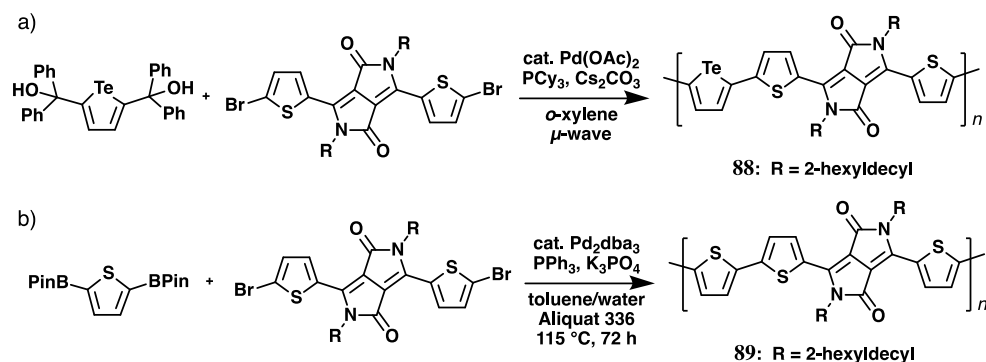


**Figure 1.12** – Chalcogenophene-containing small molecules studied as donor materials in OPVs.<sup>109</sup>

**Table 1.3** – OPV device parameters using active layers comprised of PC<sub>61</sub>BM as the acceptor and small molecules chalcogenophenes **85–87** as the donor.<sup>109</sup>

|           | $E_g$ (eV) | structure | $V_{oc}$ (V) | $J_{sc}$ (mA cm <sup>-2</sup> ) | PCE (%) |
|-----------|------------|-----------|--------------|---------------------------------|---------|
| <b>85</b> | 1.74       | BHJ       | 0.94         | 9.2                             | 4.2     |
| <b>86</b> | 1.71       | BHJ       | 0.98         | 13.2                            | 5.8     |
| <b>87</b> | 1.66       | BHJ       | 0.88         | 6.6                             | 3.0     |



**Scheme 1.17** – The synthesis of chalcogenophene-containing polymers **88** and **89** studied as donor materials in OPVs.<sup>110,111</sup>

**Table 1.4** – OPV device parameters comparing **88** to its previously reported thiophene analogue **89**;  $M_n$  values given in units of kDa.<sup>110,111</sup>

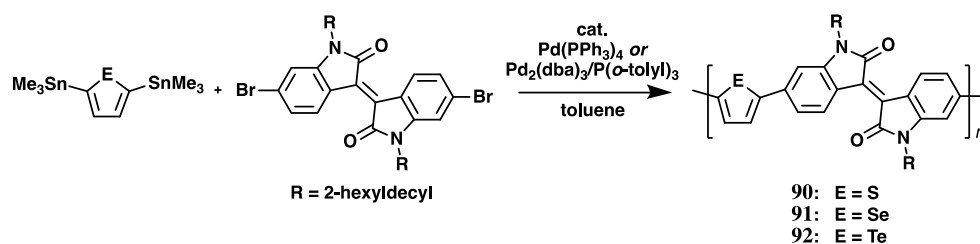
|                       | $M_n$<br>( $\bar{D}$ ) | $E_g$<br>(eV) | structure | $V_{oc}$<br>(V) | $J_{sc}$<br>(mA cm <sup>-2</sup> ) | PCE<br>(%) |
|-----------------------|------------------------|---------------|-----------|-----------------|------------------------------------|------------|
| <b>88<sup>a</sup></b> | 23.2<br>(3.7)          | 1.28          | BHJ       | 0.61            | 12.9                               | 4.4        |
| <b>89<sup>b</sup></b> | 54.0<br>(3.15)         | 1.36          | BHJ       | 0.65            | 11.8                               | 4.7        |

<sup>a</sup> Device structure: (ITO/MoO<sub>x</sub>/**88**:PC<sub>71</sub>BM/TiO<sub>x</sub>/Al)

<sup>b</sup> Device structure: (ITO/PEDOT:PSS/**89**:PC<sub>71</sub>BM/LiF/Al)

Tellurophene-containing polymers were also synthesized *via* Stille polycondensation to produce polymers **90–95** (Schemes 1.18 and 1.19)<sup>112,113</sup> These polymers were incorporated as donor materials in BHJ OPV devices using fullreene acceptors (Tables 1.5 and 1.6). For the polymeric series **90–92**, the selenium-containing polymer **91** outperformed both the sulfur and tellurium analogues (**90** and **92**, respectively), due to the expected enhancement of  $J_{sc}$ ;<sup>112</sup> surprisingly the  $J_{sc}$  is not further enhanced with tellurium. Despite the clear trend in reduced optical bandgaps for the Te-containing donor materials, this has not yet been translated into enhanced device

performance. For polymers **93–95** (Scheme 1.19), impressive PCEs approaching 9 % were achieved for inverted devices that contained a ZnO electron-transport layer treated with 1 % ethylamine in 2-methoxyethanol, which serves as an interfacial contact to facilitate charge transport.<sup>113</sup> Although similar PCEs were achieved for each of the devices, the Te-containing polymer **95** required a higher PCBM ratio in order to obtain comparable results. Nevertheless, the OPV device with **95** did achieve a PCE of 7.1 %, which is the highest value for any OPV using a tellurophene-containing donor material (Table 1.6).

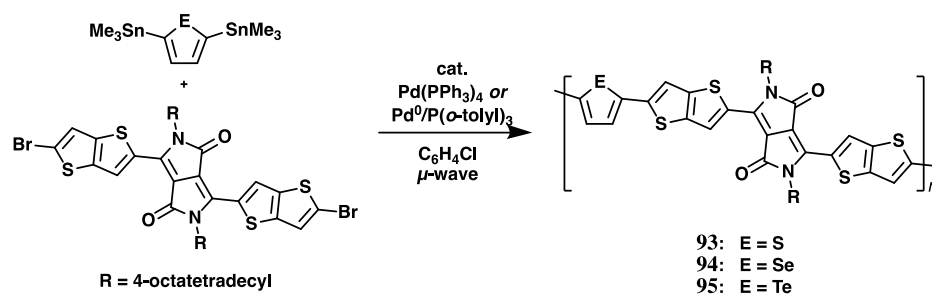


**Scheme 1.18** – Chalcogenophene-containing polymers **90–92** developed as donor materials for OPVs.<sup>112</sup>

**Table 1.5** – OPV device parameters using active layers comprised of PC<sub>61</sub>BM as the acceptor and polymers **90–92** as the donor; M<sub>n</sub> values given in units of kDa.<sup>112</sup>

|           | M <sub>n</sub> (Đ) | E <sub>g</sub> (eV) | Ratio <sup>a</sup> | V <sub>oc</sub> (V) | J <sub>sc</sub> (mA cm <sup>-2</sup> ) | PCE (%) |
|-----------|--------------------|---------------------|--------------------|---------------------|--|---------|
| <b>90</b> | 86 (1.55)          | 1.62                | 1:1                | 0.91                | 7.71                                   | 3.98    |
| <b>91</b> | 108 (1.51)         | 1.58                | 1:1                | 0.95                | 10.21                                  | 5.72    |
| <b>92</b> | 47 (1.60)          | 1.53                | 1:4                | 0.92                | 2.51                                   | 1.16    |

<sup>a</sup> Ratio of donor polymer to PC<sub>61</sub>BM



**Scheme 1.19** – Chalcogenophene-containing polymers developed as donor materials for OPVs.<sup>113</sup>

**Table 1.6** – OPV device parameters using active layers comprised of PC<sub>71</sub>BM as the acceptor and polymers **93–95** as the donor; M<sub>n</sub> values given in units of kDa.<sup>113</sup>

|           | M <sub>n</sub> (Đ) | E <sub>g</sub> (eV) | Ratio <sup>a</sup> | V <sub>oc</sub> (V) | J <sub>sc</sub> (mA cm <sup>-2</sup> ) | PCE (%) |
|-----------|--------------------|---------------------|--------------------|---------------------|--|---------|
| <b>93</b> | 80 (1.9)           | 1.39                | 1:1                | 0.57                | 23.5                                   | 8.8     |
| <b>94</b> | 95 (2.5)           | 1.37                | 1:1                | 0.56                | 21.5                                   | 7.6     |
| <b>95</b> | 91 (3.0)           | 1.32                | 1:1                | 0.62                | 19.7                                   | 6.3     |
|           |                    |                     | 1:3                | 0.63                | 21.7                                   | 7.1     |

<sup>a</sup> Ratio of donor polymer to PC<sub>71</sub>BM

Huang and coworkers are currently the only researchers to have investigated the use of tellurophene-based acceptors in the hope of being able to harvest long-lived triplet excitons. Their investigation began with copolymers **96–98** containing a tellurophene unit and either a perylene diimide (PDI) or a naphthalene diimide (NDI) unit (Figure 1.13). Although only modest PCEs up to 4.3 % were obtained (Table 1.7), encouraging evidence for strong  $\pi$ - $\pi$  interactions facilitating bulk charge transport was observed.<sup>57</sup> Next, Huang and coworkers synthesized small molecule tellurophene-based

acceptors that had different levels of ring fusion with the PDI units (**99–101**, Figure 1.14).<sup>114</sup> These acceptors achieved excellent PCEs of up to 7.5 % when incorporated into an OPV device, the highest for any tellurophene containing OPV device (Table 1.8).

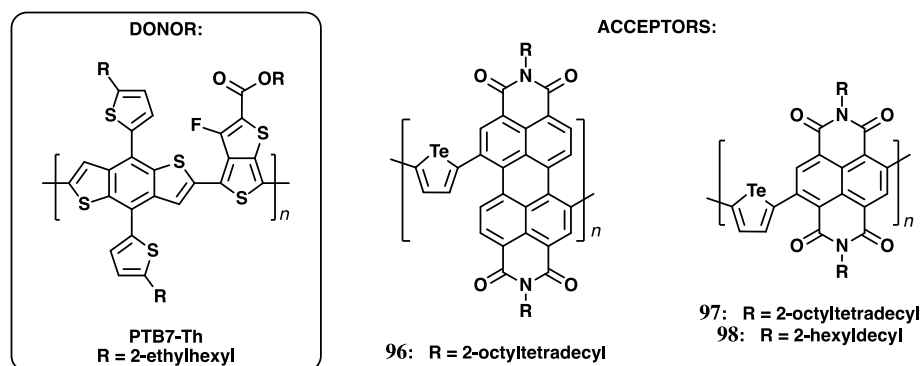


**Figure 1.13** – The donor and acceptor polymers used in the all-polymer OPVs studied by Huang and coworkers.<sup>57</sup>

**Table 1.7** – Summary of OPV device performance parameters using the donor polymer PTB7-Ph and Te-containing acceptor polymers **96–98**;  $M_n$  values given in units of kDa.<sup>57</sup>

| Acceptor  | $M_n$<br>( $\bar{M}_n$ ) | $E_g$<br>(eV) | Ratio <sup>a</sup> | $V_{oc}$<br>(V) | $J_{sc}$<br>(mA cm <sup>-2</sup> ) | PCE<br>(%) |
|-----------|--------------------------|---------------|--------------------|-----------------|------------------------------------|------------|
| <b>96</b> | 13.8<br>(2.49)           | 1.63          | 1:1                | 0.68            | 9.08                               | 2.81       |
| <b>97</b> | 67.6<br>(2.89)           | 1.51          | 1:1                | 0.71            | 9.08                               | 3.21       |
| <b>98</b> | 67.2<br>(1.85)           | 1.53          | 1:1                | 0.71            | 10.02                              | 3.54       |
|           |                          |               | 1:1.2              | 0.72            | 11.02                              | 4.29       |

<sup>a</sup> Ratio of donor polymer (PTB7-Th) to the acceptor polymer

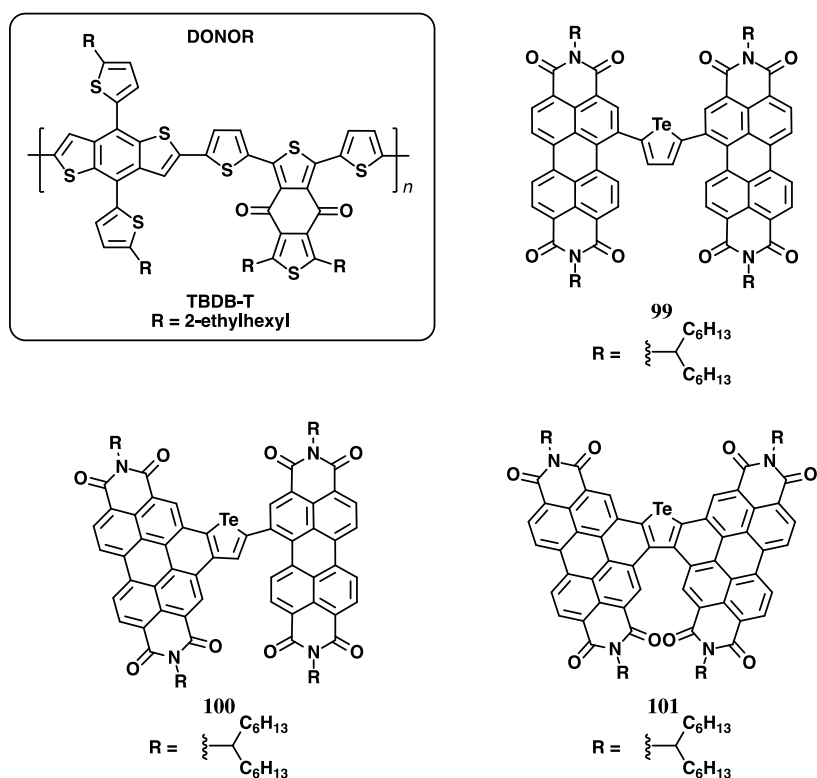


**Figure 1.14** – Small molecule acceptors **99–101** containing a tellurophene fused to PDI developed by Huang and coworkers, as well as the donor polymer used to construct OPV devices.<sup>114</sup>

**Table 1.8** – Summary of OPV device performance parameters using the donor polymer PBDB-T and Te-containing acceptors **99–101**.<sup>114</sup>

| Acceptor            | $E_g$<br>(eV) | $V_{oc}$<br>(V) | $J_{sc}$<br>( $\text{mA cm}^{-2}$ ) | PCE<br>(%) |
|---------------------|---------------|-----------------|-------------------------------------|------------|
| <b>99</b>           | 1.91          | 0.77            | 4.48                                | 1.45       |
| <b>100</b>          | 2.03          | 0.85            | 7.96                                | 3.26       |
| <b>101</b>          | 2.12          | 0.94            | 12.83                               | 7.52       |
| PC <sub>61</sub> BM | -             | 0.86            | 10.68                               | 6.67       |

Although the device performance of tellurophene-containing OPVs have not yet exceeded those based on analogous thiophene systems, the study of tellurophenes in OPVs is still nascent. It is clear from past studies that the incorporation of tellurium does lead to a reduction of the optical bandgap, thus extending the photoresponse into the near-IR. Furthermore, triplet excitons, which have long diffusion lengths, have been confirmed from several studies involving tellurophene materials.<sup>57,105</sup> However, thus far, tellurophenes have mainly been applied in situations that were examined/optimized for thiophene-based materials, which may be not be ideal for tellurophenes. For example, whereas excellent PCEs were determined for S- and Se-containing donor polymers **90–94** at a 1:1 polymer:fullerene ratio, Te-containing donor polymers **92** and **95** required larger amounts of PCBM in order to achieve similar PCEs.<sup>112,113</sup> Seferos and coworkers also established that the Te-containing polymer **84** mixes with PCBM much more intimately than its sulfur and selenium analogues (**82**, **83** respectively) disrupting the crystallinity of PCBM and reducing charge extraction efficiencies.<sup>108</sup> It is important to note that although PCBM aggregation is typically discussed in terms poor donor/acceptor phase morphology and its detrimental effect, crystalline PCBM is necessary in order to achieve appreciable charge mobility (small crystallites are necessary, but large aggregates become detrimental). Furthermore, drawbacks of fullerene acceptors include limited tunability, weak absorption in the UV and NIR regions, as well as thermal/photochemical instability.<sup>29</sup> For all of these reasons, it is necessary to continue the study of tellurophenes in OPV research, particularly in combination with non-fullerene acceptors.

### 1.2.6 OFETs devices with tellurophenes

The replacement of thiophenes with heavier Group 16 elements has been proposed to increase the charge carrier mobility within organic semiconducting polymers.<sup>113</sup> One consequence of incorporating heavier Group 16 elements into heteroles is enhanced contribution of the quinoidal form to the LUMO (with stronger E–C  $\pi$  interactions), which is known to lead to more planar geometries in the excited state by suppressing twisted intramolecular charge transfer.<sup>115</sup> Furthermore, the larger, more polarizable Se and Te atoms can lead to stronger intermolecular Te...Te interactions, which are beneficial for increasing charge transport along more directions than just along the polymer backbone.

Table 1.9 summarizes the hole mobilities ( $\mu_h$ ) and on/off ratios that have been measured for bottom-gate, top-contact OFET devices that contain tellurophenes (in chronological order). Several promising examples demonstrate that Te substitution can result in enhanced OFET performance (higher  $\mu_h$  and on/off ratios) when compared to its lighter congeners.<sup>113,116,117</sup> This is encouraging and suggests that there is room for further progress, since thiophene-based materials are currently being developed with charge carrier mobilities that rival that of polycrystalline silicon.<sup>2,32</sup> However, there also exist reports where Te substitution does not result in enhanced OFET parameters.<sup>118-120</sup> For example, within the polymer series **107–109** (Figure 1.15), the Te-containing polymer **109** gives the worst hole mobility, however the authors comment on difficulties forming homogeneous films of **109** due to its low solubility. For this reason, no  $\mu_h$  or on/off values were reported for a device containing **109** in the bottom-gate, top-contact



configuration. The authors also built devices with different architectures (top-gate, bottom-contact as well as bottom-gate, bottom-contact) incorporating **107–109**, however **109** consistently exhibited the worst performance in each configuration.

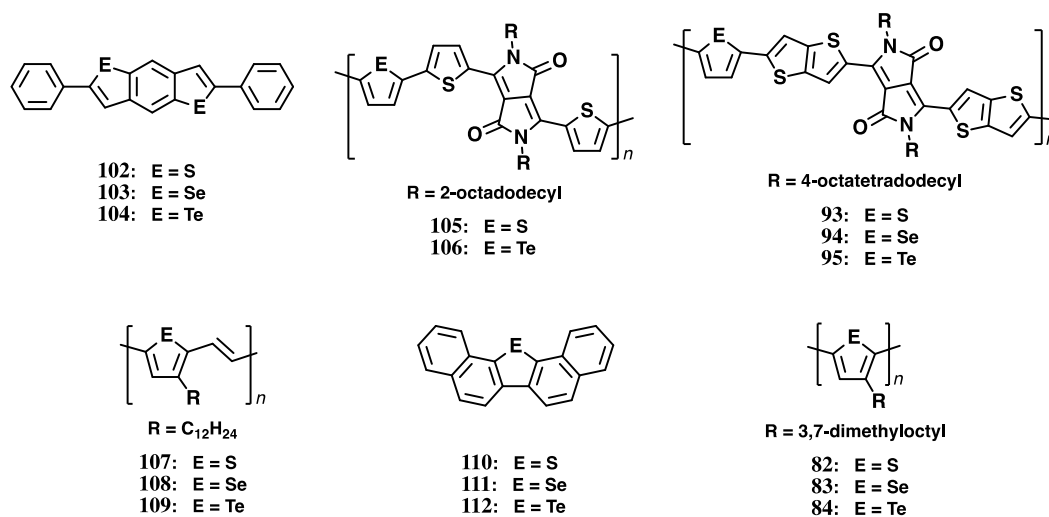


**Figure 1.15** – Chalcogenophene-containing molecules and polymers that have been incorporated into OFET devices.<sup>113,116-120</sup>

**Table 1.9** – Charge carrier mobilities ( $\text{cm}^2 \text{V}^{-1} \text{s}^{-1}$ ) and on/off ratios of bottom-gate, top-contact OFET devices incorporating chalcogenophene-containing molecules and polymers listed in chronological order.<sup>113,116-120</sup>

| Reference | S<br>$\mu_{\text{h}}$ (on/off)            | Se<br>$\mu_{\text{h}}$ (on/off)       | Te<br>$\mu_{\text{h}}$ (on/off)        |
|-----------|---|---------------------------------------|--|
| 110       | <b>102:</b> 0.0046 ( $10^3$ )             | <b>103:</b> 0.016 ( $10^4$ )          | <b>104:</b> 0.0073 ( $10^3$ )          |
| 108       | <b>105:</b> 0.77 ( $10^4$ )               |                                       | <b>106:</b> 1.78 ( $10^5$ )            |
| 105       | <b>93:</b> 0.9 ( $10^3$ )                 | <b>94:</b> 1.6 ( $10^3$ )             | <b>95:</b> 1.6 ( $10^3$ )              |
| 111       | <b>107:</b> 0.0018                        | <b>108:</b> 0.0036                    | <b>109:</b> –                          |
| 112       | <b>110:</b> 4.7 ( $10^5$ )                | <b>111:</b> 4.5 ( $10^5$ )            | <b>112:</b> 1.8 ( $10^4$ )             |
| 109       | <b>82:</b> 0.000062 ( $2.1 \times 10^2$ ) | <b>83:</b> 0.0008 ( $4 \times 10^3$ ) | <b>84:</b> 0.025 ( $1.1 \times 10^4$ ) |

### 1.2.7 Future Outlook

As heavy main group heterocycles such as tellurophenes are receiving more attention, the previously unrealized potential of these unique moieties are slowly being revealed. Although there are many promising results that have been obtained when tellurophene-containing species are used in place of typical organic semiconductors, many questions remain unanswered and many parameters are left to be optimized. For example, due to the heavy nature of the Te atom, several tellurophenes have been shown to exhibit room temperature phosphorescence in the solid state, a highly desirable feature of emitting materials. However to date, most of these species exhibit low quantum yields ( $\leq 20\%$  in air) and therefore future studies should focus on methods of tuning the emission, while also achieving high quantum yields by employing strategies

such as the use of intermolecular interactions to promote rigid molecular packing. This would minimize non-radiative decay through molecular motion, limit O<sub>2</sub> diffusion (and quenching) and enhance phosphorescence as long as self-quenching can be avoided. Furthermore, tellurophenes that are capable of forming triplet excitons have also been used to build OPV devices with efficiencies above 7 %. This ground-breaking discovery will hopefully lead to a new class of building blocks for the advancement of OPV technologies, in order to harness the sun's energy in an efficient and cost-effective manner. Future work on better understanding how tellurophenes contribute to the overall device performance (in particular, how they are different from thiophenes) and optimizing devices for tellurophenes are necessary to advance this field. Finally, several reports suggest that substituting S for Te can lead to enhanced hole mobility in OFET devices. Therefore, the careful design of tellurophenes that are solution-processible and exhibit intermolecular interactions in the solid state that allow for isotropic charge transfer to occur, is a potential solution to the problems that researchers are currently facing in the development of OFETs.

The work described in this Thesis involves the synthesis and optoelectronic properties of tellurophenes in the context of organic electronics. Inspired by the solid state, room temperature, phosphorescence of the BPin-appended tellurophene (**33**,  $\lambda_{em} = 535$  nm) which occurs in the presence of oxygen, one of the goals of my Thesis was to develop similar tellurophenes with tunable emission. In Chapter 2, I achieved a slight red-shift in emission ( $\lambda_{em} = 555$  nm) relative to **33** by forming a Lewis base/Lewis acid adduct using one available boron centre in **33**. A more significant red-shift in emission

was realized by developing methods to access previously inaccessible tellurophenes including: 1) a general boryl exchange protocol starting from reactive  $-B(O^iPr)_2$  substituents to afford several new 2,5-bis(boryl)tellurophenes; 2) improved conditions for the mild, efficient, Suzuki-Miyaura cross-coupling of borylated tellurophenes to afford novel 2,5-bis(aryl)tellurophenes. Lastly, I synthesized both a  $\pi$ -extended tellurophene (tellura(benzo)bithiophene) with PMMA-encapsulated orange-red emission ( $\lambda_{em} = 680$  nm), and a rare  $\pi$ -extended Te-containing homopolymer, with potential for harvesting triplet excitons in OPVs.

### 1.3 References

1. S. R. Forrest, *Nature*, **2004**, *428*, 911–918.
2. H. Sirringhaus, *Adv. Mater.*, **2014**, *26*, 1319–1335.
3. J. Roncali, *Chem. Rev.*, **1992**, *92*, 711–738.
4. J. Chen and Y. Cao, *Acc. Chem. Res.*, **2009**, *43*, 1709–1718.
5. A. M. Priegert, B. W. Rawe, S. C. Serin and D. P. Gates, *Chem. Soc. Rev.*, **2016**, *45*, 922–953.
6. S. M. Parke, M. P. Boone and E. Rivard, *Chem. Commun.*, **2016**, *52*, 9485–9505.
7. M. Montalti, A. Credi, L. Prodi and M. T. Gandolfi, *Handbook of Photochemistry* 3<sup>rd</sup> ed. (CRC Press, Florida, **2006**).
8. N. B. Shustova, B. D. McCarthy and M. Dinca, *J. Am. Chem. Soc.* **2011**, *133*, 20126–20129.

9. S. Xu, R. Chen, C. Zheng and W. Huang, *Adv. Mater.*, **2016**, *28*, 9920–9940.
10. T. Maldiney, A. Lecointre, B. Viana, A. Bessière, M. Bessodes, D. Gourier, C. Richard and D. Scherman, *J. Am. Chem. Soc.*, **2011**, *133*, 11810–11815.
11. M. A. Baldo, D. F. O'Brien, Y. You, A. Shoustikov, S. Sibley, M. E. Thompson and S. R. Forrest, *Nature*, **1998**, *395*, 151–154.
12. Y. Tao, K. Yuan, T. Chen, P. Xu, H. Li, R. Chen, C. Zheng, L. Zhang and W. Huang, *Adv. Mater.*, **2014**, *26*, 7931–7958.
13. Z. Yang, Z. Mao, Z. Xie, Y. Zhang, S. Liu, J. Zhao, J. Xu, Z. Chi and M. P. Aldred, *Chem. Soc. Rev.*, **2017**, *46*, 915–1016.
14. W. C. Martin, *J. of Res.*, **1971**, *2*, 109–111.
15. U. Fano and W. C. Martin, *Topics in Modern Physics A Tribute to E. U. Condon* (Editors: W.E. Britton, H. Odabasi, Colorado Associated University Press, Colorado, **1971**).
16. V. Gray, K. Moth-Poulsen, B. Albinsson and M. Abrahamsson, *Coord. Chem. Rev.*, **2018**, *362*, 54–71.
17. D. B. Papkovsky and R. I. Dmitriev, *Chem. Soc. Rev.*, **2013**, *42*, 8700–8732.
18. J. Mei, N. L. C. Leung, R. T. K. Kwok, J. W. Y. Lam and B. Z. Tang, *Chem. Rev.*, **2015**, *115*, 11718–11940.
19. J. Ohshita, S. Matsui, R. Yamamoto, T. Mizumo, Y. Ooyama, Y. Harima, T. Murafuji, K. Tao, Y. Kuramochi, T. Kaikoh and H. Higashimura, *Organometallics*, **2010**, *29*, 3239–3241.

20. S. M. Parke, M. A. B. Narreto, E. Hupf, R. McDonald, M. J. Ferguson, F. A. Hegmann and E. Rivard, *Inorg. Chem.*, **2018**, *57*, 7536–7549.
21. S. M. Parke, E. Hupf, G. K. Matharu, I. de Aguiar, L. Xu, H. Yu, M. P. Boone, G. L. C. de Souza, R. McDonald, M. J. Ferguson, G. He, A. Brown and E. Rivard, *Angew. Chem. Int. Ed.*, **2018**, *57*, 14841–14846.
22. T. Matsumoto, K. Tanaka, K. Tanaka and Y. Chujo, *Dalton Trans.*, **2015**, *44*, 8697–8708.
23. K. A. Mazzio and C. K. Luscombe, *Chem. Soc. Rev.*, **2015**, *44*, 78–90.
24. M. Sim, J. Shin, C. Shim, M. Kim, S. B. Jo, J.-H. Kim and K. Cho *J. Phys. Chem. C*, **2014**, *118*, 760–766.
25. X. Huang, S. Han, W. Huang and X. Liu, *Chem. Soc. Rev.*, **2013**, *42*, 173–201.
26. Y. Shao and Y. Yang, *Adv. Mater.*, **2005**, *17*, 2841–2844.
27. G. Winroth, D. Podobinski and F. Cacialli, *J. Appl. Phys.*, **2011**, *110*, 124504.
28. J. Hou, O. Inganäs, R. H. Friend and F. Gao, *Nat. Mater.*, **2018**, *17*, 119–128.
29. C. Yan, S. Barlow, Z. Wang, H. Yan, A. K.-Y. Jen, S. R. Marder and X. Zhan, *Nat. Rev. Mater.*, **2018**, *3*, 18003.
30. P. Cheng, G. Li, X. Zhan and Y. Yang, *Nat. Photonics*, **2018**, *12*, 131–142.
31. C. K. Lo, B. R. Gautam, P. Selter, Z. Zheng, S. D. Oosterhout, I. Constantinou, R. Knitsch, R. M. W. Wolfe, X. Yi, J.-L. Brédas, F. So, M. F. Toney, V. Coropceanu, M. R. Hansen, K. Gundogdu, and J. R. Reynolds, *Chem. Mater.*, **2018**, *30*, 2995–3009.

32. J. Mei, Y. Diao, A. L. Appleton, L. Feng and Z. Bao, *J. Am. Chem. Soc.* **2013**, *135*, 6724–6746.
33. A. A. Jahnke and D. S. Seferos, *Macromol. Rapid Commun.* **2011**, *32*, 943–951.
34. M. Jeffries-EL, B. M. Kobilka and B. J. Hale, *Macromolecules*, **2014**, *47*, 7253–7271.
35. E. Rivard, *Chem. Lett.*, **2015**, *44*, 730–736.
36. X. Wu, L. Lv, L. Hu, Q. Shi, A. Peng and H. Huang, *Chem. Phys. Chem.*, **2019**, *20*, 2600–2607.
37. E. I. Carrera and D. S. Seferos, *Macromolecules*, **2015**, *48*, 297–308.
38. J. G. Manion, J. R. Panchuk and D. S. Seferos, *Chem. Rec.*, **2019**, *19*, 1113–1122.
39. T. Chivers and R. S. Laitinen, *Chem. Soc. Rev.*, **2015**, *44*, 1725–1739.
40. Images from periodictable.com
41. A. J. Bondi, *Phys. Chem.*, **1964**, *68*, 441–451.
42. J. R. Rumble, ed., *CRC Handbook of Chemistry and Physics*, 100th ed. (Internet Version, CRC Press/Taylor & Francis, Boca Raton, Florida, **2019**.)
43. C. E. Housecroft and A. G. Sharpe, *Inorganic Chemistry*, 4<sup>th</sup> ed. (Pearson Education Ltd., Essex, England, **2012**).
44. A. A. Jahnke, B. Djukic, T. M. McCormick, E. B. Domingo, C. Hellmann, Y. Lee and D. S. Seferos, *J. Am. Chem. Soc.*, **2013**, *135*, 951–954.
45. F. Fringuelli, G. Marino, G. Savelli and A. Taticchi, *J. Chem. Soc., Chem. Commun. D*, **1971**, 1441–1441.
46. E. H. Braye, W. Hübel and I. Caplier, *J. Am. Chem. Soc.*, **1961**, *83*, 4406–4413.

47. F. Fringuelli and A. Taticchi, *J. Chem. Soc., Perkin Trans. 1*, **1972**, 199–203.
48. A. A. Jahnke, G. W. Howe and D. S. Seferos, *Angew. Chem. Int. Ed.*, **2010**, *49*, 10140–10144.
49. T. M. McCormick, A. A. Jahnke, A. J. Lough, and D. S. Seferos, *J. Am. Chem. Soc.*, **2012**, *134*, 3542–3548.
50. E. I. Carrera, T. M. McCormick, M. J. Kapp, A. J. Lough and D. S. Seferos, *Inorg. Chem.*, **2013**, *52*, 13779–13790.
51. G. He, W. Torres Delgado, D. J. Schatz, C. Merten, A. Mohammadpour, L. Mayr, M. J. Ferguson, R. McDonald, A. Brown, K. Shankar and E. Rivard, *Angew. Chem. Int. Ed.*, **2014**, *53*, 4587–4591.
52. E. I. Carrera and D. S. Seferos, *Dalton Trans.*, **2015**, *44*, 2092–2096.
53. S. Wang, X. Li, X. Hou, Y. Suna and X. Shao, *Chem. Commun.*, **2016**, *52*, 14486–14489.
54. P.-F. Li, E. I. Carrera and D. S. Seferos, *ChemPlusChem*, **2016**, *81*, 917–921.
55. W. Torres Delgado, F. Shahin, M. J. Ferguson, R. McDonald, G. He and E. Rivard, *Organometallics*, **2016**, *35*, 2140–2148.
56. E. I. Carrera, A. E. Lanterna, A. J. Lough, J. C. Scaiano and D. S. Seferos, *J. Am. Chem. Soc.*, **2016**, *138*, 2678–2689.
57. L. Lv, X. Wang, X. Wang, L. Yang, T. Dong, Z. Yang and H. Huang, *ACS Appl. Mater. Interfaces*, **2016**, *8*, 34620–34629.
58. S. Wang, Jihai Shang, C. Yan, W. Wang, C. n Yuan, H.-L. Zhang and X. Shao, *Org. Chem. Front.*, **2019**, *6*, 263–272.



59. M. Oba, M. Endo, K. Nishiyama, A. Ouchi and W. Ando, *Chem. Commun.*, **2004**, 4, 1672–1673.
60. M. Oba, Y. Okada, M. Endo, K. Tanaka, K. Nishiyama, S. Shimada and W. Ando, *Inorg. Chem.*, **2010**, 49, 10680–10686.
61. P. Serguievski and M. R. Detty, *Organometallics*, **1997**, 16, 4386–4391.
62. M. W. Kryman, G. A. Schamerhorn, K. Yung, B. Sathyamoorthy, D. K. Sukumaran, T. Y. Ohulchansky, J. B. Benedict and M. R. Detty, *Organometallics*, **2013**, 32, 4321–4333.
63. M. W. Kryman, G. A. Schamerhorn, J. E. Hill, B. D. Calitree, K. S. Davies, M. K. Linder, T. Y. Ohulchansky and M. R. Detty, *Organometallics*, **2014**, 33, 2628–2640.
64. M. W. Kryman, T. M. McCormick, and M. R. Detty, *Organometallics*, **2016**, 35, 1944–1955.
65. M. R. Detty, P. B. Merkel, R. Hilf, S. L. Gibson and S. K. Powers, *J. Med. Chem.*, **1990**, 33, 1108–1116.
66. Y. Koide, M. Kawaguchi, Y. Urano, K. Hanaoka, T. Komatsu, M. Abo, T. Teraia and T. Nagano, *Chem. Commun.*, **2012**, 48, 3091–3093.
67. K. Wen, X. Xu, J. Chen, L. Lv, L. Wu, Y. Hu, X. Wu, G. Liu, A. Peng and H. Huang, *ACS Appl. Mater. Interfaces*, **2019**, 11, 17884–17893.
68. E. I. Carrera and D. S. Seferos, *Organometallics*, **2017**, 36, 2612–2621.
69. E. Luppold, E. Müller and W. Winter, *Z. Naturforsch.*, **1976**, 31b, 1654–1657.

70. A. Maercker, H. Bodenstedt and L. Brandsma, *Angew. Chem. Int. Ed. Engl.*, **1992**, *31*, 1339–1341.
71. F. Zheng, Y. Komatsuzaki, N. Shida, H. Nishiyama, S. Inagi and I. Tomita, *Macromol. Rapid Commun.*, **2019**, *40*, 1900171.
72. W. Mack, *Angew. Chem. Int. Ed. Engl.*, **1966**, *5*, 896.
73. T. J. Barton and R. W. Roth, *J. Organometal. Chem.*, **1972**, *39*, C66–C68.
74. W. Lohner and K. Praefcke, *Chem. Ber.*, **1978**, *111*, 3745–3746.
75. E. Müller, E. Luppold and W. Winter, *Chem. Ber.*, **1975**, *108*, 237–242.
76. E. Müller, E. Luppold and W. Winter, *Synthesis*, **1975**, 265–266.
77. P. J. Fagan and W. A. Nugent, *J. Am. Chem. Soc.*, **1988**, *110*, 2310–2312.
78. X. Yan and C. Xi, *Acc. Chem. Res.*, **2015**, *48*, 935–946.
79. G. He, L. Kang, W. Torres Delgado, O. Shynkaruk, M. J. Ferguson, R. McDonald and E. Rivard, *J. Am. Chem. Soc.*, **2013**, *135*, 5360–5363.
80. K. Okuma, S. Yahata, N. Nagahora and K. Shioji, *Chem. Lett.*, **2017**, *46*, 405–407.
81. N. Nagahora, S. Yahata, S. Goto, K. Shioji and K. Okuma, *J. Org. Chem.*, **2018**, *83*, 1969–1975.
82. V. K. Karapala, H.-P. Shih and C.-C. Han, *Org. Lett.*, **2018**, *20*, 1550–1554.
83. L. Brandsma, H. Hommes, H. D. Verkruijsse and R. L. P. de Jong, *Recl. Trav. Chim. Pays-Bas*, **1985**, *104*, 226–230.
84. C. H. W. Jones and R. D. Sharma, *J. Organomet. Chem.*, **1987**, *332*, 115–121.
85. H. A. Staab, M. Höne and C. Krieger, *Tetrahedron Lett.*, **1988**, *29*, 1905–1908.

86. J. C. Hanekamp, P. A. A. Klusener and L. Brandsma, *Syn. Commun.*, **1989**, *19*, 2691–2701.
87. J. Kurita, M. Ishii, S. Yasuike and T. Tsuchiya, *J. Chem. Soc., Chem. Commun.*, **1993**, *17*, 1309–1310.
88. S. Sato and N. Furukawa, *Tetrahedron Lett.*, **1995**, *36*, 2803–2806.
89. H. Sashida, K. Sadamori and T. Tsuchiya, *Syn. Commun.*, **1998**, *28*, 713–727.
90. G. He, B. D. Wiltshire, P. Choi, A. Savin, S. Sun, A. Mohammadpour, M. J. Ferguson, R. McDonald, S. Farsinezhad, A. Brown, K. Shankar and E. Rivard, *Chem. Commun.*, **2015**, *51*, 5444–5447.
91. E. Hupf, Y. Tsuchiya, W. Moffat, L. Xu, M. Hirai, Y. Zhou, M. J. Ferguson, R. McDonald, T. Murai, G. He and E. Rivard, *Inorg. Chem.*, **2019**, *58*, 13323–13336.
92. B. Wu, Melvina, X. Wu, E. K. L. Yeow and N. Yoshikai, *Chem. Sci.*, **2017**, *8*, 4527–4532.
93. M. Jiang, J. Guo, B. Liu, Q. Tan and B. Xu, *Chem. Sci.*, **2019**, *21*, 8328–8333.
94. J. Casado, M. Moreno Oliva, M. C. Ruiz Delgado, R. Ponce Ortiz, J. Joaquín Quirante and J. T. López Navarrete, *J. Phys. Chem. A*, **2006**, *110*, 7422–7430.
95. T. Annaka, N. Nakata and A. Ishii, *Organometallics*, **2015**, *34*, 1272–1278.
96. A. K. Mahrok, E. I. Carrera, A. J. Tilley, S. Ye and D. S. Seferos, *Chem. Commun.*, **2015**, *51*, 5475–5478.
97. M. Lapkowski, R. Motyka, J. Suwiński and P. Data, *Macromol. Chem. Phys.*, **2012**, *213*, 29–35.

98. T. M. McCormick, E. I. Carrera, T. B. Schon and D. S. Seferos, *Chem. Commun.*, **2013**, *49*, 5475–11184.
99. A. Kremer, C. Aurisicchio, F. De Leo, B. Ventura, J. Wouters, N. Armaroli, A. Barbieri and D. Bonifazi, *Chem. Eur. J.*, **2015**, *21*, 15377–15387.
100. M. Zander and G. Kirsch, *Z. Naturforsch.*, **1989**, *44a*, 205–209.
101. W. Torres Delgado, C. A. Braun, M. P. Boone, O. Shynkaruk, Y. Qi, R. McDonald, M. J. Ferguson, P. Data, S. K. C. Almeida, I. de Aguiar, G. L. C. de Souza, A. Brown, G. He and E. Rivard, *ACS Appl. Mater. Interfaces*, **2018**, *10*, 12124–12134.
102. M. T. Dang, L. Hirsch and G. Wantz, *Adv. Mater.*, **2011**, *23*, 3597–3602.
103. K. Li, Y. Wu, Y. Tang, M.-A. Pan, W. Ma, H. Fu, C. Zhan and J. Yao, *Adv. Energy Mater.*, **2019**, *9*, 1901728.
104. S. S. Zade, N. Zamoshchik and M. Bendikov, *Acc. Chem. Res.*, **2011**, *44*, 14–24.
105. R. D. Pensack, Y. Song, T. M. McCormick, A. A. Jahnke, J. Hollinger, D. S. Seferos and G. D. Scholes, *J. Phys. Chem. B*, **2014**, *118*, 2589–2597.
106. S. Ye, M. Steube, E. I. Carrera and D. S. Seferos, *Macromolecules*, **2016**, *49*, 1704–1711.
107. W.-H. Lee, S. K. Lee, W. S. Shin, S.J. Moon and I.-N. Kang, *J. Polym. Sci., Part A: Polym. Chem.*, **2013**, *51*, 2753–2758.
108. J. G. Manion, S. Ye, A. H. Proppe, A. W. Laramée, G. R. McKeown, E. L. Kynaston, S. O. Kelley, E. H. Sargent and D. S. Seferos, *ACS Appl. Energy Mater.*, **2018**, *1*, 5033–5042.

109. Y. S. Park, T. S. Kale, C.-Y. Nam, D. Choi and R. B. Grubbs, *Chem. Commun.*, **2014**, *50*, 7964–7967.
110. Y. S. Park, Q. Wu, C.-Y. Nam and R. B. Grubbs, *Angew. Chem. Int. Ed.*, **2014**, *53*, 10691–10695.
111. J. C. Bijleveld, A. P. Zoombelt, S. G. J. Mathijssen, M. M. Wienk, M. Turbiez, D. M. de Leeuw, R. A. J. Janssen, *J. Am. Chem. Soc.*, **2009**, *131*, 16616–16617.
112. E. H. Jung, S. Bae, T. W. Yoo and W. H. Jo, *Polym. Chem.*, **2014**, *5*, 6545–6550.
113. R. S. Ashraf, I. Meager, M. Nikolka, M. Kirkus, M. Planells, B. C. Schroeder, S. Holliday, M. Hurhangee, C. B. Nielsen, H. Sirringhaus and I. McCulloch, *J. Am. Chem. Soc.*, **2015**, *137*, 1314–1321.
114. L. Yang, W. Gu, L. Lv, Y. Chen, Y. Yang, P. Ye, J. Wu, L. Hong, A. Peng and H. Huang, *Angew. Chem. Int. Ed.*, **2018**, *57*, 1096–1102.
115. T. Inouchi, T. Nakashima and T. Kawai, *J. Phys. Chem. A*, **2014**, *118*, 2591–2598.
116. M. Kaur, D. S. Yang, J. Shin, T. W. Lee, K. Choi, M. J. Cho and D. H. Choi, *Chem. Commun.*, **2013**, *49*, 5495–5497.
117. S. Ye, L. Janasz, W. Zajaczkowski, J. G. Manion, A. Mondal, T. Marszalek, D. Andrienko, K. Müllen, W. Pisula and D. S. Seferos, *Macromol. Rapid Commun.*, **2019**, *40*, 1800596.
118. K. Takimiya, Y. Kunugi, Y. Konda, N. Niihara and T. Otsubo, *J. Am. Chem. Soc.*, **2004**, *126*, 5084–5085.
119. M. Al-Hashimi, Y. Han, J. Smith, H. S. Bazzi, S. Y. A. Alqaradawi, S. E. Watkins, T. D. Anthopoulos and M. Heeney, *Chem. Sci.*, **2016**, *7*, 1093–1099.

120. T. Oyama, Y. S. Yang, K. Matsuo and T. Yasuda, *Chem. Commun.*, **2017**, 53, 3814–3817.

## Chapter 2 – Probing the Nature of Peripheral Boryl Groups within Luminescent Tellurophenes

### 2.1 Introduction

The development of new light-emitting materials is required to keep pace with the increasing demand for energy efficient lighting<sup>1</sup> and improved methods for bioimaging.<sup>2</sup> One prevailing effect that has hampered advances in luminogen design is aggregation-caused quenching (ACQ),<sup>3</sup> which effectively extinguishes visible light emission in the solid and aggregated states. Materials that emit *via* long-lived triplet excited states (*i.e.*, phosphorescence) are particularly prone to the ACQ effect, with triplet–triplet annihilation being a major quenching pathway. Despite the challenges associated with maintaining phosphorescence in condensed phases, researchers are continually drawn towards these materials, largely due to the possibility of attaining 100 % electroluminescence efficiencies in relation to the 25 % efficiency limit associated with traditional fluorescent materials;<sup>4</sup> however, harvesting added luminescence *via* triplet–triplet upconversion to excited singlet states<sup>5</sup> and thermally activated delayed fluorescence (TADF)<sup>6</sup> represent promising ways of enhancing fluorescence beyond the 25 % efficiency limit.

In 2014, our group noted that a series of tellurophene heterocycles containing pinacolboronate (BPin) groups at the 2- and 5-positions exhibited solid state phosphorescence in the presence of molecular oxygen and water.<sup>7</sup> This result was unexpected given that such species are either prone to self-quenching of luminescence *via* close intermolecular Te...Te contacts<sup>8</sup> or interaction of excited triplet states with

dioxygen.<sup>9</sup> This investigation indicated that phosphorescence in species such as **B-Te-6-B** (Figure 2.1) was possible *via* aggregation-induced emission (AIE) whereby intramolecular rotations could be suppressed upon aggregation, leading to enhancement of radiative decay (emission).<sup>10</sup> Furthermore, the lack of substantial self-quenching in the solid state was achieved by taking advantage of sterically encumbered BPin groups, which prevented close Te...Te intermolecular contacts from forming ( $> 5.5 \text{ \AA}$  separation in **B-Te-6-B**).<sup>7,8b</sup>

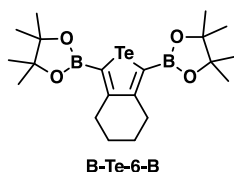


**Figure 2.1** – The structure of the BPin-flanked tellurophene, **B-Te-6-B**.

The initial family of phosphorescent tellurophenes that have been prepared in our group contained symmetrically located –BPin groups at the 2- and 5-positions of the Te heterocycle (*e.g.*, **B-Te-6-B** in Figure 2.2). These species emit green light upon excitation at *ca.* 365 nm (quantum yield,  $\Phi$ , of *ca.* 5–12 % in the solid state), and it was later noted that the relative positions of the BPin groups had an impact on the wavelength of photoluminescence. For example, the 2,4-isomer **2,4-TeC<sub>4</sub>(BPin)<sub>2</sub>Ph<sub>2</sub>** (Figure 2.2) showed a substantial red-shift in emission relative to its 2,5-isomer **2,5-TeC<sub>4</sub>(BPin)<sub>2</sub>Ph<sub>2</sub>**, with yellow-orange emission ( $\lambda_{\text{em}} = 577 \text{ nm}$ ;  $\Phi = 5.3 \%$ ;  $\tau = 17.9 \mu\text{s}$ ) measured in the solid state.<sup>11</sup> Moreover, negligible loss in emission intensity was noted



for films of **2,5-TeC<sub>4</sub>(BPin)<sub>2</sub>Ph<sub>2</sub>** exposed to 365 nm excitation under 4 atm of O<sub>2</sub>.<sup>11</sup> Thus, this species and related green emissive tellurophenes experience minimal quenching of emission by triplet oxygen (<sup>3</sup>O<sub>2</sub>) in the solid state.<sup>12</sup> Initial computational studies showed a lowering of the S<sub>0</sub>-T<sub>1</sub> energy difference in **2,4-TeC<sub>4</sub>(BPin)<sub>2</sub>Ph<sub>2</sub>** in comparison to its green emissive 2,5-isomer is due to the presence of stabilizing quinodal-type interactions between the phenyl group at the 5-position and the tellurophene ring in the excited state.<sup>11</sup> Lastly, if one cleaves the BPin groups from **B-Te-6-B** *via* protodeboronation<sup>13</sup> then the yellow emissive analogue **B-Te-6-H** and the non-emissive oil **H-Te-6-H** can be obtained (Figure 2.2); note **B-Te-6-H** is only weakly emissive at 77 K.

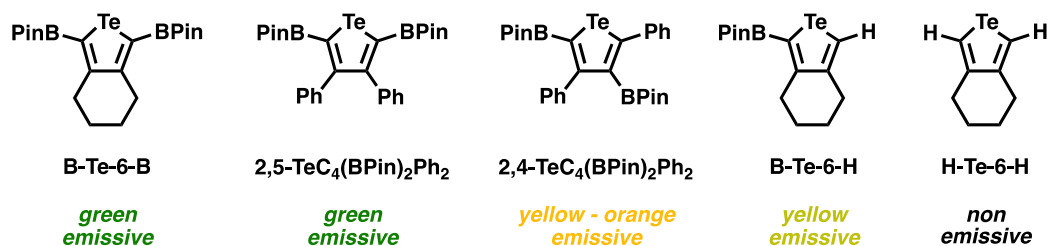


**Figure 2.2** – Selected tellurophenes reported by the Rivard group and their observed photoluminescence under irradiation with a hand-held UV-lamp (365 nm).

What remains to be understood is the full role of the BPin groups in supporting photoluminescence within tellurophenes. Prior to the work described in this Chapter, all attempts to replace the ring-appended BPin groups with  $\pi$ -conjugated units, such as thiophene moieties, have led to the loss of phosphorescence.<sup>7</sup> Herein, I describe my efforts to better understand the role of the boron centres in promoting

photoluminescence in our Te heterocycles.<sup>14</sup> Initially, the synthesis of modified –BR<sub>2</sub> appended tellurophenes was targeted, however all synthetic efforts were thwarted. In this study, it was found that the addition of a coordinating Lewis base to an accessible boron-based p-orbital in BPin enables modulation of the colour of solid state emission from green (in **B-Te-6-B**) to yellow. This represents a promising method to achieve emission colour tuning for either OLED or bioimaging applications.

## 2.2 Results and Discussion

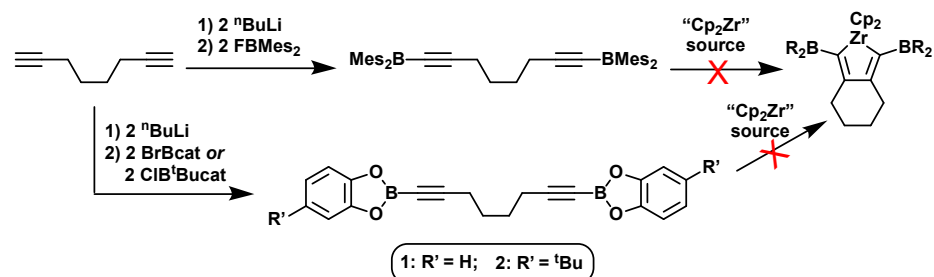
### 2.2.1 Attempted synthesis of new luminescent tellurophenes

Given the role of the BPin groups in both excitation and triplet emission, a method was sought to alter the coordination environment about boron in order to enable colour tuning of the luminescence. Previously, the preparation of a tellurophene with 2,5-positioned –BMes<sub>2</sub> groups (Mes = 2,4,6-Me<sub>3</sub>C<sub>6</sub>H<sub>2</sub>) was attempted due to the large number of luminescent species featuring this group;<sup>14</sup> not only do the hindered Mes substituents give added resistance to hydrolysis, the electron withdrawing nature of the –BMes<sub>2</sub> unit can facilitate charge delocalization in the excited state and, thus, a corresponding red-shift in emission.<sup>14</sup> The requisite diyne Mes<sub>2</sub>BC≡C(CH<sub>2</sub>)<sub>4</sub>C≡CBMes<sub>2</sub> was prepared<sup>7</sup> and exposed to standard zirconacycle forming conditions (Scheme 2.1); however no reaction was noted in the presence of the “Cp<sub>2</sub>Zr” synthon Cp<sub>2</sub>Zr(pyridine)(Me<sub>3</sub>SiC≡CSiMe<sub>3</sub>),<sup>15a</sup> while mixing the diyne with Cp<sub>2</sub>ZrCl<sub>2</sub> and 2 equivalents of <sup>n</sup>BuLi (Negishi conditions)<sup>15b</sup> gave complicated product

mixtures. An attempt to directly replace the pinacolate groups at boron *via* treatment of **B-Te-6-B** with excess MesMgBr also gave no discernable reaction (in refluxing THF or in toluene at room temperature).

Postulating that the steric bulk at boron facilitates the retention of emission in the solid state by suppressing the quenching intermolecular Te...Te interactions, Te heterocycles bearing planar catecholboronate (-Bcat) and tert-butylcatecholboronate (-B(<sup>t</sup>Bu)cat) functional groups were targeted. As catechol side groups are less hindered (versus BPin) they might encourage closer tellurophene stacking and lead to quenching of the solid state photoluminescence, thus providing insight into a possible luminescence quenching pathway in tellurophenes. Starting from the commercially available diyne HC≡C(CH<sub>2</sub>)C≡CH, double lithiation with <sup>n</sup>BuLi followed by addition of the electrophiles BrBcat or ClB<sup>t</sup>Bucat afforded the anticipated boryl-capped diynes catBC≡C(CH<sub>2</sub>)<sub>4</sub>C≡CBcat (**1**) and <sup>t</sup>BucatBC≡C(CH<sub>2</sub>)<sub>4</sub>C≡CB<sup>t</sup>Bucat (**2**), respectively, as colourless solids (Scheme 2.1). Compound **2** was further characterized using single-crystal X-ray crystallography (Figure 2.3) and showed an extended open chain form in the solid state with metrical parameters in line with previous structurally authenticated catecholboranes.<sup>16</sup> However, pure zirconacycles containing catecholboronate groups were inaccessible from the attempted cyclization of **1** and **2** with “Cp<sub>2</sub>Zr” sources<sup>15</sup> and instead afforded multiple Cp-containing products as evidenced from <sup>1</sup>H and <sup>13</sup>C{<sup>1</sup>H} NMR spectroscopy. Furthermore, although the direct replacement of the pinacolate groups in **B-Te-6-B** with 1,2-diaminonaphthalene afforded a -Bdan mono-substituted product,<sup>17</sup> the replacement of both -Bpin groups with -Bdan did not transpired despite

heating the compounds in refluxing toluene (110 °C) for 3 days. The direct formation of  $\text{danBC}\equiv\text{C}(\text{CH}_2)_4\text{C}\equiv\text{CBdan}$  was attempted by combining  $\text{LiC}\equiv\text{C}(\text{CH}_2)_4\text{C}\equiv\text{CLi}$  with  $\text{ClBdan}$ ,<sup>17</sup> however purification of the target diyne was thwarted by the extreme insolubility of the products in standard organic solvents.



**Scheme 2.1** – Attempted cyclization of borylated diynes with zirconocene reagents.

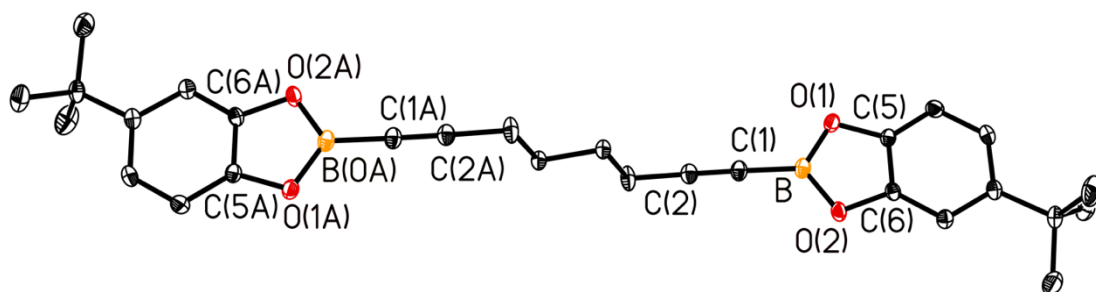


**Figure 2.3** – Molecular structure of **2** with thermal ellipsoids presented at the 30 % probability level. All hydrogen atoms and toluene solvate have been omitted for clarity. Selected bond lengths (Å) and angles (°): C(1)–C(2) 1.194(3), C(1)–B 1.514(3), B–O(1) 1.379(3), B–O(2) 1.386(3); B–C(1) C(2) 177.0(2), O(1)–B–O(2) 111.87(17), O(1)–B–C(1) 124.50(19), O(2)–B–C(1) 123.58(19).

### 2.2.2 Synthesis of B-Te-6-B adducts

In one early experiment, the green phosphorescence of **B-Te-6-B** could be completely quenched with the addition of a fluoride ion.<sup>7</sup> The absorption leading to photoluminescence in **B-Te-6-B** (HOMO to LUMO) involves a LUMO state with considerable C–B  $\pi$ -character (Figure 2.4), thus, the binding of fluoride appears to prevent an electronic transition to this orbital manifold from occurring. Attempts to form the mono-fluoride adduct [**FB-Te-6-B**]<sup>–</sup> were not successful, thus I decided to re-investigate the coordination of more sterically encumbered Lewis bases in order to probe the impact of a donor on tellurophene photoluminescence. Initially **B-Te-6-B** was combined with two equivalents of the *N*-heterocyclic olefin (NHO) IPrCH<sub>2</sub> (IPrCH<sub>2</sub> = (HCNDipp)<sub>2</sub>CCH<sub>2</sub>; Dipp = 2,6-(<sup>i</sup>Pr)<sub>2</sub>C<sub>6</sub>H<sub>3</sub>) in toluene.<sup>18</sup> Analysis of the resulting reaction mixture using <sup>1</sup>H and <sup>11</sup>B NMR spectroscopy indicated that no reaction transpired; this observation is in contrast to the NHO complexation found within the blue luminescent borafluorene adduct IPrCH<sub>2</sub>·ClBF1 (F1 = fluorenyl).<sup>19</sup> Likewise, no reaction was noted between **B-Te-6-B** and the commonly employed donors 4-dimethylaminopyridine (DMAP), PBu<sub>3</sub> or NEt<sub>3</sub>.

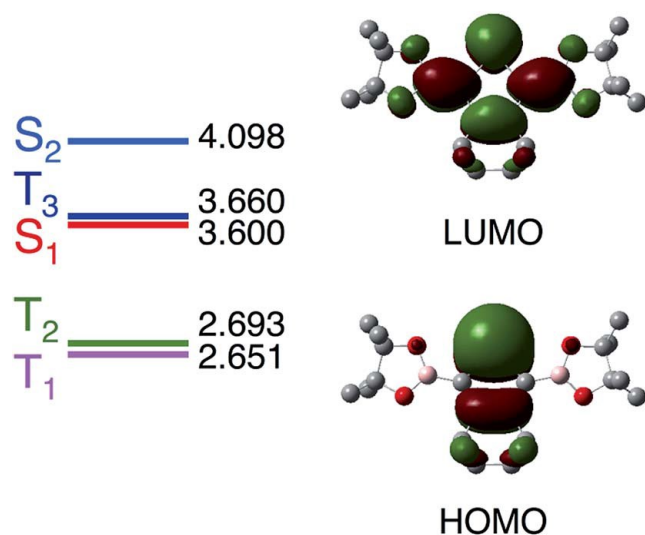
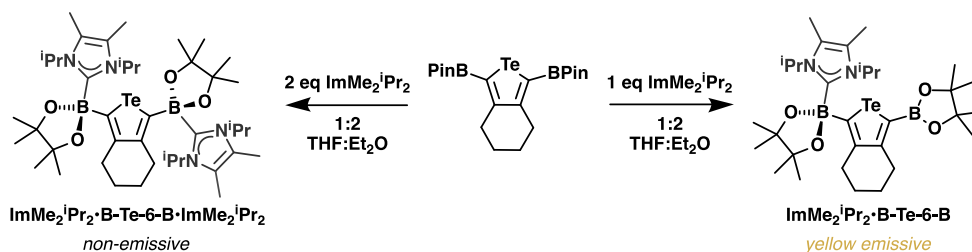


**Figure 2.4** – Computed vertical excitation energies (in eV) to singlet (S<sub>n</sub>) and triplet (T<sub>n</sub>) states from the ground state (S<sub>0</sub>) at the TD B3LYP/jun-cc-pVTZ-(PP) level of theory in the gas-phase for **B-Te-6-B** at the B3LYP/cc-pVDZ S<sub>0</sub> equilibrium geometry. Also plotted are the HOMO and LUMO for **B-Te-6-B**. Hydrogen atoms have been omitted for clarity.

When two equivalents of the *N*-heterocyclic carbene (NHC) ImMe<sub>2</sub><sup>i</sup>Pr<sub>2</sub> (ImMe<sub>2</sub><sup>i</sup>Pr<sub>2</sub> = [(MeCN<sup>i</sup>Pr)<sub>2</sub>C:]<sup>20</sup>) were combined with **B-Te-6-B**, <sup>11</sup>B NMR analysis of the reaction mixture showed the partial conversion of **B-Te-6-B** (resonance at 31.2 ppm) to two new species. One species afforded an upfield-shifted singlet at 5.3 ppm, consistent with carbene coordination at boron and the formation of a four-coordinate environment; the other product had two resonances at 31.7 and 7.9 ppm suggesting ligation of the carbene to one of the BPin groups in **B-Te-6-B** (*vide infra*). Fractional crystallization afforded a batch of pale yellow crystals that were identified as the symmetric bis(NHC) adduct **ImMe<sub>2</sub><sup>i</sup>Pr<sub>2</sub>•B-Te-6-B•ImMe<sub>2</sub><sup>i</sup>Pr<sub>2</sub>** (Scheme 2.2, Figure

2.5). As was the case with addition of  $F^-$  to **B-Te-6-B**, the bis adduct **ImMe<sub>2</sub><sup>i</sup>Pr<sub>2</sub>•B-Te-6-B•ImMe<sub>2</sub><sup>i</sup>Pr<sub>2</sub>** is non-emissive both in solution and in the solid state.



**Scheme 2.2** – Synthesis of mono- and bis-(NHC) adducts of **B-Te-6-B**.

### 2.2.3 Structural characterization of **B-Te-6-B** adducts

The solid state structure of **ImMe<sub>2</sub><sup>i</sup>Pr<sub>2</sub>•B-Te-6-B•ImMe<sub>2</sub><sup>i</sup>Pr<sub>2</sub>** is presented in Figure 2.5. As expected, the boron centres in this compound are four-coordinate with distorted tetrahedral environments. The B–C linkages involving the BPin groups and central tellurophene ring in **ImMe<sub>2</sub><sup>i</sup>Pr<sub>2</sub>•B-Te-6-B•ImMe<sub>2</sub><sup>i</sup>Pr<sub>2</sub>** have bond lengths of 1.6258(19) Å and are elongated with respect to the corresponding C–B bonds in **B-Te-6-B** [1.563(5) and 1.543(5) Å]<sup>8b</sup> due to the change in hybridization at boron from  $sp^2$  to  $sp^3$  upon binding  $\text{ImMe}_2^i\text{Pr}_2$ , leading to more p-character in the B–C bonds (and elongation by *ca.* 0.07 Å). The adjacent coordinative B–C interaction between the BPin unit and the NHC donor is 1.6985(19) Å. For comparison, the C(NHC)–B bond length in  $\text{ImMe}_2^i\text{Pr}_2 \cdot \text{BCl}_3$  is shorter by *ca.* 0.05 Å [1.644(6) Å],<sup>21</sup> while the dative C–B distance in the silapinacolborane adduct  $\text{ImMe}_2^i\text{Pr}_2 \cdot \text{B}(\text{SiPh}_3)\text{Pin}$  is also slightly contracted [1.668(2) Å]<sup>22</sup> with respect to the coordinative bonds in **ImMe<sub>2</sub><sup>i</sup>Pr<sub>2</sub>•B-Te-**

**6-B•ImMe<sub>2</sub><sup>i</sup>Pr<sub>2</sub>**; these results point toward a low Lewis acidity of the –BPin groups in **B-Te-6-Te**. The intra-ring tellurophene Te–C and C–C distances are similar in both **B-Te-6-B** and its NHC bis adduct **ImMe<sub>2</sub><sup>i</sup>Pr<sub>2</sub>•B-Te-6-B•ImMe<sub>2</sub><sup>i</sup>Pr<sub>2</sub>**.

When the reaction between **B-Te-6-B** and ImMe<sub>2</sub><sup>i</sup>Pr<sub>2</sub> was conducted in THF/Et<sub>2</sub>O and the stoichiometry strictly kept at 1:1, a new species could be isolated which had two distinct <sup>11</sup>B resonances at 31.7 and 7.9 ppm. Furthermore, <sup>13</sup>C{<sup>1</sup>H} NMR indicated the presence of two different –BPin environments, with resonances that did not correspond to either free **B-Te-6-B** or its NHC bis adduct **ImMe<sub>2</sub><sup>i</sup>Pr<sub>2</sub>•B-Te-6-B•ImMe<sub>2</sub><sup>i</sup>Pr<sub>2</sub>**. Elemental analysis also strongly supported the formation of the 1:1 NHC:tellurophene adduct **ImMe<sub>2</sub><sup>i</sup>Pr<sub>2</sub>•B-Te-6-B**, and the structure of this species was later verified using single-crystal X-ray crystallography (Figure 2.6). In line with the structures of previously known –BPin functionalized tellurophenes, the three coordinate, base-free, –BPin unit in **ImMe<sub>2</sub><sup>i</sup>Pr<sub>2</sub>•B-Te-6-B** is only slightly twisted from the plane formed by the tellurophene ring (by 13.14(17)°). The remaining –BPin group containing the ligating NHC has a distorted tetrahedral geometry at boron [bond angles at B(1) range from 104.87(13) to 117.36(14)°], while the B–C(NHC) distance of 1.696(2) Å is the same within experimental error as the corresponding distance in the bis adduct **ImMe<sub>2</sub><sup>i</sup>Pr<sub>2</sub>•B-Te-6-B•ImMe<sub>2</sub><sup>i</sup>Pr<sub>2</sub>** [1.6985(19) Å]. As expected, the average B–O distance in the three coordinate BPin unit [1.378(3) Å] of **ImMe<sub>2</sub><sup>i</sup>Pr<sub>2</sub>•B-Te-6-B** is much shorter than in the four coordinate B(1) centre [1.478(3) Å].



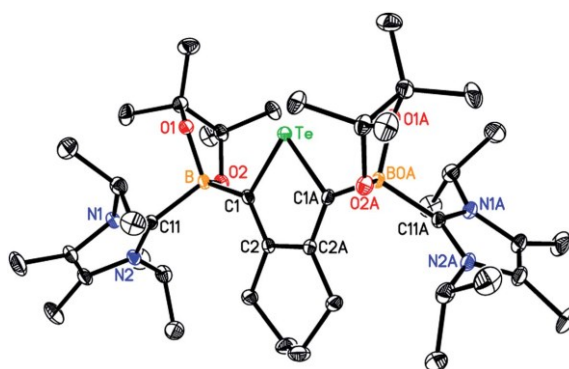


**Figure 2.5** – Molecular structure of  $\text{ImMe}_2^i\text{Pr}_2 \cdot \text{B-Te-6-B} \cdot \text{ImMe}_2^i\text{Pr}_2$  with thermal ellipsoids presented at a 30 % probability level. All hydrogen atoms and  $\text{Et}_2\text{O}$  solvate have been omitted for clarity. Selected bond lengths (Å) and angles (°): Te–C(1) 2.0776(13), C(1)–C(2) 1.3663(19), C(2)–C(2A) 1.462(3), C(1)–B 1.6258(19), C(11)–B 1.6985(19), B–O(1) 1.4833(18), B–O(2) 1.4762(17); C(1)–Te–C(1A) 84.53(8), C(1)–B–C(11) 109.70(11), O(1)–B–O(2) 104.67(11).

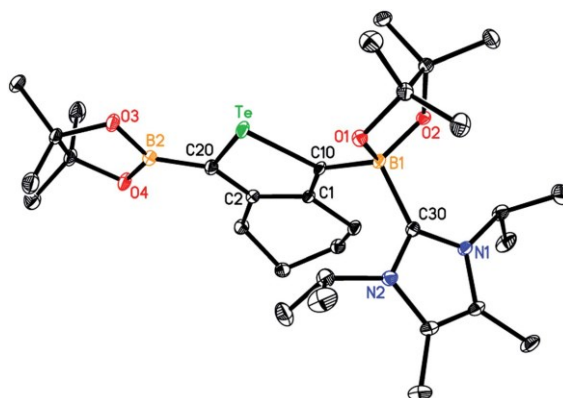


**Figure 2.6** – Molecular structure of  $\text{ImMe}_2^i\text{Pr}_2 \cdot \text{B-Te-6-B}$  with thermal ellipsoids presented at a 30 % probability level. All hydrogen atoms have been omitted for clarity. Selected bond lengths (Å) and angles (°): Te–C(10) 2.0693(17), Te–C(20) 2.0664(18), C(1)–C(10) 1.371(2), C(2)–C(20) 1.374(2), C(1)–C(2) 1.451(2), B(1)–C(10) 1.627(2), B(1)–C(30) 1.696(2), B(2)–C(20) 1.537(3), B(1)–O(1) 1.482(2), B(1)–O(2) 1.473(2), B(2)–O(3) 1.382(2), B(2)–O(4) 1.374(2); C(10)–Te–C(20) 83.58(7), C(10)–B(1)–O(1) 107.04(13), C(10)–B(1)–C(30) 108.75(13), O(1)–B(1)–O(2) 104.87(13), O(3)–B(2)–O(4) 112.46(16), C(20)–B(2)–O(3) 121.49(17).

#### 2.2.4 Photoluminescence of **ImMe<sup>i</sup>Pr<sub>2</sub>•B-Te-6-B**

Consistent with the retention of one three-coordinate BPIn environment, the air-stable solid **ImMe<sup>i</sup>Pr<sub>2</sub>•B-Te-6-B** displayed bright yellow photoluminescence when irradiated at 365 nm with a hand-held UV-lamp (Figure 2.7). Intrigued by the solid state phosphorescence of this species, the photophysical properties of this compound were explored in more detail. While **ImMe<sup>i</sup>Pr<sub>2</sub>•B-Te-6-B** showed no signs of photoluminescence in solution, a film of this adduct drop-cast from THF under N<sub>2</sub> showed yellow emission when excited at 350 nm. The resulting luminescence ( $\lambda_{em} = 555$  nm;  $\Phi_{absolute} = 1.3$  %) was found to be phosphorescence by virtue of the long-lifetimes recorded. Specifically, the decay of luminescence could be fit with a bi-exponential with a long lifetime for each component ( $\tau = 18.3$   $\mu$ s, 62 %;  $\tau = 46.2$   $\mu$ s, 38 %;  $\chi^2 = 1.007$ ); these values are consistent with emissive tellurophenes previously reported by our group.<sup>7,11</sup> Notably the  $\lambda_{em}$  in **ImMe<sup>i</sup>Pr<sub>2</sub>•B-Te-6-B** of 555 nm is red-shifted from that of **B-Te-6-B** ( $\lambda_{em} = 535$  nm) and this trend is reproduced computationally (see section 2.2.6).

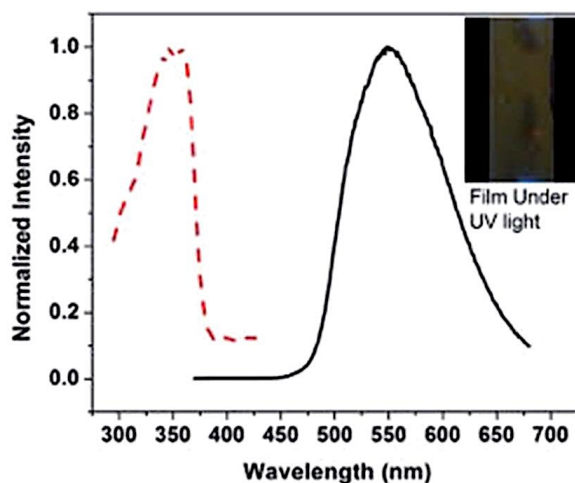


**Figure 2.7** – Excitation (dashed line) and emission (solid line) spectra for a film of **ImMe<sub>2</sub><sup>i</sup>Pr<sub>2</sub>•B-Te-6-B** drop-cast from THF under N<sub>2</sub>.

### 2.2.5 Computational study on B-Te-6-B

To gain more insight into the phosphorescence of **B-Te-6-B**, additional computations were undertaken in relation to the initial time-dependent density functional theory (TD-DFT) studies back in 2014 (originally at the B3LYP/6-31G(2d,p)/LANL2DZ for Te level for the low-lying excited singlet and triplet states).<sup>7</sup> From the 2014 study, including computations on the analogous **B-S-6-B** and **B-Se-6-B** species, the energy difference between the optically accessible S<sub>1</sub> state and the energetically closest third excited triplet state (T<sub>3</sub>) was shown to play a critical role in leading to phosphorescence. Notably, a small excited state singlet-triplet gap is found in **B-Te-6-B** (*ca.* 0.1 eV) while larger singlet-triplet gaps are computed for the S and Se analogues (> 0.8 eV), thus helping to explain the lack of phosphorescence in the lighter congeners. The present work demonstrates that this energetic argument holds true

independent of: (1) the choice of basis set, (2) the choice of functional, and (3) the inclusion of solvation effects.

The vertical excitation energies for **B-Te-6-B** were computed at the TD-B3LYP level of theory using the basis sets: cc-pVDZ, aug-cc-pVDZ, cc-pVTZ, and jun-cc-pVTZ<sup>23</sup> basis sets; for all computations, the corresponding basis sets incorporating the effective core potential (ECP) for Te were used, see Table 2.1. Relative to the computations with the largest basis set (jun-cc-pVTZ), the mean average difference (MAD) for the six states considered is  $< 0.1$  eV. Moreover, the  $S_1$  to  $T_3$  energy gap remains small ( $< 0.1$  eV) for all basis sets considered. The predicted vertical excitation energies to  $S_1$  are slightly larger than the measured peak absorption at  $S_3$  350 nm (3.5 eV) but well within the expected error for TD-DFT. Hence, computations, even with the fairly modest cc-pVDZ basis set, should be suitable for examining the photophysical properties of the tellurophenes, although cc-pVTZ or aug-cc-pVDZ would be preferred.

In addition to varying the basis sets, the vertical excitation energies of **B-Te-6-B** were also computed using TD-DFT with different functionals including the M06-2X3 and CAM-B3LYP14 functionals, *i.e.*, a hybrid meta-GGA and a range-separated hybrid functional. These computations all used the cc-pVDZ basis set. As seen in Table 2.2, the general energy ordering is similar; however, both M06-2X and CAM-B3LYP place the  $S_1$  state higher in energy than  $T_3$  but this shift moves the computed vertical excitation energy to  $S_1$  further from the experimental measurement of the UV-vis absorption maximum. With M06-2X, the energies of the lowest lying triplet states are significantly increased but this change seems to be strongly basis set dependent (Table 2.4). Overall

from the vertical excitation energies alone, there does not appear to be a strong preference for using one functional versus another; thus, the present work primarily focuses on using the B3LYP functional.

**Table 2.1** - The excitation energies (in eV) of the three lowest-lying singlet and triplet states for **B-Te-6-B** with different basis sets<sup>a</sup> at the TD-B3LYP level of theory at the gas-phase S<sub>0</sub> geometry (as determined at the B3LYP/cc-pVDZ-(PP) level of theory).

| Excited State    | Ref. 7 <sup>b</sup> | cc-pVD | aug-cc-pVDZ | cc-pVTZ | jun-ccpVTZ |
|------------------|---------------------|--------|-------------|---------|------------|
| T <sub>1</sub>   | 2.5894              | 2.6987 | 2.6682      | 2.6659  | 2.6511     |
| T <sub>2</sub>   | 2.8208              | 2.7228 | 2.6966      | 2.6951  | 2.6928     |
| S <sub>1</sub>   | 3.8070              | 3.6916 | 3.6021      | 3.6279  | 3.5955     |
| T <sub>3</sub>   | 3.8668              | 3.7444 | 3.6848      | 3.6864  | 3.6597     |
| S <sub>2</sub>   | 4.2826              | 4.2002 | 4.0958      | 4.1451  | 4.0982     |
| S <sub>3</sub>   | 4.3186              | 4.3031 | 4.2295      | 4.2546  | 4.2262     |
| MAD <sup>c</sup> | 0.1475              | 0.0729 | 0.0097      | 0.0252  | ---        |

a) For Te, the basis set employs the corresponding ECP.

b) 6-31G(2d,p)/LanL2DZ for Te.

c) Mean absolute difference (MAD) relative to the jun-cc-pVTZ results.

To assess the role of solvation on the vertical excitation energies for **B-Te-6-B**, the computations were also conducted at the TD-B3LYP/cc-pVDZ-(PP) level of theory using the polarizable continuum model (IEF-PCM<sup>24,25</sup> and universal force field (UFF) atomic radii) with parameters for THF and water (Table 2.3). The MAD for the six lowest states, when compared to the gas-phase results, is less than 0.03 eV in both water

and THF. Hence, gas-phase computations should be suitable for interpreting the photophysical properties.

**Table 2.2** – The excitation energies (in eV) of the three lowest-lying singlet and triplet states for **B-Te-6-B** at the TD-B3LYP, TD-CAM-B3LYP, and TD-M06-2X levels of theory with the cc-pVDZ-(PP) basis set at the gas-phase  $S_0$  geometry (as determined at the B3LYP/ccpVDZ-(PP) level of theory). Change relative to TD-B3LYP results given in parenthesis.

| <b>Excited State</b> | <b>B3LYP</b> | <b>CAM-B3LYP</b> | <b>M06-2X</b>    |
|----------------------|--------------|------------------|------------------|
| <b>T<sub>1</sub></b> | 2.6987       | 2.5288 (-0.1699) | 3.0331 (-0.3344) |
| <b>T<sub>2</sub></b> | 2.7228       | 2.8214 (-0.0986) | 3.0350 (-0.3122) |
| <b>S<sub>1</sub></b> | 3.6916       | 3.8938 (-0.2022) | 3.9857 (-0.2941) |
| <b>T<sub>3</sub></b> | 3.7444       | 3.7095 (-0.0349) | 3.7046 (-0.0398) |
| <b>S<sub>2</sub></b> | 4.2002       | 4.2174 (-0.0172) | 4.1652 (-0.0350) |
| <b>S<sub>3</sub></b> | 4.3031       | 4.4743 (-0.1712) | 4.5532 (-0.2501) |

**Table 2.3** – The excitation energies (in eV) of the three lowest-lying singlet and triplet states for **B-Te-6-B** at the TD-B3LYP/cc-pVDZ-(PP) level of theory for different solvents (THF and H<sub>2</sub>O treated with IEF-PCM) at the gas-phase S<sub>0</sub> geometry (as determined at the B3LYP/cc-pVDZ-(PP) level of theory). Change relative to gas-phase results given in parenthesis.

| Excited State    | Gas-phase | H <sub>2</sub> O | THF              |
|------------------|-----------|------------------|------------------|
| T <sub>1</sub>   | 2.6987    | 2.7051 (-0.0064) | 2.7033 (-0.0046) |
| T <sub>2</sub>   | 2.7228    | 2.8041 (-0.0813) | 2.7884 (-0.0656) |
| S <sub>1</sub>   | 3.6916    | 3.7172 (-0.0256) | 3.6967 (-0.0051) |
| T <sub>3</sub>   | 3.7444    | 3.7896 (-0.0452) | 3.7820 (-0.0376) |
| S <sub>2</sub>   | 4.2002    | 4.2259 (-0.0257) | 4.2166 (-0.0164) |
| S <sub>3</sub>   | 4.3031    | 4.2717 (-0.0314) | 4.2639 (-0.0392) |
| MAD <sup>a</sup> | ---       | 0.0097           | 0.0252           |

a) Mean absolute difference (MAD) compared to the gas-phase results

By determining the optimized geometry for the lowest-lying triplet state, the phosphorescence energy for **B-Te-6-B** has been determined to be 2.12 eV (Table 2.4), which can be compared to the experimentally determined value of 2.32 eV. As has been seen previously<sup>11</sup> for the **2,4-TeC<sub>4</sub>(BPin)<sub>2</sub>Ph<sub>2</sub>** and **2,5-TeC<sub>4</sub>(BPin)<sub>2</sub>Ph<sub>2</sub>** isomers, there is a systematic shift between the computed phosphorescence energy (wavelength) and the experimental measurements where the computed values are 0.2–0.5 eV too low. However, one can still predict/understand shifts in emission energy; see the discussion of **ImMe<sub>2</sub><sup>1</sup>Pr<sub>2</sub>•B-Te-6-B** in the next section.

**Table 2.4** – The excitation energies (in eV) using various levels of theory for **B-Te-6-B** at the optimized T<sub>1</sub> geometry. Experimental phosphorescence energy is 2.32 eV.

| Excited state  | TD-B3LYP/<br>cc-pVTZ-(PP) <sup>a</sup> | TD-M06-2X/<br>cc-pVTZ-(PP) <sup>a</sup> | TD-M06-2X/<br>cc-pVDZ-(PP) <sup>b</sup> |
|----------------|--|---|---|
| T <sub>1</sub> | 1.9196 (2.12) <sup>c</sup>             | 2.0915 (2.5452)                         | 2.7200                                  |
| T <sub>2</sub> | 2.5294                                 | 2.7311                                  | 2.7560                                  |
| T <sub>3</sub> | 3.6373                                 | 3.6558                                  | 3.8695                                  |
| S <sub>1</sub> | 3.3673                                 | 3.5257                                  | 3.7091                                  |
| S <sub>2</sub> | 3.8360                                 | 4.0168                                  | 4.3207                                  |
| S <sub>3</sub> | 4.4945                                 | 4.1080                                  | 4.3260                                  |

a) T<sub>1</sub> geometry determined at the UB3LYP/cc-pVTZ-(PP) level of theory.

b) T<sub>1</sub> geometry determined at the UM06-2X/cc-pVDZ-(PP) level of theory.

c) Energy computed as difference between UB3LYP/B3LYP triplet/singlet state energies.

While arguments based on the energetics and the (presumed) spin–orbit coupling due to the presence of tellurium are useful, it is interesting to determine quantitatively the role of the spin–orbit coupling in the absorption and emission processes. TD-DFT computations including spin–orbit coupling show that the S<sub>1</sub> and T<sub>3</sub> states are strongly mixed at the ground state geometry (Tables 2.5 and 2.6) and, hence, excitation will provide access to the triplet manifold needed for phosphorescence. Moreover, at the T<sub>1</sub> geometry, if one includes spin–orbit coupling (and, hence, spin is no longer a good quantum number), both the excited “triplet” state and ground “singlet” state contain contributions from T<sub>3</sub>, supporting the model for phosphorescence. From the computed oscillator strengths, the lifetimes for the three near degenerate low-lying excited states are predicted to be 4.3 ms, 2.3 ms, and 0.4 s



based on the Einstein A formulation. While these values are too long relative to the experimental measurements<sup>7</sup> by *ca.* one order of magnitude, the differences for the three “triplet” states (due to the three components) suggest an explanation for the two decay times measured experimentally; one component has too long a lifetime to be captured experimentally with our instrumentation.

**Table 2.5** – The excitation energies (in eV) at the TD-B3LYP/TZVP/ZORA of theory for **B-Te-6-B** at the specified geometries. Experimental phosphorescence energy is 2.32 eV.

| <b>Excited State</b> | <b>S<sub>1</sub> Geometry</b> | <b>T<sub>1</sub> Geometry</b> |
|----------------------|-------------------------------|-------------------------------|
| <b>T<sub>1</sub></b> | 2.7340                        | 1.9784                        |
| <b>T<sub>2</sub></b> | 2.8010                        | 2.5624                        |
| <b>T<sub>3</sub></b> | 3.6356                        | 3.6261                        |
| <b>S<sub>1</sub></b> | 3.6510                        | 3.4282                        |
| <b>S<sub>2</sub></b> | 4.0748                        | 3.8139                        |
| <b>S<sub>3</sub></b> | 4.2947                        | 4.0117                        |

**Table 2.6** – The excitation energies (in eV) to the lowest-energy “singlet” state (at the S<sub>1</sub> geometry) and “triplet” states (at the T<sub>1</sub> geometry) at the TD-B3LYP/TZVP/ZORA [+ spin–orbit coupling] level of theory for **B-Te-6-B**. Also included are the oscillator strength (*f*) and the contributions of the spin-states (the three components of the triplet state have been collected into a single contribution). The experimentally determined phosphorescence energy is 2.32 eV.

| Geometry       | Energy | Contributing States                           | <i>f</i> | Contributions to Ground State                 |
|----------------|--------|---|----------|---|
| S <sub>1</sub> | 3.5636 | 0.5509 S <sub>1</sub> + 0.4298 T <sub>3</sub> | 4.36E-02 | 0.9960 S <sub>0</sub> + 0.0030 T <sub>3</sub> |
|                | 3.7354 | 0.4287 S <sub>1</sub> + 0.5524 T <sub>3</sub> | 3.39E-02 |   |
| T <sub>1</sub> | 1.9876 | 0.9967 T <sub>1</sub> + 0.0014 T <sub>3</sub> | 1.28E-08 | 0.9962 S <sub>0</sub> + 0.0020 T <sub>3</sub> |
|                | 1.9879 | 0.9970 T <sub>1</sub> + 0.0013 T <sub>3</sub> | 2.54E-06 |   |
|                | 1.9889 | 0.9908 T <sub>1</sub> + 0.0008 T <sub>3</sub> | 1.37E-06 |   |

## 2.2.6 TD-DFT study of the B-Te-6-B adducts

To try and explain the phosphorescence in **ImMe<sub>2</sub><sup>i</sup>Pr<sub>2</sub>•B-Te-6-B** and the shift in emission relative to **B-Te-6-B**, TD-DFT computations have been carried out at the optimized geometries in the lowest-lying singlet (S<sub>0</sub>) and triplet (T<sub>1</sub>) electronic states (Tables 2.7 and 2.8). In **ImMe<sub>2</sub><sup>i</sup>Pr<sub>2</sub>•B-Te-6-B**, the S<sub>1</sub> to T<sub>3</sub> gap increases to *ca.* 0.2 eV relative to that for **B-Te-6-B**, where it is 0.06 eV; this increased energy difference could play a role in the decreased quantum yield (1.4 %) for **ImMe<sub>2</sub><sup>i</sup>Pr<sub>2</sub>•B-Te-6-B** versus 11.5 % for **B-Te-6-B**. The phosphorescence energy for **ImMe<sub>2</sub><sup>i</sup>Pr<sub>2</sub>•B-Te-6-B** is predicted to be 1.67 eV (at the B3LYP/cc-pVTZ-(PP) level of theory), which qualitatively captures the red-shift observed experimentally; the shift is overestimated,

as was observed previously when examining the different phosphorescence energies between the **2,4-TeC<sub>4</sub>(BPIn)<sub>2</sub>Ph<sub>2</sub>** and **2,5-TeC<sub>4</sub>(BPIn)<sub>2</sub>Ph<sub>2</sub>** isomers.<sup>11</sup>

**Table 2.7** – The excitation energies (in eV) at the TD-B3LYP level of theory with the cc-pVDZ-(PP) and cc-pVTZ-(PP) basis sets for **ImMe<sub>2</sub><sup>i</sup>Pr<sub>2</sub>•B-Te-6-B** at the specified geometries.

| Excited State  | cc-pVDZ-(PP) <sup>a</sup> | cc-pVDZ-(PP) <sup>b</sup> | cc-pVTZ-(PP) <sup>a</sup> | cc-pVTZ-(PP) <sup>c</sup> |
|----------------|---------------------------|---------------------------|---------------------------|---------------------------|
| T <sub>1</sub> | 2.7257                    | 2.5938                    | 2.7200                    | 2.7133                    |
| T <sub>2</sub> | 3.0698                    | 2.9938                    | 2.7560                    | 3.0068                    |
| T <sub>3</sub> | 4.1075                    | 3.9026                    | 3.8695                    | 4.0369                    |
| S <sub>1</sub> | 3.9333                    | 3.8245                    | 3.7091                    | 3.8618                    |
| S <sub>2</sub> | 4.3030                    | 4.1452                    | 4.3207                    | 4.2594                    |
| S <sub>3</sub> | 4.4045                    | 4.3242                    | 4.3260                    | 4.3565                    |

a) At the reported X-ray structure.

b) At the B3LYP/cc-pVDZ-(PP) optimized geometry for S<sub>1</sub>.

c) At the B3LYP/cc-pVTZ-(PP) optimized geometry for S<sub>1</sub>.

**Table 2.8** – The excitation energies (in eV) at the TD-B3LYP level of theory with the cc-pVDZ-(PP) and cc-pVTZ-(PP) basis sets for **ImMe<sub>2</sub><sup>i</sup>Pr<sub>2</sub>•B-Te-6-B** at the specified geometries.

| Excited State  | cc-pVDZ-(PP) <sup>a</sup> | cc-pVTZ-(PP) <sup>b</sup> |
|----------------|---------------------------|---------------------------|
| T <sub>1</sub> | 1.6107                    | 1.6702                    |
| T <sub>2</sub> | 2.7651                    | 2.7427                    |
| T <sub>3</sub> | 3.5077                    | 3.5536                    |
| S <sub>1</sub> | 3.3709                    | 3.3595                    |
| S <sub>2</sub> | 3.6973                    | 3.6966                    |

a) At the UB3LYP/cc-pVDZ-(PP) optimized geometry for T<sub>1</sub>.

b) At the UB3LYP/cc-pVTZ-(PP) optimized geometry for T<sub>1</sub>.

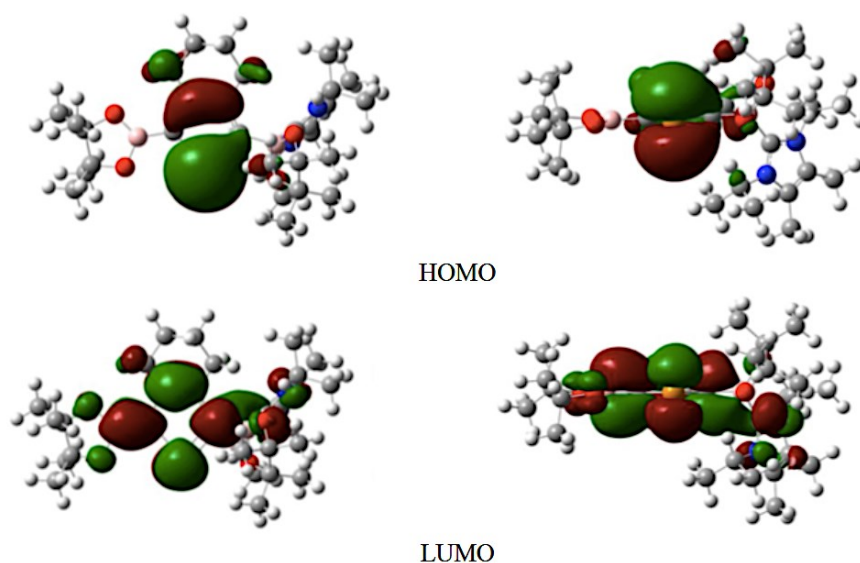


**Figure 2.8** – HOMO (*top*) and LUMO (*bottom*) of **ImMe<sub>2</sub><sup>i</sup>Pr<sub>2</sub>•B-Te-6-B** for the S<sub>0</sub> state at the (B3LYP/cc-pVDZ-(PP)) S<sub>1</sub> equilibrium geometry as determined at the B3LYP/ccpVDZ-(PP) level of theory in the gas-phase.

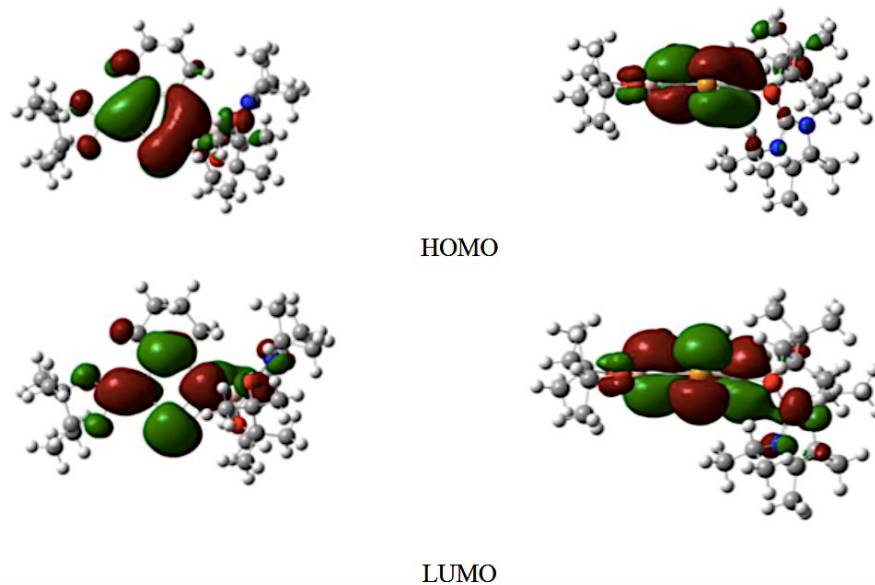


**Figure 2.9** – HOMO (*top*) and LUMO (*bottom*) of **ImMe<sub>2</sub><sup>i</sup>Pr<sub>2</sub>•B-Te-6-B** for the S<sub>0</sub> state at the (B3LYP/cc-pVDZ-(PP)) T<sub>1</sub> equilibrium geometry as determined at the B3LYP/ccpVDZ-(PP) level of theory in the gas-phase.

## 2.3 Conclusions

While initial attempts to form new tellurophenes with three-coordinate boryl ( $-BR_2$ ) substituents were not successful, coordination of the strongly donating *N*-heterocyclic carbene **ImMe<sub>2</sub><sup>i</sup>Pr<sub>2</sub>** afforded interesting results. Specifically, the initial green solid state phosphorescence in **B-Te-6-B** was quenched upon adding two equivalents of the carbene, while the mono adduct **ImMe<sub>2</sub><sup>i</sup>Pr<sub>2</sub>•B-Te-6-B** exhibited bright yellow phosphorescence. Thus, it is clear that the empty p-orbital within uncomplexed  $-BPin$  groups modulates luminescence in the corresponding tellurophenes, an observation that is supported from the accompanying computational studies. As a result, coordination of Lewis bases represents a viable and facile way to alter the emission in borylated tellurophenes.

## 2.4 Experimental

### 2.4.1 General considerations

All reactions were performed in either an inert atmosphere glove box (MBraun) or using Schlenk techniques. Solvents were dried using a Grubbs-type solvent purification system manufactured by Innovative Technology Inc.<sup>26</sup> and stored under an atmosphere of nitrogen prior to use. **B-Te-6-B**,<sup>7</sup> BrBcat,<sup>27</sup> CIB<sup>t</sup>Bucat,<sup>27</sup> CIBdan,<sup>17</sup> and ImMe<sub>2</sub><sup>i</sup>Pr<sub>2</sub><sup>22</sup> were prepared according to literature procedures. All other reagents were obtained from Sigma-Aldrich and used as received. <sup>1</sup>H, <sup>1</sup>H{<sup>31</sup>P}, <sup>13</sup>C{<sup>1</sup>H} and <sup>11</sup>B{<sup>1</sup>H} NMR spectra were recorded on a Varian VNMRS-400 or Varian VNMRS-500

spectrometer and referenced externally to SiMe<sub>4</sub> or F<sub>3</sub>B•OEt<sub>2</sub>. Elemental analyses were performed at the Analytical and Instrumentation Laboratory at the University of Alberta. Melting points were measured in sealed glass capillaries under nitrogen using a MelTemp melting point apparatus and are uncorrected.

#### 2.4.2 Synthetic procedures

**Synthesis of catBC≡C(CH<sub>2</sub>)<sub>4</sub>C≡C<sup>cat</sup> (1).** To a solution of 1,7-octadiyne (1.3 mL, 11 mmol) in Et<sub>2</sub>O (300 mL) at -78 °C was added dropwise a solution of <sup>n</sup>BuLi (7.8 mL, 2.5 M solution in hexanes, 22 mmol). After the reaction mixture was stirred at -78 °C for 1 hour, a solution of bromocatecholborane (4.37 g, 24.2 mmol) in Et<sub>2</sub>O (15 mL) was added and the mixture was stirred for 1 hour more at -78 °C, then for 16 hours at room temperature. The volatiles were removed under reduced pressure and the crude product was extracted with 300 mL of toluene. After filtration, the toluene was removed from the filtrate under reduced pressure, and the product was washed with hexanes (3 x 5 mL) to provide **1** as a white solid (1.61 g, 48 %). <sup>1</sup>H NMR (498.1 MHz, C<sub>6</sub>D<sub>6</sub>): δ = 6.89 (m, 4H, ArH), 6.68 (m, 4H, ArH), 1.76 (m, 4H, C≡C-CH<sub>2</sub>-CH<sub>2</sub>), 1.20 (m, 4H, C≡C-CH<sub>2</sub>-CH<sub>2</sub>). <sup>13</sup>C{<sup>1</sup>H} NMR (125.7 MHz, C<sub>6</sub>D<sub>6</sub>): δ = 148.4 (ArC), 123.2 (ArC), 112.8 (ArC), 107.4 (BC≡CCH<sub>2</sub>CH<sub>2</sub>), 26.9 (BC≡CCH<sub>2</sub>CH<sub>2</sub>), 19.1 (BC≡CCH<sub>2</sub>CH<sub>2</sub>). The <sup>13</sup>C{<sup>1</sup>H} resonance for B-C was not located. <sup>11</sup>B{<sup>1</sup>H} NMR (159.8 MHz, C<sub>6</sub>D<sub>6</sub>): δ = 24.5. HR-MS (EI) (C<sub>20</sub>H<sub>16</sub>B<sub>2</sub>O<sub>4</sub>): m/z calcd 342.12347; found 342.12403 (Δppm = 1.6).

**Synthesis of <sup>t</sup>BucatBC≡C(CH<sub>2</sub>)<sub>4</sub>C≡CB<sup>t</sup>Bucat (2).** To a solution of 1,7-octadiyne (0.3 mL, 2 mmol) in Et<sub>2</sub>O (100 mL) at -78 °C was added dropwise a solution of <sup>n</sup>BuLi (1.8 mL, 2.5 M solution in hexanes, 4.5 mmol). After the reaction mixture was stirred at -78 °C for 1 hour, a solution of *tert*-butylcatecholboron chloride (1.00 g, 4.75 mmol) in 15 mL of Et<sub>2</sub>O was added and the mixture was stirred for 1 hour more at -78 °C, then for 16 hours at room temperature. The resulting precipitate was allowed to settle and the mother liquor was filtered into another flask where the volatiles were then removed under reduced pressure. The crude solid was then recrystallized from toluene (at -30 °C) to provide **2** as a colourless crystalline solid of suitable quality for X-ray crystallography (0.127 g, 12 %). <sup>1</sup>H NMR (400.0 MHz, C<sub>6</sub>D<sub>6</sub>): δ = 7.19 (dd, <sup>3</sup>J<sub>HH</sub> = 2.0 Hz, <sup>4</sup>J<sub>HH</sub> = 0.4 Hz, 2H, OCCHC(CH<sub>3</sub>)<sub>3</sub>), 6.94 (d, <sup>3</sup>J<sub>HH</sub> = 8.4 Hz, <sup>4</sup>J<sub>HH</sub> = 0.4 Hz, 2H, OCCHCH), 6.86 (dd, <sup>3</sup>J<sub>HH</sub> = 8.4 Hz, <sup>4</sup>J<sub>HH</sub> = 2.0 Hz, 2H, OCCHCH), 1.83 (m, 4H, C≡CCH<sub>2</sub>CH<sub>2</sub>), 1.26 (m, 4H, C≡CCH<sub>2</sub>CH<sub>2</sub>) 1.13 (s, 18H, C(CH<sub>3</sub>)<sub>3</sub>). <sup>13</sup>C{<sup>1</sup>H} NMR (125.7 MHz, C<sub>6</sub>D<sub>6</sub>): δ = 148.4 (ArC), 146.9 (ArC), 146.2 (ArC), 120.1 (ArC), 111.9 (ArC), 110.3 (ArC), 107.2 (C≡CCH<sub>2</sub>CH<sub>2</sub>), 34.8 (C(CH<sub>3</sub>)<sub>3</sub>), 31.7 (C(CH<sub>3</sub>)<sub>3</sub>), 27.0 (C≡CCH<sub>2</sub>CH<sub>2</sub>), 19.2 (C≡CCH<sub>2</sub>CH<sub>2</sub>). The <sup>13</sup>C{<sup>1</sup>H} resonance for B-C was not located. <sup>11</sup>B{<sup>1</sup>H} NMR (128.3 MHz, C<sub>6</sub>D<sub>6</sub>): δ = 24.9. HR-MS (EI) (C<sub>28</sub>H<sub>32</sub>B<sub>2</sub>O<sub>4</sub>): m/z calcd 454.24867; found: 454.24958 (Δppm = 2.0).

**Synthesis of ImMe<sub>2</sub><sup>i</sup>Pr<sub>2</sub>•B-Te-6-B•ImMe<sub>2</sub><sup>i</sup>Pr<sub>2</sub>.** To a solution of **B-Te-6-B** (50.0 mg, 0.103 mmol) in 3 mL of a 1:2 THF:Et<sub>2</sub>O mixture was added a solution of **ImMe<sub>2</sub><sup>i</sup>Pr<sub>2</sub>** (34.7 mg, 0.193 mmol) in 3 mL of a 1:2 THF:Et<sub>2</sub>O mixture. After the

reaction mixture was stirred for 3 hours, the pale yellow solution was concentrated to *ca.* 2 mL, filtered and the resulting filtrate was cooled to  $-35\text{ }^{\circ}\text{C}$ . After 16 h, a few pale yellow crystals of **ImMe<sup>i</sup>Pr<sub>2</sub>•B-Te-6-B•ImMe<sup>i</sup>Pr<sub>2</sub>** were isolated (*ca.* 2–3 mg) that were characterized by NMR spectroscopy and X-ray crystallography. <sup>1</sup>H NMR (498.1 MHz, C<sub>6</sub>D<sub>6</sub>):  $\delta = 4.47$  (septet,  $^3J_{\text{HH}} = 6.5$  Hz, 4H, NCH(CH<sub>3</sub>)<sub>2</sub>), 3.41 (br, 4H, CCCH<sub>2</sub>CH<sub>2</sub>), 1.90 (br, 4H, CCCH<sub>2</sub>CH<sub>2</sub>), 1.61 (s, 12H, NC(CH<sub>3</sub>)C), 1.42 (s, 24H, OC(CH<sub>3</sub>)<sub>2</sub>), 1.31 (d,  $^3J_{\text{HH}} = 6.5$  Hz, 24H, NCH(CH<sub>3</sub>)<sub>2</sub>). <sup>13</sup>C{<sup>1</sup>H} NMR (125.3 MHz, C<sub>6</sub>D<sub>6</sub>):  $\delta = 161.1$  (TeC(BPin)=C), 124.3 (NC(CH<sub>3</sub>)=C), 79.5 (OC(CH<sub>3</sub>)<sub>2</sub>), 49.1 (CH(CH<sub>3</sub>)<sub>2</sub>), 34.7 (CH<sub>2</sub>CH<sub>2</sub>), 26.3 (CH<sub>2</sub>CH<sub>2</sub>), 25.1 (CH(CH<sub>3</sub>)<sub>2</sub>), 21.7 (OC(CH<sub>3</sub>)<sub>2</sub>), 10.2 (NC(CH<sub>3</sub>)C=C). The <sup>13</sup>C{<sup>1</sup>H} resonance for B-C was not located. <sup>11</sup>B{<sup>1</sup>H} NMR (159.8 MHz, C<sub>6</sub>D<sub>6</sub>):  $\delta = 5.3$  (s).

**Synthesis of ImMe<sup>i</sup>Pr<sub>2</sub>•B-Te-6-B.** To a solution of **B-Te-6-B** (103.9 mg, 0.214 mmol) in 3 mL of a 1:2 THF:Et<sub>2</sub>O mixture was added a solution of **ImMe<sup>i</sup>Pr<sub>2</sub>** (36.0 mg, 0.200 mmol) in 3 mL of 1:2 THF:Et<sub>2</sub>O. After stirring the mixture for 30 minutes, the pale yellow solution was concentrated to a volume of *ca.* 3 mL. The solvent was then allowed to slowly evaporate under nitrogen for 3 days, leading to the formation of pale yellow crystals of **ImMe<sup>i</sup>Pr<sub>2</sub>•B-Te-6-B** (50 mg, 38 %). <sup>1</sup>H NMR (400.0 MHz, C<sub>6</sub>D<sub>6</sub>):  $\delta = 4.36$  (septet,  $^3J_{\text{HH}} = 6.8$  Hz, 2H, CH(CH<sub>3</sub>)<sub>2</sub>), 3.58 (br t, 2H, CH<sub>2</sub>), 3.26 (br t, 2H, CH<sub>2</sub>), 1.81 (br, 4H, CH<sub>2</sub>), 1.58 (s, 6H, OC(CH<sub>3</sub>)<sub>2</sub>), 1.56 (s, 6H, OC(CH<sub>3</sub>)<sub>2</sub>), 1.18 (s, 6H, CH(CH<sub>3</sub>)<sub>2</sub>), 1.15 (d,  $^3J_{\text{HH}} = 6.8$  Hz, 12H, CH(CH<sub>3</sub>)<sub>2</sub>), 1.08 (s, 12H, OC(CH<sub>3</sub>)<sub>2</sub>). <sup>13</sup>C{<sup>1</sup>H} NMR (125.3 MHz, C<sub>6</sub>D<sub>6</sub>):  $\delta = 161.6$  (TeC(BPin)=C), 147.1 (TeC(BPin)=C), 136.5 (TeC(BPin)=C), 125.3 (NC(CH<sub>3</sub>)C), 82.4 (OC(CH<sub>3</sub>)<sub>2</sub>), 78.2 (OC(CH<sub>3</sub>)<sub>2</sub>), 51.3



(CH(CH<sub>3</sub>)<sub>2</sub>), 35.0 (CH<sub>2</sub>), 32.8 (CH<sub>2</sub>), 27.8 (OC(CH<sub>3</sub>)<sub>2</sub>), 27.6 (OC(CH<sub>3</sub>)<sub>2</sub>), 25.4 (CH<sub>2</sub>), 25.1 (CH<sub>2</sub>), 22.1 (NCH(CH<sub>3</sub>)<sub>2</sub>), 8.5 (NC(CH<sub>3</sub>)C). Only the <sup>13</sup>C{<sup>1</sup>H} resonance for the B-C on the tetrahedral boron centre was located (the resonance for B-C on the trigonal planar boron was not located). <sup>11</sup>B{<sup>1</sup>H} NMR (159.8 MHz, C<sub>6</sub>D<sub>6</sub>): δ = 31.6 (br, *BPin*), 7.9 (s, (ImMe<sub>2</sub><sup>i</sup>Pr<sub>2</sub>)•*BPin*). Anal. calcd for C<sub>31</sub>H<sub>52</sub>O<sub>4</sub>N<sub>2</sub>B<sub>2</sub>Te: C, 55.91; H, 7.87; N, 4.21. found: C, 56.37; H, 7.99; N, 4.26.

### 2.4.3 X-ray crystallography

Crystals for X-ray diffraction studies were removed from a vial and immediately coated with a thin layer of hydrocarbon oil (Paratone-N). A suitable crystal was then mounted on a glass fiber, and quickly placed in a low temperature stream of nitrogen on an X-ray diffractometer. All data were collected using a Bruker APEX II CCD detector/D8 diffractometer using Cu K $\alpha$  radiation with the crystals cooled to -100 °C. The data was corrected for absorption through Gaussian integration from the indexing of the crystal faces. Crystal structures were solved using intrinsic phasing SHELXT-2014<sup>28</sup> (**2** and **ImMe<sub>2</sub><sup>i</sup>Pr<sub>2</sub>•B-Te-6-B•ImMe<sub>2</sub><sup>i</sup>Pr<sub>2</sub>**) or Patterson methods (DIRDIF-2008; **ImMe<sub>2</sub><sup>i</sup>Pr<sub>2</sub>•B-Te-6-B**)<sup>29</sup> and refined using full-matrix least-squares on F<sup>2</sup>. The assignment of hydrogen atom positions was based on the sp<sup>2</sup> or sp<sup>3</sup> hybridization geometries of their attached carbon atoms, and the hydrogen atoms were given thermal parameters 20 % greater than those of their parent atoms.

**Table 2.9** – Crystallographic data for compounds **2**, **ImMe<sub>2</sub><sup>i</sup>Pr<sub>2</sub>•B-Te-6-B•ImMe<sub>2</sub><sup>i</sup>Pr<sub>2</sub>**, and **ImMe<sub>2</sub><sup>i</sup>Pr<sub>2</sub>•B-Te-6-B**.

| Compound  | <b>2</b> • toluene  | <b>ImMe<sub>2</sub><sup>i</sup>Pr<sub>2</sub>•B-Te-6-B•ImMe<sub>2</sub><sup>i</sup>Pr<sub>2</sub>•2Et<sub>2</sub>O</b> | <b>ImMe<sub>2</sub><sup>i</sup>Pr<sub>2</sub>•B-Te-6-B</b>                      |
|---|---|--|---|
| Formula   | C <sub>35</sub> H <sub>40</sub> B <sub>2</sub> O <sub>4</sub> | C <sub>50</sub> H <sub>92</sub> B <sub>2</sub> N <sub>4</sub> O <sub>6</sub> Te  | C <sub>31</sub> H <sub>52</sub> B <sub>2</sub> N <sub>2</sub> O <sub>4</sub> Te |
| form. wt. (g/mol)   | 546.29  | 994.49   | 665.96  |
| crys. dimes. (mm)   | 0.26 × 0.20 × 0.03  | 0.29 × 0.20 × 0.16   | 0.44 × 0.25 × 0.12  |
| Crystal system  | Triclinic   | monoclinic   | monoclinic  |
| Space group   | <i>P</i> $\bar{1}$  | <i>C</i> 2/ <i>c</i>   | <i>P</i> 2 <sub>1</sub> / <i>c</i> (No. 14)                                     |
| <i>a</i> (Å)  | 6.3523(2)   | 18.8131 (3)  | 10.3086 (2)   |
| <i>b</i> (Å)  | 8.0207(2)   | 11.1794 (2)  | 15.0795 (3)   |
| <i>c</i> (Å)  | 16.3894(4)  | 26.4236 (5)  | 21.3795 (4)   |
| $\alpha$ (deg)  | 92.3795(18)   | -  | -   |
| $\beta$ (deg)   | 95.9413(18)   | 93.0441 (6)  | 93.2679 (7)   |
| $\gamma$ (deg)  | 110.1138(17)  | -  | -   |
| <i>V</i> (Å <sup>3</sup> )  | 777.24(4)   | 5549.55 (17)   | 3318.01 (11)  |
| <i>Z</i>  | 1   | 4  | 4   |
| $\rho_{\text{calcd}}$ (g cm <sup>-3</sup> )   | 1.167   | 1.190  | 1.333   |
| $\mu$ (mm <sup>-1</sup> )   | 0.575   | 4.588  | 7.350   |
| temperature (°C)  | -100  | -100   | -100  |
| 2 $\theta_{\text{max}}$ (deg)   | 144.58  | 148.09   | 147.96  |
| total data  | 5411  | 19362  | 18158   |
| unique data (Rint)  | 2953(0.0549)  | 5624 (0.0136)  | 6668 (0.0281)   |
| Obs [ <i>I</i> > 2 $\sigma$ ( <i>I</i> )]   | 2310  | 5586   | 6523  |
| R <sub>1</sub> [ <i>F</i> <sub>o</sub> <sup>2</sup> ≥ 2 $\sigma$ ( <i>F</i> <sub>o</sub> <sup>2</sup> )] <sup>a</sup> | 0.0606  | 0.0212   | 0.0261  |
| wR <sub>2</sub> [all data] <sup>a</sup>   | 0.1826  | 0.0560   | 0.0668  |
| max/min $\Delta r$ (e Å <sup>-3</sup> )   | 0.462/-0.265  | 0.400/-0.412   | 0.468/-1.446  |

$$^a R_1 = \frac{\sum ||F_o| - |F_c||}{\sum |F_o|}; wR_2 = \left[ \frac{\sum w(F_o^2 - F_c^2)^2}{\sum w(F_o^4)} \right]^{1/2}$$

## 2.5 References and Notes

1. (a) I. Akasaki, *Angew. Chem., Int. Ed.*, **2015**, *54*, 7750–7763; (b) H. Amano, *Angew. Chem., Int. Ed.*, **2015**, *54*, 7764–7769; (c) S. Nakamura, *Angew. Chem., Int. Ed.*, **2015**, *54*, 7770–7788; (d) R. H. Friend, R. W. Gymer, A. B. Holmes, J. H. Burroughes, R. N. Marks, C. Taliani, D. C. C. Bradley, D. A. Dos Santos, J. L. Bredas, M. Lodgund and W. R. Salaneck, *Nature*, **1999**, *397*, 121–128; (e) M. A. Baldo, D. F. O'Brien, Y. You, A. Shoustikov, S. Sibley, M. E. Thompson and S. R. Forrest, *Nature*, **1998**, *395*, 151–154.
2. (a) B. Hein, K. I. Willig and S. W. Hell, *Proc. Natl. Acad. Sci. U.S.A.*, **2008**, *105*, 14271–14276; (b) L. Schermelleh, R. Heintzmann and H. Leonhardt, *J. Cell Biol.*, **2010**, *190*, 165–175; (c) D. Ding, K. Li, B. Liu and B. Z. Tang, *Acc. Chem. Res.*, **2013**, *46*, 2441–2453; (d) C. Wang, A. Fukazawa, M. Taki, Y. Sato, T. Higashiyama and S. Yamaguchi, *Angew. Chem., Int. Ed.*, **2015**, *54*, 15213–15217.
3. W. Z. Yuan, P. Lu, S. Chen, J. W. Y. Lam, Z. Wang, Y. Liu, H. S. Kwok, Y. Ma and B. Z. Tang, *Adv. Mater.*, **2010**, *22*, 2159–2163.
4. (a) M. A. Baldo, S. Lamansky, P. E. Burrows, M. E. Thompson and S. R. Forrest, *Appl. Phys. Lett.*, **1999**, *75*, 4–6; (b) R. C. Evans, P. Douglas and C. J. Winscom, *Coord. Chem. Rev.*, **2006**, *250*, 2093–2126.
5. T. N. Singh-Rachford and F. N. Castellano, *Coord. Chem. Rev.*, **2010**, *254*, 2560–2573.
6. H. Uoyama, K. Goushi, K. Shizu, H. Nomura and C. Adachi, *Nature*, **2012**, *492*, 234–238.

7. G. He, W. Torres Delgado, D. J. Schatz, C. Merten, A. Mohammadpour, L. Mayr, M. J. Ferguson, R. McDonald, A. Brown, K. Shankar and E. Rivard, *Angew. Chem., Int. Ed.*, **2014**, *53*, 4587–4591.
8. For selected references on the incorporation of tellurophenes into  $\pi$ -conjugated materials for optoelectronic applications, see: (a) A. A. Jahnke, G. W. Howe and D. S. Seferos, *Angew. Chem., Int. Ed.*, **2010**, *49*, 10140–10144; (b) G. He, L. Kang, W. Torres Delgado, O. Shynkaruk, M. J. Ferguson, R. McDonald and E. Rivard, *J. Am. Chem. Soc.*, **2013**, *135*, 5360–5363; (c) M. Jeffries-El, B. M. Kobilka and B. J. Hale, *Macromolecules*, **2014**, *47*, 7253–7271; (d) E. I. Carrera and D. S. Seferos, *Macromolecules*, **2015**, *48*, 297–308; (e) E. Rivard, *Chem. Lett.*, **2015**, *44*, 730–736; (f) Y. S. Park, Q. Wu, C.-Y. Nam and R. B. Grubbs, *Angew. Chem., Int. Ed.*, **2014**, *53*, 10691–10695; (g) M. Al-Hashimi, Y. Han, J. Smith, H. S. Bazzi, S. Y. A. Alqaradawi, S. E. Watkins, T. D. Anthopoulos and M. Heeney, *Chem. Sci.*, **2016**, *7*, 1093–1099; (h) T. Annaka, N. Nakata and A. Ishii, *Organometallics*, **2015**, *34*, 1272–1278; (i) S. M. Parke, M. P. Boone and E. Rivard, *Chem. Commun.*, **2016**, *52*, 9485–9505.
9. For an early report on the phosphorescence of benzotellurophenes in frozen EtOH (at 77 K), see: M. Zander and G. Kirsch, *Z. Naturforsch., A: Phys. Sci.*, **1989**, *44*, 205–209.
10. (a) J. Luo, Z. Xie, J. W. Y. Lam, L. Cheng, H. Chen, C. Qiu, H. S. Kwok, X. Zhan, Y. Liu, D. Zhu and B. Z. Tang, *Chem. Commun.*, **2001**, 1740–1741; (b) R. Hu, N. L. C. Leung and B. Z. Tang, *Chem. Soc. Rev.*, **2014**, *43*, 4494–4562; (c) J. Mei, N. L.

- C. Leung, R. T. K. Kwok, J. W. Y. Lam and B. Z. Tang, *Chem. Rev.*, **2015**, *115*, 11718–11940.
11. G. He, B. D. Wiltshire, P. Choi, A. Savin, S. Sun, A. Mohammadpour, M. J. Ferguson, R. McDonald, S. Farsinezhad, A. Brown, K. Shankar and E. Rivard, *Chem. Commun.*, **2015**, *51*, 5444–5447.
12. (a) S. Mukherjee and P. Thilagar, *Chem. Commun.*, **2015**, *51*, 10988–11003, and references therein; (b) O. Bolton, K. Lee, H.-J. Kim, K. Y. Lin and J. Kim, *Nat. Chem.*, **2011**, *3*, 205–210; (c) W. Z. Yuan, X. Y. Shen, H. Zhao, J. W. Y. Lam, L. Tang, P. Lu, C. Wang, Y. Liu, Z. Wang, Q. Zheng, J. Z. Sun, Y. Ma and B. Z. Tang, *J. Phys. Chem. C*, **2010**, *114*, 6090–6099; (d) S. Hirata, K. Totani, J. Zhang, T. Yamashita, H. Kaji, S. R. Marder, T. Watanabe and C. Adachi, *Adv. Funct. Mater.*, **2013**, *23*, 3386–3397; (e) Z. An, C. Zheng, Y. Tao, R. Chen, H. Shi, T. Chen, Z. Wang, H. Li, R. Deng, X. Liu and W. Huang, *Nat. Mater.*, **2015**, *14*, 685–690; (f) Z. Yang, Z. Mao, X. Zhang, D. Ou, Y. Mu, Y. Zhang, C. Zhao, S. Liu, Z. Chi, J. Xu, Y.-C. Wu, P.-Y. Lu, A. Lien and M. R. Bryce, *Angew. Chem., Int. Ed.*, **2016**, *55*, 2181–2185; (g) S. Hirata and M. Vacha, *J. Phys. Chem. Lett.*, **2016**, *7*, 1539–1545.
13. W. Torres Delgado, F. Shahin, M. J. Ferguson, R. McDonald, G. He and E. Rivard, *Organometallics*, **2016**, *35*, 2140–2148.
14. For selected articles on boryl ( $-BR_2$ ) promoted luminescence, see: (a) Z. M. Hudson and S. Wang, *Acc. Chem. Res.*, **2009**, *42*, 1584–1596; (b) F. Jäkle, *Chem. Rev.*, **2010**, *110*, 3985–4022; (c) A. Wakamiya and S. Yamaguchi, *Bull. Chem. Soc. Jpn.*, **2015**, *88*, 1357–1377.

15. (a) U. Rosenthal, A. Ohff, W. Baumann, A. Tillack, H. Görls, V. V. Burlakov and V. B. Shur, *Z. Anorg. Allg. Chem.*, **1995**, 621, 77–83; (b) E. Negishi, F. E. Cederbaum and T. Takahashi, *Tetrahedron Lett.*, **1986**, 27, 2829–2832.
16. (a) Y. Gu, H. Pritzkow and W. Siebert, *Eur. J. Inorg. Chem.*, **2001**, 373–379; (b) A. G. Avent, M. J. Davies, P. B. Hitchcock and M. F. Lappert, *Z. Anorg. Allg. Chem.*, **2003**, 629, 1358–1366.
17. J. A. Bailey, M. Ploeger and P. G. Pringle, *Inorg. Chem.*, **2014**, 53, 7763–7769.
18. (a) S. M. I. Al-Rafia, A. C. Malcolm, S. K. Liew, M. J. Ferguson, R. McDonald and E. Rivard, *Chem. Commun.*, **2011**, 6987–6989; (b) K. Powers, C. Hering-Junghans, R. McDonald, M. J. Ferguson and E. Rivard, *Polyhedron*, **2016**, 108, 8–14.
19. C. J. Berger, G. He, C. Merten, R. McDonald, M. J. Ferguson and E. Rivard, *Inorg. Chem.*, **2014**, 53, 1475–1486.
20. N. Kuhn and T. Kratz, *Synthesis*, **1993**, 561–562.
21. S. Muthaiah, D. C. H. Do, R. Ganguly and D. Vidovic, *Organometallics*, **2013**, 32, 6718–6724.
22. C. Kleeberg and C. Borner, *Eur. J. Inorg. Chem.*, **2013**, 2799–2806.
23. E. Papajak, J. Zheng, H. R. Leverentz and D. G. Truhlar, *J. Chem. Theory Comput.*, **2011**, 7, 3027–3034.
24. E. Cancès, B. Mennucci and J. Tomasi, *J. Chem. Phys.*, **1997**, 107, 3032–3041.
25. M. Cossi, G. Scalmani, N. Rega and V. Barone, *J. Chem. Phys.*, **2002**, 117, 43–54.
26. A. B. Pangborn, M. A. Giardello, R. H. Grubbs, R. K. Rosen and F. J. Timmers, *Organometallics*, **1996**, 15, 1518–1520.

27. X. He and J. F. Hartwig, *Organometallics*, **1996**, *15*, 400–407.
28. G. M. Sheldrick, *Acta Crystallogr., Sect. A: Found. Crystallogr.*, **2008**, *64*, 112–122.
29. P. T. Beurskens, G. Beurskens, R. de Gelder, J. M. M. Smits, S. Garcia-Granda and R. O. Gould, *DIRDIF-2008 Program. Crystallographic Laboratory*, Radboud University, Nijmegen, The Netherlands.

# Chapter 3 – Using Boryl-Substitution and Improved Suzuki-Miyaura Cross-Coupling to Access New Phosphorescent Tellurophenes

## 3.1 Introduction

Borylated compounds represent indispensable building blocks toward a variety of functional materials, ranging from fine chemicals to  $\pi$ -conjugated materials for optoelectronic applications. Most often, these borylated precursors are amenable to Suzuki-Miyaura cross coupling, arguably the most popular method for forming C(sp<sup>2</sup>)-C(sp<sup>2</sup>) linkages.<sup>1</sup> This synthetic method offers many advantages over existing coupling reactions, including high functional group tolerance and compatibility with water.

The electron-accepting ability of the three-coordinate boron centres found within boryl substituents -BR<sub>2</sub> also enables their use as colourimetric anion sensors, and as acceptor units within luminescent compounds for OLED and bioimaging applications.<sup>2</sup> The introduction of boryl-substituents to thiophenes has also led to an interesting class of fluorescent molecules and polymers, with air- and moisture-stability being a hallmark of these materials.<sup>3</sup> A commonly employed route to attach boryl groups onto  $\pi$ -conjugated heterocycles involves iridium-catalyzed C-H functionalization,<sup>4-6</sup> while metal-free approaches are now emerging as viable alternatives.<sup>7</sup> However, the preparation of borylated congeners of thiophenes, such as the heavy element-containing selenophenes (Se) and tellurophenes (Te), pose additional challenges. In particular, the enhanced reactivity of tellurophenes means that pre-



existing routes to ring functionalization can lead to competitive oxidation at the electron-rich Te atom or even ring-cleavage in some instances.<sup>9-11</sup>

Recently, the study of tellurophenes has undergone a renaissance, spurred by their advantageous properties for organic photovoltaics (OPVs),<sup>12-20</sup> organic light-emitting diodes (OLEDs),<sup>21-25</sup> and organic field effect transistors (OFETs).<sup>15,16,26-31</sup> Of particular note, OPVs featuring a tellurophene-based triplet exciton acceptor unit led to power conversion efficiencies of up to 7.5 % (Figure 3.1), and has opened a path to simplified (layered) device architectures.<sup>19</sup> Moreover, a few years ago our group uncovered efficient room temperature phosphorescence from a series of 2,5-borylated tellurophenes in the solid state (Figure 3.1), including the difficult to achieve retention of triplet state-mediated emission in the presence of O<sub>2</sub> (a known quencher of phosphorescence).<sup>21</sup> Lastly, our group and others have demonstrated the ability of tellurophenes to undergo polymerization *via* Suzuki-Miyaura cross-coupling, although usually between the difficult to prepare halogenated tellurophenes and aryl boronic acids.<sup>13,28,32,33</sup> In this regard, stable and synthetically accessible BPin-functionalized tellurophenes (BPin = pinacolatoboronate) are promising substrates for cross-coupling, however one potential drawback is their propensity to undergo base-promoted protodeboronation.<sup>34</sup>

In this Chapter, various boryl ( $-BR_2$ ) groups are placed onto tellurophenes *via* a general boryl group forming protocol starting from reactive  $-B(O^iPr)_2$  substituents. The resulting tellurophenes bearing boron-bound catecholato (cat), *tert*-butylcatecholato (<sup>t</sup>Bucat), 1,8-naphthalenediaminato (dan), and Mes (Mes = 2,4,6-Me<sub>3</sub>C<sub>6</sub>H<sub>2</sub>) groups were

previously inaccessible under the same conditions used to synthesize BPin-functionalized tellurophenes. The products of the successful condensation chemistry were studied by single-crystal X-ray crystallography, and where possible, solid state luminescence measurements. Finally, their use in high yielding Suzuki-Miyaura cross-coupling reactions is also demonstrated.

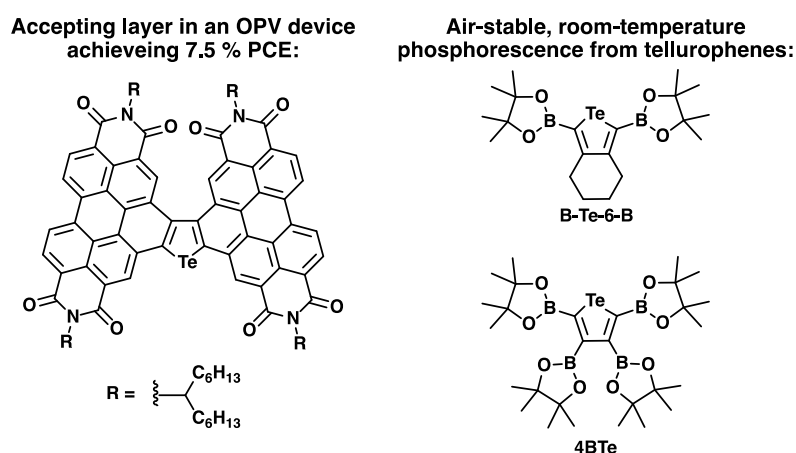


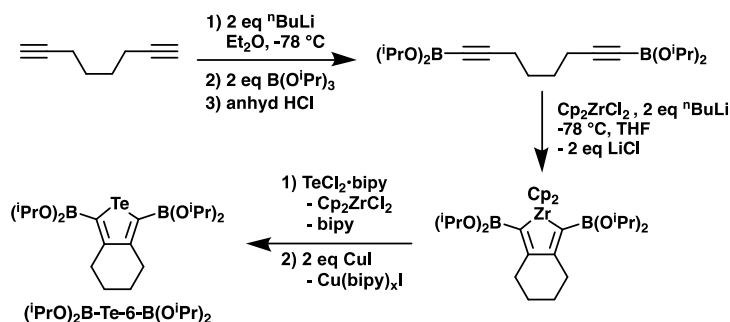
**Figure 3.1** – Tellurophenes developed for photovoltaic (*left*) and phosphorescence-based (*right*) applications.

## 3.2 Results and Discussion

### 3.2.1 Condensation reactions of $(i\text{PrO})_2\text{B-Te-6-B}(\text{O}i\text{Pr})_2$

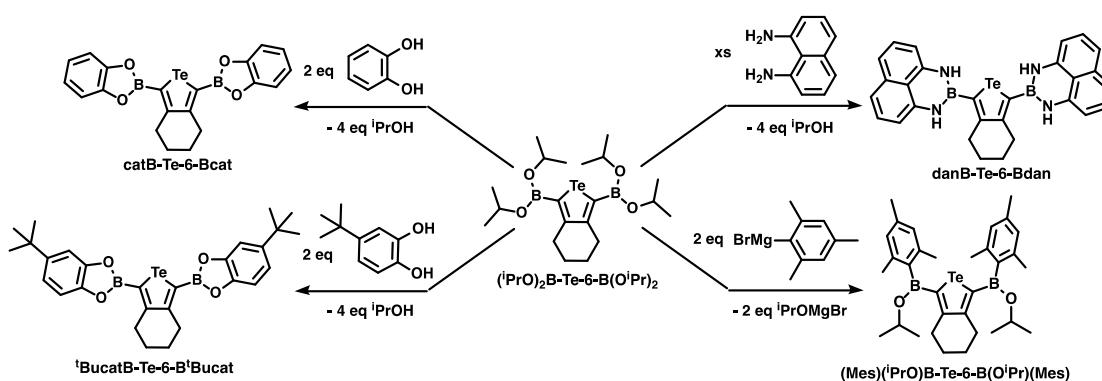
Drawing inspiration from prior condensation chemistry involving labile heteroacene-bound boryloxy  $-\text{B}(\text{OR})_2$  groups and nucleophiles,<sup>35-40</sup> the reactive precursor  $(i\text{PrO})_2\text{B-Te-6-B}(\text{O}i\text{Pr})_2$  was synthesized using a similar synthetic procedure (Scheme 3.1) as introduced in 2013 for the synthesis of the BPin analogue **B-Te-6-B**

(Figure 3.1).<sup>13,41</sup> Specifically, this procedure involved the dilithiation of 1,7-octadiyne, followed by the addition of  $B(O^iPr)_3$  and then HCl to yield the moisture-sensitive diyne  $(^iPrO)_2BC\equiv C(CH_2)_4C\equiv CB(O^iPr)_2$  (Scheme 3.1). Zirconocene-mediated diyne cyclization with Negishi's reagent (a source of "ZrCp<sub>2</sub>" generated *in situ* from two equivalents of <sup>n</sup>BuLi and Cp<sub>2</sub>ZrCl<sub>2</sub>) in THF,<sup>42</sup> followed by Zr/Te element exchange (transmetallation) with the readily available Te(II) source TeCl<sub>2</sub>·bipy (bipy = 2,2'-bipyridine) yields the target tellurophene  $(^iPrO)_2B\text{-Te-6-B}(O^iPr)_2$  in > 80 % yield (Scheme 3.1). Due to the moisture-sensitive and highly soluble nature of this di(isopropoxy)borylated tellurophene in most organic solvents, isolating the product in pure form proved challenging. Eventually it was found that the bipy byproduct could be removed *via* the addition of CuI to the crude mixture leading to insoluble, red-coloured CuI-bipy complex(es) that can be effectively removed by filtration in hexanes or pentane. While analytically pure product could still not be obtained, all borylated tellurophenes derived from this precursor were isolated as analytically pure solids.



**Scheme 3.1** – Synthesis of the di(isopropoxy)borylated tellurophene precursor  $(^iPrO)_2B\text{-Te-6-B}(O^iPr)_2$ .

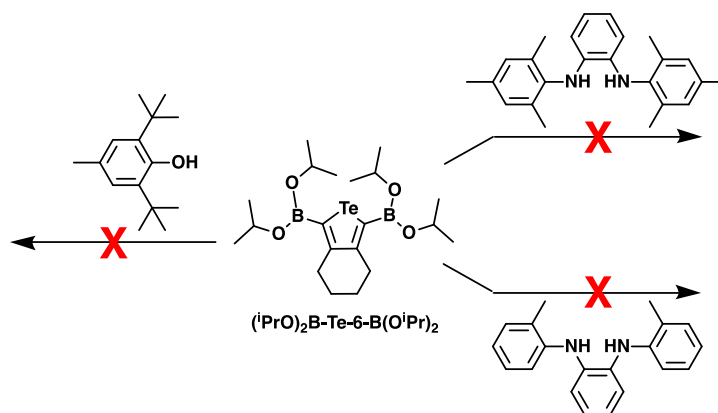
Postulating that the absence of a boryl ring chelate in  $(i\text{PrO})_2\text{B-Te-6-B(O}^i\text{Pr)}_2$  would lead to enhanced reactivity of the  $-\text{B(O}^i\text{Pr)}_2$  groups, this compound was combined with various potentially chelating nucleophiles, as well as the Grignard reagent  $\text{MesMgBr}$ . As a benchmarking reaction,  $(i\text{PrO})_2\text{B-Te-6-B(O}^i\text{Pr)}_2$  was combined with two equivalents of pinacol, leading to the formation of the well-known phosphorescent tellurophene **B-Te-6-B**<sup>13,21,41</sup> which was identified by  $^1\text{H}$ ,  $^{13}\text{C}\{^1\text{H}\}$ , and  $^{11}\text{B}\{^1\text{H}\}$  NMR spectroscopy. Addition of the less nucleophilic diol catechol (1,2-dihydroxybenzene) to  $(i\text{PrO})_2\text{B-Te-6-B(O}^i\text{Pr)}_2$  also led to boryl-substitution to yield the new tellurophene **catB-Te-6-Bcat** within one hour (Scheme 3.2). Notably, the pinacolboronate derivative **B-Te-6-B** does not react with catechol under similar conditions, showing a clear increase in reactivity by replacing the  $-\text{BPin}$  groups with  $-\text{B(O}^i\text{Pr)}_2$ .



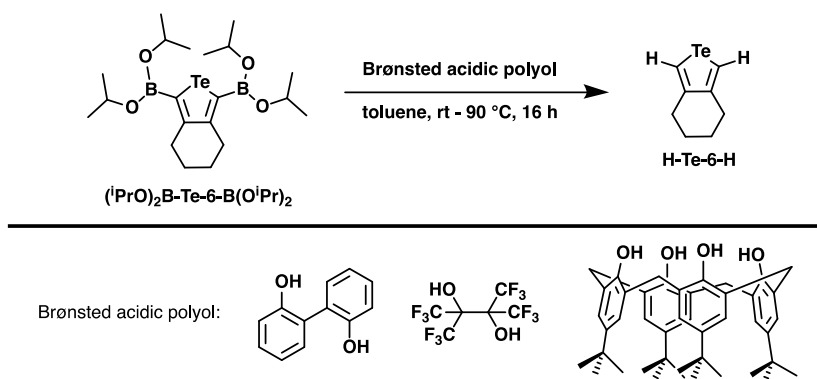
**Scheme 3.2** – Boryl exchange protocol used to access new borylated tellurophenes *via* the common building block  $(i\text{PrO})_2\text{B-Te-6-B(O}^i\text{Pr)}_2$ .

Following a similar convenient procedure,  $(i\text{PrO})_2\text{B-Te-6-B(O}^i\text{Pr)}_2$  was also combined with 4-*tert*-butylcatechol and 1,8-diaminonaphthalene to form  **${}^i\text{BucatB-Te-6-B}{}^i\text{Bucat}$**  and  **$\text{danB-Te-6-Bdan}$** , respectively (Scheme 3.2); in each case the isolated yield was *ca.* 50 %. It is important to note that these tellurophenes could not be formed *via* their respective diynes through zirconocene-mediated cyclization/metallacycle transfer.<sup>41</sup>

Although exchange reactions between  $(i\text{PrO})_2\text{B-Te-6-B(O}^i\text{Pr)}_2$  and various alcohols and amines proved to be fruitful, difficulties were encountered while attempting to extend this methodology to bulky and/or electron-deficient reagents. For example, no reaction was observed between  $(i\text{PrO})_2\text{B-Te-6-B(O}^i\text{Pr)}_2$  and the common solvent stabilizer 2,6-di-*tert*-butyl-4-methylphenol, nor with the di-imines *N,N*-dimesityl-1,2-phenylenediamine or *N,N*-dixylyl-1,2-phenylenediamine, despite allowing the reactions to go at room temperature for 7 days or heating at 50 °C for 36 hours (Scheme 3.3). In the presence of highly Brønsted acidic polyols, such as 2,2'-biphenol, perfluoropinacol [ $\text{HO}(\text{CF}_3)_2\text{C}(\text{CF}_3)_2\text{OH}$ ], and 4-*tert*-butylcalix[4]arene, the only tellurophene containing product isolated was the known protodeboronated product  **$\text{H-Te-6-H}$**  (Scheme 3.4).<sup>34</sup> A possible explanation for the observed protodeboronation is that the reaction proceeds as initially expected, however due to the more electron deficient nature of the resulting boryl-groups (*e.g.*,  $-\text{B}(\text{OC}(\text{CF}_3)_2)_2$ ), protonolysis involving the  ${}^i\text{PrOH}$  by-product is rendered more facile. I hoped to circumvent  ${}^i\text{PrOH}$ -mediated decomposition by combining dilithio-2,2'-biphenol with  $(i\text{PrO})_2\text{B-Te-6-B(O}^i\text{Pr)}_2$ , however no discernible reaction was found.



**Scheme 3.3** – Attempted reactions between  $(i\text{PrO})_2\text{B-Te-6-B(O}^i\text{Pr)}_2$  and 2,6-di-*tert*-butyl-4-methylphenol, *N,N'*-dimesityl-1,2-phenylenediamine, or *N,N'*-dixylyl-1,2-phenylenediamine.



**Scheme 3.4** – Reactions between  $(i\text{PrO})_2\text{B-Te-6-B(O}^i\text{Pr)}_2$  and various Brønsted acidic polyols that produce **H-Te-6-H** as the only tellurium containing product.

As alluded to in the introduction of this Chapter, a large number of luminescent thiophenes featuring sterically encumbered dimesitylboryl ( $-\text{BMes}_2$ ) units have been reported, with near unity fluorescence quantum yields coupled with moisture-stability and strong electronic communication in the excited state (leading to a red-shifted emission maxima *via* “push-pull” electronic arrangements).<sup>43</sup> In contrast to their

fluorescent thiophene counterparts, tellurophenes are known to exhibit long-lifetime phosphorescence due to enhanced intersystem crossing (ISC), and mixing between excited singlet ( $S_n$ ) and triplet ( $T_n$ ) states *via* the heavy atom effect.<sup>21,25,44,45</sup> In order to gain access to a new air-stable phosphorescent emitter, the synthesis of a tellurophene bearing  $-BMes_2$  groups at the 2- and 5-positions was targeted. Of note, previous attempts to yield this species *via* alkyne cyclization/metallacycle transfer from the isolable diyne  $Mes_2BC\equiv C(CH_2)_4C\equiv CBMes_2$  led to no reaction with Negishi's reagent "Cp<sub>2</sub>Zr", presumably due to the combined steric bulk of the two flanking  $-BMes_2$  groups.<sup>41</sup> While attempted reactions between **(*i*PrO)<sub>2</sub>B-Te-6-B(*O*<sup>*i*</sup>Pr)<sub>2</sub>** and MesLi were slow and gave mixtures of products, the addition of two equivalents of MesMgBr gave the new boryl tellurophene **Mes(*i*PrO)B-Te-6-B(*O*<sup>*i*</sup>Pr)Mes** in good yield (Scheme 3.2). Unfortunately, all attempts to form the fully mesityl substituted boryl tellurophene **Mes<sub>2</sub>B-Te-6-BMes<sub>2</sub>** by adding excess MesMgBr and/or refluxing in THF failed to yield any additional substitution chemistry.

### 3.2.2 Structural characterization of borylated tellurophenes

All of the four newly prepared boryl-tellurophenes discussed in this chapter were also characterized by X-ray crystallography, with the final refined structures presented in Figures 3.2–3.5. The related compounds, **catB-Te-6-Bcat** and **<sup>t</sup>BucatB-Te-6-B<sup>t</sup>Bucat** (Figures 3.2 and 3.3) both feature *cisoid* Te-C-B-O torsion angles of less than 10°, in line with mutually coplanar arrangements of the catecholboronate and tellurophene rings. Prior work with BPin has shown that when such a coplanar

arrangement is present, light absorption (excitation) can involve the vacant p-orbitals at boron.<sup>21,25,34</sup> In contrast, the solid state structure of **danB-Te-6-Bdan** (Figure 3.4) has planar  $-B(\text{dan})$  groups that are rotated by *ca.*  $50^\circ$  relative to the tellurophene ring. This compound also displays hydrogen bonding interactions between the amine protons and the oxygen atoms of  $\text{Et}_2\text{O}$  solvent molecules (N-H $\cdots$ O distances of *ca.* 2.22 Å and *ca.* 2.18 Å). Removal of the solvent molecules can be accomplished by freeze-drying a sample of **danB-Te-6-Bdan** in benzene for *ca.* 6 hours under vacuum (0.2 torr). The mesityl-substituted tellurophene **Mes(<sup>i</sup>PrO)B-Te-6-B(O<sup>i</sup>Pr)Mes** (Figure 3.5) crystallizes in the highly symmetric *Pnna* space group. The metrical parameters in this complex are as expected with one notable feature being the nearly orthogonal arrangement of the Mes ring with the plane containing the B-O, B-C(Mes) and B-C(tellurophene) bonds.<sup>43</sup>

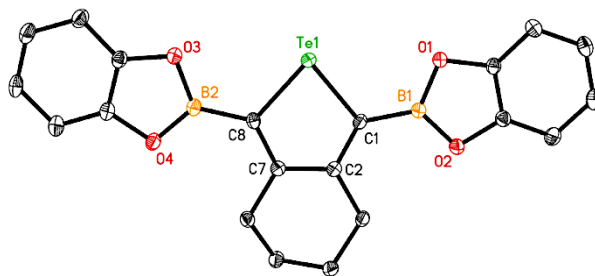


**Figure 3.2** – Molecular structure of **catB-Te-6-Bcat** with thermal ellipsoids presented at a 30 % probability level. All hydrogen atoms have been omitted for clarity. Selected bond lengths [Å] and angles [°]: Te1—C1 2.058(3), Te1—C8 2.064(3), C1—C2 1.378(4), C2—C7 1.446(4), C7—C8 1.377(4), C1—B1 1.533(4), C8—B2 1.536(4), B1—O1 1.395(3), B1—O2 1.392(4), B2—O3 1.391(4), B2—O4 1.391(4); C1—Te1—C8 82.62(11), C1—B1—O1 122.2(3), C1—B1—O2 126.3(2), C8—B2—O3 122.4(3), C8—B2—O4 126.3(3), O1—B1—O2 111.5(2), O3—B2—O4 111.3(2).



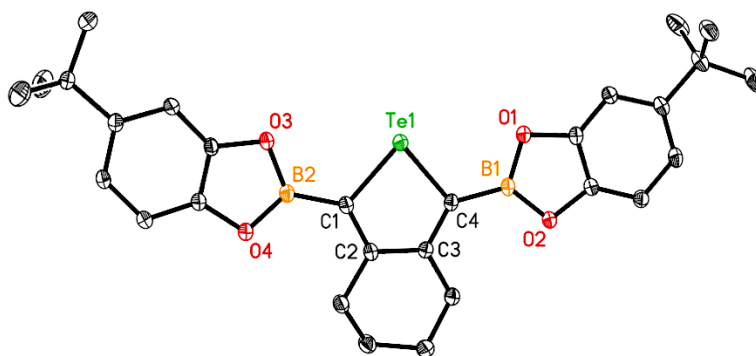


**Figure 3.3** – Molecular structure of ***t*BucatB-Te-6-Bcat<sup>t</sup>Bu** with thermal ellipsoids presented at a 30 % probability level. All hydrogen atoms have been omitted for clarity. Selected bond lengths [Å] and angles [°]: Te1—C1 2.0657(18), Te1—C4 2.0617(19), C1—C2 1.373(3), C2—C3 1.443(2), C3—C4 1.375(3), C1—B2 1.524(3), C4—B1 1.535(3), B1—O1 1.394(3), B1—O2 1.394(2), B2—O3 1.394(3), B2—O4 1.392(2); C1—Te1—C4 82.56(7), C1—B2—O3 122.64(17), C1—B2—O4 126.37(18), C4—B1—O1 120.64(18), C4—B1—O2 127.83(18), O1—B1—O2 111.48(6), O3—B2—O4 110.99(16).

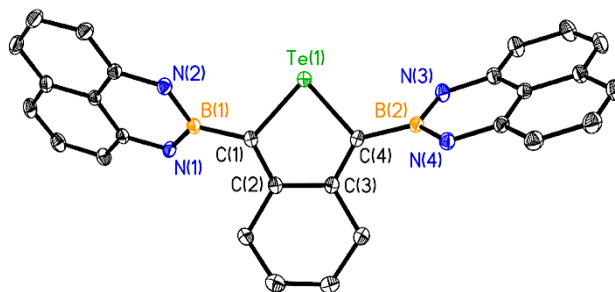


**Figure 3.4** – Molecular structure of **danB-Te-6-Bdan** with thermal ellipsoids presented at a 30 % probability level. Solvent molecules (Et<sub>2</sub>O) and H atoms have been omitted for clarity. Selected bond lengths [Å] and angles [°]: Te1—C1 2.0702(14), Te1—C4 2.0636(15), C1—C2 1.363(2), C2—C3 1.452(2), C3—C4 1.366(2), C1—B1 1.561(2), C4—B2 1.561(2), B1—N1 1.420(2), B1—N2 1.416(2), B2—N3 1.416(2), B2—N4 1.420(2); C1—Te1—C4 83.39(6), C1—B1—N1 121.57(13), C1—B1—N2 121.74(13), C4—B2—N3 122.56(14), C4—B2—N4 121.23(14), N1—B1—N2 116.58(13), N3—B2—N4 116.11(14).

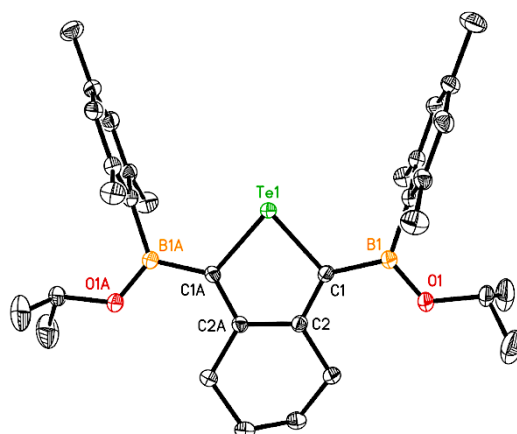


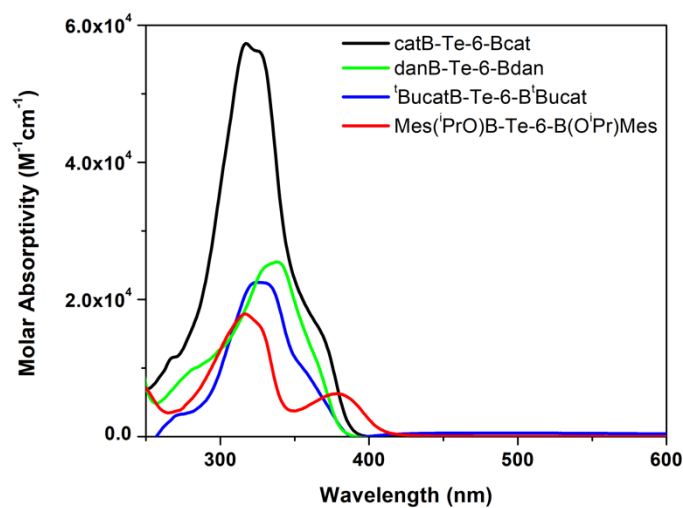
**Figure 3.5** – Molecular structure of **Mes(*i*PrO)B-Te-6-B(*O**i*Pr)Mes** with thermal ellipsoids presented at a 30 % probability level. All hydrogen atoms have been omitted for clarity. Selected bond lengths [Å] and angles [°]: Te1—C1 2.063(2), C1—C2 1.385(3), C2—C2A 1.446(5), C1—B1 1.556(3), B1—O1 1.361(3), B1—C11 1.585(3); C1—Te1—C1A 83.17(14), C1—B1—O1 117.2(2), C1—B1—C11 120.9(2), C11—B1—O1 121.9(2).

### 3.2.3 Photoluminescence characterization of borylated tellurophenes

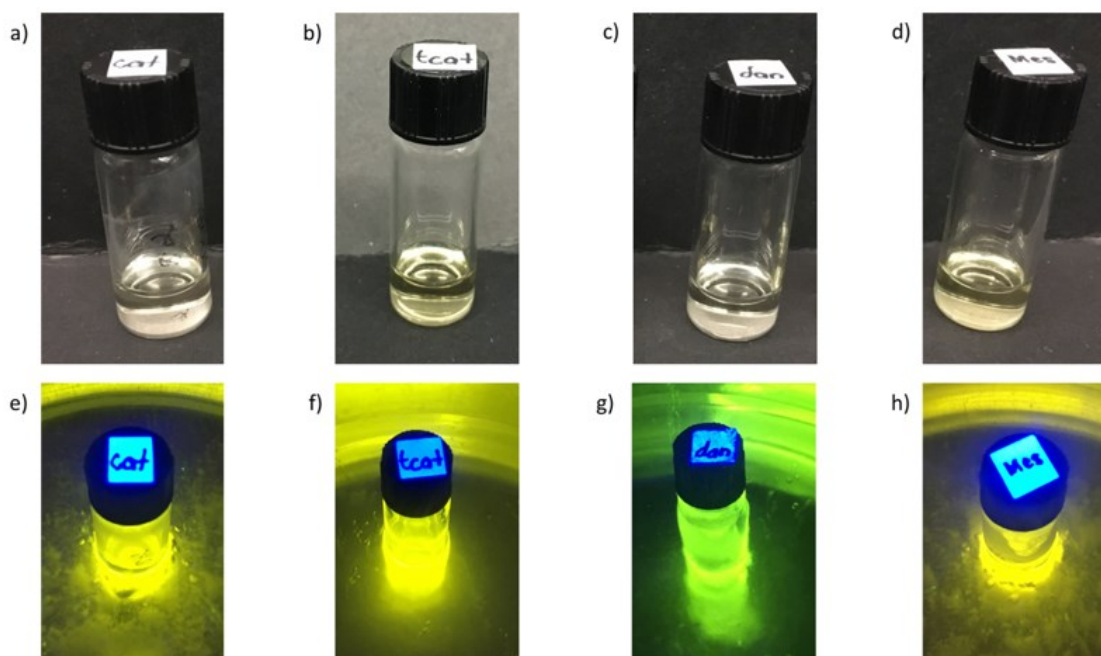
The abovementioned boryl-tellurophenes all strongly absorb UV-vis light ( $\epsilon_{\max} > 1.8 \times 10^4 \text{ M}^{-1}\text{cm}^{-1}$ ) with similar  $\lambda_{\max}$  values that range from 317 to 338 nm (

Figure 3.6). Furthermore, all four tellurophenes are emissive (green to yellow-orange) when cooled with liquid nitrogen (at 77 K) and excited at 365 nm with a hand-held UV lamp. This was true for both dilute solutions (0.01–0.02 M in frozen 2-methyltetrahydrofuran, Figure 3.7) as well as for solid samples (Figure 3.8). In the solid state at room temperature, amorphous samples of **catB-Te-6-Bcat** and **danB-Te-6-Bdan** are non-emissive, while **'BucatB-Te-6-B'Bucat** shows only very weak yellow emission ( $\lambda_{\text{em}} = 575 \text{ nm}$ ) with a measured absolute quantum yield ( $\Phi$ ) of 0.2 % (Figure

3.9). The lifetime of emission ( $\tau$ ) averaged to 22  $\mu\text{s}$  and is in the range typically found for phosphorescent tellurophenes (*ca.* 1–150  $\mu\text{s}$ ).<sup>21,25,34</sup> The mesityl-containing tellurophene **Mes(<sup>i</sup>PrO)B-Te-6-B(O<sup>i</sup>Pr)Mes** afforded a much brighter yellow-orange emission in the solid state ( $\lambda_{\text{em}} = 590 \text{ nm}$ ,  $\Phi = 15.2 \%$ ,  $\tau(\text{avg.}) = 109 \mu\text{s}$ ; Figure 3.10). **Mes(<sup>i</sup>PrO)B-Te-6-B(O<sup>i</sup>Pr)Mes** also fully retains its emission in the presence of the known triplet quencher  $\text{O}_2$ .



**Figure 3.6** – UV-vis absorption spectra recorded for  $3 \times 10^{-5} \text{ M}$  THF solutions.



**Figure 3.7** – *Top*: Solutions of a) **catB-Te-6-Bcat**, b) **<sup>t</sup>BucatB-Te-6-B<sup>t</sup>Bucat**, c) **danB-Te-6-Bdan** and d) **Mes(<sup>i</sup>PrO)B-Te-6-B(<sup>O</sup>iPr)Mes** in 2-methyltetrahydrofuran (0.01–0.02 M) at room temperature. *Bottom*: Frozen solutions of e) **catB-Te-6-Bcat**, f) **<sup>t</sup>BucatB-Te-6-B<sup>t</sup>Bucat**, g) **danB-Te-6-Bdan** and h) **Mes(<sup>i</sup>PrO)B-Te-6-B(<sup>O</sup>iPr)Mes** in 2-methyltetrahydrofuran cooled in N<sub>2</sub>(l) and irradiated with a hand-held UV lamp (365 nm).

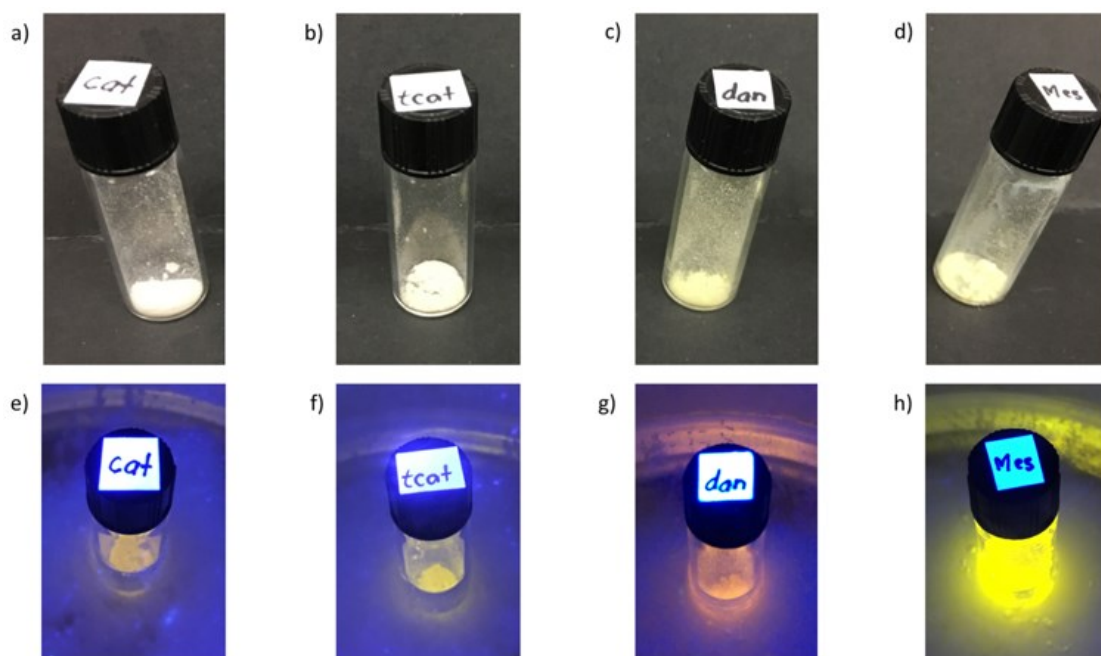


**Figure 3.8** – *Top*: Solid samples of a) **catB-Te-6-Bcat**, b) **<sup>t</sup>BucatB-Te-6-B<sup>t</sup>Bucat**, c) **danB-Te-6-Bdan** and d) **Mes(<sup>i</sup>PrO)B-Te-6-B(O<sup>i</sup>Pr)Mes** at room temperature. *Bottom*: Solid samples of e) **catB-Te-6-Bcat**, f) **<sup>t</sup>BucatB-Te-6-B<sup>t</sup>Bucat**, g) **danB-Te-6-Bdan** and h) **Mes(<sup>i</sup>PrO)B-Te-6-B(O<sup>i</sup>Pr)Mes** cooled in N<sub>2</sub> (l) and irradiated with a hand-held UV lamp (365 nm).

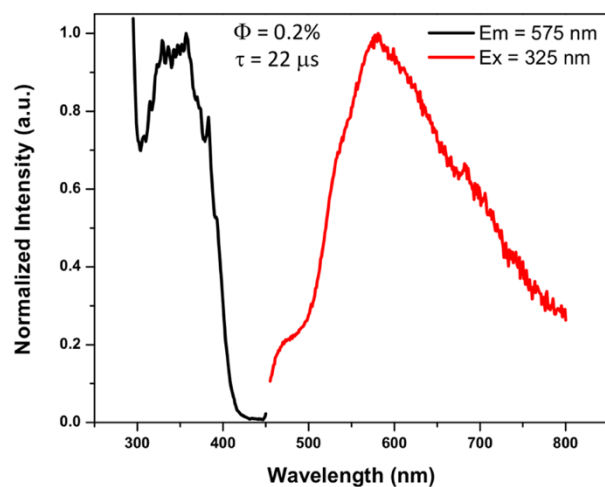


**Figure 3.9** – Solid state excitation (black) and emission (red) spectra of an amorphous sample of 'BucatB-Te-6-B'Bucat.

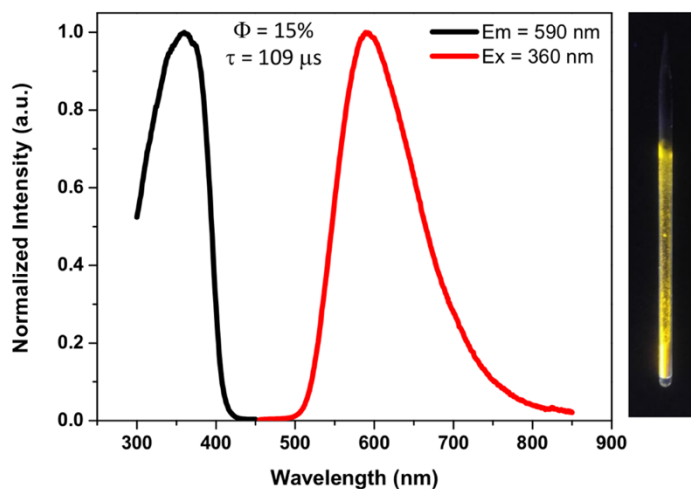


**Figure 3.10** – *Left*: Solid state excitation (black) and emission (red) spectra of an amorphous sample of Mes(<sup>i</sup>PrO)B-Te-6-B(O<sup>i</sup>Pr)Mes. *Right*: Image of the solid sample of Mes(<sup>i</sup>PrO)B-Te-6-B(O<sup>i</sup>Pr)Mes irradiated with a hand-held UV lamp (365 nm).

Previous work has shown that a decrease in phosphorescence quantum yield can occur if close intermolecular Te...Te contacts are found in the solid state (*i.e.*, below the sum of the van der Waals radii of 4.2 Å).<sup>21,46</sup> The explanation for this effect is that close contacts facilitate triplet-triplet annihilation, leading to quenching of the phosphorescence. Encouragingly, the closest Te...Te contact in the solid (crystalline) state in **<sup>t</sup>BucatB-Te-6-B<sup>t</sup>Bucat** was 4.932(1) Å, while all other tellurophenes show Te...Te separations > 5.0 Å. Although faint emission was observed for solid samples of **catB-Te-6-Bcat**, **<sup>t</sup>BucatB-Te-6-B<sup>t</sup>Bucat**, and **danB-Te-6-Bdan** at 77 K, only **Mes(<sup>i</sup>PrO)B-Te-6-B(O<sup>i</sup>Pr)Mes** showed bright emission at room temperature (Figure 3.8). In contrast to the faint emission observed for some of the solid samples, bright emission was observed for frozen (77 K) MeTHF solutions for all samples. This suggests that some self-quenching might be occurring in the pure bulk phase of the –Bcat, –B<sup>t</sup>Bucat and –Bdan analogues, where closer contacts in the amorphous solids (*vs.* in crystals) might enable self-quenching to occur. Nevertheless, the observed luminescence at 77 K (faint in the solid state and bright in dilute solution) indicates that the energy requirements for phosphorescence, *i.e.*, close excited state singlet (S<sub>n</sub>) and triplet (T<sub>n</sub>) energy levels, have been met. The observation of the brightest solid state emission for **Mes(<sup>i</sup>PrO)B-Te-6-B(O<sup>i</sup>Pr)Mes** could be due to favourable solid state packing/morphology effects, since close intermolecular contacts can restrict molecular motion and reduce the diffusion of O<sub>2</sub> through the solid, resulting in less efficient non-radiative decay (*i.e.*, less quenching of emission). Prior evidence<sup>21</sup> suggests that the solid state emission in our tellurophenes is modulated *via* aggregation-induced emission

(AIE), wherein restriction of intramolecular motion suppresses non-radiative decay pathways, leading to enhanced photoluminescence.<sup>47</sup>

### 3.2.4 Computational studies

To further explore the excitation process (light absorption) within **Mes(<sup>i</sup>PrO)B-Te-6-B(O<sup>i</sup>Pr)Mes** time-dependent density functional theory (TD-DFT) computations were conducted at the B3LYP/cc-pVDZ(-PP) level of theory. As shown in Figure 3.11, two intense transitions are predicted with absorption maxima of 315 nm and 362 nm, which are in good agreement with the experimentally derived UV-vis data ( $\lambda_{\text{max}} = 317$  and 378 nm, Figure 3.11). The lowest energy transition is attributed to a HOMO to LUMO transition, which is C-C  $\pi$  to C-C  $\pi^*$ /B-C  $\pi$  in character with significant contribution from the lone-pair (p-orbital) at the Te centre in both the HOMO and LUMO (Figure 3.12). The more intense S<sub>0</sub> to S<sub>4</sub> transition at 317 nm is attributed to a HOMO-1 to LUMO transition, which also has C-C  $\pi$  to C-C  $\pi^*$  character, however only the LUMO has a significant contribution from the Te centre. It should be stated that one needs substantial orbital participation from the heavy element (Te in this case) to gain access to enhanced spin-orbit coupling (SOC),<sup>25</sup> otherwise phosphorescence becomes less efficient.



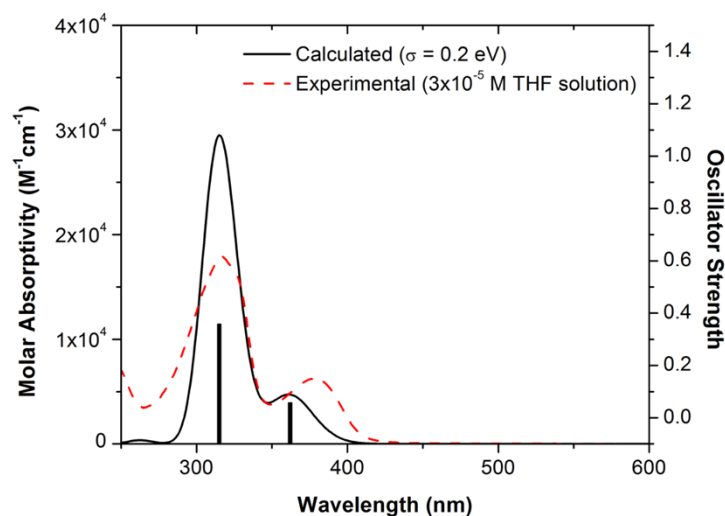


**Figure 3.11** – The experimental (red dash) and calculated (black) UV-vis absorption spectra of **Mes(<sup>i</sup>PrO)B-Te-6-B(O<sup>i</sup>Pr)Mes** at the B3LYP/cc-pVDZ(-PP) level of theory. Black bars are shown for the two electronic transitions with the highest oscillator strengths.

In accordance with the observed phosphorescence from **Mes(<sup>i</sup>PrO)B-Te-6-B(O<sup>i</sup>Pr)Mes**, TD-DFT studies also revealed the presence of several low-lying singlet excited states ( $S_n$ ;  $n < 7$ ) that are energetically close to excited triplet states ( $\Delta E_{ST} < 0.10$  eV, Figure 3.13). Therefore, the observed phosphorescence likely results from photoexcitation to an  $S_n$  state, followed by intersystem crossing to a nearby  $T_n$  state; finally, non-radiative relaxation to and emission from the  $T_1$  state occurs, in line with Kasha's rule.<sup>48</sup> Additionally, the phosphorescence energy of **Mes(<sup>i</sup>PrO)B-Te-6-B(O<sup>i</sup>Pr)Mes** was computed by calculating the difference between the zero-point corrected adiabatic energies ( $E_{0-0}$ ) of the  $S_0$  and  $T_1$  states at their optimized geometries. The computed value of 2.54 eV (488 nm) is of lower energy than the experimentally

observed phosphorescence at 590 nm (2.10 eV) in **Mes(<sup>i</sup>PrO)B-Te-6-B(O<sup>i</sup>Pr)Mes** (Figure 3.10).

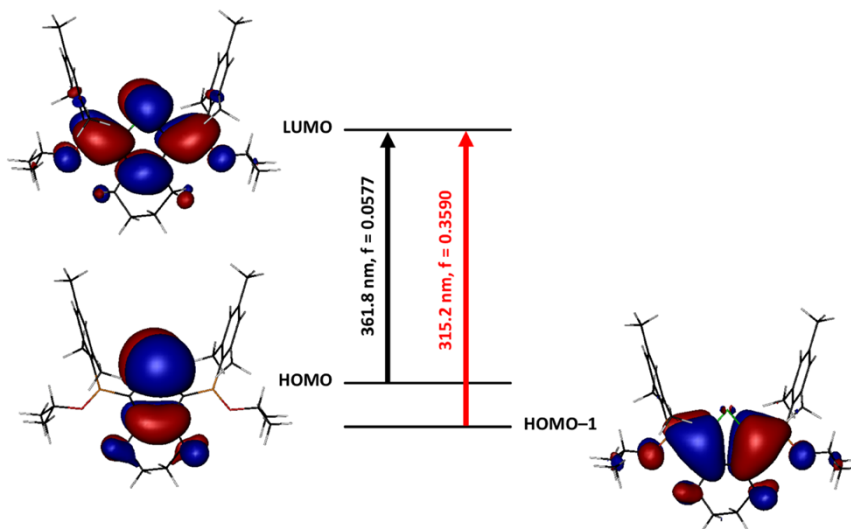


**Figure 3.12** – TD-DFT [B3LYP/cc-pVDZ(-PP)] computed main transitions for **Mes(<sup>i</sup>PrO)B-Te-6-B(O<sup>i</sup>Pr)Mes** including excitation wavelengths and oscillator strengths ( $f$ ) for the most intense transitions ( $S_0 \rightarrow S_1$ : black;  $S_0 \rightarrow S_4$ : red) along with the associated molecular orbitals; iso-surface values of +0.02/-0.02 (red/blue).

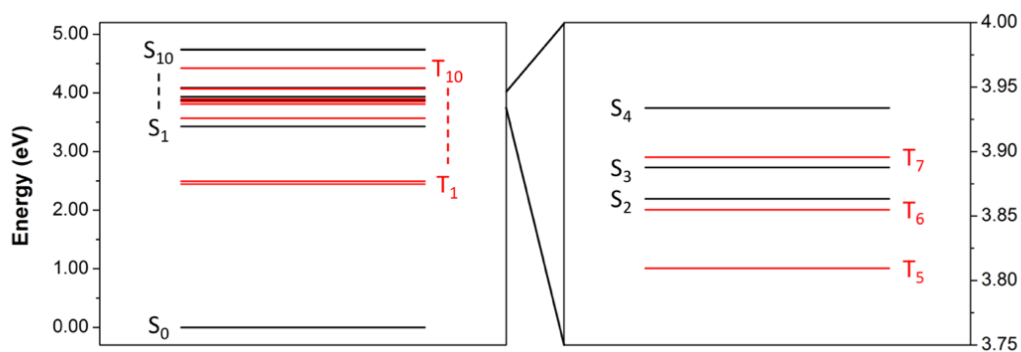
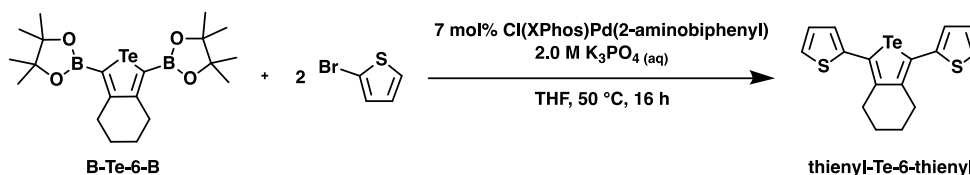


**Figure 3.13** – *Left*: Singlet and triplet states of **Mes(<sup>i</sup>PrO)B-Te-6-B(O<sup>i</sup>Pr)Mes** calculated at the B3LYP/cc-pVDZ(-PP) level of theory; *Right*: A close-up of the  $S_2$ - $S_4$  and  $T_5$ - $T_7$  states.

### 3.2.5 Suzuki-Miyaura cross-coupling involving borylated tellurophenes

The ability of the new borylated tellurophenes to act as reagents in Suzuki-Miyaura cross-coupling was investigated next. Although **B-Te-6-B** has previously been used in Suzuki-Miyaura cross-coupling to synthesize aryl-functionalized tellurophenes<sup>25</sup> as well as low molecular weight copolymers,<sup>13</sup> protodeboronation remained a continuous problem, preventing access to high molecular weight polymers. In these prior Suzuki-Miyaura coupling reactions, common pre-catalysts such as Pd(OAc)<sub>2</sub> or Pd<sub>2</sub>dba<sub>3</sub> were used. In 2010, Buchwald and coworkers reported the one-pot synthesis of an active palladium pre-catalyst featuring a 2-aminobiphenyl ligand, Cl(XPhos)Pd(2-aminobiphenyl); notably, this pre-catalyst can be activated under mild conditions (40 °C, reaction time of 2 hrs, pre-catalyst loading of 2 mol %).<sup>49</sup> Moreover, Buchwald's pre-catalyst was effective at limiting protodeboronation during the Suzuki-Miyaura cross-coupling of furan- and thiophene-containing boronic acids.<sup>49</sup> I was curious to see if this catalytic system would be suitable for electron-rich tellurophenes substrates, which are even more prone to protodeboronation than their light congeners.<sup>34</sup> As a starting point, the coupling of **B-Te-6-B** with two equivalents of 2-bromothiophene using Cl(XPhos)Pd(2-aminobiphenyl) as the pre-catalyst was examined (Scheme 3.5). A slightly higher pre-catalyst loading of 7 mol % was used since **B-Te-6-B** contains two active -BP in coupling sites per substrate instead of just one. As hoped, the resulting cross-coupling reaction transpired to yield the known tellurophene **thienyl-Te-6-thienyl**, with no detectable amounts of the known protodeboronated tellurophenes **H-Te-6-H** or **pinB-Te-6-H**.<sup>34</sup> Although slightly elevated temperatures (*ca.* 50 °C) and

higher pre-catalyst loadings (7 mol %) were required, this reaction leads to a very high isolated yield of **thienyl-Te-6-thienyl** (91 % after 16 hours). In comparison, the use of Pd(OAc)<sub>2</sub> or Pd<sub>2</sub>dba<sub>3</sub> as pre-catalysts gave yields lower than 50 %.<sup>34</sup>



**Scheme 3.5** – Improved Suzuki-Miyaura cross-coupling of **B-Te-6-B** with 2-bromothiophene to yield **thienyl-Te-6-thienyl**.

Contrary to the coupling results with **B-Te-6-B**, the Suzuki-Miyaura coupling with boryl-tellurophenes featuring –Bcat or –B<sup>t</sup>Bucat did not produce the di-substituted thienyl product **thienyl-Te-6-thienyl** in any appreciable quantity when the same cross-coupling procedure as outlined in Scheme 3.5 was applied. Despite these mild conditions, protodeboronated products were the major tellurium-containing products, along with free catechol or *tert*-butyl catechol. In addition to the known protodeboronated tellurophene, **H-Te-6-H**, a new deboronated product was also identified by the presence of an up-field singlet <sup>1</sup>H NMR resonance at 8.19 ppm, flanked by diagnostic Te satellites (Figure 3.14). This peak is tentatively assigned to the mono-substituted by-product **thienyl-Te-6-H**, which is consistent with accompanying resonances in the <sup>13</sup>C {<sup>1</sup>H} NMR spectrum, which show the expected presence of four chemically inequivalent CH<sub>2</sub> groups along the cyclohexyl backbone (Figure 3.15). The presence of the same byproduct in the coupling reactions between either **catB-Te-6-**

**Bcat** and **'BucatB-Te-6-B'Bucat** and 2-bromothiophene lends added support for the formation of **thienyl-Te-6-H**.

Finally, **danB-Te-6-Bdan** was also combined with two equivalents of 2-bromothiophene under the conditions outlined in Scheme 3.5.<sup>50</sup> In this case, no protodeboronation was detected and the desired product **thienyl-Te-6-thienyl** was formed, although not quite as cleanly (*ca.* 80 % *in situ* yield of the final product) as the coupling reaction with **B-Te-6-B** (Figures 3.14 and 3.15); after work-up, **thienyl-Te-6-thienyl** could be isolated in a 43 % yield. Overall, the above cross-coupling trials show that Buchwald's reactive Pd pre-catalyst limits protodeboronation within the Bdan- and BPin-capped tellurophenes. In particular, the use of -BPin functionalized tellurophenes in Suzuki Miyaura cross-coupling can lead to very efficient reactions to give 2,5-diaryltellurophenes in unprecedentedly high yields.

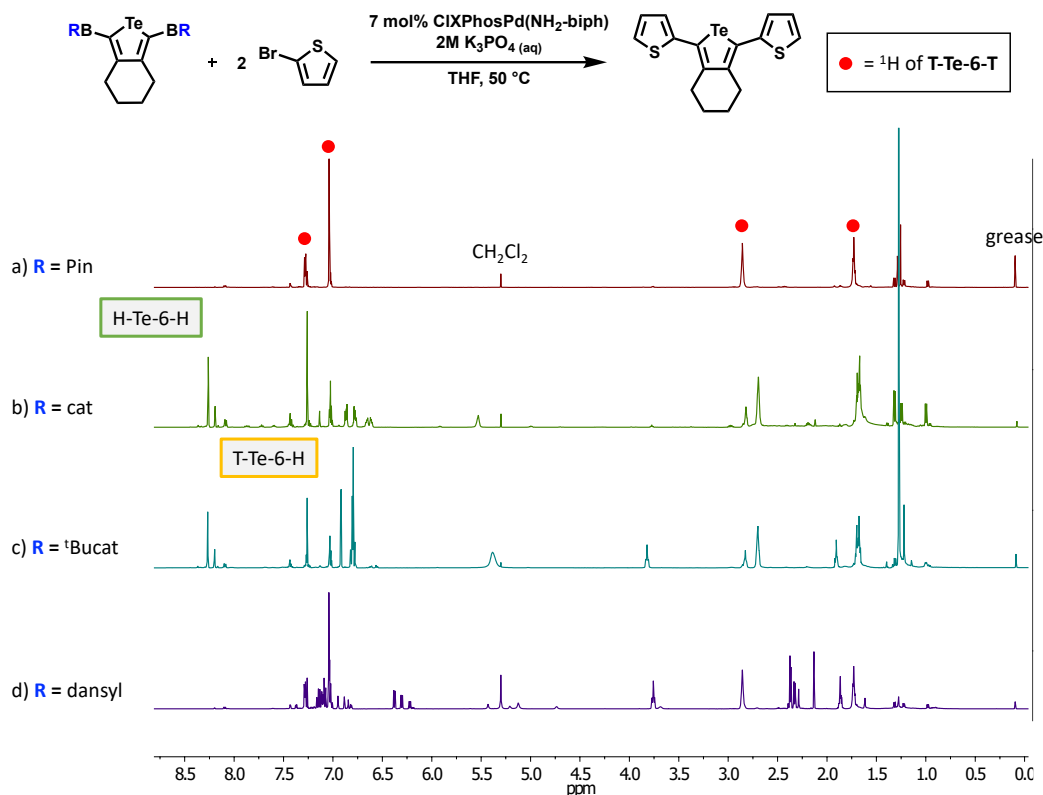


**Figure 3.14** – <sup>1</sup>H NMR spectra (CDCl<sub>3</sub>) of the attempted Suzuki-Miyaura cross coupling reactions between borylated tellurophenes and 2 equivalents of 2-bromothiophene. a) coupling with **B-Te-6-B** (16 hrs), b) coupling with **catB-Te-6-Bcat** (40 hrs), c) coupling with **<sup>t</sup>BucatB-Te-6-B<sup>t</sup>Bucat** (40 hrs), d) **danB-Te-6-Bdan** (16 hrs). All reactions were worked up by diluting the product mixtures with *ca.* 3 mL of CH<sub>2</sub>Cl<sub>2</sub>, drying over MgSO<sub>4</sub> and filtering before removing all volatiles. In the above spectra **T** = thienyl group.

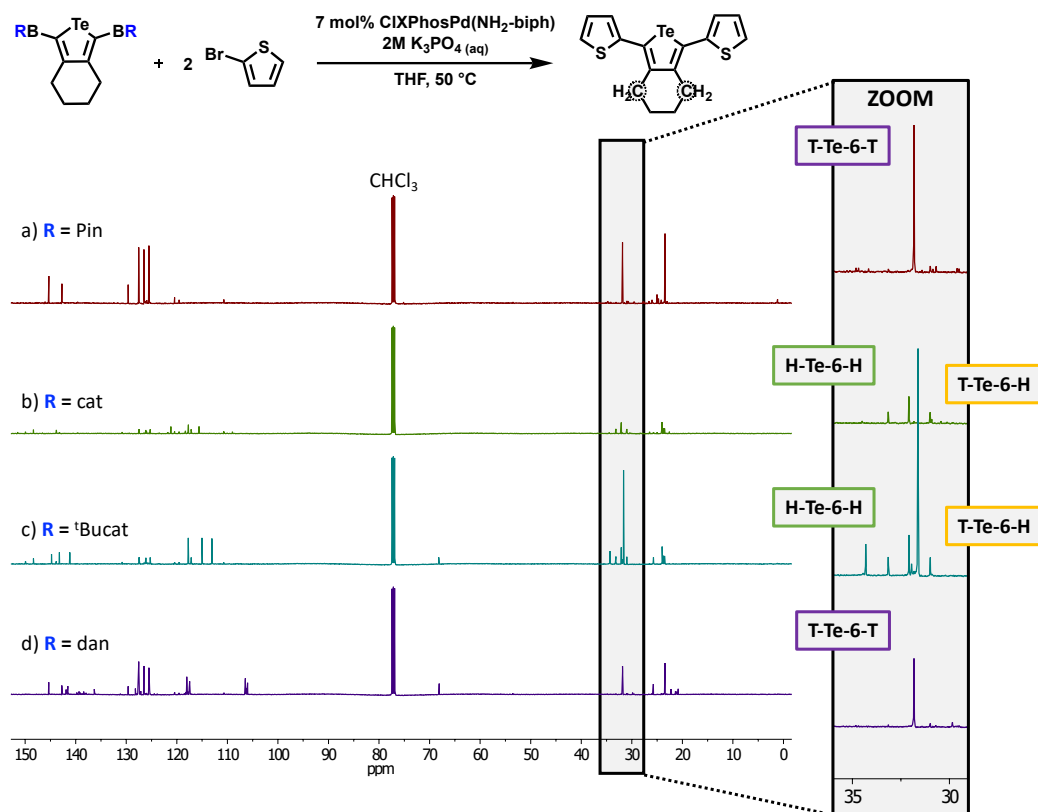


**Figure 3.15** –  $^{13}\text{C}\{^1\text{H}\}$  NMR spectra (CDCl<sub>3</sub>) of attempted Suzuki-Miyaura cross coupling reactions between borylated tellurophenes and 2-bromothiophene to produce **thienyl-Te-6-thienyl (T-Te-6-T)**. a) coupling with **B-Te-6-B** (16 hrs), b) coupling with **catB-Te-6-Bcat** (40 hrs), c) coupling with **'BucatB-Te-6-B'Bucat** (40 hrs), d) **danB-Te-6-Bdan** (16 hrs). All reactions were worked up by diluting the product mixtures with *ca.* 3 mL of CH<sub>2</sub>Cl<sub>2</sub>, drying over MgSO<sub>4</sub> and filtering before removing all volatiles. In the above spectra **T** = thienyl group.

### 3.3 Conclusions

In summary, a new di(isopropoxy)boryl-functionalized tellurophene (**<sup>i</sup>PrO**)<sub>2</sub>**B-Te-6-B(O<sup>i</sup>Pr)**<sub>2</sub> has been synthesized and used to yield new borylated tellurophenes *via* O<sup>i</sup>Pr group exchange. This method was employed to synthesize four previously

inaccessible tellurophenes: **catB-Te-6-Bcat**, **<sup>t</sup>BucatB-Te-6-B<sup>t</sup>Bucat**, **danB-Te-6-Bdan** and the mesityl-functionalized product **Mes(<sup>i</sup>PrO)B-Te-6-B(O<sup>i</sup>Pr)Mes**. **Mes(<sup>i</sup>PrO)B-Te-6-B(O<sup>i</sup>Pr)Mes** yields bright yellow-orange phosphorescence with a respectable absolute quantum yield of 15 % in the solid state and in air, which are both conditions that typically quench phosphorescence. Finally, the performance of borylated tellurophenes in Suzuki-Miyaura cross coupling reactions was investigated under mild conditions using the pre-catalyst Cl(XPhos)Pd(2-aminobiphenyl), leading to the suppression of protodeboronation. While tellurophenes bearing –BPin and –Bdan groups did not show any protodeboronation, the BPin-capped tellurophene **B-Te-6-B** was the superior substrate, yielding the coupling product **thienyl-Te-6-thienyl** cleanly in a > 90 % isolated yield. Future work will involve the utilization of this mild and effective Suzuki-Miyaura protocol to synthesize tellurophene-containing small molecules and polymers for luminescence-based applications.

## 3.4 Experimental

### 3.4.1 General procedures

Unless explicitly stated otherwise, all reactions were carried out with standard Schlenk and glovebox (MBraun) techniques using N<sub>2</sub> as the inert atmosphere and solvents that were dried using a Grubbs' type purification system manufactured by Innovative Technology Inc. 1,7-Octadiyne was purchased from GFS Chemicals, Cp<sub>2</sub>ZrCl<sub>2</sub> from Strem Chemicals Inc. and all other commercially available compounds



were obtained from Sigma-Aldrich; all commercially derived chemicals were used as received.  $\text{TeCl}_2 \cdot \text{bipy}^{51}$  and  $\text{Cl}(\text{XPhos})\text{Pd}(2\text{-aminobiphenyl})^{49}$  were synthesized according to literature procedures. Melting points were measured with a MelTemp apparatus and are reported without correction. High-resolution mass spectra were obtained on an Agilent 6220 spectrometer and Kratos Analytical MS-50G system. Elemental analyses were performed by the Analytical and Instrumentation Laboratory at the University of Alberta. UV-vis spectroscopic measurements were performed with a Varian Cary 5000 Scan Spectrophotometer.

### 3.4.2 Synthetic procedures

**Synthesis of  $(i\text{PrO})_2\text{BC}\equiv\text{C}(\text{CH}_2)_4\text{C}\equiv\text{CB}(\text{O}i\text{Pr})_2$ .**  $n\text{BuLi}$  (2.5 M solution in hexanes, 14.1 mL, 0.036 mol) was added dropwise to a cold ( $-78\text{ }^\circ\text{C}$ ) solution of 1,7-octadiyne (1.872 g, 0.01764 mol) in 350 mL of  $\text{Et}_2\text{O}$ . The mixture was stirred for 30 minutes and then a solution of  $\text{B}(\text{O}i\text{Pr})_3$  (6.634 g, 0.03527 mol) in 20 mL of  $\text{Et}_2\text{O}$  was added dropwise. The cold bath was then removed, and the mixture was stirred at room temperature for 1 hour. The reaction mixture was quenched by cooling to  $-78\text{ }^\circ\text{C}$  and adding a solution of anhydrous  $\text{HCl}$  (4.0 M solution in dioxane, 13.0 mL, 0.052 mol), followed by stirring at room temperature for 1 hour. After allowing the  $\text{LiCl}$  precipitate to settle, the supernatant was decanted into another Schlenk flask using a filter cannula. The volatiles were then removed from the filtrate under vacuum while heating to  $50\text{ }^\circ\text{C}$ , to yield  $(i\text{PrO})_2\text{BC}\equiv\text{C}(\text{CH}_2)_4\text{C}\equiv\text{CB}(\text{O}i\text{Pr})_2$  as a colourless liquid (5.006 g, 78 %)  $^1\text{H}$  NMR (498.1 MHz,  $\text{C}_6\text{D}_6$ ):  $\delta = 1.16$  (d,  $^3J_{\text{HH}} = 6.0$  Hz, 24H,  $\text{OCH}(\text{CH}_3)_2$ ), 1.39 (br, 4H,

$\text{C}\equiv\text{CCH}_2\text{CH}_2$ ), 1.94 (br, 4H,  $\text{C}\equiv\text{CCH}_2\text{CH}_2$ ), 4.68 (septet,  $^3J_{\text{HH}} = 6.0$  Hz, 4H,  $\text{OCH}(\text{CH}_3)_2$ ).  $^{13}\text{C}\{^1\text{H}\}$  NMR (176.0 MHz,  $\text{C}_6\text{D}_6$ ):  $\delta = 19.1$  ( $\text{C}\equiv\text{CCH}_2\text{CH}_2$ ), 24.7 ( $\text{OCH}(\text{CH}_3)_2$ ), 27.7 ( $\text{C}\equiv\text{CCH}_2\text{CH}_2$ ), 67.5 ( $\text{OCH}(\text{CH}_3)_2$ ), 103.2 (B-C $\equiv$ C). The  $^{13}\text{C}\{^1\text{H}\}$  resonance for B-C was not located.  $^{11}\text{B}\{^1\text{H}\}$  NMR (159.8 MHz,  $\text{C}_6\text{D}_6$ ):  $\delta = 21.5$ . HR-MS (ESI):  $m/z$  calcd. for  $[\text{C}_{20}\text{H}_{36}^{11}\text{B}_2\text{O}_4\text{Na}]^+$ : 385.2692; found: 385.2694 ( $\Delta\text{ppm} = 0.7$ ).

**Synthesis of (*i*PrO)<sub>2</sub>B-Te-6-B(O*i*Pr)<sub>2</sub>.** <sup>n</sup>BuLi (2.5 M solution in hexanes, 3.25 mL, 8.1 mmol) was added dropwise to a cold ( $-78$  °C) solution of  $\text{Cp}_2\text{ZrCl}_2$  (1.179 g, 4.033 mmol) in 100 mL of THF. The resulting mixture containing “ $\text{Cp}_2\text{Zr}$ ” (Negishi’s reagent)<sup>42</sup> was stirred for 1 hour and then a solution of (*i*PrO)<sub>2</sub>BC $\equiv$ C(CH<sub>2</sub>)<sub>4</sub>C $\equiv$ CB(O*i*Pr)<sub>2</sub> (1.391 g, 3.841 mmol) in 20 mL of THF was added. The mixture was stirred for 30 minutes at  $-78$  °C and then stirred for 16 hours at room temperature.  $\text{TeCl}_2\cdot\text{bipy}$  (1.655 g, 4.666 mmol) was added as a solid in one portion under a strong counterflow of  $\text{N}_2$ , and the reaction mixture was left to stir for 1 hour. Solid CuI (1.463 g, 7.683 mmol) was then added under a strong counterflow of  $\text{N}_2$  and the reaction mixture was left to stir for 1 more hour. The supernatant was decanted into another Schlenk flask using a filter cannula and the volatiles were removed from the filtrate *in vacuo*. In order to remove residual  $\text{Cp}_2\text{ZrCl}_2$ , the crude product was dissolved in 2 mL of pentane and filtered through a 1 cm plug of Celite. Removing the volatiles from the filtrate under vacuum afforded (*i*PrO)<sub>2</sub>B-Te-6-B(O*i*Pr)<sub>2</sub> as a red oil (1.756 g, 93 %) in *ca.* 90 % purity according to  $^1\text{H}$  NMR spectroscopy (Figure 3.19); this product was used without additional purification for all subsequent reactions.  $^1\text{H}$  NMR (699.8 MHz,  $\text{C}_6\text{D}_6$ ):  $\delta =$

1.18 (d,  $^3J_{\text{HH}} = 6.3$  Hz, 24H,  $\text{OCH}(\text{CH}_3)_2$ ), 1.50 (br, 4H,  $\text{C}=\text{CCH}_2\text{CH}_2$ ), 2.79 (br t, 4H,  $\text{C}=\text{CCH}_2\text{CH}_2$ ), 4.66 (septet,  $^3J_{\text{HH}} = 6.3$  Hz, 4H,  $\text{OCH}(\text{CH}_3)_2$ ).  $^{13}\text{C}\{^1\text{H}\}$  NMR (176.0 MHz,  $\text{C}_6\text{D}_6$ ):  $\delta = 24.0$  ( $\text{C}=\text{CCH}_2\text{CH}_2$ ), 24.9 ( $\text{OCH}(\text{CH}_3)_2$ ), 33.7 ( $\text{C}=\text{CCH}_2\text{CH}_2$ ), 66.8 ( $\text{OCH}(\text{CH}_3)_2$ ), 152.6 (Te-C=C). The  $^{13}\text{C}\{^1\text{H}\}$  resonance for B-C was not located.  $^{11}\text{B}\{^1\text{H}\}$  NMR (159.8 MHz,  $\text{C}_6\text{D}_6$ ):  $\delta = 29.9$ . HR-MS (EI):  $m/z$  calcd. for  $\text{C}_{20}\text{H}_{36}\text{O}_4^{11}\text{B}_2^{130}\text{Te}$ : 492.18619; found: 492.18642 ( $\Delta\text{ppm} = 0.5$ ).

**Synthesis of B-Te-6-B via boryl-substitution.** ( $^i\text{PrO}$ ) $_2\text{B-Te-6-B}(\text{O}^i\text{Pr})_2$  (0.060 g, 0.12 mmol) and pinacol (0.029 g, 0.25 mmol) were combined in 1 mL of THF and stirred for 16 hours. After removing the volatiles *in vacuo* the reaction mixture was dissolved in 0.7 mL of  $\text{C}_6\text{D}_6$  and analyzed by  $^1\text{H}$ ,  $^{13}\text{C}\{^1\text{H}\}$ , and  $^{11}\text{B}\{^1\text{H}\}$  NMR spectroscopy. The NMR spectra showed the quantitative conversion to **B-Te-6-B**.<sup>13</sup>

**Synthesis of catB-Te-6-Bcat.** ( $^i\text{PrO}$ ) $_2\text{B-Te-6-B}(\text{O}^i\text{Pr})_2$  (0.507 g, 1.04 mmol), catechol (0.229 g, 2.08 mmol), and 6 mL of  $\text{Et}_2\text{O}$  were stirred together for 2 hours. Afterward, the mixture was concentrated to a volume of *ca.* 1 mL and the resulting precipitate was allowed to settle. After decanting off the supernatant, the remaining solid was washed with 3 more times with 0.3 mL portions of  $\text{Et}_2\text{O}$ , each time allowing the precipitate to settle for at least 1 hour before decanting off the supernatant. After the residual solvent was removed from the remaining solid under vacuum, **catB-Te-6-Bcat** was obtained of an off-white solid (0.285 g, 59 %). Crystals suitable for single-crystal X-ray diffraction were grown by slow evaporation of a concentrated benzene solution

at room temperature.  $^1\text{H}$  NMR (699.8 MHz,  $\text{C}_6\text{D}_6$ ):  $\delta = 1.55$  (br, 4H,  $\text{C}=\text{CCH}_2\text{CH}_2$ ), 3.06 (br, 4H,  $\text{C}=\text{CCH}_2\text{CH}_2$ ), 6.81-6.83 (m, 4H,  $\text{ArH}$ ), 7.06-7.08 (m, 4H,  $\text{ArH}$ ).  $^{13}\text{C}\{^1\text{H}\}$  NMR (176.0 MHz,  $\text{C}_6\text{D}_6$ ):  $\delta = 23.5$  ( $\text{C}=\text{CCH}_2\text{CH}_2$ ), 33.8 ( $\text{C}=\text{CCH}_2\text{CH}_2$ ), 112.8 ( $\text{ArC}$ ), 123.1 ( $\text{ArC}$ ), 148.9 ( $\text{ArC}$ ), 162.2 ( $\text{Te}-\text{C}=\text{C}$ ). The  $^{13}\text{C}\{^1\text{H}\}$  resonance for B-C was not located.  $^{11}\text{B}\{^1\text{H}\}$  NMR (159.8 MHz,  $\text{C}_6\text{D}_6$ ):  $\delta = 32.5$ . Anal. calcd. (%) for  $\text{C}_{20}\text{H}_{16}\text{O}_4\text{B}_2\text{Te}$ : C, 51.16; H, 3.43. found: C, 51.22; H, 3.63. HR-MS (EI):  $m/z$  calcd. for  $\text{C}_{20}\text{H}_{16}\text{O}_4^{11}\text{B}_2^{130}\text{Te}$ : 472.02992; found: 472.02792 ( $\Delta\text{ppm} = 0.5$ ). UV-vis (in THF):  $\lambda_{\text{max}} = 317$  nm,  $\epsilon = 5.68 \times 10^4 \text{ M}^{-1}\text{cm}^{-1}$ . Mp ( $^\circ\text{C}$ ): 220 (decomposition, turned black).

**Synthesis of  $^t\text{BucatB-Te-6-B}^t\text{Bucat}$ . ( $^i\text{PrO}$ ) $_2\text{B-Te-6-B}$ ( $^o\text{Pr}$ ) $_2$**  (0.233 g, 0.476 mmol), 4-*tert*-butylcatechol (0.158 g, 0.951 mmol), and 3 mL of  $\text{Et}_2\text{O}$  were stirred together for 4 hours, after which the mixture was concentrated to a final volume of *ca.* 1 mL. The precipitate was allowed to settle, and then the supernatant was decanted off. The product was washed 3 more times with 0.5 mL portions of  $\text{Et}_2\text{O}$ , each time allowing the suspension to settle for at least 1 hour before decanting off the supernatant. Further drying of the product under vacuum yielded  **$^t\text{BucatB-Te-6-B}^t\text{Bucat}$**  as a white solid (143 mg, 52 %). Crystals suitable for single-crystal X-ray diffraction were grown by slow evaporation of a concentrated  $\text{Et}_2\text{O}$  solution at room temperature.  $^1\text{H}$  NMR (699.8 MHz,  $\text{C}_6\text{D}_6$ ):  $\delta = 1.22$  (s, 18H,  $\text{C}(\text{CH}_3)_3$ ), 1.60 (br, 4H,  $\text{C}=\text{CCH}_2\text{CH}_2$ ), 3.14 (br, 4H,  $\text{C}=\text{CCH}_2\text{CH}_2$ ), 6.93 (dd,  $^3J_{\text{HH}} = 8.4$  Hz,  $^4J_{\text{HH}} = 2.1$  Hz, 2H,  $\text{ArH}$ ), 7.06 (d,  $^3J_{\text{HH}} = 8.4$  Hz, 2H,  $\text{ArH}$ ), 7.26 (d,  $^4J_{\text{HH}} = 2.1$  Hz, 2H,  $\text{ArH}$ ).  $^{13}\text{C}\{^1\text{H}\}$  NMR (176.0 MHz,  $\text{C}_6\text{D}_6$ ):  $\delta = 23.5$  ( $\text{C}=\text{CCH}_2\text{CH}_2$ ), 31.8 ( $\text{C}(\text{CH}_3)_3$ ), 33.8 ( $\text{C}=\text{CCH}_2\text{CH}_2$ ), 34.9 ( $\text{C}(\text{CH}_3)_3$ ), 110.4

(ArC), 111.9 (ArC), 119.8 (ArC), 146.6 (ArC), 146.8 (ArC), 149.0 (ArC), 162.1 (Te-C=C<sub>2</sub>). The <sup>13</sup>C{<sup>1</sup>H} resonance for B-C was not located. <sup>11</sup>B{<sup>1</sup>H} NMR (159.8 MHz, C<sub>6</sub>D<sub>6</sub>): δ = 33.4. Anal. Calcd. (%) for C<sub>28</sub>H<sub>32</sub>O<sub>4</sub>B<sub>2</sub>Te: C, 57.81; H, 5.54. found: C, 57.09; H, 5.80. HR-MS (EI): m/z calcd. for C<sub>28</sub>H<sub>32</sub>O<sub>4</sub><sup>11</sup>B<sub>2</sub><sup>130</sup>Te: 584.15491; found: 584.15471 (Δppm = 0.3). UV/vis (in THF): λ<sub>max</sub> = 324 nm, ε = 2.25 × 10<sup>4</sup> M<sup>-1</sup>cm<sup>-1</sup>. Mp (°C): 216 (decomposition, turned black). Phosphorescence emission (powder, λ<sub>ex</sub> = 325 nm): λ<sub>em</sub> = 575 nm, Φ = 0.2 %, τ<sub>1</sub> = 9 μs, τ<sub>2</sub> = 28 μs (weighted mean τ = 22 μs).

**Synthesis of danB-Te-6-Bdan.** (iPrO)<sub>2</sub>B-Te-6-B(O<sup>i</sup>Pr)<sub>2</sub> (0.241 g, 0.493 mmol), 1,8-diaminonaphthalene (0.231 g, 1.46 mmol), and 3 mL of THF were stirred together for 3 hours followed by the removal of volatiles under vacuum. The resulting crude product was then exposed to air, dissolved in *ca.* 1 mL of a 1:1 solution of CH<sub>2</sub>Cl<sub>2</sub>:hexanes, and filtered through a glass frit containing a 10 cm pad of silica. From this filtration, only the yellow fraction was collected, which was then dried over MgSO<sub>4</sub>, filtered again and evaporated to dryness *in vacuo*. Further removal of residual solvent was accomplished by freeze drying in *ca.* 2 mL of benzene to yield 143 mg (51 %) of a yellow solid. Crystals suitable for X-ray diffraction were grown from cold (-35 °C) Et<sub>2</sub>O. <sup>1</sup>H NMR (499.8 MHz, C<sub>6</sub>D<sub>6</sub>): δ = 1.49 (br, 4H, C=CCH<sub>2</sub>CH<sub>2</sub>), 2.56 (br, 4H, C=CCH<sub>2</sub>CH<sub>2</sub>), 5.38 (s, 4H, NH), 5.95 (d, <sup>3</sup>J<sub>HH</sub> = 7.0 Hz, <sup>4</sup>J<sub>HH</sub> = 1.0 Hz, 4H, danH), 7.05-7.12 (m, 8H, danH). <sup>13</sup>C{<sup>1</sup>H} NMR (125.7 MHz, C<sub>6</sub>D<sub>6</sub>): δ = 24.1 (C=CCH<sub>2</sub>CH<sub>2</sub>), 33.6 (C=CCH<sub>2</sub>CH<sub>2</sub>), 106.6 (dan CH), 118.6 (dan CH), 120.5 (dan C), 127.9 (dan CH), 137.1 (dan C), 141.3 (dan C), 154.1 (Te-C=C). The <sup>13</sup>C{<sup>1</sup>H} resonance for B-C was not

located.  $^{11}\text{B}\{^1\text{H}\}$  NMR (128.3 MHz,  $\text{C}_6\text{D}_6$ ):  $\delta = 30.4$ . Anal. calcd. (%) for  $\text{C}_{28}\text{H}_{24}\text{N}_4\text{B}_2\text{Te}$ : C, 59.44; H, 4.28; N, 9.90. found: C, 59.13; H, 4.52; N, 8.46. Despite multiple attempts, analyses of this compound routinely gave low values for nitrogen; see Figures 3.28–3.30 for copies of the NMR data for this compound. HR-MS (EI):  $m/z$  calcd. for  $\text{C}_{28}\text{H}_{24}\text{N}_4^{11}\text{B}_2^{130}\text{Te}$ : 568.12494; found: 568.12462 ( $\Delta\text{ppm} = 0.6$ ). UV-vis (in THF):  $\lambda_{\text{max}} = 338$  nm,  $\epsilon = 2.55 \times 10^4 \text{ M}^{-1}\text{cm}^{-1}$ . Mp ( $^\circ\text{C}$ ): 170 (decomposition, turned black).

**Synthesis of (Mes)( $^i\text{PrO}$ )B-Te-6-B( $^o\text{Pr}$ )(Mes).** MesMgBr (1.74 mL, 1.0 M solution in  $\text{Et}_2\text{O}$ , 1.9 mmol) was added to a solution of ( $^i\text{PrO}$ ) $_2$ B-Te-6-B( $^o\text{Pr}$ ) $_2$  (0.425 g, 0.898 mmol) in 10 mL of  $\text{Et}_2\text{O}$  and then the reaction mixture was left to stir for 16 hours. The volatiles were removed under vacuum while heating to  $50^\circ\text{C}$ . The remaining product was then dissolved in 15 mL of hexanes and filtered through a 1 cm plug of Celite. After removal of the hexanes from the filtrate under vacuum, crude (Mes)( $^i\text{PrO}$ )B-Te-6-B( $^o\text{Pr}$ )(Mes) was recovered (397 mg, 72 %) which still contained some residual  $\text{Cp}_2\text{ZrCl}_2$  (ca. 5 %, according to  $^1\text{H}$  NMR spectroscopy) from the starting tellurophene. Spectroscopically pure material was obtained by washing the solid with  $3 \times 0.25$  mL portions of pentane to yield (Mes)( $^i\text{PrO}$ )B-Te-6-B( $^o\text{Pr}$ )(Mes) as a pale yellow solid (105 mg, 19 %). Crystals suitable for single-crystal X-ray diffraction were grown by cooling a concentrated pentane solution to  $-35^\circ\text{C}$ .  $^1\text{H}$  NMR (699.8 MHz,  $\text{C}_6\text{D}_6$ ):  $\delta = 1.08$  (d,  $^3J_{\text{HH}} = 5.6$  Hz, 12H,  $\text{OCH}(\text{CH}_3)_2$ ), 1.48 (br, 4H,  $\text{C}=\text{CCH}_2\text{CH}_2$ ), 2.17 (s, 6H,  $\text{MesCH}_3$ ), 2.30 (s, 12H,  $\text{MesCH}_3$ ), 2.84 (br, 4H,

C=CCH<sub>2</sub>CH<sub>2</sub>), 4.15 (septet, <sup>3</sup>J<sub>HH</sub> = 5.6 Hz, 2H, OCH(CH<sub>3</sub>)<sub>2</sub>), 6.76 (s, 4H, MesH). <sup>13</sup>C{<sup>1</sup>H} NMR (176.0 MHz, C<sub>6</sub>D<sub>6</sub>): δ = 21.4 (MesCH<sub>3</sub>), 22.7 (MesCH<sub>3</sub>), 24.1 (C=CCH<sub>2</sub>CH<sub>2</sub>), 24.7 (OCH(CH<sub>3</sub>)<sub>2</sub>), 34.0 (C=CCH<sub>2</sub>CH<sub>2</sub>), 70.2 (OCH(CH<sub>3</sub>)<sub>2</sub>), 127.8 (MesC), 137.6 (MesC), 138.2 (MesC), 160.4 (Te-C=C). <sup>13</sup>C{<sup>1</sup>H} resonances for Te-C-B and B-C(Mes) were not located. <sup>11</sup>B{<sup>1</sup>H} NMR (128.3 MHz, C<sub>6</sub>D<sub>6</sub>): δ = 44.6. Anal. calcd. (%) for C<sub>32</sub>H<sub>44</sub>O<sub>2</sub>B<sub>2</sub>Te: C, 63.02; H, 7.27. found: C, 62.93; H, 7.40. HR-MS (EI): m/z calcd. for C<sub>32</sub>H<sub>44</sub>O<sub>2</sub><sup>11</sup>B<sub>2</sub><sup>130</sup>Te: 612.25897; found: 612.25910 (Δppm = 0.2). UV-vis (in THF): λ<sub>max</sub> = 317 nm, ε = 1.81 × 10<sup>4</sup> M<sup>-1</sup>cm<sup>-1</sup>; λ<sub>max</sub> = 378 nm, ε = 6.46 × 10<sup>3</sup> M<sup>-1</sup>cm<sup>-1</sup>. Mp (°C): 160 (decomposition, turned black). Phosphorescence emission (powder, λ<sub>ex</sub> = 360 nm): λ<sub>em</sub> = 590 nm, Φ = 15.2 %, τ<sub>1</sub> = 82 μs, τ<sub>2</sub> = 161 μs (weighted mean τ = 109 μs).

**Improved Suzuki-Miyaura cross-coupling procedure involving B-Te-6-B and 2-bromothiophene to form thienyl-Te-6-thienyl. B-Te-6-B** (50 mg, 0.10 mmol), 2-bromothiophene (35 mg, 0.22 mmol) and the Pd pre-catalyst, Cl(XPhos)Pd(2-aminobiphenyl) (5.0 mg, 0.0060 mmol) were combined along with 2 mL of THF. To this mixture, 0.30 mL of 2.0 M K<sub>3</sub>PO<sub>4</sub> (aq) was added. After stirring at 50 °C for 16 hrs, the reaction mixture was exposed to air and diluted with 3 mL of CH<sub>2</sub>Cl<sub>2</sub>. This crude reaction mixture was dried over MgSO<sub>4</sub>, gravity filtered and upon removal of volatiles under vacuum, the resulting product was then analyzed by NMR spectroscopy. Further purification was performed by running the crude sample through a 5 cm silica plug in 3:1 hexanes:CH<sub>2</sub>Cl<sub>2</sub> which gave **thienyl-Te-6-thienyl** as a yellow solid (37 mg,

91 %) with  $^1\text{H}$  and  $^{13}\text{C}\{^1\text{H}\}$  NMR spectra which matched those found in the literature (Figure 3.34).<sup>21</sup>

### 3.4.3 Photoluminescence measurements

Steady-state photoluminescence (PL) spectra, emission lifetime ( $\lambda$ ), and photoluminescence quantum yields ( $\Phi$ ) were obtained using a Horiba PTI QuantaMaster 8075 fluorescence spectrophotometer. For the PL and quantum yield measurements, the spectrophotometer was equipped with a 75 W xenon lamp (and an integrating sphere for the quantum yield measurements). Solid samples were measured in sealed glass capillaries (melting point tubes sealed under an  $\text{N}_2$  atmosphere) mounted in a custom-made solids holder. Long-pass and short-pass cut-off filters of  $\lambda = 455$  nm and  $\lambda = 400$  nm, respectively, were used in the steady-state photoluminescence and quantum yield measurements. All quantum yields are reported as absolute values.

Lifetime measurements ( $\tau$ ) were collected on samples sealed in a melting point tube under an  $\text{N}_2$  atmosphere. The decay curves were measured using a Horiba PTI QuantaMaster 8075 fluorescence spectrometer equipped with a 75W xenon flash lamp. The resulting decay curve was fitted with the lowest exponential function that gave a suitable reduced chi-square value ( $\chi^2$ )<sup>52</sup> and a suitable Durbin Watson parameter.<sup>53-55</sup>



**Table 3.1** – The photoluminescence decay of **Mes(<sup>i</sup>PrO)B-Te-6-B(O<sup>i</sup>Pr)Mes** powder, fit with a biexponential and the resulting fitting parameters.

|   |                                    |
|---|------------------------------------|
| Number of components  | 2                                  |
| Lifetime of component 1 ( $\tau_1$ )  | $81.9517 \pm 0.641791 \mu\text{s}$ |
| Weight of component 1 ( $A_1$ )   | 0.79                               |
| Lifetime of component 2 ( $\tau_2$ )  | $160.609 \pm 0.378898 \mu\text{s}$ |
| Weight of component 2 ( $A_2$ )   | 0.21                               |
| Weighted mean lifetime $\left(\frac{\sum A_i \tau_i^2}{\sum A_i \tau_i}\right)$ | $108.893 \mu\text{s}$              |
| $\chi^2$  | 1.01188                            |
| Durbin-Watson parameter   | 2.03129                            |
| Z (run test of the residuals)   | -0.00895626                        |

**Table 3.2** – The photoluminescence decay of **<sup>t</sup>BucatB-Te-6-B<sup>t</sup>Bucat** powder, fit with a biexponential and the resulting fitting parameters.

|   |                                    |
|---|------------------------------------|
| Number of components  | 2                                  |
| Lifetime of component 1 ( $\tau_1$ )  | $9.1034 \pm 0.302457 \mu\text{s}$  |
| Weight of component 1 ( $A_1$ )   | 0.61                               |
| Lifetime of component 2 ( $\tau_2$ )  | $27.9130 \pm 0.172553 \mu\text{s}$ |
| Weight of component 2 ( $A_2$ )   | 0.39                               |
| Weighted mean lifetime $\left(\frac{\sum A_i \tau_i^2}{\sum A_i \tau_i}\right)$ | $21.5352 \mu\text{s}$              |
| $\chi^2$  | 1.03149                            |
| Durbin-Watson parameter   | 1.86808                            |
| Z (run test of the residuals)   | -0.0397772                         |

#### 3.4.4 X-ray crystallography

Crystals suitable for X-ray diffraction studies were removed from a vial and immediately coated in a thin layer of hydrocarbon oil (Paratone-N). A suitable crystal was then mounted on a glass fibre, and quickly placed in a low temperature stream of nitrogen on an X-ray diffractometer. All data was collected on a Bruker APEX II CCD detector/D8 diffractometer<sup>56</sup> using Cu K $\alpha$  radiation with the crystals cooled to  $-100$  °C. The data was corrected for absorption using Gaussian integration from the indexing of the crystal faces.<sup>57</sup> Crystal structures were solved using intrinsic phasing SHELXT-2014<sup>58</sup> and refined using full-matrix least-squares on F<sup>2</sup> (SHELXL).<sup>59</sup> The assignment of hydrogen atom positions were based on the sp<sup>2</sup> or sp<sup>3</sup> hybridization geometries of their respective carbon atoms, and were given thermal parameters 20 % greater than those of their parent atoms.

*Special refinement conditions:* In the structure of **danB-Te-6-Bdan**, the C11S-C12S distance (carbons of an Et<sub>2</sub>O solvent molecule) was constrained by DFIX command in SHELXL to be 1.4437(11) Å.

**Table 3.3** – Crystallographic data for the tellurophenes derived from (iPrO)<sub>2</sub>B-Te-6-B(O<sup>i</sup>Pr)<sub>2</sub>.

| Compound   | catB-Te-6-Bcat   | <sup>t</sup> BucatB-Te-6-B <sup>t</sup> Bucat                    | danB-Te-6-Bdan•3Et <sub>2</sub> O   | Mes( <sup>i</sup> PrO)B-Te-6-B(O <sup>i</sup> Pr)Mes             |
|--|--|--|---|--|
| formula  | C <sub>20</sub> H <sub>16</sub> B <sub>2</sub> O <sub>4</sub> Te | C <sub>28</sub> H <sub>32</sub> B <sub>2</sub> O <sub>4</sub> Te | C <sub>40</sub> H <sub>54</sub> B <sub>2</sub> N <sub>4</sub> O <sub>3</sub> Te | C <sub>32</sub> H <sub>44</sub> B <sub>2</sub> O <sub>2</sub> Te |
| form. wt. (g/mol)  | 469.55   | 581.75   | 788.09  | 609.89   |
| crys. dimes. (mm)  | 0.45×0.04×0.04   | 0.29×0.16×0.14   | 0.23×0.23×0.14  | 0.12×0.09×0.06   |
| Crystal system   | Orthorhombic   | Triclinic  | Monoclinic  | Orthorhombic   |
| Space group  | <i>P</i> 2 <sub>1</sub> 2 <sub>1</sub> 2 <sub>1</sub>            | <i>P</i> $\bar{1}$   | <i>P</i> 21/ <i>c</i>   | <i>Pnn</i> 2   |
| <i>a</i> (Å)   | 5.07070(10)  | 12.0209(3)   | 15.677(6)   | 10.0095(3)   |
| <i>b</i> (Å)   | 17.1292(3)   | 12.9608(3)   | 13.588(3)   | 12.3649(4)   |
| <i>c</i> (Å)   | 20.6984(4)   | 18.3885(4)   | 18.6150(19)   | 12.5793(4)   |
| $\alpha$ (deg)   | -  | 86.3327(10)  | -   | -  |
| $\beta$ (deg)  | -  | 77.7639(9)   | 91.140(15)  | -  |
| $\gamma$ (deg)   | -  | 69.4855(11)  | -   | -  |
| <i>V</i> (Å <sup>3</sup> )   | 1797.80(6)   | 2622.13(11)  | 3964.8(18)  | 1556.90(8)   |
| <i>Z</i>   | 4  | 4  | 4   | 2  |
| $\rho_{\text{calcd}}$ (g cm <sup>-3</sup> )  | 1.735  | 1.474  | 1.320   | 1.301  |
| $\mu$ (mm <sup>-1</sup> )  | 13.26  | 6.204  | 6.237   | 7.720  |
| temperature (°C)   | -100   | -100   | -100  | -100   |
| 2 $\theta_{\text{max}}$ (deg)  | 148.13   | 148.26   | 149.08  | 148.15   |
| total data   | 12381  | 64505  | 172797  | 10692  |
| unique data ( <i>R</i> <sub>int</sub> )  | 3595 (0.0252)  | 10160 (0.0392)   | 8062 (0.0391)   | 3126 (0.0180)  |
| Obs [ <i>I</i> > 2 $\sigma$ ( <i>I</i> )]  | 3579   | 9170   | 7701  | 3037   |
| <i>R</i> <sub>1</sub> [ <i>F</i> <sub>o</sub> <sup>2</sup> ≥ 2 $\sigma$ ( <i>F</i> <sub>o</sub> <sup>2</sup> )] <sup>a</sup> | 0.0203   | 0.0220   | 0.0207  | 0.0158   |
| <i>wR</i> <sub>2</sub> [all data] <sup>a</sup>   | 0.0490   | 0.0597   | 0.0559  | 0.0399   |
| max/min $\Delta\rho$ (e Å <sup>-3</sup> )  | 1.018/-0.717   | 0.572/-0.433   | 0.789/-0.462  | 0.220/-0.262   |

$$^a R_1 = \sum ||F_o| - |F_c|| / \sum |F_o|; wR_2 = [\sum w(F_o^2 - F_c^2)^2 / \sum w(F_o^4)]^{1/2}$$

### 3.4.5 Selected NMR spectra

$^1\text{H}$ ,  $^{13}\text{C}\{^1\text{H}\}$ ,  $^{11}\text{B}\{^1\text{H}\}$  NMR spectra were recorded on a Varian Inova spectrometer (400, 500, or 700 MHz) and referenced externally to  $\text{Me}_4\text{Si}$  ( $^1\text{H}$  and  $^{13}\text{C}\{^1\text{H}\}$ ) or  $\text{F}_3\text{B}\cdot\text{OEt}_2$  ( $^{11}\text{B}$ ).

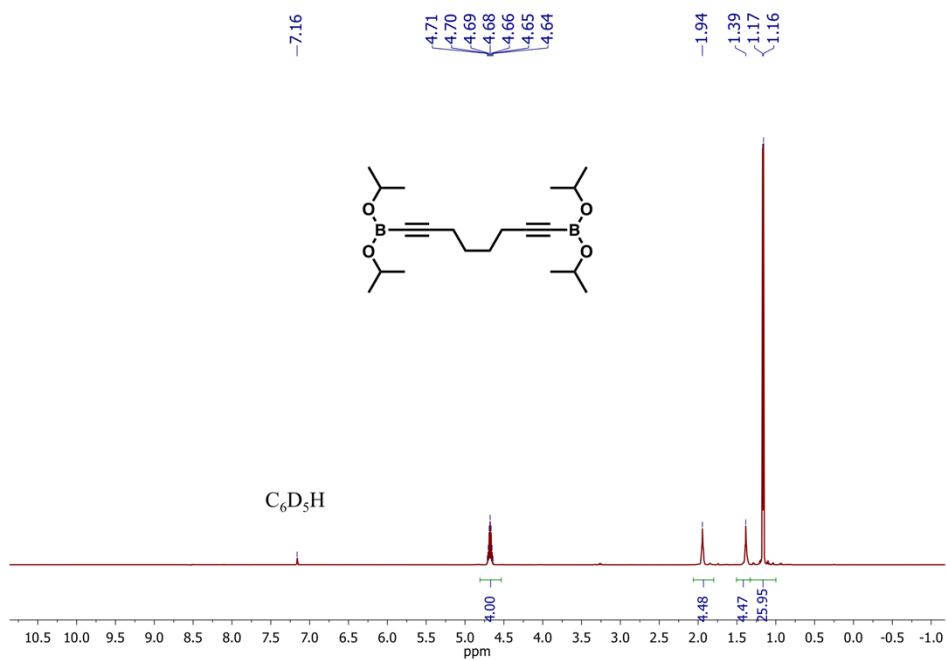


**Figure 3.16** –  $^1\text{H}$  NMR spectrum of  $(i\text{PrO})_2\text{BC}\equiv\text{C}(\text{CH}_2)_4\text{C}\equiv\text{CB}(\text{O}i\text{Pr})_2$  in  $\text{C}_6\text{D}_6$ .

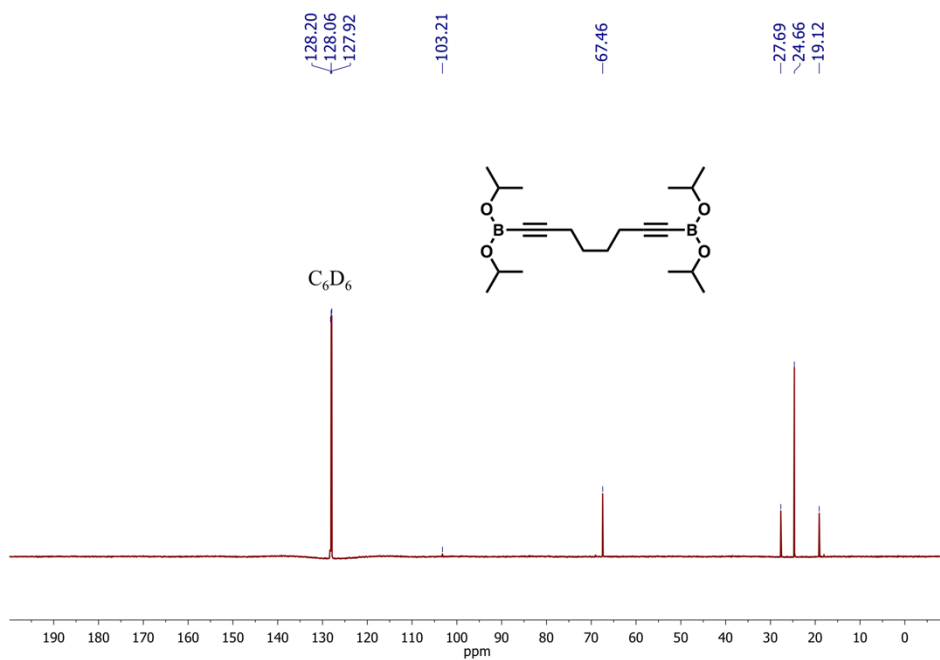


**Figure 3.17** –  $^{13}\text{C}\{^1\text{H}\}$  NMR spectrum of  $(^i\text{PrO})_2\text{BC}\equiv\text{C}(\text{CH}_2)_4\text{C}\equiv\text{CB}(\text{O}^i\text{Pr})_2$  in  $\text{C}_6\text{D}_6$ .

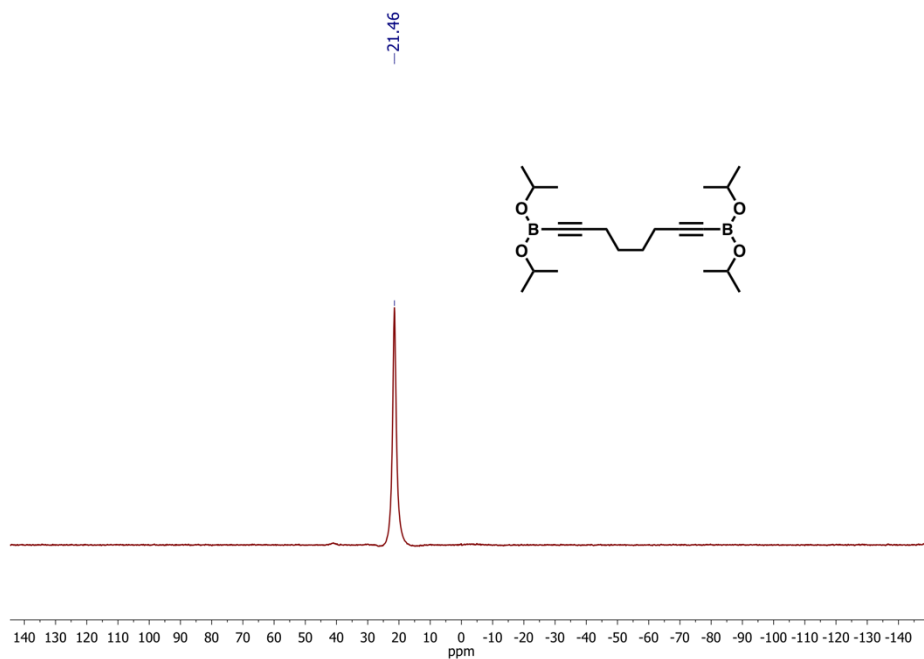


**Figure 3.18** –  $^{11}\text{B}\{^1\text{H}\}$  NMR spectrum of  $(^i\text{PrO})_2\text{BC}\equiv\text{C}(\text{CH}_2)_4\text{C}\equiv\text{CB}(\text{O}^i\text{Pr})_2$  in  $\text{C}_6\text{D}_6$ .

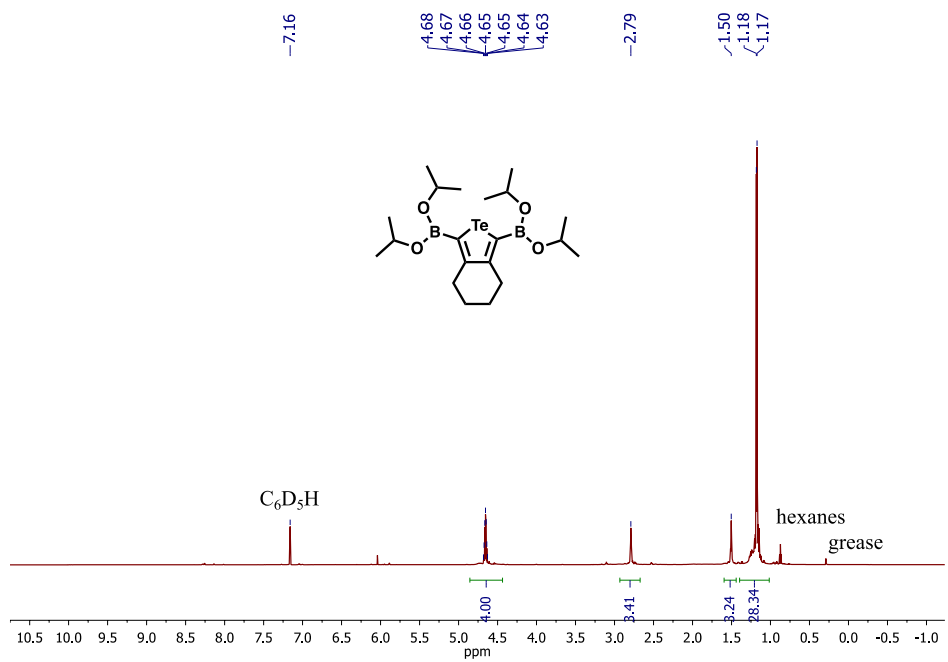


Figure 3.19 –  $^1\text{H}$  NMR spectrum of  $(i\text{PrO})_2\text{B-Te-6-B(O}i\text{Pr)}_2$  in  $\text{C}_6\text{D}_6$ .

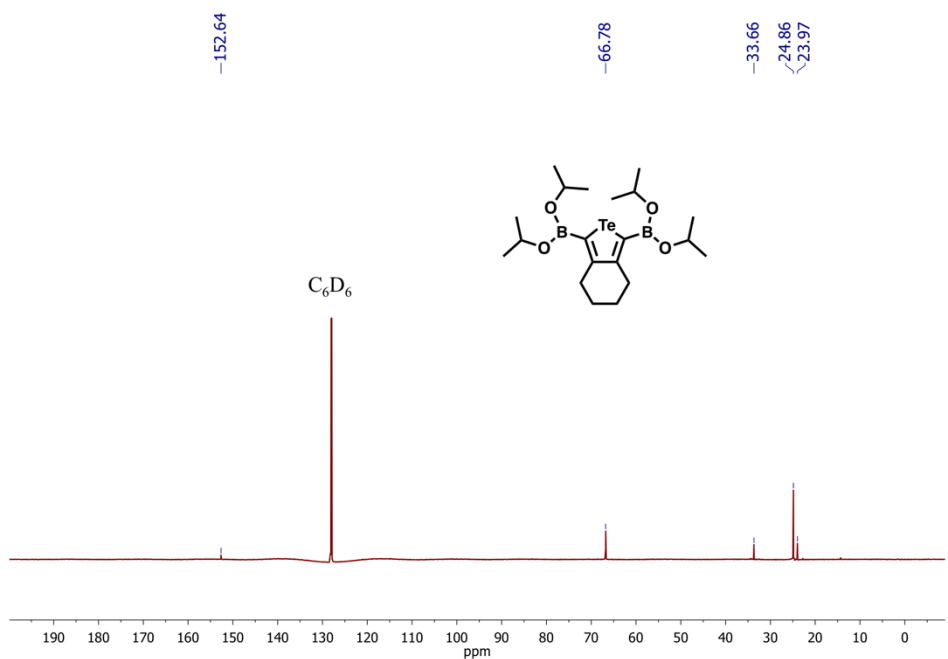


Figure 3.20 –  $^{13}\text{C}\{^1\text{H}\}$  NMR spectrum of  $(i\text{PrO})_2\text{B-Te-6-B(O}i\text{Pr)}_2$  in  $\text{C}_6\text{D}_6$ .

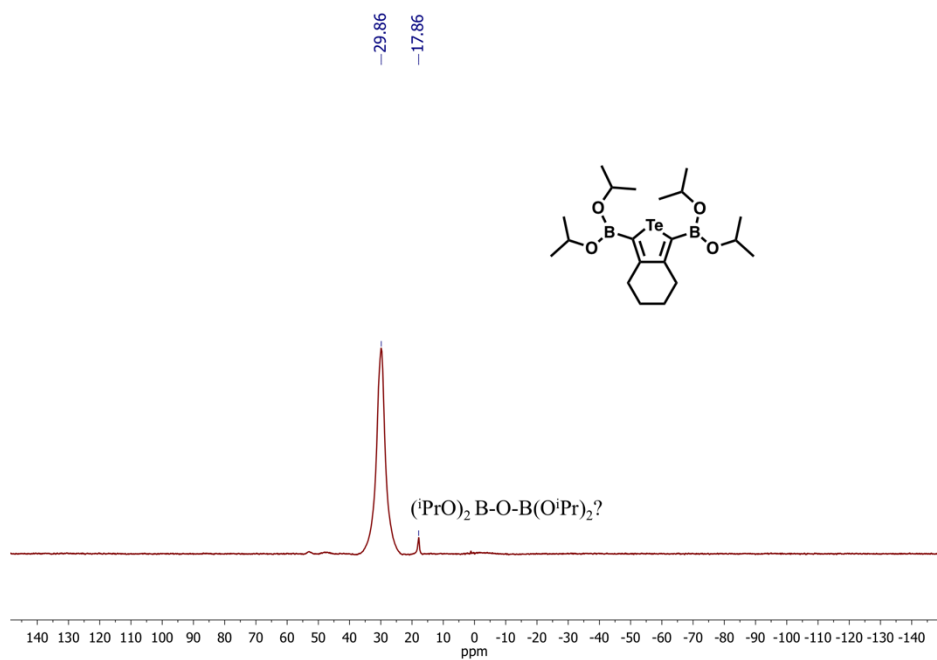


Figure 3.21 –  $^{11}B\{^1H\}$  NMR spectrum of  $(iPrO)_2B-Te-6-B(OiPr)_2$  in  $C_6D_6$ .

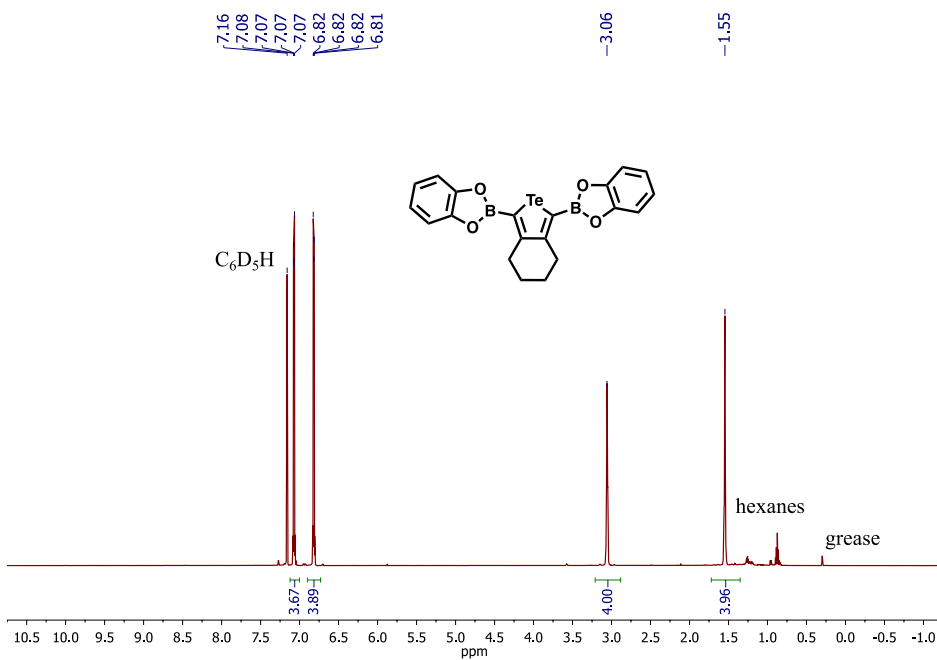
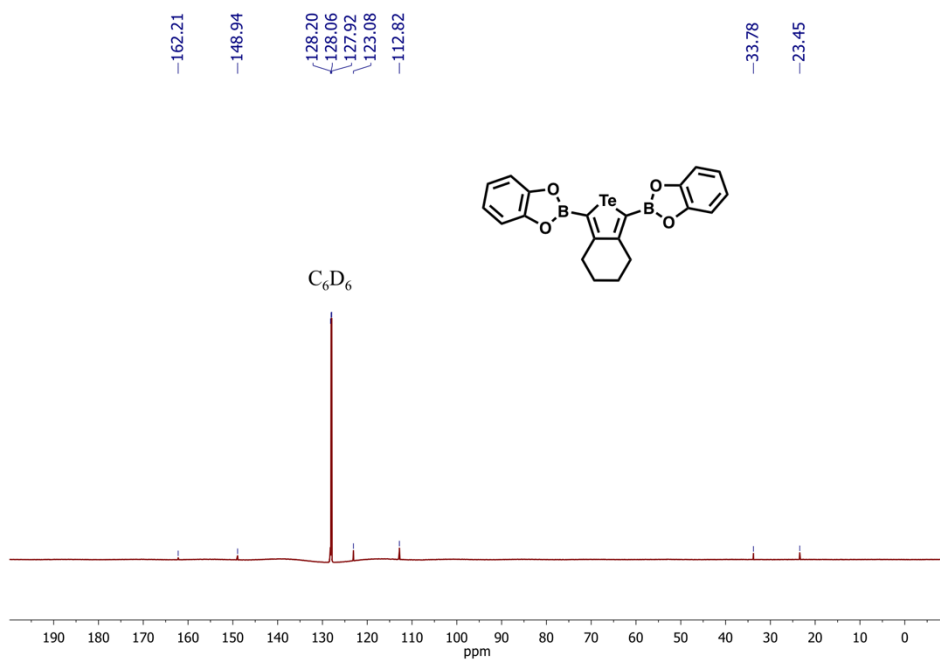
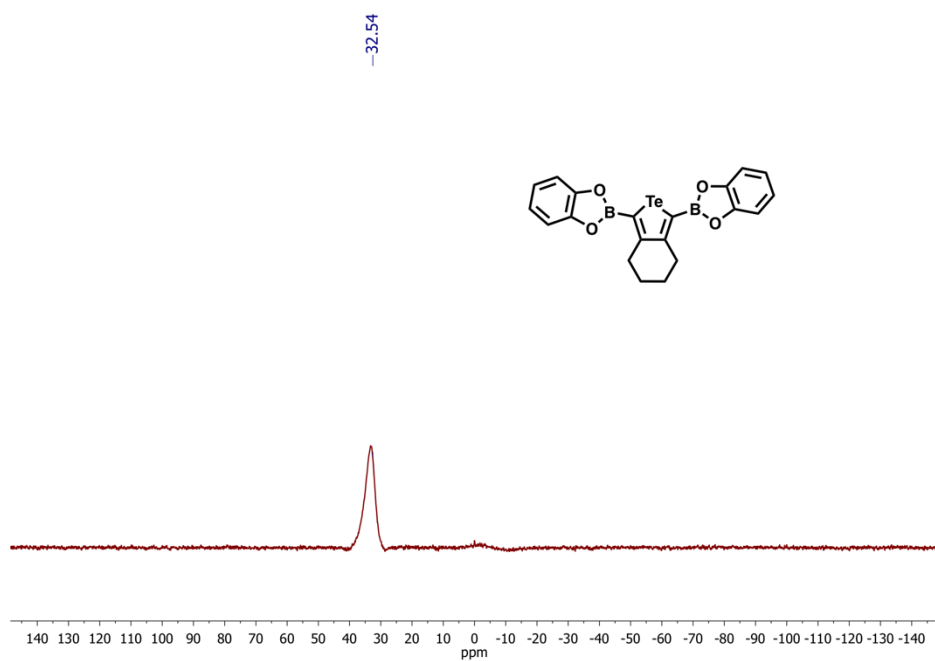


Figure 3.22 –  $^1H$  NMR spectrum of  $catB-Te-6-Bcat$  in  $C_6D_6$ .



**Figure 3.23** –  $^{13}\text{C}\{^1\text{H}\}$  NMR spectrum of *catB-Te-6-Bcat* in  $\text{C}_6\text{D}_6$ .



**Figure 3.24** –  $^{11}\text{B}\{^1\text{H}\}$  NMR spectrum of *catB-Te-6-Bcat* in  $\text{C}_6\text{D}_6$ .



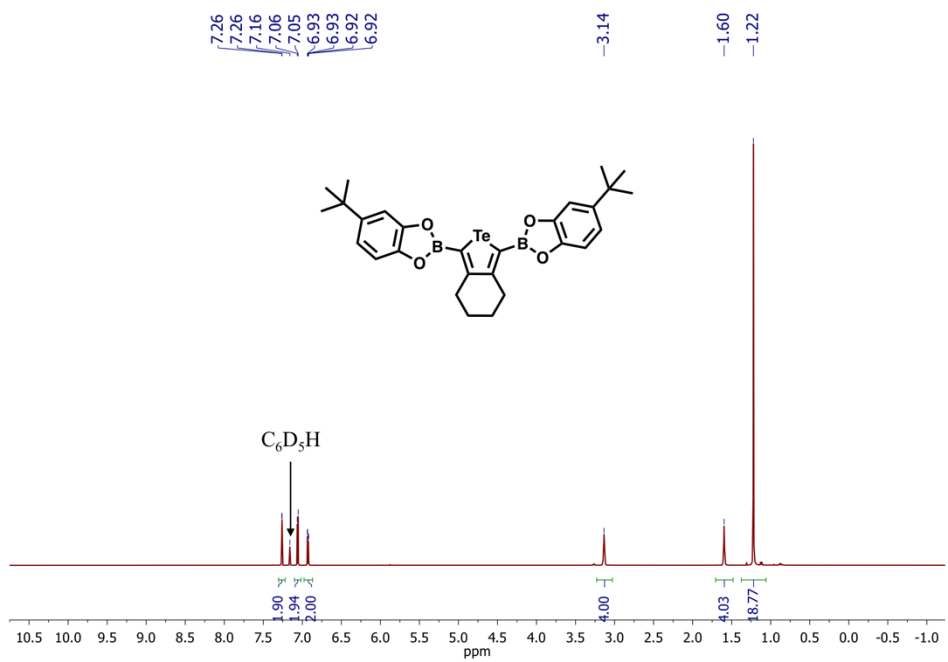


**Figure 3.25** – <sup>1</sup>H NMR spectrum of **tBucatB-Te-6-BtBucat** in C<sub>6</sub>D<sub>5</sub>H.

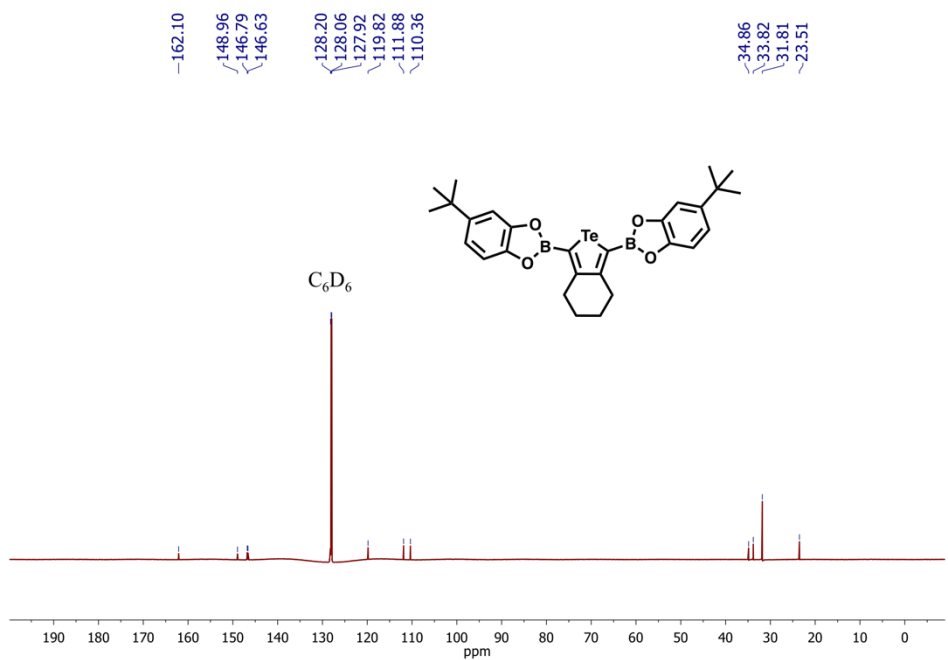


**Figure 3.26** – <sup>13</sup>C{<sup>1</sup>H} NMR spectrum of **tBucatB-Te-6-BtBucat** in C<sub>6</sub>D<sub>6</sub>.

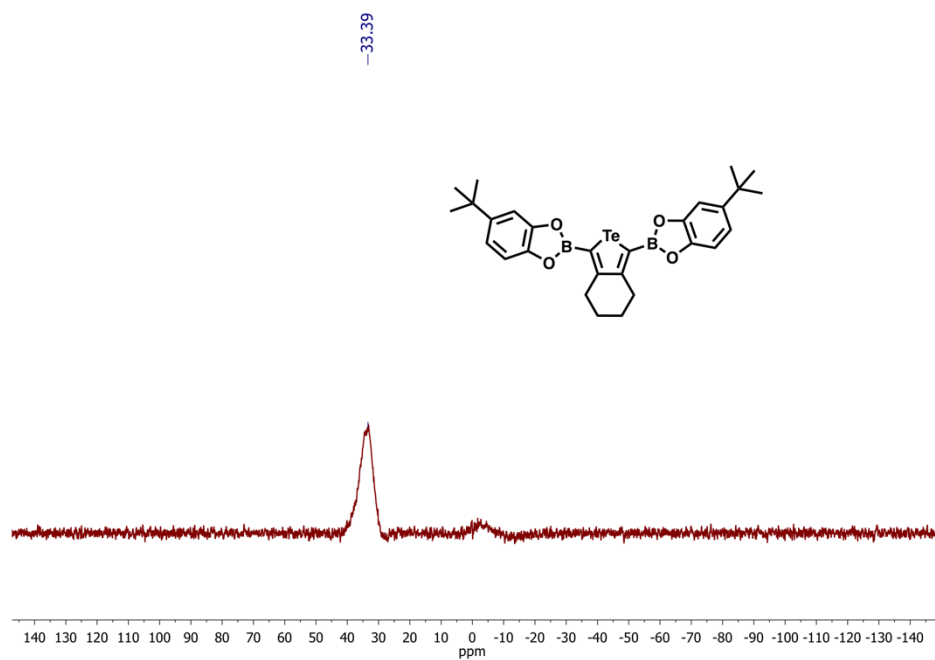


Figure 3.27 –  $^{11}\text{B}\{^1\text{H}\}$  NMR spectrum of  ${}^t\text{BucatB-Te-6-B}'\text{tBucat}$  in  $\text{C}_6\text{D}_6$ .

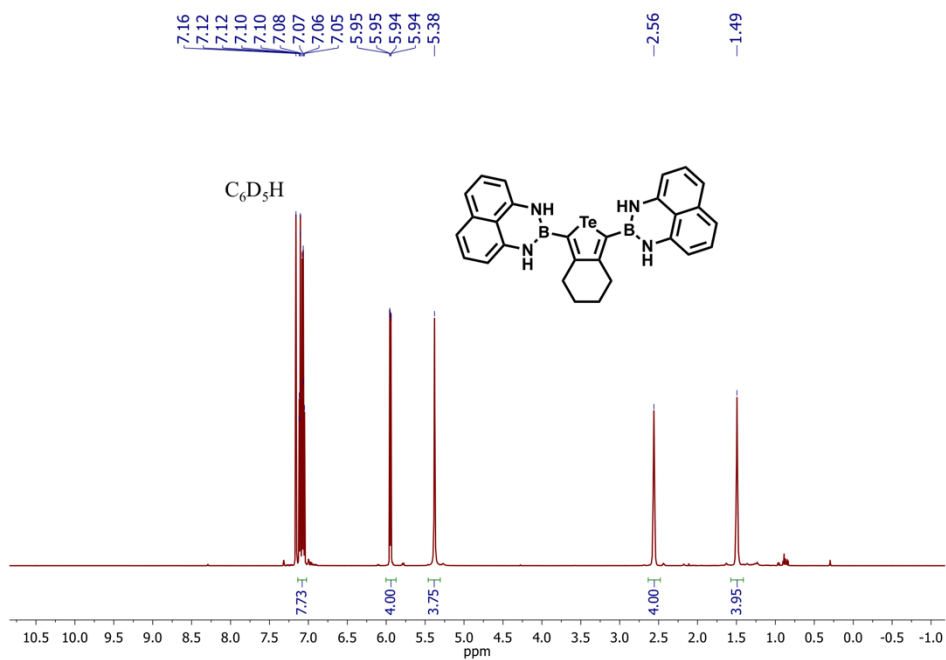
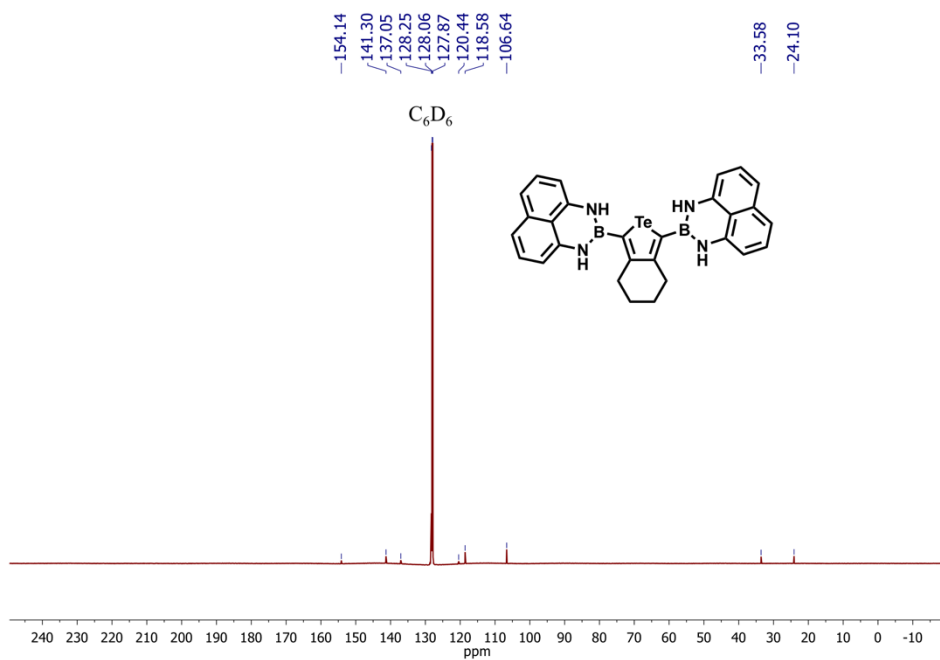
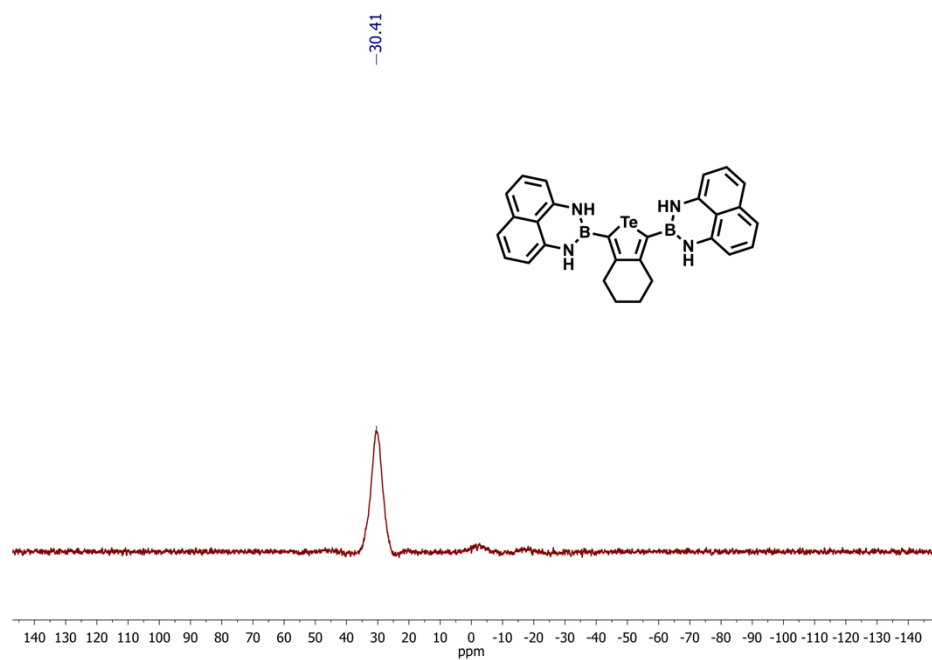


Figure 3.28 –  ${}^1\text{H}$  NMR spectrum of  $\text{danB-Te-6-Bdan}$  in  $\text{C}_6\text{D}_6$ .



**Figure 3.29** –  $^{13}\text{C}\{^1\text{H}\}$  NMR spectrum of **danB-Te-6-Bdan** in  $\text{C}_6\text{D}_6$ .



**Figure 3.30** –  $^{11}\text{B}\{^1\text{H}\}$  NMR spectrum of **danB-Te-6-Bdan** in  $\text{C}_6\text{D}_6$ .

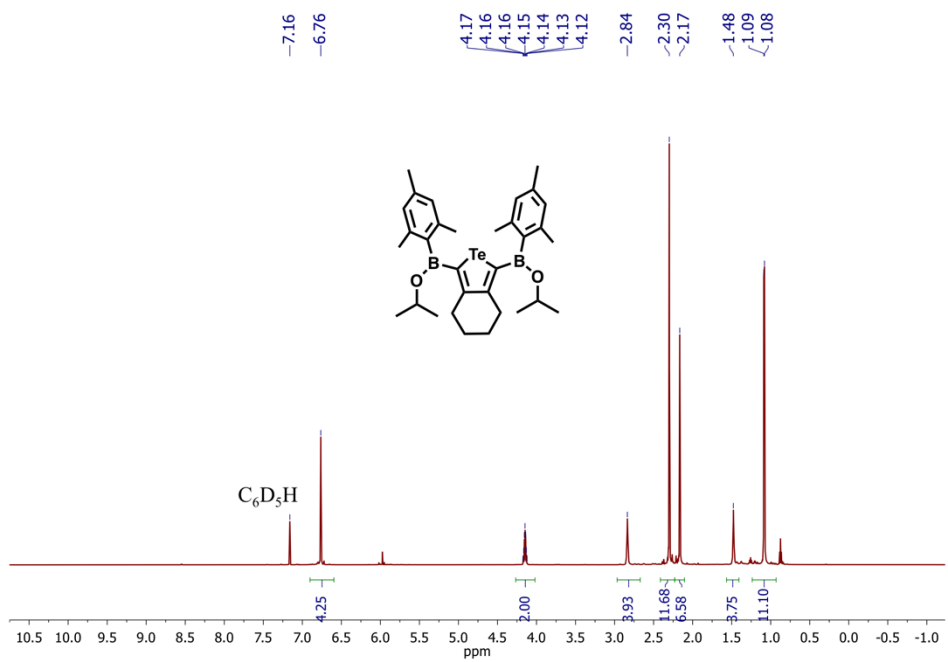


Figure 3.31 –  $^1\text{H}$  NMR spectrum of  $\text{Mes}(\text{iPrO})\text{B}-\text{Te}-6-\text{B}(\text{O}^i\text{Pr})\text{Mes}$  in  $\text{C}_6\text{D}_6$ .

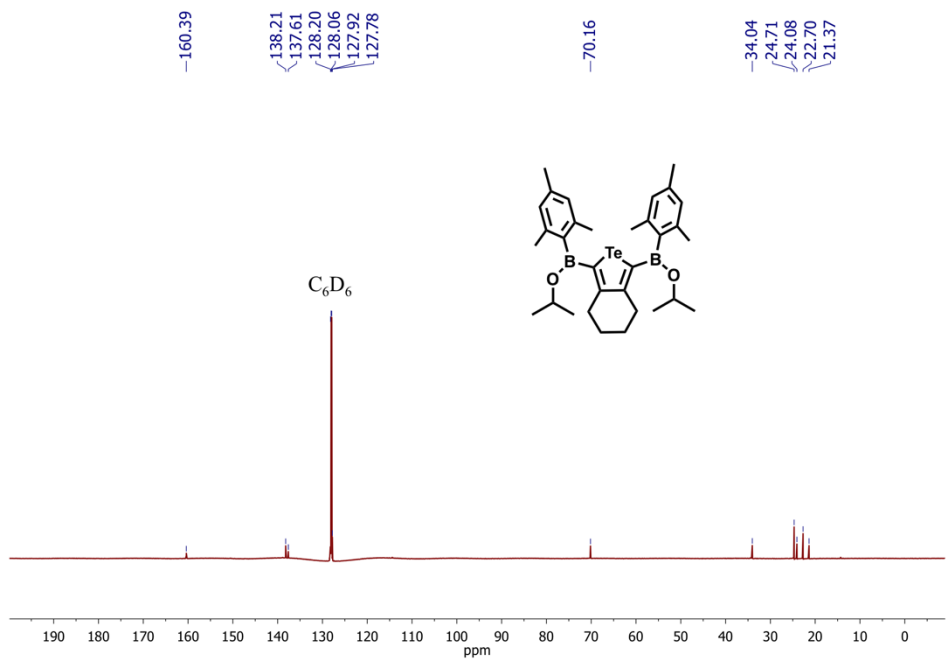
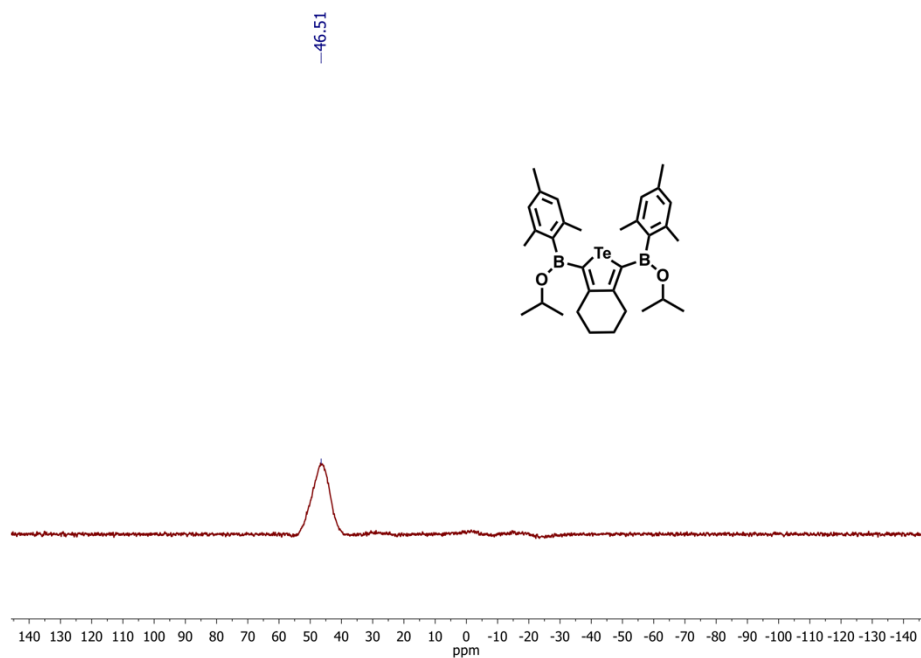
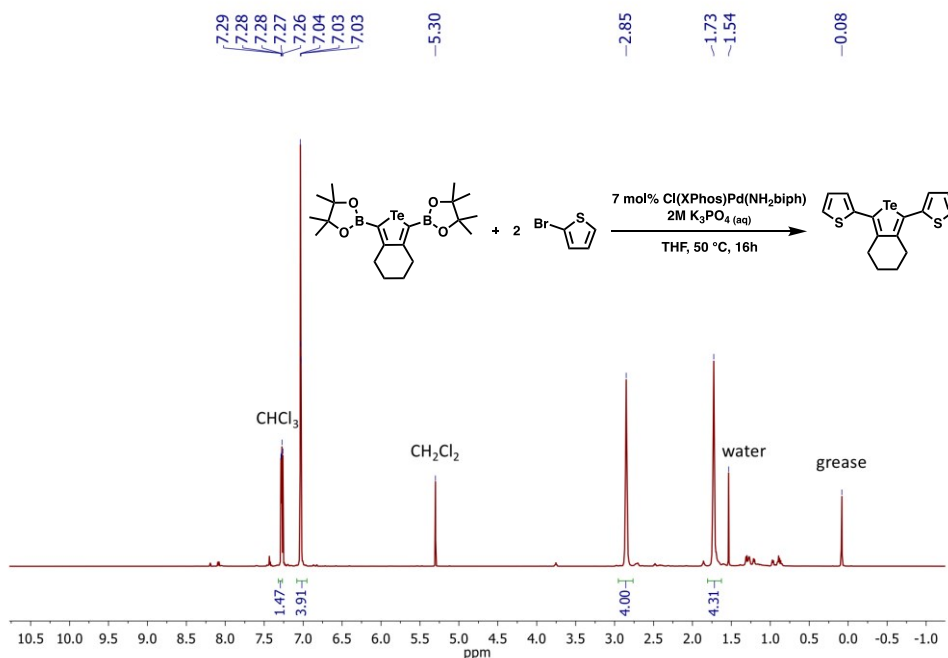


Figure 3.32 –  $^{13}\text{C}\{^1\text{H}\}$  NMR spectrum of  $\text{Mes}(\text{iPrO})\text{B}-\text{Te}-6-\text{B}(\text{O}^i\text{Pr})\text{Mes}$  in  $\text{C}_6\text{D}_6$ .



**Figure 3.33** –  $^{11}\text{B}\{^1\text{H}\}$  NMR spectrum of **Mes(*i*PrO)B-Te-6-B(*O**i*Pr)Mes** in  $\text{C}_6\text{D}_6$ .



**Figure 3.34** –  $^1\text{H}$  NMR spectrum of **thienyl-Te-6-thienyl (T-Te-6-T)** in  $\text{CDCl}_3$  produced *via* the Suzuki-Miyaura cross coupling of **B-Te-6-B** and 2 equivalents of 2-bromothiophene.

### 3.4.6 Computational methodology

All computations have been carried out with the Gaussian16 software package.<sup>60</sup> Geometry optimizations of the gas-phase structures have been performed using density functional theory (DFT) with the hybrid density functional (B3LYP)<sup>61,62</sup> in combination with the basis set cc-pVDZ (for C, H, B, O, N)<sup>63</sup> as well as the basis set cc-pVDZ(-PP) for Te.<sup>64</sup> The cc-PVDZ-PP basis set uses the corresponding effective core potential (ECP) accounting for 28 electrons. The use of the cc-PVDZ and cc-PVDZ-PP basis sets will hereafter be referred to as cc-PVDZ(-PP). The basis sets as well as the ECP for the Te atom were obtained from the Basis Set Exchange Library.<sup>65,66</sup> Initial molecular geometries were taken from the experimentally obtained X-ray structures. Subsequent frequency analysis confirmed all obtained structures to be local minima on the potential energy surface. The optimized geometry of the  $S_0$  ground state was determined at the B3LYP level of theory. The phosphorescence energy was calculated by computing the optimized geometry of the lowest lying triplet state ( $T_1$ ) using UB3LYP (spin-unrestricted B3LYP) with the same basis sets as specified above. Subsequent TD-DFT calculations were used to predict the vertical excitation energies of the first 10 singlet and first ten triplet states using the B3LYP functional as well as the cc-PVDZ(-PP) basis sets starting from the B3LYP optimized gas-phase  $S_0$  geometry. The presented molecular orbitals (MOs) were extracted from the Gaussian16 checkpoint-files and are visualized with VMD.<sup>67</sup>

**Table 3.4** – TD-DFT calculated excited states of **Mes(<sup>i</sup>PrO)B-Te-6-B(O<sup>i</sup>Pr)Mes** at the B3LYP-ccpVDZ(-PP) level of theory.

| Excited State         | Energy (eV)<br>Oscillator Strength | Wavelength<br>(nm) | Transition       |
|-----------------------|------------------------------------|--------------------|------------------|
| <b>T<sub>1</sub></b>  | 2.4463                             | 506.8              | 142 – 144        |
|                       | 0.0000                             |                    | HOMO-1 to LUMO   |
| <b>T<sub>2</sub></b>  | 2.4934                             | 497.3              | 143 – 144        |
|                       | 0.0000                             |                    | HOMO to LUMO     |
| <b>S<sub>1</sub></b>  | 3.4273                             | 361.8              | 143 – 144        |
|                       | 0.0577                             |                    | HOMO to LUMO     |
| <b>T<sub>3</sub></b>  | 3.5688                             | 347.4              | 140 – 146        |
|                       | 0.0000                             |                    | HOMO-3 to LUMO+2 |
| <b>T<sub>4</sub></b>  | 3.5691                             | 347.4              | 141 – 146        |
|                       | 0.0000                             |                    | HOMO-2 to LUMO+2 |
| <b>T<sub>5</sub></b>  | 3.8094                             | 325.5              | 141 – 144        |
|                       | 0.0000                             |                    | HOMO-2 to LUMO   |
| <b>T<sub>6</sub></b>  | 3.8548                             | 321.6              | 140 – 144        |
|                       | 0.0000                             |                    | HOMO-3 to LUMO   |
| <b>S<sub>2</sub></b>  | 3.8633                             | 320.9              | 141 – 144        |
|                       | 0.0046                             |                    | HOMO-2 to LUMO   |
| <b>S<sub>3</sub></b>  | 3.8876                             | 318.9              | 140 – 144        |
|                       | 0.0001                             |                    | HOMO-3 to LUMO   |
| <b>T<sub>7</sub></b>  | 3.8956                             | 318.3              | 143 – 145        |
|                       | 0.0000                             |                    | HOMO to LUMO+1   |
| <b>S<sub>4</sub></b>  | 3.9338                             | 315.2              | 142 – 144        |
|                       | 0.3590                             |                    | HOMO-1 to LUMO   |
| <b>T<sub>8</sub></b>  | 4.0703                             | 304.6              | 139 – 144        |
|                       | 0.0000                             |                    | HOMO-4 to LUMO   |
| <b>T<sub>9</sub></b>  | 4.0723                             | 304.5              | 138 – 144        |
|                       | 0.0000                             |                    | HOMO-5 to LUMO   |
| <b>S<sub>5</sub></b>  | 4.0831                             | 303.7              | 139 – 144        |
|                       | 0.0021                             |                    | HOMO-4 to LUMO   |
| <b>S<sub>6</sub></b>  | 4.0847                             | 303.5              | 138 – 144        |
|                       | 0.0001                             |                    | HOMO-5 to LUMO   |
| <b>S<sub>7</sub></b>  | 4.2622                             | 290.9              | 143 – 145        |
|                       | 0.0000                             |                    | HOMO to LUMO+1   |
| <b>T<sub>10</sub></b> | 4.4234                             | 280.3              | 138 – 146        |
|                       | 0.0000                             |                    | HOMO-5 to LUMO+2 |
| <b>S<sub>8</sub></b>  | 4.7159                             | 262.9              | 143 – 146        |
|                       | 0.0030                             |                    | HOMO to LUMO+2   |
| <b>S<sub>9</sub></b>  | 4.7350                             | 261.9              | 137 – 144        |
|                       | 0.0000                             |                    | HOMO-6 to LUMO   |
| <b>S<sub>10</sub></b> | 4.7407                             | 261.5              | 142 – 145        |
|                       | 0.0014                             |                    | HOMO-1 to LUMO+1 |

### 3.5 References

1. (a) C. C. C. Johansson Seechurn, M. O. Kitching, T. J. Colacot and V. Snieckus, *Angew. Chem. Int. Ed.*, **2012**, *51*, 5062–5085; (b) D. G. Hall, *Boronic Acids: Preparation and Applications in Organic Synthesis, Medicine and Materials*, 2nd ed. (Wiley-VCH Verlag GmbH & Co., Weinheim, **2011**).
2. L. Ji, S. Griesbeck and T. B. Marder, *Chem. Sci.*, **2017**, *8*, 846–863.
3. Y. Ren and F. Jäkle, *Dalton Trans.*, **2016**, *45*, 13996–14007.
4. T. Ishiyama, J. Takagi, Y. Yonekawa, J. F. Hartwig and N. Miyaura, *Adv. Synth. Catal.*, **2003**, *345*, 1103–1106.
5. K. Mertins, A. Zapf and M. Beller, *J. Mol. Catal. A: Chem.*, **2004**, *207*, 21–25.
6. G. A. Chotana, V. A. Kallepalli, R. E. Maleczka, Jr. and M. R. Smith, III, *Tetrahedron*, **2008**, *64*, 6103–6114.
7. M.-A. Légaré, M.-A. Courtemanche, É. Rochette and F.-G. Fontaine, *Science*, **2015**, *349*, 513–516.
8. (a) T. Chivers and R. S. Laitinen, *Chem. Soc. Rev.*, **2015**, *44*, 1725–1739; (b) E. Rivard, *Chem. Lett.*, **2015**, *44*, 730–736.
9. A. Aprile, K. L. Iversen, D. J. D. Wilson and J. L. Dutton, *Inorg. Chem.*, **2015**, *54*, 4934–4939.
10. E. I. Carrera, A. E. Lanterna, A. J. Lough, J. C. Scaiano and D. S. Seferos, *J. Am. Chem. Soc.*, **2016**, *138*, 2678–2689.
11. E. I. Carrera and D. S. Seferos, *Organometallics*, **2017**, *36*, 2612–2621.



12. W.-H. Lee, S. K. Lee, W. S. Shin, S.-J. Moon and I.-N. Kang, *J. Polym. Sci., Part A: Polym. Chem.*, **2013**, *51*, 2753–2758.
13. G. He, L. Kang, W. Torres Delgado, O. Shynkaruk, M. J. Ferguson, R. McDonald and E. Rivard, *J. Am. Chem. Soc.*, **2013**, *135*, 5360–5363.
14. Y. S. Park, Q. Wu, C.-Y. Nam and R. B. Grubbs, *Angew. Chem. Int. Ed.*, **2014**, *53*, 10691–10695.
15. E. H. Jung, S. Bae, T. W. Yoo and W. H. Jo, *Polym. Chem.*, **2014**, *5*, 6545–6550.
16. R. S. Ashraf, I. Meager, M. Nikolka, M. Kirkus, M. Planells, B. C. Schroeder, S. Holliday, M. Hurhangee, C. B. Nielsen, H. Sirringhaus and I. McCulloch, *J. Am. Chem. Soc.*, **2015**, *137*, 1314–1321.
17. A. A. Jahnke, B. Djukic, T. M. McCormick, E. Buchaca Domingo, C. Hellmann, Y. Lee and D. S. Seferos, *J. Am. Chem. Soc.*, **2013**, *135*, 951–954.
18. J. G. Manion, S. Ye, A. H. Proppe, A. W. Laramée, G. R. McKeown, E. L. Kynaston, S. O. Kelley, E. H. Sargent and D. S. Seferos, *ACS Appl. Energy Mater.*, **2018**, *1*, 5033–5042.
19. (a) L. Yang, W. Gu, L. Lv, Y. Chen, Y. Yang, P. Ye, J. Wu, L. Hong, A. Peng and H. Huang, *Angew. Chem. Int. Ed.*, **2018**, *57*, 1096–1102; (b) For a review on harvesting triplet excitons for OPVs, see: B. T. Luppi, D. Majak, M. Gupta, E. Rivard and K. Shankar, *J. Mater. Chem. A*, **2019**, *7*, 2445–2463.
20. W. Xing, P. Ye, J. Lu, X. Wu, Y. Chen, T. Zhu, A. Peng and H. Huang, *J. Power Sources*, **2018**, *401*, 13–19.

21. G. He, W. Torres Delgado, D. J. Schatz, C. Merten, A. Mohammadpour, L. Mayr, M. J. Ferguson, R. McDonald, A. Brown, K. Shankar and E. Rivard, *Angew. Chem. Int. Ed.*, **2014**, *53*, 4587–4591.
22. G. He, B. D. Wiltshire, P. Choi, A. Savin, S. Sun, A. Mohammadpour, M. J. Ferguson, R. McDonald, S. Farsinezhad, A. Brown, K. Shankar and E. Rivard, *Chem. Commun.*, **2015**, *51*, 5444–5447.
23. A. K. Mahrok, E. I. Carrera, A. J. Tilley, S. Ye and D. S. Seferos, *Chem. Commun.*, **2015**, *51*, 5475–5478.
24. N. Nagahora, S. Yahata, S. Goto, K. Shioji and K. Okuma, *J. Org. Chem.*, **2018**, *83*, 1969–1975.
25. W. Torres Delgado, C. A. Braun, M. P. Boone, O. Shynkaruk, Y. Qi, R. McDonald, M. J. Ferguson, P. Data, S. K. C. Almeida, I. de Aguiar, G. L. C. de Souza, A. Brown, G. He and E. Rivard, *ACS Appl. Mater. Interfaces*, **2018**, *10*, 12124–12134.
26. K. Takimiya, Y. Kunugi, Y. Konda, N. Niihara and T. Ostubo, *J. Am. Chem. Soc.*, **2004**, *126*, 5084–5085.
27. M. Kaur, D. S. Yang, J. Shin, T. W. Lee, K. Choi, M. J. Cho and D. H. Choi, *Chem. Commun.*, **2013**, *49*, 5495–5497.
28. M. Kaur, D. H. Lee, D. S. Yang, H. A. Um, M. J. Cho, J. S. Kang and D. H. Choi, *Chem. Commun.*, **2014**, *50*, 14394–14396.
29. M. Al-Hashimi, Y. Han, J. Smith, H. S. Bazzi, S. Y. A. Alqaradawi, S. E. Watkins, T. D. Anthopoulos and M. Heeney, *Chem. Sci.*, **2016**, *7*, 1093–1099.

30. T. Oyama, Y. S. Yang, K. Matsuo and T. Yasuda, *Chem. Commun.*, **2017**, *53*, 3814–3817.
31. S. Ye, L. Janasz, W. Zajaczkowski, J. G. Manion, A. Mondal, T. Marszalek, D. Andrienko, K. Müllen, W. Pisula and D. S. Seferos, *Macromol. Rapid Commun.*, **2019**, *40*, 1800596.
32. A. A. Jahnke, G. W. Howe and D. S. Seferos, *Angew. Chem. Int. Ed.*, **2010**, *49*, 10140–10144.
33. D. Moseguí González, K. N. Raftopoulos, G. He, C. N. Papadakis, A. Brown, E. Rivard and P. Müller-Buschbaum, *Macromol. Rapid Commun.*, **2017**, *38*, 1700065.
34. W. Torres Delgado, F. Shahin, M. J. Ferguson, R. McDonald, G. He and E. Rivard, *Organometallics*, **2016**, *35*, 2140–2148.
35. G. H. Herberich, W. Boveleth, B. Hessner, D. P. J. Köffer, M. Negele and R. Saive, *J. Organomet. Chem.*, **1986**, *308*, 153–166.
36. G. H. Herberich, W. Boveleth, B. Hessner, M. Hostalek, D. P. J. Köffer and M. Negele, *J. Organomet. Chem.*, **1987**, *319*, 311–326.
37. H. C. Brown, M. Srebnik, R. K. Bakshi and T. E. Cole, *J. Am. Chem. Soc.*, **1987**, *109*, 5420–5426.
38. T. Köhler, J. Faderl, H. Pritzkow and W. Siebert, *Eur. J. Inorg. Chem.*, **2002**, 2942–2946.
39. K. Durka, A. Górska, P. Jankowski, T. Kliś, M. Kublicki, J. Serwatowski, M. Urban, G. Wesela-Baumann and K. Woźniak, *Tetrahedron Lett.*, **2017**, *58*, 1185–1189.

40. S. K. Møllerup, C. Li, J. Radtke, X. Wang, Q.-S. Li and S. Wang, *Angew. Chem. Int. Ed.*, **2018**, *57*, 9634–9639.
41. C. A. Braun, D. Zommerman, I. de Aguiar, Y. Qi, W. Torres Delgado, M. J. Ferguson, R. McDonald, G. L. C. de Souza, G. He, A. Brown and E. Rivard, *Faraday Discuss.*, **2017**, *196*, 255–268.
42. (a) E. Negishi, F. E. Cederbaum and T. Takahashi, *Tetrahedron Lett.*, **1986**, *27*, 2829–2832; (b) P. J. Fagan and W. A. Nugent, *J. Am. Chem. Soc.*, **1988**, *110*, 2310–2312.
43. (a) M. Hirai, N. Tanaka, M. Sakai and S. Yamaguchi, *Chem. Rev.*, **2019**, *119*, 8291–8331, and references therein; (b) J. Merz, J. Fink, A. Friedrich, I. Krummenacher, H. H. Al Mamari, S. Lorenzen, M. Haehnel, A. Eichorn, M. Moos, M. Holzapfel, H. Braunschweig, C. Lambert, A. Steffern, L. Ji and T. B. Marder, *Chem. Eur. J.*, **2017**, *23*, 13164–13180.
44. For related work on the use of the heavy atom effect to gain access to phosphorescence in the main group, see: (a) J. Ohshita, S. Matsui, R. Yamamoto, T. Mizumo, Y. Ooyama, Y. Harima, T. Murafuji, K. Tao, Y. Kuramochi, T. Kaikoh and H. Higashimura, *Organometallics*, **2010**, *29*, 3239–3241; (b) A. Kremer, A. Fermi, N. Biot, J. Wouters and D. Bonifazi, *Chem. Eur. J.*, **2016**, *22*, 5665–5675; (c) O. Toma, M. Allain, F. Meinardi, A. Formi, C. Botta and N. Mercier, *Angew. Chem. Int. Ed.*, **2016**, *55*, 7998–8002; (d) S. M. Parke, E. Hupf, G. K. Matharu, I. de Aguiar, L. Xu, H. Yu, M. P. Boone, G. L. C. de Souza, R. McDonald, M. J. Ferguson, G. He,

- A. Brown and E. Rivard, *Angew. Chem. Int. Ed.*, **2018**, *57*, 14841–14846; (e) S. M. Parke and E. Rivard, *Isr. J. Chem.*, **2018**, *58*, 915–926 and references therein.
45. For the recent incorporation of phosphorescent tellurophene units into macrocycles, see: K. Takahashi, S. Shimo, E. Hupf, J. Ochiai, C. A. Braun, W. Torres Delgado, L. Xu, G. He, E. Rivard and N. Iwasawa, *Chem. Eur. J.*, **2019**, *25*, 8479–8483.
46. M. Mantina, A. C. Chamberlin, R. Valero, C. J. Cramer, and D. G. Truhlar, *J. Phys. Chem. A*, **2009**, *113*, 5806–5812.
47. For leading reviews on this topic, see: (a) J. Mei, N. L. C. Leung, R. T. K. Kwok, J. W. Y. Lam and B. Z. Tang, *Chem. Rev.*, **2015**, *115*, 11718–11940; (b) L. Ravotto and P. Ceroni, *Coord. Chem. Rev.*, **2017**, *346*, 62–76; (c) M. Hayduk, S. Riebe and J. Voskuhl, *Chem. Eur. J.*, **2018**, *24*, 12221–12230.
48. G. N. Lewis and M. Kasha, *J. Am. Chem. Soc.*, **1944**, *66*, 2100–2116.
49. T. Kinzel, Y. Zhang and S. L. Buchwald, *J. Am. Chem. Soc.*, **2010**, *132*, 14073–14075.
50. For a pioneering use of the Bdan group in cross-coupling, see: H. Noguchi, K. Hojo, and M. Suginome, *J. Am. Chem. Soc.*, **2007**, *129*, 758–759.
51. J. L. Dutton, G. J. Farrar, M. J. Sgro, T. L. Battista and P. J. Ragona, *Chem. Eur. J.*, **2009**, *15*, 10263–10271.
52. P. R. Bevington, *IBM J. Res. Develop.*, **1969**, *13*, 119–125.
53. J. Durbin and G. S. Watson, *Biometrika*, **1950**, *37*, 409–428.
54. J. Durbin and G. S. Watson, *Biometrika*, **1951**, *38*, 159–178.

55. D. V. O'Connor and D. Phillips, *Time Correlated Single Photon Counting* (Academic Press, New York, **1984**).
56. H. Hope, *Prog. Inorg. Chem.*, **1994**, *41*, 1–19.
57. R. H. Blessing, *Acta Crystallogr. A.*, **1995**, *51*, 33–38.
58. G. M. Sheldrick, *Acta Crystallogr. A.*, **2015**, *71*, 3–8.
59. G. M. Sheldrick, *Acta Crystallogr. C.*, **2015**, *71*, 3–8.
60. M. J. Frisch, G. W. Trucks, H. B. Schlegel, G. E. Scuseria, M. A. Robb, J. R. Cheeseman, G. Scalmani, V. Barone, G. A. Petersson, H. Nakatsuji, X. Li, M. Caricato, A. V. Marenich, J. Bloino, B. G. Janesko, R. Gomperts, B. Mennucci, H. P. Hratchian, J. V. Ortiz, A. F. Izmaylov, J. L. Sonnenberg, D. Williams-Young, F. Ding, F. Lipparini, F. Egidi, J. Goings, B. Peng, A. Petrone, T. Henderson, D. Ranasinghe, V. G. Zakrzewski, J. Gao, N. Rega, G. Zheng, W. Liang, M. Hada, M. Ehara, K. Toyota, R. Fukuda, J. Hasegawa, M. Ishida, T. Nakajima, Y. Honda, O. Kitao, H. Nakai, T. Vreven, K. Throssell, J. A. Montgomery, Jr., J. E. Peralta, F. Ogliaro, M. J. Bearpark, J. J. Heyd, E. N. Brothers, K. N. Kudin, V. N. Staroverov, T. A. Keith, R. Kobayashi, J. Normand, K. Raghavachari, A. P. Rendell, J. C. Burant, S. S. Iyengar, J. Tomasi, M. Cossi, J. M. Millam, M. Klene, C. Adamo, R. Cammi, J. W. Ochterski, R. L. Martin, K. Morokuma, O. Farkas, J. B. Foresman and D. J. Fox, *Gaussian 16, Revision A.03*, Gaussian, Inc., Wallingford CT, **2016**.
61. A. D. Becke, *J. Chem. Phys.*, **1993**, *98*, 5648–5652.
62. C. Lee, W. Yang and R. G. Parr, *Phys. Rev. B*, **1988**, *37*, 785–789.
63. T. H. Dunning, Jr., *J. Chem. Phys.*, **1989**, *90*, 1007–1023.

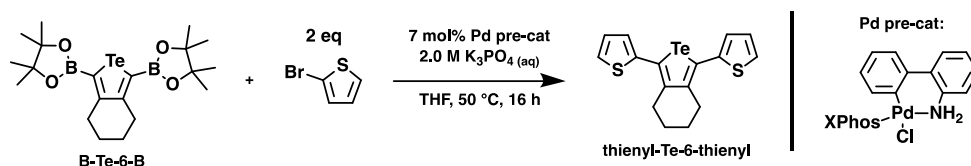
64. K. A. Peterson, D. Figgen, E. Goll, H. Stoll and M. Dolg, *J. Chem. Phys.*, **2003**, *119*, 11113–11123.
65. D. Feller, *J. Comput. Chem.*, **1996**, *17*, 1571–1586.
66. K. L. Schuchardt, B. T. Didier, T. Elsethagen, L. Sun, V. Gurumoorthi, J. Chase, J. Li and T. L. Windus, *J. Chem. Inf. Model.*, **2004**, *47*, 1045–1052.
67. W. Humphrey, A. Dalke and K. Schulten, *J. Mol. Graph.*, **1996**, *14*, 33–38.

## Chapter 4 – New Tellurophenes Derived from the Suzuki-Miyaura Cross-Coupling of a Bis(boryl)tellurophene

### 4.1 Introduction

Interest in the study of tellurophenes has increased over the past 20 years with their use being demonstrated in organic photovoltaics (OPVs),<sup>1-9</sup> organic light-emitting diodes (OLEDs),<sup>10-18</sup> and in organic field effect transistors (OFETs).<sup>1,5,6,19-24</sup> This progress can be attributed to new synthetic protocols that have made tellurophenes more accessible. To this point, although Suzuki-Miyaura cross-coupling is the most popular method for forming C(sp<sup>2</sup>)-C(sp<sup>2</sup>) bonds between aryl groups, borylated tellurophenes exhibited poor performance when common cross-coupling protocols were used. Due to the electron-rich nature of tellurophenes, the use of borylated tellurophenes as substrates often leads to undesired protodeboronation under the basic conditions of the Suzuki-Miyaura reaction, resulting in low yields.<sup>13</sup> However, it was recently shown that when Buchwald's easy to prepare and highly active pre-catalyst Cl(XPhos)Pd(2-aminobiphenyl) is used,<sup>25</sup> efficient coupling between the borylated tellurophene **B-Te-6-B** and 2-bromothiophene occurs in quantitative yield under mild conditions (Scheme 4.1).<sup>17</sup>





**Scheme 4.1** – Suzuki-Miyaura cross-coupling of **B-Te-6-B** with 2-bromothiophene to yield **thienyl-Te-6-thienyl**; XPhos = 2-dicyclohexylphosphino-2',4',6'-triisopropylbiphenyl.

One emerging application of tellurophenes is the ability of some functionalized variants to access room temperature solid state phosphorescence (often in air).<sup>10-17</sup> However, tuning the colour of emission, while maintaining moderate/high quantum yields remains a great challenge. Additionally, it is also of interest to study the effect of linking tellurophene heterocycles with redox active functional groups such as viologens. Viologens (4,4'-bipyridinium derivatives) are an interesting class of  $\pi$ -conjugated compound that can undergo two sequential, reversible one-electron reductions within a chemically accessible redox potential window, making them excellent electron-acceptors.<sup>26</sup> The first reduction event of viologen forms a thermodynamically stable radical cation with a deep purple colour, from which the name is derived. Due to their unique reduction properties, viologens have been used in a variety of functional materials including electrochromic displays, diodes and transistors, memory devices, molecular machines, antibacterial agents, electrodes for supercapacitors and batteries, catalysts for hydrogen generation, gas storage and separation, and in dye-sensitized solar cells.<sup>27</sup>

Many extended viologens, whereby an aromatic spacer separates the two pyridinium moieties, also exhibit the same reduction behaviour as the parent viologen.

Extended viologens featuring phenylene (**1**), furyl (**2**) or thienyl (**3**) spacers (Figure 4.1) also undergo a two-stage reduction similar to the parent viologen.<sup>28</sup> Whereas viologen itself is non-emissive, compounds **2** and **3** exhibit blue fluorescence in MeCN solutions with quantum yields ( $\Phi$ ) of 0.84 and 0.75, respectively. Furthermore, the incorporation of a selenophene unit to give **4** (Figure 4.1) was reported by Scherman and coworkers in 2015 and this species exhibits very weak blue fluorescence ( $\lambda_{em} = 434$  nm,  $\Phi = 0.0017$ ) in water.<sup>29</sup> The low fluorescence quantum yield of **4** was attributed to an increase in spin-orbit coupling due to the heavy nature of the Se atom, resulting in enhanced intersystem crossing (ISC) to afford a triplet excited state, followed by non-radiative decay (*e.g.*, quenching with O<sub>2</sub>) in solution.

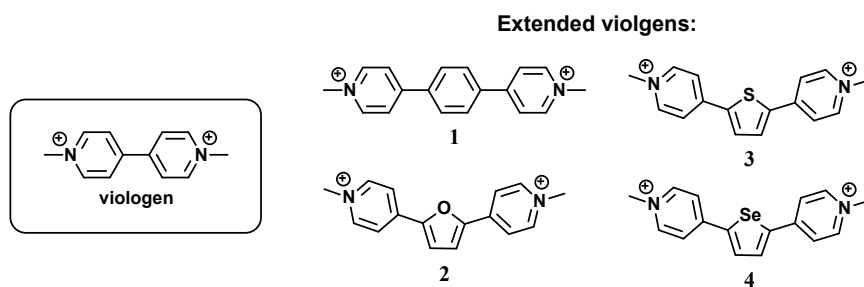


**Figure 4.1** – Viologen and examples of extended viologens featuring Group 16 heteroles as the aromatic spacer; the BF<sub>4</sub><sup>-</sup> or Cl<sup>-</sup> counterions are not shown for clarity.

Recently, a related system of chalcogen-bridged viologens was published by He and coworkers in 2018 (Figure 4.2).<sup>30</sup> These compounds were shown to undergo reversible two-stage one-electron reductions with intense colour changes, characteristic of viologens. Furthermore, the benzyl species (**5b–7b**) were all weakly fluorescent ( $\Phi$

< 1 %) in DMF solutions. No phosphorescence was observed, likely due to enhanced non-radiative decay (or quenching with O<sub>2</sub>) in solution and triplet-triplet annihilation in the solid state due to the presence of short Te...Te interactions of *ca.* 4.0 Å. Therefore, I was interested in studying whether an extended viologen containing a tellurophene unit could give way to solid state phosphorescence and if triplet-triplet annihilation *via* close intermolecular Te contacts could be prevented.

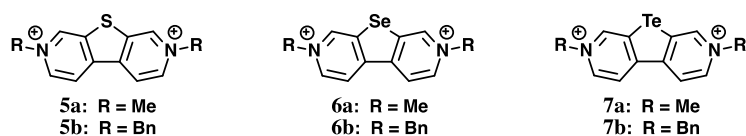


**Figure 4.2** – Chalcogen-bridged viologens developed by He and coworkers; anions Br<sup>-</sup> or <sup>-</sup>OTf are not shown for clarity.

Previously, the Rivard group has synthesized many tellurophenes exhibiting solid state phosphorescence such as the bis(pinacolatoboryl)tellurophene, **B-Te-6-B** (see Scheme 4.1 for the structure), as well as some 2,5-bis(aryl)tellurophenes prepared *via* sequential zirconocene-mediated alkyne cyclization and Zr/Te metallacycle transfer chemistry.<sup>3,15</sup> Recently I have shown that the Suzuki-Miyaura cross-coupling of **B-Te-6-B** with 2-bromothiophene affords **thienyl-Te-6-thienyl** in high yield under mild conditions with the aid of a more active Pd pre-catalyst, Cl(XPhos)Pd(2-aminobiphenyl), developed by Buchwald and coworkers (Scheme 4.1).<sup>17</sup> Thus, I decided to further explore the scope of this cross-coupling reaction and the results will be summarized in this Chapter. Herein, the Suzuki-Miyaura cross-coupling between **B-Te-6-B** and various arylhalides is reported in order to access a wider library of

potentially emissive 2,5-bis(aryl)tellurophenes. This method was used to synthesize the first extended viologen featuring a tellurophene linker, as well as the incorporation of other aryl groups that allow for further chemistry. For example, a tellurophene featuring photoactive diphenylethene (dpe) groups was synthesized in the hope that solid state photodimerization would lead to new phosphorescent tellurophene networks. Furthermore, electron-deficient dimesitylboryl ( $-BMe_2$ , Mes = 2,4,6-Me<sub>3</sub>C<sub>6</sub>H<sub>2</sub>) or *p*-nitrobenzyl groups were included in an attempt to red-shift the phosphorescence into the NIR, a desirable feature for bioimaging applications.<sup>32,33</sup>

## 4.2 Results and Discussion

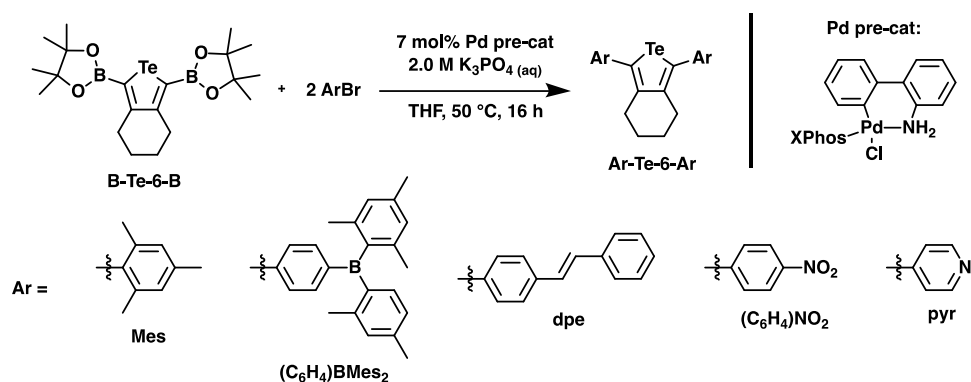
### 4.2.1 Synthesis of 2,5-bis(aryl)tellurophenes

The tellurophenes discussed in this Chapter were synthesized *via* Suzuki-Miyaura cross-coupling between **B-Te-6-B** and arylhalides under mild conditions, as shown in Scheme 4.2. The cross-coupling was first conducted between **B-Te-6-B** and bromomesitylene (BrMes, Mes = 2,4,6-Me<sub>3</sub>C<sub>6</sub>H<sub>2</sub>), leading to the formation of **Mes-Te-6-Mes** as an air- and moisture-stable white solid in a high isolated yield (> 70 %). In order to examine the compatibility of this cross-coupling protocol with even bulkier substrates, a reaction was attempted between 1-bromo-2,4,6-triisopropylbenzene (BrTrip) and **B-Te-6-B**, however no reaction transpired under the optimized conditions developed for this system (50 °C, for 20 hours).

Three-coordinate boranes ( $\text{BAr}_3$ ) featuring bulky aromatic groups are frequently employed as  $\pi$ -acceptor units in organic electronics.<sup>33-35</sup> These groups offer steric protection of the empty p-orbital at boron, which imparts air- and moisture-stability to the final products. Due to the abundance of luminescent compounds featuring  $-\text{BMes}_2$  groups,<sup>36</sup> I sought to install this group on a tellurophene with the goal of red-shifting the wavelength of phosphorescence into the near IR region. In order to do so, the reagent  $\text{Br}(\text{C}_6\text{H}_4)\text{BMes}_2$  was first prepared according to a literature procedure.<sup>37</sup> This arylhalide reacted smoothly with **B-Te-6-B** under the cross-coupling conditions outlined in Scheme 4.2 to afford **Mes<sub>2</sub>B(C<sub>6</sub>H<sub>4</sub>)-Te-6-(C<sub>6</sub>H<sub>4</sub>)BMes<sub>2</sub>** as a bright yellow solid in a 80 % yield. In a similar manner, a tellurophene featuring electron-deficient *p*-nitrophenyl groups ( $-(\text{C}_6\text{H}_4)\text{NO}_2$ ) was also synthesized by coupling **B-Te-6-B** and 4-bromonitrobenzene (Scheme 4.2) in the hopes of obtaining a NIR phosphor.

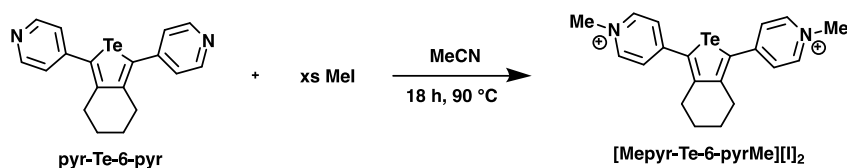
A tellurophene functionalized with diphenylethene (dpe) units was synthesized from **B-Te-6-B** and  $\text{BrC}_6\text{H}_4(\text{CH}=\text{CH})\text{C}_6\text{H}_5$  to form **dpe-Te-6-dpe** (Scheme 4.2).<sup>38</sup> If sufficiently close packing of diphenylethene-containing molecules occurs in the solid state, then the literature has shown that adjacent ethene moieties can undergo an intermolecular [2+2] photodimerization upon UV-light irradiation to produce cross-linking cyclobutane rings, forming a 2-dimensional network. This chemistry has been used previously to enhance solid state fluorescence *via* rigidification of the molecular network, as well as to sequester benzene and thiophene molecules *via* host-guest interactions.<sup>39,40</sup> However, **dpe-Te-6-dpe** is an extremely insoluble yellow powder that could not be obtained in analytically pure form, preventing further studies. Furthermore,

the inability to form a crystalline material suggests that **dpe-Te-6-dpe** would not be suitable for the solid state photodimerization to form extended networks, as pre-organization in the solid state is essential in order for this reaction to occur.



**Scheme 4.2** – Synthesis of 2,5-bis(aryl)tellurophenes derived from the Suzuki-Miyaura cross-coupling of **B-Te-6-B** with arylhalides.

Using the same cross-coupling protocol outlined in Scheme 4.2, **pyr-Te-6-pyr** was also synthesized (Scheme 4.3). In order to prepare an extended viologen with a tellurophene spacer, **pyr-Te-6-pyr** was combined with an excess of MeI to give **[MepyrTe-6-pyrMe][I]<sub>2</sub>** (Scheme 4.3). This product crystallizes out of MeCN at room temperature to give an analytically pure red solid that becomes yellow when ground into a fine powder.



**Scheme 4.3** – Synthesis of [Mepyr-Te-6-pyrMe][I]<sub>2</sub>.

#### 4.2.2 Solid state structures of the 2,5-bis(aryl)tellurophenes derived from the Suzuki-Miyaura cross-coupling protocol

Solid state structures were determined for **Mes-Te-6-Mes**, **O<sub>2</sub>N(C<sub>4</sub>H<sub>4</sub>)-Te-6-(C<sub>4</sub>H<sub>4</sub>)NO<sub>2</sub>**, **pyr-Te-6-pyr**, and **[Mepyr-Te-6-pyrMe][I]<sub>2</sub>** *via* single-crystal X-ray crystallography and the refined structures are shown in Figures 4.4–4.7. These tellurophenes adopt structural features that are common among 2,5-bis(aryl)tellurophenes including Te–C bond lengths of 2.066(4)–2.080(3) Å and C–Te–C angles of 81.21(18)–82.28(17)°,<sup>15,20</sup> with the exception of **[Mepyr-Te-6-pyrMe][I]<sub>2</sub>** which contains slightly longer Te–C bond lengths of 2.0881(16) and 2.0906(16) Å and a slightly smaller C–Te–C bond angle of 79.86(6)°. Furthermore, each of the tellurophenes described in this chapter feature aryl rings that are twisted out of the plane of the central tellurophene moiety with (C<sub>tellurophene</sub>–C<sub>tellurophene</sub>–C<sub>aryl</sub>–C<sub>aryl</sub>) torsion angles involving the tellurophene ring and aryl side groups ranging from 39.1(3)° in **pyr-Te-6-pyr** to 61.8(2) in **[Mepyr-Te-6-pyrMe][I]<sub>2</sub>**, for all tellurophenes discussed in this Chapter, except **Mes-Te-6-Mes**. This is consistent with other symmetric 2,5-bis(aryl)tellurophenes, such as tellurophenes functionalized with naphthyl or 3,5-(CF<sub>3</sub>)<sub>2</sub>C<sub>6</sub>H<sub>3</sub> groups, which adopt aryl rings canted out of the plane of the tellurophene

by 40.7(12)° to 64.0(5)°. <sup>15</sup> However, **Mes-Te-6-Mes** is the first structurally characterized 2,5-bis(aryl)tellurophene to exhibit aryl groups perpendicular to the tellurophene ring [ $C_{\text{tellurophene}}-C_{\text{tellurophene}}-C_{\text{aryl}}-C_{\text{aryl}}$  torsion angles of 89.6(4) and 92.0(4)°] likely due the steric bulk present by the *ortho*-methyl groups. In contrast, the highly planar unsymmetric tellurophene **8** (Figure 4.3) containing one electron-rich anisyl group and one electron-poor nitrophenyl group exhibits very small torsion angles of  $\leq 5.4(17)^\circ$  ( $C_{\text{tellurophene}}-C_{\text{tellurophene}}-C_{\text{aryl}}-C_{\text{aryl}}$ ). <sup>20</sup>

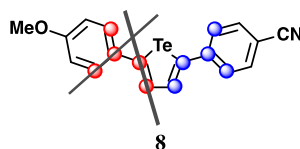


**Figure 4.3** – “Push-pull” tellurophene **8** with carbon angles used to calculate the torsion angles of interest shown with spheres.

Tellurium-containing molecules have a tendency to form close intermolecular  $\text{Te}\cdots\text{Te}$  interactions less than the sum of the van der Waals radius of Te (4.2 Å), however these interactions have been known to quench phosphorescence by encouraging triplet-triplet annihilation. <sup>15</sup> Of note, the shortest  $\text{Te}\cdots\text{Te}$  intermolecular distances observed in this study were found in the structure of **Mes-Te-6-Mes** (4.84 Å), which lies just outside the sum of the van der Waals radii of Te. This implies that negligible intermolecular interactions between the Te centres occurs in **Mes-Te-6-Mes**, **O<sub>2</sub>N(C<sub>4</sub>H<sub>4</sub>)-Te-6-(C<sub>4</sub>H<sub>4</sub>)NO<sub>2</sub>**, **pyr-Te-6-pyr**, and **[Mepyr-Te-6-pyrMe][I]<sub>2</sub>**. However, close intermolecular contacts (3.60 and 3.83 Å) were located between Te and I atoms in



[Mepyr-Te-6-pyrMe][I]<sub>2</sub>, which are less than the sum of the van der Waals radii of Te and I (4.04 Å).<sup>41</sup> These Te...I distances are comparable to the intermolecular Te...I distances observed for dibenzotellurophene diiodide **9** (3.717(1) and 3.696(1) Å as shown in Figure 4.8).<sup>42</sup>

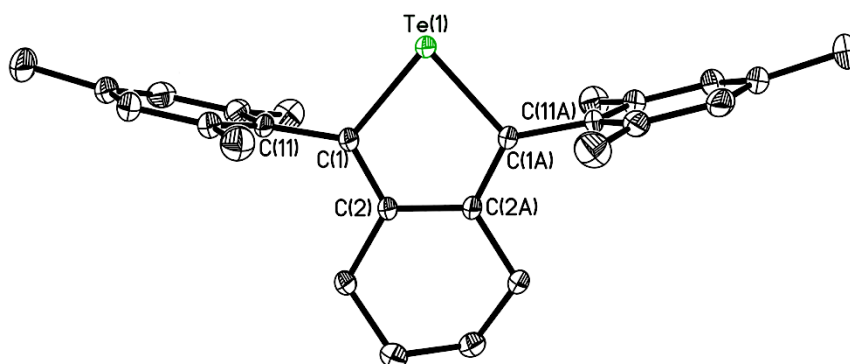


**Figure 4.4** – Molecular structure of **Mes-Te-6-Mes** with thermal ellipsoids presented at a 30 % probability level. All hydrogen atoms have been omitted for clarity. Selected bond lengths [Å] and angles [°]: Te1—C1 2.080(3), C1—C2 1.363(4), C1—C11 1.485(4), C2—C2A 1.458(5); C1—Te1—C1A 82.28(17). Selected torsion angles [°]: C2—C1—C11—C12 92.0(4), C2—C1—C11—C16 -89.6(4).

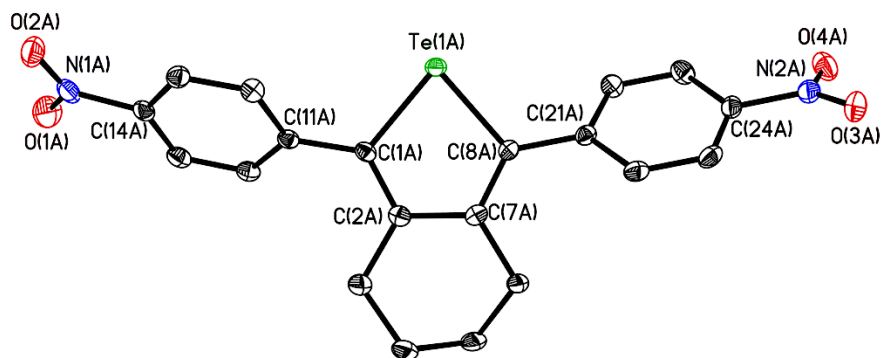


**Figure 4.5** – Molecular structure of  $\text{O}_2\text{N}(\text{C}_6\text{H}_4)\text{-Te-6-(C}_6\text{H}_4\text{)NO}_2$  with thermal ellipsoids presented at a 30 % probability level. All hydrogen atoms have been omitted for clarity. Two independent molecules of  $\text{O}_2\text{N}(\text{C}_6\text{H}_4)\text{-Te-6-(C}_6\text{H}_4\text{)NO}_2$  were located in the asymmetric unit. Selected bond lengths [ $\text{\AA}$ ] and angles [ $^\circ$ ] for molecule A with values for molecule B shown in square brackets: Te1—C1 2.069(4) [2.065(4)], Te1—C8 2.074(4) [2.066(4)], C1—C2 1.369(6) [1.371(6)], C2—C7 1.452(6) [1.452(6)], C7—C8 1.366(6) [1.365(6)]; C1—Te1—C8 81.21(18) [81.59(17)]. Selected torsion angles [ $^\circ$ ]: C2—C1—C11—C12 -48.8(7) [-45.3(7)], C2—C1—C11—C16 132.0(5) [133.4(5)], C7—C8—C21—C22 -48.6(7) [-44.3(7)], C7—C8—C21—C26 132.0(5) [133.4(5)].

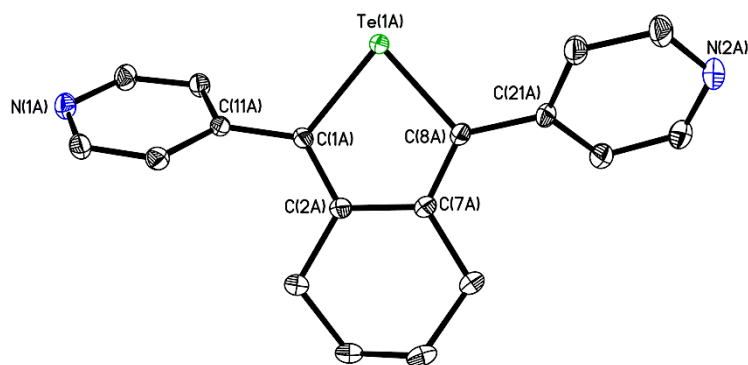


**Figure 4.6** – Molecular structure of **pyr-Te-6-pyr** with thermal ellipsoids presented at a 30 % probability level. All hydrogen atoms have been omitted for clarity. Two independent molecules of **pyr-Te-6-pyr** were located in the asymmetric unit. Selected bond lengths [Å] and angles [°] for molecule A with values for molecule B shown in square brackets: Te1—C1 2.0663(16) [2.0718(17)], Te1—C8 2.0708(16) [2.0737(16)], C1—C2 1.367(2) [1.372(2)], C2—C7 1.449(2) [1.453(2)], C7—C8 1.367(2) [1.369(2)], N1—C13 1.333(3) [1.339(3)], N1—C14 1.337(3) [1.339(3)], N2—C23 1.335(3) [1.342(3)], N2—C24 1.330(3) [1.346(3)]; C1—Te1—C8 81.46(7) [81.63(7)]. Selected torsion angles [°]: C2—C1—C11—C12 54.2(3) [43.1(3)], C2—C1—C11—C15 -125.0(2) [-139.1(2)], C7—C8—C21—C22 44.7(3) [39.1(3)], C7—C8—C21—C25 -136.1(2) [-143.50(19)].

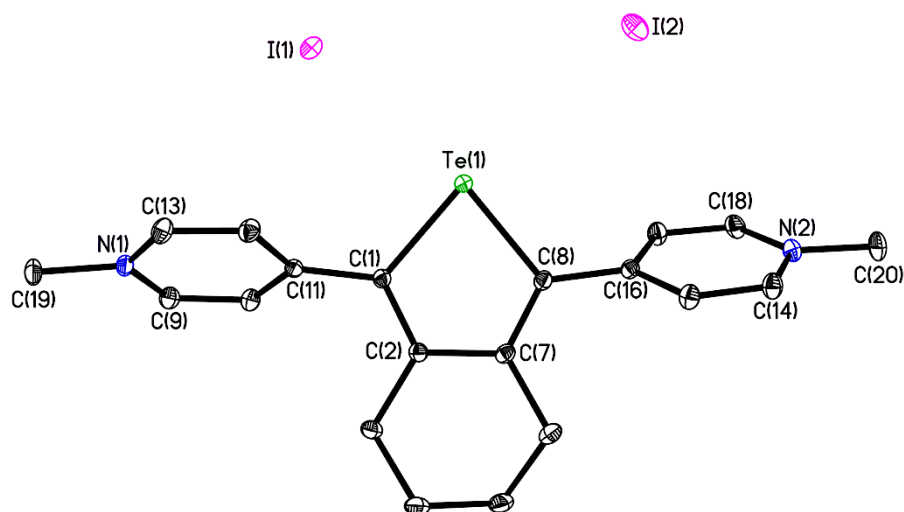


**Figure 4.7** – Molecular structure of [Mepyr-Te-6-pyrMe][I]<sub>2</sub> with thermal ellipsoids presented at a 30 % probability level. All hydrogen atoms have been omitted for clarity. Selected bond lengths [Å] and angles [°]: Te1—C1 2.0881(16), Te1—C8 2.0906(16), C1—C11 1.471(2), N1—C9 1.342(2), N1—C13 1.347(2), N1—C19 1.478(2), C2—C7 1.448(2), C7—C8 1.370(2), C8—C16 1.471(2), N2—C14 1.343(2), N2—C18 1.346(2), N2—C20 1.479(2); C1—Te1—C8 79.86(6). Selected torsion angles: C2—C1—C11—C10 -60.5(2), C2—C1—C11—C12 113.97(19), C7—C8—C16—C15 -61.8(2), C7—C8—C16—C17 116.67(19).

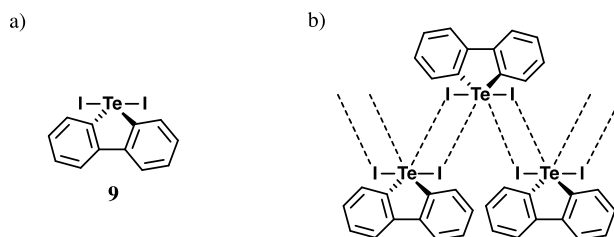


**Figure 4.8** – a) The structure of dibenzotellurophene diiodide **9**, and b) intramolecular Te...I interactions which drive the solid state packing of **9** are shown by dashed lines.

As previously mentioned in this Chapter, the aryl groups of each tellurophene are twisted out of the plane created by the tellurophene ring atoms. In particular the

solid state structure of **[Mepyr-Te-6-pyrMe][I]<sub>2</sub>** displays torsion angles of 60.5(2) and 61.8(2)° (C<sub>tellurophene</sub>-C<sub>tellurophene</sub>-C<sub>aryl</sub>-C<sub>aryl</sub>). This is in contrast to other extended viologens: for example, the related torsion angles between the pyridinium and thiophene ring in **3** (Figure 4.1) are 7.2 and 6.1°. <sup>28</sup> To examine whether the steric bulk of the fused cyclohexyl ring causes unfavourable interactions with coplanar pyridinium units, several computational studies were performed at the B3LYP/cc-pVDZ(-PP) level of theory. First, geometry optimizations were performed for **[Mepyr-Te-6-pyrMe]<sup>2+</sup>** and of **[Mepyr-Te-pyrMe]<sup>2+</sup>** (without the fused cyclohexyl group) without any geometric restrictions. The optimized torsion angle between the pyridinium and tellurophene rings were computed to be 141° and 158° for **[Mepyr-Te-6-pyrMe]<sup>2+</sup>** and **[Mepyr-Te-pyrMe]<sup>2+</sup>**, respectively. Next, several geometry optimizations were performed for both **[Mepyr-Te-6-pyrMe]<sup>2+</sup>** and **[Mepyr-Te-pyrMe]<sup>2+</sup>** with torsion angles frozen between 90° (perpendicular) and 180° (planar) (see Figure 4.9b for an illustration of the torsion angle of interest). The energy difference between each optimized structure locked at a specific torsion angle and the geometry optimizations with no geometric restrictions were plotted in Figure 4.9. Of note, geometry optimizations with torsion angles frozen at 90°, 100°, 110°, 170°, and 180° all resulted in two imaginary frequencies, which is true for both compounds. However, the computed energy for the coplanar geometry (torsion angle = 180 °) of **[Mepyr-Te-6-pyrMe]<sup>2+</sup>** is *ca.* 20 kJ/mol higher than both the unrestricted optimization and the coplanar geometry of **[Mepyr-Te-pyrMe]<sup>2+</sup>** (torsion angle = 180 °). Therefore, these gas-phase computations do suggest that unfavourable

interactions with the fused cyclohexyl group arise when the pyridinium rings are coplanar with the tellurophene heterocycle.

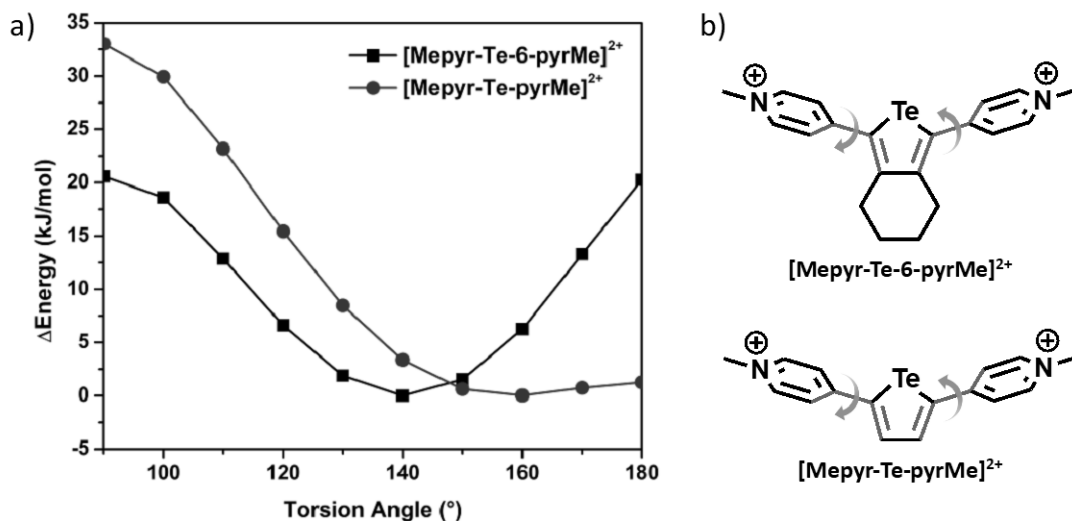


**Figure 4.9** – a) Gas-phase geometry optimizations at the B3LYP/cc-pVDZ(-PP) level of theory for [Mepyr-Te-6-pyrMe]<sup>2+</sup> and [Mepyr-Te-pyrMe]<sup>2+</sup> showing the difference in energy between structures that are optimized with frozen torsion angles (restricted optimization) and the energy of their respective optimized structures performed with no geometric restrictions (unrestricted optimization); b) structures of [Mepyr-Te-6-pyrMe]<sup>2+</sup> and [Mepyr-Te-pyrMe]<sup>2+</sup> with the torsion angle of interest shown in grey.

#### 4.2.3 Optical absorption properties of the 2,5-bis(aryl)tellurophenes

The experimental and computed UV-vis spectra of the tellurophenes derived from Suzuki-Miyaura cross-coupling discussed in this Chapter are shown in Figure 4.10. All of the 2,5-bis(aryl)tellurophenes have large molar absorptivities that range from  $9.73 \times 10^3 \text{ M}^{-1}\text{cm}^{-1}$  to  $5.69 \times 10^4 \text{ M}^{-1}\text{cm}^{-1}$ . The largest molar absorptivities are

observed in [**Mepyr-Te-6-pyr**][I<sub>2</sub>] ( $\lambda_{\text{max}} = 246 \text{ nm}$ ,  $\epsilon = 5.69 \times 10^4 \text{ M}^{-1}\text{cm}^{-1}$ ) and **dpe-Te-6-dpe** ( $\lambda_{\text{max}} = 355 \text{ nm}$ ,  $\epsilon = 5.51 \times 10^4 \text{ M}^{-1}\text{cm}^{-1}$ ), whereas the smallest molar absorptivity is observed for **Mes-Te-6-Mes** ( $\lambda_{\text{max}} = 293 \text{ nm}$ ,  $\epsilon = 9.75 \times 10^3 \text{ M}^{-1}\text{cm}^{-1}$ ). Furthermore, most tellurophenes have onsets of absorption near 450 nm, with the exception of **Mes-Te-6-Mes** and **pyr-Te-6-pyr**, which have onsets of absorption of *ca.* 400 nm, suggesting that these tellurophenes likely contain a lower degree of conjugation than the other 2,5-bis(aryl)tellurophenes discussed in this Chapter. This is consistent with the solid state structure of **Mes-Te-6-Mes**, which features mesityl groups twisted perpendicular with respect to the tellurophene core (Figure 4.4). Furthermore, gas-phase computations for **pyr-Te-6-pyr** did suggest the presence of unfavourable interactions between the pyridyl group and tellurophene ring as shown in Figure 4.9.

The UV-vis spectra for each 2,5-bis(aryl)tellurophene discussed in this Chapter were computed at the B3LYP/cc-pVDZ(-PP) level of theory in the gas-phase, and they are shown as grey inserts in Figure 4.10. Each computed spectrum matches the experimentally obtained spectra (in THF or MeCN) fairly well, correctly predicting absorption maxima and the approximate intensity of the molar absorptivity. However, the experimentally measured spectra for **Mes<sub>2</sub>B(C<sub>6</sub>H<sub>4</sub>)-Te-6-(C<sub>6</sub>H<sub>4</sub>)BMes<sub>2</sub>** and **O<sub>2</sub>N(C<sub>6</sub>H<sub>4</sub>)-Te-6-(C<sub>6</sub>H<sub>4</sub>)NO<sub>2</sub>** show additional high energy (low wavelength) bands that are not observed in the computations.

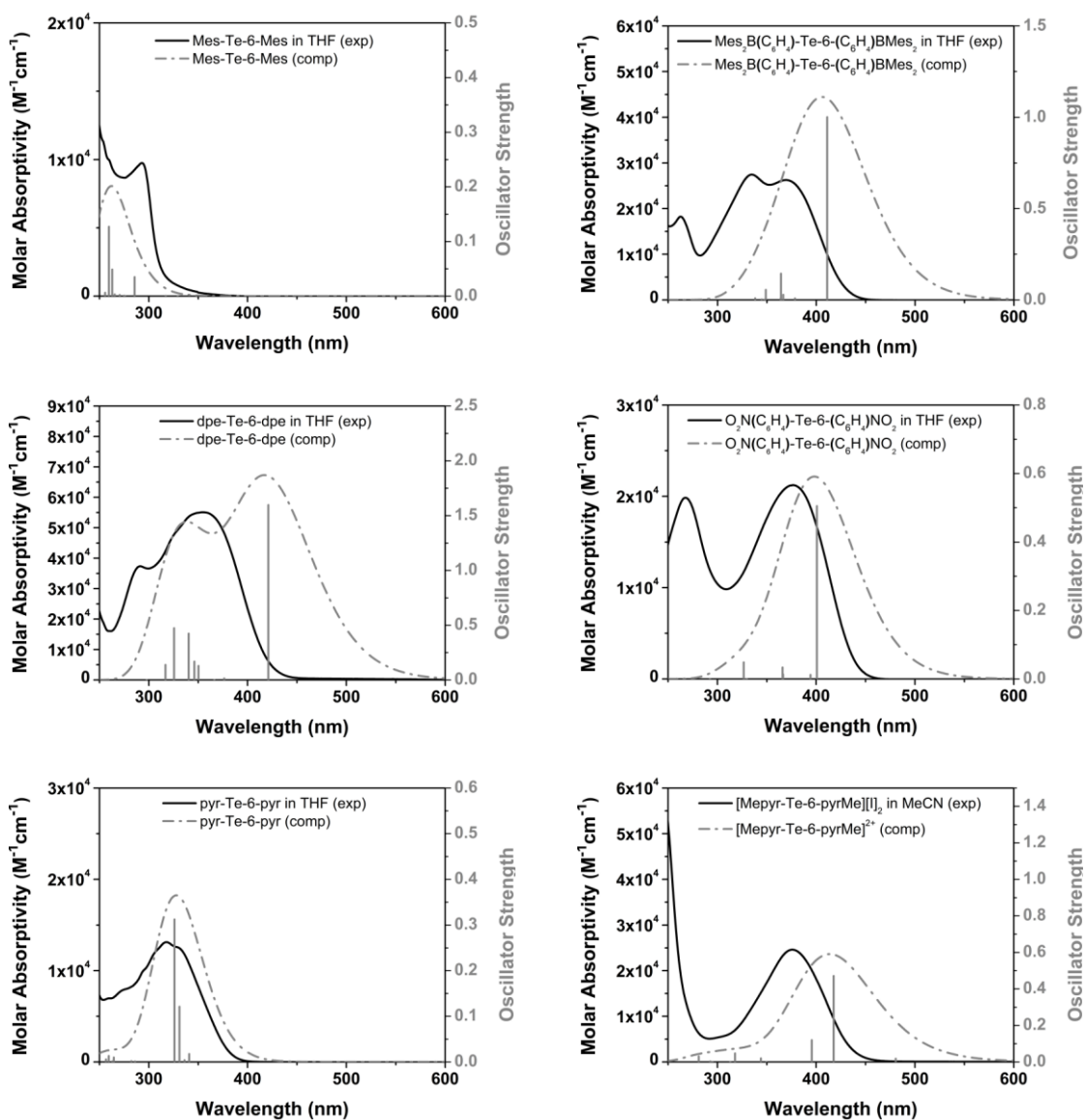


**Figure 4.10** –Experimental UV-vis spectra (black) and computed UV-vis spectra (grey) for the 2,5-bis(aryl)tellurophenes discussed in this Chapter at the B3LYP/cc-pVDZ(-PP) level of theory in the gas-phase.

#### 4.2.4 Photoluminescence of Mes<sub>2</sub>B(C<sub>6</sub>H<sub>4</sub>)-Te-6-(C<sub>6</sub>H<sub>4</sub>)BMes<sub>2</sub>

Consistent with the many luminescent compounds featuring –BMes<sub>2</sub> groups,<sup>36</sup> Mes<sub>2</sub>B(C<sub>6</sub>H<sub>4</sub>)-Te-6-(C<sub>6</sub>H<sub>4</sub>)BMes<sub>2</sub> is emissive when incorporated into a rigid



poly(methylmethacrylate) (PMMA) matrix (Figure 4.11). This compound exhibits orange emission ( $\lambda_{em} = 632$  nm) assigned as phosphorescence on the basis of the long lifetime observed ( $\tau_{avg} = 5.8$   $\mu$ s); however, the absolute quantum yield associated with phosphorescence is only 0.5 %. A second emission band is observed at 473 nm, which may result from the typical blue fluorescence observed for many aryl-BMes<sub>2</sub> compounds.<sup>43,44</sup> Of note, both of the emission peaks observed for Mes<sub>2</sub>B(C<sub>6</sub>H<sub>4</sub>)-Te-6-(C<sub>6</sub>H<sub>4</sub>)BMes<sub>2</sub> ( $\lambda_{em} = 473$  and 632 nm) do not match the emission observed for a pure sample of PMMA ( $\lambda_{em} = 415$  nm), however the small shoulder at *ca.* 415 nm does correspond to PMMA emission.

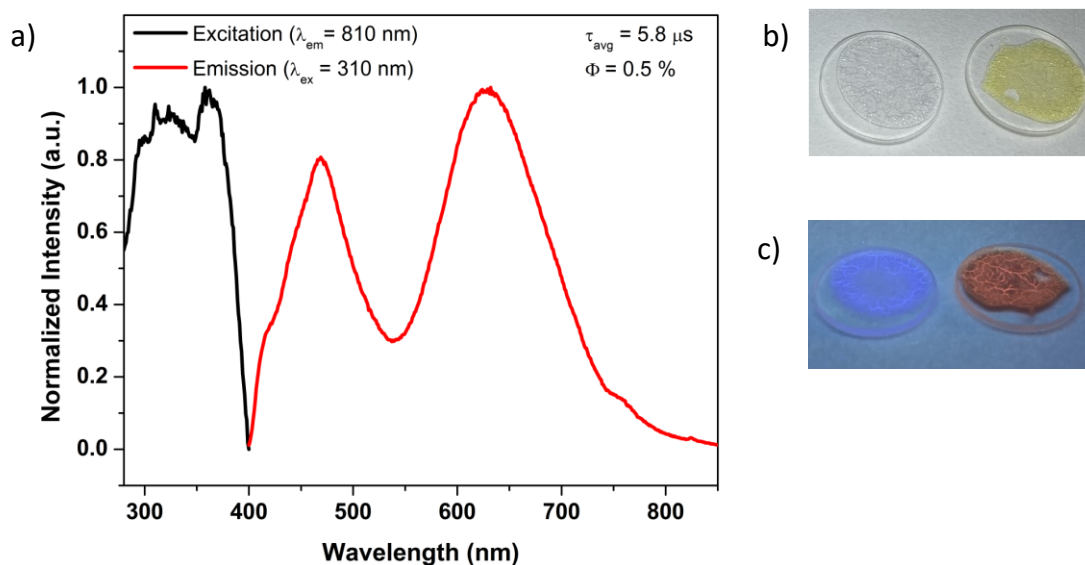


**Figure 4.11** – a) Excitation (black) and emission (red) spectra of Mes<sub>2</sub>B(C<sub>6</sub>H<sub>4</sub>)-Te-6-(C<sub>6</sub>H<sub>4</sub>)BMes<sub>2</sub>; b) images of films containing 100 % PMMA (*left*) and 1 wt% of Mes<sub>2</sub>B(C<sub>6</sub>H<sub>4</sub>)-Te-6-(C<sub>6</sub>H<sub>4</sub>)BMes<sub>2</sub> in PMMA (*right*); c) images of films containing 100 % PMMA (*left*) and 1 wt% of Mes<sub>2</sub>B(C<sub>6</sub>H<sub>4</sub>)-Te-6-(C<sub>6</sub>H<sub>4</sub>)BMes<sub>2</sub> in PMMA (*right*) irradiated with a hand-held UV lamp (254 nm).

TD-DFT computations predict one dominant transition (HOMO  $\rightarrow$  LUMO) for the excitation of **Mes<sub>2</sub>B(C<sub>6</sub>H<sub>4</sub>)-Te-6-(C<sub>6</sub>H<sub>4</sub>)BMes<sub>2</sub>**. This transition occurs from S<sub>0</sub> to S<sub>1</sub> with an oscillator strength of  $f = 1.009$  that is an order of magnitude higher than the oscillator strengths for other computed transitions in **Mes<sub>2</sub>B(C<sub>6</sub>H<sub>4</sub>)-Te-6-(C<sub>6</sub>H<sub>4</sub>)BMes<sub>2</sub>** (Figure 4.12). Although excitation to S<sub>2</sub> is associated with a significantly lower oscillator strength ( $f = 0.0083$ ) the molecular orbitals involved in this transition contain significant orbital contributions from the Te atom, unlike the excitation to S<sub>1</sub>. Furthermore, there are many pairs of energetically similar singlet and triplet excited states with  $\Delta E_{ST} < 0.1$  eV including S<sub>1</sub>/T<sub>5</sub>, S<sub>1</sub>/T<sub>6</sub>, S<sub>2</sub>/T<sub>8</sub> and S<sub>5</sub>/T<sub>9</sub> (Table 4.1). Therefore, there are several possible routes to phosphorescence in **Mes<sub>2</sub>B(C<sub>6</sub>H<sub>4</sub>)-Te-6-(C<sub>6</sub>H<sub>4</sub>)BMes<sub>2</sub>**. The zero-point corrected adiabatic energy ( $E_{0-0}$ ) difference between the optimized S<sub>0</sub> and T<sub>1</sub> geometries were used to predict a phosphorescence energy of 1.81 eV (684 nm), which is similar to the experimentally measured value (632 nm). Although the computed value of  $\lambda_{em}$  (684 nm, 1.81 eV) is more red-shifted than the experimentally measured value of 632 nm (1.96 eV), a difference of *ca.* 0.4 eV in computed energies is common with TD-DFT.<sup>11</sup> Furthermore, the relatively small difference in energy between S<sub>0</sub> and T<sub>1</sub> may be partially responsible for enhanced non-radiative decay from T<sub>1</sub>, as per the Energy Gap Law, explaining the low quantum yield ( $\Phi = 0.5$  %) measured for this sample.

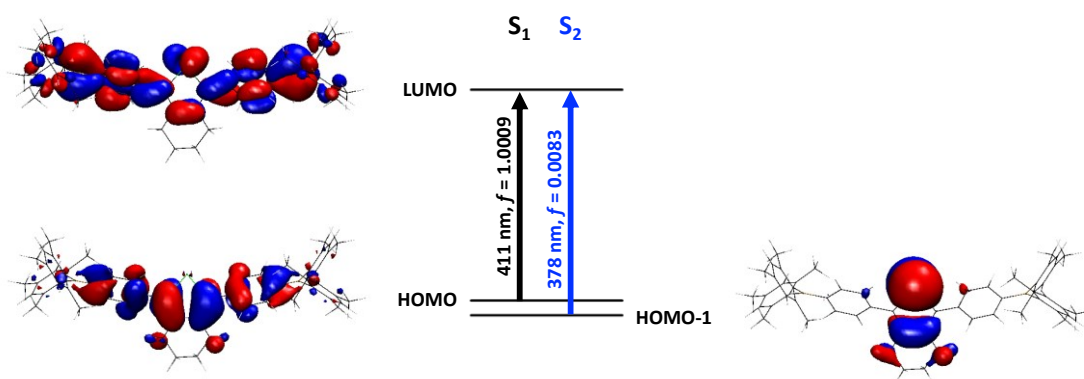


**Figure 4.12** – TD-DFT [B3LYP/cc-pVDZ(-PP)] computed transitions ( $S_0 \rightarrow S_1$ : black,  $S_0 \rightarrow S_2$ : blue) for  $\text{Mes}_2\text{B}(\text{C}_6\text{H}_4)\text{-Te-6-(C}_6\text{H}_4\text{)BMes}_2$  in the gas-phase including the excitation wavelength, oscillator strength ( $f$ ), and the associated molecular orbitals; iso-surface values of +0.02/-0.02 (red/blue).

**Table 4.1** – TD-DFT calculated excited states of **Mes<sub>2</sub>B(C<sub>6</sub>H<sub>4</sub>)-Te-6-(C<sub>6</sub>H<sub>4</sub>)BMes<sub>2</sub>** at the B3LYP-cc-pVDZ(-PP) level of theory.

| Excited State        | Energy (eV) | $\lambda$ (nm) | $f$    | Nature of Excitation (CI) <sup>a</sup>   |
|----------------------|-------------|----------------|--------|--|
| <b>T<sub>1</sub></b> | 2.2616      | 548.21         | 0.0000 | <b>HOMO</b> → <b>LUMO</b> (0.60772)  |
| <b>T<sub>2</sub></b> | 2.8207      | 439.56         | 0.0000 | <b>HOMO-1</b> → <b>LUMO</b> (0.47596)<br>HOMO → LUMO+1 (-0.37353)                  |
| <b>T<sub>3</sub></b> | 2.8608      | 433.38         | 0.0000 | <b>HOMO-1</b> → <b>LUMO</b> (0.44555)<br>HOMO → LUMO+1 (0.3945)                    |
| <b>T<sub>4</sub></b> | 3.0105      | 411.83         | 0.0000 | HOMO-2 → <b>LUMO</b> (0.46553)<br>HOMO-3 → LUMO+1 (-0.40727)                       |
| <b>T<sub>5</sub></b> | 3.0114      | 411.72         | 0.0000 | HOMO-3 → <b>LUMO</b> (0.46593)<br>HOMO-2 → LUMO+1 (-0.40894)                       |
| <b>S<sub>1</sub></b> | 3.0163      | 411.04         | 1.0009 | HOMO → <b>LUMO</b> (0.69071)   |
| <b>T<sub>6</sub></b> | 3.0729      | 403.48         | 0.0000 | HOMO-4 → LUMO+1 (0.37842)<br>HOMO-5 → <b>LUMO</b> (-0.35284)                       |
| <b>T<sub>7</sub></b> | 3.1258      | 396.65         | 0.0000 | HOMO-4 → <b>LUMO</b> (0.37911)<br>HOMO-5 → LUMO+1 (-0.34436)                       |
| <b>T<sub>8</sub></b> | 3.2626      | 380.02         | 0.0000 | HOMO → <b>LUMO+3</b> (0.39227)   |
| <b>S<sub>2</sub></b> | 3.2765      | 378.4          | 0.0083 | <b>HOMO-1</b> → <b>LUMO</b> (0.6798)   |
| <b>S<sub>3</sub></b> | 3.3821      | 366.59         | 0.0283 | HOMO → LUMO+1 (0.66937)  |
| <b>S<sub>4</sub></b> | 3.4041      | 364.23         | 0.1442 | HOMO-2 → <b>LUMO</b> (0.59218)<br>HOMO-3 → LUMO+1 (-0.36562)                       |
| <b>S<sub>5</sub></b> | 3.4057      | 364.05         | 0.0093 | HOMO-3 → <b>LUMO</b> (0.59302)<br>HOMO-2 → LUMO+1 (-0.36792)                       |
| <b>T<sub>9</sub></b> | 3.4065      | 363.96         | 0.0000 | <b>HOMO-1</b> → <b>LUMO+2</b> (0.53018)<br><b>HOMO-1</b> → <b>LUMO+3</b> (0.41366) |

a) Only coefficients (CI) > |0.31| are shown (corresponds to a contribution of 19 % to the transition).

b) Molecular orbitals involving Te are identified in bold font.

#### 4.2.5 Photoluminescence of $\text{O}_2\text{N}(\text{C}_6\text{H}_4)\text{-Te-6-(C}_6\text{H}_4\text{)NO}_2$

The tellurophene  $\text{O}_2\text{N}(\text{C}_6\text{H}_4)\text{-Te-6-(C}_6\text{H}_4\text{)NO}_2$  substituted with strongly electron-withdrawing *p*-nitrophenyl groups was also emissive when incorporated into a rigid PMMA matrix (Figure 4.13). This tellurophene exhibited the most red-shifted emission of all the tellurophenes in this Chapter with a  $\lambda_{\text{em}}$  of 695 nm. Similar to  $\text{Mes}_2\text{B}(\text{C}_6\text{H}_4)\text{-Te-6-(C}_6\text{H}_4\text{)BMes}$ , this emission is characterized as phosphorescence on the basis of the long lifetime ( $\tau_{\text{avg}} = 3.57 \mu\text{s}$ ). No emission from PMMA ( $\lambda_{\text{em}} = 415 \text{ nm}$ ) was observed in this case. A small peak in the emission spectrum of  $\text{O}_2\text{N}(\text{C}_6\text{H}_4)\text{-Te-6-(C}_6\text{H}_4\text{)NO}_2$  at *ca.* 500 nm may be due to weak fluorescence. Known tellurophenes containing a *p*-nitrophenyl group include the unsymmetrical “push-pull” diaryltellurophenes **10** and **11** (Figure 4.14) with *p*-tolyl and *p*-anisyl substituents, respectively.<sup>20</sup> No phosphorescence was reported for tellurophenes **10** or **11**, although they are fluorescent in  $\text{CH}_2\text{Cl}_2$  solutions with  $\lambda_{\text{em}}$  of 593 ( $\Phi = 2.1 \%$ ) and 643 ( $\Phi = 1.8 \%$ ), respectively.

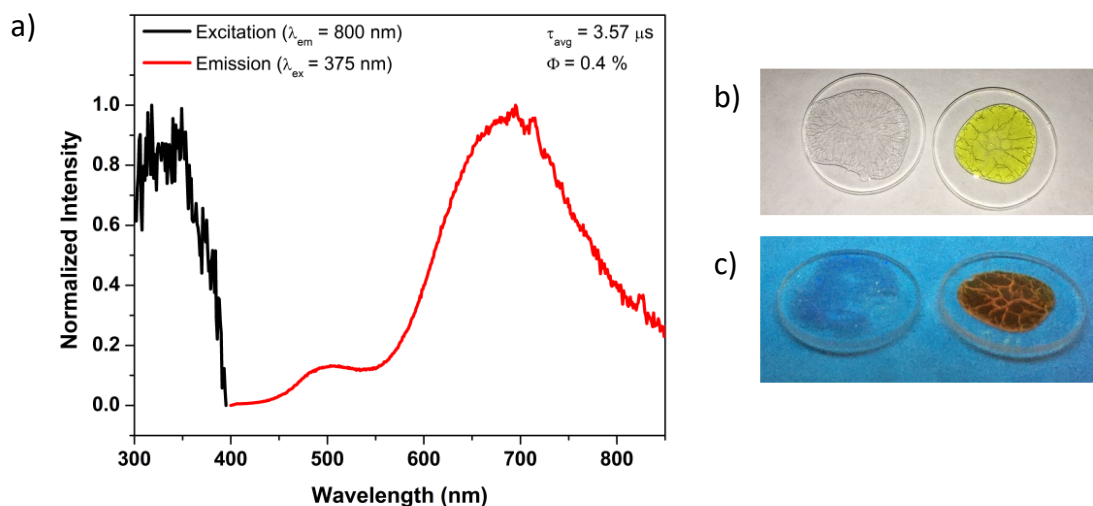


**Figure 4.13** – a) Excitation (black) and emission (red) spectra of **O<sub>2</sub>N(C<sub>6</sub>H<sub>4</sub>)-Te-6-(C<sub>6</sub>H<sub>4</sub>)NO<sub>2</sub>**; b) images of films containing 100 % PMMA (*left*) and 1 wt% of **O<sub>2</sub>N(C<sub>6</sub>H<sub>4</sub>)-Te-6-(C<sub>6</sub>H<sub>4</sub>)NO<sub>2</sub>** in PMMA (*right*); c) images of films containing 100 % PMMA (*left*) and 1 wt% of **O<sub>2</sub>N(C<sub>6</sub>H<sub>4</sub>)-Te-6-(C<sub>6</sub>H<sub>4</sub>)NO<sub>2</sub>** in PMMA (*right*) irradiated with a hand-held UV lamp (365 nm).

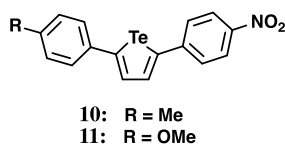


**Figure 4.14** – The structure asymmetric tellurophenes **10** and **11** featuring a *p*-nitrophenyl group.

TD-DFT computations for **O<sub>2</sub>N(C<sub>6</sub>H<sub>4</sub>)-Te-6-(C<sub>6</sub>H<sub>4</sub>)NO<sub>2</sub>** predict the most intense UV-vis absorption at 401 nm, corresponding to a HOMO→LUMO transition, to give the singlet excited state S<sub>1</sub> (Figure 4.15 and Table 4.2). This transition is π/π\* in nature but it does not contain any substantial orbital contribution from Te atom in the HOMO (Figure 4.15). The transitions from S<sub>0</sub> to S<sub>n</sub> (n = 2, 3, 8) involve modest oscillator strengths of 0.0120, 0.0131, and 0.0487, respectively. Of these, only the

excitation to  $S_2$  involves substantial Te-character in both the ground and excited states. Furthermore, the only pairs of  $S_n/T_n$  with  $\Delta E_{ST} < 0.1$  eV are  $S_2/T_6$  and  $S_3/T_{10}$  (Table 4.2). Therefore, there are two likely mechanisms to give the phosphorescence observed experimentally: absorption of light to reach excited state  $S_2$  or  $S_3$ , followed by ISC to  $T_6$  or  $T_{10}$ , radiative decay to  $T_1$ , and finally radiative decay (emission) from  $T_1$  to the ground state. The  $E_{0-0}$  between the optimized  $S_0$  and  $T_1$  geometries predicts phosphorescence at 675 nm (1.84 eV), which is similar to the experimentally measured value of 695 nm. Similar to **Mes<sub>2</sub>B(C<sub>6</sub>H<sub>4</sub>)-Te-6-(C<sub>6</sub>H<sub>4</sub>)BMes<sub>2</sub>**, the small difference in energy between  $S_0$  and  $T_1$  could partially explain the low quantum yield ( $\Phi = 0.4$  %) recorded for this tellurophene.

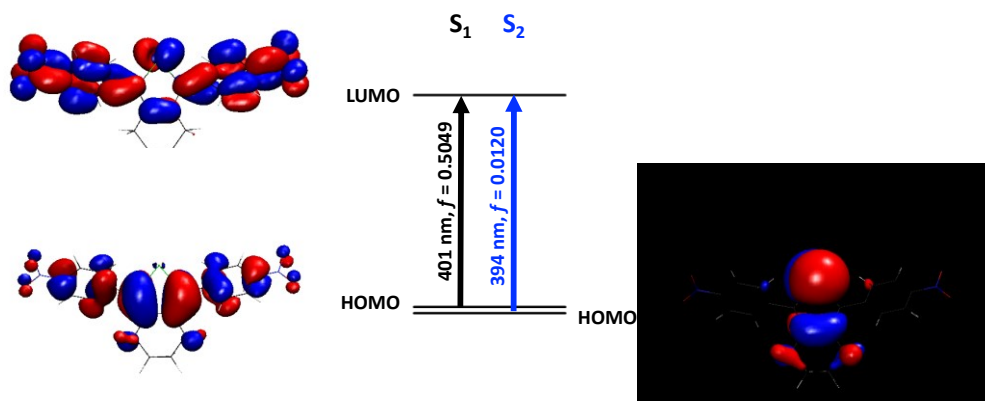


**Figure 4.15** – TD-DFT [B3LYP/cc-pVDZ(-PP)] computed transitions ( $S_0 \rightarrow S_1$ : black,  $S_0 \rightarrow S_2$ : blue) for **O<sub>2</sub>N(C<sub>6</sub>H<sub>4</sub>)-Te-6-(C<sub>6</sub>H<sub>4</sub>)NO<sub>2</sub>** in the gas-phase including the excitation wavelength, oscillator strength ( $f$ ), and the associated molecular orbitals; iso-surface values of +0.02/-0.02 (red/blue).

**Table 4.2** – TD-DFT calculated excited states of **O<sub>2</sub>N(C<sub>6</sub>H<sub>4</sub>)-Te-6-(C<sub>6</sub>H<sub>4</sub>)NO<sub>2</sub>** at the B3LYP-ccpVDZ(-PP) level of theory.

| Excited State         | Energy (eV) | $\lambda$ (nm) | $f$    | Nature of Excitation (CI) <sup>a</sup>  |
|-----------------------|-------------|----------------|--------|---|
| <b>T<sub>1</sub></b>  | 2.2791      | 544.01         | 0.0000 | <b>HOMO</b> → <b>LUMO</b> (0.61375)   |
| <b>T<sub>2</sub></b>  | 2.7391      | 452.64         | 0.0000 | <b>HOMO-1</b> → <b>LUMO</b> (0.65808)   |
| <b>T<sub>3</sub></b>  | 2.8136      | 440.65         | 0.0000 | <b>HOMO-10</b> → <b>LUMO</b> (0.42301)<br><b>HOMO-11</b> → <b>LUMO+1</b> (-0.40267) |
| <b>T<sub>4</sub></b>  | 2.8138      | 440.63         | 0.0000 | <b>HOMO-11</b> → <b>LUMO</b> (0.42303)<br><b>HOMO-10</b> → <b>LUMO+1</b> (-0.40201) |
| <b>T<sub>5</sub></b>  | 2.8678      | 432.33         | 0.0000 | <b>HOMO</b> → <b>LUMO+1</b> (0.59985)   |
| <b>S<sub>1</sub></b>  | 3.0934      | 400.81         | 0.5049 | <b>HOMO</b> → <b>LUMO</b> (0.69492)   |
| <b>S<sub>2</sub></b>  | 3.1445      | 394.29         | 0.0120 | <b>HOMO-1</b> → <b>LUMO</b> (0.69510)   |
| <b>T<sub>6</sub></b>  | 3.2088      | 386.39         | 0.0000 | <b>HOMO-5</b> → <b>LUMO+1</b> (0.35204)<br><b>HOMO-6</b> → <b>LUMO</b> (-0.32386)   |
| <b>T<sub>7</sub></b>  | 3.2196      | 385.09         | 0.0000 | <b>HOMO-6</b> → <b>LUMO+1</b> (0.44157)<br><b>HOMO-5</b> → <b>LUMO</b> (-0.43848)   |
| <b>T<sub>8</sub></b>  | 3.2349      | 383.27         | 0.0000 | <b>HOMO-1</b> → <b>LUMO+1</b> (0.38225)   |
| <b>T<sub>9</sub></b>  | 3.3677      | 368.16         | 0.0000 | <b>HOMO-1</b> → <b>LUMO+2</b> (0.62020)   |
| <b>T<sub>10</sub></b> | 3.3814      | 366.67         | 0.0000 | <b>HOMO-1</b> → <b>LUMO+1</b> (0.49458)<br><b>HOMO</b> → <b>LUMO+3</b> (-0.34285)   |
| <b>S<sub>3</sub></b>  | 3.3824      | 366.55         | 0.0131 | <b>HOMO</b> → <b>LUMO+1</b> (0.69397)   |
| <b>S<sub>4</sub></b>  | 3.3879      | 365.96         | 0.0335 | <b>HOMO-1</b> → <b>LUMO+1</b> (0.70295)   |

a) Only coefficients (CI) > |0.31| are shown (corresponds to a contribution of 19 % to the transition).

b) Molecular orbitals involving Te are identified in bold font.

#### 4.2.6 Photoluminescence of pyr-Te-6-pyr

A PMMA film containing 1 wt% of **pyr-Te-6-pyr** is also emissive, with an emission maximum centred at 614 nm (Figure 4.16). The emission is associated with an average lifetime of 7.7  $\mu$ s, consistent with phosphorescence, and a low absolute



quantum yield of 0.3 %. The peak at *ca.* 415 nm corresponds to the emission of pure PMMA.

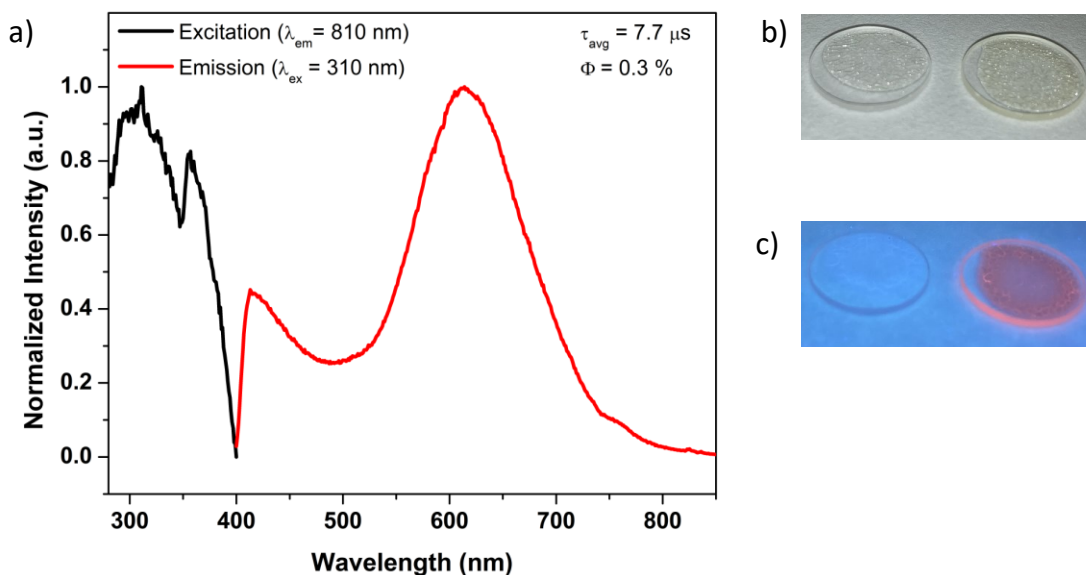


**Figure 4.16** – a) Excitation (black) and emission (red) spectra of **pyr-Te-6-pyr**; b) images of films containing 100 % PMMA (*left*) and 1 wt% of **pyr-Te-6-pyr** in PMMA (*right*); c) images of films containing 100 % PMMA (*left*) and 1 wt% of **pyr-Te-6-pyr** in PMMA (*right*) irradiated with a hand-held UV lamp (365 nm).

TD-DFT computations for **pyr-Te-6-pyr** suggest that all of the molecular orbitals involved in the main computed transitions (at 326 and 331 nm) contain significant contributions from the Te centre (Figure 4.17). The two most intense transitions computed are the  $S_0 \rightarrow S_3$  ( $f = 0.1212$ ) and  $S_0 \rightarrow S_4$  ( $f = 0.3122$ ) transitions. Due to the small energy difference between the HOMO and the HOMO-1, many transitions contain multiple contributions (*e.g.*,  $S_0 \rightarrow S_3$  contains contributions from HOMO-1  $\rightarrow$  LUMO, HOMO  $\rightarrow$  LUMO, and HOMO  $\rightarrow$  LUMO+1 as shown in Figure 4.17). There

are also two sets of  $S_n/T_n$  ( $S_3/T_5$  and  $T_6/S_4$ ) with  $\Delta E_{ST} < 0.1$  eV (Table 4.3). Therefore, a possible mechanism for phosphorescence is the absorption of light to reach excited state to  $S_3$  or  $S_4$ , followed by ISC to  $T_5$  or  $T_6$ , non-radiative decay to  $T_1$ , and finally radiative decay (emission) from  $T_1$  to  $S_0$ . The calculated  $E_{0-0}$  difference between the optimized  $S_0$  and  $T_1$  geometries predicts a phosphorescence energy of 1.97 eV (629 nm), which closely matches the experimentally measured value of 614 nm (1.91 eV).

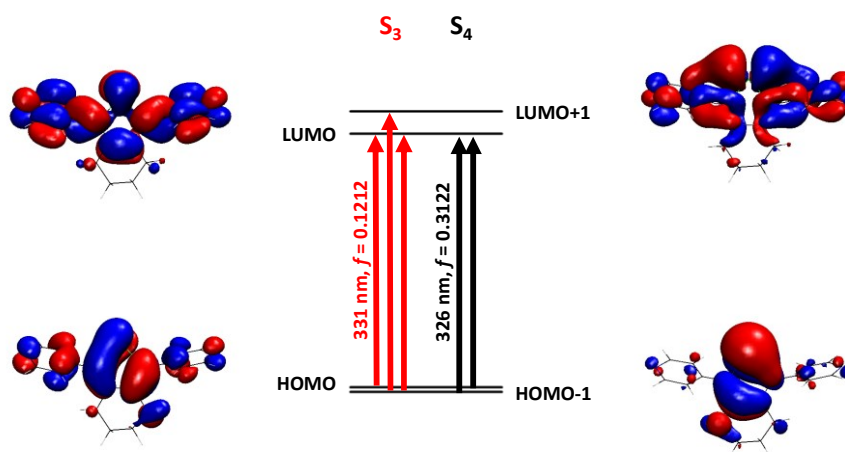


**Figure 4.17** – TD-DFT [B3LYP/cc-pVDZ(-PP)] computed main transitions for **pyr-Te-6-pyr** in the gas-phase including the excitation wavelengths and oscillator strengths ( $f$ ) for the most intense transitions ( $S_0 \rightarrow S_3$ : red;  $S_0 \rightarrow S_4$ : black) along with the associated molecular orbitals; iso-surface values of +0.02/-0.02 (red/blue).

**Table 4.3** – TD-DFT calculated excited states of **pyr-Te-6-pyr** at the B3LYP-ccpVDZ(-PP) level of theory.

| Excited State        | Energy (eV) | $\lambda$ (nm) | $f$    | Nature of Excitation (CI) <sup>a</sup>   |
|----------------------|-------------|----------------|--------|--|
| <b>T<sub>1</sub></b> | 2.4890      | 498.13         | 0.0000 | <b>HOMO</b> → <b>LUMO</b> (0.62097)  |
| <b>T<sub>2</sub></b> | 3.0691      | 403.98         | 0.0000 | <b>HOMO-1</b> → <b>LUMO</b> (0.64023)  |
| <b>T<sub>3</sub></b> | 3.2448      | 382.10         | 0.0000 | <b>HOMO-1</b> → <b>LUMO+1</b> (0.57155)<br><b>HOMO</b> → <b>LUMO+1</b> (-0.36499)  |
| <b>T<sub>4</sub></b> | 3.3659      | 368.36         | 0.0000 | <b>HOMO</b> → <b>LUMO+1</b> (0.54728)<br><b>HOMO-1</b> → <b>LUMO+1</b> (0.35714)   |
| <b>S<sub>1</sub></b> | 3.6371      | 340.88         | 0.0174 | <b>HOMO</b> → <b>LUMO+1</b> (0.50110)<br><b>HOMO-1</b> → <b>LUMO+1</b> (-0.41700)  |
| <b>S<sub>2</sub></b> | 3.6882      | 336.16         | 0.0039 | <b>HOMO</b> → <b>LUMO+1</b> (0.45274)<br><b>HOMO-1</b> → <b>LUMO+1</b> (0.41141)   |
| <b>S<sub>3</sub></b> | 3.7453      | 331.04         | 0.1212 | <b>HOMO</b> → <b>LUMO</b> (0.45958)<br><b>HOMO-1</b> → <b>LUMO+1</b> (0.37185)<br><b>HOMO-1</b> → <b>LUMO</b> (-0.35854) |
| <b>T<sub>5</sub></b> | 3.7791      | 328.08         | 0.0000 | -  |
| <b>T<sub>6</sub></b> | 3.7972      | 326.52         | 0.0000 | <b>HOMO-2</b> → <b>LUMO</b> (0.53372)  |
| <b>S<sub>4</sub></b> | 3.8041      | 325.92         | 0.3122 | <b>HOMO-1</b> → <b>LUMO</b> (0.50963)<br><b>HOMO</b> → <b>LUMO</b> (0.44009)   |

a) Only coefficients (CI) > |0.31| are shown (corresponds to a contribution of 19 % to the transition).

b) Molecular orbitals involving Te are identified in bold font.

#### 4.2.7 Photoluminescence of Mes-Te-6-Mes

Surprisingly, only very faint emission was detected from **Mes-Te-6-Mes** when incorporated into a PMMA film (Figure 4.18). The corresponding emission spectra affords a  $\lambda_{em}$  at 561 nm, but the intensity of luminescence was too faint to collect reliable lifetime or quantum yield data. Furthermore, the emission of PMMA ( $\lambda_{em} = 415$

nm) likely dominates the excitation spectrum for the film containing both **Mes-Te-6-Mes** (1 wt%) and PMMA (99 wt%).

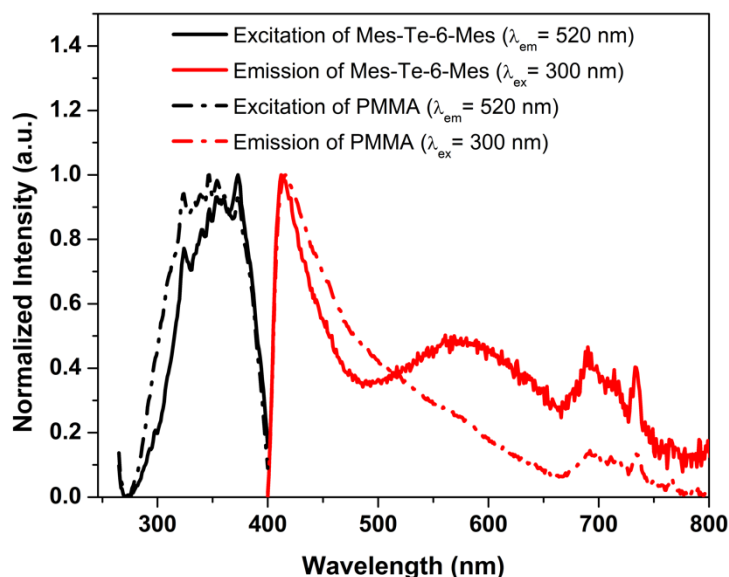


**Figure 4.18** – Excitation spectra (black) and emission spectra (red) for a film containing 1 wt% of **Mes-Te-6-Mes** in PMMA shown as a solid lines and a film of pure PMMA shown as dash-dot lines.

Computational studies on **Mes-Te-6-Mes** predict that the three most intense UV-vis transitions are  $S_0 \rightarrow S_9$  ( $f = 0.1270$ ),  $S_0 \rightarrow S_8$  ( $f = 0.0488$ ) and  $S_0 \rightarrow S_3$  ( $f = 0.0348$ ) in the 260–285 nm spectral region; each transition contains significant orbital contributions from the Te atom (Figure 4.19). Furthermore, there are two energetically accessible triplet states for ISC to occur in **Mes-Te-6-Mes** (Table 4.4), with  $T_8$  and  $T_9$  excited triplet states each within  $< 0.1$  eV from  $S_3$ . Therefore, there are many potential routes for phosphorescence to occur including the absorption of light to reach the  $S_3$  excited state, followed by intersystem crossing to  $T_8$  or  $T_9$  to access the triplet manifold.

A similar outcome could result if absorption of light to a higher excited state such as  $S_8$  or  $S_9$  was followed by non-radiative decay to  $S_3$ . Finally, non-radiative decay from  $T_n$  ( $n = 8$  or  $9$ ) to  $T_1$ , and then radiative decay from  $T_1$  to the ground state, is a viable mechanism for phosphorescence to occur. The zero-point corrected adiabatic energy ( $E_{0.0}$ ) at the optimized  $S_0$  and  $T_1$  geometries were used to predict a phosphorescence energy of 2.42 eV (513 nm) for **Mes-Te-6-Mes**. This computed value is similar to the experimental value,  $\lambda_{em} = 561$  nm. The faint emission observed for **Mes-Te-6-Mes** may be due in part to the large  $\Delta E$  between  $T_6$  and  $T_7$  (0.62 eV), which could promote reverse ISC (*e.g.*, from  $T_7$  to  $S_3$ ) giving rise to either non-radiative decay or fluorescence from  $S_1$ .

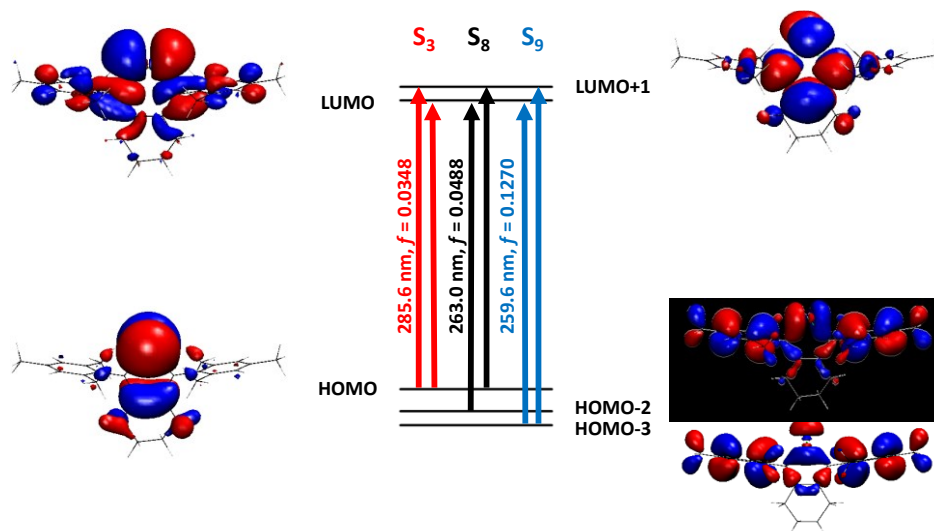


**Figure 4.19** – TD-DFT [B3LYP/cc-pVDZ(-PP)] computed main transitions for **Mes-Te-6-Mes** in the gas-phase including the excitation wavelengths and oscillator strengths ( $f$ ) for the most intense transitions ( $S_0 \rightarrow S_3$ : red;  $S_0 \rightarrow S_8$ : black;  $S_0 \rightarrow S_9$ : blue) along with the associated molecular orbitals; iso-surface values of +0.02/-0.02 (red/blue).

**Table 4.4** – TD-DFT calculated excited states of **Mes-Te-6-Mes** at the B3LYP-cc-pVDZ(-PP) level of theory.

| Excited State          | Energy (eV) | $\lambda$ (nm) | $f$    | Nature of Excitation (CI) <sup>a</sup>  |
|------------------------|-------------|----------------|--------|---|
| <b>T</b> <sub>1</sub>  | 2.8123      | 440.86         | 0.0000 | <b>HOMO-1</b> → <b>LUMO+1</b> (0.68885)   |
| <b>T</b> <sub>2</sub>  | 3.3228      | 373.13         | 0.0000 | <b>HOMO-2</b> → <b>LUMO+2</b> (0.45628)   |
| <b>T</b> <sub>3</sub>  | 3.5019      | 354.05         | 0.0000 | <b>HOMO-3</b> → <b>LUMO+2</b> (0.39481)   |
| <b>T</b> <sub>4</sub>  | 3.5058      | 353.65         | 0.0000 | <b>HOMO-2</b> → <b>LUMO</b> (-0.33660)  |
| <b>T</b> <sub>5</sub>  | 3.5710      | 347.20         | 0.0000 | <b>HOMO</b> → <b>LUMO+1</b> (0.68961)   |
| <b>T</b> <sub>6</sub>  | 3.6525      | 339.45         | 0.0000 | <b>HOMO-1</b> → <b>LUMO</b> (0.68018)   |
| <b>S</b> <sub>1</sub>  | 3.7656      | 329.25         | 0.0001 | <b>HOMO</b> → <b>LUMO</b> (0.69688)   |
| <b>S</b> <sub>2</sub>  | 3.9096      | 317.13         | 0.0006 | <b>HOMO-1</b> → <b>LUMO</b> (0.69834)   |
| <b>T</b> <sub>7</sub>  | 4.2751      | 290.01         | 0.0000 | <b>HOMO-2</b> → <b>LUMO</b> (0.52945)   |
| <b>T</b> <sub>8</sub>  | 4.3107      | 287.62         | 0.0000 | <b>HOMO</b> → <b>LUMO+2</b> (0.55702)   |
| <b>S</b> <sub>3</sub>  | 4.3412      | 285.60         | 0.0348 | <b>HOMO</b> → <b>LUMO+1</b> (0.54975)<br><b>HOMO-2</b> → <b>LUMO</b> (-0.42027)   |
| <b>T</b> <sub>9</sub>  | 4.3679      | 283.86         | 0.0000 | <b>HOMO-4</b> → <b>LUMO+2</b> (0.41276)<br><b>HOMO-5</b> → <b>LUMO</b> (-0.32301) |
| <b>T</b> <sub>10</sub> | 4.3815      | 282.97         | 0.0000 | <b>HOMO-4</b> → <b>LUMO+3</b> (0.32594)   |
| <b>S</b> <sub>4</sub>  | 4.4958      | 275.78         | 0.0002 | <b>HOMO-1</b> → <b>LUMO+2</b> (0.69996)   |
| <b>S</b> <sub>5</sub>  | 4.5084      | 275.00         | 0.0009 | <b>HOMO</b> → <b>LUMO+2</b> (0.70367)   |
| <b>S</b> <sub>6</sub>  | 4.5829      | 270.53         | 0.0021 | <b>HOMO-2</b> → <b>LUMO+1</b> (0.69723)   |
| <b>S</b> <sub>7</sub>  | 4.6699      | 265.50         | 0.0032 | <b>HOMO-1</b> → <b>LUMO+1</b> (0.51384)<br><b>HOMO-3</b> → <b>LUMO</b> (-0.45326) |
| <b>S</b> <sub>8</sub>  | 4.7145      | 262.99         | 0.0488 | <b>HOMO-2</b> → <b>LUMO</b> (0.55319)<br><b>HOMO</b> → <b>LUMO+1</b> (0.40272)    |
| <b>S</b> <sub>9</sub>  | 4.7758      | 259.61         | 0.1270 | <b>HOMO-3</b> → <b>LUMO</b> (0.44762)<br><b>HOMO-3</b> → <b>LUMO+1</b> (0.39624)  |
| <b>S</b> <sub>10</sub> | 4.8472      | 255.79         | 0.0062 | <b>HOMO-4</b> → <b>LUMO</b> (0.59627)   |

a) Only coefficients (CI) > |0.31| are shown (corresponds to a contribution of 19 % to the transition).

b) Molecular orbitals involving Te are identified in bold font.

#### 4.2.8 Photoluminescence of [Mepyr-Te-6-pyrMe][I]<sub>2</sub>

Although viologens are not usually known for their emissive properties, some examples of fluorescence have been reported.<sup>28,29</sup> Furthermore, He and coworkers reported weak fluorescence from chalcogen-bridged viologens ( $\Phi < 1$ ,  $\lambda_{em}$  were not reported).<sup>30</sup> Scherman and coworkers have recently reported the detection of solid state phosphorescence at 77 K for cyclic macrocycles containing two extended viologen units (**1**, **3**, or **4**) linked together *via* two *p*-xylene units.<sup>29</sup> Thus, the ability of [Mepyr-Te-6-pyrMe]<sup>2+</sup> to exhibit phosphorescence was computationally explored. [Mepyr-Te-6-pyrMe]<sup>2+</sup> contains two main UV-vis transitions ( $S_0 \rightarrow S_2$  and  $S_0 \rightarrow S_3$ , Figure 4.20). Of these two major transitions, only the  $S_0 \rightarrow S_3$  excitation (HOMO  $\rightarrow$  LUMO+1) involves significant contributions from the Te centre, and predominantly in the HOMO (lone pair at Te). Furthermore,  $S_2/T_4$  and  $S_3/T_5$  both have small energy differences less than 0.1 eV (Table 4.5). Therefore, absorption of light to reach excited state  $S_3$ , followed by ISC to  $T_5$  (or non-radiative decay to  $S_2$  followed by ISC to  $T_4$ ) are feasible routes to access the triplet manifold. Finally, non-radiative decay to  $T_1$  according to Kasha's rule, and then radiative decay from  $T_1$  to  $S_0$  complete the possible mechanism for phosphorescence. The calculated difference between  $E_{0,0}$  at the optimized  $S_0$  and  $T_1$  geometries yields a phosphorescence energy of 2.08 eV (597 nm). Therefore, a slight hypsochromic shift in  $\lambda_{em}$  of 32 nm is predicted for [Mepyr-Te-6-pyrMe]<sup>2+</sup> relative to pyr-Te-6-pyr. However, no phosphorescence was detected for this complex even when 1 wt% of [Mepyr-Te-6-pyrMe][I]<sub>2</sub> was incorporated into a rigid PMMA matrix.

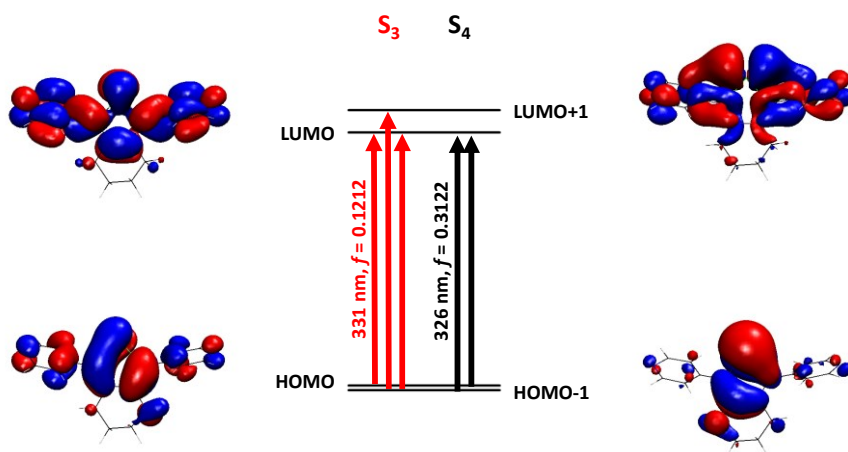


**Figure 4.20** – TD-DFT [B3LYP/cc-pVDZ(-PP)] computed main transitions for [Mepyr-Te-6-pyrMe][I]<sub>2</sub> in the gas-phase including the excitation wavelengths and oscillator strengths ( $f$ ) for the most intense transitions (S<sub>0</sub>→S<sub>3</sub>: red; S<sub>0</sub>→S<sub>4</sub>: black) along with the associated molecular orbitals; iso-surface values of +0.02/-0.02 (red/blue).



**Table 4.5** – TD-DFT calculated excited states of **[Mepyr-Te-6-pyrMe]<sup>2+</sup>** at the B3LYP-ccpVDZ(-PP) level of theory.

| Excited State        | Energy (eV) | $\lambda$ (nm) | $f$    | Nature of Excitation (CI) <sup>a</sup>   |
|----------------------|-------------|----------------|--------|--|
| <b>T<sub>1</sub></b> | 2.0620      | 601.28         | 0.0000 | <b>HOMO</b> → <b>LUMO</b> (0.69414)  |
| <b>T<sub>2</sub></b> | 2.0663      | 600.04         | 0.0000 | HOMO-1 → <b>LUMO</b> (0.67593)   |
| <b>S<sub>1</sub></b> | 2.5805      | 480.47         | 0.0184 | <b>HOMO</b> → <b>LUMO</b> (0.70114)  |
| <b>T<sub>3</sub></b> | 2.9515      | 420.07         | 0.0000 | <b>HOMO</b> → <b>LUMO+1</b> (0.69626)  |
| <b>T<sub>4</sub></b> | 2.9657      | 418.06         | 0.0000 | HOMO-1 → <b>LUMO+1</b> (0.66804)   |
| <b>S<sub>2</sub></b> | 2.9681      | 417.73         | 0.4713 | HOMO-1 → <b>LUMO</b> (0.67133)   |
| <b>S<sub>3</sub></b> | 3.1345      | 395.55         | 0.1198 | <b>HOMO</b> → <b>LUMO+1</b> (0.67766)  |
| <b>T<sub>5</sub></b> | 3.2052      | 386.82         | 0.0000 | <b>HOMO</b> → <b>LUMO+2</b> (0.57780)<br><b>HOMO</b> → <b>LUMO+4</b> (0.38902) |
| <b>S<sub>4</sub></b> | 3.5454      | 349.71         | 0.0007 | <b>HOMO</b> → <b>LUMO+2</b> (0.58238)<br>HOMO-1 → <b>LUMO+1</b> (0.33789)      |
| <b>T<sub>6</sub></b> | 3.5580      | 348.47         | 0.0000 | HOMO-1 → <b>LUMO+2</b> (0.63022)   |

a) Only coefficients (CI) > |0.31| are shown (corresponds to a contribution of 19 % to the transition).

b) Molecular orbitals involving Te are identified in bold font.

#### 4.2.9 Photoluminescence of **dpe-Te-6-dpe**

No emission was detected from samples of **dpe-Te-6-dpe**, however it should be noted that analytically pure material was not obtained for this compound. However, the viability of phosphorescence was still computationally explored. The three most intense transitions for **dpe-Te-6-dpe** are shown in Figure 4.21, with the most intense transition being excitation to **S<sub>1</sub>** (**HOMO** → **LUMO**,  $\lambda = 421$  nm,  $f = 1.5970$ ). This intense transition is also experimentally observed, with **dpe-Te-6-dpe** exhibiting the highest molar absorptivity of all of the neutral 2,5-bis(aryl)tellurophenes in this study ( $\lambda_{\text{abs}} =$

355 nm,  $\epsilon = 5.51 \times 10^4 \text{ M}^{-1}\text{cm}^{-1}$ ). However, many excited states with modest oscillator strengths of  $0.1277 \geq f \geq 0.4727$  also exist, including transitions to the S<sub>4</sub>–S<sub>7</sub> and S<sub>9</sub> excited states (Table 4.6). However, of these excited states only the S<sub>5</sub> state ( $f = 0.1680$ ) contains significant contribution from Te to the molecular orbitals involved. There are several pairs of singlet-triplet states with  $\Delta E_{\text{ST}} < 0.1 \text{ eV}$  for ISC to occur including: S<sub>1</sub>/T<sub>4</sub>, S<sub>2</sub>/T<sub>6</sub>, S<sub>2</sub>/T<sub>7</sub>, S<sub>3</sub>/T<sub>7</sub>, *etc.* (Table 4.6). Therefore, a possible mechanism for phosphorescence includes the absorption of light to reach S<sub>5</sub>, ISC to T<sub>n</sub> (*e.g.* n = 9 or 10), non-radiative decay (internal conversion) to the T<sub>1</sub> excited state, and finally radiative decay (emission) from T<sub>1</sub> to S<sub>0</sub>. Due to the large number of S<sub>n</sub>/T<sub>n</sub> pairs with  $\Delta E_{\text{ST}} < 0.1 \text{ eV}$ , it is also possible for ISC to occur after non-radiative decay to S<sub>2</sub> or S<sub>1</sub>, leading to phosphorescence. The E<sub>0-0</sub> difference between the optimized S<sub>0</sub> and T<sub>1</sub> geometries predicts phosphorescence to occur at 734 nm (1.69 eV). However, as mentioned above, the three most intense UV-vis transitions predicted in **dpe-Te-6-dpe** do not involve Te-based orbitals and this may contribute to the reduced intersystem crossing, explaining the lack of phosphorescence from this compound.

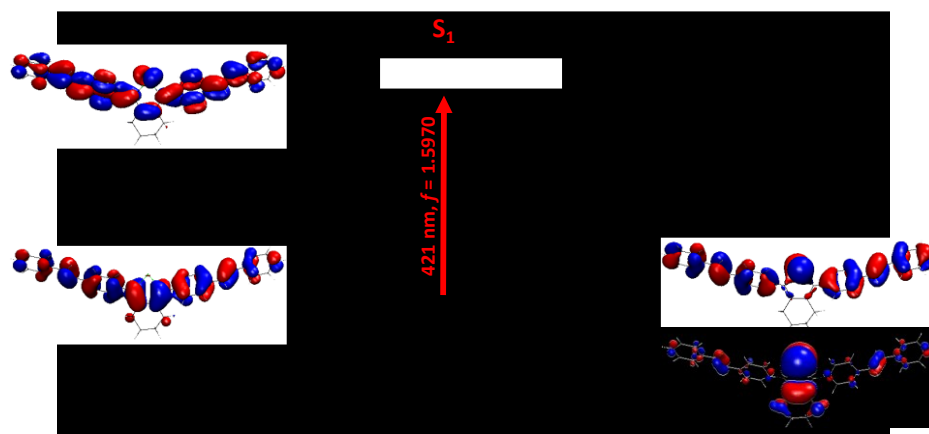


**Figure 4.21** – TD-DFT [B3LYP/cc-pVDZ(-PP)] computed transitions ( $S_0 \rightarrow S_1$ : red;  $S_0 \rightarrow S_5$ : black) for **dpe-Te-6-dpe** in the gas-phase including the excitation wavelengths, oscillator strengths ( $f$ ), and the associated molecular orbitals; iso-surface values of  $+0.02/-0.02$  (red/blue).

**Table 4.6** – TD-DFT calculated excited states of **dpe-Te-6-dpe** at the B3LYP-ccpVDZ(-PP) level of theory.

| Excited State         | Energy (eV) | $\lambda$ (nm) | $f$    | Nature of Excitation (CI) <sup>a</sup>  |
|-----------------------|-------------|----------------|--------|---|
| <b>T<sub>1</sub></b>  | 2.0109      | 616.56         | 0.0000 | <b>HOMO</b> → <b>LUMO</b> (0.59051)   |
| <b>T<sub>2</sub></b>  | 2.1551      | 575.31         | 0.0000 | <b>HOMO</b> → <b>LUMO+1</b> (0.45447)<br><b>HOMO-1</b> → <b>LUMO</b> (0.43977)  |
| <b>T<sub>3</sub></b>  | 2.5682      | 482.77         | 0.0000 | <b>HOMO-3</b> → <b>LUMO</b> (0.39388)<br><b>HOMO</b> → <b>LUMO+3</b> (-0.38207)<br><b>HOMO-1</b> → <b>LUMO+1</b> (-0.33656) |
| <b>T<sub>4</sub></b>  | 2.929       | 423.3          | 0.0000 | <b>HOMO-2</b> → <b>LUMO</b> (0.56321)   |
| <b>S<sub>1</sub></b>  | 2.9448      | 421.03         | 1.5970 | <b>HOMO</b> → <b>LUMO</b> (0.69748)   |
| <b>T<sub>5</sub></b>  | 3.2504      | 381.44         | 0.0000 | <b>HOMO</b> → <b>LUMO+1</b> (0.47494)   |
| <b>T<sub>6</sub></b>  | 3.2596      | 380.37         | 0.0000 | <b>HOMO</b> → <b>LUMO+2</b> (0.58852)   |
| <b>S<sub>2</sub></b>  | 3.2949      | 376.29         | 0.0138 | <b>HOMO</b> → <b>LUMO+1</b> (0.60771)<br><b>HOMO-1</b> → <b>LUMO</b> (-0.33608)   |
| <b>T<sub>7</sub></b>  | 3.3487      | 370.24         | 0.0000 | <b>HOMO-2</b> → <b>LUMO+2</b> (0.33004)<br><b>HOMO-1</b> → <b>LUMO+2</b> (0.32066)  |
| <b>S<sub>3</sub></b>  | 3.3859      | 366.18         | 0.0000 | <b>HOMO-2</b> → <b>LUMO</b> (0.55564)<br><b>HOMO-1</b> → <b>LUMO</b> (0.36852)  |
| <b>T<sub>8</sub></b>  | 3.4268      | 361.81         | 0.0000 | <b>HOMO-2</b> → <b>LUMO+2</b> (0.41292)   |
| <b>S<sub>4</sub></b>  | 3.5399      | 350.24         | 0.1277 | <b>HOMO</b> → <b>LUMO+2</b> (0.66069)   |
| <b>T<sub>9</sub></b>  | 3.5670      | 347.59         | 0.0000 | <b>HOMO-2</b> → <b>LUMO+1</b> (0.41833)<br><b>HOMO-1</b> → <b>LUMO+1</b> (0.30481)  |
| <b>S<sub>5</sub></b>  | 3.5813      | 346.19         | 0.1680 | <b>HOMO-1</b> → <b>LUMO</b> (0.49494)<br><b>HOMO-2</b> → <b>LUMO</b> (-0.38176)   |
| <b>T<sub>10</sub></b> | 3.5955      | 344.83         | 0.0000 | <b>HOMO-1</b> → <b>LUMO+1</b> (0.37962)   |
| <b>S<sub>6</sub></b>  | 3.6428      | 340.35         | 0.4233 | <b>HOMO-1</b> → <b>LUMO+1</b> (0.58461)<br><b>HOMO-2</b> → <b>LUMO+1</b> (0.38865)  |
| <b>S<sub>7</sub></b>  | 3.8084      | 325.55         | 0.4727 | <b>HOMO-2</b> → <b>LUMO+1</b> (0.5787)<br><b>HOMO-1</b> → <b>LUMO+1</b> (-0.37891)  |
| <b>S<sub>8</sub></b>  | 3.8118      | 325.27         | 0.0093 | <b>HOMO-2</b> → <b>LUMO+2</b> (0.5225)<br><b>HOMO-1</b> → <b>LUMO+2</b> (0.39873)   |
| <b>S<sub>9</sub></b>  | 3.9126      | 316.89         | 0.1375 | <b>HOMO-3</b> → <b>LUMO</b> (0.59416)<br><b>HOMO</b> → <b>LUMO+3</b> (0.33461)  |
| <b>S<sub>10</sub></b> | 4.1618      | 297.91         | 0.0001 | <b>HOMO-1</b> → <b>LUMO+2</b> (0.44972)<br><b>HOMO-2</b> → <b>LUMO+2</b> (-0.34819)   |

a) Only coefficients (CI) > |0.31| are shown (corresponds to a contribution of 19 % to the transition).

b) Molecular orbitals involving Te are identified in bold font.

#### 4.2.10 Comparing the HOMO/LUMO levels of 2,5-bis(aryl)tellurophenes

Figure 4.22 compares the computed HOMO and LUMO energies of each tellurophene discussed in this Chapter. Since the only difference between each tellurophene is the nature of the aryl substituents, which allows the effect of the aryl substituent on the calculated frontier molecular orbital energies to be explored. **Mes-Te-6-Mes**, with electron-donating methyl groups, features the widest HOMO-LUMO gap (4.82 eV) and the highest LUMO level (-0.86 eV). In contrast, **O<sub>2</sub>N(C<sub>6</sub>H<sub>4</sub>)-Te-6-(C<sub>6</sub>H<sub>4</sub>)NO<sub>2</sub>**, with electron-withdrawing -NO<sub>2</sub> substituents yields a much smaller HOMO-LUMO gap (3.52 eV) as well as the lowest HOMO and LUMO levels of all neutral tellurophenes (-6.34 and -2.81 eV, respectively). This illustrates the stabilizing effect of incorporating electron-withdrawing groups onto the electron-rich tellurophene ring. **[Mepyr-Te-6-pyrMe]<sup>2+</sup>** has computed HOMO and LUMO levels (-11.79 and -8.69 eV respectively) that are substantially lower in energy than that of **pyr-Te-6-pyr** (-6.09 and -1.86 eV, respectively).

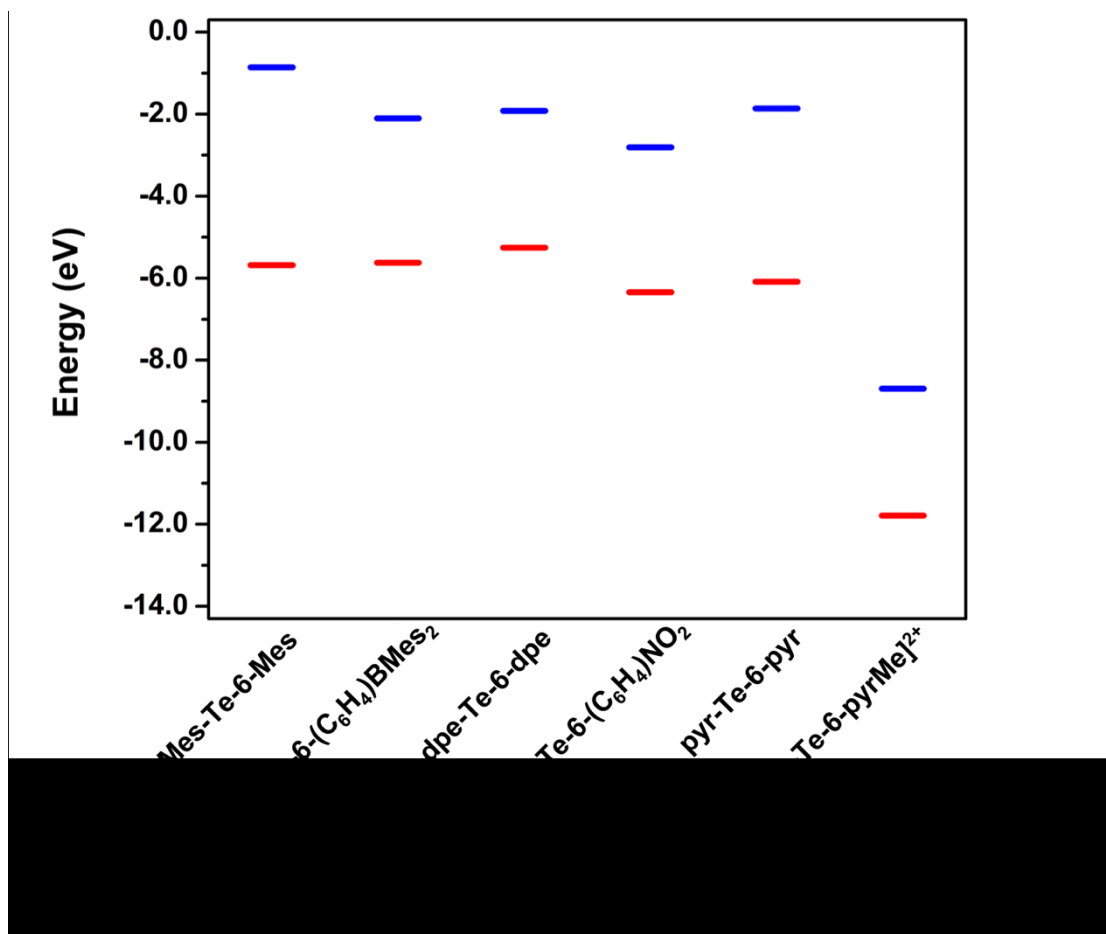


**Figure 4.22** – Computed HOMO (blue) and LUMO (red) energy levels for the optimized ground state of **Mes-Te-6-Mes**, **Mes<sub>2</sub>B(C<sub>6</sub>H<sub>4</sub>)-Te-6-(C<sub>6</sub>H<sub>4</sub>)BMes<sub>2</sub>**, **dpe-Te-6-dpe**, **O<sub>2</sub>N(C<sub>6</sub>H<sub>4</sub>)-Te-6-(C<sub>6</sub>H<sub>4</sub>)NO<sub>2</sub>**, **pyr-Te-6-pyr**, and **[Mepyr-Te-6-pyrMe]<sup>2+</sup>** in the gas-phase using B3LYP/cc-pVDZ(-PP).

### 4.3 Conclusion

Several new 2,5-bis(aryl)tellurophenes were synthesized using a mild Suzuki-Miyaura cross-coupling reaction between **B-Te-6-B** and the appropriate arylbromide. This method was used to synthesize **Mes-Te-6-Mes**, **Mes<sub>2</sub>B(C<sub>6</sub>H<sub>4</sub>)-Te-6-(C<sub>6</sub>H<sub>4</sub>)BMes<sub>2</sub>**, **dpe-Te-6-dpe**, **O<sub>2</sub>N(C<sub>6</sub>H<sub>4</sub>)-Te-6-(C<sub>6</sub>H<sub>4</sub>)NO<sub>2</sub>**, and **pyr-Te-6-pyr**.

Furthermore, an extended viologen featuring a tellurophene unit was developed by reacting **pyr-Te-6-pyr** with an excess of MeI in the hope of developing a solid state phosphorescent viologen, however phosphorescence was not achieved in this system. Of the tellurophenes in this study **Mes<sub>2</sub>B(C<sub>6</sub>H<sub>4</sub>)-Te-6-(C<sub>6</sub>H<sub>4</sub>)BMes<sub>2</sub>**, **O<sub>2</sub>N(C<sub>6</sub>H<sub>4</sub>)-Te-6-(C<sub>6</sub>H<sub>4</sub>)NO<sub>2</sub>**, and **pyr-Te-6-pyr** were all phosphorescent with  $\lambda_{em}$  of 632, 695, and 614 nm, respectively. However, each of these tellurophenes featured low quantum yields ( $\leq 0.5\%$ ) likely due to the Energy Gap Law. Future studies will focus on further red-shifting the emission into the NIR and developing more rigid structures (*e.g.*, fused aromatic rings) that should be emissive in the absence of a PMMA matrix.

## 4.4 Experimental

### 4.4.1 General procedures

Unless explicitly stated otherwise, all reactions were carried out with standard Schlenk and glovebox (MBraun) techniques using N<sub>2</sub> as the inert atmosphere and solvents that were dried using a Grubbs' type purification system manufactured by Innovative Technology Inc. 4-Bromopyridinehydrochloride was purchased from Oakwood Chemicals. 1,7-Octadiyne was purchased from GFS Chemicals, Cp<sub>2</sub>ZrCl<sub>2</sub> from Strem Chemicals Inc., and all other commercially available compounds were obtained from Sigma-Aldrich; all commercially derived chemicals were used as received. The following compounds were synthesized according to literature procedures: **B-Te-6-B**,<sup>10</sup> Cl(XPhos)Pd(2-aminobiphenyl),<sup>25</sup> (4-

bromophenyl)dimesitylborane,<sup>37</sup> and (*E*)-1-(4-bromophenyl)-2-phenylethene.<sup>38</sup> Melting points were measured with a MelTemp apparatus and are reported without correction. High-resolution mass spectra were obtained on an Agilent 6220 spectrometer and Kratos Analytical MS-50G system. Elemental analyses were performed by the Analytical and Instrumentation Laboratory at the University of Alberta. UV-vis spectroscopic measurements were performed with a Varian Cary 5000 Scan Spectrophotometer.

Steady-state photoluminescence (PL) spectra, emission lifetime ( $\lambda$ ), and photoluminescence quantum yields ( $\Phi$ ) were obtained using a Horiba PTI QuantaMaster 8075 fluorescence spectrophotometer. For the PL and quantum yield measurements, the spectrophotometer was equipped with a 75 W xenon lamp (and an integrating sphere for the quantum yield measurements). All samples were measured under ambient conditions in a poly(methylmethacrylate) (PMMA) matrix, prepared by dissolving 1 mg of sample and 99 mg of PMMA in 1 mL of THF and drop-casting the solution onto a quartz plate. Long-pass and short-pass cut-off filters of  $\lambda = 400$  nm were used in the steady-state photoluminescence and quantum yield measurements. All quantum yields are reported as absolute values.

The decay curves used to determine the emission lifetime ( $\tau$ ) were collected on a Horiba PTI QuantaMaster 8075 fluorescence spectrometer equipped with a 75 W xenon flash lamp. The resulting decay curve was fitted with the lowest exponential function that gave a suitable reduced chi-square value ( $\chi^2$ ), Durbin Watson parameter, and Z value.<sup>45-47</sup>



#### 4.4.2 Synthetic procedures

**Preparation of Mes-Te-6-Mes. B-Te-6-BP** (74.5 mg, 0.153 mmol), 2-bromomesitylene (73 mg, 0.37 mmol) and Cl(XPhos)Pd(2-aminobiphenyl) (11.1 mg, 0.0141 mmol) were dissolved in 1.5 mL of THF. Degassed 2.0 M  $\text{K}_3\text{PO}_4$  (aq) (0.50 mL, 1.0 mmol) was added to this mixture. After stirring at room temperature for 14 hours, the reaction mixture was exposed to air and 10 mL of distilled water was added. The product was extracted with  $3 \times 5$  mL of  $\text{CH}_2\text{Cl}_2$ , the combined organic fractions were washed with  $3 \times 10$  mL of distilled water, dried over  $\text{MgSO}_4$ , filtered, and then volatiles were removed from the filtrate under vacuum to yield 76 mg of a white solid. The product was further purified by column chromatography using hexanes as the eluent to yield of **Mes-Te-6-Mes** (51 mg, 71 %) as a white solid after removal of the volatiles under vacuum. Crystals suitable for single-crystal X-ray diffraction were grown by slow evaporation of a concentrated hexanes solution at room temperature.  $^1\text{H}$  NMR (699.8 MHz,  $\text{CDCl}_3$ ):  $\delta$  = 6.94 (s, 4H, Mes-CH), 2.33 (s, 6H, *p*-CH<sub>3</sub>), 2.18 (s, 12H, *o*-CH<sub>3</sub>), 2.17 (br, 4H, C=CCH<sub>2</sub>CH<sub>2</sub>), 1.55 br, 4H, C=CCH<sub>2</sub>CH<sub>2</sub>).  $^{13}\text{C}\{^1\text{H}\}$  NMR (176.0 MHz,  $\text{CDCl}_3$ ):  $\delta$  = 143.3 (Te-C=CCH<sub>2</sub>CH<sub>2</sub>), 137.1 (Te-C=CCH<sub>2</sub>CH<sub>2</sub>), 136.8 (MesC), 136.5 (MesC), 136.3 (MesC), 128.3 (MesC), 29.8 (C=CCH<sub>2</sub>CH<sub>2</sub>), 23.6 (C=CCH<sub>2</sub>CH<sub>2</sub>), 21.2 (*p*-CH<sub>3</sub>), 20.8 (*o*-CH<sub>3</sub>). Anal. calcd. (%) for  $\text{C}_{26}\text{H}_{30}\text{Te}$ : C, 66.43; H, 6.43. found: C, 66.22; H, 6.39. HR-MS (EI): *m/z* calcd for  $\text{C}_{26}\text{H}_{30}^{130}\text{Te}$ : 472.14099, found: 473.14048 ( $\Delta\text{ppm} = 1.1$ ). UV-vis (in THF):  $\lambda_{\text{max}} = 293$  nm,  $\epsilon = 9.75 \times 10^3 \text{ M}^{-1}\text{cm}^{-1}$ . Mp ( $^\circ\text{C}$ ): decomposes > 215 (under  $\text{N}_2$ ).

**Synthesis of Mes<sub>2</sub>B(C<sub>6</sub>H<sub>4</sub>)-Te-6-(C<sub>6</sub>H<sub>4</sub>)BMes<sub>2</sub>. B-Te-6-B** (51.6 mg, 0.106 mmol), (4-bromophenyl)dimesitylborane (90.4 mg, 0.223 mmol), and Cl(XPhos)Pd(2-aminobiphenyl) (5.8 mg, 0.0074 mmol) were dissolved in 5 mL of THF. Degassed 2.0 M K<sub>3</sub>PO<sub>4</sub> (aq) (0.33 mL, 0.66 mmol) was added to the reaction mixture. After stirring at 50 °C for 22 hours, the reaction mixture was exposed to air and diluted with 75 mL of CH<sub>2</sub>Cl<sub>2</sub>; the organic layer was then washed with 4 × 50 mL of distilled water. The organic layer was then dried over MgSO<sub>4</sub>, filtered, and the volatiles were removed from the filtrate under vacuum to yield 94 mg of a bright yellow solid. The product was further purified by column chromatography using 1:4 CH<sub>2</sub>Cl<sub>2</sub>:hexanes as an eluent to yield **Mes<sub>2</sub>B(C<sub>6</sub>H<sub>4</sub>)-Te-6-(C<sub>6</sub>H<sub>4</sub>)BMes<sub>2</sub>** as a yellow solid (75 mg, 80 %). <sup>1</sup>H NMR (499.8 MHz, CDCl<sub>3</sub>): δ = 7.51 (d, <sup>3</sup>J<sub>HH</sub> = 8.5 Hz, ArCH in C<sub>6</sub>H<sub>4</sub>), 4H, 7.38 (d, <sup>3</sup>J<sub>HH</sub> = 8.0 Hz, 4H, ArCH in C<sub>6</sub>H<sub>4</sub>), 6.84 (s, 8H, Mes-CH), 2.73 (br, 4H, C=CCH<sub>2</sub>CH<sub>2</sub>), 2.32 (s, 12H, *p*-CH<sub>3</sub>), 2.05 (s, 24H, *o*-CH<sub>3</sub>), 1.65 (br, 4H, C=CCH<sub>2</sub>CH<sub>2</sub>). <sup>13</sup>C{<sup>1</sup>H} NMR (125.7 MHz, CDCl<sub>3</sub>): δ = 145.3 (TeC=CCH<sub>2</sub>), 144.0 (ArC in C<sub>6</sub>H<sub>4</sub>), 140.9 (*o*-CH<sub>3</sub>), 140.0 (TeC), 138.7 (*p*-CH<sub>3</sub>), 136.8 (ArCH in C<sub>6</sub>H<sub>4</sub>), 129.0 (ArCH in C<sub>6</sub>H<sub>4</sub>), 128.3 (Mes-CH), 30.8 (C=CCH<sub>2</sub>CH<sub>2</sub>), 23.7 (*o*-CH<sub>3</sub>), 23.4 (C=CCH<sub>2</sub>CH<sub>2</sub>), 21.4 (*p*-CH<sub>3</sub>). The <sup>13</sup>C{<sup>1</sup>H} resonances for the boron-bound carbon atoms could not be located. <sup>11</sup>B{<sup>1</sup>H} NMR (128.3 MHz, CDCl<sub>3</sub>): δ = 74.3. HR-MS (MALDI): m/z calcd for C<sub>44</sub>H<sub>36</sub>B<sub>2</sub><sup>130</sup>Te: 884.39379, found: 884.39535 (Δppm = 1.8). Anal. calcd. (%) for C<sub>44</sub>H<sub>36</sub>B<sub>2</sub>Te: C, 76.23; H, 6.85; found: C, 75.43; H, 6.83. UV-vis (in THF): λ<sub>max</sub> = 335 nm, ε = 2.74 × 10<sup>4</sup> M<sup>-1</sup>cm<sup>-1</sup>, λ<sub>max</sub> = 370 nm, ε = 2.62 × 10<sup>4</sup> M<sup>-1</sup>cm<sup>-1</sup>, λ<sub>max</sub> = 263 nm, ε = 1.82 × 10<sup>4</sup> M<sup>-1</sup>cm<sup>-1</sup>. Mp (°C): 154–157 (under N<sub>2</sub>).

**Synthesis of dpe-Te-6-dpe. B-Te-6-B** (100.2 mg, 0.2063 mmol), (*E*)-1-(4-bromophenyl)-2-phenylethene (113.6 mg, 0.4384 mmol), and Cl(XPhos)Pd(2-aminobiphenyl) (11.5 mg, 0.0146 mmol) were dissolved in 8 mL of THF. Degassed 2.0 M K<sub>3</sub>PO<sub>4(aq)</sub> (0.60 mL, 0.64 mmol) was added to the reaction mixture. After stirring at 50 °C for 22 hours, a yellow precipitate formed. The reaction mixture was diluted with 225 mL CH<sub>2</sub>Cl<sub>2</sub> and washed with 4 × 125 mL of distilled water. The organic layer was then dried over MgSO<sub>4</sub>, filtered, and the volatiles were removed from the filtrate under vacuum to yield 147 mg of **dpe-Te-6-dpe**. The product was further purified by washing with 3 × 1 mL of Et<sub>2</sub>O and then 3 × 1 mL of hexanes to give **dpe-Te-6-dpe** as a yellow solid (71 mg, 58 %), however analytically pure product or crystals suitable for X-ray crystallography could not be obtained. <sup>1</sup>H NMR (699.8 MHz, CDCl<sub>3</sub>): δ = 7.53 (d, <sup>3</sup>J<sub>HH</sub> = 7.7 Hz, 4H, ArCH in C<sub>6</sub>H<sub>4</sub>), 7.52 (d, <sup>3</sup>J<sub>HH</sub> = 7.7 Hz, 4H, ArCH in C<sub>6</sub>H<sub>4</sub>), 7.42 (d, <sup>3</sup>J<sub>HH</sub> = 7.7 Hz, 4H, ArCH in C<sub>6</sub>H<sub>5</sub>), 7.37 (t, <sup>3</sup>J<sub>HH</sub> = 7.7 Hz, 4H, ArCH in C<sub>6</sub>H<sub>5</sub>), 7.28 (t, <sup>3</sup>J<sub>HH</sub> = 7.7 Hz, 2H, ArCH in C<sub>6</sub>H<sub>5</sub>), 7.14 (d, <sup>3</sup>J<sub>HH</sub> = 3.5 Hz, 4H, olefin-CH), 2.77 (br, 4H, C=CCH<sub>2</sub>CH<sub>2</sub>), 1.67 (br, 4H, C=CCH<sub>2</sub>CH<sub>2</sub>). <sup>13</sup>C {<sup>1</sup>H} NMR (176.0 MHz, CDCl<sub>3</sub>): δ = 144.8 (Te-C=CCH<sub>2</sub>CH<sub>2</sub>), 139.8, 139.3, 137.5, 136.0, 129.8, 128.9, 128.9, 128.4, 127.8, 126.7, 126.6, 30.8 (C=CCH<sub>2</sub>CH<sub>2</sub>), 23.4 (C=CCH<sub>2</sub>CH<sub>2</sub>). Due to the abundance of peaks in a similar environment, specific <sup>13</sup>C {<sup>1</sup>H} assignments for aryl carbons were not made. HR-MS (EI): m/z calcd for C<sub>36</sub>H<sub>30</sub><sup>130</sup>Te: 592.14099, found: 592.14022 (Δppm = 1.3). UV-vis (in THF): λ<sub>max</sub> = 355 nm, ε = 5.51 × 10<sup>4</sup> M<sup>-1</sup>cm<sup>-1</sup>, λ<sub>max</sub> = 291 nm, ε = 3.74 × 10<sup>4</sup> M<sup>-1</sup>cm<sup>-1</sup>. Mp (°C): 268–270 (under N<sub>2</sub>).

**Synthesis of O<sub>2</sub>N(C<sub>6</sub>H<sub>4</sub>)-Te-6-(C<sub>6</sub>H<sub>4</sub>)NO<sub>2</sub>. B-Te-6-B** (195.9 mg, 0.4033 mmol), 4-bromonitrobenzene (176.7 mg, 0.8747 mmol), and Cl(XPhos)Pd(2-aminobiphenyl) (23.7 mg, 0.0301 mmol) were dissolved in 5 mL of THF. Degassed 2.0 M K<sub>3</sub>PO<sub>4</sub>(aq) (1.30 mL, 2.60 mmol) was added to the reaction mixture. After stirring at 50 °C for 14 hours, the reaction mixture was exposed to air, diluted with 20 mL of CH<sub>2</sub>Cl<sub>2</sub>, and then washed with 4 × 30 mL of distilled water. The organic layer was dried over MgSO<sub>4</sub>, filtered, and the volatiles were removed from the filtrate under vacuum. Further purification was performed by column chromatography using 25 % CH<sub>2</sub>Cl<sub>2</sub> in hexanes as the eluent to give pure O<sub>2</sub>N(C<sub>6</sub>H<sub>4</sub>)-Te-6-(C<sub>6</sub>H<sub>4</sub>)NO<sub>2</sub> as a yellow solid (131 mg, 68 %). Yellow crystals suitable for single-crystal X-ray diffraction were grown from a saturated solution of fluorobenzene at room temperature. <sup>1</sup>H NMR (699.8 MHz, CDCl<sub>3</sub>): δ = 8.25 (d, <sup>3</sup>J<sub>HH</sub> = 9.1 Hz, 4H, ArH), 7.55 (d, <sup>3</sup>J<sub>HH</sub> = 9.1 Hz, 4H, ArH), 2.72 (br, 4H, C=CCH<sub>2</sub>CH<sub>2</sub>), 1.69 (br, 4H, C=CCH<sub>2</sub>CH<sub>2</sub>). <sup>13</sup>C {<sup>1</sup>H} NMR (125.7 MHz, CDCl<sub>3</sub>): δ = 146.9, 146.7, 146.4, 138.6 (Te-C=CCH<sub>2</sub>CH<sub>2</sub>), 130.1 (Ar-CH), 123.9 (Ar-CH), 30.7 (C=CCH<sub>2</sub>CH<sub>2</sub>), 23.0 (C=CCH<sub>2</sub>CH<sub>2</sub>). HR-MS (EI): m/z calcd for C<sub>20</sub>H<sub>16</sub>N<sub>2</sub>O<sub>4</sub><sup>130</sup>Te: 478.01724, found: 478.01764 (Δppm = 0.8). Anal. calcd. (%) for C<sub>20</sub>H<sub>16</sub>N<sub>2</sub>O<sub>4</sub>Te: C, 50.47; N, 5.89; H, 3.39; found: C, 51.18; N, 5.54; H, 3.65. UV-vis (in THF): λ<sub>max</sub> = 376 nm, ε = 2.12 × 10<sup>4</sup> M<sup>-1</sup>cm<sup>-1</sup>, λ<sub>max</sub> = 268 nm, ε = 1.99 × 10<sup>4</sup> M<sup>-1</sup>cm<sup>-1</sup>. Mp (°C): decomposes > 150 (under N<sub>2</sub>).

**Synthesis of pyr-Te-6-pyr. B-Te-6-B** (789 mg, 1.62 mmol), 4-bromopyridine hydrochloride (689 mg, 3.41 mmol), and Cl(XPhos)Pd(2-aminobiphenyl) (92 mg, 0.12 mmol) were dissolved in 50 mL of THF. Degassed 2.0 M K<sub>3</sub>PO<sub>4</sub>(aq) (4.0 mL, 8.0 mmol)

was added to the reaction mixture. After stirring at 40 °C for 14 hours, the reaction mixture was exposed to air and extracted with 3 × 150 mL of CH<sub>2</sub>Cl<sub>2</sub>. The organic fractions were combined, washed with 5 × 150 mL of distilled water, dried over MgSO<sub>4</sub>, filtered, and then the volatiles were removed from the filtrate under vacuum to yield **pyr-Te-6-pyr** (564 mg, 89 %). Further purification was performed by washing the product with 3 × 2 mL of hexanes to give **pyr-Te-6-pyr** (389 mg, 62 %) as an analytically pure white solid. Colourless crystals suitable for single-crystal X-ray diffraction were grown by slowly diffusing hexanes into a solution of **pyr-Te-6-pyr** in flourobenezene at room temperature. <sup>1</sup>H NMR (499.8 MHz, CDCl<sub>3</sub>): δ = 8.60 (dd, <sup>3</sup>J<sub>HH</sub> = 4.5 Hz, <sup>4</sup>J<sub>HH</sub> = 1.5 Hz, 4H, pyrH), 7.29 (dd, <sup>3</sup>J<sub>HH</sub> = 4.5 Hz, <sup>4</sup>J<sub>HH</sub> = 3.0 Hz, 4H, pyrH), 2.74 (br, 4H, C=CCH<sub>2</sub>CH<sub>2</sub>), 1.68 (br, 4H, C=CCH<sub>2</sub>CH<sub>2</sub>). <sup>13</sup>C{<sup>1</sup>H} NMR (125.7 MHz, CDCl<sub>3</sub>): δ = 149.9 (pyrCH), 147.7 (Te–C=CCH<sub>2</sub>CH<sub>2</sub>), 146.2 Te–C=CCH<sub>2</sub>CH<sub>2</sub>, 137.6 (pyrC), 123.8 (pyrCH), 30.6 (CH<sub>2</sub>), 22.9 (CH<sub>2</sub>). Anal. Calcd. (%) for C<sub>18</sub>H<sub>16</sub>N<sub>2</sub>Te: C, 55.73; H, 4.16; N 7.22. Found: C, 54.96; H, 4.21; N, 6.83. HR-MS (EI): m/z calcd for C<sub>18</sub>H<sub>16</sub>N<sub>2</sub><sup>130</sup>Te: 390.03757, found: 390.03760 (Δppm = 0.1). UV-vis (in THF): λ<sub>max</sub> = 318 nm, ε = 1.31 × 10<sup>4</sup> M<sup>-1</sup>cm<sup>-1</sup>. Mp (°C): 167–171 (under N<sub>2</sub>).

**Synthesis of [Mepyr-Te-6-pyrMe][I]<sub>2</sub>.** Iodomethane (372 mg, 2.62 mmol) was added to a solution of **pyr-Te-6-pyr** (102 mg, 0.262 mmol) in 30 mL of acetonitrile and the mixture was heated to 90 °C for 18 hours. The mixture was then cooled to – 30 °C and the precipitate was isolated by filtration on a Buchner funnel in air. The precipitate was washed with 50 mL of MeOH and dried under vacuum to give **[Mepyr-Te-6-pyrMe][I]<sub>2</sub>** (40 mg, 37 %) as an analytically pure red solid. Yellow crystals suitable for

single-crystal X-ray diffraction were grown by slow evaporation of an acetonitrile/methanol solution at room temperature.  $^1\text{H}$  NMR (499.8 MHz, DMSO- $d_6$ ):  $\delta$  = 8.91 (d,  $^3J_{\text{HH}} = 6.5$  Hz, 4H, pyrH), 8.08 (d,  $^3J_{\text{HH}} = 6.5$  Hz, 4H, pyrH), 4.33 (s, 6H,  $\text{CH}_3$ ), 2.76 (br, 4H,  $\text{C}=\text{CCH}_2\text{CH}_2$ ), 1.64 (br, 4H,  $\text{C}=\text{CCH}_2\text{CH}_2$ ).  $^{13}\text{C}\{^1\text{H}\}$  NMR (125.7 MHz, DMSO- $d_6$ ):  $\delta$  = 155.1 (pyrC), 148.9 (Te-C= $\text{CCH}_2\text{CH}_2$ ), 144.7 (pyrCH), 139.0 (Te-C= $\text{CCH}_2\text{CH}_2$ ), 127.2 (pyrCH), 47.1 ( $\text{CH}_3$ ), 30.2 ( $\text{CH}_2$ ), 22.1 ( $\text{CH}_2$ ). Anal. calcd. (%) for  $\text{C}_{20}\text{H}_{22}\text{N}_2\text{TeI}_2$ : C, 35.76; H, 3.30; N, 4.17; found: C, 35.18; H, 3.34; N, 4.16. HR-MS (ESI):  $m/z$  calcd for  $[\text{C}_{20}\text{H}_{22}\text{N}_2^{130}\text{Te}]^{2+}$ : 210.0417, found: 210.0417 ( $\Delta\text{ppm} = 0.1$ ). UV-vis (in THF):  $\lambda_{\text{max}} = 246$  nm,  $\varepsilon = 5.69 \times 10^4 \text{ M}^{-1}\text{cm}^{-1}$ ,  $\lambda_{\text{max}} = 376$  nm,  $\varepsilon = 2.46 \times 10^4 \text{ M}^{-1}\text{cm}^{-1}$ . Mp ( $^\circ\text{C}$ ): decomposes  $> 230$  (under  $\text{N}_2$ ).

#### 4.4.3 X-ray crystallography

Crystals suitable for X-ray diffraction studies were removed from a vial and immediately coated in a thin layer of hydrocarbon oil (Paratone-N). A suitable crystal was then mounted on a glass fibre, and quickly placed in a low temperature stream of nitrogen on an X-ray diffractometer. All data was collected on a Bruker APEX II CCD detector/D8 diffractometer<sup>48</sup> using Cu  $K\alpha$  radiation with the crystals cooled to  $-100$   $^\circ\text{C}$ . The data was corrected for absorption using Gaussian integration from the indexing of the crystal faces.<sup>49</sup> Crystal structures were solved using intrinsic phasing SHELXT-2014<sup>50</sup> and refined using full-matrix least-squares on  $F^2$  (SHELXL).<sup>51</sup> The assignment of hydrogen atom positions were based on the  $\text{sp}^2$  or  $\text{sp}^3$  hybridization geometries of

their respective carbon atoms, and were given thermal parameters 20 % greater than those of their parent atoms.

**Table 4.7** – Crystallographic data for the tellurophenes discussed in Chapter 4.

| Compound  | Mes-Te-6-Mes                       | O <sub>2</sub> N(C <sub>6</sub> H <sub>4</sub> )-<br>Te-6-<br>(C <sub>6</sub> H <sub>4</sub> )NO <sub>2</sub> | pyr-Te-6-pyr                                      | [Mepyr-Te-6-<br>pyrMe][I] <sub>2</sub>                           |
|---|------------------------------------|---|---|--|
| formula   | C <sub>26</sub> H <sub>30</sub> Te | C <sub>20</sub> H <sub>16</sub> N <sub>2</sub> O <sub>4</sub> Te  | C <sub>18</sub> H <sub>16</sub> N <sub>2</sub> Te | C <sub>20</sub> H <sub>22</sub> I <sub>2</sub> N <sub>2</sub> Te |
| form. wt. (g/mol)   | 470.10                             | 475.95  | 387.93  | 671.79   |
| crys. dimes. (mm)   | 0.27×0.20×0.19                     | 0.23×0.04×0.02  | 0.18×0.13×0.08                                    | 0.33×0.07×0.06   |
| Crystal system  | Monoclinic                         | Monoclinic  | Monoclinic  | Orthorhombic   |
| Space group   | <i>C2/c</i>                        | <i>P2<sub>1</sub>/n</i>   | <i>P2<sub>1</sub>/c</i>                           | <i>Pbca</i>  |
| <i>a</i> (Å)  | 24.245(5)                          | 8.2255(2)   | 12.8026(3)  | 14.9840(6)   |
| <i>b</i> (Å)  | 9.5267(19)                         | 18.4006(4)  | 17.6094(4)  | 9.1580(4)  |
| <i>c</i> (Å)  | 9.4788(19)                         | 23.6225(5)  | 13.5193(3)  | 31.4464(12)  |
| $\alpha$ (deg)  | -                                  | -   | -   | -  |
| $\beta$ (deg)   | 90.715(3)                          | -   | 100.3422(8)                                       | -  |
| $\gamma$ (deg)  | -                                  | -   | -   | -  |
| <i>V</i> (Å <sup>3</sup> )  | 2189.2(8)                          | 3570.53(14)   | 2998.35(12)                                       | 4315.2(3)  |
| <i>Z</i>  | 4                                  | 8   | 8   | 8  |
| $\rho_{\text{calcd}}$ (g cm <sup>-3</sup> )   | 1.426                              | 1.771   | 1.719   | 2.068  |
| $\mu$ (mm <sup>-1</sup> )   | 1.366                              | 13.41   | 15.60   | 4.246  |
| temperature (°C)  | -100                               | -100  | -100  | -100   |
| 2 $\theta_{\text{max}}$ (deg)   | 55.34                              | 140.57  | 148.42  | 64.00  |
| total data  | 9698                               | 6936  | 120069  | 55479  |
| unique data ( <i>R</i> <sub>int</sub> )   | 2535 (0.0289)                      | 6936 (0.0796)   | 6086 (0.0366)                                     | 7499 (0.0305)  |
| Obs [ <i>I</i> > 2 $\sigma$ ( <i>I</i> )]   | 2369                               | 5913  | 5913  | 6567   |
| <i>R</i> <sub>1</sub><br>[ <i>F</i> <sub>o</sub> <sup>2</sup> ≥ 2 $\sigma$ ( <i>F</i> <sub>o</sub> <sup>2</sup> )] <sup>a</sup> | 0.0376                             | 0.0359  | 0.0181  | 0.0191   |
| <i>wR</i> <sub>2</sub> [all data] <sup>a</sup>  | 0.1088                             | 0.0955  | 0.0488  | 0.0417   |
| max/min $\Delta r$<br>(e Å <sup>-3</sup> )  | 1.576/-0.525                       | 0.912/-0.656  | 0.312/-0.679                                      | 0.600/-0.723   |

$$^a R_1 = \frac{\sum ||F_o| - |F_c||}{\sum |F_o|}; wR_2 = \left[ \frac{\sum w(F_o^2 - F_c^2)^2}{\sum w(F_o^4)} \right]^{1/2}$$



#### 4.4.4 Photoluminescence data

**Table 4.8** – The photoluminescence decay of a PMMA film containing 1 wt% of **Mes<sub>2</sub>B(C<sub>6</sub>H<sub>4</sub>)-Te-6-(C<sub>6</sub>H<sub>4</sub>)BMes<sub>2</sub>**, fit with a biexponential and the resulting fitting parameters.

|   |                             |
|---|-----------------------------|
| Number of components  | 2                           |
| Lifetime of component 1 ( $\tau_1$ )  | $3.98 \pm 0.44 \mu\text{s}$ |
| Weight of component 1 ( $A_1$ )   | 0.82                        |
| Lifetime of component 2 ( $\tau_2$ )  | $9.43 \pm 0.09 \mu\text{s}$ |
| Weight of component 2 ( $A_2$ )   | 0.18                        |
| Weighted mean lifetime $\left(\frac{\sum A_i \tau_i^2}{\sum A_i \tau_i}\right)$ | 5.81 $\mu\text{s}$          |
| $\chi^2$  | 1.005                       |
| Durbin-Watson parameter   | 2.126                       |
| Z (run test of the residuals)   | -0.026                      |

**Table 4.9** – The photoluminescence decay of a PMMA film containing 1 wt% of **O<sub>2</sub>N(C<sub>6</sub>H<sub>4</sub>)-Te-6-(C<sub>6</sub>H<sub>4</sub>)NO<sub>2</sub>**, fit with a biexponential and the resulting fitting parameters.

|   |                             |
|---|-----------------------------|
| Number of components  | 2                           |
| Lifetime of component 1 ( $\tau_1$ )  | $2.15 \pm 0.13 \mu\text{s}$ |
| Weight of component 1 ( $A_1$ )   | 0.85                        |
| Lifetime of component 2 ( $\tau_2$ )  | $5.72 \pm 0.28 \mu\text{s}$ |
| Weight of component 2 ( $A_2$ )   | 0.15                        |
| Weighted mean lifetime $\left(\frac{\sum A_i \tau_i^2}{\sum A_i \tau_i}\right)$ | 3.57 $\mu\text{s}$          |
| $\chi^2$  | 1.179                       |
| Durbin-Watson parameter   | 2.353                       |
| Z (run test of the residuals)   | -0.175                      |

**Table 4.10** – The photoluminescence decay of a PMMA film containing 1 wt% of **pyr-Te-6-pyr**, fit with a biexponential and the resulting fitting parameters.

|   |                              |
|---|------------------------------|
| Number of components  | 2                            |
| Lifetime of component 1 ( $\tau_1$ )  | $4.90 \pm 0.33 \mu\text{s}$  |
| Weight of component 1 ( $A_1$ )   | 0.86                         |
| Lifetime of component 2 ( $\tau_2$ )  | $13.71 \pm 0.06 \mu\text{s}$ |
| Weight of component 2 ( $A_2$ )   | 0.14                         |
| Weighted mean lifetime $\left(\frac{\sum A_i \tau_i^2}{\sum A_i \tau_i}\right)$ | $7.72 \mu\text{s}$           |
| $\chi^2$  | 1.198                        |
| Durbin-Watson parameter   | 1.902                        |
| Z (run test of the residuals)   | -0.336                       |

#### 4.4.5 Computational methodology

All computations have been carried out with the Gaussian16 software package.<sup>52</sup> Geometry optimizations of the gas-phase structures have been performed using density functional theory (DFT) with the hybrid density functional (B3LYP)<sup>53,54</sup> in combination with the basis set cc-pVDZ (for C, H, B, O, N)<sup>55</sup> as well as the basis set cc-pVDZ(-PP) for Te.<sup>56</sup> The cc-PVDZ-PP basis set uses the corresponding effective core potential (ECP) accounting for 28 electrons. The use of the cc-PVDZ and cc-PVDZ-PP basis sets will hereafter be referred to as cc-PVDZ(-PP). The basis sets as well as the ECP for the Te atom were obtained from the Basis Set Exchange Library.<sup>57,58</sup> Frequency analysis confirmed all obtained structures to be local minima on the potential energy surface. The optimized geometry of the  $S_0$  ground state was determined at the B3LYP level of theory. The phosphorescence energy was calculated by computing the optimized

geometry of the lowest lying triplet state ( $T_1$ ) using UB3LYP (spin-unrestricted B3LYP) with the same basis sets as specified above. Subsequent TD-DFT calculations were used to predict the vertical excitation energies of the first 10 singlet states (which were used to generate the computed UV-vis spectrum)<sup>59</sup> and first ten triplet states using the B3LYP functional as well as the cc-PVDZ(-PP) basis sets starting from the B3LYP optimized gas-phase  $S_0$  geometry. The presented molecular orbitals (MOs) were extracted from the Gaussian16 checkpoint-files and are visualized with VMD.<sup>60</sup>

## 4.5 References

1. L. Yang, W. Gu, L. Lv, Y. Chen, Y. Yang, P. Ye, J. Wu, L. Hong, A. Peng, and H. Huang, *Angew. Chem. Int. Ed.*, **2018**, *57*, 1096–1102.
2. W. H. Lee, S. K. Lee, W. S. Shin, S. J. Moon and I. N. Kang, *J. Polym. Sci. Part A*, **2013**, *51*, 2753–2758.
3. G. He, L. Kang, W. Torres Delgado, O. Shynkaruk, M. J. Ferguson, R. McDonald and E. Rivard, *J. Am. Chem. Soc.*, **2013**, *135*, 5360–5363.
4. Y. S. Park, Q. Wu, C. Y. Nam and R. B. Grubbs, *Angew. Chem. Int. Ed.*, **2014**, *53*, 10691–10695.
5. E. H. Jung, S. Bae, T. W. Yoo and W. H. Jo, *Polym. Chem.*, **2014**, *5*, 6545–6550.
6. R. S. Ashraf, I. Meager, M. Nikolka, M. Kirkus, M. Planells, B. C. Schroeder, S. Holliday, M. Hurhangee, C. B. Nielsen, H. Siringhaus, and I. McCulloch, *J. Am. Chem. Soc.*, **2015**, *137*, 1314–1321.

7. A. A. Jahnke, B. Djukic, T. M. McCormick, E. Buchaca Domingo, C. Hellmann, Y. Lee and D. S. Seferos, *J. Am. Chem. Soc.*, **2013**, *135*, 951–954.
8. J. G. Manion, S. Ye, A. H. Proppe, A. W. Laramée, G. R. Mckeown, E. L. Kynaston, S. O. Kelley, E. H. Sargent and D. S. Seferos, *ACS Appl. Energy Mater.*, **2018**, *1*, 5033–5042.
9. W. Xing, P. Ye, J. Lu, X. Wu, Y. Chen, T. Zhu, A. Peng and H. Huang, *J. Power Sources*, **2018**, *401*, 13–19.
10. G. He, W. Torres Delgado, D. J. Schatz, C. Merten, A. Mohammadpour, L. Mayr, M. J. Ferguson, R. McDonald, A. Brown, K. Shankar and E. Rivard, *Angew. Chem. Int. Ed.*, **2014**, *53*, 4587–4591.
11. G. He, B. D. Wiltshire, P. Choi, A. Savin, S. Sun, A. Mohammadpour, M. J. Ferguson, R. McDonald, S. Farsinezhad, A. Brown, K. Shankar and E. Rivard, *Chem. Commun.*, **2015**, *51*, 5444–5447.
12. A. K. Mahrok, E. I. Carrera, A. J. Tilley, S. Ye and D. S. Seferos, *Chem. Commun.*, **2015**, *51*, 5475–5478.
13. W. Torres Delgado, F. Shahin, M. J. Ferguson, R. McDonald, G. He and E. Rivard, *Organometallics*, **2016**, *35*, 2140–2148.
14. C. A. Braun, D. Zomerman, I. de Aguiar, Y. Qi, W. Torres Delgado, M. J. Ferguson, R. McDonald, G. L. C. de Souza, G. He, A. Brown and E. Rivard, *Faraday Discuss.*, **2017**, *196*, 255–268.

15. W. Torres Delgado, C. A. Braun, M. P. Boone, O. Shynkaruk, Y. Qi, R. McDonald, M. J. Ferguson, P. Data, S. K. C. Almeida, I. De Aguiar, G. L. C. De Souza, A. Brown, G. He and E. Rivard, *ACS Appl. Mater. Interfaces*, **2018**, *10*, 12124–12134.
16. E. Hupf, Y. Tsuchiya, W. Moffat, L. Xu, M. Hirai, Y. Zhou, M. J. Ferguson, R. McDonald, T. Murai, G. He and E. Rivard, *Inorg. Chem.*, **2019**, *58*, 13323 – 13336.
17. C. A. Braun, N. Martinek, Y. Zhou, M. J. Ferguson and E. Rivard, *Dalton Trans.*, **2019**, *48*, 10210–10219.
18. K. Takahashi, S. Shimo, E. Hupf, J. Ochiai, C. A. Braun, W. Torres Delgado, L. Xu, G. He, E. Rivard and N. Iwasawa, *Chem. Eur. J.*, **2019**, *25*, 8479–8483.
19. K. Takimiya, Y. Kunugi, Y. Konda, N. Niihara and T. Otsubo, *J. Am. Chem. Soc.*, **2004**, *126*, 5084–5085.
20. N. Nagahora, S. Yahata, S. Goto, K. Shioji and K. Okuma, *J. Org. Chem.*, **2018**, *83*, 1969–1975.
21. M. Kaur, D. S. Yang, J. Shin, T. W. Lee, K. Choi, M. J. Cho and D. H. Choi, *Chem. Commun.*, **2013**, *49*, 5495–5497.
22. M. Kaur, D. H. Lee, D. S. Yang, H. A. Um, M. J. Cho, J. S. Kang and D. H. Choi, *Chem. Commun.*, **2014**, *50*, 14394–14396.
23. M. Al-Hashimi, Y. Han, J. Smith, H. S. Bazzi, S. Y. A. Alqaradawi, S. E. Watkins, T. D. Anthopoulos and M. Heeney, *Chem. Sci.*, **2016**, *7*, 1093–1099.
24. T. Oyama, Y. S. Yang, K. Matsuo and T. Yasuda, *Chem. Commun.*, **2017**, *53*, 3814–3817.
25. T. Kinzel, Y. Zhang and S. Buchwald, *J. Am. Chem. Soc.*, **2010**, *132*, 14073–14075.

26. P. M. S. Monk, *The Viologens: Physicochemical Properties, Synthesis, and Application of the Salt of 4,4'-Bipyridine*; Wiley: New York, **1998**.
27. J. Ding, C. Zheng, L. Wang, C. Lu, B. Zhang, Y. Chen, M. Li, G. Zhai and X. Zhuang, *J. Mater. Chem. A*, **2019**, *7*, 23337–23360.
28. K. Takahashi, T. Nihira, K. Akiyama, Y. Ikegami and E. Fukuyo, *J. Chem. Soc., Chem. Commun.*, **1992**, 620–622.
29. S. T. J. Ryan, R. M. Young, J. J. Henkelis, N. Hafezi, N. A. Vermeulen, A. Hennig, E. J. Dale, Y. Wu, M. D. Krzyaniak, A. Fox, W. M. Nau, M. R. Wasielewski, J. F. Stoddart and O. A. Scherman, *J. Am. Chem. Soc.*, **2015**, *137*, 15299–15307.
30. G. Li, L. Xu, W. Zhang, K. Zhou, Y. Ding, F. Liu, X. He and G. He, *Angew. Chem. Int. Ed.*, **2018**, *57*, 4897–4901.
31. Q. Zhao, C. Huanga and F. Li, *Chem. Soc. Rev.*, **2011**, *40*, 2508–2524.
32. Q. Zhao and J. Z. Sun, *J. Mater. Chem. C*, **2016**, *4*, 10588–10609.
33. S. K. Møllerup and S. Wang, *Chem. Soc. Rev.*, **2019**, *48*, 3537–3549.
34. L. Ji, S. Griesbeck and T. B. Marder, *Chem. Sci.*, **2017**, *8*, 846–863.
35. Y. Ren and F. Jäkle, *Dalton Trans.*, **2016**, *45*, 13996–14007.
36. J. Huo, H. Wang, S. Li, H. Shi, Y. Tang and B. Z. Tang, *Chem. Rec.*, **2020**, *20*, 556–569.
37. B. He, W. Luo, S. Hu, B. Chen, S. Zhen, H. Nie, Z. Zhao and B. Z. Tang, *J. Mater. Chem. C*, **2017**, *5*, 12553–12560.
38. A. K. Flatt, S. M. Dirk, J. C. Henderson, D. E. Shen, J. Su, M. A. Reed and J. M. Tour, *Tetrahedron*, **2003**, *59*, 8555–8570.

39. P. Wei, J. X. Zhang, Z. Zhao, Y. Chen, X. He, M. Chen, J. Gong, H. H. Y. Sung, I. D. Williams, J. W. Y. Lam and B. Z. Tang, *J. Am. Chem. Soc.*, **2018**, *140*, 1966–1975.
40. G. Campillo-Alvarado, K. P. D’mello, D. C. Swenson, S. V. Santhana Mariappan, H. Höpfl, H. Morales-Rojas and L. R. MacGillivray, *Angew. Chem. Int. Ed.*, **2019**, *58*, 5413–5416.
41. M. Mantina, A. C. Chamberlin, R. Valero, C. J. Cramer and D. G. Truhlar, *J. Phys. Chem. A*, **2009**, *113*, 5806–5812.
42. J. D. McCullough, *Inorg. Chem.*, **1975**, *14*, 1142–1146.
43. W.-L. Jia, D.-R. Bai, T. McCormick, Q.-D. Liu, M. Motala, R.-Y. Wang, C. Seward, Y. Tao and S. Wang, *Chem. Eur. J.*, **2004**, *10*, 994–1006.
44. S.-B. Zhao, P. Wucher, Z. M. Hudson, T. M. McCormick, X.-Y. Liu, S. Wang, X.-D. Feng and Z.-H. Lu, *Organometallics*, **2008**, *27*, 6446–6456.
45. P. R. Bevington, *IBM J. Res. Dev.*, **2010**, *13*, 119–125.
46. J. Durbin and G. S. Watson, *Biometrika*, **1951**, *38*, 159–177.
47. D. V. O'Connor and D. Phillips, *Time Correlated Single Photon Counting* (Academic Press, New York, **1984**).
48. H. Hope, *Prog. Inorg. Chem.*, **1994**, *41*, 1–19.
49. R. H. Blessing, *Acta Crystallogr. A.*, **1995**, *51*, 33–38.
50. G. M. Sheldrick, *Acta Crystallogr. A.*, **2015**, *71*, 3–8.
51. G. M. Sheldrick, *Acta Crystallogr. C.*, **2015**, *71*, 3–8.

52. M. J. Frisch, G. W. Trucks, H. B. Schlegel, G. E. Scuseria, M. A. Robb, J. R. Cheeseman, G. Scalmani, V. Barone, G. A. Petersson, H. Nakatsuji, X. Li, M. Caricato, A. V. Marenich, J. Bloino, B. G. Janesko, R. Gomperts, B. Mennucci, H. P. Hratchian, J. V. Ortiz, A. F. Izmaylov, J. L. Sonnenberg, D. Williams-Young, F. Ding, F. Lipparini, F. Egidi, J. Goings, B. Peng, A. Petrone, T. Henderson, D. Ranasinghe, V. G. Zakrzewski, J. Gao, N. Rega, G. Zheng, W. Liang, M. Hada, M. Ehara, K. Toyota, R. Fukuda, J. Hasegawa, M. Ishida, T. Nakajima, Y. Honda, O. Kitao, H. Nakai, T. Vreven, K. Throssell, J. A. Montgomery, Jr., J. E. Peralta, F. Ogliaro, M. J. Bearpark, J. J. Heyd, E. N. Brothers, K. N. Kudin, V. N. Staroverov, T. A. Keith, R. Kobayashi, J. Normand, K. Raghavachari, A. P. Rendell, J. C. Burant, S. S. Iyengar, J. Tomasi, M. Cossi, J. M. Millam, M. Klene, C. Adamo, R. Cammi, J. W. Ochterski, R. L. Martin, K. Morokuma, O. Farkas, J. B. Foresman and D. J. Fox, *Gaussian 16, Revision A.03*, Gaussian, Inc., Wallingford CT, **2016**.
53. A. D. Becke, *J. Chem. Phys.*, **1993**, *98*, 5648–5652.
54. C. Lee, W. Yang and R. G. Parr, *Phys. Rev. B*, **1988**, *37*, 785–789.
55. T. H. Dunning, Jr., *J. Chem. Phys.*, **1989**, *90*, 1007–1023.
56. K. A. Peterson, D. Figgen, E. Goll, H. Stoll and M. Dolg, *J. Chem. Phys.*, **2003**, *119*, 11113–11123.
57. D. Feller, *J. Comput. Chem.*, **1996**, *17*, 1571–1586.
58. K. L. Schuchardt, B. T. Didier, T. Elsethagen, L. Sun, V. Gurumoorthi, J. Chase, J. Li and T. L. Windus, *J. Chem. Inf. Model.*, **2004**, *47*, 1045–1052.
59. Procedure for generating computed UV-vis spectra: <http://gaussian.com/uvvisplot/>



60. W. Humphrey, A. Dalke and K. Schulten, *J. Mol. Graph.*, **1996**, *14*, 33–38.

## Chapter 5 – Tellura(benzo)bithiophene: A New Class of $\pi$ -Extended Tellurophene

### 5.1 Introduction

Tellurium is the lesser-known, bigger brother of sulfur and selenium, particularly in the context of  $\pi$ -conjugated heterocycles. Whereas S and Se are similar in size and electronegativity, Te is substantially larger and less electronegative, which imparts significant metalloid character to this element.<sup>1</sup> These differences can have a profound impact on the synthetic routes used to produce Te-containing materials, and on the resulting properties of the materials.

As flexible, low-cost, organic electronics are gaining momentum, tellurium presents opportunities to tune the properties of  $\pi$ -conjugated molecules in unique ways.<sup>2,3</sup> As a heavy atom, tellurium increases the efficiency of intersystem crossing (ISC), enabling access to triplet excited states and phosphorescence. Among the Group 16 cyclic chalcogenophene series, tellurophenes have the smallest optical bandgaps, mainly attributed to an energetic reduction of the LUMO. Furthermore, the metalloid character of tellurium often leads to close intermolecular Te $\cdots$ Te interactions (less than the sum of the van der Waals radius of Te) that can influence solid state packing arrangements<sup>4-6</sup> and lead to enhanced charge transport properties.<sup>7,8</sup> Thus, incorporating Te into  $\pi$ -conjugated frameworks has the potential to impart useful properties such as smaller optical bandgaps and greater electron/hole mobility.

For the reasons stated above, tellurophenes have been studied in the context of organic photovoltaics (OPVs),<sup>7,9-16</sup> organic light-emitting diodes (OLEDs),<sup>17-22</sup> organic

field effect transistors (OFETs),<sup>7,12,13,23-27</sup> self-sensitized oxidants,<sup>28,29</sup> and for anion recognition.<sup>30</sup> However, tellurophenes still represent an understudied class of compound, especially when compared to thiophenes. While thousands of polymers containing thiophene subunits have been synthesized, and many of these have been studied as active components of OPVs, only a few examples of tellurophene polymers exist and are limited mostly to copolymers. Synthesizing high molecular weight tellurophene-containing homopolymers, where delocalization spans across many tellurophene repeat units, remains a challenge but is crucial for understanding how the properties of tellurium can be harnessed to their full potential.

Figure 5.1 contains the limited number of polytellurophene homopolymers reported to date. Early examples of polymerizing the parent tellurophene involved using oxidative polymerization with FeCl<sub>3</sub> or electropolymerization; however, both polymerization methods resulted in polytellurophene (**1**) as an insoluble black powder (Figure 5.1).<sup>31,32</sup> Similarly, the electropolymerization of 3,4-dimethoxytellurophene gave a product that was too unstable to definitively characterize, although the authors did observe changes in the UV-vis absorbance spectrum consistent with their calculations on an oligomeric model for poly(3,4-dimethoxytellurophene) (**2**, Figure 5.1).<sup>5</sup> More recently, the polymerization of tellurophenes has been revisited by Seferos and coworkers, who successfully synthesized a series of poly(3-alkyltellurophene)s (**3a-d**, Figure 5.1) *via* Kumada Catalyst-Transfer Polycondensation (KCTP), representing the first solution processible polytellurophenes.<sup>14,15</sup> Rivard and coworkers have also used KCTP to synthesize: 1) polytellurophenes with a cyclohexyl or

cyclopentyl group fused to each tellurophene ring (**4a/b**), and 2) the first poly(3-aryltellurophene) (**5**), however only low molecular weights were obtained, likely due to the lack of solubility of the products leading to early termination of polymer growth.<sup>33</sup>

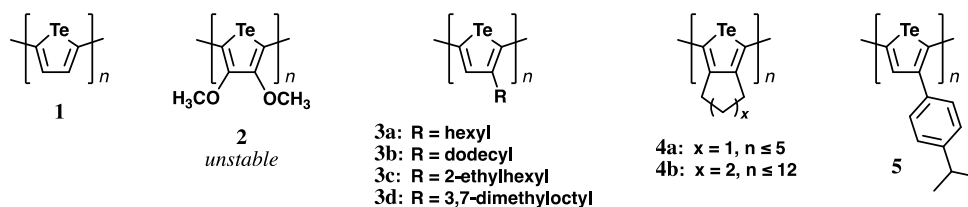


**Figure 5.1** – Known tellurophene-containing homopolymers.

In addition to extending  $\pi$ -conjugation through polymerization, it is also of interest to study  $\pi$ -extended small molecules and macrocycles. One example of an extended  $\pi$ -system incorporating tellurophene is the replacement of pyrrole rings in a porphyrin unit with tellurophene subunits, a substitution that maintains the planar/aromatic character of the porphyrin unit (**6**, Figure 5.2).<sup>34</sup> Furthermore, Xu and coworkers recently reported a versatile synthesis of  $\pi$ -extended dibenzotellurophenes, including ladder-type  $\pi$ -systems (**7**), and heterosumanene (**8**, Figure 5.2).<sup>6</sup> Heterosumanenes represent an interesting class of macrocycle, where the nature of the heteroatoms present can have drastic effects on the optoelectronic properties of the molecule. For example, tritellurasumanene (**8**, Figure 5.2) has a low oxidation potential, resulting in better electron-donating properties when compared to a trithiasumanene or a triselenasumanene.<sup>35</sup> Furthermore, tritellurasumanene (**8**) is planar whereas most other sumanenes are bowl-shaped. As a final example, Huang and coworkers systematically studied the extent of ring-fusion of 2,5-di(PDI)-tellurophene with (2, 3,

or 4 bonds between tellurophene and PDI, PDI = perylene diimide) on OPV device performance. The authors concluded that the highest degree of ring fusion (**9**, Figure 5.2) resulted in the highest power conversion efficiency of 7.5 %.

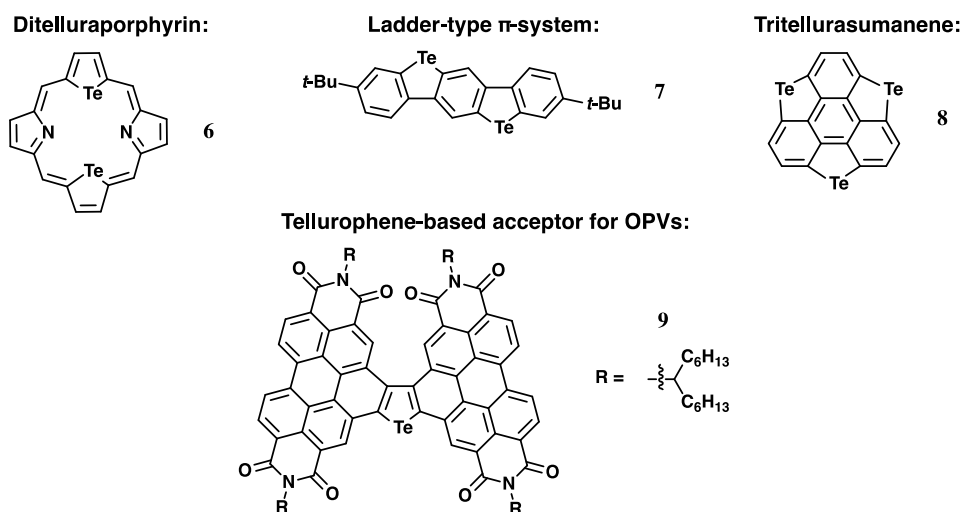


**Figure 5.2** – Examples of tellurophenes incorporated into  $\pi$ -extended molecules.

Another class of  $\pi$ -conjugated macrocycle that has received interest from the chemical community are benzotrithalogenophenes, wherein three chalcogenophene rings are fused around a benzene core. These planar electron-rich aromatics have very good light-absorbing abilities and can form supramolecular assemblies, leading to excellent charge transport properties. For example, a planar benzotrithiophene core induces strong aggregation effects when copolymerized with thiophene or thieno[3,2]thiophene leading to copolymers with hole mobilities up to  $0.24 \text{ cm}^2 \text{ V}^{-1} \text{ s}^{-1}$ .<sup>36</sup> Due to the possibility of different chalcogenophene ring orientations, there are a variety of possible regioisomers; the seven possible isomers for benzotrithiophenes are shown

in Figure 5.3. Of these isomers, the  $C_{2v}$  symmetric **bbc-BTT-3** isomer (Figure 5.3) is predicted to have the smallest HOMO-LUMO gap leading to increased light absorption at higher wavelengths.<sup>37</sup> Hetero(benzo)bithiophenes, where one thiophene is substituted for a different heterocycle, still remain limited. A series of fluorescent phospho(benzo)bithiophene isomers with small HOMO-LUMO gaps that correspond to light absorption into the near-IR region was reported by Matano and coworkers (**10–12**, Figure 5.4).<sup>38,39</sup> Unsymmetric tellura(benzo)bitiophenes (**13a/b**) and tellura(benzo)biselenophenes (**14a/b**) were synthesized by Cheng and coworkers *via* Pd-catalyzed intramolecular C-3 arylation of trichalcogenophenes (Scheme 5.1), however optoelectronic properties were not discussed in detail.<sup>40</sup>

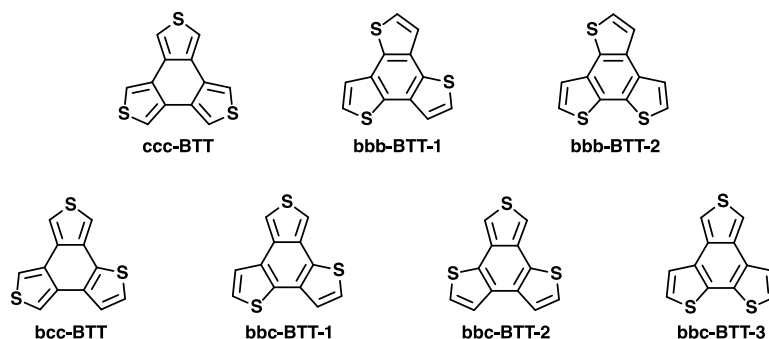


**Figure 5.3** – The seven possible isomers of benzotrithiophene (**BTT**).

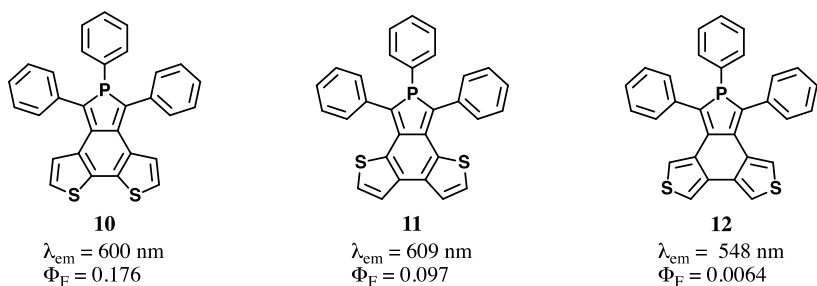
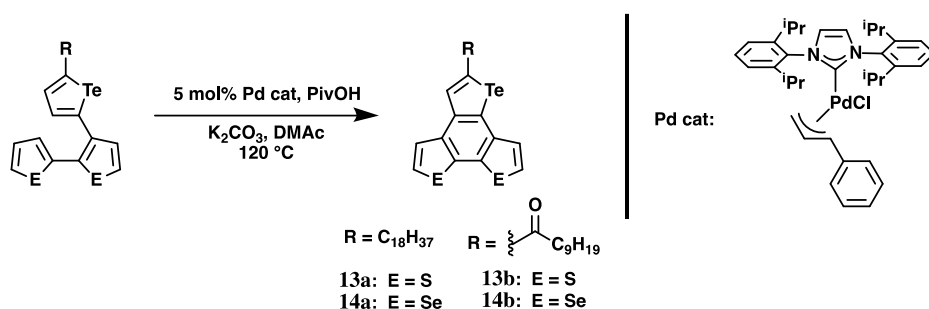


**Figure 5.4** – Phospho(benzo)bithiophene isomers and their fluorescent properties.<sup>38,39</sup>



**Scheme 5.1** – The synthesis of unsymmetrical benzotrithalcoenophenes *via* Pd-catalyzed intramolecular dehydrogenative arylation (DMAc = dimethylacetamide, PivOH = pivalic acid).<sup>40</sup>

Herein, the first synthesis of  $C_{2v}$  symmetric tellura(benzo)bithiophenes (**Te-bbts**) is reported. The incorporation of a tellurophene ring into a benzotrithalcoenophene array is expected to shift the absorbance (and emission) further into the NIR and possibly unlock phosphorescence. In order to further extend the degree of  $\pi$ -conjugation, the **Te-bbt-cumenyl** derivatives were: 1) subjected to ring annulation protocols, and 2) polymerized to form a tellurophene homopolymer (Figure 5.5). Furthermore, the optoelectronic properties **Te-bbt-cumenyl**, **Te-bbt(Me<sub>2</sub>)-f-cumenyl**, and **poly(Te-bbt-cumenyl)** were studied computationally and, where applicable, experimentally.

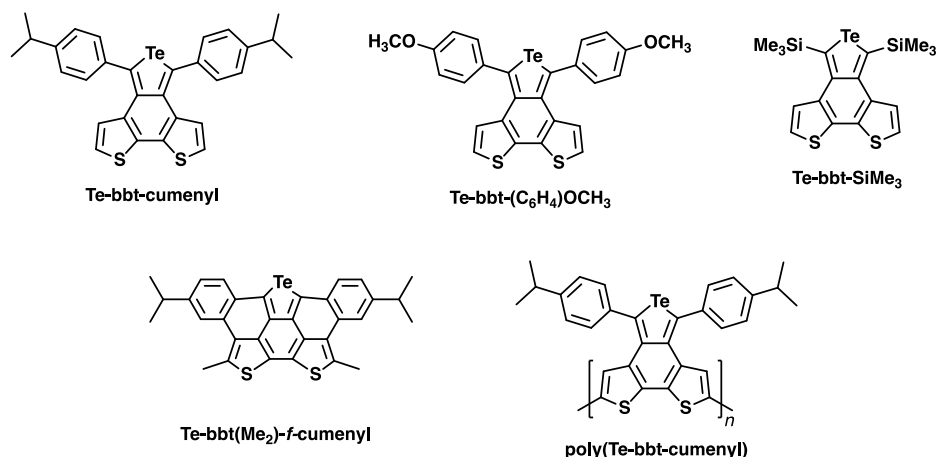


**Figure 5.5** – The  $\pi$ -extended tellura(benzo)bithiophenes mentioned in this Chapter.

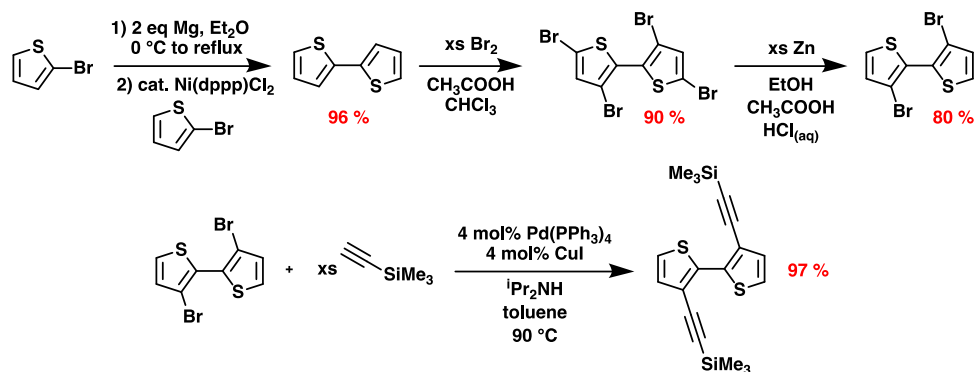
## 5.2 Results and Discussion

### 5.2.1 Synthesis of tellura(benzo)bithiophenes

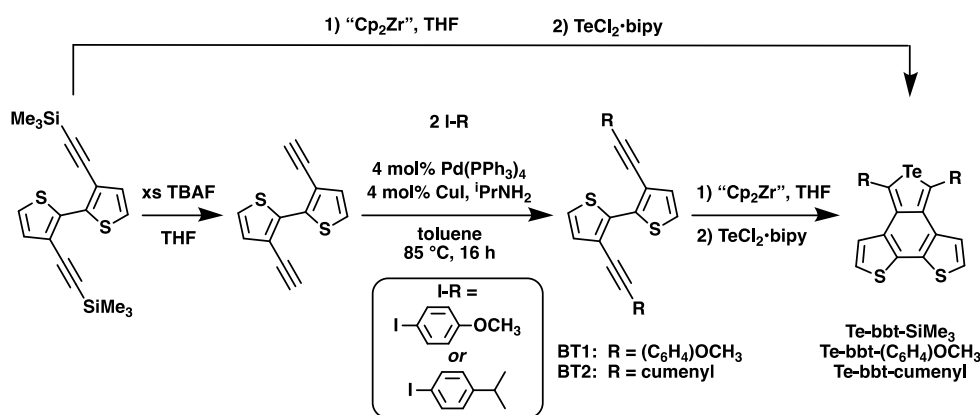
All of the tellura(benzo)bithiophenes (**Te-bbts**) discussed in this Chapter were derived from 3,3'-bis(trimethylsilylethynyl)-2,2'-bithiophene, which can be synthesized *via* a series of high-yielding literature procedures, starting from commercially available 2-bromothiophene (Scheme 5.2).<sup>41-44</sup> This silylated diyne can either be used directly for the preparation of **Te-bbt-SiMe<sub>3</sub>** or it can be deprotected with tetrabutylammonium fluoride (TBAF) to yield 3,3'-diethynyl-2,2'-bithiophene, which is then subjected to another Sonogashira reaction to yield the aryl-functionalized bithiophene diynes, **BT1** and **BT2** (Scheme 5.2). The resulting bithiophene diynes (**BT1** and **BT2**) were transformed into their corresponding **Te-bbts** by first undergoing a zirconium-mediated cyclization utilizing Cp<sub>2</sub>Zr(pyridine)(Me<sub>3</sub>SiC≡CSiMe<sub>3</sub>) as the source of “Cp<sub>2</sub>Zr” ( $\eta^5$ -C<sub>5</sub>H<sub>5</sub>). The resulting zirconacycles were combined *in situ* with the Te<sup>II</sup> source,



$\text{TeCl}_2 \cdot \text{bipy}$  ( $\text{bipy} = 2,2'$ -bipyridine), and transmetallation proceeded to give the tellura(benzo)bithiophenes in moderate yields relative to the diyne (*ca.* 60 % yield for each of **Te-bbtcumenyl** and **Te-bbt-(C<sub>6</sub>H<sub>4</sub>)OCH<sub>3</sub>**, Scheme 5.3). All three **Te-bbts** were obtained as bright yellow solids. Furthermore, **Te-bbt-(C<sub>6</sub>H<sub>4</sub>)OCH<sub>3</sub>** and **Te-bbt-cumenyl** are moisture-stable, allowing them to be purified by column chromatography under ambient conditions. However, due to the low product yields obtained for **Te-bbt-SiMe<sub>3</sub>** (*ca.* 20 %) and the extremely low solubility of **Te-bbt-(C<sub>6</sub>H<sub>4</sub>)OCH<sub>3</sub>**, further reactivity studies were focused on **Te-bbt-cumenyl**.



**Scheme 5.2** – Synthetic procedure for 3,3'-bis(trimethylsilylethynyl)-2,2'-bithiophene with the isolated yields of each reaction step shown in red.



**Scheme 5.3** – Synthesis of diynes **BT1** and **BT2**, **Te-bbt-SiMe<sub>3</sub>**, **Te-bbt-(C<sub>6</sub>H<sub>4</sub>)OCH<sub>3</sub>**, and **Te-bbt-cumenyl**; “ZrCp<sub>2</sub>” = Cp<sub>2</sub>Zr(pyridine)(Me<sub>3</sub>SiC≡CSiMe<sub>3</sub>).

### 5.2.2 Optical absorption properties of Te-bbt-cumenyl

The UV-vis spectrum of **Te-bbt-cumenyl** in THF is shown in Figure 5.6 and features a broad absorbance profile that extends to almost 500 nm. This absorption profile extends to longer wavelengths than the UV-visible spectra of the unsymmetrical tellura(benzo)bithiophene/tellura(benzo)selenophenes featuring alkyl groups (**13a/14a**), which have onsets of absorbance < 375 nm and (**14d**), and relative to analogues with acyl functional groups (**13b/14b**), which each have an onset of absorbance of *ca.* 450 nm (Scheme 5.1),<sup>40</sup> indicating a smaller optical bandgap for **Te-bbt-cumenyl**. Computations performed at the B3LYP/cc-pVDZ(-PP) level of theory were used to evaluate the nature of the excitation processes in **Te-bbt-cumenyl**. TD-DFT computations reveal three main excitations, all of which are all aromatic  $\pi$ - $\pi^*$  in nature, with some Te(p-orbital) involvement (Figure 5.7). This is consistent with the experimental data which contains three distinguishable spectral features.

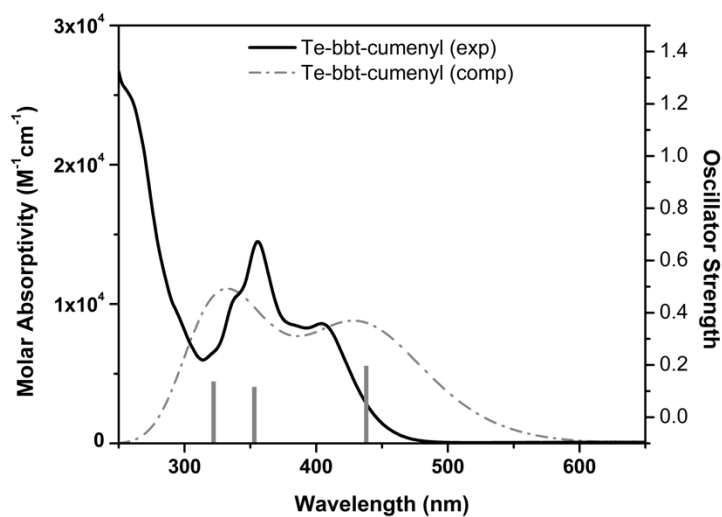


**Figure 5.6** – Experimental UV-vis spectrum of **Te-bbt-cumenyl** in THF (black line, concentration =  $2.99 \times 10^{-5}$  M) and computed UV-vis spectrum shown in grey along with oscillator strengths for the main predicted transitions (computed at the B3LYP/cc-pVDZ(-PP) level of theory).

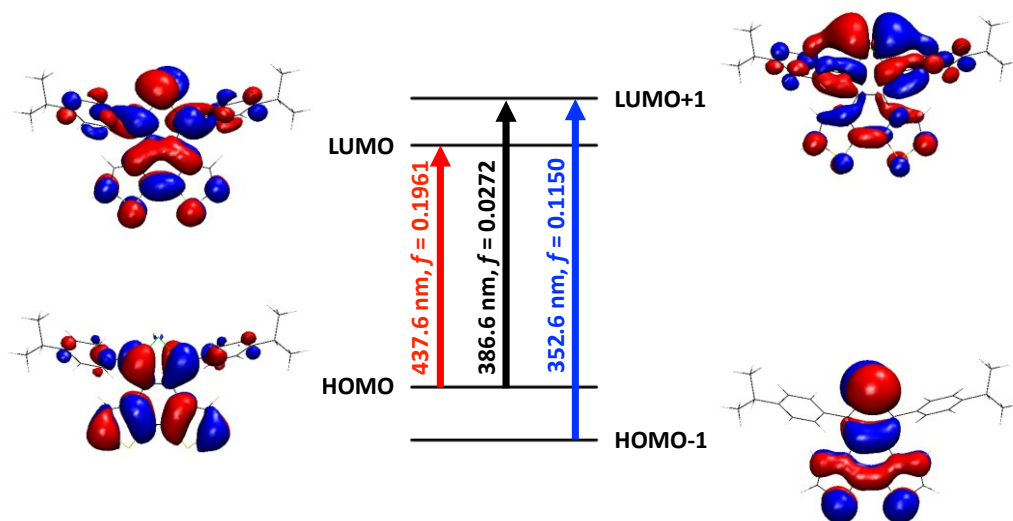


**Figure 5.7** – TD-DFT [B3LYP/cc-pVDZ(-PP)] computed main transitions for **Te-bbt-cumenyl**, including excitation wavelengths and oscillator strengths ( $f$ ) for the most intense transitions ( $S_0$ - $S_1$ : red;  $S_0$ - $S_2$ : black;  $S_0$ - $S_3$ : blue) along with the associated molecular orbitals; iso-surface values of +0.02/-0.02 (red/blue).

### 5.2.3 Investigating the oxidative decomposition of **Te-bbt-cumenyl**

**Te-bbt-cumenyl** is a thermally stable yellow solid with a decomposition temperature of 311 °C (Figure 5.8) and can be stored for over a year in the absence of light or oxygen. However, prolonged exposure to light and oxygen leads to a gradual decomposition that occurs both in the solid state and in solution. For example, a solution of **Te-bbt-cumenyl** in CDCl<sub>3</sub> produces a black precipitate if left in a lit fumehood for several days. To further explore this decomposition, a solution of **Te-bbt-cumenyl** in THF was irradiated with 355 nm light (75 W) for 20-minute time intervals and the changes in the UV-vis absorbance spectra were monitored by recording a spectrum after each irradiation event. As shown in Figure 5.9, a noticeable decrease in absorbance at 355 and 403 nm is observed after each irradiation. It should be noted that no decomposition was observed when a solution of **Te-bbt-cumenyl** in C<sub>6</sub>D<sub>6</sub>, sealed under an N<sub>2</sub> atmosphere, was irradiated with a Hg lamp (100 W) for 1 hour.

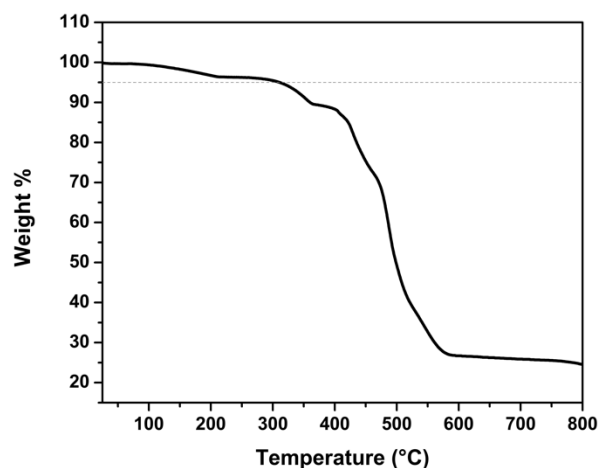


**Figure 5.8** – TGA plot of **Te-bbt-cumenyl** measured under air at 10 °C/minute. The horizontal dashed line indicates the point at which 5 % mass loss occurs.

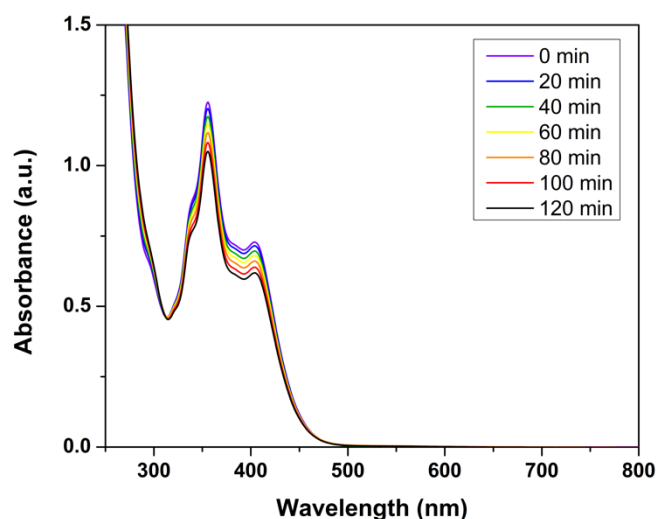


**Figure 5.9** – UV-vis absorbance spectra recorded after irradiating a solution of **Te-bbt-cumenyl** in THF with 355 nm (75 W) for 20 minute time intervals. Initial concentration of **Te-bbt-cumenyl** was  $6.00 \times 10^{-5}$  M. Before irradiation, the solution was sparged with air for one minute.

In 2010, Seferos and coworkers reported the photochemical decomposition of 2,5-diphenyltellurophene to produce an ene-dione and  $\text{TeO}_2$  in the presence of oxygen

and UV-light irradiation (365 nm).<sup>29</sup> The authors noted that the chemical oxidation of 2,5-diphenyltellurophene with *m*-CPBA (*meta*-chloroperoxybenzoic acid) also produced TeO<sub>2</sub> and the ene-dione, however an intermediate consistent with a telluroxide was detected by the emergence of a red-shifted absorbance peak, as well as *via* <sup>1</sup>H/<sup>125</sup>Te NMR spectroscopy. Interestingly, photodecomposition was still observed for 2,5-diphenyltellurophene under irradiation of UV-light (365 nm) in the absence of oxygen, likely producing elemental tellurium in this case.

The gradual decomposition of **Te-bbt-cumenyl** in the presence of both light and oxygen, prompted us to investigate whether a telluroxide and/or tellurone could also be a potential decomposition product of **Te-bbt-cumenyl** (Figure 5.10). DFT computations were performed at the B3LYP level of theory and the resulting HOMO and LUMOs of **Te-bbt-cumenyl**, **TeO-bbt-cumenyl** (telluroxide) and **TeO<sub>2</sub>-bbt-cumenyl** (tellurone) are presented in Figure 5.11. TD-DFT computations were also performed at the same level of theory in order to predict the UV-vis absorbance spectra of **Te-bbt-cumenyl**, **TeO-bbt-cumenyl** and **TeO<sub>2</sub>-bbt-cumenyl**, as well as for the corresponding ene-dione. As shown in Figure 5.12, both **TeO-bbt-cumenyl** and **TeO<sub>2</sub>-bbt-cumenyl** are predicted to have a red-shifted absorption profile relative to **Te-bbt-cumenyl**, whereas the ene-dione should increase the absorption at lower wavelengths. Although the experimentally measured decrease in absorbance at 355/403 nm is only observed when **Te-bbt-cumenyl** is irradiated with UV-light in the presence of oxygen, it does not appear to be accompanied by the appearance of new red-shifted spectral features (Figure 5.9), which are expected for the formation of a telluroxide or tellurone.

However, it is necessary to push the photodecomposition of **Te-bbt-cumenyl** to completion in order to verify this. It is possible that oxidation of the carbon framework of **Te-bbt-cumenyl** occurs in a similar fashion to 2,5-diphenyltellurophene, potentially forming the ene-dione shown in Figure 5.10 and releasing  $\text{TeO}_2$ .

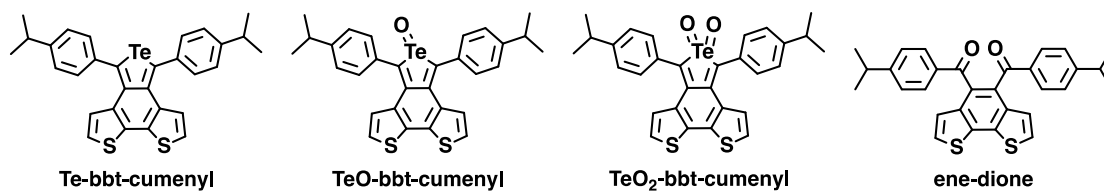


**Figure 5.10** – The structure of **Te-bbt-cumenyl** as well as the potential oxidation products: **TeO-bbt-cumenyl**, **TeO<sub>2</sub>-bbt-cumenyl**, and the corresponding ene-dione.

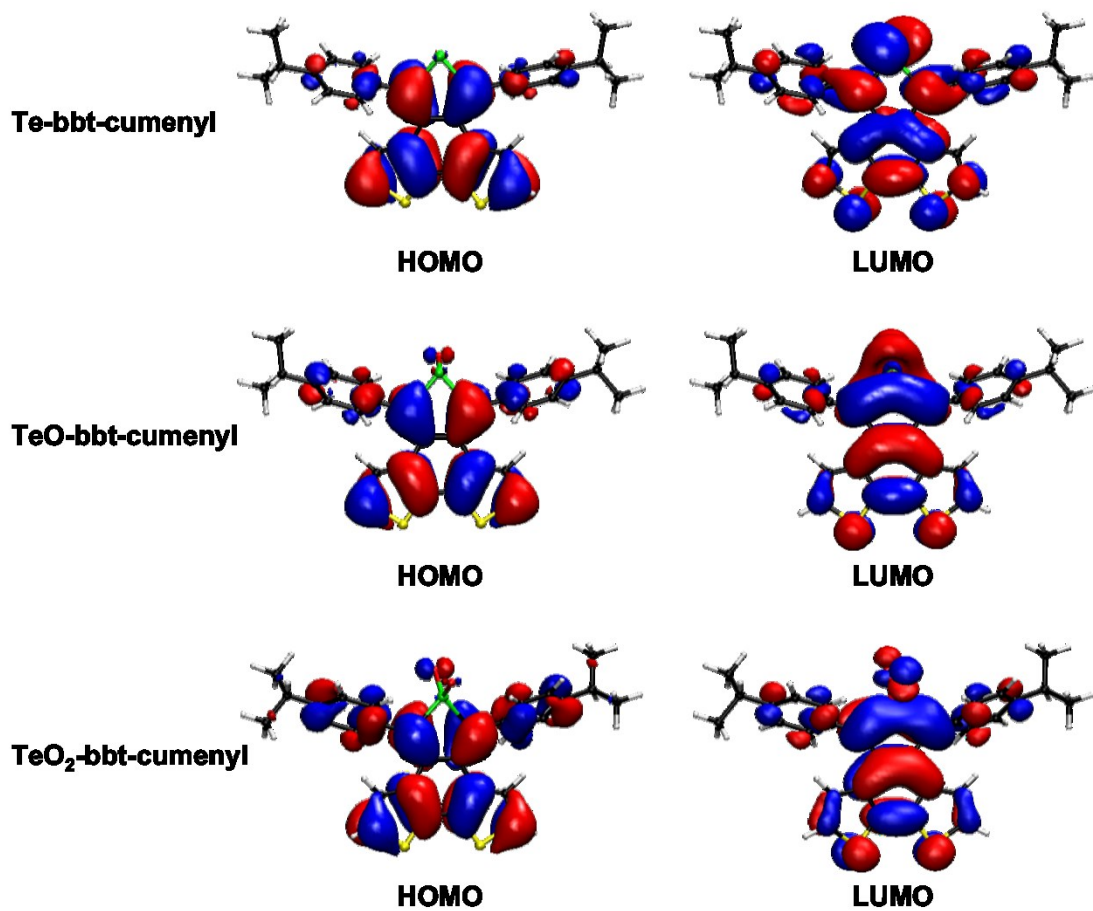


**Figure 5.11** – LUMO (*left*) and HOMO (*right*) of Te-bbt-cumenyl, TeO-bbt-cumenyl, and TeO<sub>2</sub>-bbt-cumenyl at the S<sub>0</sub> state equilibrium geometry as determined at the B3LYP/cc-pVDZ(-PP) level of theory in the gas-phase. Iso-surface values of +0.02/-0.02 (red/blue).



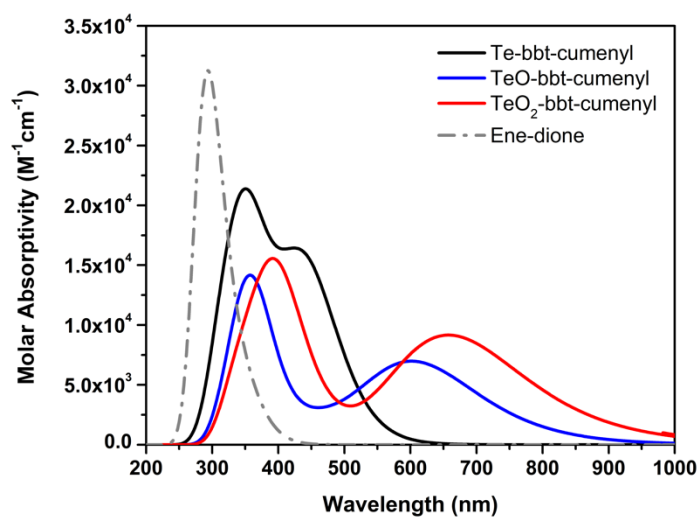
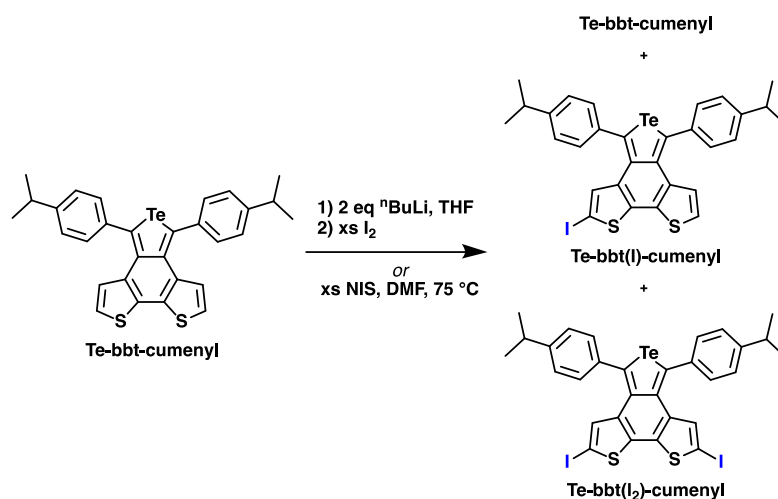


**Figure 5.12** – Calculated UV-vis spectra of **Te-bbt-cumenyl** (black), **TeO-bbt-cumenyl** (blue), **TeO<sub>2</sub>-bbt-cumenyl** (red), and the ene-dione (grey dash-dotted line) determined at the B3LYP/cc-pVDZ(-PP) level of theory using a THF polarizable continuum model (PCM).

#### 5.2.4 Synthesis of Te-bbt-cumenyl derivatives

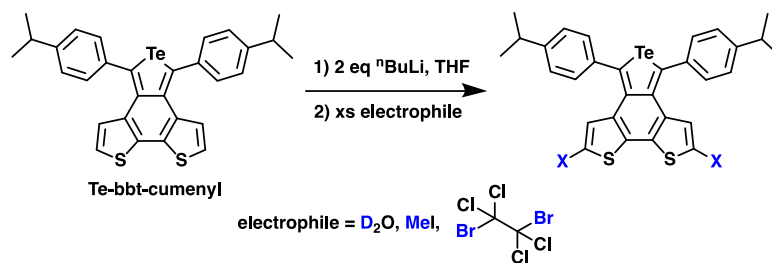
With the 2,2'-positions of the bithiophene still available for reactivity, further extension of the  $\pi$ -conjugation in **Te-bbt-cumenyl** was attempted. In the hope of forming a polymer *via* Kumada Catalyst-Transfer Polycondensation (KCTP), a dihalogenated monomer was first targeted. Due to the reactive nature of the Te centre, care must be taken to avoid halogenating the Te atom. Although facile oxidation of Te(II) to Te(IV) occurs in the presence of brominating agents such as Br<sub>2</sub>,<sup>48</sup> tellurophenes are more tolerable to ring iodination protocols, therefore the diiodinated tellurophene **Te-bbt(I<sub>2</sub>)-cumenyl** was the initial synthetic target (Scheme 5.4). Unfortunately, combining **Te-bbt-cumenyl** with NIS (*N*-iodosuccinimide) led to no discernible reaction overnight at room temperature or when the reaction mixture was

heated to 45 °C for the same time period. Increasing the reaction temperature to 75 °C with heating overnight resulted in sluggish reactivity between **Te-bbt-cumenyl** and NIS (Scheme 5.4) affording 60 % of di-iodinated (**Te-bbt(I<sub>2</sub>)-cumenyl**) and 32 % of mono-iodinated tellura(benzo)bithiophene (**Te-bbt(I)-cumenyl**), with 8 % of unreacted **Te-bbt-cumenyl** remaining. Attempts to improve the yield of **Te-bbt(I<sub>2</sub>)-cumenyl** by increasing the temperature to 110 °C or *via* the addition of acetic acid proved futile. Treatment of **Te-bbt-cumenyl** with 2 equivalents of <sup>n</sup>BuLi, followed by the addition of excess I<sub>2</sub>, also consistently gave product mixtures (di-iodinated, mono-iodinated, and unreacted **Te-bbt-cumenyl**). It should be noted that all attempts to separate the di-iodinated and mono-iodinated tellura(benzo)bithiophenes using column chromatography or fractional crystallization were unsuccessful.



**Scheme 5.4** – The partial iodination of **Te-bbt-cumenyl** and the resulting mixture of di-iodinated, mono-iodinated, and unreacted **Te-bbt-cumenyl**.

Despite the above-mentioned difficulties in forming a di-iodinated product, **Te-bbt-cumenyl** does undergo facile lithiation at the 5,5'-positions of the bithiophene unit. Addition of D<sub>2</sub>O to the di-lithiated intermediate **Te-bbt(Li<sub>2</sub>)-cumenyl** (prepared by combining **Te-bbt-cumenyl** with two equivalents of <sup>n</sup>BuLi) results in the clean conversion to **Te-bbt(D<sub>2</sub>)-cumenyl**, as evidenced by <sup>1</sup>H NMR spectroscopy. Similarly, addition of methyl iodide (MeI) to **Te-bbt(Li<sub>2</sub>)-cumenyl** produces **Te-bbt(Me<sub>2</sub>)-cumenyl** as the sole product, as determined by <sup>1</sup>H NMR spectroscopy. Furthermore, treatment of di-lithiated **Te-bbt(Li<sub>2</sub>)-cumenyl** with excess 1,2-tetrachloro-1,2-dibromoethane (Cl<sub>2</sub>BrC-CBrCl<sub>2</sub>) led to the clean formation of the dibrominated product **Te-bbt(Br<sub>2</sub>)-cumenyl** in a 70 % yield after work-up (Scheme 5.5). The attempted polymerization of **Te-bbt(Br<sub>2</sub>)-cumenyl** *via* KCTP conditions is discussed in section 5.2.7.



**Scheme 5.5** – Lithiation of **Te-bbt-cumenyl** followed by reaction with an electrophile to synthesize: **Te-bbt(D<sub>2</sub>)-cumenyl** (X = D), **Te-bbt(Me<sub>2</sub>)-cumenyl** (X = Me), and **Te-bbt(Br<sub>2</sub>)-cumenyl** (X = Br).

### 5.2.5 Solid state structures of the tellura(benzo)bithiophenes

Three tellura(benzo)bithiophenes (**Te-bbt-SiMe<sub>3</sub>**, **Te-bbt-(C<sub>6</sub>H<sub>4</sub>)OCH<sub>3</sub>**, **Te-bbt-cumenyl**) as well as the brominated product **Te-bbt(Br<sub>2</sub>)-cumenyl** were structurally characterized by single-crystal X-ray crystallography (Figures 5.14 to 5.17). To the best of my knowledge, the only other structurally characterized [*c*]-hetero(benzo)-[*b,b*]-bithiophenes include **10**, **15a**, and **15b** (Figure 5.13).<sup>37,38</sup> In each of the **Te-bbts** studied by X-ray crystallography in this Chapter, the tellurophene ring is nearly coplanar with the fused thiophene rings, with angles between the plane of the tellurophene and thiophene rings ranging from 4.67 to 11.59°. These results are similar to **10** (for angles between the phosphole and thiophene planes), however **15a/b** exhibits nearly perfect coplanarity with angles between the planes of each thiophene rings, deviating by  $\leq 1.81^\circ$ . Furthermore, the intraring C-E-C (E = P, S, or Te) angles are substantially reduced for our **Te-bbt** analogues [E = Te; 83.1(4)–85.9(2)°] when compared to the thiophene [E = S; 91.20(6)–91.42(13)°] or phosphole (E = P; 92.22(7)°] derivatives, suggesting that a higher degree of p-character exists within the Te-C bonds.

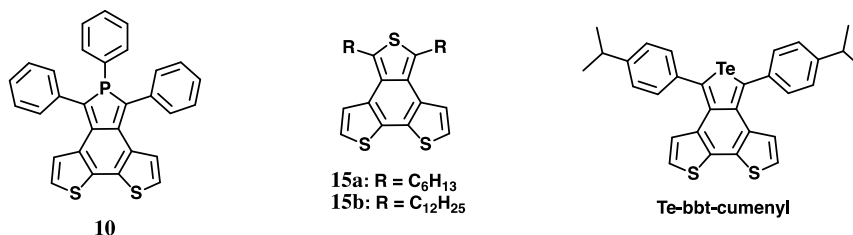


**Figure 5.13** – Structurally characterized [*c*]-hetero(benzo)-[*b,b*]-bithiophenes in the literature and **Te-bbt-cumenyl**.<sup>37,38</sup>

Due to the metalloid nature of the tellurium atom, intermolecular Te...Te interactions are of interest, as they have been reported to quench phosphorescence (*via* triplet-triplet annihilation) when the distance is less than the sum of the van der Waals radius of tellurium (4.20 Å).<sup>49</sup> The only **Te-bbt** that exhibits such close Te...Te interactions in this Chapter is **Te-bbt-(C<sub>6</sub>H<sub>4</sub>)OCH<sub>3</sub>**, which contains close intermolecular Te...Te distances of 3.78 Å in the solid state; this distance is comparable to the shortest intermolecular Te...Te interaction reported for a tellurophene (3.61 Å for **7**, Figure 5.2).<sup>6</sup> In contrast, the closest intermolecular Te...Te interactions in the solid state for **Te-bbt-SiMe<sub>3</sub>**, **Te-bbt-cumenyl**, and **Te-bbt(Br<sub>2</sub>)-cumenyl** are much longer, at 5.07 Å, 6.03 Å, and 5.23 Å respectively, suggesting that solid state phosphorescence may be possible from these tellurophenes.

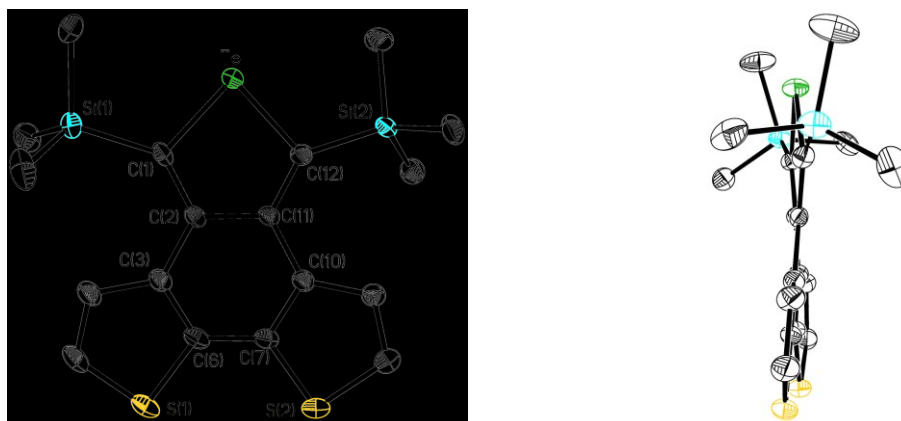


**Figure 5.14** – Molecular structure of **Te-bbt-SiMe<sub>3</sub>** (*left*) and a sideview (*right*) with thermal ellipsoids presented at a 30 % probability level. All hydrogen atoms have been omitted for clarity. Selected bond lengths [Å] and angles [°]: Te–C1 2.050(5), Te–C12 2.057(5), S1–C5 1.705(7), S1–C6 1.734(5), S2–C7 1.721(5), S2–C8 1.727(6), C1–C2 1.398(7), C2–C3 1.456(6), C2–C11 1.484(7), C3–C4 1.434(7), C4–C5 1.357(8), C6–C7 1.407(8), C8–C9 1.358 (7), C9–C10 1.431 (7), C10–C11 1.470(6), C11–C12 1.391(7); C1–Te–C12 85.9(2), C5–S1–C6 91.2(3), C7–S2–C8 91.1(3).

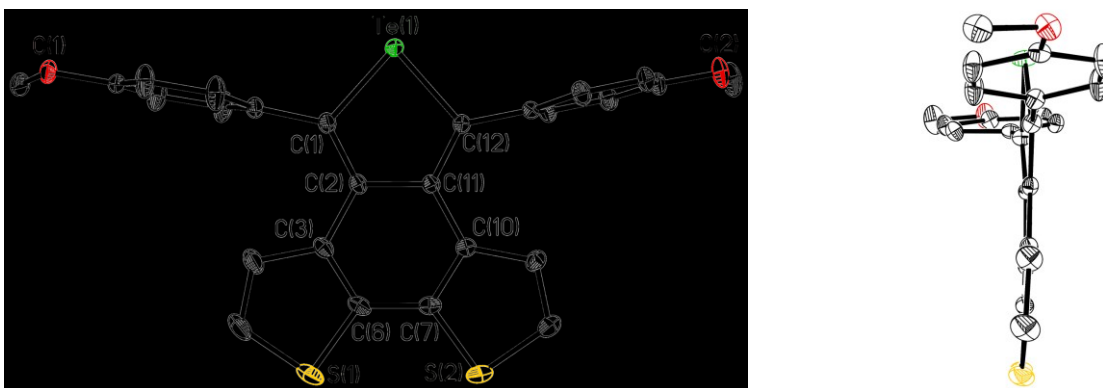


**Figure 5.15** – Molecular structure of **Te-bbt-(C<sub>6</sub>H<sub>4</sub>)OCH<sub>3</sub>** (*left*) and a sideview (*right*) with thermal ellipsoids presented at a 30 % probability level. All hydrogen atoms have been omitted for clarity. Selected bond lengths [Å] and angles [°]: Te1–C1 2.0509(14), Te1–C12 2.0567(14), S1–C5 1.714(2), S1–C6 1.7223(14), S2–C7 1.7252(15), S2–C8 1.7154(18), C1–C2 1.376(2), C2–C3 1.4631(19), C2–C11 1.4781(18), C3–C4 1.438(2), C4–C5 1.359(3), C6–C7 1.425(2), C8–C9 1.358 (2), C9–C10 1.4374 (19), C10–C11 1.4612(18), C11–C12 1.3754(19); C1–Te1–C12 83.32(5), C5–S1–C6 91.08(8), C7–S2–C8 91.07(7).

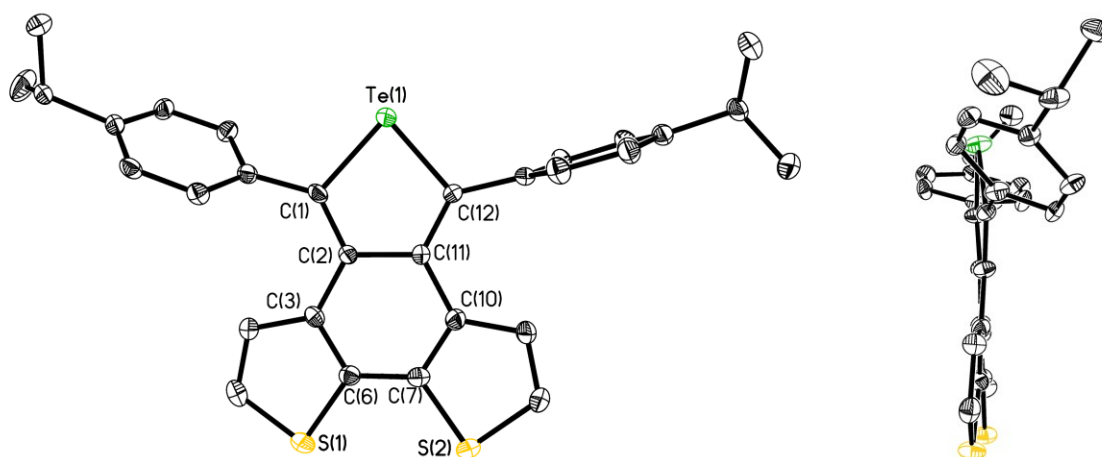


**Figure 5.16** – Molecular structure of *Te-bbt-cumenyl* (*left*) and a sideview (*right*) with thermal ellipsoids presented at a 30 % probability level. All hydrogen atoms have been omitted for clarity. Selected bond lengths [Å] and angles [°]: Te1–C1 2.062(10), Te1–C12 2.047(10), S1–C5 1.710(13), S1–C6 1.730(11), S2–C7 1.730(11), S2–C8 1.724(13), C1–C2 1.377(15), C2–C3 1.448(14), C2–C11 1.478(14), C3–C4 1.435(15), C4–C5 1.364(17), C6–C7 1.421(15), C8–C9 1.357 (17), C9–C10 1.433 (15), C10–C11 1.471(15), C11–C12 1.381(15); C1–Te1–C12 83.1(4), C5–S1–C6 90.7(6), C7–S2–C8 90.8(6).



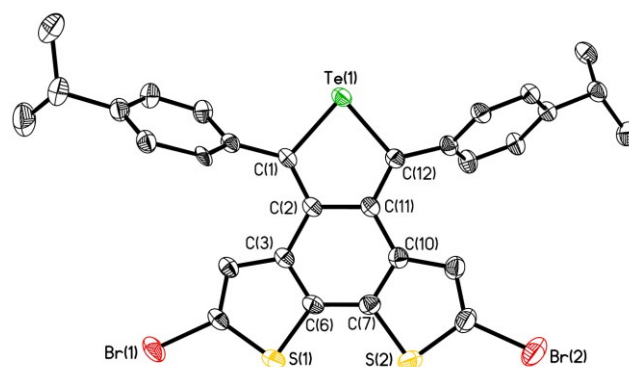


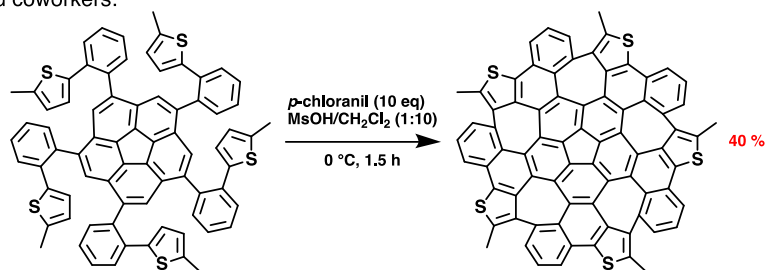
**Figure 5.17** – Molecular structure of **Te-bbt(Br<sub>2</sub>)-cumenyl** with thermal ellipsoids presented at a 30 % probability level. The diisopropyl groups are disordered and only the major orientation is shown. All hydrogen atoms have been omitted for clarity. Selected bond lengths [Å] and angles [°]: Te1–C1 2.056(3), Te1–C12 2.055(3), S1–C5 1.721(4), S1–C6 1.727(4), S2–C7 1.732(4), S2–C8 1.722(5), C1–C2 1.374(5), C2–C3 1.462(5), C2–C11 1.471(5), C3–C4 1.434(5), C4–C5 1.353(5), C6–C7 1.424(5), C8–C9 1.347 (6), C9–C10 1.437 (5), C10–C11 1.460(5), C11–C12 1.378(5); C1–Te1–C12 83.36(13), C5–S1–C6 90.11(18), C7–S2–C8 89.9(2).

### 5.2.6 Attempted intramolecular annulation of Te-bbt-cumenyl

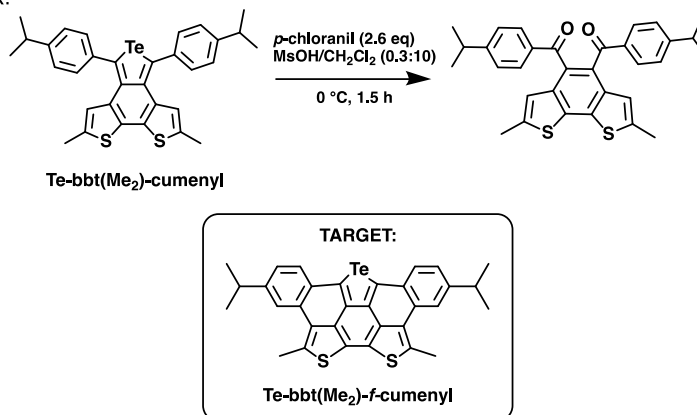
Using a Scholl-type reaction, the annulation of the 4,4'-position of the bithiophene unit in **Te-bbt-cumenyl** to produce additionally ring-fused 6-membered rings was attempted (Scheme 5.6). Such an annulation should lock all aromatic subunits into a rigid (and possibly planar) configuration and extend the  $\pi$ -conjugation further into the cumenyl side groups. One inspiration for this reaction was chemistry developed by Itami and coworkers, who successfully used *p*-chloranil to fuse aryl rings attached to a corannulene core (Scheme 5.6).<sup>50</sup> In addition, Huang and coworkers were able to use FeCl<sub>3</sub> to fuse the 3- and 4-positions of the tellurophene moiety in a 2,5-di(PDI)-tellurophene (PDI = perylene di-imide), such that each carbon atom of the tellurophene

ring was bound to a PDI unit (Scheme 5.7).<sup>7</sup> Huang discovered that the extent of ring-fusion played a critical role in the planarity and solid state packing of the resulting molecules, ultimately influencing OPV device performance when included in the active layer. Of note, Tsukamoto and Dong recently reported a cobaloxime-catalyzed dehydrogenative cyclization of *o*-teraryls under UV-light irradiation that, unlike the Scholl reaction, occurs in the absence of a strong acid or oxidant.<sup>51</sup>

a) Itami and coworkers:



b) This work:

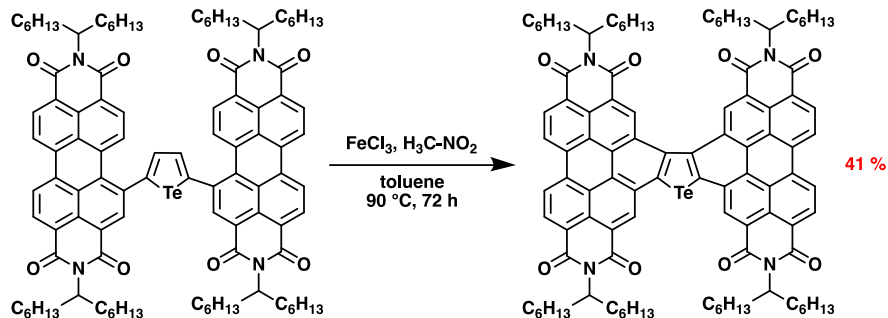


**Scheme 5.6** – a) Itami's procedure for annulating thiophene rings with aryl rings around a sumanene core; b) attempting to apply Itami's protocol to **Te-bbt(Me<sub>2</sub>)-cumenyl**.

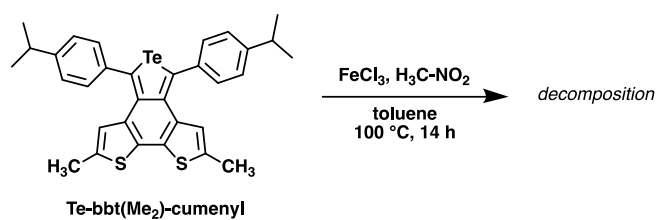
The 5,5'-positions of the bithiophene are reactive sites in **Te-bbt(Me<sub>2</sub>)-cumenyl** that must be taken into consideration, as indicated by the preferential lithiation at these

positions (Scheme 5.5). These sites are problematic since fusing the cumenyl groups with the 5,5'-positions of bithiophene would lead to large 7- or 8-membered rings. In order to encourage reactivity at the less reactive 4,4'-positions and form more rigid 6-membered rings, the methylated analogue **Te-bbt(Me<sub>2</sub>)-cumenyl** was subjected to similar reaction conditions as those implemented by the groups of Itami and Huang (Schemes 5.6 and 5.7). With methyl groups already occupying the 5,5'-positions of the bithiophene ring, this should shut down any potential reactivity at these positions. Whereas the combination of **Te-bbt(Me<sub>2</sub>)-cumenyl** with FeCl<sub>3</sub> led to decomposition into unidentified (mostly insoluble) products, the combination of **Te-bbt(Me<sub>2</sub>)-cumenyl** with *p*-chloranil did result in the formation of a new major product by <sup>1</sup>H NMR spectroscopy (Figure 5.18), however the <sup>13</sup>C{<sup>1</sup>H} NMR spectrum of this product contains a peak at 196.9 ppm (Figure 5.19) typical for carbonyls. Furthermore, mass spectrometry identified the presence of the ene-dione (expected = 510.16872, measured = 510.16817) and none of the target annulated tellurophene **Te-bbt(Me<sub>2</sub>)-f-cumenyl** (Scheme 5.6) or annulated ene-dione were detected. This reaction consistently gave the same major product even when careful attention was paid to exclude oxygen in the work-up. Furthermore, this oxidation product is occasionally detected in small amounts in the <sup>1</sup>H NMR spectrum of **Te-bbt-cumenyl** samples. These results suggest that **Te-bbt-cumenyl** is not stable to the reaction conditions, which accelerate its oxidative decomposition. The decomposition product is prematurely assigned to the ene-dione shown in Scheme 5.6 on the basis of <sup>1</sup>H NMR spectroscopy and mass spectrometry data (*vide supra*).

a) Huang and coworkers:



b) This work:



**Scheme 5.7** – a) Huang's procedure for annulating a tellurophene ring with adjoining PDI units; b) application of Huang's protocol to **Te-bbt(Me<sub>2</sub>)-cumenyl**.

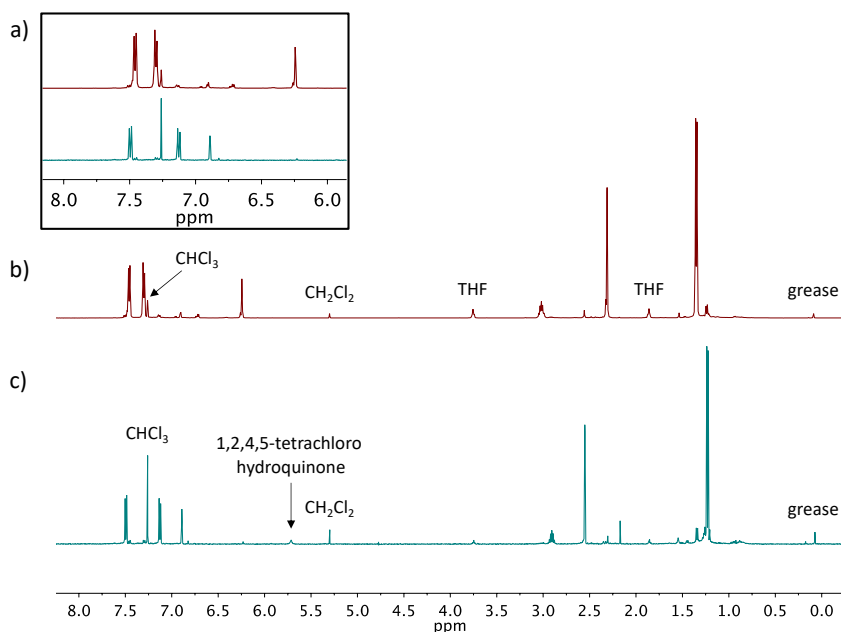


**Figure 5.18** – Stacked  $^1\text{H}$  NMR spectra (recorded in  $\text{CDCl}_3$ ) of a) a close-up of the aryl region, b) **Te-bbt(Me<sub>2</sub>)-cumenyl**, and c) reaction of **Te-bbt(Me<sub>2</sub>)-cumenyl** with *p*-chloranil after work-up.

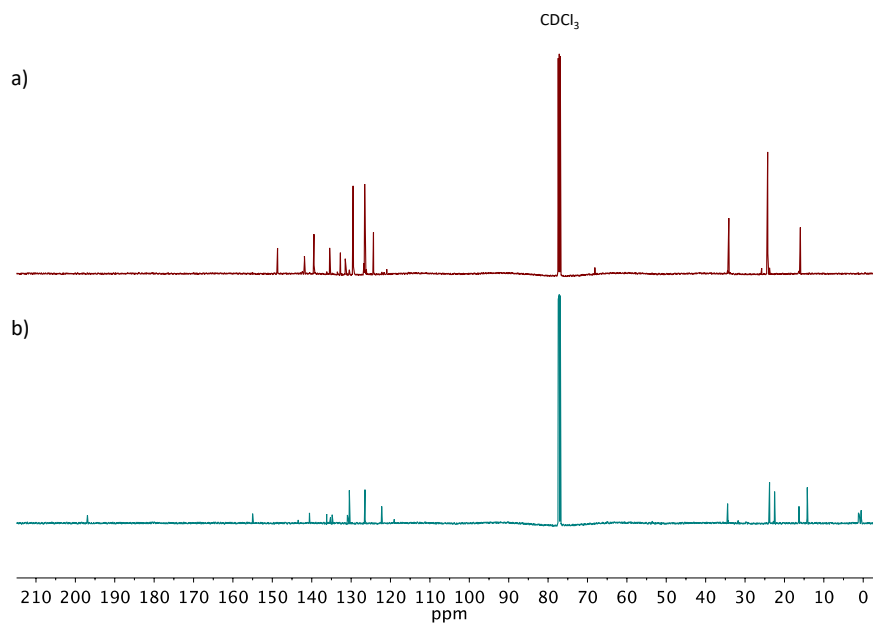


**Figure 5.19** – Stacked  $^{13}\text{C}\{^1\text{H}\}$  NMR spectra (in  $\text{CDCl}_3$ ) of a) **Te-bbt(Me<sub>2</sub>)-cumenyl**, and b) the result of combining **Te-bbt(Me<sub>2</sub>)-cumenyl** with *p*-chloranil.

### 5.2.7 A computational study on **Te-bbt(Me<sub>2</sub>)-cumenyl** and its annulated derivative **Te-bbt(Me<sub>2</sub>)-*f*-cumenyl**

Despite being unable to isolate the target annulated product **Te-bbt(Me<sub>2</sub>)-*f*-cumenyl**, ground state geometry optimizations at the B3LYP/cc-pVDZ(-PP) level of theory suggested that this compound is thermodynamically stable. In Figure 5.20, the frontier molecular orbitals of **Te-bbt(Me<sub>2</sub>)-cumenyl** and **Te-bbt(Me<sub>2</sub>)-*f*-cumenyl** are compared. The HOMO and LUMO are generally similar for both the fused and unfused compounds, with no tellurium orbital contribution to the HOMO, whereas each LUMO contains a significant amount of Te p-character along with orbital density across the entire fused arene scaffold. One notable difference is that the annulated molecule **Te-bbt(Me<sub>2</sub>)-*f*-cumenyl** contains a greater contribution from the cumenyl groups to both the HOMO and LUMO as a result of locking these groups into a coplanar arrangement, thus extending  $\pi$ -conjugation throughout the molecule. Furthermore, by extending the  $\pi$ -conjugation the LUMO energy of **Te-bbt(Me<sub>2</sub>)-*f*-cumenyl** is reduced by 0.446 eV relative to **Te-bbt(Me<sub>2</sub>)-cumenyl** (the HOMO of **Te-bbt(Me<sub>2</sub>)-*f*-cumenyl** is raised by 0.241 eV). This results in a substantial reduction of the HOMO-LUMO gap of **Te-bbt(Me<sub>2</sub>)-*f*-cumenyl** by 0.687 eV, as shown in Figure 5.20.

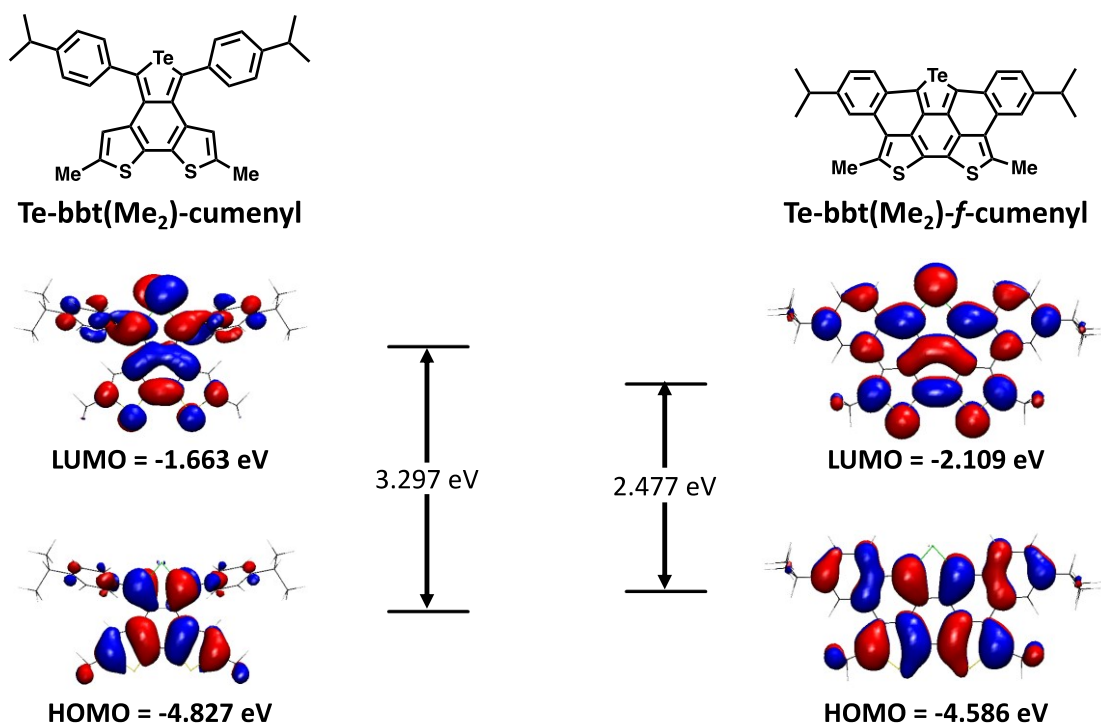


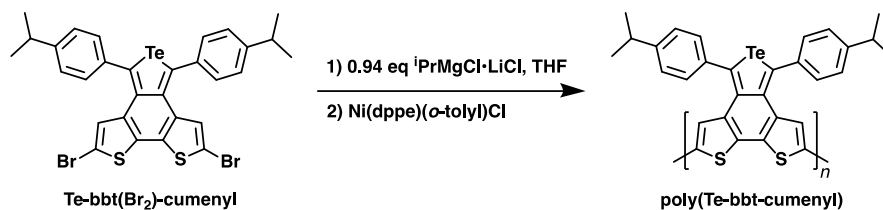
**Figure 5.20** – The HOMO and LUMO along with their corresponding energies, of **Te-bbt(Me<sub>2</sub>)-cumenyl** (*left*) and **Te-bbt(Me<sub>2</sub>)-f-cumenyl** (*right*) computed at the B3LYP/cc-pVDZ(-PP) level of theory.

### 5.2.8 Polymerization of Te-bbt(Br<sub>2</sub>)-cumenyl

As previously discussed, extending the  $\pi$ -conjugation by synthesizing a homopolymer of **Te-bbt-cumenyl** is a goal of this work (Scheme 5.8). Kumada Catalyst-Transfer Polycondensation (KCTP) was chosen as the polymerization method as it often yields high molecular weight polymers with low dispersities ( $\mathcal{D}$ ), attributed to the chain-growth mechanism involved.<sup>52</sup> Furthermore, KCTP has been used to polymerize thiophenes, selenophenes, and tellurophenes by Seferos and coworkers.<sup>14,15,53,54</sup> Following a procedure established by the Seferos group<sup>54</sup> **Te-**

**bbt(Br<sub>2</sub>)-cumenyl** was treated with a slightly sub-stoichiometric amount of <sup>i</sup>PrMg•LiCl in THF, followed by a reaction with Ni(dppe)(*o*-tolyl)Cl (dppe = bis(diphenylphosphino)ethane), a more soluble and reactive KCTP pre-catalyst in comparison to the commonly used Ni(dppe)Cl<sub>2</sub> (Scheme 5.8).<sup>55</sup> The resulting polymer was initially purified *via* Soxhlet extraction to recover a red material with a M<sub>w</sub> of 32 kDa and a *D* of 1.5, as determined by gel permeation chromatography (GPC). However, the product appears to be unstable to light/air, completely losing its colour after 2 days of light exposure under ambient conditions (Figure 5.21). Photodegradation into the ene-dione polymer without retention of the Te atom, similar to the photodegradation proposed for **Te-bbt-cumenyl** was substantiated by mass spectrometry analysis (MALDI-TOF), which confirmed the presence of oligomeric ene-diones. The decomposition is also accompanied by changes in the <sup>1</sup>H NMR spectrum. Figure 5.22 shows the full <sup>1</sup>H NMR spectrum of **Te-bbt(Br<sub>2</sub>)-cumenyl** the **poly(Te-bbt-cumenyl)** after limited exposure to air, whereas Figure 5.23 shows the changes that occur in different regions of the <sup>1</sup>H NMR spectrum after exposure to ambient conditions (including light) for 3 days. Of note, the <sup>1</sup>H NMR of the polymer purified by Soxhlet extraction matches that of the decomposed polymer.





**Scheme 5.8** – Polymerization of **Te-bbt(Br<sub>2</sub>)-cumenyl** under KCTP conditions.

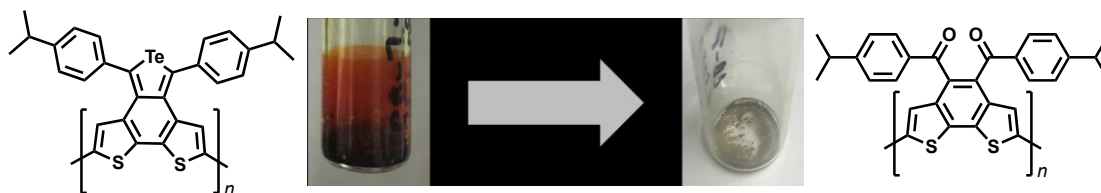


**Figure 5.21** – A sample of **poly(Te-bbt-cumenyl)** as synthesized (*left*) and after sitting in a lit room for 2 days under ambient conditions (*right*).

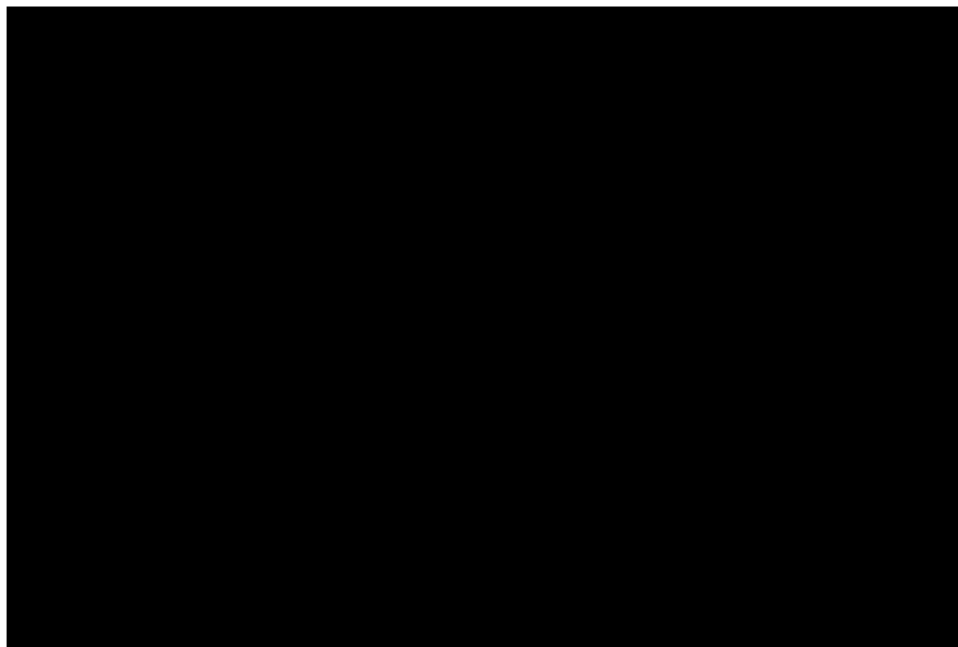


**Figure 5.22** – <sup>1</sup>H NMR spectra recorded in CDCl<sub>3</sub> of **Te-bbt(Br<sub>2</sub>)-cumenyl** (*top*) and **poly(Te-bbt-cumenyl)** (*bottom*).

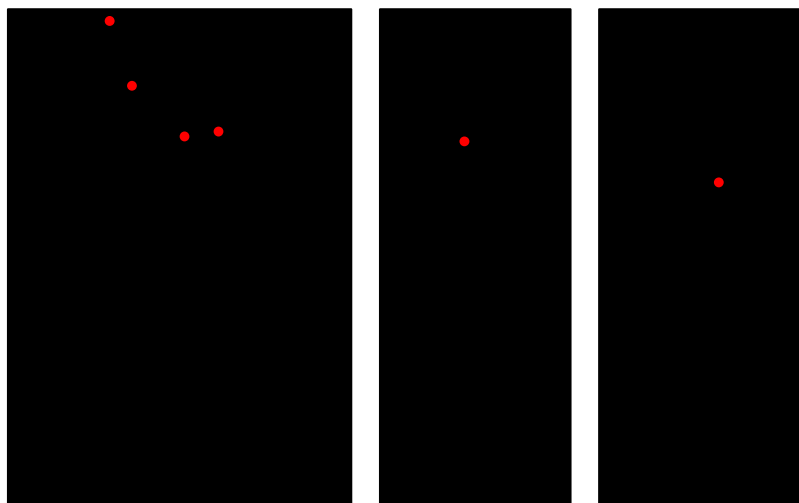


**Figure 5.23** –  $^1\text{H}$  NMR spectra of a sample of polymer in  $\text{CDCl}_3$  stored under  $\text{N}_2$  (*top*) and then exposed to air for 3 days (*bottom*) close-up of aryl,  $^1\text{Pr}(\text{CH})$  and  $^1\text{Pr}(\text{CH}_3)$  regions. Red circles indicate where the  $^1\text{H}$  NMR peaks of **Te-bbt-cumenyl** are expected to appear in  $\text{CDCl}_3$ .

In order to circumvent potential solubility issues and to hopefully allow for the synthesis of longer molecular weight polymers, the polymerization was repeated in 2-MeTHF at  $40\text{ }^\circ\text{C}$ . Once again, a red material was obtained, however this time it was purified by precipitation into cold ( $-30\text{ }^\circ\text{C}$ ) MeOH, washed with hexanes, and then stored under an inert atmosphere. Encouragingly, mass spectrometry of this sample verified the presence of a **Te-bbt-cumenyl** repeat unit, detecting molecular weights of up to 4500 Da (8–9 repeat units). Of note, many unrelated peaks were observed in the mass spectrum, indicating the presence of many different end groups and therefore suggesting that the polymerization is not very controlled. This is also observed in the  $^1\text{H}$  NMR spectrum by the presence of multiple peaks in the thienyl region and the  $^1\text{Pr}(\text{CH})$  region, which do not correspond to the decomposed ene-dione polymer (Figure

5.22). Lack of solubility has been demonstrated to effect the degree of controlled polymerization for tellurophenes under KCTP, and could be contributing to the lack of control here.

As shown in Figure 5.24, **poly(Te-bbt-cumenyl)** absorbs up to 600 nm with a  $\lambda_{\text{max}}$  of 489 nm that is red-shifted relative to **Te-bbt-cumenyl** ( $\lambda_{\text{max}} = 355$  nm, Figure 5.6). Optical bandgaps of 2.87 and 2.17 eV have been estimated using Tauc plots for **Te-bbt-cumenyl** and **poly(Te-bbt-cumenyl)**, respectively, resulting in a reduction of the optical bandgap by 0.70 eV upon polymerization. Of note, **poly(Te-bbt-cumenyl)** retains the three absorption features observed for **Te-bbt-cumenyl**, along with the appearance of a feature at 363 nm, which closely matches that of monomeric **Te-bbt-cumenyl** and **Te-bbt(Br<sub>2</sub>)-cumenyl**, although these compounds have an additional feature above 400 nm that is not present in the UV-vis spectrum of **poly(Te-bbt-cumenyl)**. In addition, the <sup>1</sup>H NMR spectrum of **poly(Te-bbt-cumenyl)** contains peaks with the same shifts that are expected for molecular **Te-bbt-cumenyl** (indicated by red circles in Figure 5.23). However, attempts to remove any monomeric material by precipitating in hexanes lead to no visible changes in the <sup>1</sup>H NMR spectrum of **poly(Te-bbt-cumenyl)**. Furthermore, these peaks disappear when a sample of **poly(Te-bbt-cumenyl)** is exposed to air/light for 3 days (Figure 5.23) even though pure samples of **Te-bbt-cumenyl** in CDCl<sub>3</sub> experience negligible decomposition in the same timeframe. Unfortunately, GPC data could not be collected on this sample due to technical issues with the instrument, leaving me unable to measure molecular weight prior to the completion of this Thesis.

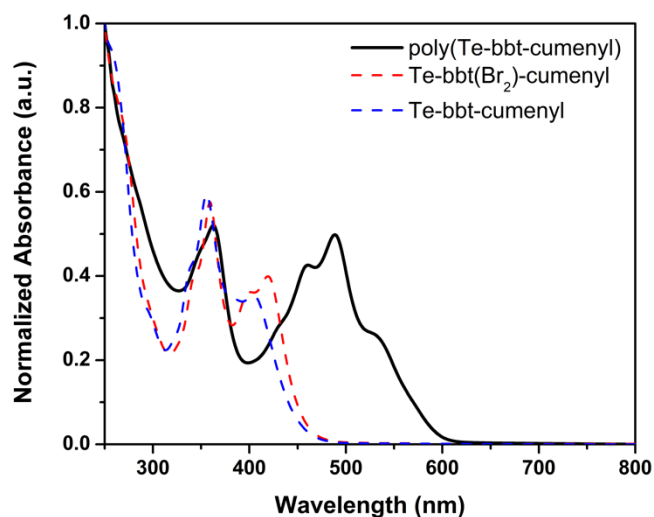


**Figure 5.24** – UV-vis spectra of **poly(Te-bbt-cumenyl)** (solid black line), **Te-bbt-cumenyl** (blue dashed line), and **Te-bbt(Br<sub>2</sub>)-cumenyl** (red dashed line line) in THF.

### 5.2.9 Photoluminescence studies of Te-bbt-cumenyl

Interestingly, no emission is observed for a pure sample of **Te-bbt-cumenyl** even at 77 K, when non-radiative decay through molecular motion is expected to be minimized. However, when a film containing 1 wt% of **Te-bbt-cumenyl** in PMMA is irradiated with UV-light, orange emission is observed under ambient conditions. The photoluminescence spectrum for **Te-bbt-cumenyl** in a PMMA matrix is shown in Figure 5.25. The emission profile is broad, extending from 550–800 nm with a maximum  $\lambda_{em}$  at 680 nm ( $\Phi = 1.3\%$ ,  $\tau = 0.6\ \mu s$ ). It should be noted that the emission at  $\lambda < 550\text{ nm}$  corresponds the emission of pure PMMA.

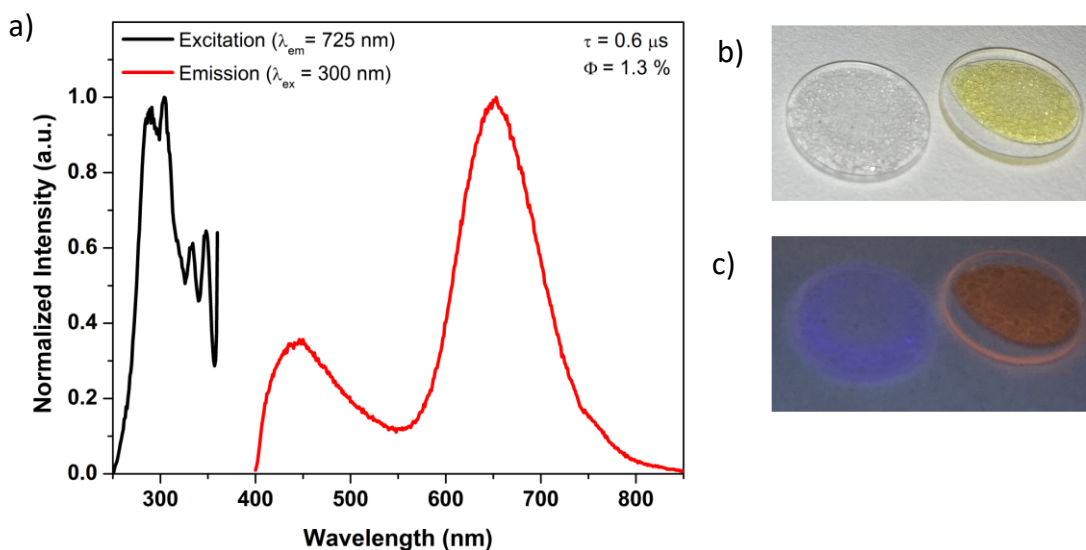


**Figure 5.25** – a) Excitation (black) and emission (red) spectra of **Te-bbt-cumenyl** in a PMMA matrix collected in air; b) images of films containing 100 % PMMA (*left*) and 1 wt% of **Te-bbt-cumenyl** in PMMA (*right*) under ambient conditions; c) images of films containing 100 % PMMA (*left*) and 1 wt% of **Te-bbt-cumenyl** in PMMA (*right*) irradiated with a hand-held UV lamp (254 nm).

The observed emission for **Te-bbt-cumenyl** is consistent with TD-DFT results computed at the B3LYP/cc-pVDZ(-PP) level of theory which suggest that the requirements for phosphorescence have been met. One requirement for phosphorescence to occur is that orbital density on the tellurium atom is involved in the excitation process, leading to a higher probability of intersystem crossing (ISC). As shown in Figure 5.7, the LUMO+1, LUMO, and HOMO–1 for **Te-bbt-cumenyl** all contain contributions from tellurium, but the HOMO does not. The predicted UV-vis absorption spectrum agrees well with the experimentally observed one and shows two pronounced transitions at 438 nm ( $S_0 \rightarrow S_1$ ; mainly HOMO to LUMO) and 353 nm ( $S_0 \rightarrow S_3$ ; mainly HOMO–1 to LUMO+1), experimentally these occur as a shoulder at

403 nm and a peak at 355 nm (Figure 5.6). The latter transition ( $S_0 \rightarrow S_3$ ) is computed to be more intense and the tellurium atom shows substantial contributions to the orbitals involved (Table 5.1). Another requirement for phosphorescence is the presence of energetically similar ( $\Delta E_{ST} < 0.1$  eV) triplet and singlet excited states, so that access to the triplet manifolds becomes energetically accessible. This requirement appears to be satisfied in **Te-bbt-cumenyl**, as there are two computed triplet states ( $T_7$  and  $T_8$ ) that are within  $< 0.03$  eV of the  $S_3$  state (Figure 5.26). These results suggest that a possible pathway to phosphorescence can be initial excitation from  $S_0$  to  $S_3$ , followed by Te-mediated ISC to  $T_7/T_8$  with relaxation to  $T_1$ , and final radiative decay (phosphorescence) to regenerate the singlet ground state,  $S_0$ . The zero-point corrected adiabatic energy ( $E_{0-0}$ ) difference calculated for the optimized  $S_0$  and  $T_1$  geometries predicts a small phosphorescence energy of 1.41 eV (881 nm). Although these computations predicted NIR emission, the computed value of  $\lambda_{em}$  is significantly more red-shifted than the experimentally measured value of 680 nm (1.82 eV), but a difference of *ca.* 0.4 eV in the computed energies is common with TD-DFT.<sup>18</sup>

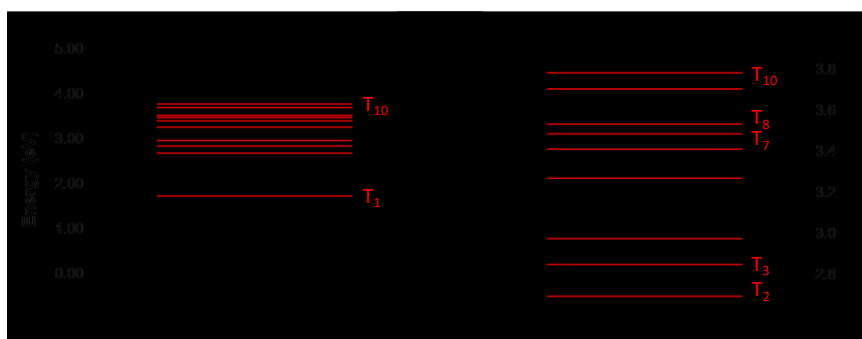


**Figure 5.26** – *Left*: Singlet (black) and triplet (red) states of **Te-bbt-cumenyl** calculated at the B3LYP/cc-pVDZ(-PP) level of theory; *Right*: A close-up of the  $S_1$ – $S_7$  and  $T_2$ – $T_{10}$  states. All energies are calculated relative to  $S_0 = 0.00$  eV.

**Table 5.1** – TD-DFT calculated excited states of **Te-bbt-cumenyl** at the B3LYP-ccpVDZ(-PP) level of theory.

| Excited State        | Energy (eV) | $\lambda$ (nm) | $f$    | Nature of Excitation (CI, %) <sup>a</sup>  |
|----------------------|-------------|----------------|--------|--|
| <b>T<sub>1</sub></b> | 1.7439      | 710.97         | 0.0000 | <b>HOMO</b> → <b>LUMO</b> (0.67697, 92 %)  |
| <b>T<sub>2</sub></b> | 2.6969      | 459.73         | 0.0000 | <b>HOMO-2</b> → <b>LUMO</b> (-0.37783, 29 %)<br><b>HOMO</b> → <b>LUMO+1</b> (0.37400, 28 %)<br><b>HOMO</b> → <b>LUMO+2</b> (0.38230, 29 %) |
| <b>S<sub>1</sub></b> | 2.8332      | 437.61         | 0.1961 | <b>HOMO</b> → <b>LUMO</b> (0.67714, 92 %)  |
| <b>T<sub>3</sub></b> | 2.8528      | 434.61         | 0.0000 | <b>HOMO-1</b> → <b>LUMO</b> (0.69231, 96 %)  |
| <b>T<sub>4</sub></b> | 2.9780      | 416.33         | 0.0000 | <b>HOMO</b> → <b>LUMO+1</b> (0.55418, 61 %)  |
| <b>S<sub>2</sub></b> | 3.2069      | 386.61         | 0.0272 | <b>HOMO</b> → <b>LUMO+1</b> (0.66115, 87 %)  |
| <b>T<sub>5</sub></b> | 3.2727      | 378.85         | 0.0000 | <b>HOMO-3</b> → <b>LUMO</b> (-0.34692, 24 %)<br><b>HOMO</b> → <b>LUMO+3</b> (0.38773, 30 %)  |
| <b>T<sub>6</sub></b> | 3.4144      | 363.12         | 0.0000 | <b>HOMO-1</b> → <b>LUMO+1</b> (0.61549, 76 %)  |
| <b>T<sub>7</sub></b> | 3.4887      | 355.39         | 0.0000 | <b>HOMO-2</b> → <b>LUMO</b> (0.53156, 57 %)<br><b>HOMO</b> → <b>LUMO+2</b> (0.40219, 32 %)   |
| <b>S<sub>3</sub></b> | 3.5168      | 352.55         | 0.1150 | <b>HOMO-1</b> → <b>LUMO</b> (0.62414, 78 %)  |
| <b>T<sub>8</sub></b> | 3.5371      | 350.53         | 0.0000 | <b>HOMO-3</b> → <b>LUMO+3</b> (0.38107, 29 %)  |

a) Only coefficients (CI) > |0.31| are shown; % = % contribution of the molecular orbitals to the corresponding transition.

b) Molecular orbitals involving Te are identified in bold font.

A computational investigation of potential phosphorescence from the target annulated species **Te-bbt(Me<sub>2</sub>)-f-cumenyl** was also conducted using TD-DFT at the B3LYP/cc-pVDZ(-PP) level of theory. Two main transitions are predicted in the UV-vis spectrum for this compound, including the S<sub>0</sub>→S<sub>1</sub> (HOMO → LUMO) and S<sub>0</sub>→S<sub>5</sub> (HOMO-1 → LUMO and HOMO → LUMO+3) transitions (Figure 5.27). Although the HOMO and LUMO+3 do not contain any orbital contribution from Te, the HOMO-1 and LUMO do contain major contributions from Te. Therefore, the Te contributions to the orbitals involved in the excitation to S<sub>5</sub> could promote ISC to a triplet excited state. Furthermore, four pairs of S<sub>n</sub>/T<sub>n</sub> excited states with ΔE<sub>ST</sub> < 0.1 eV exist including: S<sub>3</sub>/T<sub>6</sub>, S<sub>4</sub>/T<sub>7</sub>, S<sub>5</sub>/T<sub>9</sub>, S<sub>6</sub>/T<sub>10</sub> (Table 5.2). Therefore, a potential path for phosphorescence is excitation to S<sub>5</sub>, ISC to T<sub>9</sub>, non-radiative decay to T<sub>1</sub> and finally radiative (phosphorescence) from T<sub>1</sub> to S<sub>0</sub>. The E<sub>0-0</sub> at optimized S<sub>0</sub> and T<sub>1</sub> geometries were used to predict a phosphorescence energy of 1.10 eV (1124 nm). This is substantially red-shifted from the predicted phosphorescence energy for **Te-bbt-cumenyl** (881 nm). However, such a small energy difference between S<sub>0</sub> and T<sub>1</sub> may result in enhanced non-radiative decay due to the Energy Gap Law, suppressing phosphorescence from being observed experimentally.



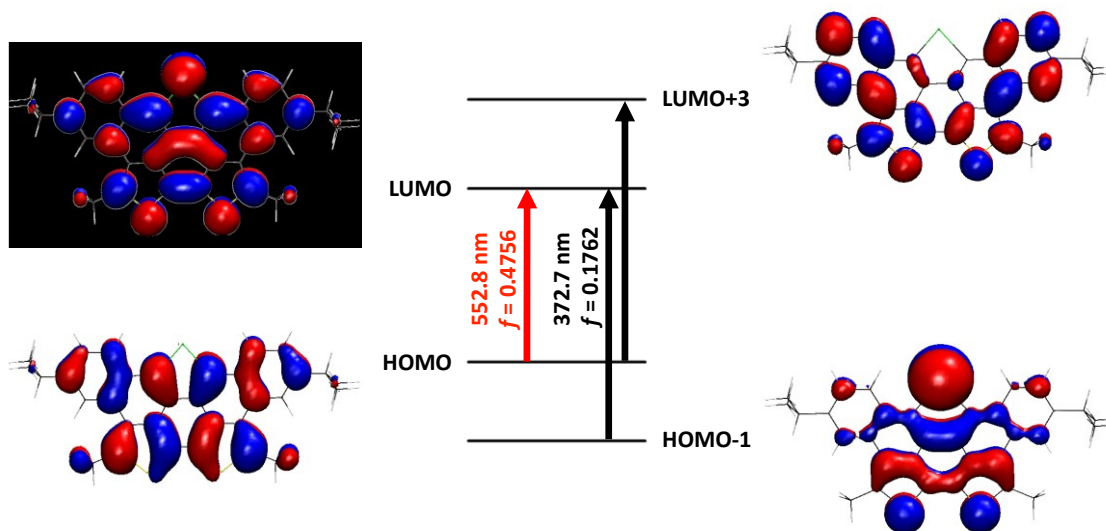


**Figure 5.27** – TD-DFT [B3LYP/cc-pVDZ(-PP)] computed main transitions for **Te-bbt(Me<sub>2</sub>)-f-cumenyl** including excitation wavelengths and oscillator strengths ( $f$ ) for the most intense transitions ( $S_0 \rightarrow S_1$ : red;  $S_0 \rightarrow S_5$ : black) along with the associated molecular orbitals; iso-surface values of +0.02/-0.02 (red/blue).

**Table 5.2** – TD-DFT calculated excited states of **Te-bbt(Me<sub>2</sub>)-f-cumenyl** at the B3LYP-ccpVDZ(-PP) level of theory.

| Excited State         | Energy (eV) | $\lambda$ (nm) | $f$    | Nature of Excitation (CI, %) <sup>a</sup>  |
|-----------------------|-------------|----------------|--------|--|
| <b>T<sub>1</sub></b>  | 1.1721      | 1057.8         | 0.0000 | HOMO → <b>LUMO</b> (0.70268, 99 %)   |
| <b>S<sub>1</sub></b>  | 2.2428      | 552.81         | 0.4756 | HOMO → <b>LUMO</b> (0.70395, 99 %)   |
| <b>T<sub>2</sub></b>  | 2.3686      | 523.44         | 0.0000 | HOMO → <b>LUMO+2</b> (0.55649, 62 %)<br>HOMO-2 → <b>LUMO</b> (-0.36913, 27 %)                                  |
| <b>T<sub>3</sub></b>  | 2.5993      | 476.99         | 0.0000 | HOMO → LUMO+3 (0.5262, 55 %)<br><b>HOMO-1</b> → <b>LUMO</b> (0.36332, 26 %)                                    |
| <b>T<sub>4</sub></b>  | 2.6486      | 468.12         | 0.0000 | <b>HOMO-1</b> → <b>LUMO</b> (0.5957, 71 %)   |
| <b>T<sub>5</sub></b>  | 2.7272      | 454.63         | 0.0000 | HOMO → LUMO+1 (0.69581, 97 %)  |
| <b>S<sub>2</sub></b>  | 2.8623      | 433.17         | 0.0000 | HOMO → LUMO+1 (0.70205, 99 %)  |
| <b>T<sub>6</sub></b>  | 3.0454      | 407.12         | 0.0000 | HOMO-2 → <b>LUMO</b> (0.48968, 48 %)<br>HOMO → <b>LUMO+2</b> (0.39714, 32 %)                                   |
| <b>S<sub>3</sub></b>  | 3.1068      | 399.07         | 0.0058 | HOMO → <b>LUMO+2</b> (0.60255, 73 %)<br>HOMO-2 → <b>LUMO</b> (0.35132, 25 %)                                   |
| <b>S<sub>4</sub></b>  | 3.1513      | 393.44         | 0.0166 | HOMO → LUMO+3 (0.50995, 52 %)<br><b>HOMO-1</b> → <b>LUMO</b> (-0.46024, 42 %)                                  |
| <b>T<sub>7</sub></b>  | 3.1528      | 393.26         | 0.0000 | HOMO → LUMO+4 (0.48128, 46 %)<br>HOMO-4 → <b>LUMO</b> (0.32999, 22 %)<br>HOMO-2 → <b>LUMO</b> (-0.31636, 20 %) |
| <b>T<sub>8</sub></b>  | 3.2193      | 385.13         | 0.0000 | HOMO → LUMO+5 (0.40158, 32 %)<br>HOMO-5 → <b>LUMO</b> (0.34578, 24 %)  |
| <b>S<sub>5</sub></b>  | 3.3266      | 372.71         | 0.1762 | <b>HOMO-1</b> → <b>LUMO</b> (0.50394, 51 %)<br>HOMO → LUMO+3 (0.4424, 39 %)                                    |
| <b>T<sub>9</sub></b>  | 3.3609      | 368.91         | 0.0000 | <b>HOMO-1</b> → <b>LUMO+1</b> (0.66807, 89 %)  |
| <b>T<sub>10</sub></b> | 3.4348      | 360.96         | 0.0000 | <b>HOMO-3</b> → <b>LUMO</b> (0.57891, 67 %)  |
| <b>S<sub>6</sub></b>  | 3.5278      | 351.45         | 0.0481 | HOMO-2 → <b>LUMO</b> (0.59052, 70 %)<br>HOMO → LUMO+2 (-0.33721, 23 %)   |
| <b>S<sub>7</sub></b>  | 3.5896      | 345.4          | 0.0028 | HOMO → LUMO+4 (0.67328, 91 %)  |
| <b>S<sub>8</sub></b>  | 3.7601      | 329.74         | 0.0000 | <b>HOMO-1</b> → <b>LUMO+1</b> (0.69069, 95 %)  |
| <b>S<sub>9</sub></b>  | 3.8281      | 323.88         | 0.0185 | HOMO-4 → <b>LUMO</b> (0.56991, 65 %)<br><b>HOMO-3</b> → <b>LUMO</b> (-0.33791, 23 %)                           |
| <b>S<sub>10</sub></b> | 3.8425      | 322.67         | 0.0468 | <b>HOMO-3</b> → <b>LUMO</b> (0.54142, 59 %)<br>HOMO-4 → <b>LUMO</b> (0.30495, 19%)                             |

a) Only coefficients (CI) > |0.31| are shown; % = % contribution of the molecular orbitals to the corresponding transition.

b) Molecular orbitals involving Te are identified in bold font.

## 5.3 Conclusion

In summary, a series of new tellurophenes with ring-fused bithiophene units were developed. Three such tellura(benzo)bithiophenes featuring SiMe<sub>3</sub>, (C<sub>6</sub>H<sub>4</sub>)OCH<sub>3</sub>, and cumenyl as side groups were synthesized. **Te-bbt-SiMe<sub>3</sub>** and **Te-bbt-(C<sub>6</sub>H<sub>4</sub>)OCH<sub>3</sub>** were obtained in poor isolated yield and with low solubility, respectively, so further studies focused mainly on **Te-bbt-cumenyl**. Several derivatives were synthesized *via* the di-lithiation of **Te-bbt-cumenyl** and reaction with the appropriate electrophile; these include: 1) **Te-bbt(Me<sub>2</sub>)-cumenyl**, which was used in the attempt to form the annulated product **Te-bbt(Me<sub>2</sub>)-f-cumenyl**, and 2) **Te-bbt(Br<sub>2</sub>)-cumenyl**, which was polymerized to form **poly(Te-bbt-cumenyl)**. Although the annulation reaction proved unsuccessful, the optoelectronic properties of the  $\pi$ -extended **Te-bbt-cumenyl** and **poly(Te-bbt-cumenyl)** revealed broad features in the UV-vis that spans across a large portion of the visible spectrum. Furthermore, the newly synthesized **Te-bbt-cumenyl** exhibits orange phosphorescence when incorporated into a rigid matrix such as a PMMA film. Future work will involve the investigation of these unique  $\pi$ -delocalized species as NIR emitters or as components in solar cells.

## 5.4 Experimental

### 5.4.1 General procedures

Unless explicitly stated otherwise, all reactions were carried out with standard Schlenk and glovebox (MBraun) techniques using N<sub>2</sub> as the inert atmosphere and

solvents that were dried using a Grubbs' type purification system manufactured by Innovative Technology Inc. 1,7-Octadiyne was purchased from GFS Chemicals,  $\text{Cp}_2\text{ZrCl}_2$  from Strem Chemicals Inc., trimethylsilylacetylene from Matrix Scientific, and all other commercially obtained compounds were obtained from Sigma-Aldrich; all commercially derived chemicals were used as received. The following compounds were synthesized according to literature procedures:  $\text{TeCl}_2\cdot\text{bipy}$ ,<sup>56</sup>  $\text{Cp}_2\text{Zr}(\text{pyridine})(\text{Me}_3\text{SiCCSiMe}_3)$ ,<sup>57</sup> 2,2'-bithiophene,<sup>41</sup> 3,3',5,5'-tetrabromo-2,2'-bithiophene,<sup>42</sup> 3,3'-dibromo-2,2'-bithiophene,<sup>43</sup> 3,3'-bis(trimethylsilylethynyl)-2,2'-bithiophene,<sup>44</sup> 3,3'-diethynyl-2,2'-bithiophene<sup>44</sup> and  $\text{Ni}(\text{dppe})(o\text{-tolyl})\text{Cl}$ .<sup>55</sup> The molarity of  ${}^n\text{BuLi}$  was determined by a titration with *N*-benzylbenzamide in THF (indicated by a colour change from colourless to a persistent blue).<sup>58</sup> The concentration of  ${}^i\text{PrMgCl}\cdot\text{LiCl}$  solutions (supplied as a solution in THF) were determined by  ${}^1\text{H}$  NMR spectroscopy using 1,5-cyclooctadiene (COD) as an internal standard.<sup>59</sup> Melting points were measured with a MelTemp apparatus and are reported without correction. Gel permeation chromatography (GPC) was performed at 40 °C using THF as the eluent at a flow rate 0.5 mL per minute. A Viscotek VE 2001 autosampler, Malvern T6000M column, GPC 270 Max dual detector, and a Viscotek VE 3580 refractive index detector (RI) were used for GPC sample analysis and data collection. High-resolution mass spectra were obtained on an Agilent 6220 spectrometer and Kratos Analytical MS-50G instrument. Elemental analyses were performed by the Analytical and Instrumentation Laboratory at the University of Alberta. UV-vis spectroscopic measurements were

performed with a Varian Cary 5000 Scan spectrophotometer. Thermogravimetric analysis was performed on a PerkinElmer Pyris 1 TGA instrument.

Steady-state photoluminescence (PL) spectra, emission lifetime ( $\lambda$ ), and photoluminescence quantum yields ( $\Phi$ ) were obtained using a Horiba PTI QuantaMaster 8075 fluorescence spectrophotometer. For the PL and quantum yield measurements, the spectrophotometer was equipped with a 75W xenon lamp (and an integrating sphere for the quantum yield measurements). The luminescence of **Te-bbt-cumenyl** was measured under ambient conditions in a poly(methylmethacrylate) (PMMA) matrix, prepared by dissolving 1 mg of sample and 99 mg of PMMA in 1 mL of THF and drop-casting the solution on to a quartz plate. Long-pass and short-pass cut-off filters of  $\lambda = 400$  nm were used in the steady-state photoluminescence and quantum yield measurements. All quantum yields are reported as absolute values.

The decay curves used to determine the emission lifetime ( $\tau$ ) were collected on a Horiba PTI QuantaMaster 8075 fluorescence spectrometer equipped with a 75W xenon flash lamp. The resulting decay curve was fitted with the lowest exponential function that gave a suitable reduced chi-square value ( $\chi^2$ ), Durbin Watson parameter, and Z value.<sup>60,61</sup>

#### 5.4.2 Synthetic procedures

**Synthesis of BT1.** 3,3'-Diethynyl-2,2'-bithiophene (244 mg, 1.14 mmol), 4-iodoanisole (560 mg, 2.39 mmol), Pd(PPh<sub>3</sub>)<sub>4</sub> (54 mg, 0.047 mmol), CuI (10 mg, 0.053 mmol) and 3 mL of toluene were loaded into a flask. To this mixture, 0.4 mL of <sup>i</sup>Pr<sub>2</sub>NH

was added. The reaction mixture was heated to 80 °C for 15 hours, cooled to room temperature and the solvent was removed *in vacuo* with gradual heating from room temperature to 50 °C. The product mixture was exposed to air, extracted with 100 mL of CH<sub>2</sub>Cl<sub>2</sub>, and washed with 3 × 50 mL of distilled water. The organic layer was dried over MgSO<sub>4</sub>, gravity filtered, and then the solvent was removed from the filtrate. The remaining solid was washed with 3 × 2 mL of CH<sub>2</sub>Cl<sub>2</sub> to give 251 mg of pure **BT1**. Another 152 mg of pure **BT1** was recovered by combining the CH<sub>2</sub>Cl<sub>2</sub> washes, removing the solvent and purifying the product *via* flash column chromatography through silica gel with a 1:1 CH<sub>2</sub>Cl<sub>2</sub>:hexanes solvent mixture as the eluent (total yield of **BT1** = 403 mg, 83 %). <sup>1</sup>H NMR (499.8 MHz, CDCl<sub>3</sub>): δ = 7.53 (d, <sup>3</sup>J<sub>HH</sub> = 8.5 Hz, 4H, CHCHC-OCH<sub>3</sub>), 7.24 (d, <sup>3</sup>J<sub>HH</sub> = 5.5 Hz, 2H, SCHCH), 7.15 (d, <sup>3</sup>J<sub>HH</sub> = 5.0 Hz, 2H, SCHCH), 6.91 (d, <sup>3</sup>J<sub>HH</sub> = 8.5 Hz, 4H, CHCHC-OCH<sub>3</sub>), 3.84 (s, 6H, OCH<sub>3</sub>). <sup>13</sup>C{<sup>1</sup>H} NMR (125.7 MHz, CDCl<sub>3</sub>): δ = 159.9 (COCH<sub>3</sub>), 138.0 (SCCS), 133.0 (CHCHC-OCH<sub>3</sub>), 130.4 (SCHCH), 124.1 (SCHCH), 119.6, (SCCC≡C) 115.7 (CCHCHC-OCH<sub>3</sub>), 114.3 (CHCHC-OCH<sub>3</sub>), 95.7 (SCCC≡C), 84.8 (SCCC≡C), 55.5 (OCH<sub>3</sub>). HR-MS (EI): m/z calcd. for [C<sub>26</sub>H<sub>18</sub>S<sub>2</sub>O<sub>2</sub>]<sup>+</sup>: 426.0748; found: 426.0747 (Δppm = 0.3).

**Synthesis of BT2.** 3,3'-Diethynyl-2,2'-bithiophene (0.457 g, 2.13 mmol), 4-iodocumene (1.171 g, 4.758 mmol), Pd(PPh<sub>3</sub>)<sub>4</sub> (0.100 g, 0.0865 mmol), CuI (0.016 g, 0.085 mmol), and 25 mL of toluene were loaded into a flask. To this mixture, 2.5 mL of <sup>i</sup>Pr<sub>2</sub>NH was added. The reaction mixture was heated to 85 °C for 15 hours, cooled to room temperature and then the solvent was removed *in vacuo* with gradual heating from room temperature to 50 °C. The crude product was exposed to air, extracted with 3 ×

50 mL of CH<sub>2</sub>Cl<sub>2</sub>, and washed with 3 × 100 mL of distilled water. The organic layer was dried over MgSO<sub>4</sub>, gravity filtered, and then the solvent was removed from the filtrate under vacuum. The resulting solid was combined with 1 mL of a 1:1 CH<sub>2</sub>Cl<sub>2</sub>/hexanes solvent mixture. The resulting suspension was allowed to settle and the mother liquor was decanted. This procedure was repeated three more times with a CH<sub>2</sub>Cl<sub>2</sub>/hexanes solvent mixture, and then three more times with pure hexanes. Removal of the residual solvent from the remaining precipitate under vacuum gave 586 mg of pure **BT2**. The CH<sub>2</sub>Cl<sub>2</sub>/hexanes extracts were combined, concentrated under vacuum and then subjected to flash column chromatography through silica gel with 10 % CH<sub>2</sub>Cl<sub>2</sub> in hexanes as the eluent to afford another 154 mg of pure **BT2**. The total amount of **BT2** obtained was 0.740 g (77 %). <sup>1</sup>H NMR (499.8 MHz, CDCl<sub>3</sub>): δ = 7.53 (d, <sup>3</sup>J<sub>HH</sub> = 8.5 Hz, 4H, CHCHC-CH(CH<sub>3</sub>)<sub>2</sub>), 7.25 (d, <sup>3</sup>J<sub>HH</sub> = 8.0 Hz, 4H, CHCHC-CH(CH<sub>3</sub>)<sub>2</sub>), 7.25 (d, <sup>3</sup>J<sub>HH</sub> = 5.5 Hz, 2H, SCHCH), 7.17 (d, <sup>3</sup>J<sub>HH</sub> = 5.5 Hz, 2H, SCHCH), 2.94 (septet, <sup>3</sup>J<sub>HH</sub> = 7.0 Hz, 2H, CH(CH<sub>3</sub>)<sub>2</sub>), 1.28 (d, <sup>3</sup>J<sub>HH</sub> = 7.0 Hz, 12H, CH(CH<sub>3</sub>)<sub>2</sub>). <sup>13</sup>C{<sup>1</sup>H} NMR (125.7 MHz, CDCl<sub>3</sub>): δ = 149.6 (CCH(CH<sub>3</sub>)<sub>2</sub>), 138.3 (SCCS), 131.5 (C≡C-CCHCHC-CH(CH<sub>3</sub>)<sub>2</sub>), 130.5 (SCHCH), 126.7 (C≡C-CCHCHC-CH(CH<sub>3</sub>)<sub>2</sub>), 124.2 (SCHCH), 120.9 (C≡C-CCHCHC-CH(CH<sub>3</sub>)<sub>2</sub>), 119.5 (SCCC≡C), 95.9 (SCCC≡C), 85.3 (SCCC≡C), 34.3 (CH(CH<sub>3</sub>)<sub>2</sub>), 24.0 (CH(CH<sub>3</sub>)<sub>2</sub>). Anal. calcd. (%) for C<sub>30</sub>H<sub>26</sub>S<sub>2</sub>: C, 79.96; H, 5.82; S, 14.23. found: C, 79.13; H, 5.78; S, 13.54. HR-MS (EI): m/z calcd. for [C<sub>30</sub>H<sub>26</sub>S<sub>2</sub>]<sup>+</sup>: 450.1476; found: 450.1474 (Δppm = 0.3). TGA: 5 % mass loss at 373 °C (in air).

**Synthesis of Te-bbt-SiMe<sub>3</sub>.** A solution of Cp<sub>2</sub>Zr(pyridine)(Me<sub>3</sub>SiCCSiMe<sub>3</sub>) (102 mg, 0.217 mmol) in 5 mL of THF was added to a solution of 3,3'-bis(trimethylsilylethynyl)-2,2'-bithiophene (60 mg, 0.17 mmol) in 5 mL of THF. The resulting solution was stirred for 8 hours and then transferred to another vial containing solid TeCl<sub>2</sub>•bipy (92 mg, 0.26 mmol). The reaction mixture was then stirred for 1 hour, filtered through a plug of glass fibre and the volatiles were removed from the filtrate under vacuum. The crude product was then stirred vigorously in 2 mL of pentane and filtered through Celite, before volatiles were removed from the filtrate under vacuum. Further purification was performed by exposing the sample to air (to degrade residual zirconocene-containing impurities) and then heating the product to 50 °C under vacuum in order to remove residual pyridine and Me<sub>3</sub>SiCCSiMe<sub>3</sub>. Finally, the product was dissolved in 2 mL of hexanes, filtered through a glass fibre plug (in a pipette), and then purified by cooling the resulting solution to –30 °C to give **Te-bbt-SiMe<sub>3</sub>** as a yellow solid (16 mg, 19 %). Crystals suitable for single-crystal X-ray diffraction were grown from a concentrated hexamethyldisiloxane (Me<sub>3</sub>SiOSiMe<sub>3</sub>) solution at –30 °C. <sup>1</sup>H NMR (400.0 MHz, C<sub>6</sub>D<sub>6</sub>): δ = 7.90 (d, <sup>3</sup>J<sub>HH</sub> = 5.6 Hz, 2H, SCHCH), 6.81 (d, <sup>3</sup>J<sub>HH</sub> = 5.6 Hz, 2H, SCHCH), 0.51 (s, 18H, Si(CH<sub>3</sub>)<sub>3</sub>). <sup>13</sup>C {<sup>1</sup>H} NMR (100.6 MHz, C<sub>6</sub>D<sub>6</sub>): δ = 152.0 (TeCC), 144.9 (TeCC), 136.8 (SCC), 132.6 (SCC), 127.6 (SCHCH), 121.9 (SCHCH), 2.8 (Si(CH<sub>3</sub>)<sub>3</sub>). Anal. calcd. (%) for C<sub>18</sub>H<sub>22</sub>S<sub>2</sub>Si<sub>2</sub>Te: C, 44.46; H, 4.56; S, 13.19. found: C, 44.61; H, 4.60; S, 13.19. HR-MS (EI): m/z calcd. for [C<sub>26</sub>H<sub>18</sub>O<sub>2</sub>S<sub>2</sub><sup>130</sup>Te]<sup>+</sup>: 487.97638; found: 487.97613 (Δppm = 0.5). UV/vis (in THF): λ<sub>max</sub> = 369 nm, ε = 1.67 × 10<sup>4</sup> M<sup>-1</sup>cm<sup>-1</sup>.



**Synthesis of Te-bbt-(C<sub>6</sub>H<sub>4</sub>)OCH<sub>3</sub>.** A solution of Cp<sub>2</sub>Zr(pyridine)(Me<sub>3</sub>SiCCSiMe<sub>3</sub>) (342 mg, 0.726 mmol) in 2 mL of THF was added to a solution of diyne **BT1** (236 mg, 0.553 mmol) in 15 mL of THF. The resulting solution was stirred for 3.5 hours and then transferred to another vial containing solid TeCl<sub>2</sub>•bipy (259 mg, 0.730 mmol). The reaction mixture was then stirred for 2 hours before the volatiles were removed under vacuum; the crude product was exposed to air for the subsequent work-up procedure. The crude product was dissolved in 250 mL of CH<sub>2</sub>Cl<sub>2</sub>, filtered through a frit that was loaded with a 3 cm pad of Florisil and the volatiles were removed from the filtrate under vacuum. Further purification was performed *via* flash column chromatography through silica gel with a mixture of 1:1 CH<sub>2</sub>Cl<sub>2</sub>:hexanes as the eluent to give **Te-bbt-(C<sub>6</sub>H<sub>4</sub>)OCH<sub>3</sub>** as a yellow solid (168 mg, 55 %). Crystals suitable for single-crystal X-ray diffraction were grown from a concentrated CH<sub>2</sub>Cl<sub>2</sub> solution layered with hexanes at room temperature. <sup>1</sup>H NMR (499.8 MHz, CDCl<sub>3</sub>): δ = 7.47 (d, <sup>3</sup>J<sub>HH</sub> = 8.5 Hz, 4H, CCHCHC-OCH<sub>3</sub>), 6.99 (d, <sup>3</sup>J<sub>HH</sub> = 8.5 Hz, 4H, CCHCHC-OCH<sub>3</sub>), 6.96 (d, <sup>3</sup>J<sub>HH</sub> = 5.5 Hz, 2H, SCHCH), 6.74 (d, <sup>3</sup>J<sub>HH</sub> = 5.5 Hz, 2H, SCHCH), 3.90 (s, 6H, OCH<sub>3</sub>). <sup>13</sup>C{<sup>1</sup>H} NMR (125.7 MHz, CDCl<sub>3</sub>): δ = 159.5 (COCH<sub>3</sub>), 142.3 (CCHCHC-OCH<sub>3</sub>), 139.5 (TeC=C), 134.1 (TeC=C), 133.5 (SCC), 132.7 (SCC), 130.7 (CHCHC-OCH<sub>3</sub>), 126.2 (SCHCH), 121.7 (SCHCH), 114.2 (CHCHC-OCH<sub>3</sub>), 55.6 (OCH<sub>3</sub>). Anal. calcd. (%) for C<sub>26</sub>H<sub>18</sub>O<sub>2</sub>S<sub>2</sub>Te: C, 56.35; H, 3.27; S, 11.57. found: C, 56.24; H, 3.56; S, 11.24. HR-MS (EI): m/z calcd. for [C<sub>26</sub>H<sub>18</sub>O<sub>2</sub>S<sub>2</sub><sup>130</sup>Te]<sup>+</sup>: 555.98108; found: 555.97913 (Δppm = 3.5). UV/vis (in THF): λ<sub>max</sub> = 356 nm, ε = 1.89 × 10<sup>4</sup> M<sup>-1</sup>cm<sup>-1</sup>. Mp (°C): 254 – 256 (under N<sub>2</sub>).

**Synthesis of Te-bbt-cumenyl.** A solution of Cp<sub>2</sub>Zr(pyridine)(Me<sub>3</sub>SiCCSiMe<sub>3</sub>) (1.016 g, 2.158 mmol) in 5 mL of THF was added to a solution of diyne **BT2** (0.744 g, 1.65 mmol) in 30 mL of THF. The resulting solution was stirred for 15 hours and then a suspension of TeCl<sub>2</sub>•bipy (0.765 g, 2.16 mmol) in 12 mL of THF was added. The reaction mixture was then stirred for 15 hours before exposing to air, diluted with 300 mL of CH<sub>2</sub>Cl<sub>2</sub>, and the resulting mixture was filtering through a frit loaded with Celite. After removal of the volatiles from the filtrate, further purification of the product was accomplished *via* flash column chromatography through silica gel with 10 % CH<sub>2</sub>Cl<sub>2</sub> in hexanes as the eluent to give **Te-bbt-cumenyl** as a yellow solid (0.550 g, 58 %). Crystals suitable for single-crystal X-ray diffraction were grown from a concentrated Et<sub>2</sub>O solution held at -30 °C. <sup>1</sup>H NMR (499.8 MHz, CDCl<sub>3</sub>): δ = 7.47 (d, <sup>3</sup>J<sub>HH</sub> = 8.0 Hz, 4H, CCHCHC-CH(CH<sub>3</sub>)<sub>2</sub>), 7.31 (d, <sup>3</sup>J<sub>HH</sub> = 8.0 Hz, 4H, CCHCHC-CH(CH<sub>3</sub>)<sub>2</sub>), 6.96 (d, <sup>3</sup>J<sub>HH</sub> = 5.0 Hz, 2H, SCHCH), 6.72 (d, <sup>3</sup>J<sub>HH</sub> = 5.0 Hz, 2H, SCHCH), 3.01 (septet, <sup>3</sup>J<sub>HH</sub> = 7.0 Hz, 2H, CH(CH<sub>3</sub>)<sub>2</sub>), 1.35 (d, 12H, <sup>3</sup>J<sub>HH</sub> = 7.0 Hz, CH(CH<sub>3</sub>)<sub>2</sub>). <sup>13</sup>C {<sup>1</sup>H} NMR (125.7 MHz, CDCl<sub>3</sub>): δ = 148.7 (CCH(CH<sub>3</sub>)<sub>2</sub>), 142.9 (CCHCHC-CH(CH<sub>3</sub>)<sub>2</sub>), 139.2 (TeC=C), 139.1 (TeC=C), 133.5 (SCC), 132.7 (SCC), 129.4 (CCHCHC-CH(CH<sub>3</sub>)<sub>2</sub>), 126.8 (CCHCHC-CH(CH<sub>3</sub>)<sub>2</sub>), 126.2 (SCHCH), 121.6 (SCHCH), 34.1 (CH(CH<sub>3</sub>)<sub>2</sub>), 24.2 (CH(CH<sub>3</sub>)<sub>2</sub>). <sup>125</sup>Te {<sup>1</sup>H} NMR (157.2 MHz, C<sub>6</sub>D<sub>6</sub>): δ = 976.8 (s). Anal. calcd. (%) for C<sub>30</sub>H<sub>26</sub>S<sub>2</sub>Te: C, 62.31; H, 4.53; S, 11.09. found: C, 62.76; H, 4.60; S, 11.10. HR-MS (EI): m/z calcd. for [C<sub>30</sub>H<sub>26</sub>S<sub>2</sub><sup>130</sup>Te]<sup>+</sup>: 580.0538; found: 580.0536 (Δppm = 0.5). UV/vis (in THF): λ<sub>max</sub> = 356 nm, ε = 1.88 × 10<sup>4</sup> M<sup>-1</sup>cm<sup>-1</sup>, λ<sub>max</sub> = 404 nm, ε = 1.05 × 10<sup>4</sup> M<sup>-1</sup>cm<sup>-1</sup>. TGA: 5 % mass loss at 311 °C (in air). Mp (°C): 208–210 (in air).

**Synthesis of Te-bbt(D<sub>2</sub>)-cumenyl.** <sup>n</sup>BuLi (3.25 M solution in hexanes) was added to a solution of **Te-bbt-cumenyl** (47 mg, 0.081 mmol) in 3 mL of THF. This mixture was stirred at room temperature for 16 hours and then 0.20 mL of D<sub>2</sub>O was added. The mixture was then treated with MgSO<sub>4</sub>, filtered, and the volatiles were removed from the filtrate *in vacuo*. The crude product was then dissolved in 0.7 mL of CDCl<sub>3</sub> for analysis by <sup>1</sup>H and <sup>13</sup>C{<sup>1</sup>H} NMR spectroscopy. The NMR spectra showed the quantitative formation of **Te-bbt(D<sub>2</sub>)-cumenyl**. <sup>1</sup>H NMR (498.1 MHz, CDCl<sub>3</sub>): δ = 7.48 (d, <sup>3</sup>J<sub>HH</sub> = 8.0 Hz, 4H, CHCHC-CH(CH<sub>3</sub>)<sub>2</sub>), 7.31 (d, <sup>3</sup>J<sub>HH</sub> = 8.0 Hz, 4H, CHCHC-CH(CH<sub>3</sub>)<sub>2</sub>), 6.74 (s, 2H, SC(D)CH), 3.02 (septet, <sup>3</sup>J<sub>HH</sub> = 7.0 Hz, 2H, CH(CH<sub>3</sub>)<sub>2</sub>), 1.36 (d, <sup>3</sup>J<sub>HH</sub> = 7.0 Hz, 4H, CH(CH<sub>3</sub>)<sub>2</sub>). <sup>13</sup>C{<sup>1</sup>H} NMR (125.3 MHz, CDCl<sub>3</sub>): δ = 148.7 (CCH(CH<sub>3</sub>)<sub>2</sub>), 142.9 (CCHCHC-CH(CH<sub>3</sub>)<sub>2</sub>), 139.2 (TeC=C), 139.1(TeC=C), 133.5 (SCC), 132.6 (SCC), 129.4 (CCHCHC-CH(CH<sub>3</sub>)<sub>2</sub>), 126.7 (CCHCHC-CH(CH<sub>3</sub>)<sub>2</sub>), 126.0 (SC(D)CH), 121.6 (SC(D)CH), 34.1 (CH(CH<sub>3</sub>)<sub>2</sub>), 24.2 (CH(CH<sub>3</sub>)<sub>2</sub>).

**Synthesis of Te-bbt(Me<sub>2</sub>)-cumenyl.** <sup>n</sup>BuLi (3.1 M solution in hexanes, 80 μL, 0.25 mmol) was added to a solution of **Te-bbt-cumenyl** (65 mg, 0.11 mmol) in 5 mL of THF. This mixture was stirred for 30 minutes, and then cooled to -78 °C before adding iodomethane (50 mg, 0.35 mmol) dropwise. The mixture was stirred at room temperature for 16 hours and then 5 mL of distilled water was added. The product was extracted using 3 × 5 mL of CH<sub>2</sub>Cl<sub>2</sub> (in air). The organic layer was then washed with 3 × 5 mL of distilled water, dried over MgSO<sub>4</sub>, and then filtered. Removal of the solvent from the filtrate under vacuum gave **Te-bbt(Me<sub>2</sub>)-cumenyl** as a yellow-orange solid (60 mg, 88 %). <sup>1</sup>H NMR (499.8 MHz, CDCl<sub>3</sub>): δ = 7.46 (d, <sup>3</sup>J<sub>HH</sub> = 8.0 Hz, 4H, CHCHC-

CH(CH<sub>3</sub>)<sub>2</sub>), 7.30 (d, <sup>3</sup>J<sub>HH</sub> = 8.0 Hz, 4H, CHCHC-CH(CH<sub>3</sub>)<sub>2</sub>), 6.24 (s, 2H, SC(CH<sub>3</sub>)CH), 3.02 (septet, <sup>3</sup>J<sub>HH</sub> = 7.0 Hz, 2H, CH(CH<sub>3</sub>)<sub>2</sub>), 2.31 (s, 6H, SCCH<sub>3</sub>), 1.35 (d, <sup>3</sup>J<sub>HH</sub> = 7.0 Hz, 4H, CH(CH<sub>3</sub>)<sub>2</sub>). <sup>13</sup>C{<sup>1</sup>H} NMR (125.7 MHz, CDCl<sub>3</sub>): δ = 148.7 (CCH(CH<sub>3</sub>)<sub>2</sub>), 141.8 (CCHCHC-CH(CH<sub>3</sub>)<sub>2</sub>), 139.4 (SC(CH<sub>3</sub>)CH), 135.5 (TeC=C), 135.5 (TeC=C), 132.7 (SCC), 131.5 (SCC), 129.5 (CCHCHC-CH(CH<sub>3</sub>)<sub>2</sub>), 126.6 (CCHCHC-CH(CH<sub>3</sub>)<sub>2</sub>), 124.3 (SC(CH<sub>3</sub>)CH), 34.1 (CH(CH<sub>3</sub>)<sub>2</sub>), 24.3 (CH(CH<sub>3</sub>)<sub>2</sub>), 16.0 (SC(CH<sub>3</sub>)). Anal. calcd. (%) for C<sub>32</sub>H<sub>30</sub>S<sub>2</sub>Te: C, 63.39; H, 4.99; S, 10.58; found: C, 63.53; H, 5.16; S, 10.66. HR-MS (MALDI): m/z calcd for C<sub>32</sub>H<sub>30</sub>S<sub>2</sub><sup>130</sup>Te: 680.08457, found: 680.08512 (Δppm = 1.5). UV-vis (in THF): λ<sub>max</sub> = 356 nm, ε = 1.33 × 10<sup>4</sup> M<sup>-1</sup>cm<sup>-1</sup>, λ<sub>max</sub> = 418 nm, ε = 8.48 × 10<sup>3</sup> M<sup>-1</sup>cm<sup>-1</sup>. Mp (°C): decomposes > 200 (under N<sub>2</sub>).

**Attempted annulation of Te-bbt(Me<sub>2</sub>)-cumenyl. Te-bbt(Me<sub>2</sub>)-cumenyl** (43 mg, 0.071 mmol) was dissolved in 14 mL of CH<sub>2</sub>Cl<sub>2</sub> and cooled to 0 °C before adding *p*-chloranil (35 mg, 0.14 mmol) as a solid under a strong counterflow flow of N<sub>2</sub>. This mixture was stirred for 20 minutes before adding 0.40 mL of H<sub>3</sub>CSO<sub>3</sub>H that had been sparged with N<sub>2</sub> for 15 minutes. The reaction mixture was then stirred for 1.5 hours at 0 °C, before removing the solvent under vacuum. The product was extracted using 4 mL of Et<sub>2</sub>O, filtered, and the solvent was removed from the filtrate using vacuum. The crude product was dissolved in 3 mL of a 1:1 solvent mixture and then filtered through silica. Removal of the solvent from the filtrate under vacuum gave 29.5 mg (81 %) of a major product (assigned as the ene-dione) contaminated with tetrachlorohydroquinone. <sup>1</sup>H NMR (498.1 MHz, CDCl<sub>3</sub>): δ = 7.49 (d, <sup>3</sup>J<sub>HH</sub> = 8.5 Hz, 4H, CHCHC-CH(CH<sub>3</sub>)<sub>2</sub>), 7.13 (d, <sup>3</sup>J<sub>HH</sub> = 8.5 Hz, 4H, CHCHC-CH(CH<sub>3</sub>)<sub>2</sub>), 6.89 (s, <sup>3</sup>J<sub>HH</sub>

= 1.5 Hz, 2H, SC(CH<sub>3</sub>)CH), 2.91 (septet, <sup>3</sup>J<sub>HH</sub> = 7.0 Hz, 2H, CH(CH<sub>3</sub>)<sub>2</sub>), 2.55 (s, 6H, SCCH<sub>3</sub>), 1.23 (d, <sup>3</sup>J<sub>HH</sub> = 7.0 Hz, 12H, CH(CH<sub>3</sub>)<sub>2</sub>). <sup>13</sup>C {<sup>1</sup>H} NMR (125.7 MHz, CDCl<sub>3</sub>): δ = 196.9 (C=O), 155.0 (ArC), 136.2 (ArC), 135.2 (ArC), 134.8 (ArC), 130.9 (ArC), 130.4 (ArC), 126.5 (ArC), 122.2 (ArC), 124.3 (ArC), 34.1 (CH(CH<sub>3</sub>)<sub>2</sub>), 24.3 (CH(CH<sub>3</sub>)<sub>2</sub>), 16.0 SC(CH<sub>3</sub>). HR-MS (MALDI): m/z calcd for C<sub>32</sub>H<sub>30</sub>S<sub>2</sub>O<sub>2</sub>: 510.16872, found: 510.16817 (Δppm = 0.5).

**Synthesis of Te-bbt(Br<sub>2</sub>)-cumenyl.** <sup>n</sup>BuLi (2.71 M solution in hexanes, 0.89 mL, 2.4 mmol) was added to a cold (−30 °C) solution of **Te-bbt-cumenyl** (549 mg, 0.949 mmol) in 40 mL of THF. This mixture was stirred for 1.5 hours at room temperature, after which time it was cooled to −30 °C and a cold (−30 °C) solution of 1,2-dibromotetrachloroethane (788 mg, 2.42 mmol) in 1 mL of THF was added. The mixture was then warmed to room temperature and left to stir for 16. The volatiles were removed under vacuum and the crude product was purified via flash chromatography through silica gel with 5 % CH<sub>2</sub>Cl<sub>2</sub> in hexanes as the eluent. After evaporation of the solvent, **Te-bbt(Br<sub>2</sub>)-cumenyl** was obtained as a yellow solid (490 mg, 70 %). Crystals suitable for single-crystal X-ray diffraction were grown from a concentrated Et<sub>2</sub>O solution at room temperature. <sup>1</sup>H NMR (499.8 MHz, CDCl<sub>3</sub>): δ = 7.42 (d, <sup>3</sup>J<sub>HH</sub> = 8.0 Hz, 4H, CHCHC-CH(CH<sub>3</sub>)<sub>2</sub>), 7.33 (d, <sup>3</sup>J<sub>HH</sub> = 8.0 Hz, 4H, CHCHC-CH(CH<sub>3</sub>)<sub>2</sub>), 6.50 (s, 2H, SCBrCH), 3.03 (septet, <sup>3</sup>J<sub>HH</sub> = 7.0 Hz, 2H, CH(CH<sub>3</sub>)<sub>2</sub>), 1.35 (d, <sup>3</sup>J<sub>HH</sub> = 7.0 Hz, 12H, CH(CH<sub>3</sub>)<sub>2</sub>). <sup>13</sup>C {<sup>1</sup>H} NMR (125.7 MHz, CDCl<sub>3</sub>): δ = 149.4 (CCH(CH<sub>3</sub>)<sub>2</sub>), 143.8 (CCHCHC-CH(CH<sub>3</sub>)<sub>2</sub>), 138.5 (TeC=C), 138.1 (TeC=C), 133.4 (SCC), 132.6 (SCC), 129.3 (CCHCHC-CH(CH<sub>3</sub>)<sub>2</sub>), 129.1 (SCBrCH), 126.9 (CCHCHC-CH(CH<sub>3</sub>)<sub>2</sub>), 110.0

(SCBr), 34.2 (CH(CH<sub>3</sub>)<sub>2</sub>), 24.3 (CH(CH<sub>3</sub>)<sub>2</sub>). Anal. Calcd. (%) for C<sub>30</sub>H<sub>24</sub>Br<sub>2</sub>S<sub>2</sub>Te: C, 48.95; H, 3.29; S, 8.71. Found: C, 48.85; H, 3.37; S, 8.67. HR-MS (EI): m/z calcd. for [C<sub>30</sub>H<sub>24</sub><sup>81</sup>Br<sub>2</sub>S<sub>2</sub><sup>130</sup>Te]<sup>+</sup>: 739.87073; found: 739.87396 ( $\Delta$ ppm = 4.4). UV-vis (in THF):  $\lambda_{\max}$  = 359 nm,  $\epsilon$  =  $2.22 \times 10^4$  M<sup>-1</sup>cm<sup>-1</sup>;  $\lambda_{\max}$  = 419 nm,  $\epsilon$  =  $1.53 \times 10^4$  M<sup>-1</sup>cm<sup>-1</sup>. Mp (°C): 169–175 (under N<sub>2</sub>).

**Synthesis of Poly(Te-bbt-cumenyl).** <sup>i</sup>PrMgCl•LiCl (0.74 M solution in THF, 0.023 mL, 0.17 mmol) was added to a solution of **Te-bbt(Br<sub>2</sub>)-cumenyl** (130.0 mg, 0.1766 mmol) in 10 mL of 2-MeTHF, resulting in a colour change from yellow to orange. The mixture was stirred for 15 minutes and then transferred to a flask containing solid Ni(dppe)(*o*-tolyl)Cl (1.03 mg, 0.00177 mmol) and the mixture was heated to 40 °C for 15 hours. The reaction mixture was quenched by adding 1.0 M HCl<sub>(aq)</sub> (2.5 mL, 2.5 mmol). The reaction mixture was then concentrated to a volume of *ca.* 4 mL under vacuum and added dropwise to a 100 mL of cold (–30 °C) MeOH while vigorously stirring. The precipitate was isolated by vacuum filtration, washed with 100 mL of MeOH, and then washed with 200 mL of hexanes. The remaining solid dissolved in 50 mL of THF and then the solvent was removed under vacuum to obtain **poly(Te-bbt-cumenyl)** as a red solid (27 mg, 26 %) that was stored under an inert atmosphere. <sup>1</sup>H NMR (499.8 MHz, CDCl<sub>3</sub>):  $\delta$  = 7.55–7.27, 6.96 (br t, ArH), 6.73 (br t, thienylH), 6.48 (br d, thienylH), 3.12 (br septet, CH(CH<sub>3</sub>)<sub>2</sub>), 3.01 (br septet, CH(CH<sub>3</sub>)<sub>2</sub>), 1.56–1.19 (br d, CH(CH<sub>3</sub>)<sub>2</sub>). UV-vis (in THF):  $\lambda_{\max}$  = 363,  $\epsilon$  =  $1.95 \times 10^4$  M<sup>-1</sup>cm<sup>-1</sup>;  $\lambda_{\max}$  = 492 nm,  $\epsilon$  =  $1.83 \times 10^4$  M<sup>-1</sup>cm<sup>-1</sup>.

### 5.4.3 GPC results

**Table 5.3** – Initial GPC results for partially oxidized **poly(Te-bbt-cumenyl)** in THF.

| Run | $M_n$ (kDa) | $M_w$ (kDa) | $M_w/M_n$   |
|-----|-------------|-------------|-------------|
| 1   | 21.5        | 31.8        | 1.48        |
| 2   | 21.6        | 32.3        | 1.50        |
| 3   | 22.0        | 32.3        | 1.47        |
| AVG | <b>21.7</b> | <b>32.1</b> | <b>1.48</b> |

### 5.4.4 Photoluminescent lifetimes

**Table 5.4** – The photoluminescence decay of a PMMA film containing 1 wt% of **Te-bbt-cumenyl** and the resulting fitting parameters.

|                                      |                             |
|--------------------------------------|-----------------------------|
| Number of components                 | 1                           |
| Lifetime of component 1 ( $\tau_1$ ) | $0.59 \pm 0.02 \mu\text{s}$ |
| Weight of component 1 ( $A_1$ )      | 1.0                         |
| $\chi^2$                             | 0.98                        |
| Durbin-Watson parameter              | 1.45                        |
| Z (run test of the residuals)        | -1.01                       |

### 5.4.5 X-ray crystallography

Crystals suitable for X-ray diffraction studies were removed from a vial and immediately coated in a thin layer of hydrocarbon oil (Paratone-N). A suitable crystal was then mounted on a glass fibre, and quickly placed in a low temperature stream of nitrogen on an X-ray diffractometer. All data was collected on a Bruker APEX II CCD

detector/D8 diffractometer using Cu K $\alpha$  radiation with the crystals cooled to  $-100\text{ }^{\circ}\text{C}$ .<sup>62</sup> The data was corrected for absorption using Gaussian integration from the indexing of the crystal faces.<sup>63</sup> Crystal structures were solved using intrinsic phasing SHELXT-2014<sup>64</sup> and refined using full-matrix least-squares on F<sup>2</sup> (SHELXL).<sup>65</sup> The assignment of hydrogen atom positions were based on the sp<sup>2</sup> or sp<sup>3</sup> hybridization geometries of their respective carbon atoms, and were given thermal parameters 20 % greater than those of their parent atoms.

*Special refinement conditions for Te-bbt-cumenyl:* The crystal used for data collection was found to display non-merohedral twinning. Both components of the twin were indexed with the program *CELL\_NOW* (Bruker AXS Inc., Madison, WI, 2004). The second twin component can be related to the first component by 180° rotation about the [0.464 0 1] axis in real space and about the [0 0 1] axis in reciprocal space. Integrated intensities for the reflections from the two components were written into a *SHELXL-2014* HKLF 5 reflection file with the data integration program *SAINTE* (version 8.38A), using all reflection data (exactly overlapped, partially overlapped and non-overlapped). The refined value of the twin fraction (*SHELXL-2014* BASF parameter) was 0.382(2).

*Special refinement conditions for Te-bbt(Br<sub>2</sub>)-cumenyl:* The disordered isopropylphenyl groups had the following restraints applied: **SADI** (66 total restraints) applied to the phenyl C–C distances, and to isopropyl group (defined by atoms C19, C20, C21) C–C distances; **RIGU** (240 total restraints) applied to the anisotropic displacement parameters.



**Table 5.5** – Crystallographic data for the **Te-bbts** discussed in this Chapter.

| <b>Compound</b>  | <b>Te-bbt-SiMe<sub>3</sub></b>                                    | <b>Te-bbt-(C<sub>6</sub>H<sub>4</sub>)OCH<sub>3</sub></b>        | <b>Te-bbt-cumenyl</b>                             | <b>Te-bbt(Br<sub>2</sub>)-cumenyl</b>                             |
|--|---|--|---|---|
| formula  | C <sub>18</sub> H <sub>22</sub> S <sub>2</sub> Si <sub>2</sub> Te | C <sub>26</sub> H <sub>18</sub> O <sub>2</sub> S <sub>2</sub> Te | C <sub>30</sub> H <sub>26</sub> S <sub>2</sub> Te | C <sub>30</sub> H <sub>24</sub> Br <sub>2</sub> S <sub>2</sub> Te |
| form. wt. (g/mol)  | 486.25  | 554.12   | 578.23  | 736.03  |
| crys. dimes. (mm)  | 0.19×0.15×0.09  | 0.47×0.35×0.18   | 0.54×0.09×0.06                                    | 0.35×0.14×0.03  |
| Crystal system   | Monoclinic  | Triclinic  | Monoclinic  | Triclinic   |
| Space group  | <i>P</i> 2 <sub>1</sub> / <i>c</i>                                | <i>P</i> $\bar{1}$   | <i>P</i> 2 <sub>1</sub> / <i>n</i>                | <i>P</i> $\bar{1}$  |
| <i>a</i> (Å)   | 15.7083(15)   | 10.0707(4)   | 9.7421(7)   | 9.8771(2)   |
| <i>b</i> (Å)   | 10.8790(12)   | 10.0864(4)   | 14.1876(7)  | 11.0801(2)  |
| <i>c</i> (Å)   | 12.3190(15)   | 13.5383(6)   | 18.7139(9)  | 14.3139(3)  |
| $\alpha$ (deg)   | -   | 91.7026(6)   | -   | 74.4813(10)   |
| $\beta$ (deg)  | 101.950(7)  | 110.2996(5)  | 102.393(3)  | 85.1080(10)   |
| $\gamma$ (deg)   | -   | 118.4913(5)  | -   | 67.9060(5)  |
| <i>V</i> (Å <sup>3</sup> )   | 2059.6(4)   | 1101.32(8)   | 2526.3(3)   | 1398.35(5)  |
| <i>Z</i>   | 4   | 2  | 4   | 2   |
| $\rho_{\text{calcd}}$ (g cm <sup>-3</sup> )  | 1.568   | 1.671  | 1.520   | 1.748   |
| $\mu$ (mm <sup>-1</sup> )  | 14.37   | 1.562  | 10.94   | 13.26   |
| temperature (°C)   | -100  | -100   | -100  | -100  |
| 2 $\theta_{\text{max}}$ (deg)  | 145.18  | 55.13  | 145.51  | 145.02  |
| total data   | 13946   | 10139  | 5502  | 9849  |
| unique data ( <i>R</i> <sub>int</sub> )  | 4070 (0.0607)   | 5080 (0.0061)  | 5502 (0.1202)                                     | 5347 (0.0222)   |
| Obs [ <i>I</i> > 2 $\sigma$ ( <i>I</i> )]  | 3481  | 4924   | 5175  | 4960  |
| <i>R</i> <sub>1</sub> [ <i>F</i> <sub>o</sub> <sup>2</sup> ≥ 2 $\sigma$ ( <i>F</i> <sub>o</sub> <sup>2</sup> )] <sup>a</sup> | 0.0498  | 0.0175   | 0.0834  | 0.0323  |
| <i>wR</i> <sub>2</sub> [all data] <sup>a</sup>   | 0.1372  | 0.0470   | 0.2296  | 0.0884  |
| max/min $\Delta\rho$ (e Å <sup>-3</sup> )  | 1.668/-1.366  | 0.323/-0.270   | 1.011/-1.505                                      | 1.052/-1.394  |

$$^a R_1 = \sum ||F_o| - |F_c|| / \sum |F_o|; wR_2 = [\sum w(F_o^2 - F_c^2)^2 / \sum w(F_o^4)]^{1/2}$$

#### 5.4.6 Computational methodology

All computations have been carried out with the Gaussian16 software package.<sup>66</sup> Geometry optimizations of the gas-phase structures have been performed using density functional theory (DFT) with the hybrid density functional (B3LYP)<sup>67,68</sup> in combination with the basis set cc-pVDZ (for C, H, B, O, N)<sup>69</sup> as well as the basis set cc-pVDZ(-PP) for Te.<sup>70</sup> The cc-PVDZ-PP basis set uses the corresponding effective core potential (ECP) accounting for 28 electrons. The use of the cc-PVDZ and cc-PVDZ-PP basis sets will hereafter be referred to as cc-PVDZ(-PP). The basis sets as well as the ECP for the Te atom were obtained from the Basis Set Exchange Library.<sup>71,72</sup> Frequency analysis confirmed all obtained structures to be local minima on the potential energy surface. The optimized geometry of the  $S_0$  ground state was determined at the B3LYP level of theory. The phosphorescence energy was calculated by computing the optimized geometry of the lowest lying triplet state ( $T_1$ ) using UB3LYP (spin-unrestricted B3LYP) with the same basis sets as specified above. Subsequent TD-DFT calculations were used to predict the vertical excitation energies of the first 10 singlet states (which were used to generate the computed UV-vis spectrum)<sup>73</sup> and first ten triplet states using the B3LYP functional as well as the cc-PVDZ(-PP) basis sets starting from the B3LYP optimized gas-phase  $S_0$  geometry. The presented molecular orbitals (MOs) were extracted from the Gaussian16 checkpoint-files and are visualized with VMD.<sup>74</sup>

## 5.5 References

1. T. Chivers and R. S. Laitinen, *Chem. Soc. Rev.*, **2015**, *44*, 1725–1739.
2. E. Rivard, *Chem. Lett.*, **2015**, *44*, 730–736.
3. E. I. Carrera and D. S. Seferos, *Macromolecules*, **2015**, *48*, 297–308.
4. M. Pittelkow, T. K. Reenberg, K. T. Nielsen, M. J. Magnussen, T. I. Sølling, F. C. Krebs and J. B. Christensen, *Angew. Chem. Int. Ed.*, **2006**, *45*, 5666–5670.
5. A. Patra, Y. H. Wijsboom, G. Leitius and M. Bendikov, *Org. Lett.*, **2009**, *11*, 1487–1490.
6. M. Jiang, J. Guo, B. Liu, Q. Tan and B. Xu, *Org. Lett.*, **2019**, *21*, 8328–8333.
7. L. Yang, W. Gu, L. Lv, Y. Chen, Y. Yang, P. Ye, J. Wu, L. Hong, A. Peng, and H. Huang, *Angew. Chem. Int. Ed.*, **2018**, *57*, 1096–1102.
8. S. Ye, L. Janasz, W. Zajaczkowski, J. G. Manion, A. Mondal, T. Marszalek, D. Andrienko, K. Müllen, W. Pisula and D. S. Seferos, *Macromol. Rapid Commun.*, **2019**, *40*, 1800596.
9. W. H. Lee, S. K. Lee, W. S. Shin, S. J. Moon and I. N. Kang, *J. Polym. Sci. Part A*, **2013**, *51*, 2753–2758.
10. G. He, L. Kang, W. Torres Delgado, O. Shynkaruk, M. J. Ferguson, R. McDonald and E. Rivard, *J. Am. Chem. Soc.*, **2013**, *135*, 5360–5363.
11. Y. S. Park, Q. Wu, C. Y. Nam and R. B. Grubbs, *Angew. Chem. Int. Ed.*, **2014**, *53*, 10691–10695.
12. E. H. Jung, S. Bae, T. W. Yoo and W. H. Jo, *Polym. Chem.*, **2014**, *5*, 6545–6550.

13. R. S. Ashraf, I. Meager, M. Nikolka, M. Kirkus, M. Planells, B. C. Schroeder, S. Holliday, M. Hurhangee, C. B. Nielsen, H. Sirringhaus, and I. McCulloch, *J. Am. Chem. Soc.*, **2015**, *137*, 1314–1321.
14. A. A. Jahnke, B. Djukic, T. M. McCormick, E. Buchaca Domingo, C. Hellmann, Y. Lee and D. S. Seferos, *J. Am. Chem. Soc.*, **2013**, *135*, 951–954.
15. J. G. Manion, S. Ye, A. H. Proppe, A. W. Laramée, G. R. Mckeown, E. L. Kynaston, S. O. Kelley, E. H. Sargent and D. S. Seferos, *ACS Appl. Energy Mater.*, **2018**, *1*, 5033–5042.
16. W. Xing, P. Ye, J. Lu, X. Wu, Y. Chen, T. Zhu, A. Peng and H. Huang, *J. Power Sources*, **2018**, *401*, 13–19.
17. G. He, W. Torres Delgado, D. J. Schatz, C. Merten, A. Mohammadpour, L. Mayr, M. J. Ferguson, R. McDonald, A. Brown, K. Shankar and E. Rivard, *Angew. Chem. Int. Ed.*, **2014**, *53*, 4587–4591.
18. G. He, B. D. Wiltshire, P. Choi, A. Savin, S. Sun, A. Mohammadpour, M. J. Ferguson, R. McDonald, S. Farsinezhad, A. Brown, K. Shankar and E. Rivard, *Chem. Commun.*, **2015**, *51*, 5444–5447.
19. A. K. Mahrok, E. I. Carrera, A. J. Tilley, S. Ye and D. S. Seferos, *Chem. Commun.*, **2015**, *51*, 5475–5478.
20. N. Nagahora, S. Yahata, S. Goto, K. Shioji and K. Okuma, *J. Org. Chem.*, **2018**, *83*, 1969–1975.

21. W. Torres Delgado, C. A. Braun, M. P. Boone, O. Shynkaruk, Y. Qi, R. McDonald, M. J. Ferguson, P. Data, S. K.C. Almeida, I. De Aguiar, G. L. C. De Souza, A. Brown, G. He and E. Rivard, *ACS Appl. Mater. Interfaces*, **2018**, *10*, 12124–12134.
22. K. Takahashi, S. Shimo, E. Hupf, J. Ochiai, C. A. Braun, W. Torres Delgado, L. Xu, G. He, E. Rivard and N. Iwasawa, *Chem. Eur. J.*, **2019**, *25*, 8479–8483.
23. K. Takimiya, Y. Kunugi, Y. Konda, N. Niihara and T. Otsubo, *J. Am. Chem. Soc.*, **2004**, *126*, 5084–5085.
24. M. Kaur, D. S. Yang, J. Shin, T. W. Lee, K. Choi, M. J. Cho and D. H. Choi, *Chem. Commun.*, **2013**, *49*, 5495–5497.
25. M. Kaur, D. H. Lee, D. S. Yang, H. A. Um, M. J. Cho, J. S. Kang and D. H. Choi, *Chem. Commun.*, **2014**, *50*, 14394–14396.
26. M. Al-Hashimi, Y. Han, J. Smith, H. S. Bazzi, S. Y. A. Alqaradawi, S. E. Watkins, T. D. Anthopoulos and M. Heeney, *Chem. Sci.*, **2016**, *7*, 1093–1099.
27. T. Oyama, Y. S. Yang, K. Matsuo and T. Yasuda, *Chem. Commun.*, **2017**, *53*, 3814–3817.
28. T. M. McCormick, E. I. Carrera, T. B. Schon and D. S. Seferos, *Chem. Commun.*, **2013**, *49*, 11182–11184.
29. E. I. Carrera and D. S. Seferos, *Organometallics*, **2017**, *36*, 2612–2621.
30. G. E. Garrett, E. I. Carrera, D. S. Seferos and M. S. Taylor, *Chem. Commun.*, **2016**, *52*, 9881–9884.
31. R. I. Sugimoto, K. Yoshino, S. Inoue and K. Tsukagoshi, *Jpn. J. Appl. Phys.*, **1985**, *24*, L425–L427.

32. S. Inoue, T. Jigami, H. Nozoe, T. Otsubo and F. Ogura, *Tetrahedron Lett.*, **1994**, *35*, 8009–8012.
33. B. T. Luppi, R. McDonald, M. J. Ferguson, L. Sang and E. Rivard, *Chem. Commun.*, **2019**, *55*, 14218–14221.
34. A. Alka, V. S. Shetti and M. Ravikanth, *Dalton Trans.*, **2019**, *48*, 4444–4459.
35. S. Wang, X. Li, X. Hou, Y. Sun and X. Shao, *Chem. Commun.*, **2016**, *52*, 14486–14489.
36. B. C. Schroeder, C. B. Nielsen, Y. J. Kim, J. Smith, Z. Huang, J. Durrant, S. E. Watkins, K. Song, T. D. Anthopoulos, and I. McCulloch, *Chem. Mater.*, **2011**, *23*, 4025–4031.
37. X. Guo, S. Wang, V. Enkelmann, M. Baumgarten, and K. Müllen, *Org. Lett.*, **2011**, *13*, 6062–6065.
38. Y. Matano, T. Miyajima, T. Fukushima, H. Kaji, Y. Kimura and H. Imahori, *Chem. Eur. J.*, **2008**, *14*, 8102–8115.
39. T. Miyajima, Y. Matano and H. Imahori, *Eur. J. Org. Chem.*, **2008**, 255–259.
40. S. Y. Chen, Y. C. Pao, S. K. Sahoo, W. C. Huang, Y. Y. Lai and Y. J. Cheng, *Chem. Commun.*, **2018**, *54*, 1517–1520.
41. C.-Y. Kuo, Y.-C. Huang, C.-Y. Hsiow, Y.-W. Yang, C.-I. Huang, S.-P. Rwei, H.-L. Wang and L. Wang, *Macromolecules*, **2013**, *46*, 5985–5997.
42. P. M. Beaujuge, H. N. Tsao, M. R. Hansen, C. M. Amb, C. Risko, J. Subbiah, K. R. Choudhury, A. Mavrinskiy, W. Pisula, J. L. Bredas, F. So, K. Müllen and J. R. Reynolds, *J. Am. Chem. Soc.*, **2012**, *134*, 8944–8957.

43. J. A. Letizia, M. R. Salata, C. M. Tribout, A. Facchetti, M. A. Ratner and T. J. Marks, *J. Am. Chem. Soc.*, **2008**, *130*, 9679–9694.
44. B. Djukic, P. K. Poddutoori, P. A. Dube, T. Seda, H. A. Jenkins and M. T. Lemaire, *Inorg. Chem.*, **2009**, *48*, 6109–6116.
45. M. Oba, M. Endo, K. Nishiyama, A. Ouchi and W. Ando, *Chem. Commun.*, **2004**, 1672–1673.
46. M. Oba, Y. Okada, M. Endo, K. Tanaka, K. Nishiyama, S. Shimada and W. Ando, *Inorg. Chem.*, **2010**, *49*, 10680–10686.
47. P. Serguievski and M. R. Detty, *Organometallics*, **1997**, *16*, 4386–4391.
48. A. A. Jahnke, G. W. Howe and D. S. Seferos, *Angew. Chem. Int. Ed.*, **2010**, *49*, 10140–10144.
49. M. Mantina, A. C. Chamberlin, R. Valero, C. J. Cramer and D. G. Truhlar, *J. Phys. Chem. A*, **2009**, *113*, 5806–5812.
50. H. A. Lin, K. Kato, Y. Segawa, L. T. Scott and K. Itami, *Chem. Sci.*, **2019**, *10*, 2326–2330.
51. T. Tsukamoto and G. Dong, *Angew. Chem. Int. Ed.*, **2020**, DOI:10.1002/anie.202004719.
52. A. Kiriya, V. Senkovskyy and M. Sommer, *Macromol. Rapid Commun.*, **2011**, *32*, 1503–1517.
53. S. Ye, M. Steube, E. I. Carrera and D. S. Seferos, *Macromolecules*, **2016**, *49*, 1704–1711.

54. S. Ye, S. M. Foster, A. A. Pollit, S. Cheng and D. S. Seferos, *Chem. Sci.*, **2019**, *10*, 2075–2080.
55. E. A. Standley, S. J. Smith, P. Müller and T. F. Jamison, *Organometallics*, **2014**, *33*, 2012–2018.
56. J. L. Dutton, G. J. Farrar, M. J. Sgro, T. L. Battista and P. J. Ragoona, *Chem. Eur. J.*, **2009**, *15*, 10263–10271.
57. J. Linshoef, E. J. Baum, A. Hussain, P. J. Gates, C. Näther, and A. Staubitz, *Angew. Chem. Int. Ed.*, **2014**, *53*, 12916–12920.
58. A. F. Burchat, J. M. Chong and N. Nielsen, *J. Organomet. Chem.*, **1997**, *542*, 281–283.
59. T. R. Hoye, B. M. Eklov and M. Voloshin, *Org. Lett.*, **2004**, *6*, 2567–2570.
60. J. Durbin and G. S. Watson, *Biometrika*, **1951**, *38*, 159–177.
61. D. V. O'Connor and D. Phillips, *Time Correlated Single Photon Counting*; Academic Press: New York, **1984**.
62. H. Hope, *Prog. Inorg. Chem.*, **1994**, *41*, 1–19.
63. R. H. Blessing, *Acta Crystallogr. A*, **1995**, *51*, 33–38.
64. G. M. Sheldrick, *Acta Crystallogr. A*, **2015**, *71*, 3–8.
65. G. M. Sheldrick, *Acta Crystallogr. C*, **2015**, *71*, 3–8.
66. M. J. Frisch, G. W. Trucks, H. B. Schlegel, G. E. Scuseria, M. A. Robb, J. R. Cheeseman, G. Scalmani, V. Barone, G. A. Petersson, H. Nakatsuji, X. Li, M. Caricato, A. V. Marenich, J. Bloino, B. G. Janesko, R. Gomperts, B. Mennucci, H. P. Hratchian, J. V. Ortiz, A. F. Izmaylov, J. L. Sonnenberg, D. Williams-Young, F.



- Ding, F. Lipparini, F. Egidi, J. Goings, B. Peng, A. Petrone, T. Henderson, D. Ranasinghe, V. G. Zakrzewski, J. Gao, N. Rega, G. Zheng, W. Liang, M. Hada, M. Ehara, K. Toyota, R. Fukuda, J. Hasegawa, M. Ishida, T. Nakajima, Y. Honda, O. Kitao, H. Nakai, T. Vreven, K. Throssell, J. A. Montgomery, Jr., J. E. Peralta, F. Ogliaro, M. J. Bearpark, J. J. Heyd, E. N. Brothers, K. N. Kudin, V. N. Staroverov, T. A. Keith, R. Kobayashi, J. Normand, K. Raghavachari, A. P. Rendell, J. C. Burant, S. S. Iyengar, J. Tomasi, M. Cossi, J. M. Millam, M. Klene, C. Adamo, R. Cammi, J. W. Ochterski, R. L. Martin, K. Morokuma, O. Farkas, J. B. Foresman and D. J. Fox, *Gaussian 16, Revision A.03*, Gaussian, Inc., Wallingford CT, **2016**.
67. A. D. Becke, *J. Chem. Phys.*, **1993**, *98*, 5648–5652.
68. C. Lee, W. Yang and R. G. Parr, *Phys. Rev. B*, **1988**, *37*, 785–789.
69. T. H. Dunning, Jr. *J. Chem. Phys.*, **1989**, *90*, 1007–1023.
70. K. A. Peterson, D. Figgen, E. Goll, H. Stoll and M. Dolg, *J. Chem. Phys.*, **2003**, *119*, 11113–11123.
71. D. Feller, *J. Comput. Chem.*, **1996**, *17*, 1571–1586.
72. K. L. Schuchardt, B. T. Didier, T. Elsethagen, L. Sun, V. Gurumoorthi, J. Chase, J. Li and T. L. Windus, *J. Chem. Inf. Model.*, **2004**, *47*, 1045–1052.
73. Procedure for generating computed UV-vis spectra: <http://gaussian.com/uvvisplot/>
74. W. Humphrey, A. Dalke and K. Schulten, *J. Mol. Graph.*, **1996**, *14*, 33–38.

## Chapter 6 –Summary and Future Directions

### 6.1 Tuning the Emission and Enhancing the Quantum Yield of Phosphorescence from Borylated Tellurophenes

To date, the highest quantum yield of phosphorescence from a tellurophene is the borylated tellurophene **1** ( $\Phi = 20\%$ , Figure 6.1).<sup>1</sup> This tellurophene features three-coordinate boryl groups, which are intrinsically electron-deficient due to the presence of an empty p-orbital on each boron centre, with some steric protection supplied by the adjacent pinacol (Pin) groups. In Chapter 2, the tuning of emission *via* the coordination of a Lewis base to the boron centre of the bis(pinacolatoboryl)tellurophene **2** ( $\lambda_{em} = 535$  nm ( $\Phi = 11.5\%$ ) was discussed (Scheme 6.1). The electron-donating nature of the methyl groups in pinacol (along with weak O→B  $\pi$ -donation) resulted in a low Lewis acidity at the boron centres, only allowing for the coordination of a very small, strongly Lewis basic *N*-heterocyclic carbene (NHC), as shown in Scheme 6.1. Coordination of one equivalent of the NHC was found to slightly red-shift the emission, while the coordination of two equivalents of NHC to **2** quench the emission (Scheme 6.1).

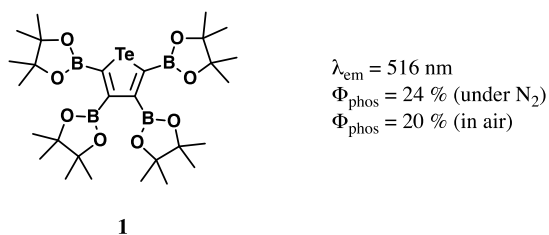
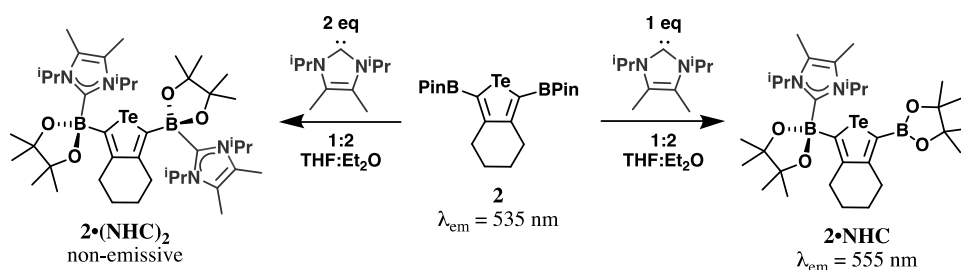


**Figure 6.1** – The highest reported quantum yield of phosphorescence from a tellurophene.



**Scheme 6.1** – Coordination of an NHC to the boron centres in **2** to form **2•NHC** and **2•(NHC)<sub>2</sub>**.

In Chapter 3, the bis(diisopropoxy)boryl)tellurophene precursor **3** was subjected to exchange reactions with diols or bis(amines), or reacted with MesMgBr, to afford the new bis(boryl)tellurophenes **4–7** (Figure 6.2). In particular, the boron centres in **4** should be more reactive than **2**, since catechol is planar and electron-withdrawing in nature. Tellurophene **4** only exhibited emission at 77 K, suggesting that molecular motion is a common mechanism for the non-radiative decay of the triplet excited state. Therefore, I propose that the coordination of an aryl anion to **4** could provide steric bulk and rigidity to this tellurophene, suppressing molecular motion and enhancing room temperature phosphorescence in the solid state (Scheme 6.2). Furthermore, **4** is a more suitable substrate than **2** for exploring how the emission can be tuned upon the addition

of one equivalent of an aryl anion, such as a Grignard reagent or a lithiated aryl species. Therefore, this reaction can also be used to probe whether the aryl anion (featuring electron-rich or electron-poor groups) can enable the emission of **4** to be tuned.

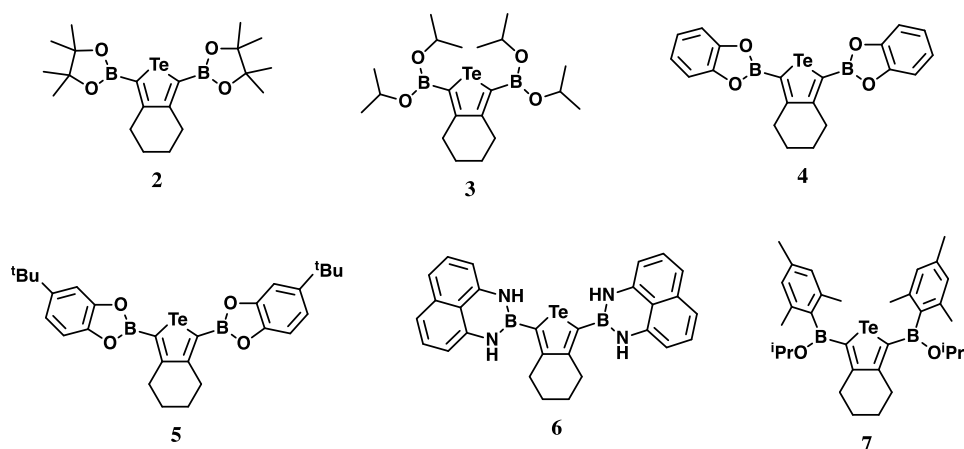
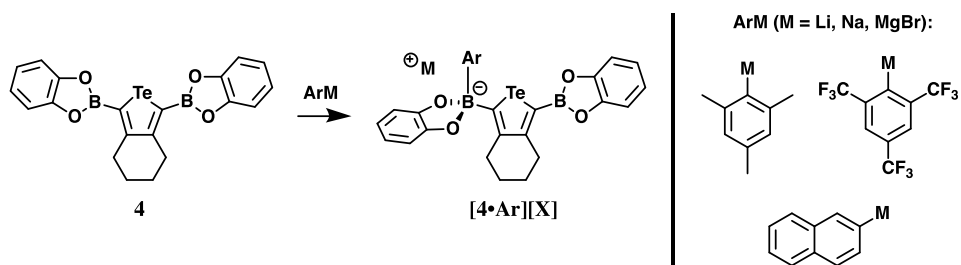


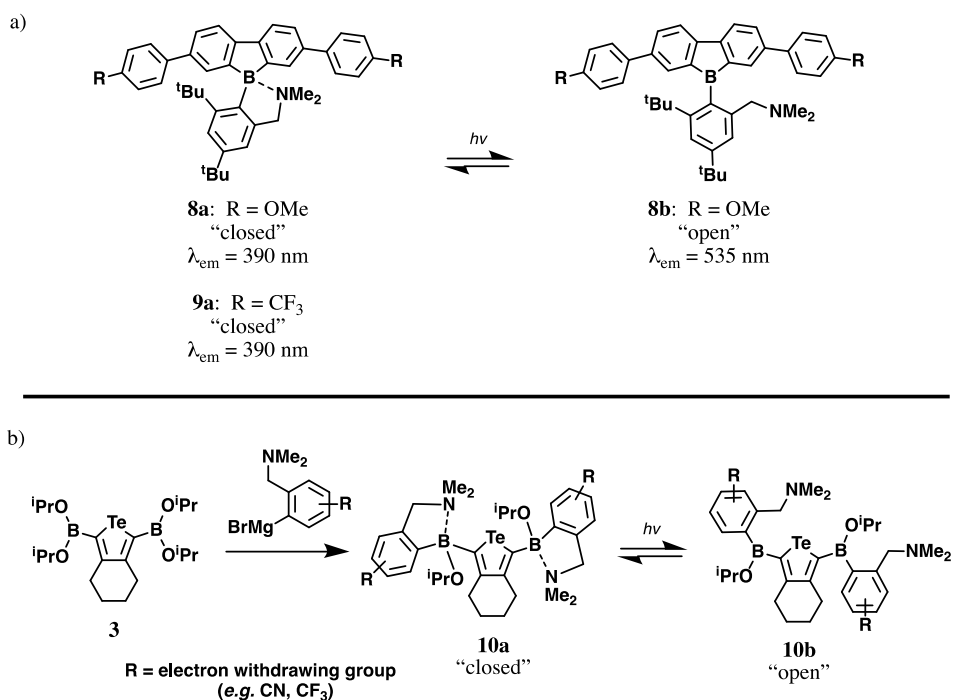
**Figure 6.2** – Bis(boryl)tellurophenes discussed in this Thesis.



**Scheme 6.2** – The proposed coordination of aryl salts to **4** in order to tune the emission wavelength and enhance RTP.

Boron-bound substituents that include a pendant Lewis basic unit can be used as a means to tune the emission in response to an external stimuli, such as UV-light.<sup>2</sup> For example, Chujo and coworkers have used the mamx ligand (mamx = 2,4-di-*tert*-butyl-6-[(dimethylamino)methyl]phenyl) to make emissive boron compounds (Scheme

6.3a) which contains a pendant dimethylamino group that can interact with a boron centre.<sup>3</sup> Upon excitation, dual emission was observed for the dibenzoborole **8a** featuring methoxy side groups (Scheme 6.3a). This dual emission was attributed to emission from the closed form (**8a**,  $\lambda_{em} = 330$  nm) and emission from a twisted intramolecular charge transfer (TICT) state enabled by the dissociation of the B–N bond under UV-light irradiation to give the open form (**8b**,  $\lambda_{em} = 535$  nm). However, the longer wavelength emission was not observed when the methoxy groups (OMe) were replaced with electron-withdrawing trifluoromethyl groups (CF<sub>3</sub>) in **9a**, likely due to a stronger B–N interaction inhibiting the open form (and thus prevent the formation of a TICT state).



**Scheme 6.3** – a) Borafluorenes with pendant amines, and b) the proposed use of tellurophenes featuring boryl groups with pendant amines to increase atmospheric stability of the tellurophene and potentially turn the emission “on” and “off”.

White light emission is frequently used in everyday applications, such as room lighting and the backlighting in displays, making its efficiency an important parameter to optimize.<sup>4,5</sup> White light is usually generated by blending or layering several emissive components, which together emit white light. Achieving white light emission from the dual emission of a single compound would simplify device fabrication and reproducibility, while making the devices less susceptible to colour aging or phase segregation of the various components. Furthermore, phosphors are particularly desirable due to the higher theoretical maximum electroluminescent efficiency enabled by the allowed emission from triplet excited states, which comprise 75 % of all electrically generated excitons.<sup>6</sup>

Due to the modest quantum yields of phosphorescence observed for several borylated tellurophenes in air,<sup>1</sup> there is interest in tuning the emission of these systems and increasing the efficiency of the light-emission properties. Furthermore, coaxing dual emission in order to achieve white light emission out of a single molecule is highly desirable. Therefore, it would be of great interest to study the use of a pendant amine on a borylated tellurophene, to see if dual emission is possible *via* emission from the closed form and emission from a TICT state enabled by B–N dissociation under UV-light irradiation (Scheme 6.3b).

It is possible that similar to **1** (Scheme 6.1), coordination to the B centres could quench the emission from the proposed bis(boryl)tellurophene (**10a**, Scheme 6.3). However, an added feature is that the pendant amine should allow for air- and moisture-stability of the Lewis acidic boron centres. Therefore, even if dual emission is not

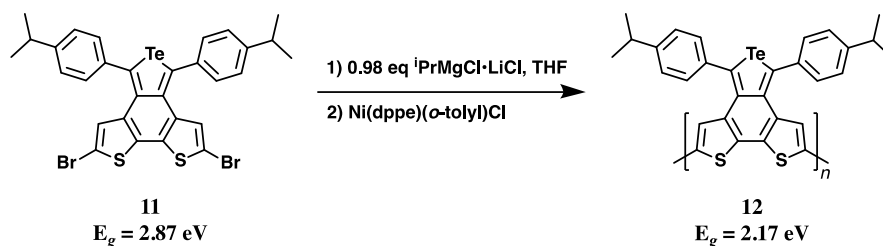
possible from this system, it is still of interest to study the reversible B–N interaction as a means of stabilizing the empty p-orbital on boron. For example, boron-bound electron-withdrawing groups could be incorporated in order to tune the emission of the bis(boryl)tellurophene **10a/b**, with stability provided by the reversible B–N interaction. In the “closed” form (**10a**) the boron centre is fully saturated and therefore less prone to react with moisture, however the emissive “open” form (**10b**) is generated upon UV-light irradiation (Scheme 6.3b).

## 6.2 Optimizing OPV Devices with Tellurophenes

In Chapter 5, the synthesis of  $\pi$ -extended tellura(benzo)bithiophenes such **11**, and its corresponding polymer **12** synthesized *via* Kumada Catalyst-Transfer Polycondensation (KCTP), were discussed (Scheme 6.4). These materials were initially developed in the hope that long delocalized polymer chains with repeat units featuring the heavy atom Te, could lead to small bandgap polymers for OPVs. However, the optical bandgap of **12** (2.17 eV) is too large to make this polymer suitable as a donor material for OPVs, since optical bandgaps of 1.2–1.7 eV are required to achieve the highest theoretical OPV device efficiencies.<sup>7</sup>

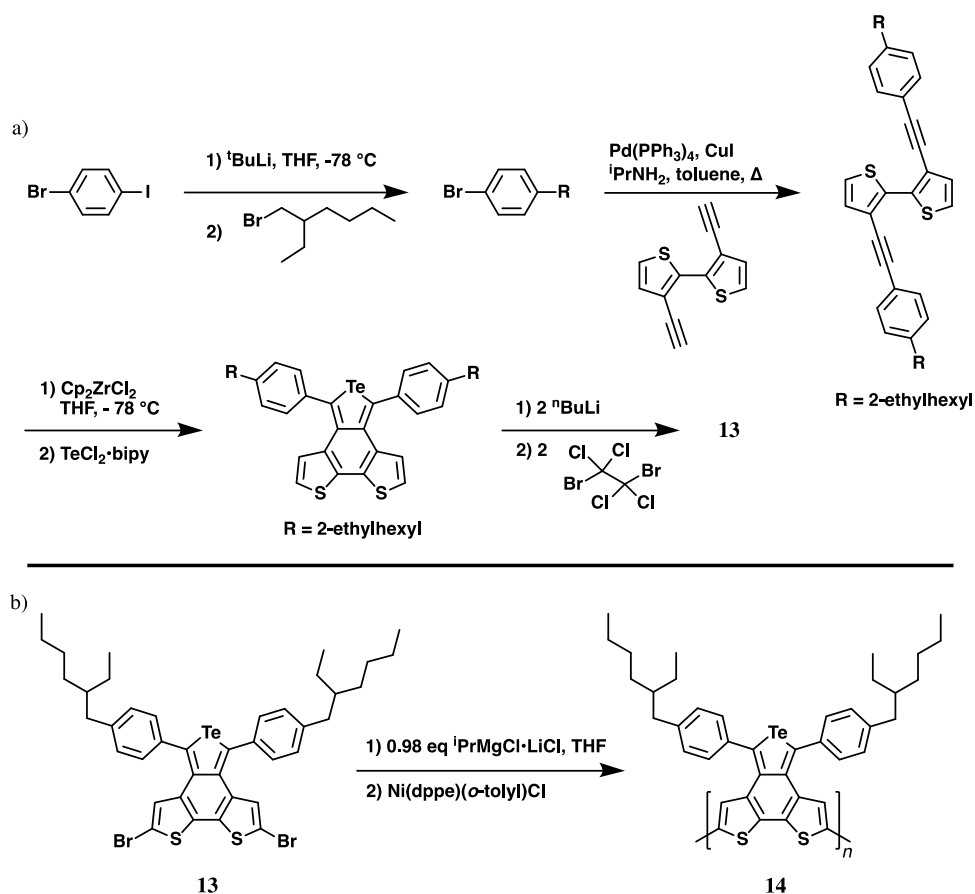
Despite the low suitability of **Te-bbt** homopolymers such as **12** for OPV devices, tellurophene-containing polymers are not well studied and there is still interest in these polymers as RTP phosphors or as semiconductors for OFETs. In order to overcome the poor solubility of **12** and gain access to higher molecular weight Te-

polymers, the incorporation of alkyl groups such as 2-ethylhexyl groups is proposed for the dibrominated monomer **11** and the corresponding polymer **12** (Scheme 6.5). However, one concern with incorporating alkyl groups in this way is that it will sterically prevent monomer units from achieving a coplanar arrangement, disrupting extended  $\pi$ -conjugation throughout the polymer backbone, although it is also possible that van der Waals interactions between the alkyl chain will still allow for a coplanar arrangement between **Te-bbt** repeat units.



**Scheme 6.4** – The polymerization of **11** to form polymer **12** via KCTP.





**Scheme 6.5** – a) The proposed synthesis, and b) the polymerization, of a **Te-bbt** monomer with solubilizing alkyl groups **13** in the hope of obtaining higher molecular weights for polymer **14** *via* KCTP.

As described in this Thesis, many research groups have explored the incorporation of tellurophene-based donors and acceptors to give functioning OPVs with power conversion efficiencies of up to 7.5%.<sup>8</sup> However, most often tellurophenes are incorporated into systems that have been optimized for thiophenes, however studies have shown that tellurophene-containing molecules and polymers often behave differently than their thiophene analogues.<sup>9</sup> For example, studies comparing different chalcogenophene-based donors, usually obtain better results for tellurophene analogues

at lower donor:acceptor ratios than that of thiophene/selenophene active layers.<sup>7,10,11</sup> Furthermore, the field of OPVs has moved beyond fullerene-based acceptors, but Te-based donor polymers have only been incorporated into devices with these early benchmarking fullerene acceptors. Selection of the acceptor relative to the donor is extremely important with both donor/acceptor miscibility as well as the relative LUMO levels being important parameters within OPV devices; the LUMO level of the acceptor must be lower in energy than that of the donor in order to overcome the binding energy of the exciton, however it is also important that the energy levels of the LUMOs are not too high, in order to minimize thermalization loss.<sup>12,13</sup> State-of-the-art non-fullerene acceptors are typically either: 1) based on fused aromatics diimides such as PDI or NDI (Figure 6.3), or 2) macrocycles that incorporate strong intramolecular push-pull electronic effects such as the popular acceptor unit, ITIC (Figure 6.3).<sup>14-16</sup> Careful selection of a non-fullerene acceptor (considering miscibility and relative LUMO levels) are routes with a high potential to elevate Te-based OPVs. It would also be very interesting to combine a low band-gap Te-based donor with a Te-based acceptor such as Huang's PDI acceptor (**13**).<sup>17</sup> This may result in enhanced formation of long-lived triplet excitons and may also lead to beneficial bulk charge transport properties due to Te...Te interactions.

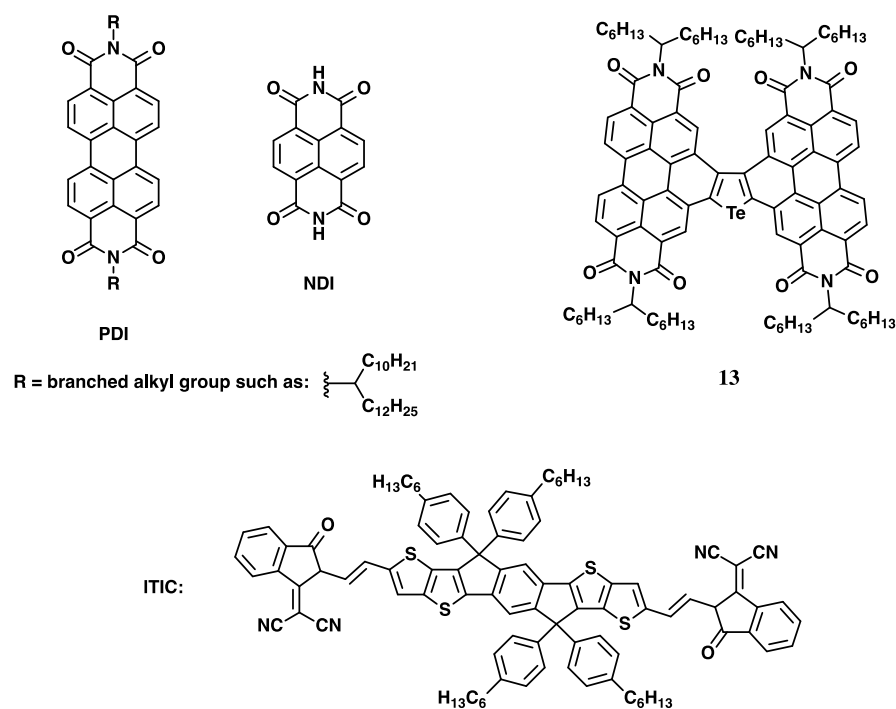


**Figure 6.3** – Examples of non-fullerene acceptors for OPVs.

### 6.3 Future Outlook

With increasing attention placed on heavy main group heterocycles such as tellurophenes, the previously untapped potential of these unique moieties are slowly being uncovered. Encouragingly, room temperature phosphorescence (RTP) with quantum yields of up to 20 % in air has been noted from tellurophenes in the solid state, although tuning the emission, while maintaining high quantum yields remains a challenge. In addition, promising results have been reported when tellurophene-based molecules/polymers are incorporated into organic photovoltaics and organic field-effect transistors, although there is still a lot of room for growth in these fields. Of note, tellurophenes have been used to build OPV devices with efficiencies above 7 %,

however further progress can undoubtedly be realized if non-fullerene acceptors are selected to compliment Te-based donor materials. This will hopefully lead to a new class of building blocks for the advancement of OPV technology in order to harness the sun's energy in an efficient and cost-effective manner.

## 6.4 References

1. G. He, W. Torres Delgado, D. J. Schatz, C. Merten, A. Mohammadpour, L. Mayr, M. J. Ferguson, R. McDonald, A. Brown, K. Shankar and E. Rivard, *Angew. Chem. Int. Ed.*, **2014**, *53*, 4587–4591.
2. S. K. Mellerup and S. Wang, *Chem. Soc. Rev.*, **2019**, *48*, 3537–3549.
3. T. Matsumoto, H. Takamine, K. Tanaka and Y. Chujo, *Mater. Chem. Front.*, **2017**, *1*, 2368–2375.
4. M. C. Gather, A. Köhnen and K. Meerholz, *Adv. Mater.*, **2011**, *23*, 233–248.
5. M. Shang, C. Li and J. Lin, *Chem. Soc. Rev.*, **2014**, *43*, 1372–1386.
6. Z. He, W. Zhao, J. W.Y. Lam, Q. Peng, H. Ma, G. Liang, Z. Shuai and B. Z. Tang, *Nat. Commun.*, **2017**, *8*, 416.
7. G. Dennler, M. C. Scharber and C. J. Brabec, *Adv. Mater.*, **2009**, *21*, 1323–1338.
8. L. Yang, W. Gu, L. Lv, Y. Chen, Y. Yang, P. Ye, J. Wu, L. Hong, A. Peng and H. Huang, *Angew. Chem. Int. Ed.*, **2018**, *57*, 1096–1102.

9. J. G. Manion, S. Ye, A. H. Proppe, A. W. Laramée, G. R. McKeown, E. L. Kynaston, S. O. Kelley, E. H. Sargent and D. S. Seferos, *ACS Appl. Energy Mater.*, **2018**, *1*, 5033–5042.
10. E. H. Jung, S. Bae, T. W. Yoo and W. H. Jo, *Polym. Chem.*, **2014**, *5*, 6545–6550.
11. R. S. Ashraf, I. Meager, M. Nikolka, M. Kirkus, M. Planells, B. C. Schroeder, S. Holliday, M. Hurhangee, C. B. Nielsen, H. Sirringhaus and I. McCulloch, *J. Am. Chem. Soc.*, **2015**, *137*, 1314–1321.
12. C. J. Brabec, S. Gowrisanker, J. J. M. Halls, D. Laird, S. Jia and S. P. Williams, *Adv. Mater.*, **2010**, *22*, 3839–3856.
13. G. Li, R. Zhu and Y. Yang, *Nat. Photonics*, **2012**, *6*, 153–161.
14. J. Hou, O. Inganäs, R. H. Friend and F. Gao, *Nat. Mater.*, **2018**, *17*, 119–128.
15. C. Yan, S. Barlow, Z. Wang, H. Yan, A. K.-Y. Jen, S. R. Marder and X. Zhan, *Nat. Rev. Mater.*, **2018**, *3*, 18003.
16. P. Cheng, G. Li, X. Zhan and Y. Yang, *Nat. Photonics*, **2018**, *12*, 131–142.
17. L. Yang, W. Gu, L. Lv, Y. Chen, Y. Yang, P. Ye, J. Wu, L. Hong, A. Peng and H. Huang, *Angew. Chem. Int. Ed.*, **2018**, *57*, 1096–1102.

## Complete Bibliography

### Chapter 1:

18. S. R. Forrest, *Nature*, **2004**, *428*, 911–918.
19. H. Sirringhaus, *Adv. Mater.*, **2014**, *26*, 1319–1335.
20. J. Roncali, *Chem. Rev.*, **1992**, *92*, 711–738.
21. J. Chen and Y. Cao, *Acc. Chem. Res.*, **2009**, *43*, 1709–1718.
22. A. M. Prieger, B. W. Rawe, S. C. Serin and D. P. Gates, *Chem. Soc. Rev.*, **2016**, *45*, 922–953.
23. S. M. Parke, M. P. Boone and E. Rivard, *Chem. Commun.*, **2016**, *52*, 9485–9505.
24. M. Montalti, A. Credi, L. Prodi and M. T. Gandolfi, *Handbook of Photochemistry* 3<sup>rd</sup> ed. (CRC Press, Florida, **2006**).
25. N. B. Shustova, B. D. McCarthy and M. Dinca, *J. Am. Chem. Soc.* **2011**, *133*, 20126–20129.
26. S. Xu, R. Chen, C. Zheng and W. Huang, *Adv. Mater.*, **2016**, *28*, 9920–9940.
27. T. Maldiney, A. Lecointre, B. Viana, A. Bessière, M. Bessodes, D. Gourier, C. Richard and D. Scherman, *J. Am. Chem. Soc.*, **2011**, *133*, 11810–11815.
28. M. A. Baldo, D. F. O'Brien, Y. You, A. Shoustikov, S. Sibley, M. E. Thompson and S. R. Forrest, *Nature*, **1998**, *395*, 151–154.
29. Y. Tao, K. Yuan, T. Chen, P. Xu, H. Li, R. Chen, C. Zheng, L. Zhang and W. Huang, *Adv. Mater.*, **2014**, *26*, 7931–7958.
30. Z. Yang, Z. Mao, Z. Xie, Y. Zhang, S. Liu, J. Zhao, J. Xu, Z. Chi and M. P. Aldred, *Chem. Soc. Rev.*, **2017**, *46*, 915–1016.

31. W. C. Martin, *J. of Res.*, **1971**, 2, 109–111.
32. U. Fano and W. C. Martin, *Topics in Modern Physics A Tribute to E. U. Condon* (Editors: W.E. Britton, H. Odabasi, Colorado Associated University Press, Colorado, **1971**).
33. V. Gray, K. Moth-Poulsen, B. Albinsson and M. Abrahamsson, *M. Coord. Chem. Rev.*, **2018**, 362, 54–71.
34. D. B. Papkovsky and R. I. Dmitriev, *Chem. Soc. Rev.*, **2013**, 42, 8700–8732.
35. J. Mei, N. L. C. Leung, R. T. K. Kwok, J. W. Y. Lam and B. Z. Tang, *Chem. Rev.*, **2015**, 115, 11718–11940.
36. J. Ohshita, S. Matsui, R. Yamamoto, T. Mizumo, Y. Ooyama, Y. Harima, T. Murafuji, K. Tao, Y. Kuramochi, T. Kaikoh and H. Higashimura, *Organometallics*, **2010**, 29, 3239–3241.
37. S. M. Parke, M. A. B. Narreto, E. Hupf, R. McDonald, M. J. Ferguson, F. A. Hegmann and E. Rivard, *Inorg. Chem.*, **2018**, 57, 7536–7549.
38. S. M. Parke, E. Hupf, G. K. Matharu, I. de Aguiar, L. Xu, H. Yu, M. P. Boone, G. L. C. de Souza, R. McDonald, M. J. Ferguson, G. He, A. Brown and E. Rivard, *Angew. Chem. Int. Ed.*, **2018**, 57, 14841–14846.
39. T. Matsumoto, K. Tanaka, K. Tanaka and Y. Chujo, *Dalton Trans.*, **2015**, 44, 8697–8708.
40. K. A. Mazzio and C. K. Luscombe, *Chem. Soc. Rev.*, **2015**, 44, 78–90.
41. M. Sim, J. Shin, C. Shim, M. Kim, S. B. Jo, J.-H. Kim and K. Cho *J. Phys. Chem. C*, **2014**, 118, 760–766.

42. X. Huang, S. Han, W. Huang and X. Liu, *Chem. Soc. Rev.*, **2013**, *42*, 173–201.
43. Y. Shao and Y. Yang, *Adv. Mater.*, **2005**, *17*, 2841–2844.
44. G. Winroth, D. Podobinski and F. Cacialli, *J. Appl. Phys.*, **2011**, *110*, 124504.
45. J. Hou, O. Inganäs, R. H. Friend and F. Gao, *Nat. Mater.*, **2018**, *17*, 119–128.
46. C. Yan, S. Barlow, Z. Wang, H. Yan, A. K.-Y. Jen, S. R. Marder and X. Zhan, *Nat. Rev. Mater.*, **2018**, *3*, 18003.
47. P. Cheng, G. Li, X. Zhan and Y. Yang, *Nat. Photonics*, **2018**, *12*, 131–142.
48. C. K. Lo, B. R. Gautam, P. Selter, Z. Zheng, S. D. Oosterhout, I. Constantinou, R. Knitsch, R. M. W. Wolfe, X. Yi, J.-L. Brédas, F. So, M. F. Toney, V. Coropceanu, M. R. Hansen, K. Gundogdu, and J. R. Reynolds, *Chem. Mater.*, **2018**, *30*, 2995–3009.
49. J. Mei, Y. Diao, A. L. Appleton, L. Feng and Z. Bao, *J. Am. Chem. Soc.* **2013**, *135*, 6724–6746.
50. A. A. Jahnke and D. S. Seferos, *Macromol. Rapid Commun.* **2011**, *32*, 943–951.
51. M. Jeffries-EL, B. M. Kobilka and B. J. Hale, *Macromolecules*, **2014**, *47*, 7253–7271.
52. E. Rivard, *Chem. Lett.*, **2015**, *44*, 730–736.
53. X. Wu, L. Lv, L. Hu, Q. Shi, A. Peng and H. Huang, *Chem. Phys. Chem.*, **2019**, *20*, 2600–2607.
54. E. I. Carrera and D. S. Seferos, *Macromolecules*, **2015**, *48*, 297–308.
55. J. G. Manion, J. R. Panchuk and D. S. Seferos, *Chem. Rec.*, **2019**, *19*, 1113–1122.
56. T. Chivers and R. S. Laitinen, *Chem. Soc. Rev.*, **2015**, *44*, 1725–1739.



57. Images from [periodictable.com](http://periodictable.com)
58. A. J. Bondi, *Phys. Chem.*, **1964**, *68*, 441–451.
59. J. R. Rumble, ed., *CRC Handbook of Chemistry and Physics*, 100th ed. (Internet Version, CRC Press/Taylor & Francis, Boca Raton, Florida, **2019**.)
60. C. E. Housecroft and A. G. Sharpe, *Inorganic Chemistry*, 4<sup>th</sup> ed. (Pearson Education Ltd., Essex, England, **2012**).
61. A. A. Jahnke, B. Djukic, T. M. McCormick, E. B. Domingo, C. Hellmann, Y. Lee and D. S. Seferos, *J. Am. Chem. Soc.*, **2013**, *135*, 951–954.
62. F. Fringuelli, G. Marino, G. Savelli and A. Taticchi, *J. Chem. Soc., Chem. Commun. D*, **1971**, 1441–1441.
63. E. H. Braye, W. Hübel and I. Caplier, *J. Am. Chem. Soc.*, **1961**, *83*, 4406–4413.
64. F. Fringuelli and A. Taticchi, *J. Chem. Soc., Perkin Trans. 1*, **1972**, 199–203.
65. A. A. Jahnke, G. W. Howe and D. S. Seferos, *Angew. Chem. Int. Ed.*, **2010**, *49*, 10140–10144.
66. T. M. McCormick, A. A. Jahnke, A. J. Lough, and D. S. Seferos, *J. Am. Chem. Soc.*, **2012**, *134*, 3542–3548.
67. E. I. Carrera, T. M. McCormick, M. J. Kapp, A. J. Lough and D. S. Seferos, *Inorg. Chem.*, **2013**, *52*, 13779–13790.
68. G. He, W. Torres Delgado, D. J. Schatz, C. Merten, A. Mohammadpour, L. Mayr, M. J. Ferguson, R. McDonald, A. Brown, K. Shankar and E. Rivard, *Angew. Chem. Int. Ed.*, **2014**, *53*, 4587–4591.
69. E. I. Carrera and D. S. Seferos, *Dalton Trans.*, **2015**, *44*, 2092–2096.

70. S. Wang, X. Li, X. Hou, Y. Suna and X. Shao, *Chem. Commun.*, **2016**, *52*, 14486–14489.
71. P.-F. Li, E. I. Carrera and D. S. Seferos, *ChemPlusChem*, **2016**, *81*, 917–921.
72. W. Torres Delgado, F. Shahin, M. J. Ferguson, R. McDonald, G. He and E. Rivard, *Organometallics*, **2016**, *35*, 2140–2148.
73. E. I. Carrera, A. E. Lanterna, A. J. Lough, J. C. Scaiano and D. S. Seferos, *J. Am. Chem. Soc.*, **2016**, *138*, 2678–2689.
74. L. Lv, X. Wang, X. Wang, L. Yang, T. Dong, Z. Yang and H. Huang, *ACS Appl. Mater. Interfaces*, **2016**, *8*, 34620–34629.
75. S. Wang, Jihai Shang, C. Yan, W. Wang, C. n Yuan, H.-L. Zhang and X. Shao, *Org. Chem. Front.*, **2019**, *6*, 263–272.
76. M. Oba, M. Endo, K. Nishiyama, A. Ouchi and W. Ando, *Chem. Commun.*, **2004**, *4*, 1672–1673.
77. M. Oba, Y. Okada, M. Endo, K. Tanaka, K. Nishiyama, S. Shimada and W. Ando, *Inorg. Chem.*, **2010**, *49*, 10680–10686.
78. P. Serguievski and M. R. Detty, *Organometallics*, **1997**, *16*, 4386–4391.
79. M. W. Kryman, G. A. Schamerhorn, K. Yung, B. Sathyamoorthy, D. K. Sukumaran, T. Y. Ohulchansky, J. B. Benedict and M. R. Detty, *Organometallics*, **2013**, *32*, 4321–4333.
80. M. W. Kryman, G. A. Schamerhorn, J. E. Hill, B. D. Calitree, K. S. Davies, M. K. Linder, T. Y. Ohulchansky and M. R. Detty, *Organometallics*, **2014**, *33*, 2628–2640.

81. M. W. Kryman, T. M. McCormick, and M. R. Detty, *Organometallics*, **2016**, *35*, 1944–1955.
82. M. R. Detty, P. B. Merkel, R. Hilf, S. L. Gibson and S. K. Powers, *J. Med. Chem.*, **1990**, *33*, 1108–1116.
83. Y. Koide, M. Kawaguchi, Y. Urano, K. Hanaoka, T. Komatsu, M. Abo, T. Teraia and T. Nagano, *Chem. Commun.*, **2012**, *48*, 3091–3093.
84. K. Wen, X. Xu, J. Chen, L. Lv, L. Wu, Y. Hu, X. Wu, G. Liu, A. Peng and H. Huang, *ACS Appl. Mater. Interfaces*, **2019**, *11*, 17884–17893.
85. E. I. Carrera and D. S. Seferos, *Organometallics*, **2017**, *36*, 2612–2621.
86. E. Luppold, E. Müller and W. Winter, *Z. Naturforsch.*, **1976**, *31b*, 1654–1657.
87. A. Maercker, H. Bodenstedt and L. Brandsma, *Angew. Chem. Int. Ed. Engl.*, **1992**, *31*, 1339–1341.
88. F. Zheng, Y. Komatsuzaki, N. Shida, H. Nishiyama, S. Inagi and I. Tomita, *Macromol. Rapid Commun.*, **2019**, *40*, 1900171.
89. W. Mack, *Angew. Chem. Int. Ed. Engl.*, **1966**, *5*, 896.
90. T. J. Barton and R. W. Roth, *J. Organometal. Chem.*, **1972**, *39*, C66–C68.
91. W. Lohner and K. Praefcke, *Chem. Ber.*, **1978**, *111*, 3745–3746.
92. E. Müller, E. Luppold and W. Winter, *Chem. Ber.*, **1975**, *108*, 237–242.
93. E. Müller, E. Luppold and W. Winter, *Synthesis*, **1975**, 265–266.
94. P. J. Fagan and W. A. Nugent, *J. Am. Chem. Soc.*, **1988**, *110*, 2310–2312.
95. X. Yan and C. Xi, *Acc. Chem. Res.*, **2015**, *48*, 935–946.

96. G. He, L. Kang, W. Torres Delgado, O. Shynkaruk, M. J. Ferguson, R. McDonald and E. Rivard, *J. Am. Chem. Soc.*, **2013**, *135*, 5360–5363.
97. K. Okuma, S. Yahata, N. Nagahora and K. Shioji, *Chem. Lett.*, **2017**, *46*, 405–407.
98. N. Nagahora, S. Yahata, S. Goto, K. Shioji and K. Okuma, *J. Org. Chem.*, **2018**, *83*, 1969–1975.
99. V. K. Karapala, H.-P. Shih and C.-C. Han, *Org. Lett.*, **2018**, *20*, 1550–1554.
100. L. Brandsma, H. Hommes, H. D. Verkruijsse and R. L. P. de Jong, *Recl. Trav. Chim. Pays-Bas*, **1985**, *104*, 226–230.
101. C. H. W. Jones and R. D. Sharma, *J. Organomet. Chem.*, **1987**, *332*, 115–121.
102. H. A. Staab, M. Höne and C. Krieger, *Tetrahedron Lett.*, **1988**, *29*, 1905–1908.
103. J. C. Hanekamp, P. A. A. Klusener and L. Brandsma, *Syn. Commun.*, **1989**, *19*, 2691–2701.
104. J. Kurita, M. Ishii, S. Yasuie and T. Tsuchiya, *J. Chem. Soc., Chem. Commun.*, **1993**, *17*, 1309–1310.
105. S. Sato and N. Furukawa, *Tetrahedron Lett.*, **1995**, *36*, 2803–2806.
106. H. Sashida, K. Sadamori and T. Tsuchiya, *Syn. Commun.*, **1998**, *28*, 713–727.
107. G. He, B. D. Wiltshire, P. Choi, A. Savin, S. Sun, A. Mohammadpour, M. J. Ferguson, R. McDonald, S. Farsinezhad, A. Brown, K. Shankar and E. Rivard, *Chem. Commun.*, **2015**, *51*, 5444–5447.
108. E. Hupf, Y. Tsuchiya, W. Moffat, L. Xu, M. Hirai, Y. Zhou, M. J. Ferguson, R. McDonald, T. Murai, G. He and E. Rivard, *Inorg. Chem.*, **2019**, *58*, 13323–13336.

109. B. Wu, Melvina, X. Wu, E. K. L. Yeow and N. Yoshikai, *Chem. Sci.*, **2017**, *8*, 4527–4532.
110. M. Jiang, J. Guo, B. Liu, Q. Tan and B. Xu, *Chem. Sci.*, **2019**, *21*, 8328–8333.
111. J. Casado, M. Moreno Oliva, M. C. Ruiz Delgado, R. Ponce Ortiz, J. Joaquín Quirante and J. T. López Navarrete, *J. Phys. Chem. A*, **2006**, *110*, 7422–7430.
112. T. Annaka, N. Nakata and A. Ishii, *Organometallics*, **2015**, *34*, 1272–1278.
113. A. K. Mahrok, E. I. Carrera, A. J. Tilley, S. Ye and D. S. Seferos, *Chem. Commun.*, **2015**, *51*, 5475–5478.
114. M. Lapkowski, R. Motyka, J. Suwiński and P. Data, *Macromol. Chem. Phys.*, **2012**, *213*, 29–35.
115. T. M. McCormick, E. I. Carrera, T. B. Schon and D. S. Seferos, *Chem. Commun.*, **2013**, *49*, 5475–11184.
116. A. Kremer, C. Aurisicchio, F. De Leo, B. Ventura, J. Wouters, N. Armaroli, A. Barbieri and D. Bonifazi, *Chem. Eur. J.*, **2015**, *21*, 15377–15387.
117. M. Zander and G. Kirsch, *Z. Naturforsch.*, **1989**, *44a*, 205–209.
118. W. Torres Delgado, C. A. Braun, M. P. Boone, O. Shynkaruk, Y. Qi, R. McDonald, M. J. Ferguson, P. Data, S. K. C. Almeida, I. de Aguiar, G. L. C. de Souza, A. Brown, G. He and E. Rivard, *ACS Appl. Mater. Interfaces*, **2018**, *10*, 12124–12134.
119. M. T. Dang, L. Hirsch and G. Wantz, *Adv. Mater.*, **2011**, *23*, 3597–3602.
120. K. Li, Y. Wu, Y. Tang, M.-A. Pan, W. Ma, H. Fu, C. Zhan and J. Yao, *Adv. Energy Mater.*, **2019**, *9*, 1901728.

121. S. S. Zade, N. Zamoshchik and M. Bendikov, *Acc. Chem. Res.*, **2011**, *44*, 14–24.
122. R. D. Pensack, Y. Song, T. M. McCormick, A. A. Jahnke, J. Hollinger, D. S. Seferos and G. D. Scholes, *J. Phys. Chem. B*, **2014**, *118*, 2589–2597.
123. S. Ye, M. Steube, E. I. Carrera and D. S. Seferos, *Macromolecules*, **2016**, *49*, 1704–1711.
124. W.-H. Lee, S. K. Lee, W. S. Shin, S.J. Moon and I.-N. Kang, *J. Polym. Sci., Part A: Polym. Chem.*, **2013**, *51*, 2753–2758.
125. J. G. Manion, S. Ye, A. H. Proppe, A. W. Laramée, G. R. McKeown, E. L. Kynaston, S. O. Kelley, E. H. Sargent and D. S. Seferos, *ACS Appl. Energy Mater.*, **2018**, *1*, 5033–5042.
126. Y. S. Park, T. S. Kale, C.-Y. Nam, D. Choi and R. B. Grubbs, *Chem. Commun.*, **2014**, *50*, 7964–7967.
127. Y. S. Park, Q. Wu, C.-Y. Nam and R. B. Grubbs, *Angew. Chem. Int. Ed.*, **2014**, *53*, 10691–10695.
128. J. C. Bijleveld, A. P. Zoombelt, S. G. J. Mathijssen, M. M. Wienk, M. Turbiez, D. M. de Leeuw, R. A. J. Janssen, *J. Am. Chem. Soc.*, **2009**, *131*, 16616–16617.
129. E. H. Jung, S. Bae, T. W. Yoo and W. H. Jo, *Polym. Chem.*, **2014**, *5*, 6545–6550.
130. R. S. Ashraf, I. Meager, M. Nikolka, M. Kirkus, M. Planells, B. C. Schroeder, S. Holliday, M. Hurhangee, C. B. Nielsen, H. Sirringhaus and I. McCulloch, *J. Am. Chem. Soc.*, **2015**, *137*, 1314–1321.
131. L. Yang, W. Gu, L. Lv, Y. Chen, Y. Yang, P. Ye, J. Wu, L. Hong, A. Peng and H. Huang, *Angew. Chem. Int. Ed.*, **2018**, *57*, 1096–1102.

132. T. Inouchi, T. Nakashima and T. Kawai, *J. Phys. Chem. A*, **2014**, *118*, 2591–2598.
133. M. Kaur, D. S. Yang, J. Shin, T. W. Lee, K. Choi, M. J. Cho and D. H. Choi, *Chem. Commun.*, **2013**, *49*, 5495–5497.
134. S. Ye, L. Janasz, W. Zajaczkowski, J. G. Manion, A. Mondal, T. Marszalek, D. Andrienko, K. Müllen, W. Pisula and D. S. Seferos, *Macromol. Rapid Commun.*, **2019**, *40*, 1800596.
135. K. Takimiya, Y. Kunugi, Y. Konda, N. Niihara and T. Otsubo, *J. Am. Chem. Soc.*, **2004**, *126*, 5084–5085.
136. M. Al-Hashimi, Y. Han, J. Smith, H. S. Bazzi, S. Y. A. Alqaradawi, S. E. Watkins, T. D. Anthopoulos and M. Heeney, *Chem. Sci.*, **2016**, *7*, 1093–1099.
137. T. Oyama, Y. S. Yang, K. Matsuo and T. Yasuda, *Chem. Commun.*, **2017**, *53*, 3814–3817.

## Chapter 2:

1. (a) I. Akasaki, *Angew. Chem., Int. Ed.*, **2015**, *54*, 7750–7763; (b) H. Amano, *Angew. Chem., Int. Ed.*, **2015**, *54*, 7764–7769; (c) S. Nakamura, *Angew. Chem., Int. Ed.*, **2015**, *54*, 7770–7788; (d) R. H. Friend, R. W. Gymer, A. B. Holmes, J. H. Burroughes, R. N. Marks, C. Taliani, D. C. C. Bradley, D. A. Dos Santos, J. L. Bredas, M. Lodglund and W. R. Salaneck, *Nature*, **1999**, *397*, 121–128; (e) M. A. Baldo, D. F. O'Brien, Y. You, A. Shoustikov, S. Sibley, M. E. Thompson and S. R. Forrest, *Nature*, **1998**, *395*, 151–154.
2. (a) B. Hein, K. I. Willig and S. W. Hell, *Proc. Natl. Acad. Sci. U.S.A.*, **2008**, *105*, 14271–14276; (b) L. Schermelleh, R. Heintzmann and H. Leonhardt, *J. Cell Biol.*,

- 2010**, *190*, 165–175; (c) D. Ding, K. Li, B. Liu and B. Z. Tang, *Acc. Chem. Res.*, **2013**, *46*, 2441–2453; (d) C. Wang, A. Fukazawa, M. Taki, Y. Sato, T. Higashiyama and S. Yamaguchi, *Angew. Chem., Int. Ed.*, **2015**, *54*, 15213–15217.
3. W. Z. Yuan, P. Lu, S. Chen, J. W. Y. Lam, Z. Wang, Y. Liu, H. S. Kwok, Y. Ma and B. Z. Tang, *Adv. Mater.*, **2010**, *22*, 2159–2163.
4. (a) M. A. Baldo, S. Lamansky, P. E. Burrows, M. E. Thompson and S. R. Forrest, *Appl. Phys. Lett.*, **1999**, *75*, 4–6; (b) R. C. Evans, P. Douglas and C. J. Winscom, *Coord. Chem. Rev.*, **2006**, *250*, 2093–2126.
5. T. N. Singh-Rachford and F. N. Castellano, *Coord. Chem. Rev.*, **2010**, *254*, 2560–2573.
6. H. Uoyama, K. Goushi, K. Shizu, H. Nomura and C. Adachi, *Nature*, **2012**, *492*, 234–238.
7. G. He, W. Torres Delgado, D. J. Schatz, C. Merten, A. Mohammadpour, L. Mayr, M. J. Ferguson, R. McDonald, A. Brown, K. Shankar and E. Rivard, *Angew. Chem., Int. Ed.*, **2014**, *53*, 4587–4591.
8. For selected references on the incorporation of tellurophenes into  $\pi$ -conjugated materials for optoelectronic applications, see: (a) A. A. Jahnke, G. W. Howe and D. S. Seferos, *Angew. Chem., Int. Ed.*, **2010**, *49*, 10140–10144; (b) G. He, L. Kang, W. Torres Delgado, O. Shynkaruk, M. J. Ferguson, R. McDonald and E. Rivard, *J. Am. Chem. Soc.*, **2013**, *135*, 5360–5363; (c) M. Jeffries-El, B. M. Kobilka and B. J. Hale, *Macromolecules*, **2014**, *47*, 7253–7271; (d) E. I. Carrera and D. S. Seferos, *Macromolecules*, **2015**, *48*, 297–308; (e) E. Rivard, *Chem. Lett.*, **2015**, *44*, 730–736;



- (f) Y. S. Park, Q. Wu, C.-Y. Nam and R. B. Grubbs, *Angew. Chem., Int. Ed.*, **2014**, *53*, 10691–10695; (g) M. Al-Hashimi, Y. Han, J. Smith, H. S. Bazzi, S. Y. A. Alqaradawi, S. E. Watkins, T. D. Anthopoulos and M. Heeney, *Chem. Sci.*, **2016**, *7*, 1093–1099; (h) T. Annaka, N. Nakata and A. Ishii, *Organometallics*, **2015**, *34*, 1272–1278; (i) S. M. Parke, M. P. Boone and E. Rivard, *Chem. Commun.*, **2016**, *52*, 9485–9505.
9. For an early report on the phosphorescence of benzotellurophenes in frozen EtOH (at 77 K), see: M. Zander and G. Kirsch, *Z. Naturforsch., A: Phys. Sci.*, **1989**, *44*, 205–209.
10. (a) J. Luo, Z. Xie, J. W. Y. Lam, L. Cheng, H. Chen, C. Qiu, H. S. Kwok, X. Zhan, Y. Liu, D. Zhu and B. Z. Tang, *Chem. Commun.*, **2001**, 1740–1741; (b) R. Hu, N. L. C. Leung and B. Z. Tang, *Chem. Soc. Rev.*, **2014**, *43*, 4494–4562; (c) J. Mei, N. L. C. Leung, R. T. K. Kwok, J. W. Y. Lam and B. Z. Tang, *Chem. Rev.*, **2015**, *115*, 11718–11940.
11. G. He, B. D. Wiltshire, P. Choi, A. Savin, S. Sun, A. Mohammadpour, M. J. Ferguson, R. McDonald, S. Farsinezhad, A. Brown, K. Shankar and E. Rivard, *Chem. Commun.*, **2015**, *51*, 5444–5447.
12. (a) S. Mukherjee and P. Thilagar, *Chem. Commun.*, **2015**, *51*, 10988–11003, and references therein; (b) O. Bolton, K. Lee, H.-J. Kim, K. Y. Lin and J. Kim, *Nat. Chem.*, **2011**, *3*, 205–210; (c) W. Z. Yuan, X. Y. Shen, H. Zhao, J. W. Y. Lam, L. Tang, P. Lu, C. Wang, Y. Liu, Z. Wang, Q. Zheng, J. Z. Sun, Y. Ma and B. Z. Tang, *J. Phys. Chem. C*, **2010**, *114*, 6090–6099; (d) S. Hirata, K. Totani, J. Zhang, T.

- Yamashita, H. Kaji, S. R. Marder, T. Watanabe and C. Adachi, *Adv. Funct. Mater.*, **2013**, *23*, 3386–3397; (e) Z. An, C. Zheng, Y. Tao, R. Chen, H. Shi, T. Chen, Z. Wang, H. Li, R. Deng, X. Liu and W. Huang, *Nat. Mater.*, **2015**, *14*, 685–690; (f) Z. Yang, Z. Mao, X. Zhang, D. Ou, Y. Mu, Y. Zhang, C. Zhao, S. Liu, Z. Chi, J. Xu, Y.-C. Wu, P.-Y. Lu, A. Lien and M. R. Bryce, *Angew. Chem., Int. Ed.*, **2016**, *55*, 2181–2185; (g) S. Hirata and M. Vacha, *J. Phys. Chem. Lett.*, **2016**, *7*, 1539–1545.
13. W. Torres Delgado, F. Shahin, M. J. Ferguson, R. McDonald, G. He and E. Rivard, *Organometallics*, **2016**, *35*, 2140–2148.
14. For selected articles on boryl ( $-BR_2$ ) promoted luminescence, see: (a) Z. M. Hudson and S. Wang, *Acc. Chem. Res.*, **2009**, *42*, 1584–1596; (b) F. Jäkle, *Chem. Rev.*, **2010**, *110*, 3985–4022; (c) A. Wakamiya and S. Yamaguchi, *Bull. Chem. Soc. Jpn.*, **2015**, *88*, 1357–1377.
15. (a) U. Rosenthal, A. Ohff, W. Baumann, A. Tillack, H. Görls, V. V. Burlakov and V. B. Shur, *Z. Anorg. Allg. Chem.*, **1995**, *621*, 77–83; (b) E. Negishi, F. E. Cederbaum and T. Takahashi, *Tetrahedron Lett.*, **1986**, *27*, 2829–2832.
16. (a) Y. Gu, H. Pritzkow and W. Siebert, *Eur. J. Inorg. Chem.*, **2001**, 373–379; (b) A. G. Avent, M. J. Davies, P. B. Hitchcock and M. F. Lappert, *Z. Anorg. Allg. Chem.*, **2003**, *629*, 1358–1366.
17. J. A. Bailey, M. Ploeger and P. G. Pringle, *Inorg. Chem.*, **2014**, *53*, 7763–7769.
18. (a) S. M. I. Al-Rafia, A. C. Malcolm, S. K. Liew, M. J. Ferguson, R. McDonald and E. Rivard, *Chem. Commun.*, **2011**, 6987–6989; (b) K. Powers, C. Hering-Junghans, R. McDonald, M. J. Ferguson and E. Rivard, *Polyhedron*, **2016**, *108*, 8–14.

19. C. J. Berger, G. He, C. Merten, R. McDonald, M. J. Ferguson and E. Rivard, *Inorg. Chem.*, **2014**, *53*, 1475–1486.
20. N. Kuhn and T. Kratz, *Synthesis*, **1993**, 561–562.
21. S. Muthaiah, D. C. H. Do, R. Ganguly and D. Vidovic, *Organometallics*, **2013**, *32*, 6718–6724.
22. C. Kleeberg and C. Borner, *Eur. J. Inorg. Chem.*, **2013**, 2799–2806.
23. E. Papajak, J. Zheng, H. R. Leverentz and D. G. Truhlar, *J. Chem. Theory Comput.*, **2011**, *7*, 3027–3034.
24. E. Cancès, B. Mennucci and J. Tomasi, *J. Chem. Phys.*, **1997**, *107*, 3032–3041.
25. M. Cossi, G. Scalmani, N. Rega and V. Barone, *J. Chem. Phys.*, **2002**, *117*, 43–54.
26. A. B. Pangborn, M. A. Giardello, R. H. Grubbs, R. K. Rosen and F. J. Timmers, *Organometallics*, **1996**, *15*, 1518–1520.
27. X. He and J. F. Hartwig, *Organometallics*, **1996**, *15*, 400–407.
28. G. M. Sheldrick, *Acta Crystallogr., Sect. A: Found. Crystallogr.*, **2008**, *64*, 112–122.
29. P. T. Beurskens, G. Beurskens, R. de Gelder, J. M. M. Smits, S. Garcia-Granda and R. O. Gould, *DIRDIF-2008 Program. Crystallographic Laboratory*, Radboud University, Nijmegen, The Netherlands.

### Chapter 3:

1. (a) C. C. C. Johansson Seechurn, M. O. Kitching, T. J. Colacot and V. Snieckus, *Angew. Chem. Int. Ed.*, **2012**, *51*, 5062–5085; (b) D. G. Hall, *Boronic Acids*:

- Preparation and Applications in Organic Synthesis, Medicine and Materials*, 2nd ed. (Wiley-VCH Verlag GmbH & Co., Weinheim, **2011**).
2. L. Ji, S. Griesbeck and T. B. Marder, *Chem. Sci.*, **2017**, *8*, 846–863.
  3. Y. Ren and F. Jäkle, *Dalton Trans.*, **2016**, *45*, 13996–14007.
  4. T. Ishiyama, J. Takagi, Y. Yonekawa, J. F. Hartwig and N. Miyaura, *Adv. Synth. Catal.*, **2003**, *345*, 1103–1106.
  5. K. Mertins, A. Zapf and M. Beller, *J. Mol. Catal. A: Chem.*, **2004**, *207*, 21–25.
  6. G. A. Chotana, V. A. Kallepalli, R. E. Maleczka, Jr. and M. R. Smith, III, *Tetrahedron*, **2008**, *64*, 6103–6114.
  7. M.-A. Légaré, M.-A. Courtemanche, É. Rochette and F.-G. Fontaine, *Science*, **2015**, *349*, 513–516.
  8. (a) T. Chivers and R. S. Laitinen, *Chem. Soc. Rev.*, **2015**, *44*, 1725–1739; (b) E. Rivard, *Chem. Lett.*, **2015**, *44*, 730–736.
  9. A. Aprile, K. L. Iversen, D. J. D. Wilson and J. L. Dutton, *Inorg. Chem.*, **2015**, *54*, 4934–4939.
  10. E. I. Carrera, A. E. Lanterna, A. J. Lough, J. C. Scaiano and D. S. Seferos, *J. Am. Chem. Soc.*, **2016**, *138*, 2678–2689.
  11. E. I. Carrera and D. S. Seferos, *Organometallics*, **2017**, *36*, 2612–2621.
  12. W.-H. Lee, S. K. Lee, W. S. Shin, S.-J. Moon and I.-N. Kang, *J. Polym. Sci., Part A: Polym. Chem.*, **2013**, *51*, 2753–2758.
  13. G. He, L. Kang, W. Torres Delgado, O. Shynkaruk, M. J. Ferguson, R. McDonald and E. Rivard, *J. Am. Chem. Soc.*, **2013**, *135*, 5360–5363.

14. Y. S. Park, Q Wu, C.-Y. Nam and R. B. Grubbs, *Angew. Chem. Int Ed.*, **2014**, *53*, 10691–10695.
15. E. H. Jung, S. Bae, T. W. Yoo and W. H. Jo, *Polym. Chem.*, **2014**, *5*, 6545–6550.
16. R. S. Ashraf, I. Meager, M. Nikolka, M. Kirkus, M. Planells, B. C. Schroeder, S. Holliday, M. Hurhangee, C. B. Nielsen, H. Sirringhaus and I. McCulloch, *J. Am. Chem. Soc.*, **2015**, *137*, 1314–1321.
17. A. A. Jahnke, B. Djukic, T. M. McCormick, E. Buchaca Domingo, C. Hellmann, Y. Lee and D. S. Seferos, *J. Am. Chem. Soc.*, **2013**, *135*, 951–954.
18. J. G. Manion, S. Ye, A. H. Proppe, A. W. Laramée, G. R. McKeown, E. L. Kynaston, S. O. Kelley, E. H. Sargent and D. S. Seferos, *ACS Appl. Energy Mater.*, **2018**, *1*, 5033–5042.
19. (a) L. Yang, W. Gu, L. Lv, Y. Chen, Y. Yang, P. Ye, J. Wu, L. Hong, A. Peng and H. Huang, *Angew. Chem. Int. Ed.*, **2018**, *57*, 1096–1102; (b) For a review on harvesting triplet excitons for OPVs, see: B. T. Luppi, D. Majak, M. Gupta, E. Rivard and K. Shankar, *J. Mater. Chem. A*, **2019**, *7*, 2445–2463.
20. W. Xing, P. Ye, J. Lu, X. Wu, Y. Chen, T. Zhu, A. Peng and H. Huang, *J. Power Sources*, **2018**, *401*, 13–19.
21. G. He, W. Torres Delgado, D. J. Schatz, C. Merten, A. Mohammadpour, L. Mayr, M. J. Ferguson, R. McDonald, A. Brown, K. Shankar and E. Rivard, *Angew. Chem. Int. Ed.*, **2014**, *53*, 4587–4591.

22. G. He, B. D. Wiltshire, P. Choi, A. Savin, S. Sun, A. Mohammadpour, M. J. Ferguson, R. McDonald, S. Farsinezhad, A. Brown, K. Shankar and E. Rivard, *Chem. Commun.*, **2015**, *51*, 5444–5447.
23. A. K. Mahrok, E. I. Carrera, A. J. Tilley, S. Ye and D. S. Seferos, *Chem. Commun.*, **2015**, *51*, 5475–5478.
24. N. Nagahora, S. Yahata, S. Goto, K. Shioji and K. Okuma, *J. Org. Chem.*, **2018**, *83*, 1969–1975.
25. W. Torres Delgado, C. A. Braun, M. P. Boone, O. Shynkaruk, Y. Qi, R. McDonald, M. J. Ferguson, P. Data, S. K. C. Almeida, I. de Aguiar, G. L. C. de Souza, A. Brown, G. He and E. Rivard, *ACS Appl. Mater. Interfaces*, **2018**, *10*, 12124–12134.
26. K. Takimiya, Y. Kunugi, Y. Konda, N. Niihara and T. Ostubo, *J. Am. Chem. Soc.*, **2004**, *126*, 5084–5085.
27. M. Kaur, D. S. Yang, J. Shin, T. W. Lee, K. Choi, M. J. Cho and D. H. Choi, *Chem. Commun.*, **2013**, *49*, 5495–5497.
28. M. Kaur, D. H. Lee, D. S. Yang, H. A. Um, M. J. Cho, J. S. Kang and D. H. Choi, *Chem. Commun.*, **2014**, *50*, 14394–14396.
29. M. Al-Hashimi, Y. Han, J. Smith, H. S. Bazzi, S. Y. A. Alqaradawi, S. E. Watkins, T. D. Anthopoulos and M. Heeney, *Chem. Sci.*, **2016**, *7*, 1093–1099.
30. T. Oyama, Y. S. Yang, K. Matsuo and T. Yasuda, *Chem. Commun.*, **2017**, *53*, 3814–3817.

31. S. Ye, L. Janasz, W. Zajaczkowski, J. G. Manion, A. Mondal, T. Marszalek, D. Andrienko, K. Müllen, W. Pisula and D. S. Seferos, *Macromol. Rapid Commun.*, **2019**, *40*, 1800596.
32. A. A. Jahnke, G. W. Howe and D. S. Seferos, *Angew. Chem. Int. Ed.*, **2010**, *49*, 10140–10144.
33. D. Moseguí González, K. N. Raftopoulos, G. He, C. N. Papadakis, A. Brown, E. Rivard and P. Müller-Buschbaum, *Macromol. Rapid Commun.*, **2017**, *38*, 1700065.
34. W. Torres Delgado, F. Shahin, M. J. Ferguson, R. McDonald, G. He and E. Rivard, *Organometallics*, **2016**, *35*, 2140–2148.
35. G. H. Herberich, W. Boveleth, B. Hessner, D. P. J. Köffer, M. Negele and R. Saive, *J. Organomet. Chem.*, **1986**, *308*, 153–166.
36. G. H. Herberich, W. Boveleth, B. Hessner, M. Hostalek, D. P. J. Köffer and M. Negele, *J. Organomet. Chem.*, **1987**, *319*, 311–326.
37. H. C. Brown, M. Srebnik, R. K. Bakshi and T. E. Cole, *J. Am. Chem. Soc.*, **1987**, *109*, 5420–5426.
38. T. Köhler, J. Faderl, H. Pritzkow and W. Siebert, *Eur. J. Inorg. Chem.*, **2002**, 2942–2946.
39. K. Durka, A. Górska, P. Jankowski, T. Kliś, M. Kublicki, J. Serwatowski, M. Urban, G. Wesela-Baumann and K. Woźniak, *Tetrahedron Lett.*, **2017**, *58*, 1185–1189.
40. S. K. Møllerup, C. Li, J. Radtke, X. Wang, Q.-S. Li and S. Wang, *Angew. Chem. Int. Ed.*, **2018**, *57*, 9634–9639.

41. C. A. Braun, D. Zommerman, I. de Aguiar, Y Qi, W. Torres Delgado, M. J. Ferguson, R. McDonald, G. L. C. de Souza, G. He, A. Brown and E. Rivard, *Faraday Discuss.*, **2017**, *196*, 255–268.
42. (a) E. Negishi, F. E. Cederbaum and T. Takahashi, *Tetrahedron Lett.*, **1986**, *27*, 2829–2832; (b) P. J. Fagan and W. A. Nugent, *J. Am. Chem. Soc.*, **1988**, *110*, 2310–2312.
43. (a) M. Hirai, N. Tanaka, M. Sakai and S. Yamaguchi, *Chem. Rev.*, **2019**, *119*, 8291–8331, and references therein; (b) J. Merz, J. Fink, A. Friedrich, I. Krummenacher, H. H. Al Mamari, S. Lorenzen, M. Haehnel, A. Eichorn, M. Moos, M. Holzapfel, H. Braunschweig, C. Lambert, A. Steffern, L. Ji and T. B. Marder, *Chem. Eur. J.*, **2017**, *23*, 13164–13180.
44. For related work on the use of the heavy atom effect to gain access to phosphorescence in the main group, see: (a) J. Ohshita, S. Matsui, R. Yamamoto, T. Mizumo, Y. Ooyama, Y. Harima, T. Murafuji, K. Tao, Y. Kuramochi, T. Kaikoh and H. Higashimura, *Organometallics*, **2010**, *29*, 3239–3241; (b) A. Kremer, A. Fermi, N. Biot, J. Wouters and D. Bonifazi, *Chem. Eur. J.*, **2016**, *22*, 5665–5675; (c) O. Toma, M. Allain, F. Meinardi, A. Formi, C. Botta and N. Mercier, *Angew. Chem. Int. Ed.*, **2016**, *55*, 7998–8002; (d) S. M. Parke, E. Hupf, G. K. Matharu, I. de Aguiar, L. Xu, H. Yu, M. P. Boone, G. L. C. de Souza, R. McDonald, M. J. Ferguson, G. He, A. Brown and E. Rivard, *Angew. Chem. Int. Ed.*, **2018**, *57*, 14841–14846; (e) S. M. Parke and E. Rivard, *Isr. J. Chem.*, **2018**, *58*, 915–926 and references therein.



45. For the recent incorporation of phosphorescent tellurophene units into macrocycles, see: K. Takahashi, S. Shimo, E. Hupf, J. Ochiai, C. A. Braun, W. Torres Delgado, L. Xu, G. He, E. Rivard and N. Iwasawa, *Chem. Eur. J.*, **2019**, *25*, 8479–8483.
46. M. Mantina, A. C. Chamberlin, R. Valero, C. J. Cramer, and D. G. Truhlar, *J. Phys. Chem. A*, **2009**, *113*, 5806–5812.
47. For leading reviews on this topic, see: (a) J. Mei, N. L. C. Leung, R. T. K. Kwok, J. W. Y. Lam and B. Z. Tang, *Chem. Rev.*, **2015**, *115*, 11718–11940; (b) L. Ravotto and P. Ceroni, *Coord. Chem. Rev.*, **2017**, *346*, 62–76; (c) M. Hayduk, S. Riebe and J. Voskuhl, *Chem. Eur. J.*, **2018**, *24*, 12221–12230.
48. G. N. Lewis and M. Kasha, *J. Am. Chem. Soc.*, **1944**, *66*, 2100–2116.
49. T. Kinzel, Y. Zhang and S. L. Buchwald, *J. Am. Chem. Soc.*, **2010**, *132*, 14073–14075.
50. For a pioneering use of the Bdan group in cross-coupling, see: H. Noguchi, K. Hojo, and M. Suginome, *J. Am. Chem. Soc.*, **2007**, *129*, 758–759.
51. J. L. Dutton, G. J. Farrar, M. J. Sgro, T. L. Battista and P. J. Ragona, *Chem. Eur. J.*, **2009**, *15*, 10263–10271.
52. P. R. Bevington, *IBM J. Res. Develop.*, **1969**, *13*, 119–125.
53. J. Durbin and G. S. Watson, *Biometrika*, **1950**, *37*, 409–428.
54. J. Durbin and G. S. Watson, *Biometrika*, **1951**, *38*, 159–178.
55. D. V. O'Connor and D. Phillips, *Time Correlated Single Photon Counting* (Academic Press, New York, **1984**).
56. H. Hope, *Prog. Inorg. Chem.*, **1994**, *41*, 1–19.

57. R. H. Blessing, *Acta Crystallogr. A.*, **1995**, *51*, 33–38.
58. G. M. Sheldrick, *Acta Crystallogr. A.*, **2015**, *71*, 3–8.
59. G. M. Sheldrick, *Acta Crystallogr. C.*, **2015**, *71*, 3–8.
60. M. J. Frisch, G. W. Trucks, H. B. Schlegel, G. E. Scuseria, M. A. Robb, J. R. Cheeseman, G. Scalmani, V. Barone, G. A. Petersson, H. Nakatsuji, X. Li, M. Caricato, A. V. Marenich, J. Bloino, B. G. Janesko, R. Gomperts, B. Mennucci, H. P. Hratchian, J. V. Ortiz, A. F. Izmaylov, J. L. Sonnenberg, D. Williams-Young, F. Ding, F. Lipparini, F. Egidi, J. Goings, B. Peng, A. Petrone, T. Henderson, D. Ranasinghe, V. G. Zakrzewski, J. Gao, N. Rega, G. Zheng, W. Liang, M. Hada, M. Ehara, K. Toyota, R. Fukuda, J. Hasegawa, M. Ishida, T. Nakajima, Y. Honda, O. Kitao, H. Nakai, T. Vreven, K. Throssell, J. A. Montgomery, Jr., J. E. Peralta, F. Ogliaro, M. J. Bearpark, J. J. Heyd, E. N. Brothers, K. N. Kudin, V. N. Staroverov, T. A. Keith, R. Kobayashi, J. Normand, K. Raghavachari, A. P. Rendell, J. C. Burant, S. S. Iyengar, J. Tomasi, M. Cossi, J. M. Millam, M. Klene, C. Adamo, R. Cammi, J. W. Ochterski, R. L. Martin, K. Morokuma, O. Farkas, J. B. Foresman and D. J. Fox, *Gaussian 16, Revision A.03*, Gaussian, Inc., Wallingford CT, **2016**.
61. A. D. Becke, *J. Chem. Phys.*, **1993**, *98*, 5648–5652.
62. C. Lee, W. Yang and R. G. Parr, *Phys. Rev. B*, **1988**, *37*, 785–789.
63. T. H. Dunning, Jr., *J. Chem. Phys.*, **1989**, *90*, 1007–1023.
64. K. A. Peterson, D. Figgen, E. Goll, H. Stoll and M. Dolg, *J. Chem. Phys.*, **2003**, *119*, 11113–11123.
65. D. Feller, *J. Comput. Chem.*, **1996**, *17*, 1571–1586.

66. K. L. Schuchardt, B. T. Didier, T. Elsethagen, L. Sun, V. Gurumoorthi, J. Chase, J. Li and T. L. Windus, *J. Chem. Inf. Model.*, **2004**, *47*, 1045–1052.

67. W. Humphrey, A. Dalke and K. Schulten, *J. Mol. Graph.*, **1996**, *14*, 33–38.

#### **Chapter 4:**

1. L. Yang, W. Gu, L. Lv, Y. Chen, Y. Yang, P. Ye, J. Wu, L. Hong, A. Peng, and H. Huang, *Angew. Chem. Int. Ed.*, **2018**, *57*, 1096–1102.

2. W. H. Lee, S. K. Lee, W. S. Shin, S. J. Moon and I. N. Kang, *J. Polym. Sci. Part A*, **2013**, *51*, 2753–2758.

3. G. He, L. Kang, W. Torres Delgado, O. Shynkaruk, M. J. Ferguson, R. McDonald and E. Rivard, *J. Am. Chem. Soc.*, **2013**, *135*, 5360–5363.

4. Y. S. Park, Q. Wu, C. Y. Nam and R. B. Grubbs, *Angew. Chem. Int. Ed.*, **2014**, *53*, 10691–10695.

5. E. H. Jung, S. Bae, T. W. Yoo and W. H. Jo, *Polym. Chem.*, **2014**, *5*, 6545–6550.

6. R. S. Ashraf, I. Meager, M. Nikolka, M. Kirkus, M. Planells, B. C. Schroeder, S. Holliday, M. Hurhangee, C. B. Nielsen, H. Sirringhaus, and I. McCulloch, *J. Am. Chem. Soc.*, **2015**, *137*, 1314–1321.

7. A. A. Jahnke, B. Djukic, T. M. McCormick, E. Buchaca Domingo, C. Hellmann, Y. Lee and D. S. Seferos, *J. Am. Chem. Soc.*, **2013**, *135*, 951–954.

8. J. G. Manion, S. Ye, A. H. Proppe, A. W. Laramée, G. R. Mckeown, E. L. Kynaston, S. O. Kelley, E. H. Sargent and D. S. Seferos, *ACS Appl. Energy Mater.*, **2018**, *1*, 5033–5042.

9. W. Xing, P. Ye, J. Lu, X. Wu, Y. Chen, T. Zhu, A. Peng and H. Huang, *J. Power Sources*, **2018**, *401*, 13–19.
10. G. He, W. Torres Delgado, D. J. Schatz, C. Merten, A. Mohammadpour, L. Mayr, M. J. Ferguson, R. McDonald, A. Brown, K. Shankar and E. Rivard, *Angew. Chem. Int. Ed.*, **2014**, *53*, 4587–4591.
11. G. He, B. D. Wiltshire, P. Choi, A. Savin, S. Sun, A. Mohammadpour, M. J. Ferguson, R. McDonald, S. Farsinezhad, A. Brown, K. Shankar and E. Rivard, *Chem. Commun.*, **2015**, *51*, 5444–5447.
12. A. K. Mahrok, E. I. Carrera, A. J. Tilley, S. Ye and D. S. Seferos, *Chem. Commun.*, **2015**, *51*, 5475–5478.
13. W. Torres Delgado, F. Shahin, M. J. Ferguson, R. McDonald, G. He and E. Rivard, *Organometallics*, **2016**, *35*, 2140–2148.
14. C. A. Braun, D. Zomerman, I. de Aguiar, Y. Qi, W. Torres Delgado, M. J. Ferguson, R. McDonald, G. L. C. de Souza, G. He, A. Brown and E. Rivard, *Faraday Discuss.*, **2017**, *196*, 255–268.
15. W. Torres Delgado, C. A. Braun, M. P. Boone, O. Shynkaruk, Y. Qi, R. McDonald, M. J. Ferguson, P. Data, S. K. C. Almeida, I. De Aguiar, G. L. C. De Souza, A. Brown, G. He and E. Rivard, *ACS Appl. Mater. Interfaces*, **2018**, *10*, 12124–12134.
16. E. Hupf, Y. Tsuchiya, W. Moffat, L. Xu, M. Hirai, Y. Zhou, M. J. Ferguson, R. McDonald, T. Murai, G. He and E. Rivard, *Inorg. Chem.*, **2019**, *58*, 13323 – 13336.
17. C. A. Braun, N. Martinek, Y. Zhou, M. J. Ferguson and E. Rivard, *Dalton Trans.*, **2019**, *48*, 10210–10219.

18. K. Takahashi, S. Shimo, E. Hupf, J. Ochiai, C. A. Braun, W. Torres Delgado, L. Xu, G. He, E. Rivard and N. Iwasawa, *Chem. Eur. J.*, **2019**, *25*, 8479–8483.
19. K. Takimiya, Y. Kunugi, Y. Konda, N. Niihara and T. Otsubo, *J. Am. Chem. Soc.*, **2004**, *126*, 5084–5085.
20. N. Nagahora, S. Yahata, S. Goto, K. Shioji and K. Okuma, *J. Org. Chem.*, **2018**, *83*, 1969–1975.
21. M. Kaur, D. S. Yang, J. Shin, T. W. Lee, K. Choi, M. J. Cho and D. H. Choi, *Chem. Commun.*, **2013**, *49*, 5495–5497.
22. M. Kaur, D. H. Lee, D. S. Yang, H. A. Um, M. J. Cho, J. S. Kang and D. H. Choi, *Chem. Commun.*, **2014**, *50*, 14394–14396.
23. M. Al-Hashimi, Y. Han, J. Smith, H. S. Bazzi, S. Y. A. Alqaradawi, S. E. Watkins, T. D. Anthopoulos and M. Heeney, *Chem. Sci.*, **2016**, *7*, 1093–1099.
24. T. Oyama, Y. S. Yang, K. Matsuo and T. Yasuda, *Chem. Commun.*, **2017**, *53*, 3814–3817.
25. T. Kinzel, Y. Zhang and S. Buchwald, *J. Am. Chem. Soc.*, **2010**, *132*, 14073–14075.
26. P. M. S. Monk, *The Viologens: Physicochemical Properties, Synthesis, and Application of the Salt of 4,4'-Bipyridine*; Wiley: New York, **1998**.
27. J. Ding, C. Zheng, L. Wang, C. Lu, B. Zhang, Y. Chen, M. Li, G. Zhai and X. Zhuang, *J. Mater. Chem. A*, **2019**, *7*, 23337–23360.
28. K. Takahashi, T. Nihira, K. Akiyama, Y. Ikegami and E. Fukuyo, *J. Chem. Soc., Chem. Commun.*, **1992**, 620–622.

29. S. T. J. Ryan, R. M. Young, J. J. Henkelis, N. Hafezi, N. A. Vermeulen, A. Hennig, E. J. Dale, Y. Wu, M. D. Krzyaniak, A. Fox, W. M. Nau, M. R. Wasielewski, J. F. Stoddart and O. A. Scherman, *J. Am. Chem. Soc.*, **2015**, *137*, 15299–15307.
30. G. Li, L. Xu, W. Zhang, K. Zhou, Y. Ding, F. Liu, X. He and G. He, *Angew. Chem. Int. Ed.*, **2018**, *57*, 4897–4901.
31. Q. Zhao, C. Huanga and F. Li, *Chem. Soc. Rev.*, **2011**, *40*, 2508–2524.
32. Q. Zhao and J. Z. Sun, *J. Mater. Chem. C*, **2016**, *4*, 10588–10609.
33. S. K. Mellerup and S. Wang, *Chem. Soc. Rev.*, **2019**, *48*, 3537–3549.
34. L. Ji, S. Griesbeck and T. B. Marder, *Chem. Sci.*, **2017**, *8*, 846–863.
35. Y. Ren and F. Jäkle, *Dalton Trans.*, **2016**, *45*, 13996–14007.
36. J. Huo, H. Wang, S. Li, H. Shi, Y. Tang and B. Z. Tang, *Chem. Rec.*, **2020**, *20*, 556–569.
37. B. He, W. Luo, S. Hu, B. Chen, S. Zhen, H. Nie, Z. Zhao and B. Z. Tang, *J. Mater. Chem. C*, **2017**, *5*, 12553–12560.
38. A. K. Flatt, S. M. Dirk, J. C. Henderson, D. E. Shen, J. Su, M. A. Reed and J. M. Tour, *Tetrahedron*, **2003**, *59*, 8555–8570.
39. P. Wei, J. X. Zhang, Z. Zhao, Y. Chen, X. He, M. Chen, J. Gong, H. H. Y. Sung, I. D. Williams, J. W. Y. Lam and B. Z. Tang, *J. Am. Chem. Soc.*, **2018**, *140*, 1966–1975.
40. G. Campillo-Alvarado, K. P. D’mello, D. C. Swenson, S. V. Santhana Mariappan, H. Höpfl, H. Morales-Rojas and L. R. MacGillivray, *Angew. Chem. Int. Ed.*, **2019**, *58*, 5413–5416.

41. M. Mantina, A. C. Chamberlin, R. Valero, C. J. Cramer and D. G. Truhlar, *J. Phys. Chem. A*, **2009**, *113*, 5806–5812.
42. J. D. McCullough, *Inorg. Chem.*, **1975**, *14*, 1142–1146.
43. W.-L. Jia, D.-R. Bai, T. McCormick, Q.-D. Liu, M. Motala, R.-Y. Wang, C. Seward, Y. Tao and S. Wang, *Chem. Eur. J.*, **2004**, *10*, 994–1006.
44. S.-B. Zhao, P. Wucher, Z. M. Hudson, T. M. McCormick, X.-Y. Liu, S. Wang, X.-D. Feng and Z.-H. Lu, *Organometallics*, **2008**, *27*, 6446–6456.
45. P. R. Bevington, *IBM J. Res. Dev.*, **2010**, *13*, 119–125.
46. J. Durbin and G. S. Watson, *Biometrika*, **1951**, *38*, 159–177.
47. D. V. O'Connor and D. Phillips, *Time Correlated Single Photon Counting* (Academic Press, New York, **1984**).
48. H. Hope, *Prog. Inorg. Chem.*, **1994**, *41*, 1–19.
49. R. H. Blessing, *Acta Crystallogr. A.*, **1995**, *51*, 33–38.
50. G. M. Sheldrick, *Acta Crystallogr. A.*, **2015**, *71*, 3–8.
51. G. M. Sheldrick, *Acta Crystallogr. C.*, **2015**, *71*, 3–8.
52. M. J. Frisch, G. W. Trucks, H. B. Schlegel, G. E. Scuseria, M. A. Robb, J. R. Cheeseman, G. Scalmani, V. Barone, G. A. Petersson, H. Nakatsuji, X. Li, M. Caricato, A. V. Marenich, J. Bloino, B. G. Janesko, R. Gomperts, B. Mennucci, H. P. Hratchian, J. V. Ortiz, A. F. Izmaylov, J. L. Sonnenberg, D. Williams-Young, F. Ding, F. Lipparini, F. Egidi, J. Goings, B. Peng, A. Petrone, T. Henderson, D. Ranasinghe, V. G. Zakrzewski, J. Gao, N. Rega, G. Zheng, W. Liang, M. Hada, M. Ehara, K. Toyota, R. Fukuda, J. Hasegawa, M. Ishida, T. Nakajima, Y. Honda, O.

- Kitao, H. Nakai, T. Vreven, K. Throssell, J. A. Montgomery, Jr., J. E. Peralta, F. Ogliaro, M. J. Bearpark, J. J. Heyd, E. N. Brothers, K. N. Kudin, V. N. Staroverov, T. A. Keith, R. Kobayashi, J. Normand, K. Raghavachari, A. P. Rendell, J. C. Burant, S. S. Iyengar, J. Tomasi, M. Cossi, J. M. Millam, M. Klene, C. Adamo, R. Cammi, J. W. Ochterski, R. L. Martin, K. Morokuma, O. Farkas, J. B. Foresman and D. J. Fox, *Gaussian 16, Revision A.03*, Gaussian, Inc., Wallingford CT, **2016**.
53. A. D. Becke, *J. Chem. Phys.*, **1993**, *98*, 5648–5652.
54. C. Lee, W. Yang and R. G. Parr, *Phys. Rev. B*, **1988**, *37*, 785–789.
55. T. H. Dunning, Jr., *J. Chem. Phys.*, **1989**, *90*, 1007–1023.
56. K. A. Peterson, D. Figgen, E. Goll, H. Stoll and M. Dolg, *J. Chem. Phys.*, **2003**, *119*, 11113–11123.
57. D. Feller, *J. Comput. Chem.*, **1996**, *17*, 1571–1586.
58. K. L. Schuchardt, B. T. Didier, T. Elsethagen, L. Sun, V. Gurumoorthi, J. Chase, J. Li and T. L. Windus, *J. Chem. Inf. Model.*, **2004**, *47*, 1045–1052.
59. Procedure for generating computed UV-vis spectra: <http://gaussian.com/uvvisplot/>
60. W. Humphrey, A. Dalke and K. Schulten, *J. Mol. Graph.*, **1996**, *14*, 33–38.
- Chapter 5:**
1. T. Chivers and R. S. Laitinen, *Chem. Soc. Rev.*, **2015**, *44*, 1725–1739.
2. E. Rivard, *Chem. Lett.*, **2015**, *44*, 730–736.
3. E. I. Carrera and D. S. Seferos, *Macromolecules*, **2015**, *48*, 297–308.
4. M. Pittelkow, T. K. Reenberg, K. T. Nielsen, M. J. Magnussen, T. I. Sølling, F. C. Krebs and J. B. Christensen, *Angew. Chem. Int. Ed.*, **2006**, *45*, 5666–5670.



5. A. Patra, Y. H. Wijsboom, G. Leitus and M. Bendikov, *Org. Lett.*, **2009**, *11*, 1487–1490.
6. M. Jiang, J. Guo, B. Liu, Q. Tan and B. Xu, *Org. Lett.*, **2019**, *21*, 8328–8333.
7. L. Yang, W. Gu, L. Lv, Y. Chen, Y. Yang, P. Ye, J. Wu, L. Hong, A. Peng, and H. Huang, *Angew. Chem. Int. Ed.*, **2018**, *57*, 1096–1102.
8. S. Ye, L. Janasz, W. Zajaczkowski, J. G. Manion, A. Mondal, T. Marszalek, D. Andrienko, K. Müllen, W. Pisula and D. S. Seferos, *Macromol. Rapid Commun.*, **2019**, *40*, 1800596.
9. W. H. Lee, S. K. Lee, W. S. Shin, S. J. Moon and I. N. Kang, *J. Polym. Sci. Part A*, **2013**, *51*, 2753–2758.
10. G. He, L. Kang, W. Torres Delgado, O. Shynkaruk, M. J. Ferguson, R. McDonald and E. Rivard, *J. Am. Chem. Soc.*, **2013**, *135*, 5360–5363.
11. Y. S. Park, Q. Wu, C. Y. Nam and R. B. Grubbs, *Angew. Chem. Int. Ed.*, **2014**, *53*, 10691–10695.
12. E. H. Jung, S. Bae, T. W. Yoo and W. H. Jo, *Polym. Chem.*, **2014**, *5*, 6545–6550.
13. R. S. Ashraf, I. Meager, M. Nikolka, M. Kirkus, M. Planells, B. C. Schroeder, S. Holliday, M. Hurhangee, C. B. Nielsen, H. Siringhaus, and I. McCulloch, *J. Am. Chem. Soc.*, **2015**, *137*, 1314–1321.
14. A. A. Jahnke, B. Djukic, T. M. McCormick, E. Buchaca Domingo, C. Hellmann, Y. Lee and D. S. Seferos, *J. Am. Chem. Soc.*, **2013**, *135*, 951–954.

15. J. G. Manion, S. Ye, A. H. Proppe, A. W. Laramée, G. R. Mckeown, E. L. Kynaston, S. O. Kelley, E. H. Sargent and D. S. Seferos, *ACS Appl. Energy Mater.*, **2018**, *1*, 5033–5042.
16. W. Xing, P. Ye, J. Lu, X. Wu, Y. Chen, T. Zhu, A. Peng and H. Huang, *J. Power Sources*, **2018**, *401*, 13–19.
17. G. He, W. Torres Delgado, D. J. Schatz, C. Merten, A. Mohammadpour, L. Mayr, M. J. Ferguson, R. McDonald, A. Brown, K. Shankar and E. Rivard, *Angew. Chem. Int. Ed.*, **2014**, *53*, 4587–4591.
18. G. He, B. D. Wiltshire, P. Choi, A. Savin, S. Sun, A. Mohammadpour, M. J. Ferguson, R. McDonald, S. Farsinezhad, A. Brown, K. Shankar and E. Rivard, *Chem. Commun.*, **2015**, *51*, 5444–5447.
19. A. K. Mahrok, E. I. Carrera, A. J. Tilley, S. Ye and D. S. Seferos, *Chem. Commun.*, **2015**, *51*, 5475–5478.
20. N. Nagahora, S. Yahata, S. Goto, K. Shioji and K. Okuma, *J. Org. Chem.*, **2018**, *83*, 1969–1975.
21. W. Torres Delgado, C. A. Braun, M. P. Boone, O. Shynkaruk, Y. Qi, R. McDonald, M. J. Ferguson, P. Data, S. K.C. Almeida, I. De Aguiar, G. L. C. De Souza, A. Brown, G. He and E. Rivard, *ACS Appl. Mater. Interfaces*, **2018**, *10*, 12124–12134.
22. K. Takahashi, S. Shimo, E. Hupf, J. Ochiai, C. A. Braun, W. Torres Delgado, L. Xu, G. He, E. Rivard and N. Iwasawa, *Chem. Eur. J.*, **2019**, *25*, 8479–8483.
23. K. Takimiya, Y. Kunugi, Y. Konda, N. Niihara and T. Otsubo, *J. Am. Chem. Soc.*, **2004**, *126*, 5084–5085.

24. M. Kaur, D. S. Yang, J. Shin, T. W. Lee, K. Choi, M. J. Cho and D. H. Choi, *Chem. Commun.*, **2013**, *49*, 5495–5497.
25. M. Kaur, D. H. Lee, D. S. Yang, H. A. Um, M. J. Cho, J. S. Kang and D. H. Choi, *Chem. Commun.*, **2014**, *50*, 14394–14396.
26. M. Al-Hashimi, Y. Han, J. Smith, H. S. Bazzi, S. Y. A. Alqaradawi, S. E. Watkins, T. D. Anthopoulos and M. Heeney, *Chem. Sci.*, **2016**, *7*, 1093–1099.
27. T. Oyama, Y. S. Yang, K. Matsuo and T. Yasuda, *Chem. Commun.*, **2017**, *53*, 3814–3817.
28. T. M. McCormick, E. I. Carrera, T. B. Schon and D. S. Seferos, *Chem. Commun.*, **2013**, *49*, 11182–11184.
29. E. I. Carrera and D. S. Seferos, *Organometallics*, **2017**, *36*, 2612–2621.
30. G. E. Garrett, E. I. Carrera, D. S. Seferos and M. S. Taylor, *Chem. Commun.*, **2016**, *52*, 9881–9884.
31. R. I. Sugimoto, K. Yoshino, S. Inoue and K. Tsukagoshi, *Jpn. J. Appl. Phys.*, **1985**, *24*, L425–L427.
32. S. Inoue, T. Jigami, H. Nozoe, T. Otsubo and F. Ogura, *Tetrahedron Lett.*, **1994**, *35*, 8009–8012.
33. B. T. Luppi, R. McDonald, M. J. Ferguson, L. Sang and E. Rivard, *Chem. Commun.*, **2019**, *55*, 14218–14221.
34. A. Alka, V. S. Shetti and M. Ravikanth, *Dalton Trans.*, **2019**, *48*, 4444–4459.
35. S. Wang, X. Li, X. Hou, Y. Sun and X. Shao, *Chem. Commun.*, **2016**, *52*, 14486–14489.

36. B. C. Schroeder, C. B. Nielsen, Y. J. Kim, J. Smith, Z. Huang, J. Durrant, S. E. Watkins, K. Song, T. D. Anthopoulos, and I. McCulloch, *Chem. Mater.*, **2011**, *23*, 4025–4031.
37. X. Guo, S. Wang, V. Enkelmann, M. Baumgarten, and K. Müllen, *Org. Lett.*, **2011**, *13*, 6062–6065.
38. Y. Matano, T. Miyajima, T. Fukushima, H. Kaji, Y. Kimura and H. Imahori, *Chem. Eur. J.*, **2008**, *14*, 8102–8115.
39. T. Miyajima, Y. Matano and H. Imahori, *Eur. J. Org. Chem.*, **2008**, 255–259.
40. S. Y. Chen, Y. C. Pao, S. K. Sahoo, W. C. Huang, Y. Y. Lai and Y. J. Cheng, *Chem. Commun.*, **2018**, *54*, 1517–1520.
41. C.-Y. Kuo, Y.-C. Huang, C.-Y. Hsiow, Y.-W. Yang, C.-I. Huang, S.-P. Rwei, H.-L. Wang and L. Wang, *Macromolecules*, **2013**, *46*, 5985–5997.
42. P. M. Beaujuge, H. N. Tsao, M. R. Hansen, C. M. Amb, C. Risko, J. Subbiah, K. R. Choudhury, A. Mavrinskiy, W. Pisula, J. L. Bredas, F. So, K. Müllen and J. R. Reynolds, *J. Am. Chem. Soc.*, **2012**, *134*, 8944–8957.
43. J. A. Letizia, M. R. Salata, C. M. Tribout, A. Facchetti, M. A. Ratner and T. J. Marks, *J. Am. Chem. Soc.*, **2008**, *130*, 9679–9694.
44. B. Djukic, P. K. Poddutoori, P. A. Dube, T. Seda, H. A. Jenkins and M. T. Lemaire, *Inorg. Chem.*, **2009**, *48*, 6109–6116.
45. M. Oba, M. Endo, K. Nishiyama, A. Ouchi and W. Ando, *Chem. Commun.*, **2004**, 1672–1673.

46. M. Oba, Y. Okada, M. Endo, K. Tanaka, K. Nishiyama, S. Shimada and W. Ando, *Inorg. Chem.*, **2010**, *49*, 10680–10686.
47. P. Serguievski and M. R. Detty, *Organometallics*, **1997**, *16*, 4386–4391.
48. A. A. Jahnke, G. W. Howe and D. S. Seferos, *Angew. Chem. Int. Ed.*, **2010**, *49*, 10140–10144.
49. M. Mantina, A. C. Chamberlin, R. Valero, C. J. Cramer and D. G. Truhlar, *J. Phys. Chem. A*, **2009**, *113*, 5806–5812.
50. H. A. Lin, K. Kato, Y. Segawa, L. T. Scott and K. Itami, *Chem. Sci.*, **2019**, *10*, 2326–2330.
51. T. Tsukamoto and G. Dong, *Angew. Chem. Int. Ed.*, **2020**, DOI:10.1002/anie.202004719.
52. A. Kiriya, V. Senkovskyy and M. Sommer, *Macromol. Rapid Commun.*, **2011**, *32*, 1503–1517.
53. S. Ye, M. Steube, E. I. Carrera and D. S. Seferos, *Macromolecules*, **2016**, *49*, 1704–1711.
54. S. Ye, S. M. Foster, A. A. Pollit, S. Cheng and D. S. Seferos, *Chem. Sci.*, **2019**, *10*, 2075–2080.
55. E. A. Standley, S. J. Smith, P. Müller and T. F. Jamison, *Organometallics*, **2014**, *33*, 2012–2018.
56. J. L. Dutton, G. J. Farrar, M. J. Sgro, T. L. Battista and P. J. Ragona, *Chem. Eur. J.*, **2009**, *15*, 10263–10271.

57. J. Linshoef, E. J. Baum, A. Hussain, P. J. Gates, C. Näther, and A. Staubitz, *Angew. Chem. Int. Ed.*, **2014**, *53*, 12916–12920.
58. A. F. Burchat, J. M. Chong and N. Nielsen, *J. Organomet. Chem.*, **1997**, *542*, 281–283.
59. T. R. Hoye, B. M. Eklov and M. Voloshin, *Org. Lett.*, **2004**, *6*, 2567–2570.
60. J. Durbin and G. S. Watson, *Biometrika*, **1951**, *38*, 159–177.
61. D. V. O'Connor and D. Phillips, *Time Correlated Single Photon Counting*; Academic Press: New York, **1984**.
62. H. Hope, *Prog. Inorg. Chem.*, **1994**, *41*, 1–19.
63. R. H. Blessing, *Acta Crystallogr. A*, **1995**, *51*, 33–38.
64. G. M. Sheldrick, *Acta Crystallogr. A*, **2015**, *71*, 3–8.
65. G. M. Sheldrick, *Acta Crystallogr. C*, **2015**, *71*, 3–8.
66. M. J. Frisch, G. W. Trucks, H. B. Schlegel, G. E. Scuseria, M. A. Robb, J. R. Cheeseman, G. Scalmani, V. Barone, G. A. Petersson, H. Nakatsuji, X. Li, M. Caricato, A. V. Marenich, J. Bloino, B. G. Janesko, R. Gomperts, B. Mennucci, H. P. Hratchian, J. V. Ortiz, A. F. Izmaylov, J. L. Sonnenberg, D. Williams-Young, F. Ding, F. Lipparini, F. Egidi, J. Goings, B. Peng, A. Petrone, T. Henderson, D. Ranasinghe, V. G. Zakrzewski, J. Gao, N. Rega, G. Zheng, W. Liang, M. Hada, M. Ehara, K. Toyota, R. Fukuda, J. Hasegawa, M. Ishida, T. Nakajima, Y. Honda, O. Kitao, H. Nakai, T. Vreven, K. Throssell, J. A. Montgomery, Jr., J. E. Peralta, F. Ogliaro, M. J. Bearpark, J. J. Heyd, E. N. Brothers, K. N. Kudin, V. N. Staroverov, T. A. Keith, R. Kobayashi, J. Normand, K. Raghavachari, A. P. Rendell, J. C. Burant,

- S. S. Iyengar, J. Tomasi, M. Cossi, J. M. Millam, M. Klene, C. Adamo, R. Cammi, J. W. Ochterski, R. L. Martin, K. Morokuma, O. Farkas, J. B. Foresman and D. J. Fox, *Gaussian 16, Revision A.03*, Gaussian, Inc., Wallingford CT, **2016**.
67. A. D. Becke, *J. Chem. Phys.*, **1993**, *98*, 5648–5652.
68. C. Lee, W. Yang and R. G. Parr, *Phys. Rev. B*, **1988**, *37*, 785–789.
69. T. H. Dunning, Jr. *J. Chem. Phys.*, **1989**, *90*, 1007–1023.
70. K. A. Peterson, D. Figgen, E. Goll, H. Stoll and M. Dolg, *J. Chem. Phys.*, **2003**, *119*, 11113–11123.
71. D. Feller, *J. Comput. Chem.*, **1996**, *17*, 1571–1586.
72. K. L. Schuchardt, B. T. Didier, T. Elsethagen, L. Sun, V. Gurumoorthi, J. Chase, J. Li and T. L. Windus, *J. Chem. Inf. Model.*, **2004**, *47*, 1045–1052.
73. Procedure for generating computed UV-vis spectra: <http://gaussian.com/uvvisplot/>
74. W. Humphrey, A. Dalke and K. Schulten, *J. Mol. Graph.*, **1996**, *14*, 33–38.
- Chapter 6:**
1. G. He, W. Torres Delgado, D. J. Schatz, C. Merten, A. Mohammadpour, L. Mayr, M. J. Ferguson, R. McDonald, A. Brown, K. Shankar and E. Rivard, *Angew. Chem. Int. Ed.*, **2014**, *53*, 4587–4591.
2. S. K. Mellerup and S. Wang, *Chem. Soc. Rev.*, **2019**, *48*, 3537–3549.
3. T. Matsumoto, H. Takamine, K. Tanaka and Y. Chujo, *Mater. Chem. Front.*, **2017**, *1*, 2368–2375.
4. M. C. Gather, A. Köhnen and K. Meerholz, *Adv. Mater.*, **2011**, *23*, 233–248.
5. M. Shang, C. Li and J. Lin, *Chem. Soc. Rev.*, **2014**, *43*, 1372–1386.

6. Z. He, W. Zhao, J. W.Y. Lam, Q. Peng, H. Ma, G. Liang, Z. Shuai and B. Z. Tang, *Nat. Commun.*, **2017**, *8*, 416.
7. G. Dennler, M. C. Scharber and C. J. Brabec, *Adv. Mater.*, **2009**, *21*, 1323–1338.
8. L. Yang, W. Gu, L. Lv, Y. Chen, Y. Yang, P. Ye, J. Wu, L. Hong, A. Peng and H. Huang, *Angew. Chem. Int. Ed.*, **2018**, *57*, 1096–1102.
9. J. G. Manion, S. Ye, A. H. Proppe, A. W. Laramée, G. R. McKeown, E. L. Kynaston, S. O. Kelley, E. H. Sargent and D. S. Seferos, *ACS Appl. Energy Mater.*, **2018**, *1*, 5033–5042.
10. E. H. Jung, S. Bae, T. W. Yoo and W. H. Jo, *Polym. Chem.*, **2014**, *5*, 6545–6550.
11. R. S. Ashraf, I. Meager, M. Nikolka, M. Kirkus, M. Planells, B. C. Schroeder, S. Holliday, M. Hurhangee, C. B. Nielsen, H. Sirringhaus and I. McCulloch, *J. Am. Chem. Soc.*, **2015**, *137*, 1314–1321.
12. C. J. Brabec, S. Gowrisanker, J. J. M. Halls, D. Laird, S. Jia and S. P. Williams, *Adv. Mater.*, **2010**, *22*, 3839–3856.
13. G. Li, R. Zhu and Y. Yang, *Nat. Photonics*, **2012**, *6*, 153–161.
14. J. Hou, O. Inganäs, R. H. Friend and F. Gao, *Nat. Mater.*, **2018**, *17*, 119–128.
15. C. Yan, S. Barlow, Z. Wang, H. Yan, A. K.-Y. Jen, S. R. Marder and X. Zhan, *Nat. Rev. Mater.*, **2018**, *3*, 18003.
16. P. Cheng, G. Li, X. Zhan and Y. Yang, *Nat. Photonics*, **2018**, *12*, 131–142.
17. L. Yang, W. Gu, L. Lv, Y. Chen, Y. Yang, P. Ye, J. Wu, L. Hong, A. Peng and H. Huang, *Angew. Chem. Int. Ed.*, **2018**, *57*, 1096–1102.